

Applications of Spatially-Resolved Hybrid Hydrogels

Phillip Robert Anthony Chivers

Doctor of Philosophy

University of York

Chemistry

January 2019

Abstract

Low-molecular-weight gelators (LMWGs) form gel networks through non-covalent interactions. Materials formed from these small molecules are often responsive to external stimuli, making them attractive for high-tech applications. This responsiveness often comes at the expense of durability. In contrast, polymer gelators form crosslinked networks which are often robust, but unresponsive.

To harness the desirable properties of both classes of material, a robust hybrid hydrogel comprising the LMWG 1,3:2,4-dibenzylidene-D-sorbitol diacylhydrazide (DBS-CONH₂) and a photo-inducible PG (poly(ethylene glycol)dimethacrylate), PEGDM) was developed. PEGDM was crosslinked within a supporting DBS-CONH₂ gel matrix by photoirradiation. Spectroscopic studies indicated that non-covalent interactions between the LMWG and PG networks subtly modified the material properties (e.g. gel stiffness). The use of a printed mask during photoirradiation enabled spatial control of PEGDM crosslinking.

We demonstrated the application of these hybrid gels as active drug release matrices. Specific interactions between naproxen (NPX) and the DBS-CONH₂ nanofibres mediated pH-dependent release. DBS-CONH₂ was found to largely retain its responsiveness within the hybrid gel, which demonstrated a good degree of pH-dependent NPX release. A photo-patterned hybrid gel preferentially delivered NPX into a compartment at pH 7 compared to one at pH 2.8, illustrating potential for targeted drug release.

The applications of photo-patterned hybrid gels as enzyme bioreactors were explored next. Alkaline phosphatase retained its activity within hybrid gels which behaved as a semi-permeable membrane - entrapping the enzyme but allowing diffusion of reactants and products. First generation reactors showed good reaction conversion over relatively short timescales.

Cytocompatibility studies indicated that hybrid hydrogels were compatible with mesenchymal stem cells, supporting cell growth over one month. Gel matrix-regulated stem cell differentiation was apparent on the stiffest hybrid gels tested. Cells cultured on these materials exhibited elevated alkaline phosphatase content and calcium deposition, indicators of osteoblast formation. Preliminary studies suggest that spatially-resolved hybrid gels induce spatially-resolved stem cell morphology.

Table of Contents

Abstract	2
List of Figures	9
List of Tables	25
List of Schemes	26
List of Accompanying Material	27
Acknowledgements	28
Declaration	29
1 Introduction	30
1.1 Low-Molecular-Weight Gels.....	30
1.2 Dual Network ‘Hybrid Gels’	33
1.2.1 Hybrid organogels.....	34
1.2.2 Hybrid hydrogels.....	35
1.3 Spatial Control of Low-Molecular-Weight Gel Structure	41
1.3.1 Photo-patterned LMWGs	42
1.3.2 3D-printed LMWGs	52
1.3.3 Diffusion-controlled LMWGs	54
1.3.4 Surface-patterned LMWGs	56
1.3.5 Self-healing LMWGs	58
1.4 Project Aims	60
1.4.1 Drug release.....	60
1.4.2 Enzyme reactivity.....	61
1.4.3 Stem cell differentiation.....	61
2 Fabrication and Characterisation of Spatially-Resolved Hybrid Hydrogels	62
2.1 Introduction.....	62
2.1.1 DBS gels	62
2.1.2 PEG gels	64
2.2 Chapter aims	65
2.3 Synthesis of Gelators	66
2.3.1 Synthesis of 1,3:2,4-dibenzylidene-D-sorbitol- <i>p,p'</i> -diacyl hydrazide (DBS-CONHNH ₂)	66
2.3.2 Synthesis of poly(ethylene glycol) dimethacrylate	67
2.4 Preparation of Hydrogels	67
2.4.1 Preparation of DBS-CONHNH ₂ hydrogels and initial characterisation	67
2.4.2 Preparation of PEGDM hydrogels	68

2.4.3	Preparation of DBS-CONHNH ₂ /PEGDM hybrid hydrogels.....	69
2.5	Characterisation of Dual-Network Hydrogels	70
2.5.1	Quantification of hybrid hydrogel PEGDM content by NMR.....	70
2.5.2	T _{gel} studies.....	73
2.5.3	Rheological studies	73
2.5.4	SEM imaging	80
2.5.5	IR spectroscopy.....	81
2.6	Photo-patterning of DBS-CONHNH ₂ /PEGDM Hybrid Gels	83
2.7	Conclusions and Future Work	89
3	Hybrid and Multidomain Hydrogels for Controlled Drug Release	90
3.1	Introduction – LMW hydrogels for controlled drug release	90
3.1.1	Physical encapsulation	91
3.1.2	Covalent conjugation	94
3.1.3	Gel-forming drugs	96
3.2	Chapter aims	98
3.3	Preparation of NPX-loaded hydrogels	101
3.4	Characterisation of NPX-loaded hydrogels	103
3.4.1	T _{gel} studies.....	103
3.4.2	Rheological studies	104
3.4.3	SEM imaging	108
3.4.4	IR spectroscopy.....	109
3.4.5	NMR study.....	110
3.5	pH controlled NPX release from hydrogels.....	111
3.6	Photo-patterned NPX-loaded hybrid hydrogels.....	119
3.7	Differential NPX release from photo-patterned hybrid gels.....	120
3.8	The influence of network order – reverse hybrid gels.....	122
3.9	Conclusions.....	129
4	Spatially-Resolved Enzyme Bioreactors	131
4.1	Enzyme Bioreactions.....	131
4.1.1	Membrane Bioreactors	132
4.1.2	Enzymatic Reactions in LMW Hydrogels	135
4.2	Chapter Aims.....	138
4.3	Alkaline Phosphatase.....	139
4.4	Gel Permeability	140
4.5	Solution-phase studies.....	145
4.6	ALP-encapsulation and activity	151

4.6.1	Solution-phase	152
4.6.2	DBS-CONHNH ₂ gels.....	153
4.6.3	PEGDM and hybrid gels	155
4.6.4	Enzyme leaching	157
4.6.5	Gel-phase studies.....	159
4.7	Photo-patterned bioreactors	162
4.8	An alternative reactor design – small molecule exclusion.....	170
4.9	Conclusions.....	181
5	Towards Spatially-Programmed Stem Cell Behaviour	183
5.1	Introduction.....	183
5.1.1	Polymer gels for the spatiotemporal control	183
5.1.2	LMW hydrogels for cell growth	186
5.2	Chapter aims	190
5.3	Mesenchymal stem cells.....	191
5.4	MSC compatibility and seeding density.....	192
5.4.1	DBS-CONHNH ₂ hydrogels	193
5.4.2	PEGDM hydrogels	197
5.4.3	Hybrid hydrogels.....	199
5.4.4	Gel swelling.....	202
5.4.5	Cell seeding on larger gels	203
5.4.6	Photoinitiator concentration in cell culture media.....	203
5.5	Matrix-dependent Y201 growth	205
5.6	Quantifying cell growth.....	210
5.7	Oil Red O Adipogenesis Assay	211
5.8	Osteogenesis Assays	214
5.8.1	Alizarin Red S	214
5.8.2	Wnt reporter cells.....	216
5.8.3	Alkaline phosphatase	218
5.9	Photo-patterned gels for spatially-resolved stem cell properties.....	221
5.10	Conclusions.....	223
6	Conclusions and Future Work	225
6.1	Fabrication and characterisation of hybrid hydrogels	225
6.2	Drug delivery	226
6.3	Enzyme bioreactors	227
6.4	Tissue engineering	228
6.5	Summary	228

7	Experimental	230
7.1	General Experimental Methods	230
7.2	Chapter 2	231
7.2.1	Synthetic procedures	231
7.2.2	Preparation of hydrogels	233
7.2.3	Estimation of DBS-CONHNH ₂ gelation percentage	234
7.2.4	Estimation of PEGDM concentration in hybrid gels	234
7.2.5	Preparation of samples for FT-IR analysis	234
7.2.6	Preparation of samples for SEM analysis	234
7.2.7	T _{gel} analysis	235
7.2.8	Rheology sample preparation	235
7.2.9	Rheology methods	236
7.2.10	Photo-patterned hybrid gels	237
7.3	Chapter 3	238
7.3.1	Preparation of NPX-loaded hydrogels	238
7.3.2	NPX-loaded rheology sample preparation	238
7.3.3	Characterisation of NPX-loaded hydrogels	239
7.3.4	NPX encapsulation study	239
7.3.5	NPX release studies	239
7.3.6	Preparation of NPX-loaded photo-patterned hybrid gels	240
7.3.7	Differential release	240
7.3.8	Preparation of reverse hybrid gels	240
7.3.9	Preparation of reverse hybrid rheology samples	241
7.3.10	NPX release study	242
7.4	Chapter 4	242
7.4.1	Preparation of hydrogels in cuvettes	242
7.4.2	Diffusion studies	242
7.4.3	Preparation of enzyme stock solution	243
7.4.4	Solution phase studies	243
7.4.5	DBS-CONHNH ₂ pH determination	244
7.4.6	Qualitative ALP activity tests	244
7.4.7	Enzyme leaching experiments	244
7.4.8	CD spectroscopy	245
7.4.9	Gel-phase ALP activity	245
7.4.10	Substrate/product uptake studies	246
7.4.11	NMR study	246

7.4.12	<i>p</i> NPP diffusion through a hybrid gel ring	246
7.4.13	ALP bioreactor with enzyme immobilised in the hybrid gel ring	246
7.4.14	ALP bioreactor with enzyme free in the outer compartment	247
7.4.15	AP bioreactor with enzyme in the outer compartment	247
7.4.16	Dye diffusion through DBS-CONH ₂ LMW hydrogels.....	248
7.4.17	Dye diffusion through hybrid hydrogels.....	248
7.4.18	Dye diffusion through photo-patterned hybrid hydrogels.....	249
7.4.19	ALP controlled diffusion reactor	250
7.5	Chapter 5.....	250
7.5.1	Preparation of gels in 24-well plates.....	250
7.5.2	Gel sterilisation	251
7.5.3	2D cell culture	252
7.5.4	Optical and fluorescence microscopy	252
7.5.5	Gel swelling test.....	252
7.5.6	PI leaching.....	253
7.5.7	SEM sample preparation	253
7.5.8	Confocal microscopy	253
7.5.9	Cell lysis	254
7.5.10	BCA total protein assay	254
7.5.11	Oil Red O assay.....	254
7.5.12	Alizarin Red S assay	255
7.5.13	Wnt Reporter Assay	256
7.5.14	ALP assay	256
7.5.15	Photo-patterned gels in well plates	256
7.5.16	Spatially-resolved stem cell growth	257
7.5.17	Gradient patterning	257
Appendices	258
Appendix 1:	Characterisation of DBS-CO ₂ Me	258
Appendix 2:	Characterisation of DBS-CONH ₂	259
Appendix 3:	Characterisation of PEGDM.....	261
Appendix 4:	Scanning Electron Micrographs of Hydrogels.....	262
Appendix 5:	IR spectra (all gels are xerogels)	266
Appendix 6:	Representative rheology traces of hydrogels.....	270
	Gels without NPX: Frequency sweeps	270
	DBS-CONH ₂ gels (6 mM) – solvent system test	272
	Crosslinking Density Test (10% hybrid gel)	273

Appendix 7: Photo-patterning resolution test, 20% EtOH gel	273
Appendix 8: Example NMR quantification experiment	274
Appendix 9: UV-vis spectra of ALP solution-phase reactions	275
Appendix 10: 3-month old bioreactors	279
Appendix 11: Acid phosphatase reactor	280
Appendix 12: Diffusion reactor images	281
Appendix 13: Fluorescence microscopy images	284
Appendix 14: Scanning electron micrographs of MSCs cultured on hybrid hydrogels	285
Appendix 15: Optical microscopy images of Alizarin Red S stained samples	286
List of Abbreviations	287
References	292

List of Figures

Figure 1.1: Summary of some characteristic macroscale and nanoscale features of gel-phase materials. Rheologically, gels exhibit solid-like properties and stress-relaxation. The precise macroscale properties of a gel network are determined by the porous nanoscale network from which it is formed. Images adapted from [5].	30
Figure 1.2: Self-assembly of low-molecular weight gelators into a bulk gel-phase material	31
Figure 1.3: Partial gelator structures which may show responsiveness to electromagnetic irradiation (a), changes in pH (b) and enzymatic activity (c).	32
Figure 1.4: Cartoon representation and generalised characteristics of low-molecular weight gels (a), hybrid gels (b) and polymer gels (c).	34
Figure 1.5: Guenet and co-workers' early example of a hybrid organogel. Structures of the OPV LMWG (a), isotactic polystyrene PG (b). AFM image of the hybrid gel formed in <i>cis</i> -decalin (c). Two fibre sizes are evident. The thicker structures are LMWG fibres, the thin fibres are the PG network. A thermo-reversible colour change was seen for the hybrid gels due to assembly and disassembly of the LMWG fibres. Adapted from [38].	35
Figure 1.6: The method of assembly can have a significant impact on hybrid gel structure and property. He and Denkbaş used the same two components – the LMWG Fmoc-Phe-Phe (a) and an alginate PG (b) to yield materials with different nanoscale structures. Using a single Ca ²⁺ source to trigger both LMWG and PG assembly results in the formation of narrower Fmoc-Phe-Phe nanofibres (c) compared to when this network is assembled prior to alginate crosslinking (d). Scale bars = 1 µm. SEM images are from [43] and [44].	36
Figure 1.7: The combination of a tetrapeptide LMWG (a) and a PPV PG network (b) resulted in fluorescence enhancement (c) and sustained methylene blue release (d) compared to the individual gel networks. Adapted from [51].	38
Figure 1.8: A single material with multiple applications. The orthogonally assembled hybrid gel of DBS-CONHNH ₂ (a) and agarose (b) has been used for the extraction of precious metals, palladium-catalysed Suzuki couplings and the growth of mouse fibroblasts. Images adapted from [55], [56] and [56], [57] and [58].	39
Figure 1.9: Watanabe's two-component LMWG network based on octylaldonamide (a) enhances the mechanical properties of an acrylamide (b) network which had been crosslinked by methylenbisacrylamide (c). Schematic illustration of the templating of acrylamide PG network within a pre-formed LMW hydrogel (d). Adapted from [60].	40
Figure 1.10: Eastoe's gemini surfactant (a) undergoes photo-dimerisation on UV exposure, resulting in gel disassembly with spatial control (b). ⁷⁰ Adapted from [70].	42

Figure 1.11: Cooling the isotropic LC/LMWG liquid under UV irradiation results in the formation of an anisotropic gel network (a). In the absence of UV light an isotropic gel network is formed (b). Micro-patterned LC gels were visualised by polarised light microscopy (c).⁷² Adapted from [72]. 43

Figure 1.12: Light-driven dynamic pattern formation.⁷³ (a) Open (left) and closed (right) forms of dithienylcyclopentene can be switched between through exposure to specific wavelength of light. Micrographs (b-d) of spatially-controlled gel formation (magnification $\times 20$). All were exposed to a homogeneous visible light source throughout the experiment. A horizontal grating pattern (a) was formed after 10 min UV exposure. An additional diagonal pattern was then formed after rotation and a further 10 min exposure (b). After 90 min UV diagonal UV exposure the horizontal pattern has been ‘erased’ whilst the diagonal patterning remains (c). Adapted from [73]. 43

Figure 1.13: Photoacid-catalysed formation of a tris-hydrazone gelator from hydrazide and aldehyde starting materials (a). Spatially-controlled gel formation on the microscale (b). Photomask design (i) and fluorescent microscopy images (ii and iii). Scale bar (ii) = 500 μm . Scale bar (iii) = 100 μm . Adapted from [74]. 44

Figure 1.14: Fumaric acid gelator reported by Matsumoto et. al. (a). Directional control of *E. coli* spreading through spatially-resolved gel breakdown (b). Dark spots are *E. coli*, arrows indicate direction of motion. Scale bar = 100 μm . Adapted from [76]. 45

Figure 1.15: An azobenzene-based gelator (a) can undergo spatially-resolved reversible gel-sol transitions (b). UV-promoted *trans-cis* isomerisation breaks down the gel network to form a pattern. This pattern was erased using visible light, then re-written in another write-read-erase cycle. Adapted from [77]. 46

Figure 1.16: Structures of the perylene bisimide gelator (a) and photo-degradable macrocycle (b). Spatial resolution of gel formation could be achieved in dioxane (c) but not in water (d). Adapted from [78]. 47

Figure 1.17: Structure of Feringa’s dithienylethene gelator in the open form (a). Gel morphology observed by TEM is significantly different for untreated (b) and UV-exposed (c) gels (scale bar = 1 μm). Spatial control of the gel-gel morphology transition was achieved using a photomask (d). This was easily observable due to a change in gel absorbance properties on irradiation. Adapted from [79]. 48

Figure 1.18: Structure of PBI-valine gelator (a). Photo-patterned gel (b). Exposure to UV light reduces the distance between gelator molecules in the nanofibres, resulting in increased mechanical strength (c) in the irradiated (left) vs non-irradiated (right) regions. Adapted from [80]. 48

Figure 1.19: Structures of calixarene (a) and stilbene (b) gelator precursors. The calixarene gel's fluorescent properties are modified by UV light (c). Prior to photo-patterning, the gel is fluorescent (i). A mask is applied to the gel (ii) and in the exposed areas fluorescence is lost over time (iii and iv). Adapted from [81]. 49

Figure 1.20: Structures of the *trans*-stilbene (a) and dipeptide (b) gelators used by Adams and co-workers. The spatially-resolved disassembly of the dipeptide network could be visualised using a low-powered UV lamp (c). The star shape represents the irradiated gel. Adapted from [82]. 50

Figure 1.21: Structures of the self-sorting hydrazide (a) and acylhydrazone (b) organogelators. Dual-network gels were partially exposed to visible (350-570 nm) light (c) and visualised under natural (green) and UV (blue) light. The irradiated areas appear darker due to loss of fluorescence *via* disassembly of the acylhydrazone network. Adapted from [83]. 50

Figure 1.22: Combination of a sugar-based LMWG (a) with a PG (b) allows photo-patterning of multidomain hybrid hydrogels. The areas exposed to UV light are robust (c) whilst shielded regions are easily broken down. Adapted from [55]. 51

Figure 1.23: Structure of DBS-glycine (a) which, through a sequential acidification, was photo-patterned into a DBS-CO₂H gel with excellent resolution (b). No significant diffusion of protons out of the UV-exposed area (top-half) occurs over several hours (c), indicating sustained pattern integrity over this timescale. Adapted from [84]. 52

Figure 1.24: Dual-enzyme catalysed 3D-printing of a naphthalene-tripeptide gel. LMWG fibres (blue chains) are crosslinked by PEGMA molecules (red chains) to form printed hydrogel matrices (top right). Adapted from [90]. 53

Figure 1.25: Tetra-substituted calix[4]arene (a) form gels in organic solvents. These gels are able to recover their mechanical properties on removal of the applied strain (b). This allows them to be extruded as printed materials (c). Adapted from [91]. 54

Figure 1.26: Fmoc-diphenylalanine, one example of a dipeptide hydrogelator used to illustrate the optimisation of LMWGs for 3D-printing (a). 3D-printed lines (b) and layers (c) were printed. Dyes were added to each line/layer for clarity. Adapted from [92]. 54

Figure 1.27: Spatially-resolved tris-hydrazone gel formation controlled by reaction-diffusion (a). H = tris-hydrazide, A = aldehyde. In a reaction-diffusion configuration, a chemical gradient, in this case of fluorescent aldehyde, could be introduced into the free-standing gels (b). Microscale objects were fabricated using a wet stamping methodology (c). Scale bar (a), (b) = 1 cm. Scale bar (c) = 1 mm. Adapted from [94]. 55

Figure 1.28: Thermolysin catalyses the formation of Fmoc-diphenylalanine from gelator precursors (a). Visualisation of spatially-resolved gel formation using a Congo Red stain under cross-polarised

light (b). Green region represents association of Congo Red with self-assembled β -sheets. Scale bar = 0.3 μ m. Adapted from [97].	57
Figure 1.29: Confocal microscopy images of van Esch's surface-patterned tris-hydrazone gels (a). Yellow regions represent the surface pattern dimensions. Adams' electrochemically-triggered dipeptide hydrogels (b). Top (left) and side-on (b) views. Gel thickness was controlled by the applied current and the patterning time. Adapted from [105] and [106].	58
Figure 1.30: Spontaneous separation of peptide amphiphile and protein pre-gelators occurs on mixing (a). Altering the number of interfaces between the gel and an external surface altered the anisotropic gel structure (b and c). NIH/3T3 mouse fibroblasts were formulated into these cytocompatible materials by 3D printing (d). Adapted from [111].	59
Figure 1.31: Structures of the LMWG (a) and PG (b) used to develop photo-patternable hybrid hydrogels in this thesis.	60
Figure 2.1: Meunier's synthesis of DBS from D-sorbitol and benzaldehyde.	62
Figure 2.2: Structure of 1,3:2,4-di(3,4-dichloro benzylidene)-D-sorbitol studied by Song and co-workers (a). This DBS derivative self-assembled into straight nanofibres in 7:3 DMSO-H ₂ O (b) and helical nanofibres in n-octanol. Adapted from [141].	63
Figure 2.3: PEG diacrylate hydrogels with different polymer chain lengths display different cell viability. Gels with average molecular weight 3,000 Da showed poor cell viability (A and E) whilst a gel formed from PEG diacrylate with average mass 10,000 Da showed good cell survival over the same timeframe. Green cells = live, red cells = dead. Adapted from [171].	65
Figure 2.4: Representative images of inverted hydrogels formed from 6 mM DBS-CONH ₂ (a) and 3% wt/vol PEGDM (b).	69
Figure 2.5: Schematic representation of the hybrid gel fabrication process. A DBS-CONH ₂ hydrogel is formed first <i>via</i> a heat/cool cycle (a). A solution of PEGDM and PI is pipetted on top (b) and left for 3 days for these species to diffuse into the gel (c). The supernatant is removed and the PEGDM photo-polymerised by exposure to UV light (d).	70
Figure 2.6: Representative NMR spectrum of a hybrid gel (10% wt/vol PEGDM, 24 h diffusion), dried and dissolved in DMSO-d ₆ prior to UV exposure. Peaks at 9.80 (DBS-CONH ₂) and 1.93 (PEGDM CH ₃) were used to calculate the percentage PEGDM diffused into the gel.	71
Figure 2.7: Storage (G' , black) and loss (G'' , red) moduli of the different prepared hydrogels in response to varying shear strain at a constant frequency (1 Hz). Rheological traces for: 6 mM DBS-CONH ₂ (a), 8 mM DBS-CONH ₂ (b), 5% PEGDM (c), 10% PEGDM (d), 5% hybrid (e) and 10% hybrid (f). Features of interest are highlighted on the trace of 6mM DBS-CONH ₂ (a). Errors are <i>ca.</i> \pm 10% for all samples.	75

Figure 2.8: Representative rheological trace of 6 mM DBS-CONH₂ in response to varying frequency with features of interest highlighted (a). Storage (G') and loss (G'') moduli of the different prepared hydrogels (b). G' = black circles/bars, G'' = red circles/bars. Errors are *ca.* $\pm 10\%$ for all samples..... 77

Figure 2.9: Storage modulus (G') of the top and bottom halves of a 10% hybrid gel disc (height *ca.* 1 cm) in response to changes in frequency. Red squares = top half, blue circles = bottom half. Error bars are standard deviation, $n = 3$ 78

Figure 2.10: Storage (G' , black) and loss (G'' , red) moduli of the different prepared hydrogels in response to varying temperature at constant shear strain and frequency. Rheological traces for: 6 mM DBS-CONH₂ (a), 7% PEGDM (b), 10% PEGDM (c), 7% hybrid (d) and 10% hybrid (e). Features of interest are highlighted on the trace of 6mM DBS-CONH₂ (a). Errors are *ca.* $\pm 10\%$ for all samples..... 79

Figure 2.11: SEM images of 6 mM DBS-CONH₂ (left), 10% PEGDM (middle) and 10% hybrid (right) gels. Image magnification is given at the left of each row. Scale bars are as follows: 5,000 $\times = 1 \mu\text{m}$, 20,000 $\times = 1 \mu\text{m}$, 50,000 $\times = 100 \text{ nm}$ 81

Figure 2.12: Excerpts from IR spectra of 6 mM DBS-CONH₂ (a) and 10% hybrid (b) gels. Changes in the O-H and N-H peaks of DBS-CONH₂ are observed. 82

Figure 2.13: Gels were prepared in bottomless vials, which could be removed from the glass tray they were adhered to (a). This allowed a glass slide and cardboard 'photomask to be applied to the top of the gel, shielding the centre of the disc from UV exposure for patterning of a gel 'ring'. Side (a) and top (b) views of this system are shown. 84

Figure 2.14: Schematic of the masking procedure to create photo-patterned gels (a). UV light is represented by purple wavy arrows. Masking the exterior of the gel discs during photo-patterning as well as the region desired to remain soft resulting in improved photo-patterning resolution. Samples of 10 mm thickness and exposed to UV light for 20 min yielded the highest resolution multidomain gels (b), comprising a soft centre and a robust exterior. Physical manipulation of the outer edge was possible (c) and this region could be easily separated from the uncured centre. . 84

Figure 2.15: Comparison of 10 mL DBS-CONH₂ gels prepared by heating in H₂O directly (a) and by adding gelator pre-dissolved in DMSO to boiling H₂O..... 86

Figure 2.16: Photo-patterning resolution test. 10% hybrid gel samples were exposed to UV-irradiation for 0.5 h. Non-crosslinked regions were washed away with a low-pressure water stream to reveal the patterned regions. As seen from the side (a) and above (b). Mask 'gap' diameters are (from top to bottom) 2 mm, 3 mm, 4 mm and 5 mm respectively. 87

Figure 2.17: Gels were photo-patterned using a mask with a ring geometry printed on (a). The thickness of the photomask has a profound impact on the patterning efficacy. Masks 1 layer thick showed very poor patterning resolution (b), but this was much improved with a 4 layer thick mask (c). 88

Figure 3.1: Cartoon representation of strategies for encapsulation of drugs within a LMWG matrix. Physical encapsulation (a), covalent conjugation to LMWGs (b) and self-assembly of drugs (c)... 90

Figure 3.2: Structures of the *para*- (a) and *meta*- (b) bis-imidazolium gelators reported by Limon et. al. Regions of each gelator which interact with ibuprofen and indomethacin are highlighted in red. Release profiles of physically encapsulated ibuprofen (c) and indomethacin (d) from bis-imidazolium amphiphile hydrogels. Figure adapted from [213]. 92

Figure 3.3: Reversible light-induced *trans-cis* isomerisation of an azobenzene pentapeptide gelator (a). Exposure to UV light results in gel breakdown (b). Rapid release of Vitamin B₁₂ (c) is seen for samples exposed to UV light (black squares) compared to a sample kept in the dark (red circles). Figure adapted from [216]. 93

Figure 3.4: Structure of Xu's pioneering vancomycin-pyrene conjugate (left) which self-assembles in water to yield a hydrogel (right). Adapted from [220]. 94

Figure 3.5: Structures of the bolo-amphiphile drug-conjugate gelator reported by Vemula et. al. (a). Acetaminophen portions of the molecule are highlighted in red. Structure of curcumin (b). Schematic of single and dual drug release from acetaminophen gelators (c). Adapted from [101]. 95

Figure 3.6: Gels formed by the reaction of acetylcysteine with gold (a), silver (b) and copper (c) salts. (d) Supramolecular synthons formed in the reaction of anti-inflammatory drugs with amantadine. Top = 'W' synthon, bottom = 'X' synthon. Adapted from [229] and [230]. 97

Figure 3.7: Structures of the NSAIDs naproxen (a), ibuprofen (b) and aspirin (c). Surface displays of COX-2 bound by naproxen (d) and COX-1 bound by indomethacin-(R)- α -ethyl-ethanolamide (e). 98

Figure 3.8: NPX release profiles for PASP (black diamonds) and PASP-EC hybrid (white diamonds) under simulated intestinal (a) and gastric (b) conditions. Figure adapted from [245]. 99

Figure 3.9: pH-dependent release of NPX from DBS-CONHNH₂ hydrogels (a), as reported by Smith and co-workers [114]. The proposed mode of interaction between DBS-CONHNH₂ and NPX (b). Only a fragment of DBS-CONHNH₂ has been drawn for clarity. 100

Figure 3.10: Images of hydrogels loaded with NPX (6 mM). 6 mM DBS-CONHNH₂ (a), 10% PEGDM (b) and hybrid gels (c: left = 5% hybrid, middle = 7% hybrid, right = 10% hybrid). 102

Figure 3.11: Storage (G' , black) and loss (G'' , red) moduli of NPX (6 mM) loaded hydrogels in response to varying shear strain at a constant frequency (1 Hz). Rheological traces for: 6 mM DBS-

CONHNH ₂ (a), 8 mM DBS-CONHNH ₂ (b), 5% PEGDM (c), 10% PEGDM (d), 5% hybrid (e) and 10% hybrid (f). Errors are <i>ca.</i> ± 10% for all samples. Breaks in the data in (a) and (b) are due to sample slipping.	105
Figure 3.12: Storage (<i>G'</i> , black) and loss (<i>G''</i> , red) moduli of NPX (6 mM) loaded hydrogels in response to varying frequency at a constant shear strain. Rheological traces for: 6 mM DBS-CONHNH ₂ (a), 8 mM DBS-CONHNH ₂ (b), 5% PEGDM – poor quality data due to gel slipping (c), 10% PEGDM (d), 5% hybrid (e) and 10% hybrid (f). Errors are <i>ca.</i> ± 10% for all samples.	107
Figure 3.13: SEM images of 6 mM DBS-CONHNH ₂ (top) and 10% hybrid (bottom) gels loaded with 6 mM NPX. Image magnification is given above each column. Scale bars are as follows: 5,000 × = 1 μm, 20,000 × = 1 μm, 50,000 × = 100 nm.	108
Figure 3.14: Excerpts from IR spectra of 6 mM DBS-CONHNH ₂ (a) and 10% hybrid (b) gels. Changes in the O-H and N-H peaks of DBS-CONHNH ₂ are observed.	109
Figure 3.15: ¹ H NMR spectrum of NPX (6 mM) loaded DBS-CONHNH ₂ (6 mM) hydrogel made in D ₂ O solvent. Solution was spiked with DMSO (0.028 M) to quantify unbound NPX.	111
Figure 3.16: Representative absorption spectra of all gel components used in this study. PI = blue, DBS-CONHNH ₂ = red, NPX = grey, PEGDM = orange.	112
Figure 3.17: Release of NPX from DBS-CONHNH ₂ hydrogels at LMWG concentration of 6 mM (a) and 8 mM (b) into buffers of different pH. Black diamond = pH 2.8, red square = pH 4, purple inverted triangle = pH 5.5, green circle = pH 7, blue triangle = pH 8.	114
Figure 3.18: SEM images of NPX-loaded DBS-CONHNH ₂ hydrogels after submersion in pH 4 buffer for 72 h. Magnifications are 5,000 × (left), 20,000 × (middle) and 75,000 × (right). Scale bars are as follows: 5,000 × = 1 μm, 20,000 × = 1 μm, 75,000 × = 100 nm.	115
Figure 3.19: Release of NPX from 5% (a) and 10% (b) PEGDM hydrogels into buffers of different pH. Red square = pH 4, green circle = pH 7, blue triangle = pH 8.	116
Figure 3.20: Release of NPX from 5% (a) and 10% (b) hybrid hydrogels into buffers of different pH. Red square = pH 4, pink inverted triangle = pH 5.5, green circle = pH 7, blue triangle = pH 8.	117
Figure 3.21: SEM images of NPX-loaded 10% hybrid hydrogels after submersion in pH 4 buffer for 72 h. Magnifications are 5,000 × (left), 20,000 × (middle) and 50,000 × (right). Scale bars are as follows: 5,000 × = 1 μm, 20,000 × = 1 μm, 50,000 × = 100 nm.	118
Figure 3.22: A ring-shaped photomask (a) was applied over the NPX-loaded LMWG gel and the pattern transferred to the gel by UV-photopatterning (b). The weak LMWG interior and exterior were easily removed to leave the more robust hybrid hydrogel ring (c).	119
Figure 3.23: Summary of the differential release experiment (a). Release into two compartments of different pH values, separated by a gel band (diameter = 2 cm). NPX release profiles (b). Red circles	

= pH 2.8, green circles = pH 7. Increased transparency of the gel is observed from 0.5 h (top) to 3 h (bottom) as NPX is released (c).....	121
Figure 3.24: Crystallisation of NPX at the top of the PEGDM hydrogel during attempted diffusion-loading (a). Schematic of the optimised reverse hybrid gel fabrication methodology (b).	123
Figure 3.25: Images of 1 mL (a) and 10 mL (right) 5% reverse hybrid gels loaded with NPX (6 mM). Note that crystallisation of NPX is observed after 24 h, as seen in (a).	124
Figure 3.26: Storage (G' , black) and loss (G'' , red) moduli of a 5% reverse hybrid gel prepared using a pre-heated solution of PEGDM/PI. Changes in G' and G'' are given in response to increasing shear strain (a), frequency (b) and temperature (c). Errors are <i>ca.</i> $\pm 10\%$ for all samples.	125
Figure 3.27: Storage (G' , black) and loss (G'' , red) moduli of a 5% reverse hybrid gel prepared using a room temperature solution of PEGDM/PI. Changes in G' and G'' are given in response to increasing shear strain (a), frequency (b) and temperature (c). Errors are <i>ca.</i> $\pm 10\%$ for all samples.	126
Figure 3.28: Release of NPX into buffers of different pH from a 5% reverse hybrid gel. Red circles = pH 4, green squares = pH 7, blue triangles = pH 8.	128
Figure 4.1: Schematic representation of a traditional MBR. Macromolecules and biocatalysts can't pass the membrane, whereas small molecule products can diffuse through, eliminating the need for post-reaction separation.....	132
Figure 4.2: Industrially relevant MBR reactions. Effective separation of lactase starting material and lactic acid was demonstrated by Najafpour (a), whilst Liu demonstrated that only glucose and no oligosaccharide species could pass through a PES membrane (b). Pinelo used the selective oxidation of glucose (c) to achieve efficient separation from xylose in solution.....	133
Figure 4.3: Cartoon representation of strategies for enzyme immobilisation in MBRs. Covalent immobilisation (a), physical entrapment (b) and crosslinking-mediated physical entrapment (c).	134
Figure 4.4: (a) Scheme of 2-hydroxybiphenyl hydroxylation catalysed by HbpA with concomitant NADH regeneration by formate dehydrogenase (FDH). (b) Schematic representation of the tube-in-tube reactor including separation of gas and liquid phases by inner membrane. Figure adapted from [289].	134
Figure 4.5: Schematic representation of Xu's super-active LMWG-immobilised enzyme (a). The amphiphilic nature of the LMWG accompanied by large pore size facilitates mass transfer of substrate (S) and products (P) to and from the enzyme (E) sites in the hydrogel. The Hb catalysed oxidation of pyrogallol was tested (b). Turnover rates (c) of Hb immobilised in the LMW hydrogel (squares) were much greater than free Hb in water (triangles) and Hb immobilised in a PG matrix (circles). Figure adapted from [291].	136

Figure 4.6: Immobilised enzyme assays reported by Hamachi et. al. Fluorescence assay for N-terminal lysine residues (a). 5-Dimethylaminonaphthalene-1-(N-2-aminoethyl)sulfonamide is liberated selectively in LMW hydrogels containing lysyl endoprotease (LEP), resulting in a change in colour from pink to green for these samples only. Adapted from [34]. Oxidase-mediated LMWG breakdown assay (b). Oxidation of the relevant biomolecule results in formation of H₂O₂, which reductively cleaves the Npmoc protecting group and induces LMWG disassembly. Adapted from [296]. 137

Figure 4.7: Cartoon representation of a challenging two-step photo-patterned enzyme reactor configuration. To proceed to the next compartment, each reagent must pass through an enzyme-loaded gel barrier. In theory this results in a ‘product’ compartment with no reactant impurities. Example reaction shown here is the dephosphorylation of *para*-nitrophenyl phosphate by alkaline phosphatase (ALP),²⁹ followed by O-glucosylation using β-glucosidase (BGL).⁴⁰ 138

Figure 4.8: Structure of rat intestinal alkaline phosphatase with *p*NP located at the active site (a). Enzyme was recombinantly expressed in Sf9 lepidoptera cells and the two monomers are coloured in green and yellow respectively.⁴⁸ Image from [302]. ALP-catalysed dephosphorylation of *p*NPP yields *p*NP, which undergoes a pH-induced colour change based on deprotonation of the phenol (b). 139

Figure 4.9: Schematic representation of the proposed enzyme bioreactor. *p*NPP (colourless) diffuses from a central ‘reactant’ compartment through an ALP-loaded gel membrane (purple ring) which catalyses its dephosphorylation into *p*NPP (yellow). Therefore, the outer ‘product’ compartment should consist solely of *p*NP. 140

Figure 4.10: Concentration of fluorophores at the base of gels of dimension 1 cm × 1 cm × 0.5 cm (height). Diffusion through 6 mM DBS-CONHNH₂ (a), 10% hybrid (b) and 10% PEGDM (c) hydrogels. Errors given as standard deviation (n = 3). 142

Figure 4.11: Two possible tautomeric forms of fluorescein – free acid (left) and lactone (right). 144

Figure 4.12: UV spectra of *p*NPP (solid) and *p*NP (hollow) at pH 4 (red) and pH 9 (blue). All spectra recorded at a concentration of 0.016 mM (a). Structures and absorption maxima of *p*NPP and *p*NP at pH 4 and pH 9 (b). 145

Figure 4.13: Representative changes in ALP-catalysed *p*NP formation over time at different substrate concentrations. ALP concentration was 0.1 U mL⁻¹ for all samples. 146

Figure 4.14: Michaelis-Menten kinetic plot for the hydrolysis of *p*NPP using ALP at a concentration of 0.1 U mL⁻¹. Error bars represent one standard deviation and where not seen are smaller than the data points (n = 3). 147

Figure 4.15: Lineweaver-Burk plot for the hydrolysis of <i>p</i> NPP using ALP at a concentration of 0.1 U mL ⁻¹ . Error bars represent one standard deviation and where not seen are smaller than the data points (n = 3).	148
Figure 4.16: Change in the initial rate of hydrolysis of <i>p</i> NPP (0.1 mM) with ALP concentration.	149
Figure 4.17: Total conversion of <i>p</i> NPP over time at different concentrations of ALP in pH 9 buffer (a), pH 11 buffer (b) and in unbuffered water (c). Orange bars = 2 h, blue bars = 24 h, yellow bars = 48 h.	150
Figure 4.18: Solution-phase studies of gelation stimuli on the bioactivity of ALP (0.2 U mL ⁻¹). Activity in the hydrolysis of <i>p</i> NPP (5 mM) was tested in response to sonication (a: left = control, right = sample) and heat (b: left = control, middle = heated, right = heated and cooled in ice).	152
Figure 4.19: Gel-phase studies of gelation stimuli on the bioactivity of ALP (0.4 U mL ⁻¹ in each gel). All gels are 6 mM DBS-CONH ₂ . Gel prepared by standard DBS-CONH ₂ procedure (a: left = sample, right = control). Gels prepared by holding the hot sol at 70°C (b: left = untreated solution control, middle-left = treated solution control, middle-right = gel injected with ALP, right = gel sample). ALP gel prepared by holding the hot sol at 80°C (c). ALP-gel containing DMSO has similar activity to a gel with no DMSO (d: left = DMSO gel, right = gel control).	153
Figure 4.20: Images of dyes injected into hydrogels. Fluorescein injected into DBS-CONH ₂ (a) and hybrid (b) gels. Methylene blue injected into a hybrid gel (b).	154
Figure 4.21: Effect of UV light on the bioactivity of ALP in solution (0.2 U mL ⁻¹). Control (left), 0.5 h UV exposure (middle) and 0.5 h UV exposure in 0.05% wt/vol PI solution (right). <i>p</i> NPP concentration was 5 mM in all cases.	156
Figure 4.22: Uptake of <i>p</i> NPP (left) and <i>p</i> NP (right) into DBS-CONH ₂ (top), 10% PEGDM (middle) and 10% hybrid (bottom) hydrogels. Red bars = pH 4, blue bars = pH 11. Green bars are uptakes at pH 7. For <i>p</i> NP two distinct species are observed by UV at pH 7. The protonated and deprotonated forms are denoted by the dark and light green bars respectively. The dashed black line represents 25% uptake, the expected dilution based solely on equilibration of concentration. Errors given as standard deviation (n = 3).	160
Figure 4.23: NMR spectrum of a DBS-CONH ₂ (6 mM) hydrogel formed in an aqueous solution of <i>p</i> NP (10 mM). Peaks of interest for determining the proportion of mobile and immobile <i>p</i> NP are highlighted.	162
Figure 4.24: Change in concentration of <i>p</i> NPP (red), <i>p</i> NP (grey) and the total molar concentration (yellow) in the 'product' compartment over time for an ALP-loaded hybrid gel reactor (a). The dotted blue line represents the rate of diffusion of <i>p</i> NPP into the 'product' compartment with no	

ALP present. Images of the bioreactor taken after 1 h (left), 2 h (middle) and 5 h (right) reaction time.	164
Figure 4.25: Change in concentration of <i>p</i> NPP (red), <i>p</i> NP (grey) and the total molar concentration (yellow) in the ‘product’ compartment over time for a reactor with ALP present in the ‘product’ compartment (a). The dotted blue line represents the rate of diffusion of <i>p</i> NPP into the ‘product’ compartment with no ALP present. Images of the bioreactor taken every 30 min (b). Pictures span the time from 0 h (left) to 3 h (right).	165
Figure 4.26: Schematic of how a bioreactor with ‘reactive’ enzyme compartment would function. ALP is encapsulated between two photo-patterned hybrid gel rings. <i>p</i> NPP must diffuse from the ‘reactant’ compartment (centre, white), through the ‘reactive’ compartment (middle), conceptually yielding pure <i>p</i> NP in the ‘product’ compartment (outside, yellow).	168
Figure 4.27: (a) Change in concentration of <i>p</i> NPP (red), <i>p</i> NP (grey) and the total molar concentration (yellow) in the ‘product’ compartment over time for a reactor with AP present in the ‘product’ compartment. (b) Images of the bioreactor taken after 2 h (left), 4 h (middle) and 6 h (right). (c) Image of the bioreactor after being submerged in pH 9 buffer for 24 h. Errors given as standard deviation (n = 3).	170
Figure 4.28: Schematic representation of an exclusion bioreactor. Dense, photo-patterned hybrid gel (purple) does not allow passage of reactant or product, whilst an enzyme-loaded, soft LMWG (blue) allows reagent diffusion and reaction.	171
Figure 4.29: Storage (G' , black) and loss (G'' , red) moduli of the different prepared hydrogels in response to varying shear strain at a constant frequency (1 Hz, left) and to varying frequency at a constant shear strain (right). Rheological traces for: 20% hybrid (a), 40% hybrid (b), and 60% hybrid (c) hydrogels. At 40 and 60% PEGDM loading slipping of the gels lead to poor quality data, in particular in the frequency sweep experiments. Errors given as standard deviation (n = 3).	172
Figure 4.30: Concentration of fluorophores at the base of gels of dimension 1 cm × 1 cm × 0.5 cm (b). Diffusion through 20% (blue), 40% (red) and 60% (green) hybrid gels. Errors give as standard deviation (n = 3).	173
Figure 4.31: Cartoon representation of the reactor design (a). Fluorescein (b, yellow) and MB (c, blue) diffuse through the less dense reactor channels and mix prior to collection in the ‘product’ well.	174
Figure 4.32: Diffusion of MB and fluorescein through 6 mM DBS-CONH ₂ (a) and 60% hybrid (b) hydrogels. Pictures were taken after 0 h (left), 5 h (middle) and 24 h (right). Both dyes are at concentrations of 0.5 M.	175

Figure 4.33: Photomask (a) and resulting pattern (b) used to study the diffusion of MB and fluorescein in photo-patterned 60% hybrid gels. MB and fluorescein at 0.5 M (a) and as saturated solutions (b) after 0 h (left), 5 h (middle) and 24 h (right).	176
Figure 4.34: Diffusion of saturated solution of MB and fluorescein in photo-patterned 20% hybrid (a) and 40% hybrid (b) reactors.	177
Figure 4.35: Diffusion of saturated MB and fluorescein solutions through photo-patterned 40% hybrid (top) and 60% hybrid (bottom) gels (a). Pictures represent the reactor (from left to right) after 1, 3, 5, 7 and 24 h. Cumulative molar quantities of dyes (top graph) and percentage of total added moles (bottom graph) measured in the 'product' compartment for 40% hybrid (b) and 60% hybrid (c) reactors. Yellow circles = fluorescein, blue circles = MB.	178
Figure 4.36: Change in concentration of <i>p</i> NPP (red) and <i>p</i> NP (grey) in the product well of the diffusion bioreactor at room temperature (a) and images of the bioreactor (b) after 1 h (left) and 6 h. Change in concentration of <i>p</i> NPP (red) and <i>p</i> NP (grey) in the product well of the diffusion bioreactor at 50 °C (c) and images of the bioreactor (d) after 1 h (left) and 6 h.	180
Figure 5.1: Orthogonal triggers can be used to achieve complex control of gel properties and stem cell behaviour. Anseth and co-workers used SPAAC reactivity between a tetra-arm PEG and a functionalised aldehyde to form a PG network (a). Conjugation of biomolecules to the gel network was achieved with spatial control <i>via</i> a visible light-initiated thiol-ene reaction (b). Orange circle = biomolecule. Two-photon laser methods were used to spatially control the expression of fluorescent peptides in 3-dimensions (c). Gel breakdown was initiated by UV-mediated cleavage of a nitrobenzyl ether (d). UV light was used to pattern channels in the PEG hydrogel. Cell migration was only seen in the channel which had been functionalised with an RGD peptide (e). Adapted from [349].	184
Figure 5.2: Reversible oxime ligation can be used to conjugate proteins to the PEG hydrogel with spatiotemporal control (a). UV-initiated cleavage of the nitrobenzyl ether moiety reveals an alkoxyamine, which in turn reacts with an aldehyde-functionalised protein to form an oxime linkage between hydrogel and protein (b). Reversible oxime ligation was used to spatiotemporally control mesenchymal stem cell (MSC) adherence to the gel network (c, MSCs shown in green). Images adapted from [350].	185
Figure 5.3: Peptide amphiphile developed by Schneider and co-workers (a). Peptide amphiphile gels implanted into a brain lesion (b) allows migration and growth of cells into the gap (c). Hamsters treated with the peptide amphiphile recovered vision in most cases, as evidenced by the response of the subjects to a visual stimulus (d). Images adapted from [358].	186

Figure 5.4: (a) Co-assembly of Fmoc-Phe-Phe (top) and Fmoc-Ser (bottom) allowed the fabrication of robust, cytocompatible amino acid hydrogels. (b) The ratio of the two gelators could be altered to control hydrogel stiffness. Greater proportions of Fmoc-Phe-Phe increased hydrogel stiffness. (c) Soft, stiff and rigid gels could be used to stimulate the formation of adipocytes (left), chondrocytes (middle) and osteocytes (right) respectively. Images taken from [64]. 187

Figure 5.5: Barthelemy’s glycosylated thymidine gelator (a). Little ASC adherence is seen after 14 days on the LMW hydrogel alone (b). When co-assembled with collagen however, much greater ASC adherence and proliferation is observed. Figure adapted from [374]. 189

Figure 5.6: Cartoon representation of the influence of matrix stiffness on mesenchymal stem cell fate (a). The example fates given here are those of human bone marrow mesenchymal stem cells. The specific stem cell type alters the available lineages, and other possible stem cell fates are possible. For example, with a different subset of stem cells, Engler et. al. showed that MSCs undertook different morphologies when cultured on gels of high (b), medium (c) and low (d) stiffness. These different morphologies were the result of the formation of bone, muscle and fat tissue respectively. Images taken from [63]. 190

Figure 5.7: Gels were prepared in the centre of washers adhered to the bottom of the wells in a 24 well plate (a). A typical experiment is shown in (b). Brightfield (top) and fluorescence (bottom) images of a DBS-CONHNH₂ (6 mM) hydrogel incubated in media for 24 h (c). The LMW hydrogel features seen in the Brightfield images are not observed in the fluorescence image. Cells seeded on LMW hydrogels at densities of 10,000 (d) and 50,000 (e) cells mL⁻¹ showed good adherence after 24 h and adopted extended, fibroblast-like morphologies. Scale bars = 500 μm. 193

Figure 5.8: Representative fluorescence microscopy images of Y201 XGreen cells cultured on DBS-CONHNH₂ hydrogels washed with 70% ethanol followed by three washes with PBS. Cells were cultured for 1, 5 and 7 days. Seeding densities are given on the left-hand side of the figure. Good adherence and proliferation were seen for cells up to 40,000 cells mL⁻¹. At a seeding density of 50,000 cells mL⁻¹ aggregated structures were observed. This is indicative of cell apoptosis and agglomeration occurring at high cell confluency. Scale bar = 500 μm. 195

Figure 5.9: Representative fluorescence microscopy images of Y201 XGreen cells cultured on DBS-CONHNH₂ hydrogels washed with PBS only for 1, 5 and 7 days. Seeding densities are given on the left-hand side of the figure. Good adherence and proliferation were seen for cells seeded at 10 and 20,000 cells mL⁻¹. At higher seeding densities large, round, aggregated structures were observed. This is indicative of cell apoptosis and agglomeration occurring at high cell confluency. Scale bar = 500 μm. 196

Figure 5.10: Brightfield (top) and fluorescence (bottom) images of PEGDM samples. Gels were washed with 70% ethanol followed by three washes with PBS. Images of the gel seeded with no cells indicate that the gel does not fluoresce under ZsGreen excitation conditions (a). Poor Y201 XGreen adherence was seen on PEGDM gels, shown at a seeding of 30,000 cells mL⁻¹ (b). This is indicated by the rounded morphology of the cells after 24 h. Similar cell morphologies were observed at higher and lower Y201 XGreen seeding densities (see Appendix 13). Good adherence of cells to the polystyrene well plate surrounding the gel and washer was observed over 24 h (c), indicating that lack of adhesion is a property of the gel and not of experiment error. 198

Figure 5.11: Representative fluorescence microscopy images of Y201 XGreen cells cultured on 10% hybrid hydrogels washed with 70% ethanol followed by three washes with PBS. Cells were imaged after 1, 5 and 7 days culture. Seeding densities are given on the left-hand side of the figure. Good adherence and proliferation is seen for cells seeded between 10,000 and 40,000 cells mL⁻¹ over 7 days. Poor adhesion is seen in some samples after 24 h At an initial seeding density of 50,000 cell mL⁻¹, evidence of large, round, aggregated structures were observed. This is indicative of cell apoptosis and agglomeration occurring at high cell confluency. Scale bar = 500 μm. 200

Figure 5.12: Elastic moduli (stiffnesses) of the gels tested in this cytocompatibility study. Errors given as standard deviation (n=3)..... 201

Figure 5.13: Y201 XGreen cells cultured on 20% (a, b), 40% (c, d) and 60% (e, f) hybrid gels for 7 days. Reasonable cell adhesion is seen on the 20% hybrid gels, with cells adopting an extended morphology. MSCs cultured on 40% hybrid gels show no adherence and display spherical morphology reminiscent of that seen for PEGDM hydrogels. Almost no cells were observed on the surface of the 60% hybrid gels, indicating that they are not compatible with Y201 cells. Scale bar = 500 μm. 202

Figure 5.14: Concentration of PI in PBS solution used to wash gels in prepared in well plates. Errors given as standard deviation (n = 4). 204

Figure 5.15: Representative optical microscopy images of Y201 XGreen cells cultured on plastic and gel matrices. Images were taken after 7, 14 and 21 days. Initial cell seeding densities of 10,000 cells mL⁻¹ were used for all samples. Cells cultured on LMW hydrogel matrices appear more disperse than those cultured on the stiffer hybrid gels. All individual cells showed elongated morphologies on these materials. Cells grown on 10% PEGDM hydrogels showed no adherence over 21 days, indicated by the rounded aggregates. Scale bar = 500 μm. 206

Figure 5.16: Representative fluorescence microscopy images of Y201 XGreen cells cultured on plastic and gel matrices. Images were taken after 7, 14 and 21 days. Initial cell seeding densities of 10,000 cells mL⁻¹ were used for all samples. Cells cultured on LMW hydrogel matrices appear more

disperse than those cultured on the stiffer hybrid gels. All individual cells showed elongated morphologies on these materials. Cells grown on 10% PEGDM hydrogels showed no adherence over 21 days, indicated by the rounded aggregates. Scale bar = 500 μm 207

Figure 5.17: SEM images of 10% hybrid (top) and 20% hybrid (bottom) hydrogels with Y201 MSCs cultured on top for 3 weeks. Further images are provided in Appendix 14. 209

Figure 5.18: Confocal microscopy images of Y201 XGreen cells cultured on a 20% hybrid gel. Views are from beneath (a), side-on (b) and above (c). Scale bar = 500 μm 209

Figure 5.19: Complexation of Cu^+ by bicinchonic acid (a). This complex is responsible for purple coloration in the presence of protein. Total protein recorded for each of the cell treatments (b). Errors given as standard deviation ($n = 6$). 210

Figure 5.20: Oil Red O staining of Y201 cells cultured on different materials after 3 weeks (top). Images of Oil Red O stained control samples with no cells seeded (bottom). Scale bar = 1 mm. 212

Figure 5.21: Absorption of solutions of Oil Red O eluted from Y201 cells cultured for 3 weeks. Absorbance of eluent from control samples with no seeded cells were subtracted from the original absorbance to yield these values. Errors given as standard deviation ($n = 6$). 213

Figure 5.22: Mode of calcium binding by Alizarin Red S (a). Cumulative elution of Alizarin Red S from each cell growth matrix (d) Scanned images of the 24 well plates containing Alizarin Red S stained samples. Controls without cells are shown in (b). Stained test samples with cells cultured for 3 weeks are shown in (c). Values are corrected for staining on control samples where no cells were seeded and against. Errors given as standard deviation ($n = 6$). 215

Figure 5.23: Fluorescence intensity normalised against total sample protein content for cells cultured on four different matrices. Solid bars represent fluorescence from Wnt-3a treated positive controls for fluorescence, whilst striped bars represent fluorescence from the untreated test samples. Errors given as standard deviation ($n = 6$). 217

Figure 5.24: ALP content normalised against total protein for samples cultured on different matrices. Errors given as standard deviation ($n = 6$). 219

Figure 5.25: Cartoon representation of photopatterning of gels in well plates. Gels are formed in the well plates. The plate is turned upside down and a photomask placed over the top such that half of each well is shielded from UV irradiation. Gels are then irradiated with long wavelength UV light for 20 min. 221

Figure 5.26: Brightfield (a) and fluorescent (b) images of cells growing at the interface of 'stiff' hybrid gel (top half) and 'soft' LMW hydrogel (bottom half) after 2 weeks. The yellow dashed lines guide the eye as to the location of the interface. Scale bars = 500 μm . Average fluorescence intensity

from the 'stiff' and 'soft' regions of the multi-domain gels (c). Errors given as standard deviation (n = 3). 222

Figure 5.27: Gradient patterning mask (a). Increasingly light regions of the mask (moving from top-left to bottom-right) should allow greater UV penetration and PG crosslinking, resulting in greater gel stiffness. Sampling pattern for rheology is given in (b). Storage modulus (G') of the gels sampled from each region of the gel (c). Errors given as standard deviation (n = 3). 224

Figure 6.1: Spatially-resolved hybrid hydrogels have been shown to have potential applications for differential release (left), spatially-controlled tissue engineering (middle) and spatially-resolved bioreactors (right). 229

List of Tables

Table 2.1: Uptake of PEGDM from a solution of concentration 10% wt/vol (0.5 mL) over time. Hydrogels of volume 0.5 mL were used in this study and were not exposed to UV light before analysis. Errors given as standard deviation (n = 3).	72
Table 2.2: Uptake of PEGDM into DBS-CONH ₂ hydrogel after 3 days. Hydrogels of volume 0.5 mL were used in this study and were not exposed to UV light before analysis. Errors given as standard deviation (n = 3).	72
Table 2.3: T _{gel} values of DBS-CONH ₂ and UV-cured hybrid gels. Errors given as standard deviation (n = 3).	73
Table 2.4: Gelation of DBS-CONH ₂ in different solvent mixtures. All samples were prepared in 10 mL total solvent volume and transferred to a glass mould (dimensions 5 cm, × 5 cm × 1 cm) before cooling to room temperature.	86
Table 3.1: T _{gel} values of DBS-CONH ₂ and UV-cured hybrid gels with and without NPX at a concentration of 6 mM. Errors given as standard deviation (n = 3).	103
Table 3.2: Percentage deprotonation of NPX in each buffer solution as calculated by the Henderson-Hasselbalch equation, and the observed release of NPX into buffer solution from 6 mM DBS-CONH ₂ gels after 24 h.....	114
Table 3.3: Initial NPX release rates into buffers of varying pH. All rates assume zero-order release kinetics.	118
Table 4.1: Physical characteristics of the fluorophores used in this study. Absorption maxima (recorded at 50 μM), calculated Stokes radius and literature gyration radius values for each compound.....	141
Table 4.2: Initial diffusion rates through each gel and concentration at the base of the gel after 24 h. Diffusion rates calculated assuming zero order kinetics.	143
Table 4.3: Calculated percentage ALP release from each gel type into pH 9 buffer. Errors given as standard deviation (n = 3).	157
Table 4.4: Quantities of pNPP and pNP in the different compartments of the photo-patterned bioreactor after 6 h reaction time. The initial amount of pNPP added to the reactant compartment was 300 × 10 ⁻⁸ mol (10 mM, 0.3 mL).	167
Table 5.1: Swelling of DBS-CONH ₂ , PEGDM and hybrid hydrogels in water; measured by changes in gel height. LMWG and PG tests were carried out in triplicate, hybrid gel samples in duplicate. Errors given as standard deviation.....	203
Table 7.1: Suppliers, stated mass and wavelengths of fluorescence intensity maxima for each fluorophore at 50 μM.....	243

List of Schemes

Scheme 2.1: Synthesis of DBS-CO ₂ Me.....	66
Scheme 2.2: Synthesis of DBS-CONHNH ₂	67
Scheme 2.3: Synthesis of PEGDM.....	67

List of Accompanying Material

Supplementary Video 1: Photo-patterned 10% hybrid gel has different properties in the regions shielded from (centre) and exposed to (outer edge) UV light.

Supplementary Video 2: Confocal microscopy image of Y201 XGreen cells on 20% hybrid gel – 3D rotation.

Acknowledgements

There are many people I must acknowledge for their help towards the work presented in this thesis. First and foremost, big thanks must go to Professor David Smith for his support and guidance throughout my PhD, and for being a good sport with his Secret Santa presents. Hopefully someone else will take up the mantle of chief tormentor. Thanks too, to Professor Paul Genever and his group, in particular Andrew Stone, Dr. Alasdair Kay and David Kuntin, for helping a simple chemist learn at least some biology.

On the technical side, thanks go to Heather Fish (NMR), Karl Heaton (mass spectrometry), Laurence Abbott (fluorimetry) and Abi Storey (glassblowing) in the Department of Chemistry, as well as Meg Stark (SEM) and Andrew Leech (CD) in the Biology Technology Facility.

To all members of the DKS group, past and present, thank you for making this such a brilliant, bonkers place to work. Thanks to Jorge (the Master of the Universe) for teaching me more than I ever needed to know about tractors, and sorry for ruining the Grease Megamix for you. Thanks also to Jamie, not just for contributing to the enzyme work, but for being a good laugh. Jonny, good luck with doing real synthetic chemistry. Best of luck to all the back office post-docs. Carmen, enjoy your new life as a biologist! To my girls, Kirtens, Branna and Batty Pop – you're all mental, but never change. I don't know what you'll do with your newfound freedom, but I know I'm going to miss the noise.

Thanks as well to our neighbours in the PAC group, in particular to Drs. Andy Steer and Sam Griggs for adopting me as a fresh-faced PhD student. I already miss the long coffee breaks and the banter. Thanks to you both, as well as Nik (Rik, Wasgij, Rajesh) and Pavan for our daily football chat. Without the constant reminders my Fantasy League team will no doubt fall apart. Maddocks, you tried... I hope your plants all live happy and healthy lives.

Thanks as well to everyone on the Wentworth squash and Organics football teams. Sports have kept me (relatively) sane during my PhD, and we even managed to win a few titles! A special thanks to my family, without whom I'd never have made it this far. Thanks to mum and dad for their support throughout my education, to Alex for his unending supply of hot drinks, and to Helen for... something, I'm sure. Last, but not least, to Becks. You've been there for me from the start. Thanks for putting up with everything and good luck when it's your turn!

York, it's been a blast. Until next time.

Declaration

I declare that the work presented in this thesis is entirely my own, except where otherwise acknowledged. This work has not been submitted in part or fully for examination towards any other degree or qualification. All sources are acknowledged as References. Aspects of this work have been published in the following journal article: *Chem. Sci.*, 2017, **8**, 7218-7227.

1 Introduction

1.1 Low-Molecular-Weight Gels

Gels are a colloidal state of matter – where colloidal refers to the microscopic dispersion of one phase within another - in which bulk flow of a liquid-like phase is prevented by the presence of a solid-like sample-spanning network. The solid-like network – formed from molecules known as gelators - is able to do this despite comprising a very small percentage of the overall material (typically less than 1% wt/vol).¹ The macroscopic consequence of the mixing of the two phases is one which most people are familiar. The ‘wobble’ associated with jellies alludes to the fact that the properties of these materials are somewhere between solid and liquid.²

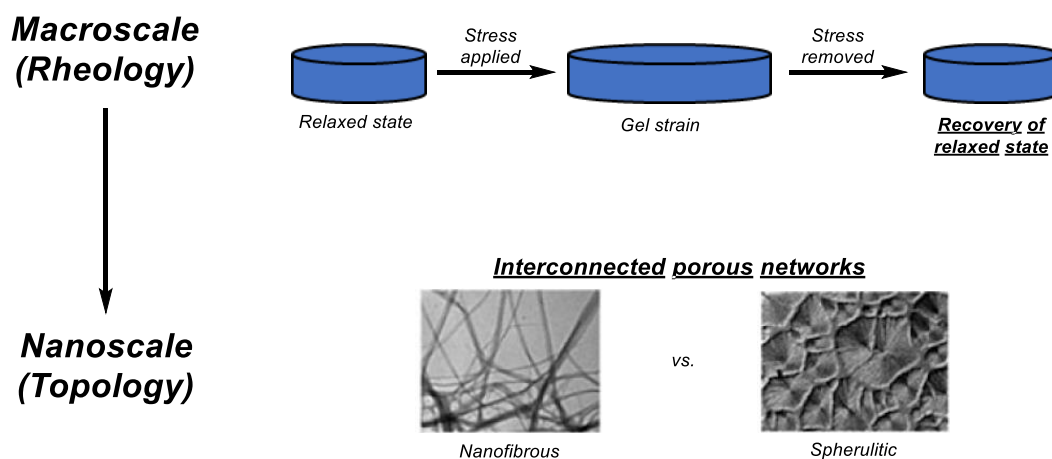


Figure 1.1: Summary of some characteristic macroscale and nanoscale features of gel-phase materials. Rheologically, gels exhibit solid-like properties and stress-relaxation. The precise macroscale properties of a gel network are determined by the porous nanoscale network from which it is formed. Images adapted from [5].

However, despite the ease with which this phase can be identified macroscopically, a universal definition of a gel is yet to be fully established.³ Almost ubiquitous in discussions of gel-phase materials is Dorothy Jordan Lloyd’s 1926 statement that “The colloidal condition, the gel, is one which is easier to recognise than to define”.⁴ This statement was made in the absence of some of the analytical techniques available to the gel chemist today, yet still holds surprisingly true. Nonetheless a number of characteristic features that gels often display have been identified, which include the recovery of mechanical properties after the removal of a straining force and the formation of a porous network (Figure 1.1).⁵

Within the more general field of gel chemistry, so-called low-molecular-weight gelators (LMWGs) have become of increasing interest in recent years. These are molecules with a molecular weight < 2000 Da which self-assemble through non-covalent interactions (including hydrogen bonding, van der Waals forces, π - π stacking and solvophobic effects) to form the 1-dimensional fibres required for solvent immobilisation (Figure 1.2) and formation of a bulk material. Gels of this type are commonly known as low-molecular-weight gels, supramolecular gels, physical gels and molecular gels. This type of gelation can be considered a type of crystallisation, in which the formation of directional interactions between gelators usually induces the formation of 1-dimensional fibres, rather than 2- or 3-dimensional crystals.

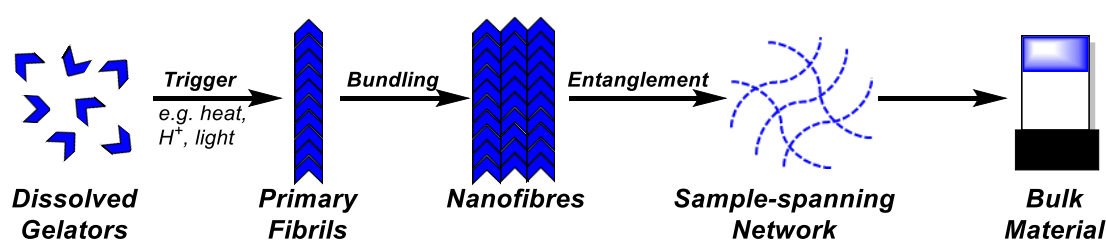


Figure 1.2: Self-assembly of low-molecular weight gelators into a bulk gel-phase material

The formation of these fibres is highly dependent on both the structure of the LMWG and the solvent in which the gel is formed. The interactions between gelator molecules and between the gelator and the solvent must be finely balanced for gelation to occur.^{6,7} If the former are too strong, the gelators will not disperse in the liquid, whilst if the latter prevail, solid-like nanofibres will not precipitate out of the solution phase. Therefore, not every LMWG will form a sample-spanning network in every solvent. Those which undergo gelation in water are known as hydrogelators, whilst those which form gels in organic solvents are termed organogelators.

LMWGs are of particular interest because the weak, reversible, non-covalent interactions through which the nanofibres are assembled are susceptible to changes in their environment. The formation or disassembly of a gel network can be triggered by the application of a range of external stimuli including heating/cooling, changes in the concentration of H⁺ or other ions and the use of a specific enzyme to form/cleave bonds; all of which change the solubility of the gelator in the given solvent (Figure 1.3).⁸⁻¹⁰ Reaction between two pre-gelators to form a self-assembling compound is also known, although less widely reported.¹¹ The properties of the bulk gels, including the stimuli to which they are responsive, are determined by the nature of the gelators from which they are formed. The properties of the individual molecules are translated up through the hierarchical self-

assembly process into the macroscopic material. In this way the organic chemist can design material properties based on their knowledge of the behaviour of small molecules.

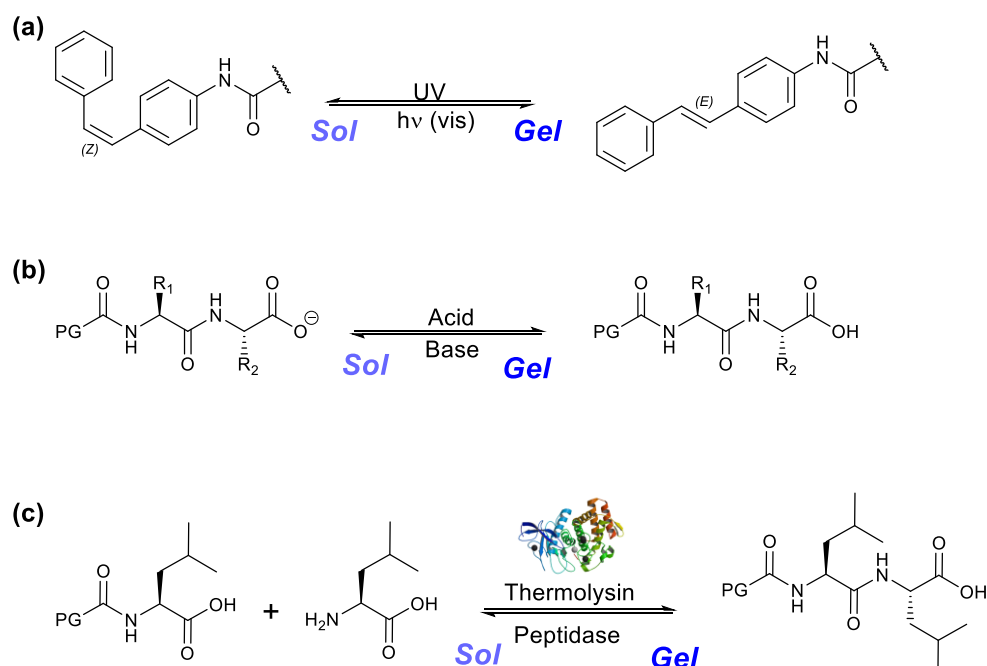


Figure 1.3: Partial gelator structures which may show responsiveness to electromagnetic irradiation (a), changes in pH (b) and enzymatic activity (c).

Due to their responsiveness and tuneability, LMWGs find increasing use in a wide range of high-tech applications.¹² LMW hydrogels are of particular interest as matrices for drug delivery and tissue engineering.^{13–15} These will be discussed in more detail later in this thesis. Supramolecular gels have also been explored as a solution to a range of environmental problems.¹⁶ For example, LMWGs which spontaneously self-assemble in organic media could be used for water purification (e.g. by entrapping crude oil in a solid-like phase),^{17,18} whilst conductive gel matrices have potential for use in optoelectronic devices.^{19,20} LMWG matrices have also been used for the crystallisation of previously inaccessible polymorphs of pharmaceutical compounds,^{21,22} as well as the encapsulation of said pharmaceuticals to prevent extraction for the synthesis of illegal drugs.²³ These high-tech applications build upon the more traditional and industrial applications of LMWGs in the food, lubricant and adhesives industries among others. Such applications (as well as more cutting edge ones) have recently been extensively reviewed.²⁴

1.2 Dual Network ‘Hybrid Gels’

One approach to achieving enhanced functionality of a LMWG is to combine it with a polymer gel (PG). PGs are a second category of gelator, encompassing natural and synthetic long chain polymers which form gel networks through either covalent or non-covalent crosslinking (termed chemical and physical gels respectively).^{25,26} The consequence of this is that compared to LMWGs, these materials are often relatively robust and durable. As such PGs have found increasing industrial relevance through the years, and are currently available in commercial products in the form of foods (such as jelly sweets),²⁷ contact lenses^{28–30} and as absorbent materials in sanitary products amongst others.³¹

This durability, however, often comes at the cost of stimulus responsiveness. The comparative robustness – and in the case of covalently linked PGs, the permanence – of crosslinking in these materials can prevent them from responding to changes in their external environment. PGs often swell in aqueous solution or in response to temperature changes, representing a type of ‘responsiveness’, and the incorporation of, for example, pH-sensitive units can imbue these materials with responsiveness to certain stimuli.³² However, the programming of more sophisticated responses into PGs is often synthetically more challenging than for LMWGs. As such examples of these types of materials are, perhaps, surprisingly limited. Practically, this limits the usefulness of these materials in high-tech biomedical applications, where responsive and adaptive changes in material properties can be used to control the delivery of drugs or growth factors at defined locations and times.

As such there is increasing interest in the synergistic combination of responsive LMWG networks with polymer-based materials to utilise the desirable properties of the respective components. In a key recent review, Cornwell and Smith identified five categories of LMWG-polymer combination, namely: (i) polymerisation of gel fibres; (ii) capture of LMWG fibres in a polymer matrix; (iii) addition of non-gelling polymers to LMWGs; (iv) directed interactions between LMWG and polymer networks; and (v) hybrid LMWG/PG networks.³³

Of particular interest is the final category. In such hybrid gels, orthogonal assembly of the two network types results in a material which, at least in theory, can demonstrate the properties of the two individual networks (Figure 1.4). Informed selection of the two gel networks allows a material to be created which demonstrates the desirable properties of the two individual networks whilst mitigating the drawbacks. Often this means that the stimulus-responsiveness of the LMWG network is retained, but the mechanical weakness of this material is offset by the incorporation of the robust polymer gel.

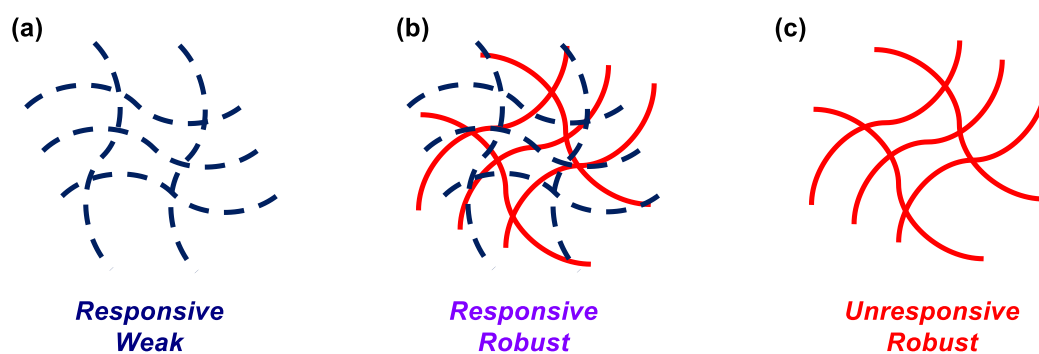


Figure 1.4: Cartoon representation and generalised characteristics of low-molecular weight gels (a), hybrid gels (b) and polymer gels (c).

This section will describe key reports in which this hybrid gel approach has been utilised. For each example discussed, the importance of assembly methodology on maintenance of the individual network properties will be highlighted, as well as how incorporating two networks proves advantageous over the constituent parts. It is worth noting that the concept of dual-network gels is not a new one. In fact, myriad publications describe so-called interpenetrating polymer network (IPN) gels – in which two independent polymer networks exist in a single material.^{34–37}

1.2.1 Hybrid organogels

Somewhat surprisingly, it was not until 2009 that the first reports of hybrid LMWG/PG gels were published. Dasgupta *et. al.* formed an oligo(*p*-phenylene vinylene) (OPV) organogel (Figure 1.5a) within an isotactic polystyrene gel (Figure 1.5b) network to yield a hybrid gel structure.³⁸ Cooling of the mixed components from the hot sol resulted in sequential assembly of the two components (polystyrene first, then OPV) due to the significant difference in sol-gel transition temperature between the two networks. The Differential Scanning Calorimetry (DSC) trace of the hybrid gel displayed two distinct sol-gel transitions, whilst Atomic Force Microscopy (AFM) images showed evidence of two distinct sets of nanofibres, both indicating orthogonality of the structures (Figure 1.5c). Heating the gel to a temperature between the gelation temperatures of the two networks resulted in selective disassembly of OPV within the supporting polystyrene framework (Figure 1.5d).

Fmoc-Phe-Phe gelation motif into a glucomannan polysaccharide gel *via* a solvent switching method.⁴² The presence of glucomannan significantly retarded the gelation kinetics of Fmoc-Phe-Phe, however the stability of the LMWG network in neutral/alkaline buffer was greatly enhanced. This stability slowed the release of docetaxel from the hybrid gel compared to the LMWG matrix alone. A significant degree of control over release could be achieved by modifying the molecular weight of the glucomannan chains, gel ageing time, and administration of β -mannanase (which breaks down the supporting PG network). In later work, this group used calcium chloride to simultaneously trigger the assembly of Fmoc-Phe-Phe and alginate (a biologically derived PG) nanofibres. Again, tuning the ratio of LMWG and PG allowed a degree of control of docetaxel release.⁴³

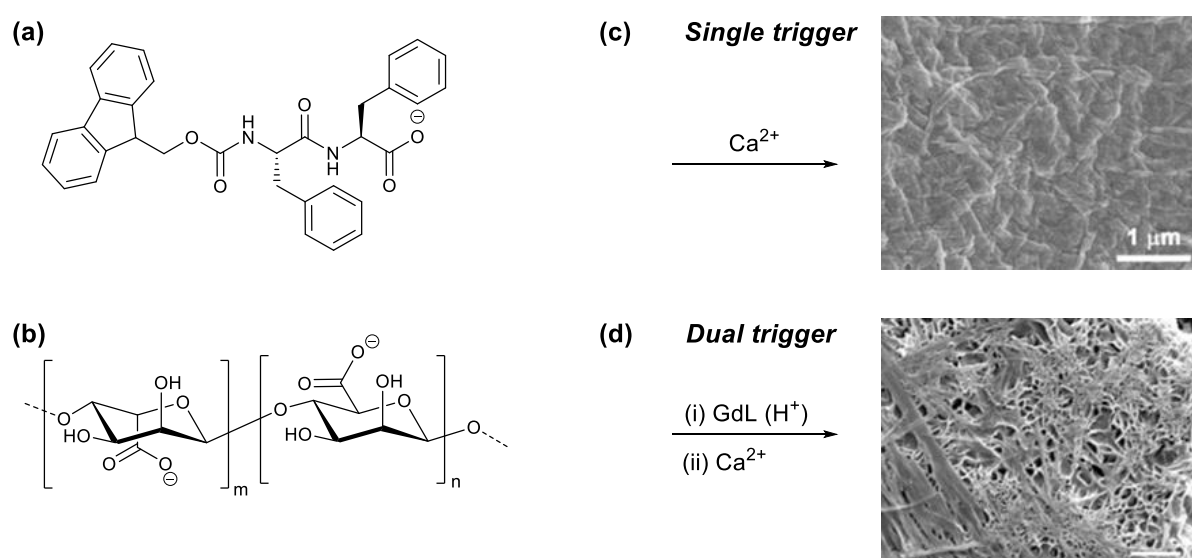


Figure 1.6: The method of assembly can have a significant impact on hybrid gel structure and property. He and Denkbař used the same two components – the LMWG Fmoc-Phe-Phe (a) and an alginate PG (b) to yield materials with different nanoscale structures. Using a single Ca^{2+} source to trigger both LMWG and PG assembly results in the formation of narrower Fmoc-Phe-Phe nanofibres (c) compared to when this network is assembled prior to alginate crosslinking (d). Scale bars = 1 μm . SEM images are from [43] and [44].

Denkbař and co-workers used the same two components to prepare hybrid hydrogels for cell culture applications.⁴⁴ However, to ensure complete orthogonality of the two networks they first triggered the formation of Fmoc-Phe-Phe using glucono- δ -lactone (GdL) – a slow hydrolysing source of acidic protons – followed by addition of calcium chloride to crosslink the alginate PG network. Importantly, these materials had subtly different properties to those described by He and co-workers (see above).⁴³ The nanoscale networks, for example, possessed subtly different morphologies (Figure 1.6). Denkbař' gels were also homogeneous, whilst a gradient of crosslinking

density was seen in He's gels. This illustrates the importance of sample history, processing conditions and assembly order in determining the properties of hybrid gels, a factor that also applies to self-assembled materials in general.⁴⁵⁻⁴⁷ The hybrid gels prepared by Denkbaş were significantly more robust than Fmoc-Phe-Phe gels and prevented burst release of vancomycin HCl. However, some detrimental effects on chondrocyte viability was observed for more densely crosslinked hybrid gels. Liu and co-workers also used a stepwise assembly approach to ensure the orthogonality of the Fmoc-Tyr and alginate networks in their hybrid gels.⁴⁸ The LMWG was triggered *via* a solvent switch – Fmoc-Tyr in DMSO was diluted in an aqueous solution of sodium alginate. After LMWG formation, calcium chloride was again used to trigger the formation of the PG network. Unlike calcium alginate alone, the IPN hybrid gels showed sustained release of both rhodamine blue and methylene blue dyes, demonstrating the potential applications of these materials for controlled drug release.

Enzymatic formation of amino acid hydrogels is, as outlined in Section 1.1, relatively common. Wang *et. al.* used alkaline phosphatase to trigger the formation of a naphthalene-protected tetrapeptide, followed by soaking in calcium chloride solution to induce alginate network formation.⁴⁹ The phosphatase enzyme immobilised in the hybrid gel retained its activity for over 20 reaction cycles, whereas neither enzyme loaded LMW or polymer hydrogels could be re-used, due to gel breakdown and enzyme leaching respectively. A dual-enzyme approach to hybrid gel formation was later reported by Mao *et. al.* Self-assembly of Fmoc-Tyr was induced by hydrolysis of a phosphorylated precursor to form a LMW hydrogel.⁵⁰ An *N*-hydroxyimide was added which interacted with the surface of the nanofibres. Reduction of this compound in a glucose oxidase (GOx)-mediated process resulted in the formation of a carbon centred radical, which initiated propagation of a dimethylacrylamide polymer chain. Through this process, the polymer network formed crosslinks between the self-assembled LMWG fibres, significantly enhancing the mechanical properties compared to the LMWG alone.

An interesting example of a hybrid gel from Surin, Escuder and co-workers combined a tetrapeptide (Figure 1.7a) LMWG network with the polymer gel poly(*para*-phenylene vinylene) (PPV, Figure 1.7b).⁵¹ Interactions between the cationic LMWG chain and the anionic PG network resulted in intimate assembly of the two networks, in contrast to the works described above. This co-assembly had a profound impact on the nanoscale morphology, resulting in thicker and more highly connected fibrils compared to the peptides alone. Macroscopically, a significant fluorescence enhancement was seen from the PG network incorporated into a hybrid gel (Figure 1.7c). Electrostatic and aromatic interactions with dyes such as methylene blue also reduced the rate of release of these model drugs compared to the LMW hydrogels (Figure 1.7d).

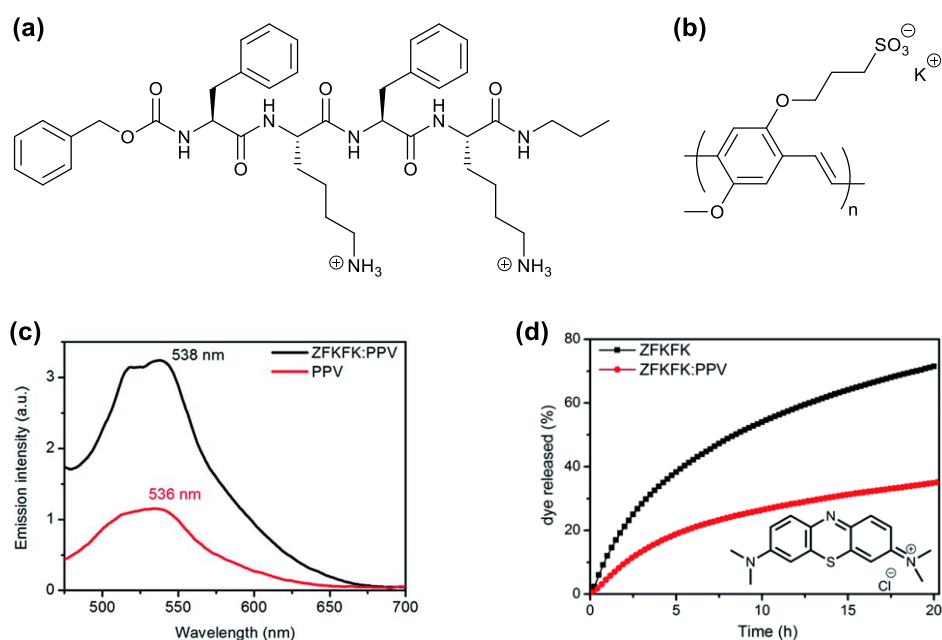


Figure 1.7: The combination of a tetrapeptide LMWG (a) and a PPV PG network (b) resulted in fluorescence enhancement (c) and sustained methylene blue release (d) compared to the individual gel networks. Adapted from [51].

Feng and co-workers incorporated a novel bola-amphiphile amino acid gelator within an agarose network, again using the difference in assembly temperatures to ensure orthogonality.⁵² SEM and IR spectroscopy suggested little interaction between the networks. The stiffness of the samples increased approximately five-fold compared to the LMWG alone. Disappointingly, no applications of this system were demonstrated or proposed.

The Smith group have developed a number of hybrid gels using functionalised sugar-based gelators. Their first report in this area described the combination of 1,3:2,4-dibenzylidene-D-sorbitol-*p,p'*-dicarboxylic acid (DBS-CO₂H) with agarose. DBS-CO₂H nanofibres formed slowly by acidification within an agarose supporting matrix which had been formed *via* a heat/cool cycle.⁵³ The orthogonality of the two networks was confirmed by a range of spectroscopic techniques. Interestingly, cycles of DBS-CO₂H assembly or disassembly could be achieved within the agarose gel by repeated exposure to acidic and basic conditions respectively. Later, the co-assembly of this hybrid gel system with a heparin-binding micelle was demonstrated.⁵⁴ Release of heparin (a widely used anti-coagulant) could be controlled by altering the composition of the gel. Increasing the concentration of either DBS-CO₂H or the micellar component reduced heparin release due to stronger binding, whilst greater agarose concentrations prevented release of the biomolecule by sterically hindering its diffusion into solution.

DBS-CO₂H has also been combined with the synthetic polymer gelator poly(ethylene glycol) dimethacrylate (PEGDM) in a hybrid gel.⁵⁵ Again, orthogonal triggers were used to assemble the two networks. In this case, UV irradiation was used to initiate radical crosslinking of a PEGDM network containing dissolved DBS-CO₂H gelator. Slow acidification of this gel resulted in the formation of a robust hybrid gel. Each network impacted on the release of dye molecules from the materials. The dense, crosslinked PEGDM network completely prevented diffusion of a large dye, whilst specific interactions between gelators and amine-bearing dyes significantly slowed the release of these molecules compared to PEGDM alone.

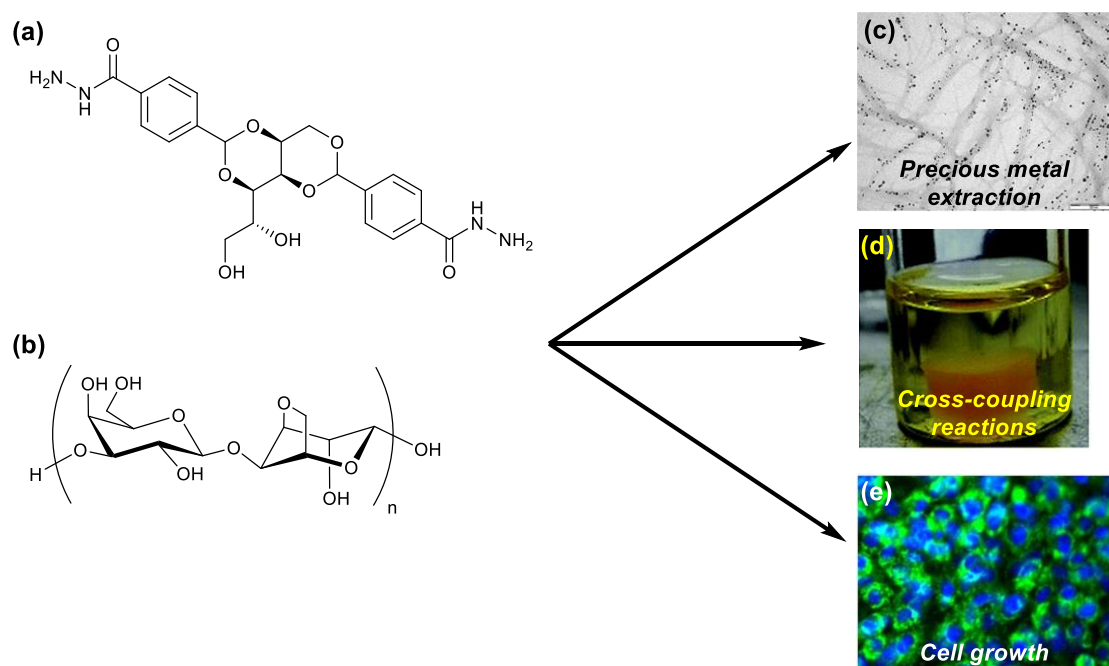


Figure 1.8: A single material with multiple applications. The orthogonally assembled hybrid gel of DBS-CONHNH₂ (a) and agarose (b) has been used for the extraction of precious metals, palladium-catalysed Suzuki couplings and the growth of mouse fibroblasts. Images adapted from [56], [57] and [58].

By combining a different DBS-derivative with agarose, a wholly different set of functionalities could be accessed (Figure 1.8), highlighting the importance of retention of LMWG properties in this class of material. In this case, a LMWG bearing acyl hydrazide moieties (DBS-CONHNH₂) was shown to extract a range of metals from solution, generating *in situ* nanoparticles along the lengths of the LMWG nanofibres (Figure 1.8c). These hybrid gel/nanoparticle composites are electrically conducting,⁵⁶ and – as demonstrated for palladium-containing materials – are able to act as catalysts in industrially relevant chemical processes (Figure 1.8d).⁵⁷ In the latter case, the additional stability provided by the supporting agarose network was crucial for the recyclability of the material. In the absence of the PG the gel network is not robust enough to withstand stirring in a

reaction setting. The same gel (but without abstracted metal) has also shown potential as a commercially-relevant, biocompatible matrix for tissue engineering.⁵⁸ Agarose itself was unable to support cell growth, whilst DBS-CONHNH₂ could, but was challenging to handle owing to its mechanical weakness. Combining both networks in a hybrid gel combined the best features of both individual gels, being both easily handleable and supportive of fibroblast growth (Figure 1.8e). These three examples of hybrid gels containing DBS-CONHNH₂ were all published concurrent with the research presented in this thesis.

Xhang and co-workers also described the development of a hybrid hydrogel for cell culture applications.⁵⁹ A C₂-symmetric phenyl derived LMWG was self-assembled using a thermal trigger to form a hydrogel containing alginate, which was then crosslinked by addition of calcium chloride. Interpenetrating and orthogonal networks were formed – confirmed by X-ray diffraction and infrared spectroscopy. The crosslinked materials were up to five times stiffer than the LMW hydrogels and showed improved cell fibroblast adherence and proliferation.

As well as hybrid gels being used to enhance the physical properties of LMWG-containing materials, the inverse has also been recently reported. The same C₂-symmetric phenyl gelator described by Xhang was incorporated into a kappa-carrageenan PG network to increase the hydrophilicity and thermal stability of the materials.⁶⁰ These changes were reflected in the enhanced viability of a commonly used cell line. Watanabe and co-workers showed that templating a UV-crosslinked polyacrylamide network by a pre-formed octylaldonamide/sodium dodecyl sulfate LMWG network significantly enhances the ability of the PG to resist crushing stress, even after the LMWG was removed (Figure 1.9).⁶¹ This was attributed to the templating effect of the LMWG network, which it was argued would reduce network inhomogeneity and improve the energy dissipation properties of the polyacrylamide network.

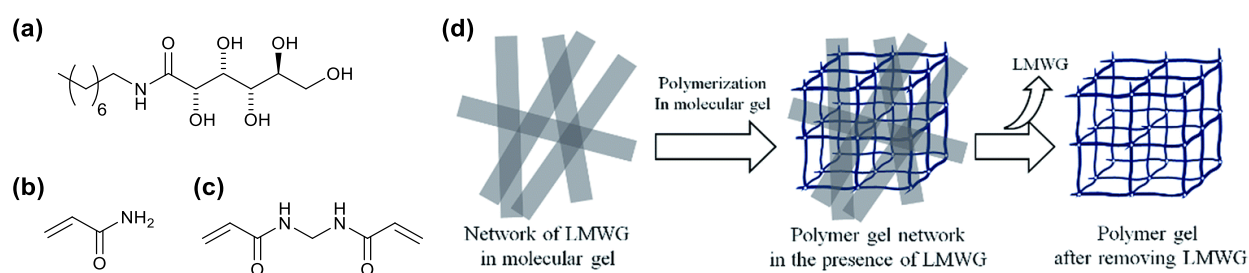


Figure 1.9: Watanabe's two-component LMWG network based on octylaldonamide (a) enhances the mechanical properties of an acrylamide (b) network which had been crosslinked by methylenbisacrylamide (c). Schematic illustration of the templating of acrylamide PG network within a pre-formed LMW hydrogel (d). Adapted from [60].

Chen *et. al.* also recently described the *in situ* reaction and self-assembly of a LMWG as part of the hybrid gel formation process. Guanosine and boric acid were mixed in the presence of dimethylacrylamide, a crosslinker and photoinitiator resulting in formation of guanosine borate diesters.⁶² On addition of KOH, these species assembled into tetrameric species which could stack further to form nanofibres. A LMW hydrogel formed, which underwent significant stiffening on the application of UV to crosslink the polymer network. These materials were significantly stiffer than either the guanosine-based LMW hydrogel or the dimethylacrylamide network individually. These materials also show remarkable elasticity and stress recovery properties. The authors propose that the LMWG contributes to these properties by reversibly dissipating the energy which would otherwise result in permanent deformation and weakening of the covalently crosslinked network.

1.3 Spatial Control of Low-Molecular-Weight Gel Structure

A major drawback of LMWGs is the homogeneity of the materials which are produced. Gels are usually formed from the solution state through either cooling or addition of a chemical trigger. The gels produced are therefore homogeneous, with no changes in structural or chemical properties across the material. This equally applies to almost all the examples of hybrid gels described above. For more complex applications of LMWGs to be realised, it is essential to be able to spatially control the formation and properties of the resulting gels. For example, stem cells are highly responsive to the properties of the matrix they are grown on.⁶³⁻⁶⁵ Properties ranging from thickness and stiffness to the presentation of cell adhesion moieties all influence the fate of stem cells undergoing differentiation. Uniform gels therefore limit the complexity of the tissue that can be grown on them. Gels are often explored for microfluidic applications, but again, if the materials produced have uniform properties, they are unable to direct flow or demonstrate spatially-defined chemical reactivity.⁶⁶

There exist in the literature myriad examples of gel assembly/disassembly mediated by light, redox processes and other spatially-controllable stimuli.⁶⁷⁻⁶⁹ Too frequently though these processes are only performed on a whole sample, resulting in a homogeneous material. Therefore, we will focus here on examples in which chemical and/or structural heterogeneity are introduced to a gel sample through spatially-controlled application of an appropriate stimulus.

1.3.1 Photo-patterned LMWGs

In recent years significant effort has been made to spatially control the properties of LMWGs. Often, approaches popularised by PG chemists are adapted for use in LMWGs. In particular photo-patterning has been widely utilised to control sol-gel phase transition. LMWGs incorporating photo-isomerisable moieties are particularly attractive, as the transition between *trans*- and *cis*- forms of a chemical structure can control the ability of the gelators to stack into 1-dimensional nanofibres.

The first example of a spatially-resolved LMWG was reported by, Eastoe *et. al.* in 2004.⁷⁰ They demonstrated the spatially-resolved gel-sol transition of a photo-dimerisable stilbene organogelator (Figure 1.10a), the *trans*-isomer of which formed gels in toluene via a heat/cool cycle in the presence of trace amounts of *N,N'*-dimethyldodecylamine. The authors attribute the gelation to the aggregation of inverse micellar structures. Upon photo-irradiation, the gelator undergoes a dimerisation process, resulting in disassembly of the opaque gel in the regions exposed to UV light (Figure 1.10b). This change in the aggregation state was confirmed using small-angle neutron scattering (SANS) and was non-reversible.

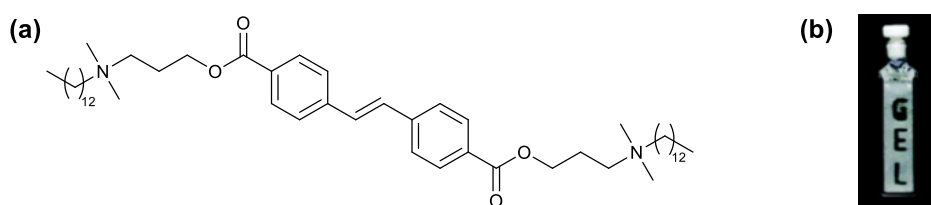


Figure 1.10: Eastoe's gemini surfactant (a) undergoes photo-dimerisation on UV exposure, resulting in gel disassembly with spatial control (b).⁷⁰ Adapted from [70].

In the same year, Kato and co-workers also used light to impose spatial resolution on a LMW gel. They incorporated a photo-switchable di-azobenzene gelator into a cyanobiphenyl liquid crystal (LC).⁷¹ Cooling of the hot sol resulted in formation of a nematic LC-templated gel, as visualised by polarised microscopy. Exposure of regions of the sample to UV-light induced a *trans-cis* isomerisation of the azobenzene moieties, resulting in gel breakdown in these areas. This was accompanied by the conversion of the nematic LC to a cholesteric phase. Over time (or by exposure to visible light) as the isomerisation process is reversed, the gel-phase is re-formed and is templated by the cholesteric LC phase. On heating and re-cooling, the system reverts to a nematic gel phase, making the patterns erasable and rewritable.

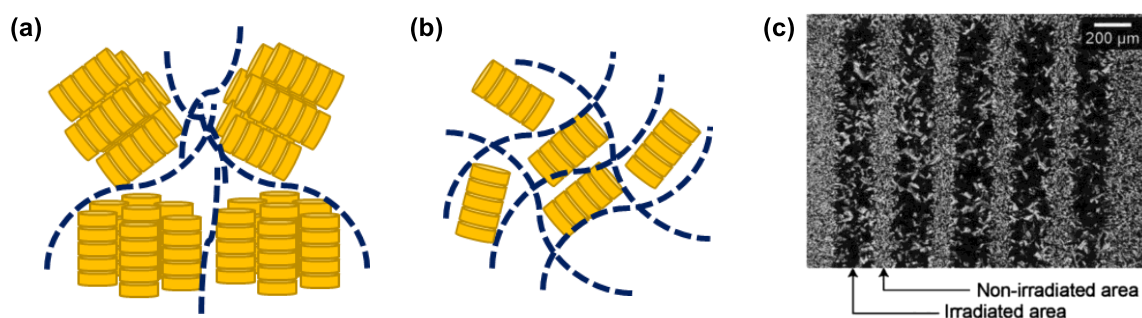


Figure 1.11: Cooling the isotropic LC/LMWG liquid under UV irradiation results in the formation of an anisotropic gel network (a). In the absence of UV light an isotropic gel network is formed (b). Micro-patterned LC gels were visualised by polarised light microscopy (c). Adapted from [72].

In subsequent work, the same group applied this synergistic approach to LC and gel-phase patterning in a discotic LC-templated system.⁷² Again, the gel was controlled by *cis-trans* isomerisation process. Under UV irradiation, the proportion of *cis*-azobenzene is greatly increased, depressing the T_{gel} . Therefore, upon cooling the isotropic LC/LMWG liquid, the discotic LC assembles first into a columnar hexagonal (Col_h) phase. Further cooling results in LMWG self-assembly. The presence of the Col_h phase templates the gel, resulting in formation of an anisotropic material (Figure 1.11a). In contrast, in the absence of UV light, an isotropic gel phase forms at a higher temperature than the Col_h phase due to the greater abundance of *trans*-gelators (Figure 1.11b). Again, these reversible phase changes were spatially-controlled on the microscale using a photomask and visualised by polarised light microscopy (Figure 1.11c).

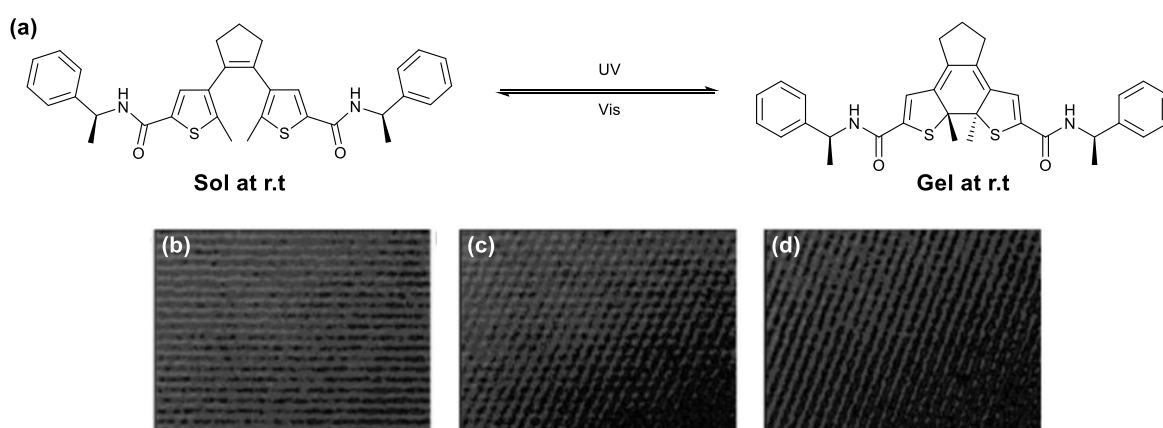


Figure 1.12: Light-driven dynamic pattern formation.⁷³ (a) Open (left) and closed (right) forms of dithienylcyclopentene can be switched between through exposure to specific wavelength of light. Micrographs (b-d) of spatially-controlled gel formation (magnification $\times 20$). All were exposed to a homogeneous visible light source throughout the experiment. A horizontal grating pattern (a) was formed after 10 min UV exposure. An additional diagonal pattern was then formed after rotation and a further 10 min exposure (b). After 90 min UV diagonal UV exposure the horizontal pattern has been 'erased' whilst the diagonal patterning remains (c). Adapted from [73].

Soon after this report, van Esch, Feringa and co-workers performed reversible ring-closure on a dithienylcyclopentene derivative to develop reversibly-patternable organogels (Figure 1.12a).⁷³ At room temperature, UV-initiated ($\lambda = 330$ nm) ring-closure results in the formation of a sample-spanning gel network in toluene. Visible-light ($\lambda > 420$ nm) was then used to reverse this reaction and induce gel disassembly. Spatiotemporally controlled exposure of the solutions to UV and visible light sources allowed the formation of dynamic and reversible patterned gels on the microscale. The lifetime of the materials at each point in space could be defined by the exposure time and intensity of the individual light sources, as well as the regime of exposure (Figure 1.12b-d). For example, further UV-irradiation of the gel state resulted in better-defined and longer lasting patterns compared to those patterned into the sol.

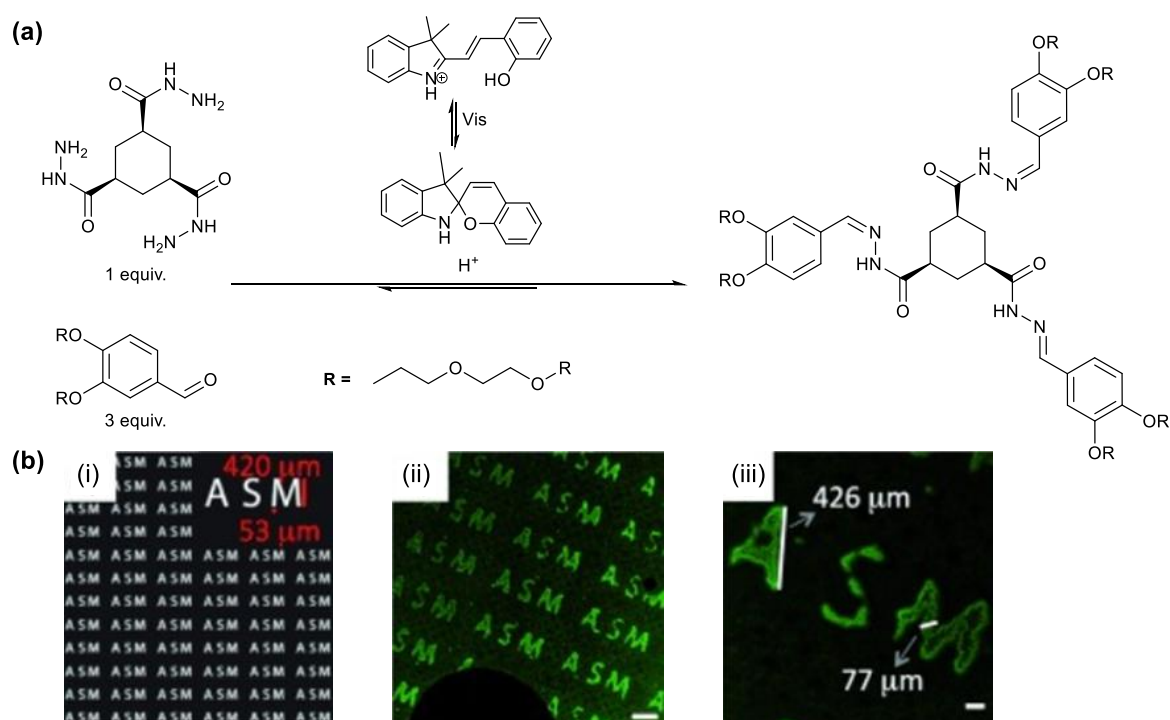


Figure 1.13: Photoacid-catalysed formation of a tris-hydrazone gelator from hydrazide and aldehyde starting materials (a). Spatially-controlled gel formation on the microscale (b). Photomask design (i) and fluorescent microscopy images (ii and iii). Scale bar (ii) = 500 μm . Scale bar (iii) = 100 μm . Adapted from [74].

More recently, the same group have developed a system for the light-induced formation of hydrogel patterns. The acid-promoted reaction of a *tris*-hydrazide with three equivalents of aldehyde forms a *tris*-hydrazone which spontaneously self-assembles into a sample-spanning gel network (Figure 1.13a).⁷⁴ Merocyanine is a photoacid generator (PAG) which under visible light undergoes cyclisation to form the corresponding spiropyran. This process liberates a proton which catalyses the formation of the gelator, ultimately resulting in gel formation. Crucially, when

irradiation stops the spiropyran rapidly converts back to the merocyanine, ensuring that gel formation is localised to regions of light exposure. Laser printed photomasks were used for fine control of this acidification (and gelation) process with excellent microscale resolution (Figure 1.13b). Adams and co-workers have also described the use of a PAG to spatially control the formation of a gel network, in their case using UV-light to protonate naphthalene-dipeptide hydrogelators, which self-assemble rapidly to form nanofibres.⁷⁵ The rapid rate of fibre formation ensures good patterning resolution for this system.

The first example of a photo-patternable hydrogelator was reported by Matsumoto *et. al.* in 2008. They synthesised a range of glycolipid-based hydrogelators, which, through *trans-cis* isomerisation of an appended fumaric acid moiety, underwent reversible gel-sol transitions at room temperature (Figure 1.14a).⁷⁶ The sugar head and lipid tail of these molecules contribute to gelation through solubility modification. However, it is intermolecular hydrogen bonding associated with the amide groups of fumaric acid which are crucial for the formation of 1D fibres. Exposure to UV light converts this moiety into the maleic acid form, resulting in disruption of these hydrogen bonds and gel disassembly. This change could be reversed by exposure to visible light or a bromine source. Again, by using a laser/photomask, this sol/gel transition could be spatiotemporally controlled. Figure 1.14

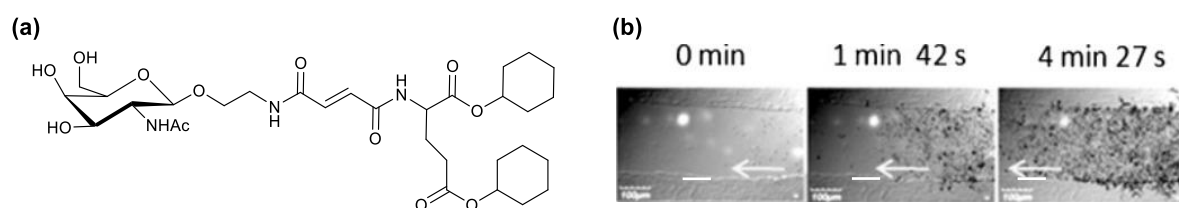


Figure 1.14: Fumaric acid gelator reported by Matsumoto *et. al.* (a). Directional control of *E. coli* spreading through spatially-resolved gel breakdown (b). Dark spots are *E. coli*, arrows indicate direction of motion. Scale bar = 100 μm . Adapted from [76].

As well as being the first patternable hydrogel, this was also the first work to demonstrate an application of photo-patterned gels, specifically the controlled diffusion of bacterial movement. *Escherichia coli* (*E. coli*) was localised to the sol region of a bulk gel sample. Size exclusion prevented passage of the bacteria through the gel membrane. Upon exposure to UV-light however, channels of sol were produced along which the *E. coli* could migrate and proliferate (Figure 1.14b). Controlled cell motion is an important consideration for applications such as tissue engineering and this type of approach holds promise for the control of, for example, stem cell penetration into a 3D gel matrix.

More recently Kim and co-workers developed the *tris*-(4-((*E*)-phenyldiazenyl)phenyl)benzene-1,3,5-tricarboxamide gelator (Figure 1.15a), which forms a sample spanning gel through a solvent switch.⁷⁷ This network could subsequently be disassembled by exposure to UV-light. Using a photomask, patterns of sol were created in a bulk gel matrix. These patterns could be erased by exposure to visible light, which reverses the *trans-cis* isomerisation of the peripheral azobenzene moieties. Multiple write-read-erase cycles were performed on this material (Figure 1.15b). The whole cycle is complete in under 4 min, in contrast to the longer timescales (*ca.* 1 h) reported for van Esch's organogel patterns (see above).⁷³ This fast cycle time makes this system practical for use in functional supramolecular memory systems. However, the resolution achievable in this process was only demonstrated on the mm scale.

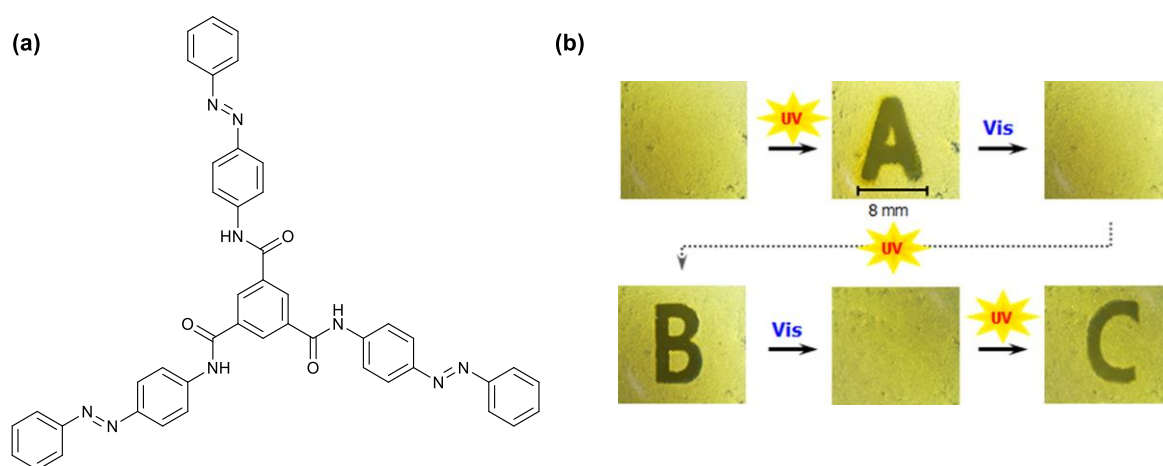


Figure 1.15: An azobenzene-based gelator (a) can undergo spatially-resolved reversible gel-sol transitions (b). UV-promoted *trans-cis* isomerisation breaks down the gel network to form a pattern. This pattern was erased using visible light, then re-written in another write-read-erase cycle. Adapted from [77].

A recent contribution to the field comes from the Chiu lab. They used a degradable macrocycle to shield interactions between perylene-bisimide (PBI) gelator molecules (Figure 1.16a) *via* the formation of a rotaxane-like structure.⁷⁸ The macrocycle utilised (Figure 1.16b) is photo-degradable, and on exposure to UV light breaks down to reveal hydrogen bonding moieties on the free gelator, encouraging nanofibre formation. Rapid gelation in organic solvents limits diffusion of the free gelator prior to forming nanofibres, resulting in good photo-patterning resolution (Figure 1.16c). By contrast the gelation process in aqueous solution was much slower compared to the rate of gelator diffusion. As a result, no resolution was observed for gels photo-patterned in aqueous solution (Figure 1.16d).

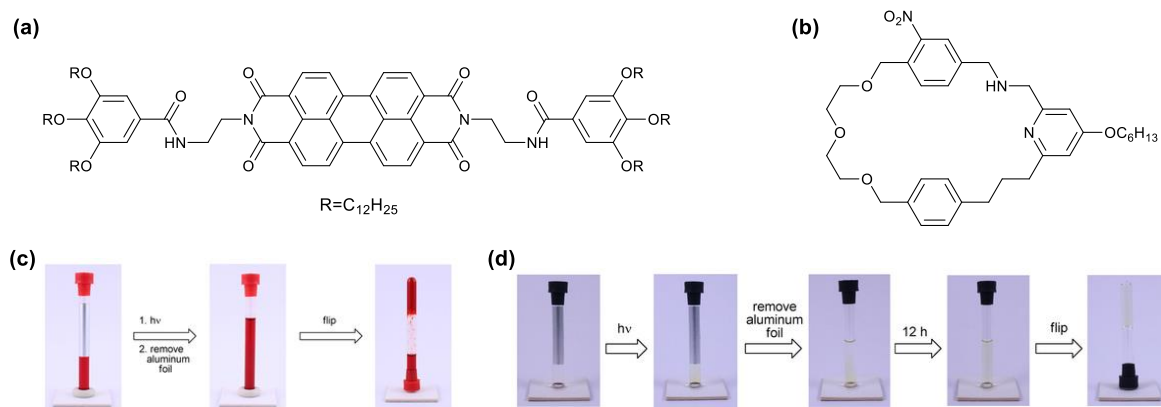


Figure 1.16: Structures of the perylene bisimide gelator (a) and photo-degradable macrocycle (b). Spatial resolution of gel formation could be achieved in dioxane (c) but not in water (d). Adapted from [78].

The examples of photo-patterned gels discussed so far have detailed spatial control of either the formation or breakdown of gel networks. Of great potential interest are gels which can modulate their structures in response to a stimulus whilst remaining in the gel phase throughout the process.

An excellent example of this approach was reported in 2014 by the Feringa group. They performed a reversible photo-cyclisation reaction on a dithienylethene-appended peptide hydrogelator (Figure 1.17a) to generate changes in absorption and fluorescence properties of the material.⁷⁹ As in his earlier collaborative work with van Esch (see above), exposure of the gelators to UV light resulted in cyclisation of the dithienylethene moiety (open/closed ratio = 52:48), whilst visible light reversed this reaction (open/closed ratio = 92:8). Throughout this process reversible changes in the nanostructure of the gel could be observed by electron microscopy (Figure 1.17b and c). Unusually, despite these changes in structure, this did not manifest in rheological changes. The UV-vis emission spectrum was significantly changed upon irradiation however. This could easily be visualised by a change in gel colour from yellow to red. This change could be spatially controlled using a photomask to yield gels with domains of different colour (Figure 1.17d). To date, this remains the only example of a photo-patterned gel-gel morphology (in a single-component gel) in which the patterned state is indefinitely stable until a reversing stimulus is applied.

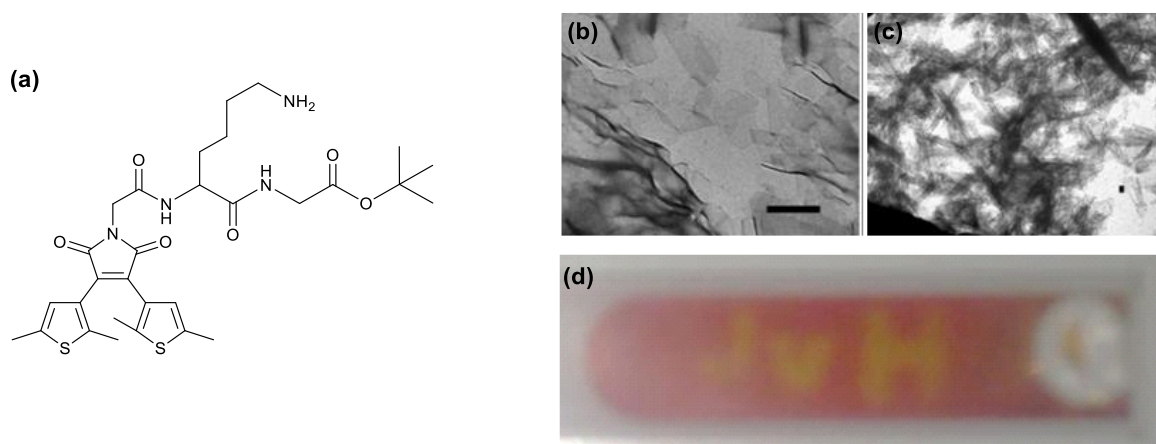


Figure 1.17: Structure of Feringa's dithienylethene gelator in the open form (a). Gel morphology observed by TEM is significantly different for untreated (b) and UV-exposed (c) gels (scale bar = 1 μm). Spatial control of the gel-gel morphology transition was achieved using a photomask (d). This was easily observable due to a change in gel absorbance properties on irradiation. Adapted from [79].

In contrast, Draper *et. al.* reported a temporarily stable change in gel morphology upon photoreduction of a PBI gelator (Figure 1.18a).⁸⁰ Protonation of an appended valine initially resulted in bulk gel formation. Exposure of the sample to UV light ($\lambda = 365 \text{ nm}$) initiates the formation of a radical anionic PBI species, which both quenches fluorescence (Figure 1.18b) and increases the mechanical strength of the bulk material (Figure 1.18c) only in those areas which were exposed to UV irradiation. These changes were confirmed through SANS to be the result of an increase in fibre density, itself predicted by density functional theory (DFT) calculations to be caused by the enhancement of anion- π interactions in the excited state. The radical anion has a surprisingly long lifetime ($> 24 \text{ h}$) due to stabilisation of this species through gelator stacking, but unlike Feringa's example, does eventually revert to the ground state in the absence of any further stimuli.

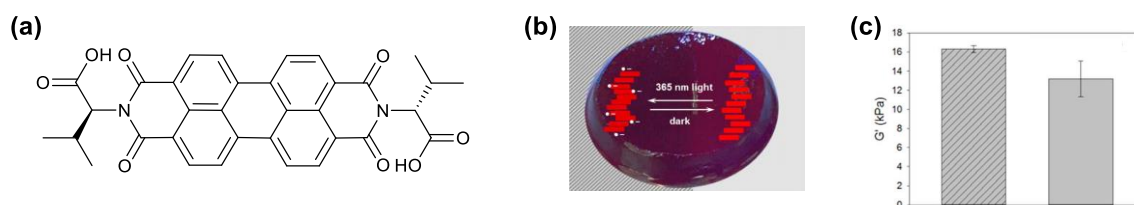


Figure 1.18: Structure of PBI-valine gelator (a). Photo-patterned gel (b). Exposure to UV light reduces the distance between gelator molecules in the nanofibres, resulting in increased mechanical strength (c) in the irradiated (left) vs non-irradiated (right) regions. Adapted from [80].

In recent work, calixarene-derived gelators were shown to be able to undergo spatially-controlled morphological changes in response to UV light.⁸¹ *In situ* gel formation was achieved through the reaction of an aldehyde-bearing stilbene derivative (Figure 1.19a) with an acyl hydrazide-functionalised calixarene (Figure 1.19b) over 2 days in DMSO. These hydrazone gels exhibited blue fluorescence (attributed to H-aggregates), which was quenched under UV light (Figure 1.19c). This quenching was shown to be the result of photo-dimerisation of the stilbene moieties and was accompanied by a 1000 × increase in the mechanical strength of the gel in exposed regions. Finer control of the gel properties was achieved by incorporating a heat-treatment step, which modifies the proportion of H-aggregates in the gel and therefore alters the changes observed on UV-exposure.

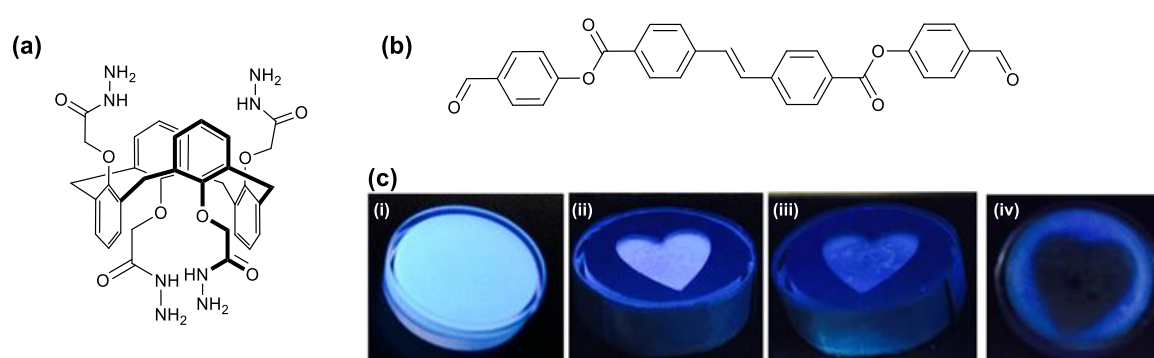


Figure 1.19: Structures of calixarene (a) and stilbene (b) gelator precursors. The calixarene gel's fluorescent properties are modified by UV light (c). Prior to photo-patterning, the gel is fluorescent (i). A mask is applied to the gel (ii) and in the exposed areas fluorescence is lost over time (iii and iv). Adapted from [81].

An alternative approach to maintaining the gel state during photo-patterning is to selectively disassemble one network of a dual-network gel. Seminal work in this field was reported by Adams *et. al.* in 2014. They used a stepwise acidification to induce orthogonal self-assembly of: (i) a bis-phenylalanine-functionalised stilbene (Figure 1.20a, pK_a ca. 5.8), followed by (ii) a dipeptide gelator (Figure 1.20b, pK_a ca. 5.0).⁸² The application of UV-light ($\lambda = 365$ nm) then induces spatially selective breakdown of the stilbene gelator by way of a *trans-cis* isomerisation over 2 h. The mechanical properties of gels exposed to UV light were similar to those of the dipeptide gelator alone, suggesting that the second network was unaffected by the loss of the stilbene nanofibres. NMR and fluorescence studies also indicated that the network breakdown was localised exclusively to areas where light was allowed to penetrate the bulk sample (Figure 1.20c).

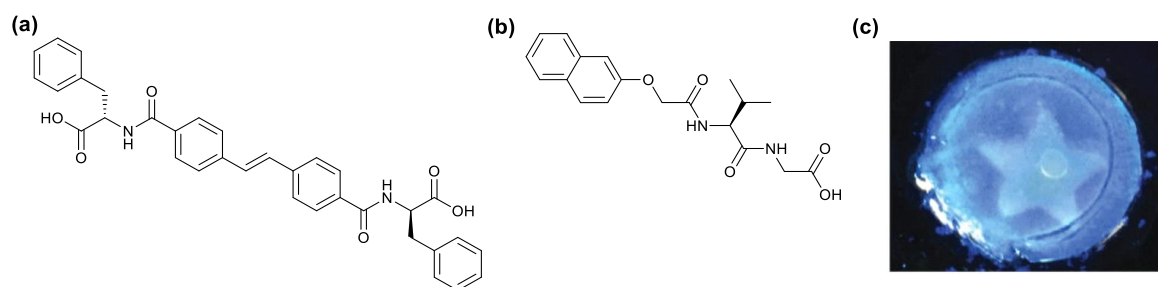


Figure 1.20: Structures of the *trans*-stilbene (a) and dipeptide (b) gelators used by Adams and co-workers. The spatially-resolved disassembly of the dipeptide network could be visualised using a low-powered UV lamp (c). The star shape represents the irradiated gel. Adapted from [82].

More recently, Che *et al.* prepared organogels comprising self-sorted diacylhydrazide (Figure 1.21a) and acylhydrazone (Figure 1.21b) networks.⁸³ In contrast to Adams, the orthogonality of the networks in this case was ensured by the significant difference in T_{gel} values (57 °C and 15 °C respectively). Crucially, in these dual-network gels the emission profile of the dihydrazide undergoes a bathochromic shift such that the emission maximum overlaps with the absorption profile of the acylhydrazone. In an elegant step, visible light irradiation and subsequent fluorescence of the dihydrazide network was used to induce a *trans-cis* isomerisation in the acylhydrazone network, resulting in selective disassembly of this second network with good spatial resolution (Figure 1.21c). Interestingly, in contrast to Adams' photo-patterned gels, the properties of the gel after irradiation (mechanical strength, wettability) do not return to that of the dihydrazide gel alone. This suggests the networks may not be completely self-sorted, or that they may interact during formation, altering the properties compared to the single-component gels.

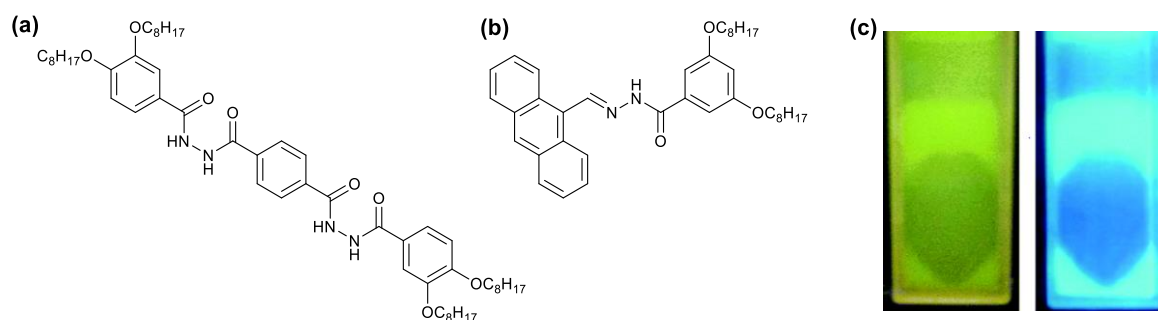


Figure 1.21: Structures of the self-sorting hydrazide (a) and acylhydrazone (b) organogelators. Dual-network gels were partially exposed to visible (350-570 nm) light (c) and visualised under natural (green) and UV (blue) light. The irradiated areas appear darker due to loss of fluorescence via disassembly of the acylhydrazone network. Adapted from [83].

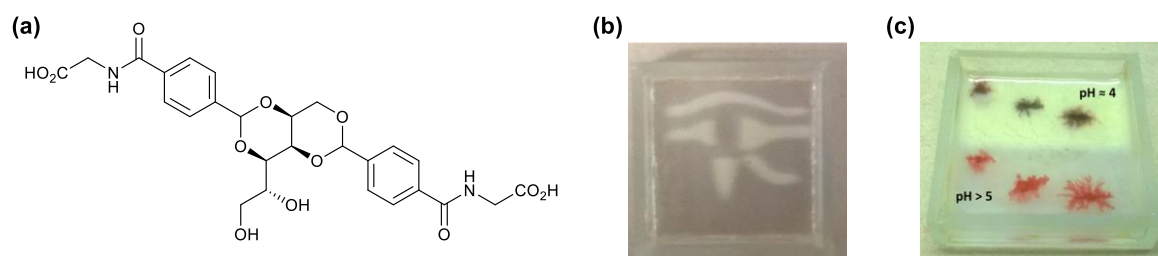


Figure 1.23: Structure of DBS-glycine (a) which, through a sequential acidification, was photo-patterned into a DBS- CO_2H gel with excellent resolution (b). No significant diffusion of protons out of the UV-exposed area (top-half) occurs over several hours (c), indicating sustained pattern integrity over this timescale. Adapted from [84].

1.3.2 3D-printed LMWGs

The advent of commercially-available 3D-printing technologies has afforded gel chemists unprecedented control over the complex and reproducible shaping of materials. The state-of-the-art in the field is the fine control of gel structures through 2-photon stereolithography, which allows materials to be fabricated with exquisite detail and resolution on the nanoscale. Cutting-edge research has also shown that gels can be utilised as a suspension matrix for Rapid Liquid Printing.⁸⁵ A thixotropic, granular, polymer gel in this case allows an extruder to deposit material at defined points without leakage of the ‘ink’ into cavities left during this process.

3D-printing is a particularly attractive approach for the development of tissue engineering scaffolds. Using mild gelation methods, encapsulation of cells in pre-shaped materials which can be inserted directly into a patient represents a promising approach for regenerative medicine.⁸⁶ Numerous examples of 3D-printed and (both covalently and non-covalently) crosslinked polymers have been reported in recent years,^{87–89} however few reports exist of 3D-printed LMW gels. The relatively slow rate of progress in this field can be attributed to a number of factors. The comparative difficulty in handling these materials makes them less attractive candidates for study, whilst the relatively small number of LMWGs demonstrating the required thixotropy for extrusion-based technologies limits their scope compared to covalently crosslinked gels which are cured rapidly during the extrusion process. Fundamentally, the difficulty associated with rational prediction of LMWG gel-forming ability and macroscale properties limits the rate at which advancement can be made.

Despite these difficulties, a number of recent reports suggest an emergence of interest in using LMWGs for 3D-printing. In 2016, Wei *et. al.* reported the development of an elegant two-step enzyme-based printing method in which glucose oxidase (GOx) and horseradish peroxidase (HRP) work in tandem to crosslink LMWG fibres *in situ* (Figure 1.24).⁹⁰ Both enzymes were added to a

supramolecular hydrogel formed from an acrylate-functionalised tripeptide gel, along with glucose, acetylacetone (AcAc) and poly(ethylene glycol) methacrylate. Glucose oxidation by GOx produces one equivalent of H_2O_2 , which is converted by horseradish peroxidase into water. AcAc intercepts the intermediate radical in this process to generate $\text{AcAc}\cdot$. This species initiates a radical polymerisation of the LMWG with poly(ethylene glycol) methacrylate (PEGMA), crosslinking the LMWG fibres.

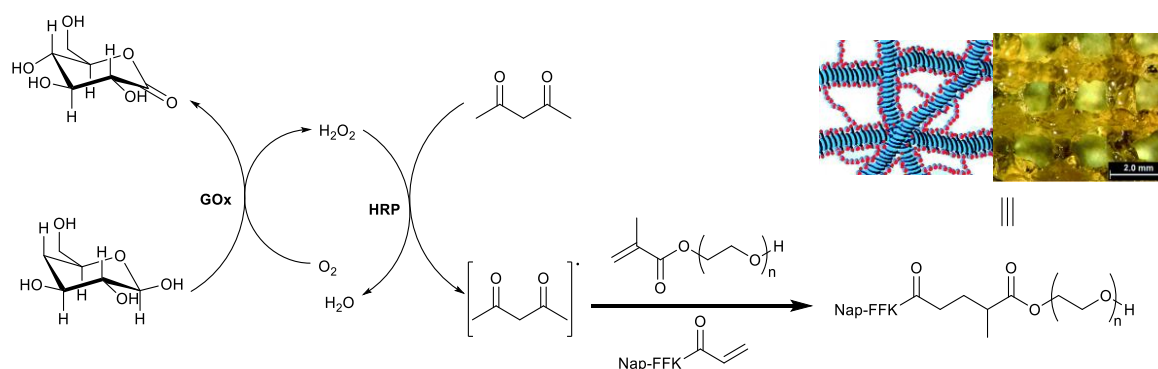


Figure 1.24: Dual-enzyme catalysed 3D-printing of a naphthalene-tripeptide gel. LMWG fibres (blue chains) are crosslinked by PEGMA molecules (red chains) to form printed hydrogel matrices (top right). Adapted from [90].

Performing this process in the gel state prevents reactions between individual LMWGs and enhances enzyme activity compared to the solution state reaction by trapping the enzymes (and their reaction products) in close proximity. The rapid rate of enzyme turnover in this case is crucial to the 3D-printing process. As the gel sets rapidly after mixing with the enzymes, the precursor solution was used as an ink for an extrusion-based printing process. Additionally, this co-localisation of enzymes prevents radical processes from causing significant damage to encapsulated fibroblasts, which showed excellent viability over 48 h.

A simpler approach to 3D-printing was reported in the same year by Fang and co-workers. They synthesised a tetra-substituted calix[4]arene (Figure 1.25a) which formed gels *via* a heat/cool cycle in a range of organoalkoxysilanes.⁹¹ Importantly, these gels demonstrate thixotropy. After breaking by shear, upon removal of the straining force they are able to rapidly recover their original mechanical properties and reform a gel network (Figure 1.25b). By forming a gel in a syringe barrel and applying pressure, the gel could be extruded and reformed *in situ* to create basic 3D-printed shapes (Figure 1.25c). Finer control and reproducibility could in this case be achieved, at least in principle, through the use of a dedicated 3D-printer.

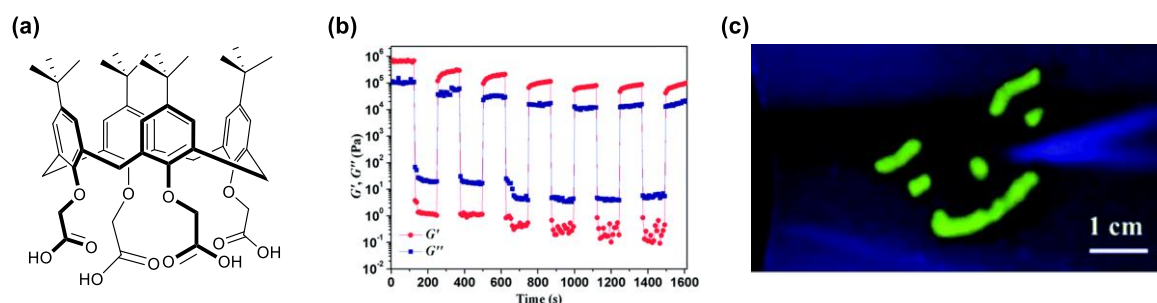


Figure 1.25: Tetra-substituted calix[4]arene (a) form gels in organic solvents. These gels are able to recover their mechanical properties on removal of the applied strain (b). This allows them to be extruded as printed materials (c). Adapted from [91].

More recently, the Adams group have outlined an approach to the design and optimisation of the 3D-printing process for LMWGs.⁹² Using a range of dipeptide hydrogels (Figure 1.26a), they optimised parameters including gelation trigger, extrusion volume and speed, printing height and printer movement speed. Their efforts culminated in the printing of well-defined multi-layered gel structures on the millimetre scale (Figure 1.26b and c). The approach reported here represents the current standard for the development of LMWGs for 3D-printing, and it is expected that it will be further developed by others in the future.

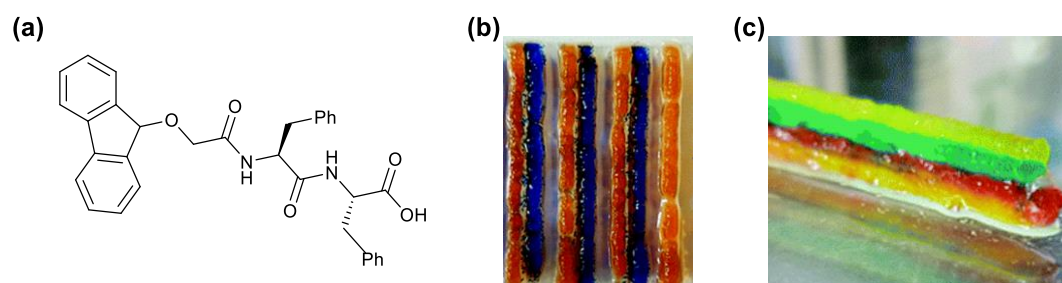


Figure 1.26: Fmoc-diphenylalanine, one example of a dipeptide hydrogelator used to illustrate the optimisation of LMWGs for 3D-printing (a). 3D-printed lines (b) and layers (c) were printed. Dyes were added to each line/layer for clarity. Adapted from [92].

1.3.3 Diffusion-controlled LMWGs

Hierarchical self-assembly is a diffusion-controlled process, in which the rate of transport to the site of fibre nucleation or extension plays a key role in determining the kinetics of gel network formation. This in turn has profound implications for the macroscopic properties displayed by the gel-phase materials.⁹³ Recently, some research groups have looked to exert kinetic control over the diffusion of specific molecules to spatiotemporally control the shape and lifetime of gels.

In a seminal paper, van Esch and co-workers used alginate gels to spatially control the formation of a *tris*-hydrazone hydrogel (see above).⁹⁴ Shaped calcium alginate gels were used to enforce spatial separation of the aldehyde and *tris*-hydrazide gel precursors at the beginning of an experiment. Over time, these species diffused through the alginate matrix and spontaneously formed an opaque gel network upon reaction. Rapid self-assembly of the gel matrix on reaction ensured that well-resolved structures were formed, the final shape of which was determined by the geometries of the reservoir and separating alginate gel. Dissolution of the alginate gel using ethylenediaminetetraacetic acid (EDTA) yielded well-defined and self-standing *tris*-hydrazone gels of multiple millimetres in diameter (Figure 1.27a). Using a fluorescently tagged aldehyde it was also shown that chemical gradients could be introduced into the sample (Figure 1.27b), an important feature for the design of materials for more complex applications such as tissue engineering. To fabricate smaller shaped gels, the researchers employed a wet stamping approach, in which a shaped agar stamp containing dissolved *tris*-hydrazide was pressed onto an alginate gel containing the reactive aldehyde. At the interface between the gels diffusional exchange allows the two components to react in a spatially-defined manner (Figure 1.27c). Gel formation was observed and again the addition of EDTA allowed separation of the *tris*-hydrazone gel from the alginate supporting matrix. Well-resolved objects could be produced down to 300 μm in size and were visualised by fluorescence microscopy.

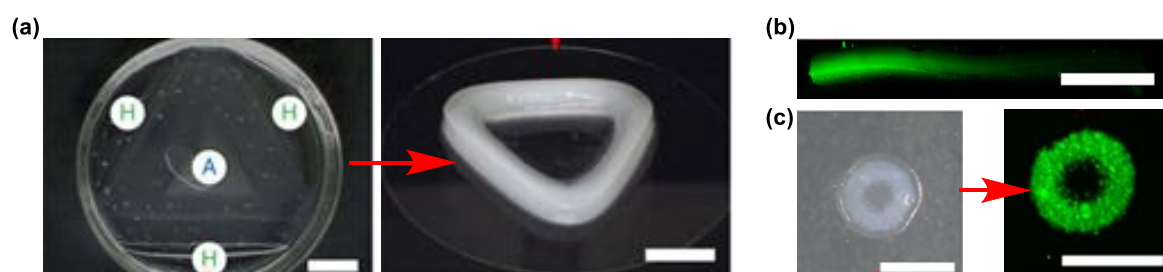


Figure 1.27: Spatially-resolved *tris*-hydrazone gel formation controlled by reaction-diffusion (a). H = *tris*-hydrazide, A = aldehyde. In a reaction-diffusion configuration, a chemical gradient, in this case of fluorescent aldehyde, could be introduced into the free-standing gels (b). Microscale objects were fabricated using a wet stamping methodology (c). Scale bar (a), (b) = 1 cm. Scale bar (c) = 1 mm. Adapted from [94].

Control of reaction-diffusion processes is a new but powerful approach to the spatiotemporal control of gel structure. Limited systems complexity has been achieved thus far, but it can be envisioned that a combination of spatiotemporally controlled gel formation and disassembly approaches outlined above could be used to create dynamic gel-forming processes with programmable kinetic profiles. For example, Bon and co-workers have spatiotemporally controlled

alginate gel breakdown by enzymatic methods.⁹⁵ Defined breakdown of an alginate gel over time could alter favourable diffusion paths of van Esch's gelator precursors. In this way, dynamic spatiotemporal control of macroscale gel shaping could be achieved.

Ruiz-Olles *et. al.* have also studied the structural alteration of an acid/amine two-component organogel caused by diffusion of the gelator precursors across a gel-gel interface.⁹⁶ When two gels containing different combinations of acid and amine were placed in contact, exchange of the gelator components occurred to create a gradient of gel composition across the length of the sample. The nanoscale gel networks were modified across the material and changed with time, again demonstrating how diffusion can be used to create LMWGs with spatiotemporally defined properties.

1.3.4 Surface-patterned LMWGs

Given that the formation of a LMWG is initiated by some external stimulus, patterning these triggers onto a surface is a simple way to spatially-control the formation of a bulk gel. An early example of this approach came from the Ulijn group in 2009.⁹⁷ Through immobilisation of an endoprotease (thermolysin) on a poly(ethylene glycol) (PEG)-coated surface, they were able to confine enzyme activity exclusively to regions where it was covalently bound. Fmoc-phenylalanine was only coupled to a further phenylalanine residue in the regions of enzymatic activity (Figure 1.28a). Rapid self-assembly of the resulting Fmoc-Phe-Phe LMWG meant that gel formation could be spatially defined with excellent resolution. This was visualised using a Congo Red stain (Figure 1.28b). Interestingly, in follow-up work it was shown that the composition of reversibly (non-covalently) and irreversibly (covalently) bound thermolysin on a polymer layer has a significant impact on gelation.⁹⁸ A greater proportion of non-covalently bound enzyme results in a greater gel height compared to when only covalently bound thermolysin is present. A combination of the two studies outlined here could be used to achieve 3-dimensional control of the supramolecular gel shape.

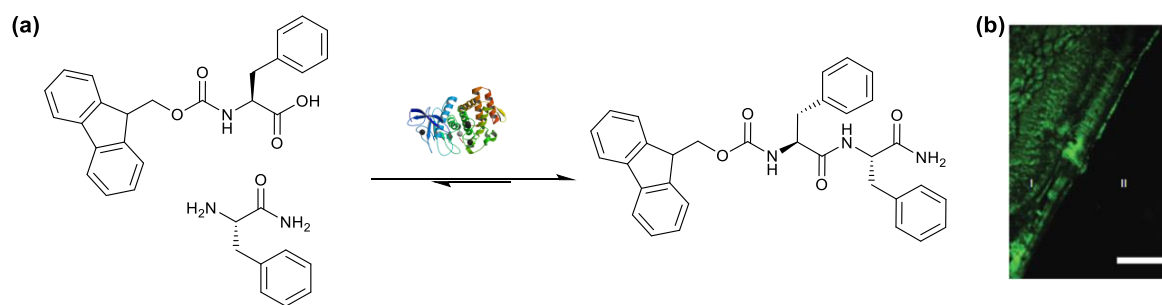


Figure 1.28: Thermolysin catalyses the formation of Fmoc-diphenylalanine from gelator precursors (a). Visualisation of spatially-resolved gel formation using a Congo Red stain under cross-polarised light (b). Green region represents association of Congo Red with self-assembled β -sheets. Scale bar = 0.3 mm. Adapted from [97].

Xu and Vemula have reported several examples of LMWG precursors which self-assemble on cleavage by phosphatase enzymes.^{99–102} Hydrolysis of the phosphate group from an amino acid pre-gelator lowers the solubility of the peptide LMWG and induces self-assembly, enabling the formation of hydrogels capable of controlled drug delivery^{100,103} or enzymatic reactivity.^{49,104} The immobilisation/incorporation of two different enzymes, which promote self-assembly *via* orthogonal reactions, can be envisaged to induce the formation of dual-network hydrogels. For example, the confinement of both thermolysin and alkaline phosphatase specific regions of a gel surface (as described by Ulijn) would enable complex shaping of dual-network peptide hydrogels to be achieved.

Similarly, the van Esch group demonstrated the surface-mediated patterning of their *tris*-hydrazone hydrogel. Rather than using enzymes, they spatially defined the display of sulfonic acid moieties on the surface of a glass slide.¹⁰⁵ When submerged in a solution of *tris*-hydrazide and aldehyde, localised dissociation of the acid catalysed the rapid reaction between pre-gelators in a shape defined by the ‘stamp’ used to pattern the glass slide. Confocal microscopy and AFM were used to confirm that hydrogel patterns down to 10 μm in diameter could be produced with excellent spatial resolution (Figure 1.29a). Interestingly, rapid gel formation prevents protons from diffusing a significant distance from the surface, and as such gels could only be formed up to 5.5 μm in thickness.

An alternative approach to acid-triggered patterning of peptide gels was reported by Adams and co-workers in the same year. In this unique work, patterns of conductive and insulating regions on a fluorine-doped tin oxide (FTO) slide.¹⁰⁶ These slides were submerged in a solution of a dipeptide hydrogelator and hydroquinone. On passage of a current through the FTO slides, hydroquinone undergoes an electrochemical oxidation, liberating two protons. The localised pH change on

oxidation results in the rapid protonation of the dipeptide LMWGs and formation of a gel network in the regions of conductivity. As well as the regions of the slide in which the gels formed, the height of the gel could also be controlled by altering either the applied current or the 'exposure' time of the precursor solution (Figure 1.29b). In contrast to van Esch's acid-catalysed approach to gel patterning, materials with thicknesses in the millimetre range could easily be fabricated *via* this method.

The researchers went on to demonstrate excellent examples of the potential to create complex patterned materials using this system. For example, they fabricated multi-layer gels by exposing a sample of electrochemically patterned gel to another solution of gelator and hydroquinone. They were also able to make multi-domain gels by taking a patterned gel and exposing the previously insulated areas to a current in the presence of a different gelator. Perhaps most impressively however, through careful control of the applied current, slow acidification of a solution of mixed peptide gelators was achieved. As the pK_a of each gelator (see above) was reached, a sample spanning network was formed, with the two networks remaining orthogonal.

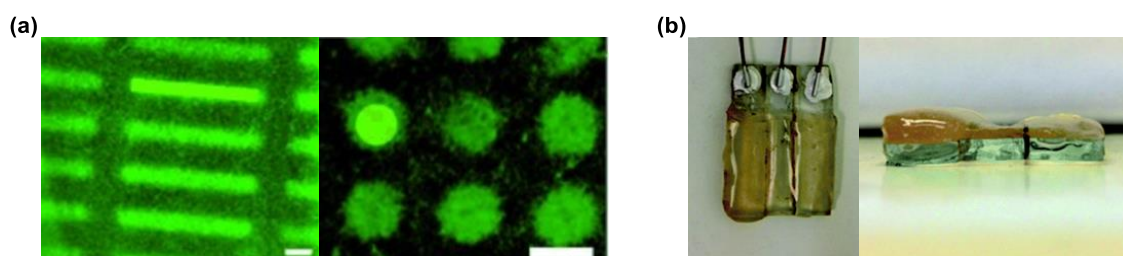


Figure 1.29: Confocal microscopy images of van Esch's surface-patterned tris-hydrazone gels (a). Yellow regions represent the surface pattern dimensions. Adams' electrochemically-triggered dipeptide hydrogels (b). Top (left) and side-on (right) views. Gel thickness was controlled by the applied current and the patterning time. Adapted from [105] and [106].

1.3.5 Self-healing LMWGs

Self-healing gels are of great interest in a diverse range of technologies.^{107,108} In particular, these materials have great potential as healable adhesives and sealants for the aerospace industry, as well as for biomedical applications where injection is required for minimally invasive therapies. An excellent recent review of self-healing LMWGs and their applications in devices was recently published by Li *et. al.*¹⁰⁹ In this report, they highlight a number of 'shaped' materials formed by the 'healing' of two or more low-molecular-weight gel discs to form a cylinder. Various chemistries have been utilised to achieve chemical or physical healing including the formation of dynamic covalent bonds (imines, oximes etc.) or the re-arrangement of nanoscale networks to form enthalpically

favourable non-covalent interactions. In LMWGs, the exchange of material at the gel-gel interface has also been shown to have important implications in the self-healing process.⁹⁶

Examples where self-healing has been used to create more complex shapes than cylinders are few in number. Bera and Haldar described in 2016 the formation of a gel 'gate' by healing of multiple gel cylinders.¹¹⁰ Self-assembly of this material in a range of alcohols occurred specifically on addition of aqueous potassium hydroxide. The specificity of gelation with respect to base suggests that specific interactions between the gelator, potassium cations and hydroxide anions are essential for the assembly and re-healing properties of these materials. These gels were mechanically robust and largely thixotropic, evidencing the self-healing nature of the gel networks.

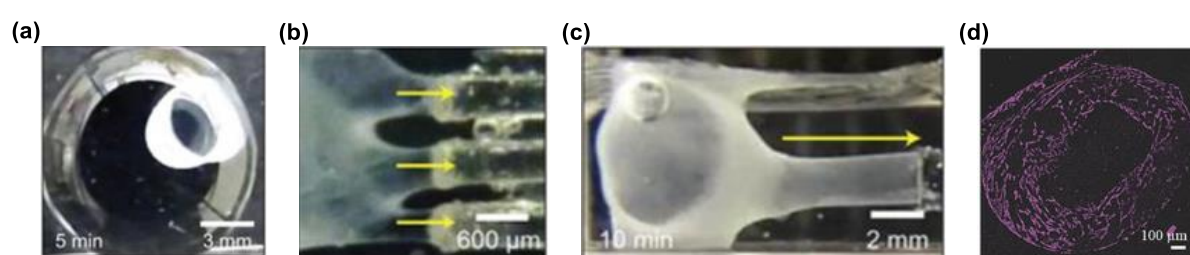


Figure 1.30: Spontaneous separation of peptide amphiphile and protein pre-gelators occurs on mixing (a). Altering the number of interfaces between the gel and an external surface altered the anisotropic gel structure (b and c). NIH/3T3 mouse fibroblasts were formulated into these cytocompatible materials by 3D printing (d). Adapted from [111].

A unique self-healing gel was recently reported by Mata and co-workers. Spontaneous biphasic separation of an elastin-like protein and a peptide amphiphile resulted from the self-assembly of a two-component membrane-like gel at the interface of the two aqueous solutions.¹¹¹ Interactions between hydrophobic domains was postulated to result in this spontaneous self-assembly. Neither of the two pre-gelator species are capable of forming gels, however, non-covalent interactions between these molecules results in alignment and assembly of the two-component gelator. Interestingly, this membrane spontaneously adheres to any surface it comes into contact with. Moving the surface away from the membrane resulted in anisotropic extension of the material to generate complex macroscopic structures (Figure 1.30a-c). Structural integrity of the material was maintained throughout this process due to the assembly of further pre-gelators in a self-healing process. This intriguing self-assembling system has since been combined with 3D-printing technologies to develop defined 3-dimensional materials for cell culture (Figure 1.30d).^{112,113}

1.4 Project Aims

As alluded to above, for LMWGs to find more widespread application, issues regarding the mechanical weakness of these materials must first be addressed. The ubiquitous image of the gel in the upturned vial masks the fact that most are too fragile to be removed from these containers. Similarly, for these materials to be fabricated as devices to interface with systems, whether biological or electronic, the ability to process such materials into a desired shape is essential.

The aim of this project is therefore to combine an industrially-relevant, functional LMWG (Figure 1.31a) with a robust and photo-patternable PG (Figure 1.31b) in a single hybrid material; and to demonstrate its use as a functional material in a variety of applications. To understand the macroscale behaviour of these materials, they must be characterised fully to determine the degree of interaction between the LMWG and PG, and in turn the extent of orthogonality of the two networks. This has important implications on how the two gel networks retain and express their individual properties in a hybrid material. Having developed a photo-patternable hybrid gel, we aimed to use them to achieve a degree of spatial control of three key bio-relevant processes: (i) drug release; (ii) stem cell differentiation; and (iii) enzyme reactivity.

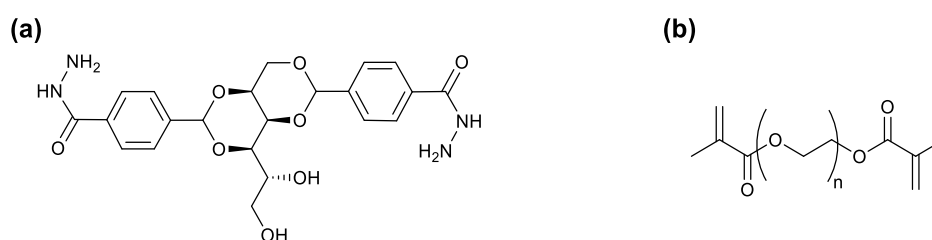


Figure 1.31: Structures of the LMWG (a) and PG (b) used to develop photo-patternable hybrid hydrogels in this thesis.

1.4.1 Drug release

We aim to build on previous work describing the pH-dependent release of carboxylic acid containing drugs by LMWGs.¹¹⁴ By incorporating a orthogonal PG network into this material, it is thought that these materials will be made more robust without significantly hindering the pH-dependent release of the LMWG. Characterisation of the interactions between all three components of this network (LMWG, PG and drug) will help to rationalise any differences seen. In addition, we aim to use photo-patterned materials to spatially control the release of drug molecules, taking this class of material a step closer to application as a controlled/targeted release system.

1.4.2 Enzyme reactivity

The encapsulation of enzymes within a gel matrix is well known. However, examples in which they are formulated within an LMWG are relatively few. Additionally, in all examples, a simple block of an enzyme-loaded gel is added to a reaction mixture. We aim to use a shaped hybrid gel to create diffusion-driven enzyme bioreactors. It was hoped that formulation of an enzyme within a shaped hybrid gel would allow for the conversion of reactant into product to be achieved with a degree of spatial and temporal control, bringing these materials closer to being considered as reactor devices in their own right, rather than as passive reaction additives.

1.4.3 Stem cell differentiation

By confining the formation of the PG network to defined regions in space, spatial control of the mechanical properties of a gel can be controlled. We aim to exploit this spatial resolution to achieve spatial control over stem cell behaviour. The differentiation process, for example, is well known to be dependent on the stiffness of the matrix on which the cells are grown. We aim to characterise the growth of stem cells on each class of gel developed here (LMWG, PG and hybrid gel) and to determine how these materials direct stem cell behaviour.

2 Fabrication and Characterisation of Spatially-Resolved Hybrid Hydrogels

Aspects of this research have been published in: P. R. A. Chivers and D. K. Smith, *Chem. Sci.*, 2017, **8**, 7218-7227.

2.1 Introduction

As seen in Chapter 1, examples of hybrid hydrogels are somewhat rare. Considered choices of gelators with assembly methods which are orthogonal and compatible with each monomer species are necessary to create functional materials combining the properties of both individual gel networks. As such, researchers often turn to thoroughly studied families of gelators. In this thesis, we have focused on a single derivative of each of the LMWG 1,3:2,4-dibenzylidene-D-sorbitol (DBS), and the PG poly(ethylene glycol) (PEG), both of which are well-established gelator frameworks.

2.1.1 DBS gels

The first reported synthesis of DBS came as early as 1981. Meunier described the formation of this compound *via* the acid-catalysed condensation of D-sorbitol with two equivalents of benzaldehyde (Figure 2.1).¹¹⁵ A mixture of compounds was obtained, which was originally ascribed to the formation of isomeric diacetal species. This interpretation was later revised in the light of structural studies carried out by Wolfe in the early 1940s.¹¹⁶ They first showed that a non-gelling mixture of mono-, di- and tri-substituted derivatives were formed during the reaction procedure. Treatment with triphenylmethyl chloride showed only the presence of a single DBS-structure containing only one tritylated alcohol. Acid hydrolysis of this 6-OH protected DBS-derivative resulted in the formation of L-xylose, confirming acetal substitution in the 1, 2, 3 and 4-OH positions. Angyal and Lawler carefully hydrolysed DBS to yield 2,4-monobenzylidene-D-sorbitol, confirming the now accepted 1,3:2,4 acetal substitution pattern.¹¹⁷

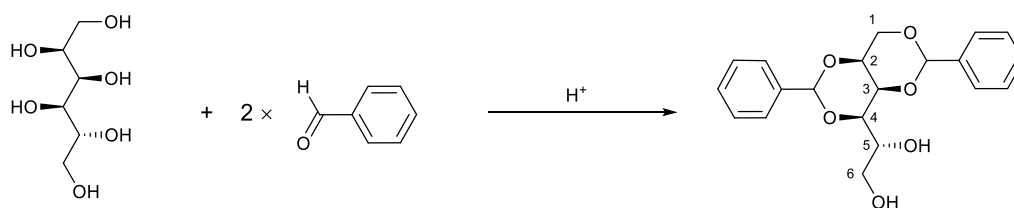


Figure 2.1: Meunier's synthesis of DBS from D-sorbitol and benzaldehyde.

In the years since its discovery, DBS has become widely used in a range of commercial products.¹¹⁸ It is present as a textural modifier in a range of personal care products^{119–126} and is formulated into plastics where it acts as a clarifying agent.^{127–131} To tailor the properties of this LMWG for the different applications outlined above, extensive research into the derivatisation of DBS has been carried out. A wide range of functional groups have been installed on the aromatic ‘wings’ of the LMWG, including halogens^{132,133}, amines,¹³⁴ acyl hydrazones,¹³⁵ and alkyl groups.¹³³ Functionalisation of the reactive 6-OH position is also relatively common, whilst protection of this primary alcohol allows facile derivatisation at the 5-OH position.^{136,137} Alternatively, by using glucono- δ -lactone as the starting “sugar”, a gluconic acid derivative with only one free alcohol in the 5-position was obtained.¹³⁸ Functionalisation of the 5-OH followed by reduction of the acid yielded this type of DBS-derivative in fewer steps than by traditional protection/deprotection strategies. In unique work, Xie *et. al.* showed that by using a modified sorbitol as reagent, functionalisation at the 1-position of the sugar chain was possible.

More recently, studies regarding the nature of the self-assembled structures in DBS-based gels have begun to emerge. Modification of the 6-OH demonstrated the importance of this moiety in the self-assembly process in non-polar solvents – no gelation was observed on its conversion into a methoxy group, whilst functionalisation with a hydrogen bond donor moiety did not prevent self-assembly.¹³⁹ In contrast Watase *et. al.* showed that π - π stacking was the major attractive interaction between monomers in polar solvents.¹⁴⁰ Interestingly, the consequence of the differences in assembly mechanisms is manifested in changes in the nanoscale network morphology (Figure 2.2).¹⁴¹ Planar stacking resulting from π - π interactions in polar solvents results in the formation of straight nanofibres as observed by SEM. In contrast, a slight twisting is induced to minimise the energy of the structures formed by interactions between the 6-OH and acetal oxygens of adjacent monomers.¹⁴² This confers helicity onto the nanoscale structures observed.

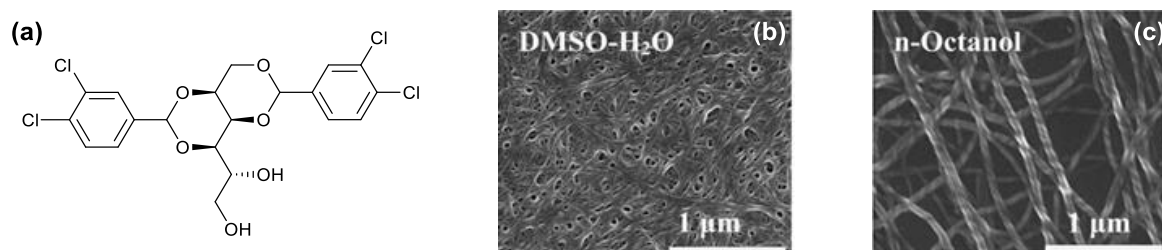


Figure 2.2: Structure of 1,3:2,4-di(3,4-dichloro benzylidene)-D-sorbitol studied by Song and co-workers (a). This DBS derivative self-assembled into straight nanofibres in 7:3 DMSO-H₂O (b) and helical nanofibres in n-octanol. Adapted from [141].

Despite the large library of DBS derivatives reported to date, surprisingly only three examples of hydrogelators have been developed within this family of molecules. Using a divergent synthetic procedure the Smith group synthesised DBS derivatives functionalised at the *para*-position of the aromatic 'wings' with either a carboxylic acid⁵³ (DBS-CO₂H) or an acyl hydrazide¹⁴³ (DBS-CONHNH₂). The incorporation of these relatively polar groups overcame the solubility issues preventing dissolution and gelation in water associated with this class of molecule. The two LMWGs form sample spanning networks in water at relatively low concentrations, but using different triggering mechanisms – DBS-CO₂H forms in response to acidification, whilst DBS-CONHNH₂ forms *via* a heat/cool cycle. Reaction of DBS-CO₂H with the amino acid glycine yielded another pH responsive LMW hydrogelator with a pK_a value distinct from that of its precursor.⁸⁴ The development of these LMW hydrogels opens the possibility of DBS-based materials to be used for biomedical applications.

2.1.2 PEG gels

Poly(ethylene glycol), also known as poly(ethylene oxide), is a commercially available polymer which is widely used for tissue engineering^{144–146} and drug delivery.^{147–150} Its relatively low cost, biocompatibility and low toxicity make it suitable for these applications. In addition the flexibility and electron donation ability of PEG gels makes them suitable materials for energy storage devices as electrolytes/polymeric separators.¹⁵¹

Covalent crosslinking of the PEG 'monomers' results in the formation of a solvent-encapsulating, sample-spanning network. This crosslinking can be initiated by a number of methods,^{152–156} the most common of which is UV-irradiation^{157–159}. These techniques are compatible with a range of alkene-derivatised PEG species. Reaction at one or both of the hydroxyl end groups can yield PEG bearing acrylate or methacrylate groups which facilitate the crosslinking process.^{160,161} Copolymerisation of these species with bioactive species (for example Arg-Gly-Asp sequences or peptides)^{36,162–165} and the incorporation of degradable linking groups^{166–169} has imbued this type of hydrogel with great versatility, which has contributed to its widespread use in biomaterials research.

The chain length of crosslinked PEG hydrogels can have a significant impact on its properties. At the same concentration (% wt/vol) crosslinked PEG diacrylate and PEG dimethacrylate gels are significantly less stiff than their short-chained counterparts, presumably due to the presence of a greater number of cross-linkable moieties in the latter. However, low molecular weight PEG gels were also more brittle (less elastic), demonstrated lesser release of bioactive molecules and showed comparatively poor cell viability over 7 days (Figure 2.3).^{170–173} These effects must be

considered when selecting a specific mass fraction polymer for a given application, however the rationale for these decisions is often omitted from publications.

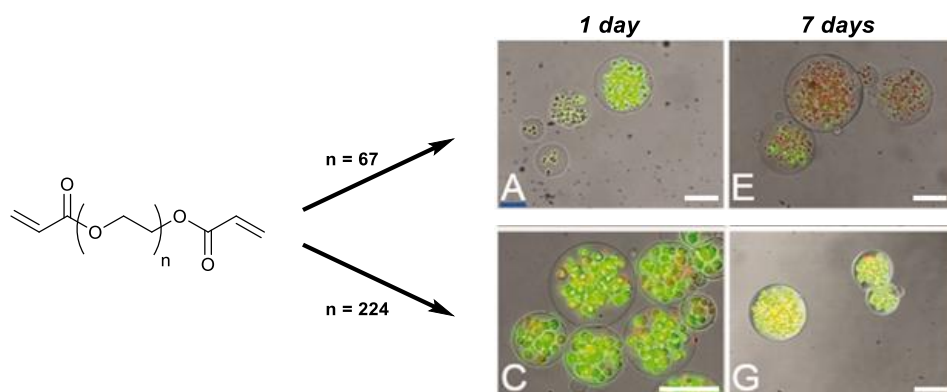


Figure 2.3: PEG diacrylate hydrogels with different polymer chain lengths display different cell viability. Gels with average molecular weight 3,000 Da showed poor cell viability (A and E) whilst a gel formed from PEG diacrylate with average mass 10,000 Da showed good cell survival over the same timeframe. Green cells = live, red cells = dead. Adapted from [171].

2.2 Chapter aims

In this chapter we aimed to develop a novel hybrid hydrogel based on a commercially relevant LMWG (DBS-CONH₂) and a photo-patternable PG (PEGDM). It was hypothesised that the orthogonal assembly of the two gel networks would allow us to harness the desirable properties of each class of material, namely the stimulus-responsiveness of the LMWG and the robustness of the PG. Having demonstrated the formation of such a hybrid gel, we targeted the full characterisation of the materials on a number of length scales:

- i) The **macroscopic** properties of the material were analysed using techniques such as rheology
- ii) The **nanoscale** morphology of the network was observed through electron microscopy
- iii) On the **molecular** level we probed gelator interactions using NMR and IR spectroscopy

The incorporation of PEGDM as a PG in this system will also allow us to induce spatial control over the gel properties. We aimed to exemplify the spatially-controlled application of light (photo-patterning) as a method to define the areas under which the photo-polymerisation of the polymeric species occurs and demonstrate that the changes in material properties are confined to those regions where exposure to UV light is allowed.

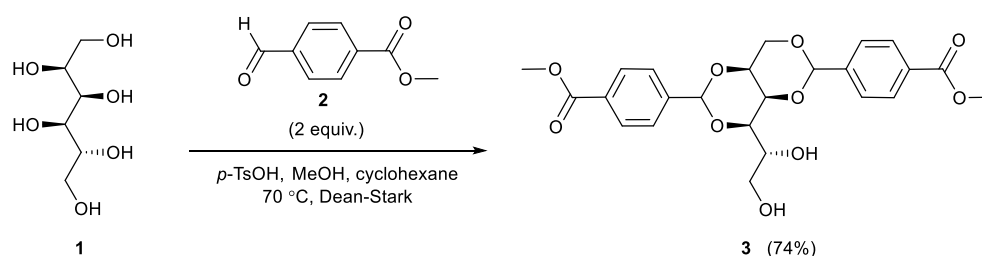
Given the range of applications we envisaged these hybrid gels being utilised for, we elected to use a medium-sized PEG chain length for these studies. Whilst less stiff (an important consideration for

tissue engineering applications) we also considered the greater cell viability and greater rate of small molecule diffusion associated with this chain length compared to shorter analogues.

2.3 Synthesis of Gelators

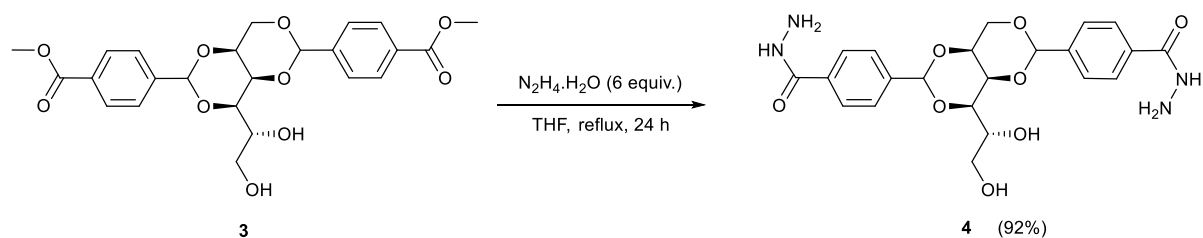
2.3.1 Synthesis of 1,3:2,4-dibenzylidene-D-sorbitol-*p,p'*-diacyl hydrazide (DBS-CONHNH₂)

1,3:2,4-Dibenzylidene-D-sorbitol-*p,p'*-dihydrazide (DBS-CONHNH₂) was synthesised in two steps as previously reported by Okesola *et. al.* (Scheme 2.1).¹⁴³ First, the acid-catalysed condensation of D-sorbitol (**1**) with two equivalents of methyl-4-formyl benzoate (**2**) under Dean Stark conditions yielded a mixture of mono-, di- and tri-substituted benzylidene methyl esters. The desired di-substituted compound, 1,3:2,4-dibenzylidene-D-sorbitol-*p,p'*-dimethyl ester (DBS-CO₂Me, **3**) was isolated by washing the crude mixture first with boiling dichloromethane (DCM, to remove the tri-substituted derivative), then with boiling water (to remove the mono-substituted compound). This yielded **3** in good yield. No features corresponding to starting material or undesired side-products were observed by either NMR or mass spectrometry, suggesting the product was obtained with good purity (*ca.* 95%). To ascertain whether a greater level of purity is achieved by this method, further characterisation techniques, such as elemental analysis or high-pressure liquid chromatography, need to be employed.



Scheme 2.1: Synthesis of DBS-CO₂Me.

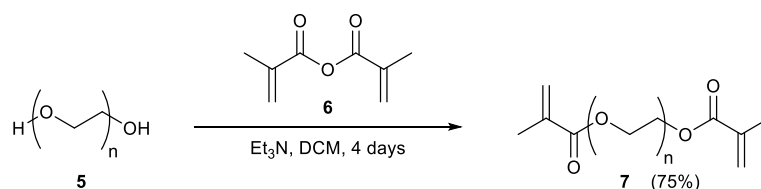
The reaction of **3** with a large excess of hydrazine monohydrate (Scheme 2.2) under reflux resulted in formation of 1,3:2,4-dibenzylidene-D-sorbitol-*p,p'*-diacyl hydrazide (DBS-CONHNH₂), **4**. This nucleophilic substitution reaction proceeds in excellent yield and the compound was isolated on the gram scale without the need for column chromatography. Again, no evidence of impurities were observed by NMR or mass spectrometry, and the purity of the compound is estimated at *ca.* 95%. A greater level of purity has not been ascertained at this time, and the presence of some impurities cannot be ruled out, a factor which must be considered when interpreting the results in subsequent chapters.



Scheme 2.2: Synthesis of DBS-CONHNH₂.

2.3.2 Synthesis of poly(ethylene glycol) dimethacrylate

Poly(ethylene glycol) dimethacrylate (PEGDM), with an average molecular mass of 8000 Da was synthesised as previously reported (Scheme 2.3).^{55,160} Poly(ethylene glycol) (**5**, Average M_w = 8000 Da) was stirred in dry DCM for 4 days in the presence of triethylamine and methacrylic anhydride (**6**) to yield the desired compound (**7**), which was isolated by filtration through alumina and precipitation in diethyl ether. Yields for this reaction were variable (*ca.* 30-80%) but were enhanced by using ice cold diethyl ether and elution with a large volume of DCM. Consistent yields in the region of 60-80% could be achieved by control of these parameters. The purity of these compounds, as above, are estimated at *ca.* 95% based on NMR and mass spectrometric analysis. Whilst every effort was taken to remove residual DCM from the product, the presence of small amounts of this solvent has not been confirmed by elemental analysis at this time. Again, this must be taken into consideration, in particular regarding the findings relating to stem cell growth in Chapter 5.



Scheme 2.3: Synthesis of PEGDM.

2.4 Preparation of Hydrogels

2.4.1 Preparation of DBS-CONHNH₂ hydrogels and initial characterisation

DBS-CONHNH₂ gels were prepared by weighing out a known amount of gelator in 0.5 mL deionised H₂O. Dispersion of the solid in solution followed by heating to dissolution and subsequent cooling under ambient conditions resulted in the rapid formation of LMW hydrogels. A qualitative assessment of gel formation was carried out initially. The so-called 'inversion test' was utilised for this purpose.¹⁷⁴ In this test the mould in which the material has been formed is inverted. Should a

sample-spanning network have formed, bulk flow of the liquid phase is prevented and the gel remains at the base of the container. Using the inversion test, it was found that DBS-CONHNH₂ forms hydrogels (Figure 2.4a) over a relatively narrow concentration range (4-10 mM, 0.19-0.47% wt/vol). Both above and below this concentration, on cooling after dissolution, DBS-CONHNH₂ precipitated from the solution without forming a uniformly dispersed sample-spanning network.

NMR spectroscopy was used to assess the proportion of DBS-CONHNH₂ gelator which had undergone self-assembly. Monomeric species (i.e. free gelator) has a longer T_2 relaxation time due to their relative freedom to tumble and diffuse in solution. This gives them well-defined peaks in an NMR spectrum. In contrast, nanofibrillar assemblies are much more constrained and therefore are not observed in the spectrum due to peak broadening. Using this knowledge, the relative proportions of a gelator species present in the solution and gel-phase respectively can be inferred by comparison to a mobile internal standard.

A DBS-CONHNH₂ hydrogel was formed in an NMR tube by addition of a hot solution of gelator (6 mM, 0.7 mL in D₂O) containing DMSO (0.04% vol/vol) as internal standard to a hot NMR tube. Comparison of the relative integrals of the aromatic peaks of DBS-CONHNH₂ to the DMSO standard confirmed that for gels prepared at a concentration of 6 mM, less than 0.01% of the gelator is free in solution after the heat/cool cycle. DBS-CONHNH₂ has previously been reported to be stable across a wide range of pH values,⁵⁰ likely due to the relatively low pK_a of the acylhydrazide moiety (typically *ca.* 2-4).^{52,53}

2.4.2 Preparation of PEGDM hydrogels

PEGDM hydrogels were fabricated by dissolution of a known mass of gelator in 0.5 mL H₂O with 2-hydroxy-4'-(2-hydroxyethoxy)-2-methylpropiophenone (0.05% wt/vol) as a photoinitiator (PI), followed by exposure to a high-powered UV lamp. This concentration of PI was chosen as it has previously been shown to be effective for initiation of radical crosslinking reactions whilst remaining compatible with a range of cell types in *in vitro* and *in vivo* experiments.^{177,178} UV exposure for 0.5 h induced in the crosslinking of the polymer chains and resulted in gel formation at a minimum concentration of 3% wt/vol (Figure 2.4b) and a maximum of 60% wt/vol, again assessed *via* tube inversion. Below the minimum gelation concentration (MGC), there may be insufficient crosslinking to induce the formation of the sample-spanning network. Above 60% wt/vol PEGDM the polymer was not completely soluble.

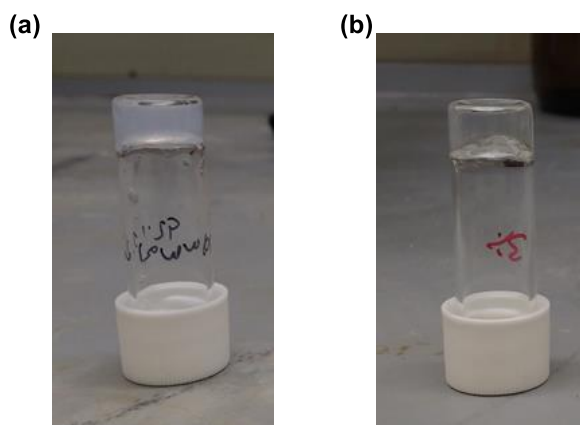


Figure 2.4: Representative images of inverted hydrogels formed from 6 mM DBS-CONH₂ (a) and 3% wt/vol PEGDM (b).

2.4.3 Preparation of DBS-CONH₂/PEGDM hybrid hydrogels

As a result of the different assembly methods of the two gelators, it was envisaged that the LMWG and PG could be fabricated as a dual-network hydrogel. The formation of orthogonal gel networks would in theory allow us to utilise the desirable properties of the two individual materials. Initially, we attempted to prepare such a material *via* a method similar to that described by Cornwell *et. al.* for DBS-CO₂H/PEGDM hybrid gels.⁵⁵ They reported that orthogonal photo-polymerisation and LMWG self-assembly could be initiated from a mixed solution of the two gelators. In our case, the rapidly forming DBS-CONH₂ network would be formed first by a heat/cool cycle, after which UV exposure would cross-link the PG network.

DBS-CONH₂ (6 mM) was suspended in an aqueous solution of PEGDM (5% wt/vol) and PI (0.05% wt/vol) by sonication. On heating the DBS-CONH₂ dissolved, but the solution became cloudy, possibly due to aggregation of the polymers in solution. On cooling, a weak LMWG network was formed. Qualitatively, this appeared less stable than DBS-CONH₂ gels formed in the absence of PEGDM and PI. This can be rationalised by a difference in solubility of the LMWG in water and the more hydrophobic PEGDM solution. A DBS-CONH₂ hydrogel submerged in a PEGDM solution does not dissolve however, suggesting that the presence of the PG may disrupt the fibre nucleation/aggregation process.

Due to the imperfect gelation from using this directly mixed system, we developed an alternative method to formulate PEGDM into the DBS-CONH₂ gel (Figure 2.5). First, the DBS-CONH₂ gel (6 mM) was formed *via* a heat/cool cycle. Following network formation, a solution of the same volume as the LMWG and containing a known concentration of PEGDM and PI was pipetted on top

of the LMWG. This solution was left for 3 days to allow an equilibrium to be reached, after which time the supernatant was removed. Exposure of this gel to UV light for 0.5 h resulted in a noticeable stiffening of the sample, confirming that a proportion of the PEGDM had diffused into the pre-existing gel network and subsequently been polymerised. This was also confirmed by the appearance of peaks corresponding to the ethylene glycol moiety in the NMR spectrum of a sample prior to UV-exposure. Both before and after the photo-polymerisation step, no DBS-CONH₂ was seen in the spectrum, suggesting that diffusion of PEGDM into the gel and formation of the second PG network does not result in significant disassembly of the LMWG nanofibres. Hybrid gels formed by this method will be referred to as $x\%$ hybrid, where x is the concentration of PEGDM in the supernatant (wt/vol). It should be noted, however, that not all of this PEGDM will have diffused into the gel (see below for quantification).

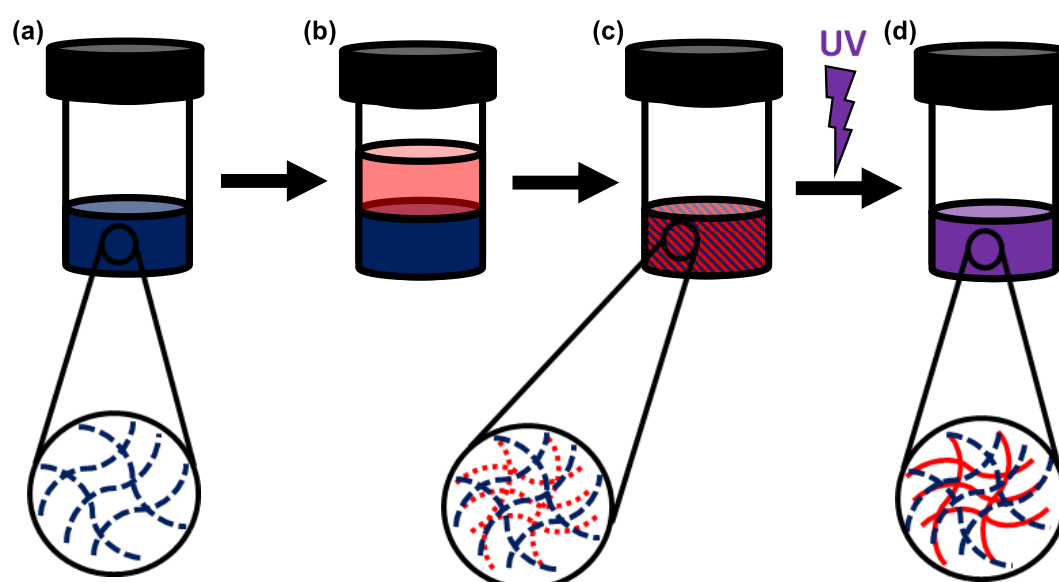


Figure 2.5: Schematic representation of the hybrid gel fabrication process. A DBS-CONH₂ hydrogel is formed first via a heat/cool cycle (a). A solution of PEGDM and PI is pipetted on top (b) and left for 3 days for these species to diffuse into the gel (c). The supernatant is removed and the PEGDM photo-polymerised by exposure to UV light (d).

2.5 Characterisation of Dual-Network Hydrogels

2.5.1 Quantification of hybrid hydrogel PEGDM content by NMR

To quantify PEGDM incorporation into the low-molecular-weight gel (0.5 mL), we again formed a DBS-CONH₂ gel and then pipetted a solution of a known concentration of PEGDM on top. The supernatant was removed and the gel dried *in vacuo* after a defined period of time. The contents of the gel were then fully dissolved in DMSO-*d*₆ and analysed by ¹H NMR. Given that the concentration of DBS-CONH₂ in the sample is known (6 mM), it was possible to quantify the

PEGDM content of the gel by comparison of the integrals of non-overlapping peaks in the spectrum (Figure 2.6). Using a calibration curve of peak integral ratio against mass of PEGDM - plotted by dissolving known quantities of PEGDM monomer and DBS-CONH₂ in DMSO-*d*₆ – data regarding the effect of time (Table 2.1) and PEGDM concentration (Table 2.2) on uptake were deduced.

The quantity of PEGDM taken up by the gel, as expected, increases over time (Table 2.1). A time period of 3 days maximised uptake. Additionally, the concentration of the supernatant determines the final concentration of PEGDM in the hybrid gel (Table 2.2). As expected, a higher PEGDM concentration in the solution results in a higher overall uptake into the gel. A similar uptake by mass was observed for solutions of identical concentrations, but different volumes. This data thus confirms that 3 days is sufficient to allow equilibration of PEGDM uptake into the gel and quantifies the concentration of PG in the hybrid gels. Interestingly, the uptake of PEGDM is greater than expected based on simple equilibration of concentration (50% for 0.5 mL supernatant, 33% for 1 mL). It is possible that the PEGDM monomers favour the more hydrophobic environment in the DBS-CONH₂ hydrogel, and therefore partitions preferentially into this phase.

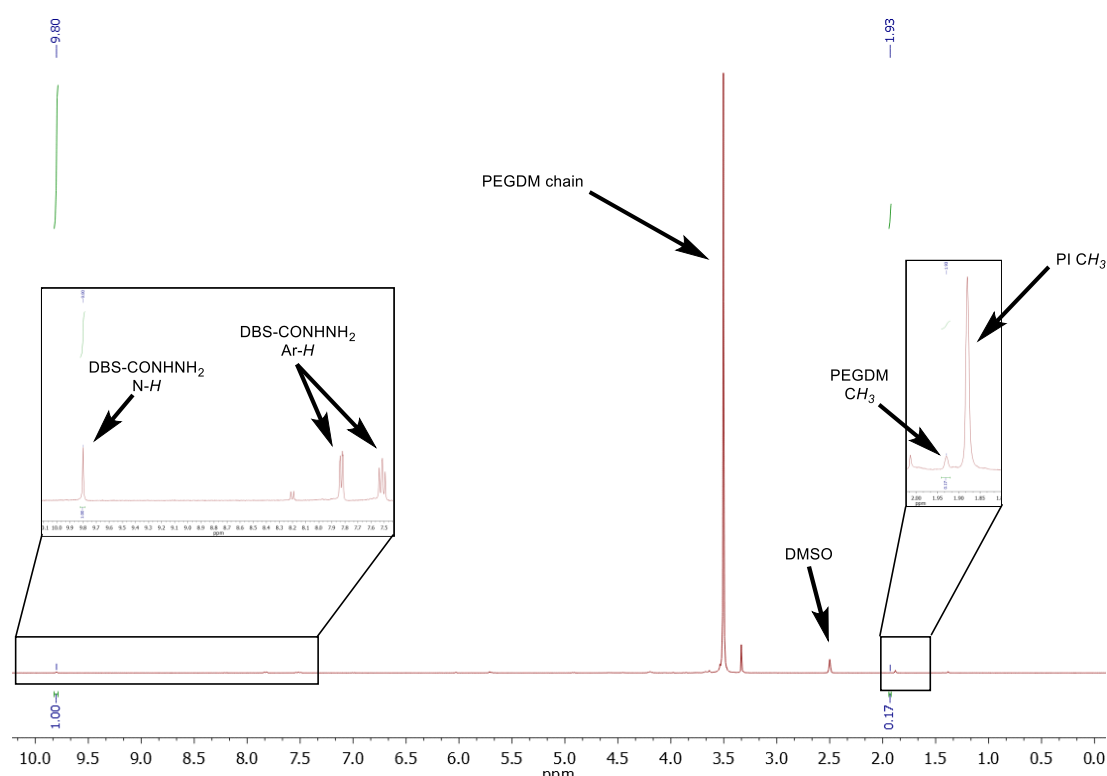


Figure 2.6: Representative NMR spectrum of a hybrid gel (10% wt/vol PEGDM, 24 h diffusion), dried and dissolved in DMSO-*d*₆ prior to UV exposure. Peaks at 9.80 (DBS-CONH₂) and 1.93 (PEGDM CH₃) were used to calculate the percentage PEGDM diffused into the gel.

Table 2.1: Uptake of PEGDM from a solution of concentration 10% wt/vol (0.5 mL) over time. Hydrogels of volume 0.5 mL were used in this study and were not exposed to UV light before analysis. Errors given as standard deviation (n = 3).

Time / h	PEGDM uptake / mg	% uptake	PEGDM conc in gel / % wt/vol
24	15 ± 8	30 ± 16	3.0 ± 1.6
48	31 ± 10	62 ± 20	6.2 ± 2.0
72	41 ± 4	82 ± 8	8.2 ± 0.8

Table 2.2: Uptake of PEGDM into DBS-CONHNH₂ hydrogel after 3 days. Hydrogels of volume 0.5 mL were used in this study and were not exposed to UV light before analysis. Errors given as standard deviation (n = 3).

PEGDM mass / mg	Supernatant volume / ml	PEGDM conc (sol) / % wt/vol	PEGDM uptake / mg	% uptake	PEGDM conc in gel / % wt/vol
15	0.5	3	13.5 ± 0.5	90 ± 3	2.7 ± 0.1
25	0.5	5	22.2 ± 0.2	89 ± 1	4.5 ± 0.1
35	0.5	7	27.3 ± 1.4	78 ± 4	5.5 ± 0.3
50	0.5	10	43.2 ± 1.0	86 ± 2	8.6 ± 0.2
50	1	5	27.5 ± 1.5	55 ± 3	5.6 ± 0.3

These studies were carried out in sample vials with diameter 1.0 cm. Samples prepared in these vials have a smaller ratio of the gel:sol interface area to gel volume than those prepared in the vials/moulds described later. It was therefore considered likely that the diffusion processes in this setup would be slowest, and therefore that a diffusion time of 3 days for all samples would result in samples with similar properties regardless of container dimensions.

The influence of errors on these results was minimised by regular calibration of the equipment used (weighing balance, Gilson pipette). In particular, this should minimise the influence of systematic errors on the results here. The effect of instrument precision on random error has also been considered. The error associated with the mass of gelator measured is ± 0.005 mg, and the precision of the 1000 µL pipette is ± 1 µL. Therefore, for this experiment, the error associated with the weighing out of DBS-CONHNH₂ and PEGDM are 0.25% and 0.03% respectively. Pipetting error was calculated as 0.14%. The total error associated with reagent quantity measurement is 0.42%. In addition to this, errors associated with NMR experiments can typically be 5%. In addition to these errors, whilst the greatest efforts were taken to make the gel formation process consistent, the

nature of the heat/cool cycle is such that complete reproducibility cannot be ensured. The random error associated with the readings here is therefore expected to be in excess of 5%. This is in line with the errors reported in the measurements in Tables 2.1 and 2.2.

2.5.2 T_{gel} studies

We initially probed the macroscopic properties of the prepared gels. Using the tube inversion method described above, the response of selected hydrogels to changes in temperature was determined. Gels (0.5 mL) were prepared in sample vials (diameter 1 cm) and placed in a thermoregulated oil bath. The temperature was raised slowly ($0.5\text{ }^{\circ}\text{C min}^{-1}$) and the vials inverted at each whole degree. The gel-sol transition temperature (T_{gel}) was recorded as the temperature at which the gel no longer adhered to the surface of the vial (Table 2.3). As is often reported for LMWGs, the thermal stability of the DBS-CONH NH_2 hydrogel network improves with increased gelator concentration. Increasing the PEGDM loading in the hybrid gel also raises the T_{gel} due to an increase in the crosslinking density of the material and an increase in the number of adhesion points with the glass surface. The anticipated errors associated with measurement are anticipated to be similar to those noted above. In addition, vial inversion may disrupt the gels, introducing a high degree of potential error in the readings here. The qualitative nature of this T_{gel} study makes it difficult to estimate errors by comparison to prior literature, however the trends observed here are in line with a similar hybrid gel reported by Cornwell *et. al.*⁵⁵

Table 2.3: T_{gel} values of DBS-CONH NH_2 and UV-cured hybrid gels. Errors given as standard deviation ($n = 3$).

DBS CONH NH_2	PEGDM	$T_{gel} / ^{\circ}\text{C}$
6 mM	-	80 ± 1
8 mM	-	94 ± 1
6 mM	5%	85 ± 2
6 mM	7%	91 ± 1
6 mM	10%	> 100

2.5.3 Rheological studies

To further study the macroscale properties of these gels, we employed parallel plate rheology to characterise the mechanical properties. Rheology is a technique which measures the response of a bulk material to the application of an oscillatory shear stress.^{179,180} A perfectly elastic material will

demonstrate an oscillatory strain proportional to and exactly in phase with the applied stress at any moment (phase angle, $\delta = 0^\circ$). Conversely, a perfectly viscous material will have a strain curve out of phase with the applied stress by 90° . For viscoelastic materials, the reality will be somewhere between the two ($0^\circ < \delta < 90^\circ$). Conversion of the phase angle into two components, one describing the elasticity of the material (G') and one describing the viscosity (G'') can be achieved using the following treatments:

$$G' = G^* \cos\delta \quad \text{Equation 2.1}$$

$$G'' = G^* \sin\delta \quad \text{Equation 2.2}$$

G' , the storage modulus, represents the amount of stress stored in the material as energy, whilst G'' represents the dissipated energy and is known as the loss modulus. G^* is the complex shear modulus and is calculated from the ratio of the applied stress and the observed material strain.

A value of G' greater than that of G'' is characteristic of the gel phase. A simple measurement of the viscoelasticity of the material of interest can therefore quickly reveal whether or not the sample is a gel or some other phase (e.g. a viscous liquid would show $G'' > G'$, but may not flow on tube inversion). Additionally, the magnitude of G' and G'' reveal information regarding the stiffness of the gel whilst the point at which the two values become equal can be considered the maximum stress the material can withstand. Measurement of these properties with increasing temperature provides an alternative measure of the T_{gel} for comparison to the methods outlined above.

In an effort to minimise systematic errors, the rheometer used was periodically calibrated using viscous liquids with known rheological behaviour. Random error in the experiments described below can be introduced by a number of sources. Similar sources of error as described above were expected with regards to the quantities of gelator and water used (total no more than 0.5%). Additionally, for this particular technique, differences in the adhesion of the gel-phase materials to the upper and lower rheometer plates can be significant. The effects of slight differences in sample slipping can be significant. These typically account for errors in rheological measurements on the order of 10%. Errors of this magnitude (measured as the standard deviation of the mean) are typical of the data presented in this thesis. Where sample slipping results in greater error this is noted in the figure legends.

First, we monitored the gel properties in response to an applied shear strain whilst maintaining a constant frequency (Figure 2.7). In general, the G' value of the hybrid gels was very similar to a PEGDM gel of the same concentration – for both types of material the stiffness increases with PEGDM concentration. This suggests that the polymer component of these materials is dominant

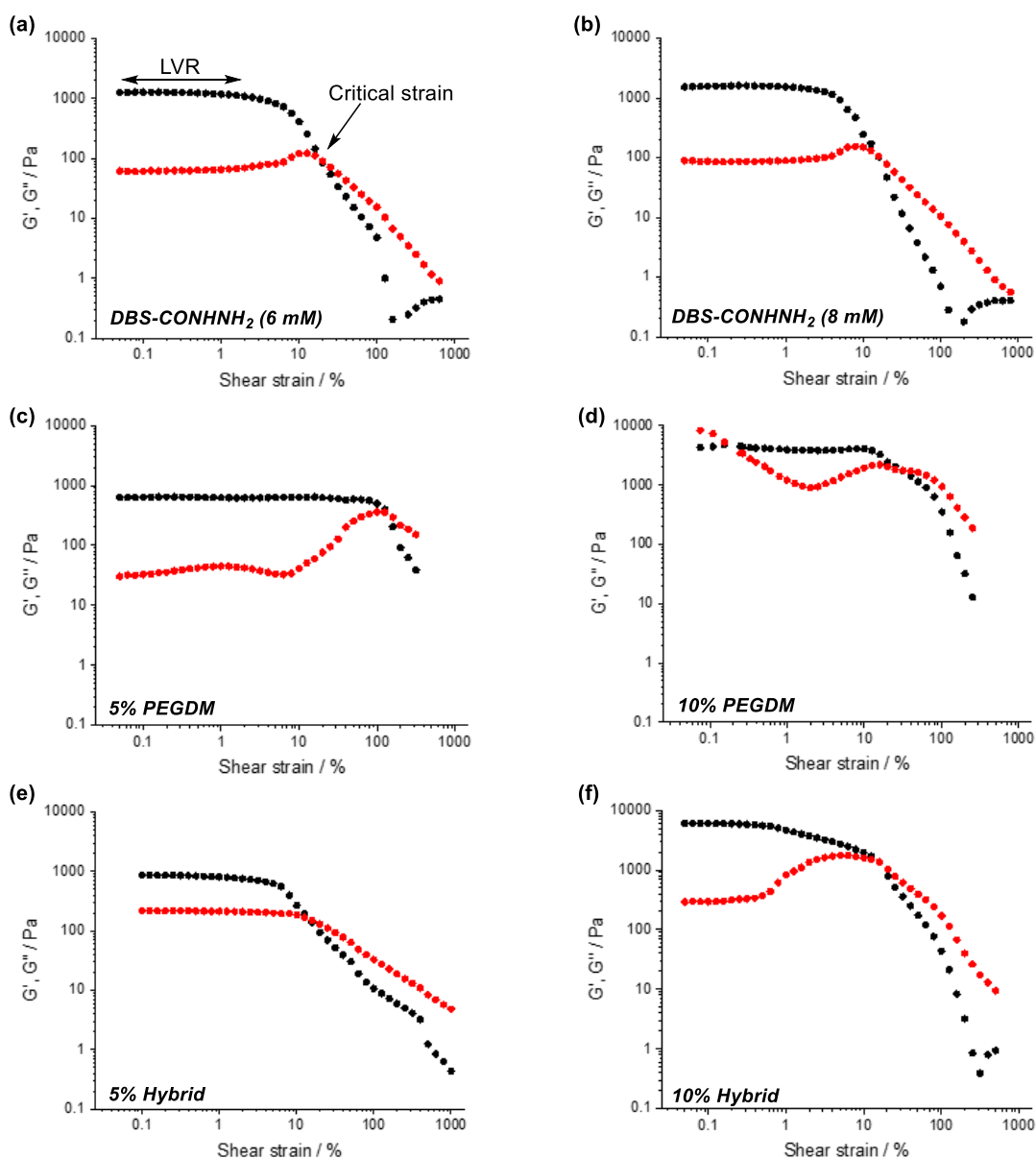


Figure 2.7: Storage (G' , black) and loss (G'' , red) moduli of the different prepared hydrogels in response to varying shear strain at a constant frequency (1 Hz). Rheological traces for: 6 mM DBS-CONH₂ (a), 8 mM DBS-CONH₂ (b), 5% PEGDM (c), 10% PEGDM (d), 5% hybrid (e) and 10% hybrid (f). Features of interest are highlighted on the trace of 6mM DBS-CONH₂ (a). Errors are ca. $\pm 10\%$ for all samples.

in determining the stiffness of these materials. Of particular interest is the 10% hybrid gel. This material has a stiffness significantly (ca. three times) greater than DBS-CONH₂ gels (Figure 2.8a). By comparing the values at which G' and G'' cross over (the critical shear strain) the resistance of the gels to deformation can also be determined. DBS-CONH₂ gels yield at shear strains of 13 and 20% at 6 mM and 8 mM respectively. For PEGDM hydrogels this process occurs at >100% strain. The hybrid gels break down at intermediate values of ca. 30%. Clearly, both networks have an

impact on the ability of the gels to resist changes in strain, but the incorporation of the crosslinked PG network makes the hybrid both stiffer and more resistant to strain than the LMWG alone. These changes account for the relative robustness and ease of handling of the hybrid gels compared the DBS-CONH₂ gels (see above).

Significant differences in the shapes of the traces corresponding to DBS-CONH₂ and PEGDM hydrogels are observed. The value of G'' increase significantly in the latter prior to the decrease in G' value associated with breakdown of the gel state. By comparison, only a small increase in G'' is observed in the LMW hydrogels. We propose that these differences are due to the differences in the response of the two network types to the increasing strain. The more elastic, covalently-crosslinked PEGDM network likely undergoes significant rearrangement with increasing shear prior to breaking down. The dip in G'' at low shear in the 10% PEGDM gels is reproducible and may also be the result of nanoscale rearrangements. Due to the non-covalent nature of the bonding in the DBS-CONH₂ gels, the nanofibres are less able to dissipate energy in this manner and therefore only a small increase in G'' is seen before the crossover point. Interestingly, the 5% hybrid gel behaves more like the DBS-CONH₂ gels, with no observed increase in G'' at higher shears, whilst the trace of the 10% hybrid gels closely resembles that of the PEGDM gels. Whilst the critical strain of the 5 and 10% hybrid gels is very similar, the behaviour of the gels prior to their breakdown is clearly influenced by the PG content of the material.

The response of the gels to a change in frequency at a fixed shear strain – selected from the linear viscoelastic region (LVR, see Figure 2.7a) of the shear strain sweep - was also probed (Figure 2.8). The LVR is the range of shear strains for which the value of G' does not change significantly and is usually identified qualitatively. In this region, the mechanical properties of the hydrogels are not expected to deviate with any small changes in the applied strain. As such, any features seen in the rheological traces below are the result of changes in frequency, and not error in the strain applied to the materials. The relative values of G' and G'' were broadly similar to those observed with changing shear strain and no changes in these values was observed over the standard LMWG testing range (1-100 rad s⁻¹ \equiv 0.7-16 Hz). On increasing the frequency to much higher values (*ca.* 100 Hz, 628 rad s⁻¹) both G' and G'' increase rapidly, indicating a hardening process in the gel-phase materials on the short timescales studied. Similar effects have been reported previously by the groups of Adams and Verdier, who attribute this behaviour to a glass-like transition.^{181,182} The frequency at which this stiffening occurs is significantly impacted by the hydrogel composition. PEGDM hydrogels appear to harden at frequencies of *ca.* 16 Hz, whilst the DBS-CONH₂ LMWGs only undergo this process at much higher values (*ca.* 40 Hz). Interestingly, the hybrid gels, with both LMWG and PG networks present, stiffen at intermediate frequencies (*ca.* 25-30 Hz). No changes

were observed in the rheological properties of DBS-CONHNH₂ hydrogels after exposure to UV light for 0.5 h, supporting the hypothesis that PEGDM is responsible for the differences seen here, rather than any photo-induced thermal/evaporation effects.

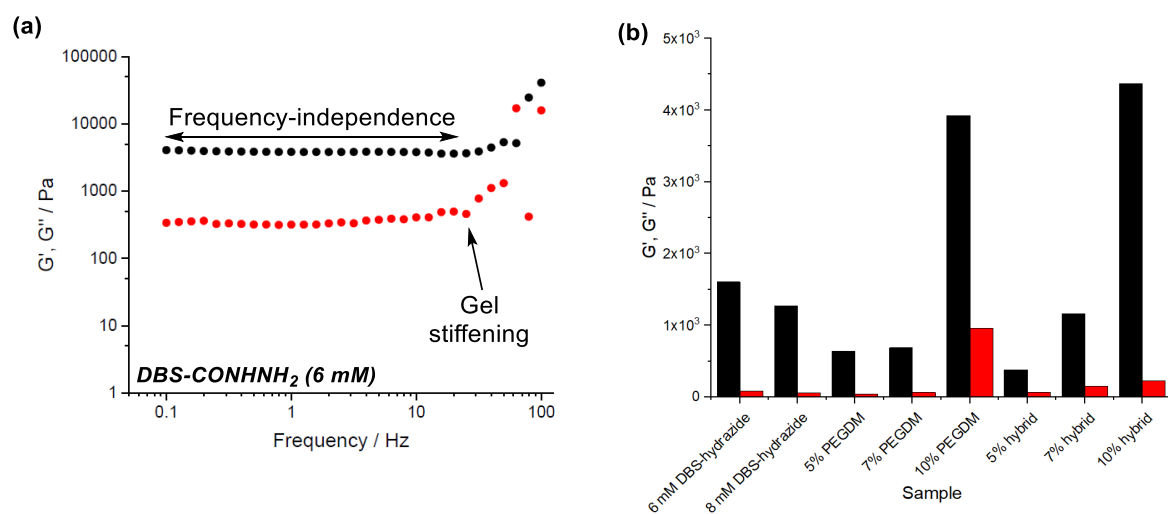


Figure 2.8: Representative rheological trace of 6 mM DBS-CONHNH₂ in response to varying frequency with features of interest highlighted (a). Storage (G') and loss (G'') moduli of the different prepared hydrogels (b). G' = black circles/bars, G'' = red circles/bars. Errors are ca. $\pm 10\%$ for all samples.

As all these gels were exposed to UV from above, it was important to determine whether the extent of crosslinking was identical throughout the depth of the gels. As a proxy measurement of this, we prepared a 10% hybrid gel disc as described above. In this case, the gel had a total volume of 2 mL, resulting in a gel height of ca. 1 cm. Importantly this is double the thickness of the other prepared rheological samples, but is also at least as thick as any other gel prepared as part of this thesis. This 2 mL gel was halved horizontally, to yield two identical gel discs. The rheological properties of the top and bottom halves of the gel were almost identical (Figure 2.9), suggesting that for all hybrid gels reported herein, no significant differences in the crosslinking density - and therefore material properties - are significant in the height axis. Changes (or lack thereof) in crosslinking density could also be measured directly using techniques such as spatially-resolved Raman and NMR spectroscopy. We reasoned that the macroscopic impact was the most relevant measure of this effect, therefore these methods have not been employed here.^{183,184}

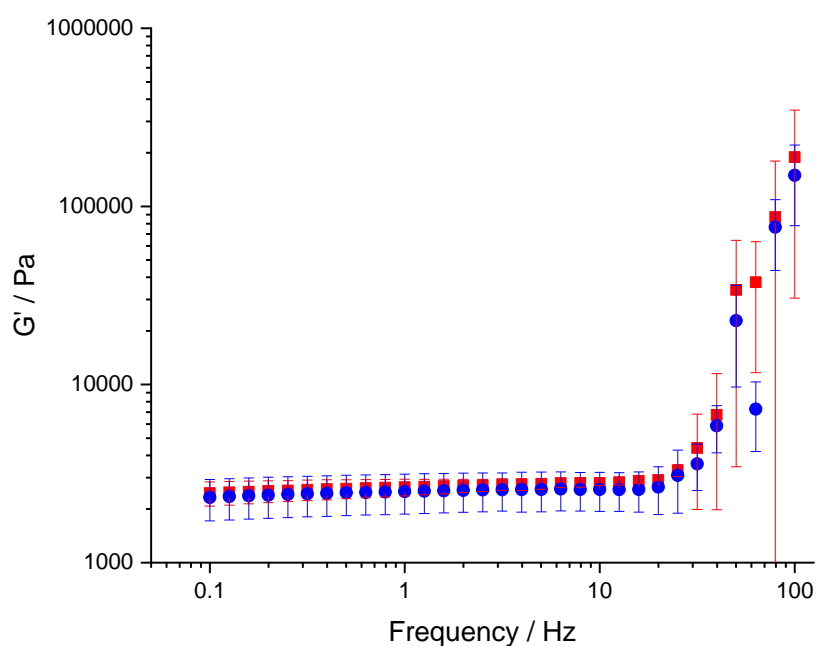


Figure 2.9: Storage modulus (G') of the top and bottom halves of a 10% hybrid gel disc (height ca. 1 cm) in response to changes in frequency. Red squares = top half, blue circles = bottom half. Error bars are standard deviation, $n = 3$.

Finally, the response of the various hydrogels to an increase in temperature – recorded at a shear strain and frequency within the plateau regions – was measured (Figure 2.10). DBS-CONHNH₂ hydrogels showed a slight increase in the elastic and inelastic moduli on increasing the temperature up until a critical point, which can be interpreted as the T_{gel} . This crossover point is ca. 75 °C, in good agreement with the T_{gel} observed in bulk gel samples. The increase in stiffness up to this point could be explained by the conversion of a kinetically stable form to a slightly stiffer equilibrium structure. Alternatively, these observations may be an artefact of the methodology – solvent evaporation over time may increase the effective concentration of DBS-CONHNH₂ resulting in increased stiffness, or may alter the applied force of the rheometer plate as the sample shrinks.

By contrast PEGDM hydrogels do not show an increase in stiffness as the temperature is increased. After a certain temperature (ca 65 °C for 7% PEGDM and ca. 75 °C for 10% PEGDM), G' and G'' then decrease, with samples having lower PEGDM loadings showing greater susceptibility to thermally-initiated gel breakdown.

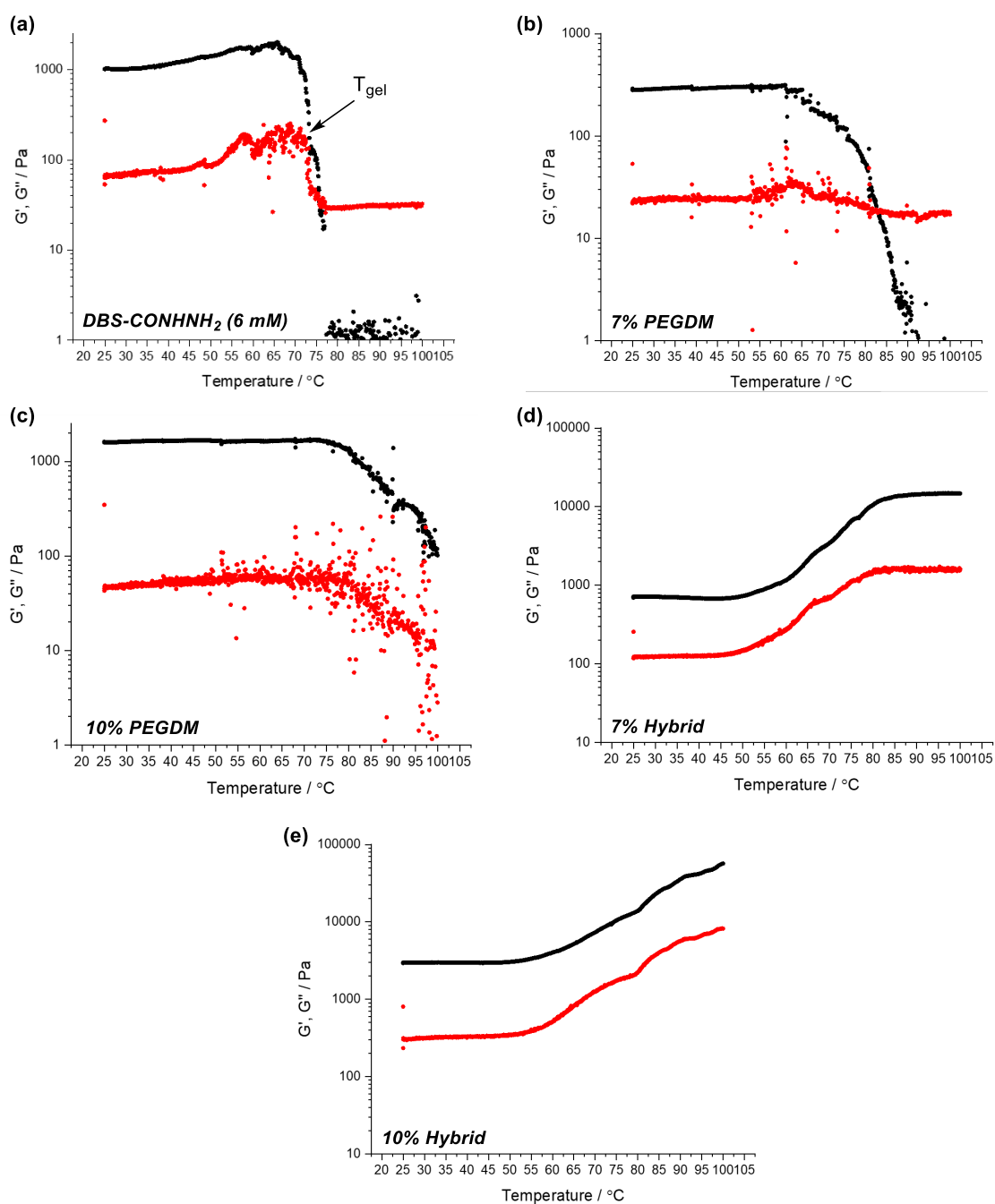


Figure 2.10: Storage (G' , black) and loss (G'' , red) moduli of the different prepared hydrogels in response to varying temperature at constant shear strain and frequency. Rheological traces for: 6 mM DBS-CONH₂ (a), 7% PEGDM (b), 10% PEGDM (c), 7% hybrid (d) and 10% hybrid (e). Features of interest are highlighted on the trace of 6mM DBS-CONH₂ (a). Errors are ca. $\pm 10\%$ for all samples.

In the hybrid gel samples, however, very interesting behaviour is observed. These gels increase significantly in stiffness as the temperature increases. Whilst the 7% hybrid gel stiffness plateaus at ca. 80 °C, the 10% hybrid gel increases in stiffness up to 100 °C. The reasons for this behaviour are not clear at this time. In the gel phase, the methacrylate groups were not visible using solution state

NMR spectroscopy even prior to UV exposure, thus it was not possible to probe the degree of crosslinking by this method. The decrease in stiffness observed for DBS-CONH₂ gels is not observed in the hybrid gel samples, indicating that the PEGDM network stabilises the LMWG nanofibres with respect to heat, preventing network breakdown. However, given that the stiffness of the samples (G') is determined by the PEGDM content of the hydrogels, it is more likely that any changes in LMWG structure are simply not visible in these experiments.

These rheological tests demonstrate that the combination of the two gel network types in a single hybrid gel results in synergistic modification of the mechanical properties. The incorporation of PEGDM enhances the stiffness of the material, improving the handleability, whilst DBS-CONH₂ appears to increase the resistance to high frequency oscillations compared to the PG alone.

2.5.4 SEM imaging

Next, the nanoscale morphology of the gels was assessed by electron microscopy. Transmission and scanning electron microscopy (TEM and SEM respectively) allow 'direct' visualisation of the gel nanofibres in 2 and 3-dimensions respectively on this scale. The collection of meaningful data from these techniques is less than trivial however and relies heavily on proper sample preparation. For traditional EM techniques, samples must be dry. Adams has discussed at length the effects of drying on the network observed by EM.^{185,186} To prevent collapse of the gel networks to a xerogel, samples are often prepared for TEM by a freeze-fracture method, where rapid freezing of the solvent helps preserve the gel nanostructure.¹⁸⁷ For SEM, freeze-drying under vacuum in liquid N₂ is a suitable preparation method to preserve a more aerogel-like structure.^{188,189}

We elected to use SEM to visualise the gel networks in our LMWG, PG and hybrid hydrogels (Figure 2.11). DBS-CONH₂ exhibited a nanofibrous morphology characteristic of LMWGs, with fibre diameters of 25 ± 11 nm. By comparison, PEGDM hydrogels adopt a more extended sheet-like structure due to the covalent nature of the bonding in this material.

For a sample of 10% hybrid gel, both the sheet-like structures associated with PEGDM and the DBS-CONH₂ nanofibres (diameter *ca.* 20 nm) can be seen in the electron micrograph. This indicates that both networks have formed orthogonally in the hybrid gel as hypothesised. The presence of the pre-existing LMWG fibres does not prevent formation of a sample-spanning PG network, and the PG crosslinking process does not result in LMWG disassembly. This orthogonality, allowing full formation of the PEGDM network, could explain why the rheological stiffnesses of the hybrid gels (Section 2.5.3) are very close to those of PEGDM hydrogels of a similar loading. It should be noted

that whilst the assembly of the two gel networks is orthogonal, it does appear that the DBS-CONH₂ nanofibres aggregate somewhat along the sheet-like structures of the PEGDM network. This indicates that there may be some interactions between the two networks in the hybrid gel, which could explain the responses of these materials to high shear strain and frequency, both of which are intermediate between gels formed from the individual components. It is possible that this observation is an artefact of the drying process, however efforts were taken to minimise any induced structural changes by freeze-drying all samples at low temperatures (as described above).^{185,186} Further SEM images with different magnifications are given in Appendix 4.

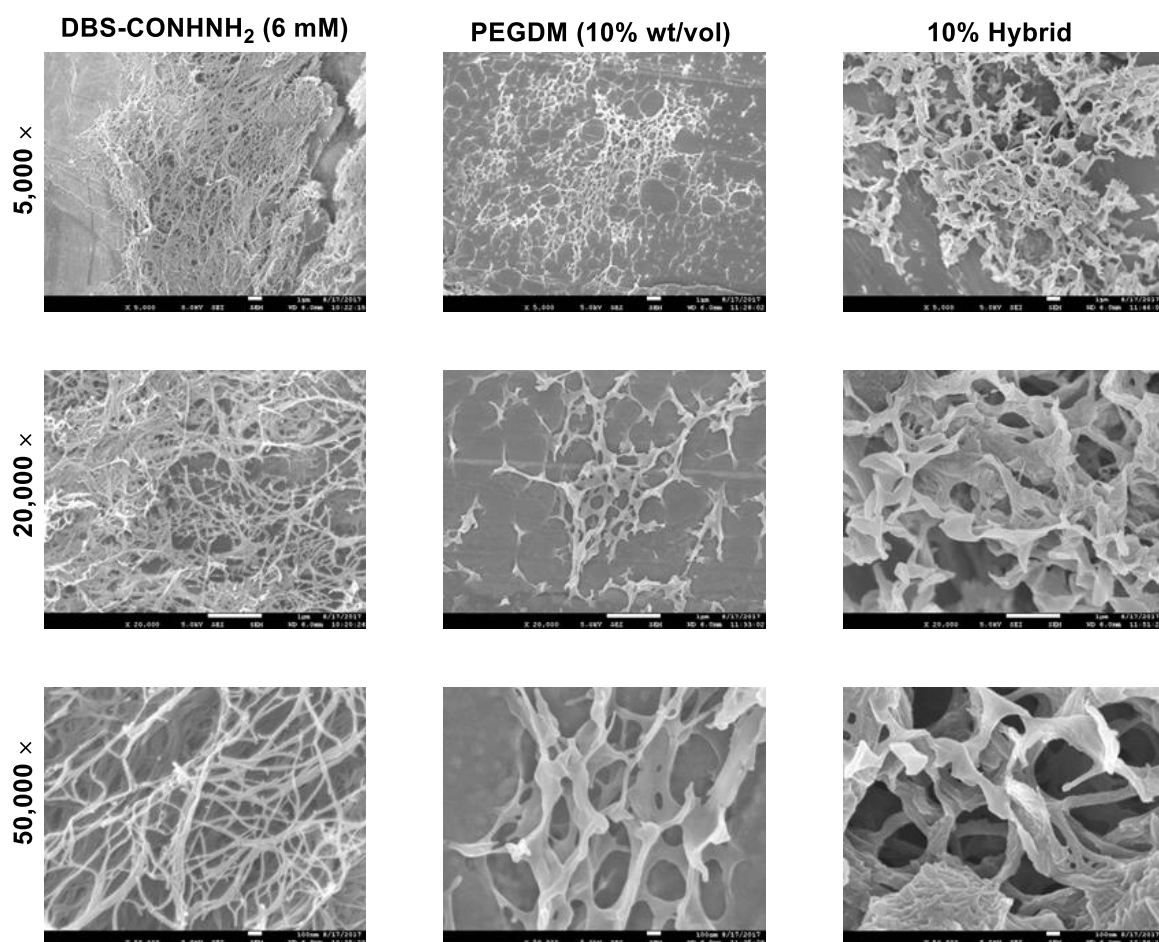


Figure 2.11: SEM images of 6 mM DBS-CONH₂ (left), 10% PEGDM (middle) and 10% hybrid (right) gels. Image magnification is given at the left of each row. Scale bars are as follows: 5,000 × = 1 μm, 20,000 × = 1 μm, 50,000 × = 100 nm.

2.5.5 IR spectroscopy

Infra-red (IR) spectroscopy is a useful tool for understanding the specific interactions a gelator has with both other gelator molecules and the solvent in which the gel is formed. Changes in

wavenumber in the IR spectrum can be indicative of hydrogen bonding interaction, solvophobic effects or van der Waals interactions and can reveal which moieties in a gelator compound are responsible for the assembly of fibrils.¹⁹⁰ It is preferable to measure the IR spectrum of a sample in the gel phase. Depending on the nature of the interactions and the solvent however, the relevant peaks in the spectrum may be obscured. For example, the large percentage by mass of water in a hydrogel sample often obscures the hydroxyl and amine peaks of interest.

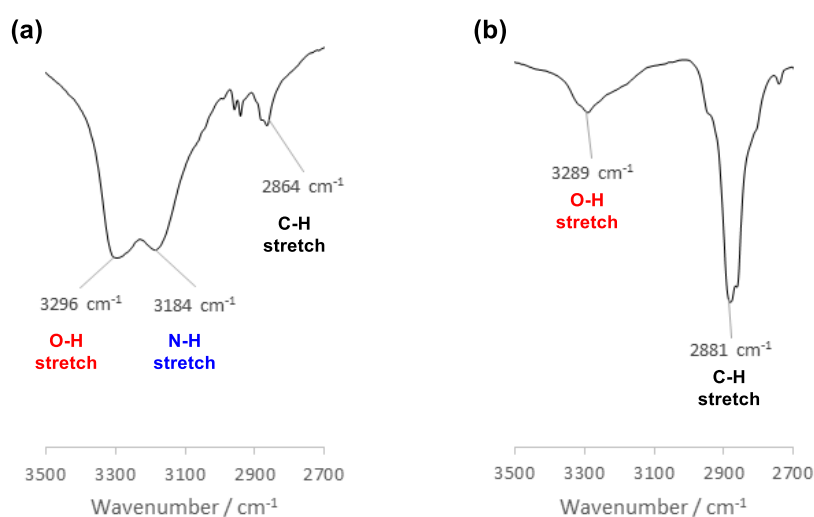


Figure 2.12: Excerpts from IR spectra of 6 mM DBS-CONH₂ (a) and 10% hybrid (b) gels. Changes in the O-H and N-H peaks of DBS-CONH₂ are observed.

With this in mind, we elected to analyse the IR spectra of dried xerogels to prevent masking of O-H and N-H stretches of interest (Appendix 5).^{114,191,192} In DBS-CONH₂ xerogels these stretches appear at 3296 cm⁻¹ and 3184 cm⁻¹ respectively (Figure 2.12a). A characteristic C=O stretch is observed at 1724 cm⁻¹ in 10% PEGDM hydrogels. Importantly, for a dried 10% hybrid xerogel, the peaks associated with both individual components can be seen. This emphasises that the two gel networks are present in a single material. Interestingly however, the IR spectrum of the hybrid gel does not correspond simply to an overlay of the LMWG and PG spectra. The DBS-CONH₂ O-H stretch is shifted significantly (7 cm⁻¹), whilst the N-H stretch is broadened (Figure 2.12b). Whilst these changes appear significant, they are relatively small when considering the full width at half maximum (FWHM) of the peaks. The FWHM of the O-H stretch are ca. 140 cm⁻¹ and 230 cm⁻¹ in the LMW and hybrid hydrogels respectively. Therefore, whilst the peak broadening observed may be indicative of non-covalent interactions, this data does not provide conclusive evidence of these. More significantly, a difference in wavenumber of 4 cm⁻¹ in the carbonyl stretch of DBS-CONH₂ is seen in the LMW (1639 cm⁻¹) and hybrid (1635 cm⁻¹) hydrogels. These peaks are much sharper

(ca. 30 cm^{-1}) and therefore give a much better indication that the two networks interact to some extent. A similar change is seen in the PEGDM IR spectrum. The carbonyl stretch is seen at 1732 cm^{-1} in the hybrid gel, a shift of 8 cm^{-1} compared to the PG alone. This data is indicative of attractive interactions between the DBS-CONH₂ and PEGDM networks in the hybrid gel, and supports the observation by SEM that the LMWG nanofibres appear to aggregate along the PG sheets (Section 2.5.4). Again though, caution must be taken when drawing conclusions from this data. Difficulties associated with drying of the hybrid gels mean that interactions with water cannot be ruled out. Additionally, as for SEM images, the data must be regarded with the caveat that the interactions observed may not be identical to those of the native gel.^{185,186,193}

2.6 Photo-patterning of DBS-CONH₂/PEGDM Hybrid Gels

Having demonstrated the formation of hybrid gels comprising two largely orthogonal gel networks, we aimed to prepare photo-patterned gels with non-uniform mechanical properties in two-dimensions. We sealed bottomless glass vials to a glass tray using silicone. A hot solution of DBS-CONH₂ (6 mM, 1 mL) was added to this vial. On cooling, the LMWG network formed and a bulk gel could be seen. A solution of PEGDM (10% wt/vol) and PI (0.05% wt/vol) was added on top and left for three days as described above (Figure 2.13a). At this point, the vial was carefully removed to leave the DBS-CONH₂ gel standing in the tray. A glass disc (diameter = 18 mm) was applied to the top of the gel and a circular cardboard photomask (diameter = 10 mm) was placed on top (Figure 2.13b and c). The glass slide was applied so the cardboard mask was not in direct contact with - and therefore not removing water from - the hydrogel. It was expected that in regions exposed to UV light that the photo-polymerisation of PEGDM would result in stiffening of the gel, whilst shielded areas would remain as a weak LMWG material composed of DBS-CONH₂ nanofibres and unpolymerised PEGDM. We began by studying the potential to create a stiff hybrid gel 'ring' with a soft LMWG centre. The diameter of the gel in this case was 17 mm whilst the cardboard mask had a diameter of 10 mm.

Using this system, poor patterning resolution was achieved for exposure times between 10 and 30 minutes, with the centre of the gel stiffening (qualitatively) to approximately the same extent as the outer edge in all cases. This was considered to be the result of one of the following effects:

- i) Refraction of light by the glass disc to the centre of the gel
- ii) Diffusion of propagative radical species to the centre of the disc prior to termination
- iii) Penetration of UV light through the sides of the gel to the centre of the disc.

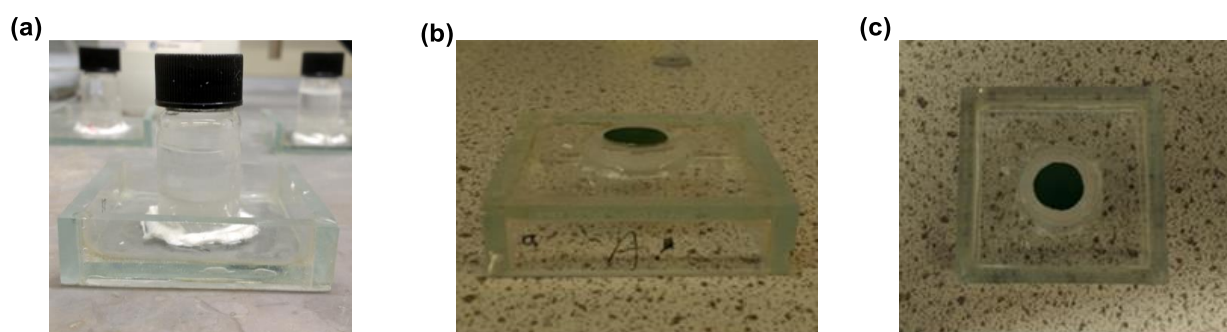


Figure 2.13: Gels were prepared in bottomless vials, which could be removed from the glass tray they were adhered to (a). This allowed a glass slide and cardboard 'photomask' to be applied to the top of the gel, shielding the centre of the disc from UV exposure for patterning of a gel 'ring'. Side (a) and top (b) views of this system are shown.

The first of these hypotheses was tested by the use of a smaller glass disc, in this case the same diameter as the photomask (10 mm). No improvement in the patterning resolution was observed. Nor was an increase in resolution achieved by cooling the gels in ice for the duration of the photo-patterning. This suggests that diffusional effects were unlikely to have significantly affected the process. However, when a mask was used which shielded not only the centre of the gel, but also the area outside the gel diameter (Figure 2.14a), a significant level of spatial control was achieved. Optimisation of the patterning process with respect to gel thickness and UV-exposure time was carried out, with 1 cm height and 20 min patterning time found to result in the highest resolution (Figure 2.14b).

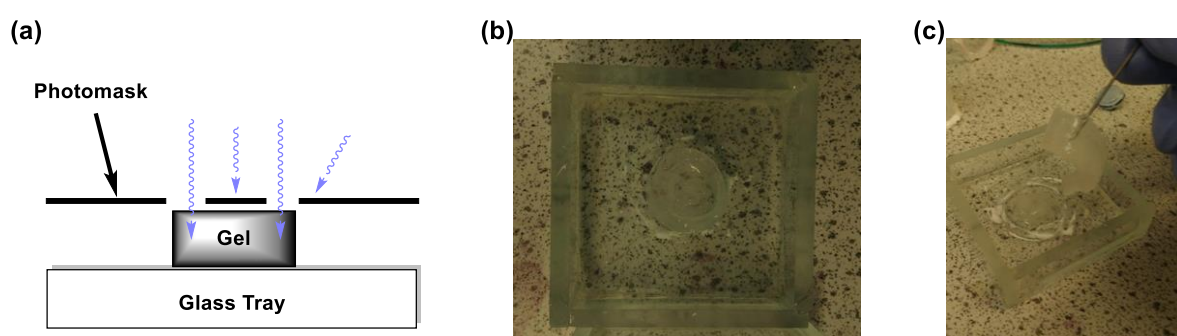


Figure 2.14: Schematic of the masking procedure to create photo-patterned gels (a). UV light is represented by purple wavy arrows. Masking the exterior of the gel discs during photo-patterning as well as the region desired to remain soft resulting in improved photo-patterning resolution. Samples of 10 mm thickness and exposed to UV light for 20 min yielded the highest resolution multidomain gels (b), comprising a soft centre and a robust exterior. Physical manipulation of the outer edge was possible (c) and this region could be easily separated from the uncured centre.

Clear differences in the material properties of the gels in the centre and at the edge of the disc were observed. The soft centre of the gel could not be manipulated easily with either a spatula or a needle. By contrast, the robust exterior region could be handled with ease and facile separation of this region from the uncured LMWG region was achieved by piercing with a needle and removing by hand (Figure 2.14c, Supplementary Video 1).

Whilst this initial approach to the photo-patterning of DBS-CONHNH₂/PEGDM hydrogels provided evidence of the feasibility of the technique, the fact that a glass slide is placed on the gel to apply the mask limits the utility of this method. Application of the glass slide and subsequent removal sometimes resulted in breakdown of the shielded regions of the gels, a problem which we expected to be exacerbated with scale. Therefore, it was desirable to develop a methodology which did not require this step.

Therefore, in a manner analogous to that reported by Cornwell *et. al.*, we attempted to prepare hybrid gels in a larger (5 cm × 5 cm × 1 cm) tray, over which could be placed a laser-printed acetate photomask without contacting the gel. Interestingly, on the 10 mL scale it was not possible to fully dissolve a 6 mM suspension of DBS-CONHNH₂ in water alone. This was believed to be the result of inhomogeneous heating of the sample. Some of these samples were able to form turbid gels (Figure 2.15a), however, reproducibility in the proportion of sample dissolved could not be ensured and inconsistent gel robustness was observed. Efforts were made to heat the suspensions throughout by heating in glass containers of various shape (in the mould, round bottomed flask, large vials etc.), as well as by heating to reflux. However, none of these methods resulted in total dissolution of the sample.

Addition of either ethanol or methanol to the starting solution aided solubility in certain ratios. However, this often led to the formation of gels which were too weak to allow addition of a PEGDM/PI solution for subsequent hybrid gel formation (Table 2.4). Of the mixtures trialled, only a 10% solution of ethanol resulted in gelator dissolution followed by formation of a robust gel. Either increasing the ethanol content to 20% or reducing it to 0% resulted in the formation of a less stiff gel as measured by rheology (Appendix 6). Presumably this is due to an increased proportion of gelator remaining soluble in the former case, whilst lower initial solubility in pure water likely means fewer gelator molecules are available to form nanofibres in the latter. Whilst there is an interest in the effects of solvent properties on the gelation process and material properties,^{194,195} given the cytotoxicity of ethanol and methanol – and bearing in mind the target biomedical applications for these materials - we chose not to pursue this avenue of research further.

Table 2.4: Gelation of DBS-CONH₂ in different solvent mixtures. All samples were prepared in 10 mL total solvent volume and transferred to a glass mould (dimensions 5 cm, × 5 cm × 1 cm) before cooling to room temperature.

% H ₂ O / v/v	% MeOH / v/v	% EtOH / v/v	Total dissolution on heating?	Gel formation?
90	10	0	No	Yes (robust)
80	20	0	No	Yes (robust)
70	30	0	No	Yes (fairly robust)
65	35	0	Yes	Yes (weak)
50	50	0	Yes	Yes (very weak)
90	0	10	Yes	Yes (robust)
80	0	20	Yes	Yes (weak)
50	0	50	Yes	No

Instead, to overcome the solubility issues, samples of DBS-CONH₂ were first dissolved in DMSO with sonication before adding to boiling H₂O. Samples were prepared such that the final concentration of DMSO was between 2 and 4% v/v. At these concentrations Okesola *et. al.* demonstrated that the DMSO has no significant effect on the bulk properties of the material.¹⁴³ Additionally, with biomedical applications in mind, these concentrations of DMSO are widely reported to have little effect on human cell cultures *in vitro* or *in vivo*.^{196,197} Using this method reproducible, uniform, translucent DBS-CONH₂ gels of 10 mL volume were produced in the glass moulds (Figure 2.15b). To prepare hybrid gels, an aqueous solution (10 mL total) of PEGDM (10% wt/vol) and PI (0.05% wt/vol) was carefully pipetted on top of the LMW hydrogel. As for the gels in vials, diffusion of the polymer and PI was allowed to reach equilibrium over 3 days before the supernatant was removed. On UV-irradiation, the gels stiffened as expected.

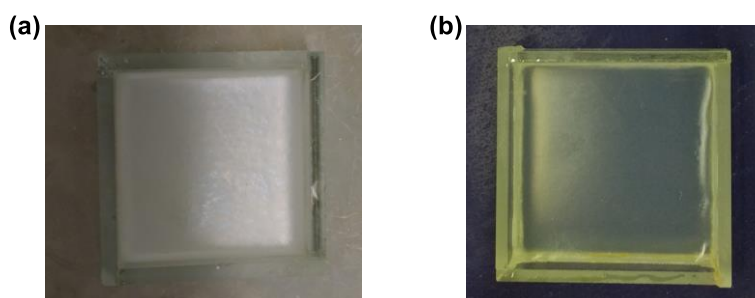


Figure 2.15: Comparison of 10 mL DBS-CONH₂ gels prepared by heating in H₂O directly (a) and by adding gelator pre-dissolved in DMSO to boiling H₂O.

To prepare UV-patterned multi-domain gels, a cardboard photomask was placed over the mould such that it was not in contact with the surface of the gel. As before, the area surrounding the gel was also shielded from UV-irradiation to improve patterning resolution. We initially tested the resolution we could achieve *via* this method by using a standard mask with circles of increasing diameter cut into them. Gels were partially exposed to UV light for 0.5 h, after which time the light source was removed, and the soft, non-polymerised regions washed away with a low power stream of H₂O. This revealed the patterned regions, which were formed with relatively good resolution (Figure 2.16). Gel pattern diameters were *ca.* 1.3 × the mask pattern diameter. It should be noted that an identical resolution was observed for hybrid gels formed in a 10% v/v EtOH solution (in water).

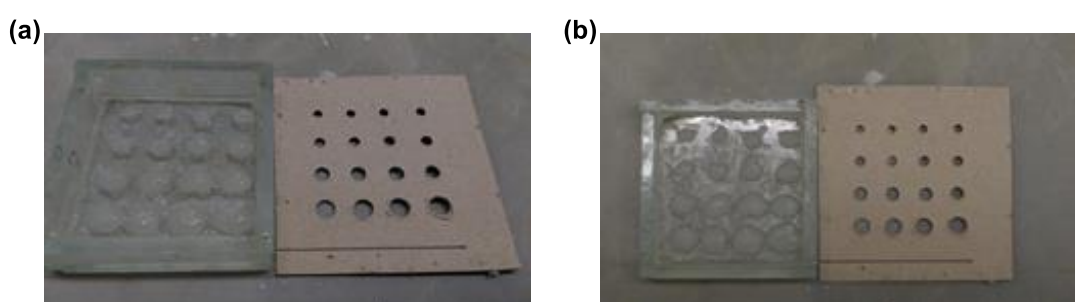


Figure 2.16: Photo-patterning resolution test. 10% hybrid gel samples were exposed to UV-irradiation for 0.5 h. Non-crosslinked regions were washed away with a low-pressure water stream to reveal the patterned regions. As seen from the side (a) and above (b). Mask ‘gap’ diameters are (from top to bottom) 2 mm, 3 mm, 4 mm and 5 mm respectively.

This slight loss in fidelity is thought to be the result of the mask being held around 0.5 cm above the gel (because room must be left in the tray for PEGDM/PI solution). This allows light to reach regions of the gel which were not accessible when the mask was in direct contact with the gel. Such issues were not encountered when the mask was in direct contact with the gel (see above). Better resolution could therefore likely be achieved by using a more sophisticated mask ‘holder’ which lowers the photomask closer to the surface of the gel, but this was not explored within the scope of this project.

An advantage of using the acetate photomasks is that it is possible to print any 2D geometry onto them, which can then in theory be patterned into the gel-phase materials. We chose to exemplify this approach by printing and patterning a simple ring, with an internal diameter of 2 cm and thickness 0.5 cm (Figure 2.17a). Acetate masks were placed above (and not in contact with) the gel as described for the cardboard photomasks above. Optimisation of the process with respect to a number of variables was carried out in this case. Considerations included the number of acetate

masks layered on each other (i.e. the mask ‘thickness’), the curing time and the temperature. Using too few photomasks resulted in poor resolution of the ring pattern (Figure 2.17b), as a proportion of the UV light could pass through the black regions of the mask, which were not completely opaque. Longer patterning times also resulted in a lower resolution, however incomplete patterns were observed at short exposure times. It was found that 4-layer mask and 0.5 h UV-exposure resulted in optimal photo-patterning of this geometry (Figure 2.17c). The regions shielded from UV light in this case were washed away easily with a low-pressure water stream, whilst the robust hybrid gel ring remained intact throughout this process. Cooling the gel with ice during the process also slightly enhanced the pattern fidelity, presumably by limiting diffusion.

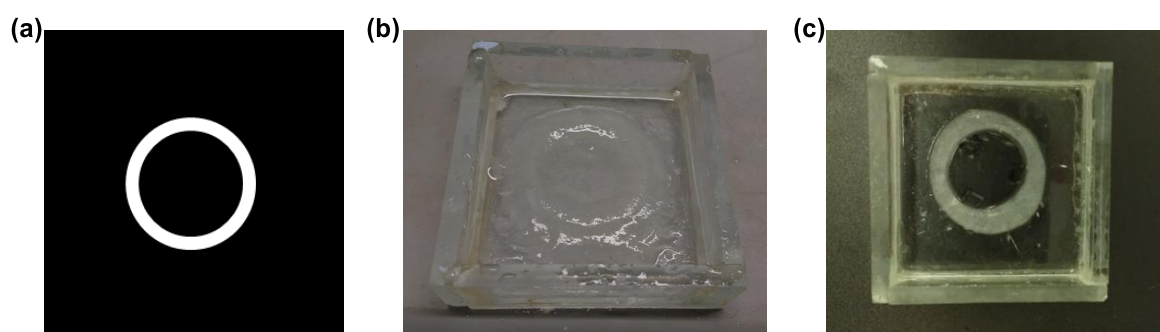


Figure 2.17: Gels were photo-patterned using a mask with a ring geometry printed on (a). The thickness of the photomask has a profound impact on the patterning efficacy. Masks 1 layer thick showed very poor patterning resolution (b), but this was much improved with a 4 layer thick mask (c).

Control experiments in which a solution of PEGDM was exposed to UV light under a photomask were also carried out. Interestingly, regardless of the patterning time, no spatial control over the photo-polymerisation process could be achieved in the absence of the pre-existing DBS-CONH₂ self-assembled network. Presumably, the LMWG network limits diffusion of propagating radical species, allowing spatial control over the crosslinking reaction which is not possible when the monomeric species are free to diffuse in solution. This finding, as with the rheological data, demonstrates that the synergy between the two-components in this hybrid gel is crucial to the properties and function of the material. Both components of the hydrogel are essential to be able to fabricate hydrogels with spatially-controlled properties.

2.7 Conclusions and Future Work

In this chapter, we have synthesised and characterised DBS-CONH₂, a LMWG which has previously been shown to have potential applications for controlled drug delivery and precious metal remediation. Despite the interesting properties of DBS-CONH₂ gels, they are too mechanically weak to be of significant practical use. We have therefore developed a novel hybrid gel, in which the DBS-CONH₂ LMWG network is supported by the by a biocompatible PEGDM PG network.

Importantly, in this novel hybrid gel, the two networks have orthogonal methods of assembly. The DBS-CONH₂ sample-spanning network is formed *via* a heat/cool cycle, whilst UV photopolymerisation is used to crosslink the PEGDM network. Evidence that the two networks are largely independent is seen in the SEM images and by IR spectroscopy. However, the synergy between the two networks has a profound impact on the material in a number of ways:

- i) Whilst the PEGDM component of the hybrid hydrogels determines the rheological stiffness, the resistance to increased frequency of shear oscillations is enhanced by the incorporation of the LMWG;
- ii) The use of PEGDM allows the stiffening of the hydrogel to be spatially-controlled through selective irradiation of regions of the gel;
- iii) Photo-patterning is not possible in the absence of the DBS-CONH₂ network, which helps provide spatial resolution by acting as a supporting gel matrix and limiting diffusion effects.

Given that incomplete gelation was observed for hybrid gels prepared via a 'one-pot' method, as described by Cornwell *et. al.*,^{53,84} we believe that the method outlined herein, where the LMWG network is formed first, followed by incorporation of the PG component, may provide a more general route to hybrid LMWG/PG hybrid gels. In the future, this approach could be used to explore different combinations of LMWGs and PGs to develop hybrid materials with unique properties. In particular, the combination of PEGDM with a wide range of hydrogelators may allow the development of a versatile family of shaped, functional hybrid gel devices.

3 Hybrid and Multidomain Hydrogels for Controlled Drug Release

Aspects of this research have been published in: P. R. A. Chivers and D. K. Smith, *Chem. Sci.*, 2017, **8**, 7218-7227

3.1 Introduction – LMW hydrogels for controlled drug release

Gels are widely used as excipients in drug formulations, with the majority of both academic reports and patent literature describing the use of PGs as carriers of active pharmaceutical ingredients (APIs). Recently, however, a significant increase in the number of formulations utilising a responsive LMWG as a responsive matrix have been reported. LMW hydrogels are of particular interest for controlled drug delivery – the combination of responsiveness, biodegradability and biocompatibility makes them highly attractive candidates for this purpose. Two excellent recent reviews have set the field in context,^{13,198} and have identified three major approaches (Figure 3.1) to the capture and release of drugs from LMW hydrogel matrices:

- 1) Physical encapsulation within an LMWG scaffold
- 2) Covalent conjugation of drugs to self-assembling LMWGs
- 3) Gel-forming drugs

Rather than providing an exhaustive overview of the area, in this chapter introduction, important and illustrative examples of each of these three approaches will be highlighted with a focus on how controlled release is achieved from each system. It should be noted that organogels formed in relatively benign solvents are also of significant interest for drug delivery, but these materials will not be discussed here.¹⁹⁹

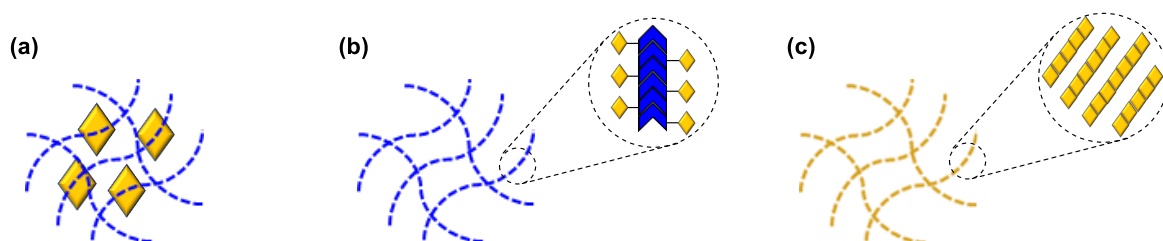


Figure 3.1: Cartoon representation of strategies for encapsulation of drugs within a LMWG matrix. Physical encapsulation (a), covalent conjugation to LMWGs (b) and self-assembly of drugs (c).

3.1.1 Physical encapsulation

By far the most common method of API formulation, physical entrapment within a gel matrix provides a very simple method to enhance the stability of drugs within the body.²⁰⁰ Traditionally, densely crosslinked polymers have been used to prolong drug release by limiting the rate of diffusion out of the hydrogel matrix.²⁰¹ This is often not a viable approach for LMW hydrogels, which tend to be formed from relatively small quantities of gelator in a large volume of solvent. For limited examples however, an increase in LMWG loading has been shown to influence the release of therapeutic agents. Das and co-workers decreased the rate of Vitamin B₆ release from cationic dipeptide gels from 100% to 70% over 48 h by increasing the gelator loading from 0.5 to 3.0% wt/vol.²⁰² Similarly, Cao *et. al.* showed that the release of salicylic acid was inversely proportional to the concentration of gelator, although the changes in release were modest in this case – doubling the gelator concentration decreased API release by *ca.* 10%.²⁰³ Puramatrix® is one example of a commercially available peptide LMW hydrogel which demonstrates similar loading-dependent release properties.^{204–206} Increasing the time for which a gel is stable under physiological conditions is also a promising approach to achieving sustained release. The use of LMW hydrogels formed from D-peptide or unnatural amino acid gelators can result in enhanced lifetimes and slower release of the drug payload.^{207–210}

A more widespread approach to limit release rate is to tune the structure of the gelator such that it interacts relatively strongly with the encapsulated API. Pioneering work in this field came from the Zhang group. They demonstrated the self-assembly of a β -sheet 16 amino acid sequence into sample-spanning hydrogel networks and, as in the examples above, reported an inverse relationship between LMWG loading and release rate.²¹¹ More importantly, they showed that the structure of the encapsulated drug has a profound effect on its release rate. With this particular amino acid sequence, highly acidic species such as bromophenol blue remained in the peptide hydrogel whilst the less acidic phenol red diffused freely out. Small release differences were also seen for triply and quadruply substituted sulfonic acid pyrene derivatives, with the more highly charged species interacting more strongly with the gel. This research highlights the importance of non-covalent interactions for controlled release from LMW hydrogels.

More recently, Palocci and co-workers showed that differences in release rate were observed for enantiomeric forms of a tripeptide gel. Dexamethasone, a corticosteroid, was released from Fmoc-Phe-Phe-Phe hydrogels with L-chirality at a much greater rate than for its D-chiral enantiomer,²¹² likely due to differences in specific interactions between the chiral drug and the gel network. Limón *et. al.* also recently showed that changes in the substitution pattern of a bis-imidazolium gelator

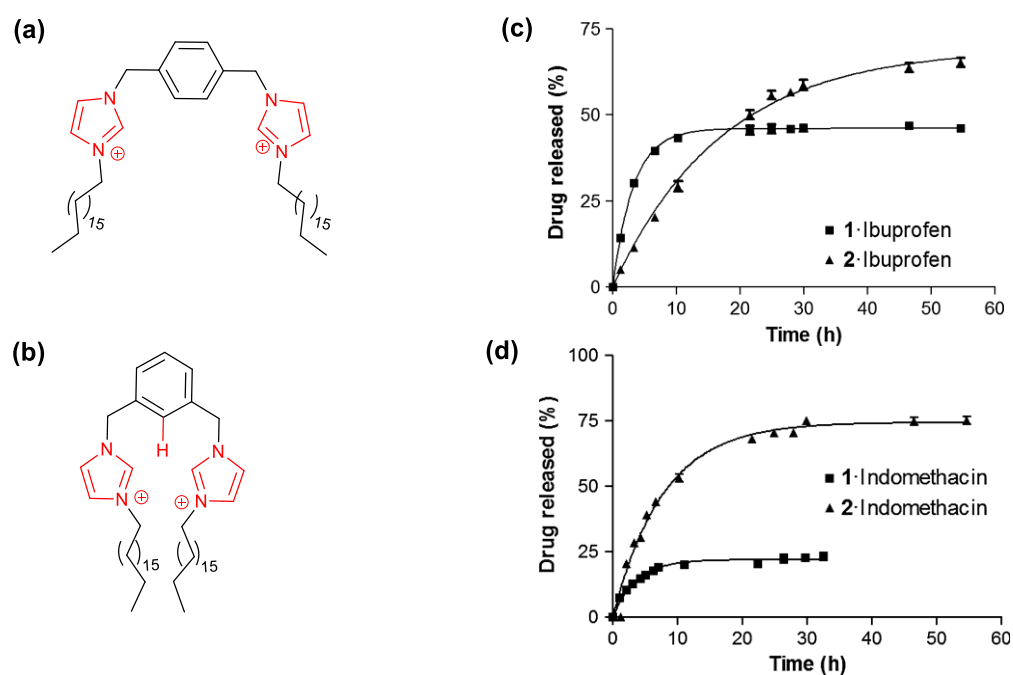


Figure 3.2: Structures of the *para*- (a) and *meta*- (b) bis-imidazolium gelators reported by Limon et. al. Regions of each gelator which interact with ibuprofen and indomethacin are highlighted in red. Release profiles of physically encapsulated ibuprofen (c) and indomethacin (d) from bis-imidazolium amphiphile hydrogels. Figure adapted from [213].

significantly affects the release of APIs including ibuprofen and indomethacin. The positively charged gel amphiphiles interact with the anionic drug molecules in a manner determined by the substitution pattern of the central phenyl ring (Figure 3.2).²¹³ In solution, the *para*-substituted gelator interacts with the two drugs only through the imidazolium group, whereas additional interactions with the phenyl group were present with the *meta*-gelator. Surprisingly then, release of both ibuprofen and indomethacin was less in a hydrogel formed from the *para*-gelator. It was suggested that in the presence of the drugs, the self-assembly modes of the two gelators are altered, resulting in API internalisation within the nanofibres of the *para*-gel, reducing the release rate. In subsequent work, the *meta*-linked bis-imidazolium was co-assembled in the presence of a serine protease inhibitor, which resulted in the formation of coiled nanofibres rather than the long, straight nanofibres associated with the gelator alone.²¹⁴ The presence of the drug also modified the gel properties, making it softer and more elastic. These rheological properties, combined with the high permeation of inhibitor into skin, makes this gel formulation appropriate for topical application in the treatment of Rosacea.

As well as modifying the gelator-drug interactions, the timing and location of release can be controlled by designing stimuli-responsive systems. As described in Chapter 1, LMW hydrogels are

inherently responsive materials, able to undergo morphological changes or disassembly in response to an external stimulus. Zhang and co-workers demonstrated UV-induced gel breakdown of an azobenzene-pentapeptide hydrogel and its application in temporally controlled drug release. Gels formed in the presence of Vitamin B₁₂ released the biomolecule over a period of 48 hours when relying on diffusion alone. On irradiation, complete release was achieved over 4 h, a 12-fold increase in the release rate.²¹⁵ Schneider and co-workers adopted a similar approach, utilising an azobenzene-appended cyclic dipeptide which, as above, underwent UV-induced disassembly.²¹⁶ Significantly greater release of both DNA oligomers and doxorubicin were seen on UV-irradiation, highlighting the potential of this approach for gene therapy.

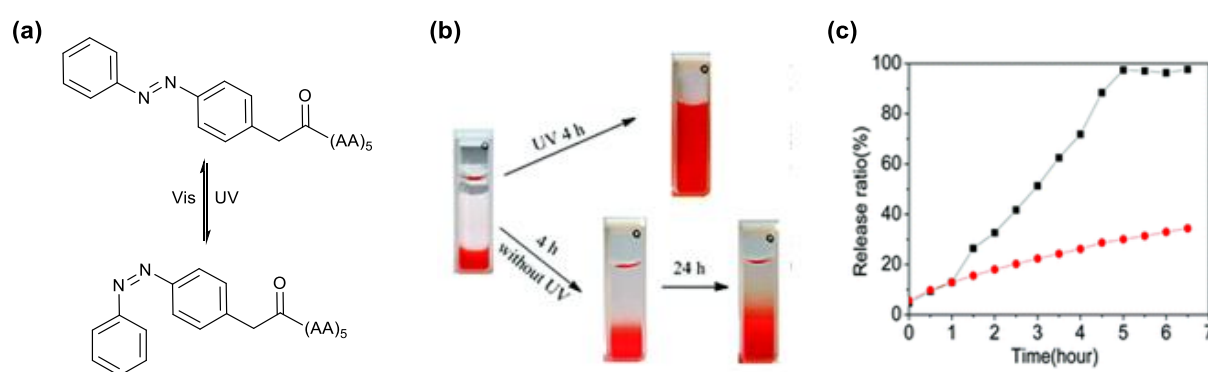


Figure 3.3: Reversible light-induced trans-cis isomerisation of an azobenzene pentapeptide gelator (a). Exposure to UV light results in gel breakdown (b). Rapid release of Vitamin B₁₂ (c) is seen for samples exposed to UV light (black squares) compared to a sample kept in the dark (red circles). Figure adapted from [216].

The controlled shrinking of a hydrogel matrix in response to environmental changes has been demonstrated by several groups. Notable contributions regarding drug release include those from Liu and Hamachi, who have utilised the response of such gelators to metal ions²¹⁷ and pH²¹⁸ respectively. Gel shrinkage encouraged expulsion of large molecules such as vitamins from the hydrogel matrices, with the degree of release determined by the relative affinity of the species for the gel and aqueous phase respectively. Hamachi also developed a multi-stimulus responsive LMW hydrogel for fine control of API release.²¹⁹ Phosphate groups in these molecules were sensitive to changes in pH and Ca²⁺ concentration, whilst the double bond in the 'spacer' group determined gelation efficiency in response to light exposure. Complex temporal control of vitamin B₁₂ release was achieved by application of these stimuli in different sequences.

3.1.2 Covalent conjugation

Covalent conjugation of bioactive drugs to a LMWG can have a number of advantages compared to physical encapsulation. In particular, this approach can prevent burst release which is often associated with physically encapsulated drug molecules. The stability of the self-assembling 'prodrugs' prevents this, as they are designed to be selectively cleaved only under certain conditions. In this way, selective release at a target position in the body can be achieved, provided the triggering species is specifically produced at the target site.

Xu and co-workers pioneered this approach to controlled drug delivery in the early 2000s. In seminal work they reported the self-assembly of vancomycin-containing structures formed through conjugation of the C-terminal backbone of the antibiotic to a pyrene unit which exhibited π - π stacking (Figure 3.4).²²⁰ Gels formed at a relatively low concentration and retained a good degree of the antibiotic activity of vancomycin against a range of bacteria. Some years later, the same group reported that the conjugation of taxol to a tetrapeptide unit gave a molecule that underwent self-assembly to form a gel on enzymatic dephosphorylation.²²¹ Slow and sustained release of the prodrug from the LMW hydrogel meant that this prodrug hydrogel exhibited comparable cytotoxicity to that of free taxol. Subsequent work demonstrated hydrogelation of the same tetrapeptide formed using D-amino acids, and showed that in an *in vivo* mouse model, improved biostability and longer term activity was exhibited compared to the L-prodrug.¹⁰⁰ Improved resistance to enzymatic hydrolysis makes D-amino acids attractive candidates for sustained *in vivo* delivery. Dastidar and co-workers used a similar approach to enhance the lifetime of naproxen-conjugated dipeptide hydrogels. Rather than D-amino acids, the incorporation of β -amino acids in the prodrug structure prevented rapid enzymatic cleavage, instead enabling slow release of the prodrug into solution.²²²

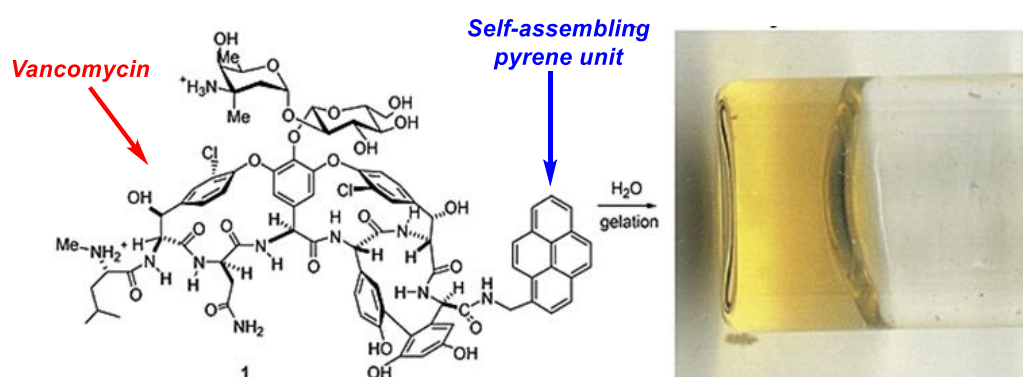


Figure 3.4: Structure of Xu's pioneering vancomycin-pyrene conjugate (left) which self-assembles in water to yield a hydrogel (right). Adapted from [220].

In the above examples, the self-assembling prodrug retains the activity associated with the free API and sustained release of this species is dependent on the dissolution rate of the gel. More common however, is cleavage of the prodrug species to yield an active API in response to the external environment. Enzymes represent the most widely used cleavage trigger for this purpose. Kim and co-workers demonstrated as early as 2006 the enzyme-induced release of ibuprofen from a drug: dipeptide conjugate hydrogel.²²³ Diglycyl-ibuprofen underwent self-assembly due to a combination of hydrogen bonding interactions between the amino acid residues, and aromatic interactions of peripheral ibuprofen moieties. Amide bond cleavage was initiated by addition of carboxypeptidase Y, liberating ibuprofen and inducing gel breakdown. A similar report from Xu and co-workers described the conjugation of mesalazine to a D-tripeptide assembly sequence, and its subsequent release was triggered by azo-reductase, an enzyme produced specifically in the colon.²²⁴ Importantly, the amino acid sequence was stable to a powerful protease, suggesting the utility of this material for oral delivery of this anti-inflammatory.

In a highly influential report, Vemula *et. al.* described the formulation of acetaminophen as a bola-amphiphilic prodrug with lipase-cleavable ester linkages (Figure 3.5a).¹⁰¹ This structure forms a hydrogel via a heat/cool cycle which can be degraded upon exposure to lipase. On addition of enzyme, gel disassembly and acetaminophen release occurred, with total gel breakdown observed over 48 h. Encapsulation of the anti-cancer agent curcumin (Figure 3.5b) in the hydrogel allowed for the dual-release of drugs from the matrix upon ester hydrolysis (Figure 3.5c). Crucially, no drug release was reported in the absence of lipase, demonstrating the potential for targeted release in the small intestine where this enzyme is most prevalent. By combining the physical encapsulation and release of a drug with a covalently captured API, a more complex and therapeutically relevant release system was developed.

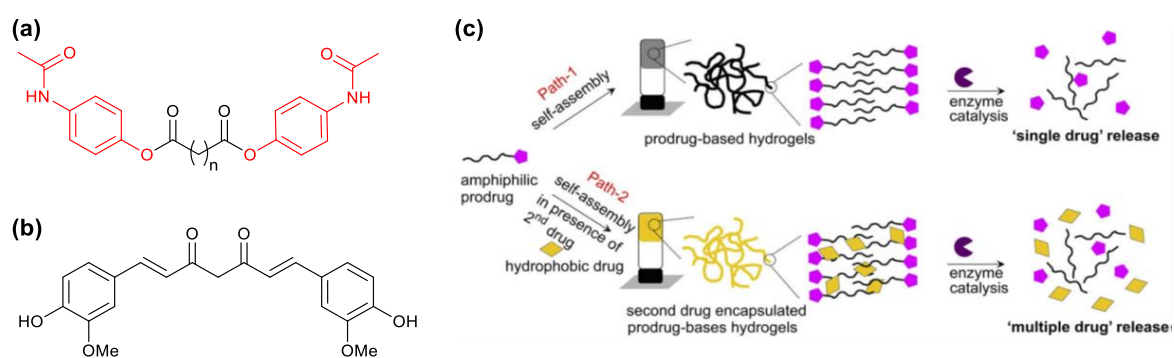


Figure 3.5: Structures of the bola-amphiphile drug-conjugate gelator reported by Vemula *et. al.* (a). Acetaminophen portions of the molecule are highlighted in red. Structure of curcumin (b). Schematic of single and dual drug release from acetaminophen gelators (c). Adapted from [101].

Limited examples of non-enzymatic triggers have been reported for the liberation of APIs from prodrug hydrogels. Matson and Stupp, for example, connected the drug nabumetone to a peptide amphiphile *via* a hydrolytically-labile hydrazone linkage.²²⁵ Site-specific addition of a hydrazide group to a short peptide amphiphile allowed well-defined nabumetone functionalisation using solid-phase peptide synthesis. Slow hydrolysis of the hydrazone linkage in pH 7 buffer solution resulted in sustained release over 24 days. In novel work, Chen and co-workers linked naproxen to a peptide unit through a photolytically cleavable nitrobenzyl ester group.²²⁶ Exposure of the LMW hydrogel to UV light led to release of free naproxen and concomitant gel breakdown. The use of a UV trigger may limit the applications of this approach for *in vivo* drug release, however the use of two-photon techniques may open this up to more widespread use, in particular for the release of anti-cancer drugs.

3.1.3 Gel-forming drugs

A much more recent approach to gel-based drug release is the development of triggers which induce gelation of an API itself. Most early examples of this approach describe self-assembling peptide sequences which happen to possess some therapeutic activity.^{227,228} Conceptually, these works are therefore very similar to the works presented at the beginning of Section 3.1.2. Additionally, in these examples, release of the bioactive gelator was not demonstrated, therefore they will not be discussed further other than to note that these gels may be interesting for further study as part of a dual-API release formulation.

Novel research from Odriozola and co-workers detailed the formation of hydrogels induced by ligation of group 11 metal salts by acetylcysteine (Figure 3.6a-c).²²⁹ Co-ordination of the cysteine thiol to the metal centre resulted in the formation of a sample spanning network which demonstrated pH-responsiveness – deprotonation of the carboxylic acid group using a base increases the solubility of the compound in water, inducing gel disassembly and API release. The authors proposed that thiol-containing peptides would displace the acetylcysteine *in vivo*, providing an alternative release mechanism.

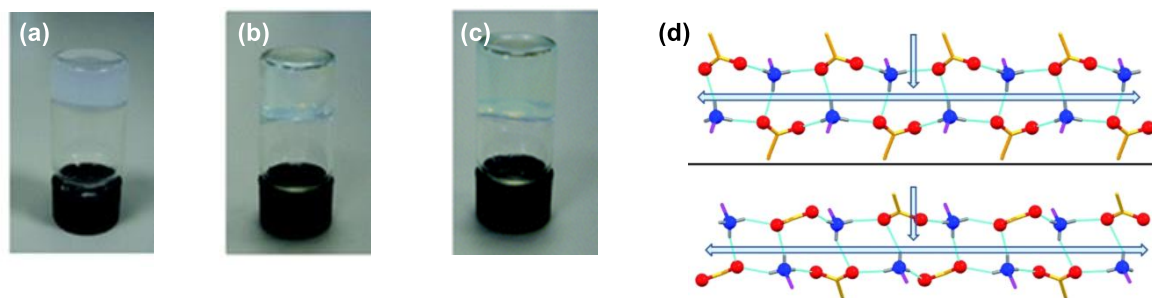


Figure 3.6: *Gels formed by the reaction of acetylcysteine with gold (a), silver (b) and copper (c) salts. (d) Supramolecular synthons formed in the reaction of anti-inflammatory drugs with amantadine. Top = 'W' synthon, bottom = 'X' synthon. Adapted from [229] and [230].*

Dastidar has contributed significantly to this area through the design of supramolecular synthons based on the salts of common APIs. The group first described this approach to gelation in a 2014 paper, where they developed a range of gels based on primary ammonium (PAM) carboxylate synthons (Figure 3.6d).²³⁰ APIs including indomethacin, tolfenamic acid and flurbiprofen were reacted with amantadine to yield 1-dimensional hydrogen bonding networks which aggregate to form sample-spanning gel networks. Whilst the PAMs studied here were too insoluble in water to form LMW hydrogels, judicious selection of amine and drug combinations has yielded hydrogels with potential applications as anti-cancer agents²³¹ or for live cell imaging.²³² Nandi and co-workers have developed similar bicomponent LMW hydrogels based on the supramolecular assembly of riboflavin and a range of small molecule therapeutics.²³³ As with many of the studies in this field however, only hydrogel formation was studied. Subsequent release of the APIs was not demonstrated.

The controlled release of drugs from LMW hydrogels is clearly a highly active area of research, and one which is developing rapidly. The examples highlighted herein illustrate the relative advantages and drawbacks of each approach. Dependent on the application, burst release of a physically encapsulated drug under programmed conditions, or sustained release of covalently conjugated API may be more appropriate. However, as has become clear in the text, surprisingly few examples of LMWG-containing hydrogels exist which demonstrate multiple encapsulation and release methods. We propose that to achieve sophisticated controlled release of multiple bioactive components for disease treatment or tissue engineering, such materials will have to be developed.

3.2 Chapter aims

Despite the many papers detailing the formulation and release of APIs in LMW hydrogels, very few of these materials represent viable administration methods in a clinical setting. Whilst LMW hydrogels have the potential for controlled and targeted release mediated by interactions with the drug of interest, their mechanical weakness limits their utility for oral administration or implantation. On the other hand, polymer hydrogels are often much more robust, providing the strength required to withstand the stresses applied by the body. However, with a few exceptions, release from these materials is controlled only by the rate of diffusion out of the porous polymer gel structure.

Using the hybrid hydrogel developed in Chapter 2 we aimed to demonstrate its utility for controlled release, using naproxen (NPX) as a model drug. NPX is a non-steroidal anti-inflammatory drug (NSAID) related to ibuprofen and aspirin (Figure 3.7). NSAIDs function by inhibition of cyclooxygenase-2 (COX-2), which is responsible for the production of prostaglandins at sites of tissue damage (Figure 3.7d).²³⁴ These prostaglandins induce vasodilation which can in turn lead to acute or chronic pain in a patient. Naproxen reversibly binds COX-2 to reduce the rate of prostaglandin formation, reducing inflammation around damaged tissue.

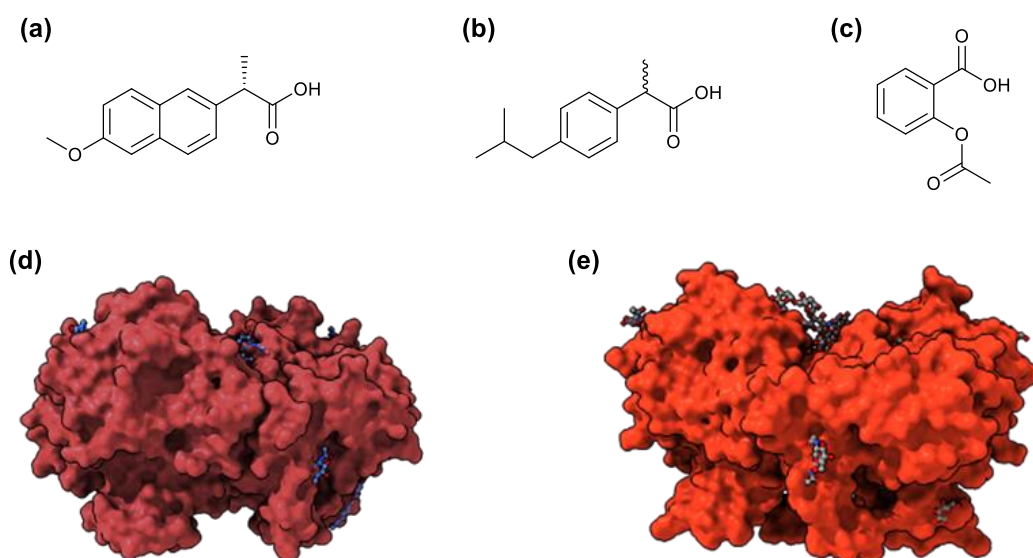


Figure 3.7: Structures of the NSAIDs naproxen (a), ibuprofen (b) and aspirin (c). Surface displays of COX-2 bound by naproxen (d) and COX-1 bound by indomethacin-(R)- α -ethyl-ethanolamide (e).

However, significant adverse effects of naproxen in the stomach have recently been reported.²³⁵ As well as inhibiting COX-2, naproxen also reversibly inhibits COX-1, another cyclooxygenase enzyme

(Figure 3.7e). COX-1 stimulates the formation of mucus in the stomach lining, an important defence against the strongly acidic conditions in the stomach. Side-effects of NPX are therefore reported to include irritation, ulceration and bleeding of the stomach. Selective COX-2 inhibiting drugs have been synthesised and tested in recent years, however, a significant increase in the incidence of cardiovascular disease was reported in clinical trials. As such, NPX remains in use and the development of matrices which encourage specific release in the intestine are of increasing importance. Not only does this reduce the risk of side-effects, as uptake from the intestine is high it ensures a greater therapeutic effect is provided with each dose.^{236,237}

A number of reports describing approaches to controlled release of NPX from hydrogels have been published in recent years. The majority of these examples achieve a degree of controlled release by using high loadings of a polymer to decrease the rate of diffusion out of the gel.^{238–241} This method is not dependent on changes in conditions which may be experienced in the body however, and as such does not represent true controlled release. More novel approaches to controlled NPX release include conjugation to magnetic nanoparticles²⁴² and encapsulation in a temperature sensitive poly(*N*-isopropyl)acrylamide (PNIPAAm) matrix,²⁴³ which utilise differences in the permeability and temperature of healthy and inflamed tissues respectively.

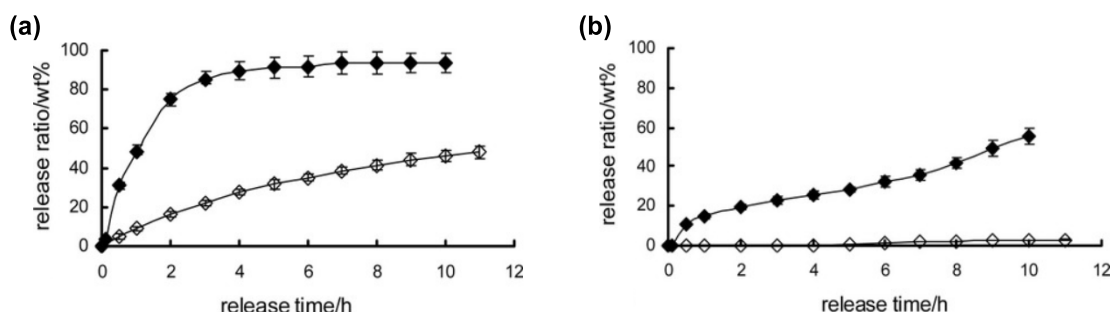


Figure 3.8: NPX release profiles for PASP (black diamonds) and PASP-EC hybrid (white diamonds) under simulated intestinal (a) and gastric (b) conditions. Figure adapted from [245].

Works describing the pH-dependent swelling of polymer hydrogels, and enhanced release from the ‘swollen’ hydrogels have also been described. Subuddhi and Das prepared dual-PG materials comprising poly(vinyl alcohol) and chitosan.²⁴⁴ Swelling of this second network at pH 7 allows rapid release of NPX compared to under more acidic or alkaline conditions. Cao *et. al.* also used an interpenetrating polymer network (IPN) to achieve the same ends.²⁴⁵ In their case polyaspartic acid (PASP) showed pH dependent swelling within an ethyl cellulose (EC) supporting matrix. Very slow

NPX release was observed into simulated gastric fluid (pH 1.05) from the IPN compared to the PASP alone (Figure 3.8a). In contrast, some NPX release (although still relatively slow) was still observed under simulated intestinal conditions (pH 6.8) for the IPN (Figure 3.8b). The release of NPX from a sugar-based LMW gelator was reported by Wang and co-workers in 2014. Using a methoxybenzylidene protected monosaccharide, release of NPX from the gel matrix was stimulated by addition of acid, which hydrolysed the gelator acetal groups, resulting in gel disassembly.²⁴⁶ However, significant release was observed over 9 h even in the absence of this acid trigger.

The above examples utilise non-specific diffusional effects to control drug release. To our knowledge, DBS-CONH₂ remains the only gel which mediates release of this NSAID *via* the formation and disruption of drug: nanofibre interactions (Figure 3.9). Smith and co-workers demonstrated that under acidic conditions the protonated carboxylic acid moiety of NPX interacts with the acyl hydrazide groups presented on the LMWG nanofibres, limiting release into a solution adjusted to pH 7.¹¹⁴ Deprotonation of the acid at pH 8 encouraged rapid release of NPX through disruption of these interactions.

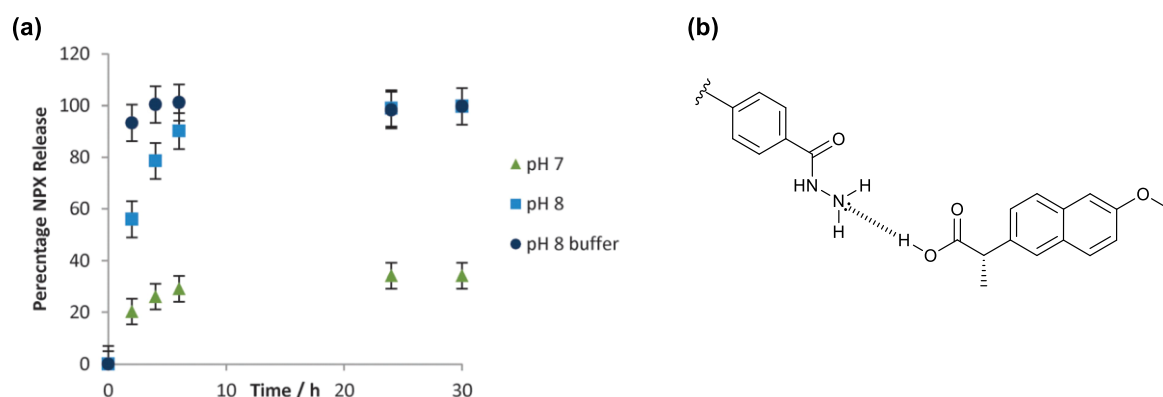


Figure 3.9: pH-dependent release of NPX from DBS-CONH₂ hydrogels (a), as reported by Smith and co-workers [114]. The proposed mode of interaction between DBS-CONH₂ and NPX (b). Only a fragment of DBS-CONH₂ has been drawn for clarity.

Given the orthogonal assembly of the DBS-CONH₂ and PEGDM networks in our hybrid hydrogel (Chapter 2), we proposed that a similar pH-dependent release behaviour would be observed for these dual-network materials. The incorporation of the PG network would also bestow the material with additional desirable properties compared to the LMWG alone, including increased resistance to strain and the capacity for photo-induced shaping. We aimed to formulate NPX within this hybrid hydrogel and assess the characteristics of the system compared to both NPX-loaded DBS-CONH₂ and PEGDM gels reported in Chapter 2. We then planned to determine the influence of each gel

network on the pH-dependent release of NPX. Finally, we proposed to use the photo-patternable nature of the hybrid gels to achieve a degree of spatial control over NPX 'delivery', highlighting the power of the LMWG/PG hybrid gel approach for developing functional drug release materials.

3.3 Preparation of NPX-loaded hydrogels

NPX was formulated into DBS-CONH₂ hydrogels as previously reported by Smith and co-workers.¹¹⁴ DBS-CONH₂ and NPX were mixed as solids and water added such that the concentration of NPX was 6 mM. These samples were sonicated to break up any aggregates and the resulting suspension heated to dissolution. The hot sol was allowed to cool to room temperature under ambient conditions. NPX-loaded gels formed on cooling in a few minutes over the same concentration range as in the absence of NPX (*ca.* 4-10 mM). No NPX precipitation or crystallisation was observed on cooling, although a slight turbidity of the samples (Figure 3.10a) was observed compared to gels prepared in the absence of NPX.

NPX-loaded PEGDM hydrogels were prepared by sonicating a mixture of NPX (6 mM), PEGDM (known mass) and PI (0.05% wt/v) in water before curing under a high-powered UV lamp at room temperature (0.5 h). This yielded clear hydrogels in which small clumps of NPX could be seen (Figure 3.10b). This suggests that the NPX is not properly incorporated into the PG nanostructure. We suggest that the absence of specific interactions between the gel fibres and NPX, along with the low solubility of NPX in water (partition coefficient, $\log P = 3.34$)²⁴⁷ prevents proper formulation into the PG matrix.

For the preparation of NPX-loaded DBS-CONH₂/PEGDM hybrid hydrogels, we initially attempted to formulate all three components directly into the gel *via* a heat/cool cycle. In Chapter 2 it was shown that this approach resulted in the formation of weak gels, we proposed due to a difference in solubility of DBS-CONH₂ in the PEGDM solution. Smith and co-workers have previously suggested that the formulation of drugs with high $\log P$ values can encourage more efficient network aggregation.¹¹⁴ Therefore we proposed that NPX may have the same effect here, encouraging formation of a sample-spanning network within the PEGDM solution. This was not the case, however. Little to no evidence of gel formation was observed after the heat/cool cycle. ¹H NMR spectra of mixed solutions NPX and PEGDM (both heated and not) show no evidence of structural changes in either species, or any shifts indicative of interactions between the two which may hinder DBS-CONH₂ gelation. Just as for the samples without NPX, the LMW hydrogels themselves were not soluble in the PEGDM/PI solution. As proposed in Chapter 2, the nucleation

and/or aggregation of DBS-CONH₂ is likely inhibited by formulation in the PEGDM solution, and the presence of NPX appears to exacerbate this effect.

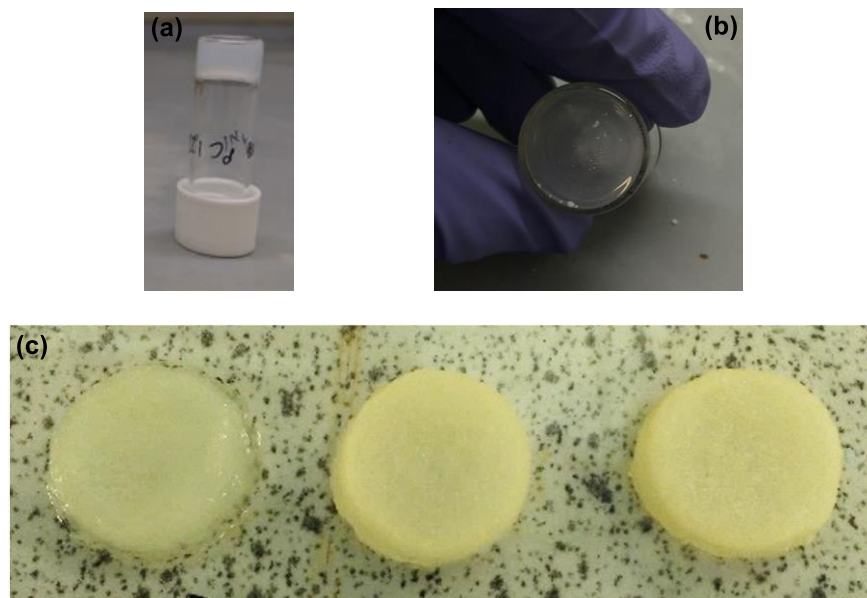


Figure 3.10: Images of hydrogels loaded with NPX (6 mM). 6 mM DBS-CONH₂ (a), 10% PEGDM (b) and hybrid gels (c: left = 5% hybrid, middle = 7% hybrid, right = 10% hybrid).

We therefore adopted the approach developed in Chapter 2 for the formation of hybrid hydrogels. A solution of PEGDM (known mass) and PI (0.05% wt/vol) was pipetted on top of an NPX-loaded DBS-CONH₂ hydrogel. This solution was left for three days to allow PEGDM and PI diffusion into the gel. After this time the supernatant was removed and the gels irradiated with long wavelength UV light for 0.5 h to yield robust, drug-loaded hybrid gels. These gels are opaque, in contrast to the translucent hybrid gels formed in the absence of NPX (Figure 3.10c).

No NPX was detected by ¹H NMR in the supernatant, and measurements performed on the dried gels after PEGDM diffusion showed equimolar quantities of DBS-CONH₂ and NPX (NPX concentration = 6.15 ± 0.3 mM). Therefore, it can be inferred that no drug was released into the solution during the hybrid gel preparation and that the concentration of NPX in these gels is 6 mM. This is in line with the results reported by Howe *et. al.*, which showed that minimal release of NPX was seen into unbuffered water.¹¹⁴ We suggest this is due to binding of NPX to the gel fibres under these conditions. Additionally, no significant change in the uptake of PEGDM ($84 \pm 4\%$) was observed compared to samples without NPX in 10% hybrid gel samples ($86 \pm 2\%$). NPX and PEGDM concentration in the gels was calculated by comparison of the integrals of the DBS-CONH₂ acyl hydrazide peak ($\delta = 9.81$) to the peaks corresponding to either the NPX ($\delta = 1.27$) or the PEGDM

($\delta = 1.93$) methyl group. As the concentration of DBS-CONHNH₂ is 6 mM in all the samples, the concentration of NPX and PEGDM could be extrapolated.

3.4 Characterisation of NPX-loaded hydrogels

3.4.1 T_{gel} studies

To assess the impact of NPX on the macroscopic properties of the hydrogels, we applied the same methodology as outlined in Chapter 2 to study the gel-sol transition temperature (T_{gel}). Gels (0.5 mL) containing NPX were placed in a thermoregulated oil bath and the temperature raised at a rate of 0.5 °C min⁻¹. The T_{gel} was assessed by tube inversion (Table 2.3). Interestingly, the T_{gel} values of both the LMWG and the hybrid gel samples increased by *ca.* 10 °C on incorporation of NPX. We suggest that this may be the result of the high partition coefficient of NPX. Interactions between the NPX and DBS-CONHNH₂ formed in solution may increase the effective hydrophobicity of the gelator species compared to DBS-CONHNH₂ alone. This may encourage self-assembly or fibre aggregation by reducing the solubility in water, in turn increasing the gel-sol transition temperature.

Table 3.1: T_{gel} values of DBS-CONHNH₂ and UV-cured hybrid gels with and without NPX at a concentration of 6 mM. Errors given as standard deviation (n = 3).

DBS CONHNH ₂	PEGDM / % wt/vol	NPX / mM	T _{gel} / °C
6 mM	-	0	80 ± 1
8 mM	-	0	94 ± 1
6 mM	5	0	85 ± 2
6 mM	7	0	91 ± 1
6 mM	10	0	> 100 °C
6 mM	-	6	90 ± 1
6 mM	5	6	94 ± 1
6 mM	7	6	99 ± 2
6 mM	10	6	> 100 °C

As for the hybrid gels in Chapter 2, increasing concentration of PEGDM resulted in an increase in the T_{gel} of the resulting hybrid gel. Interestingly, the loading of NPX in hybrid gels also raised the T_{gel} compared to those prepared in its absence. This suggests that the response of the gels to

temperature is not solely determined by the PEGDM network in the hybrid hydrogels. Errors associated with this study are similar to those described in Chapter 2. An additional small contribution to the random error from the weighing of NPX is expected, but overall this should contribute relatively little to differences in the data (0.7% based on the smallest samples used).

3.4.2 Rheological studies

We further probed the macroscopic properties of the drug-loaded hydrogels by parallel plate rheology. The response of the gels to an applied shear strain was first studied (Figure 3.11). Little difference was observed between the rheological properties of 6 mM (*ca.* 2300 Pa) and 8 mM (*ca.* 2700 Pa) DBS-CONH₂ hydrogels in the presence of NPX. However, they are approximately twice as stiff as DBS-CONH₂ hydrogels in the absence of NPX (1600 and 1260 Pa for 6 mM and 8 mM hydrogels respectively, see page 75). This supports the idea that NPX encourages DBS-CONH₂ network assembly due to its high $\log P$ value (see above). As in the absence of NPX (page 75), higher PEGDM concentrations resulted in greater stiffnesses of the PG and hybrid hydrogels. Formulation of NPX did not induce significant changes in the rheological properties of PEGDM hydrogels. The 5% PEGDM hydrogels had stiffnesses of *ca.* 600 Pa both with and without NPX, whilst the 10% PEGDM gels had a G' value of *ca.* 5000 Pa. A slight decrease in the stiffness of the hybrid gels was observed in NPX-loaded samples, which may be attributable to a slight disruptive effect of NPX on PEGDM crosslinking, or due to the presence of NPX limiting the interactions between the DBS-CONH₂ and PEGDM networks. In the presence of NPX, the storage moduli of the 5% and 10% hybrid gels were 368 and 3738 Pa respectively, whilst in the absence of NPX these values were 381 and 4370 Pa (page 75).

Generally, similar characteristic features in the rheological data were seen as for the hydrogels prepared in the absence of NPX (page 76). Breaks in the data for DBS-CONH₂ gels make it difficult to interpret the changes in G'' at frequencies lower than the critical strain, but it does appear that this value increases slightly, indicative of dissipative nanoscale rearrangements. This may suggest that the presence of NPX not only raises the stiffness of the hydrogels, but increases their ability to deform prior to gel breakdown. This is not manifested in an increase in the LVR or critical strain value in this case. The shape of the rheological traces of the 5% and 10% PEGDM gels are very similar to those seen in Chapter 2. Again, a significant increase in G'' is seen before the decrease in elastic modulus is observed. This is again rationalised as the dissipative effect of nanoscale network rearrangements. Interestingly, in this case the dip in G'' value of 10% PEGDM is not seen when NPX is formulated. Crystallised NPX may disfavour changes in the network at low shear in this case. As

in the absence of NPX, differences in the behaviour of 5% and 10% hybrid gels were seen. Both gels demonstrate the increase in G'' associated with the PG network, although this

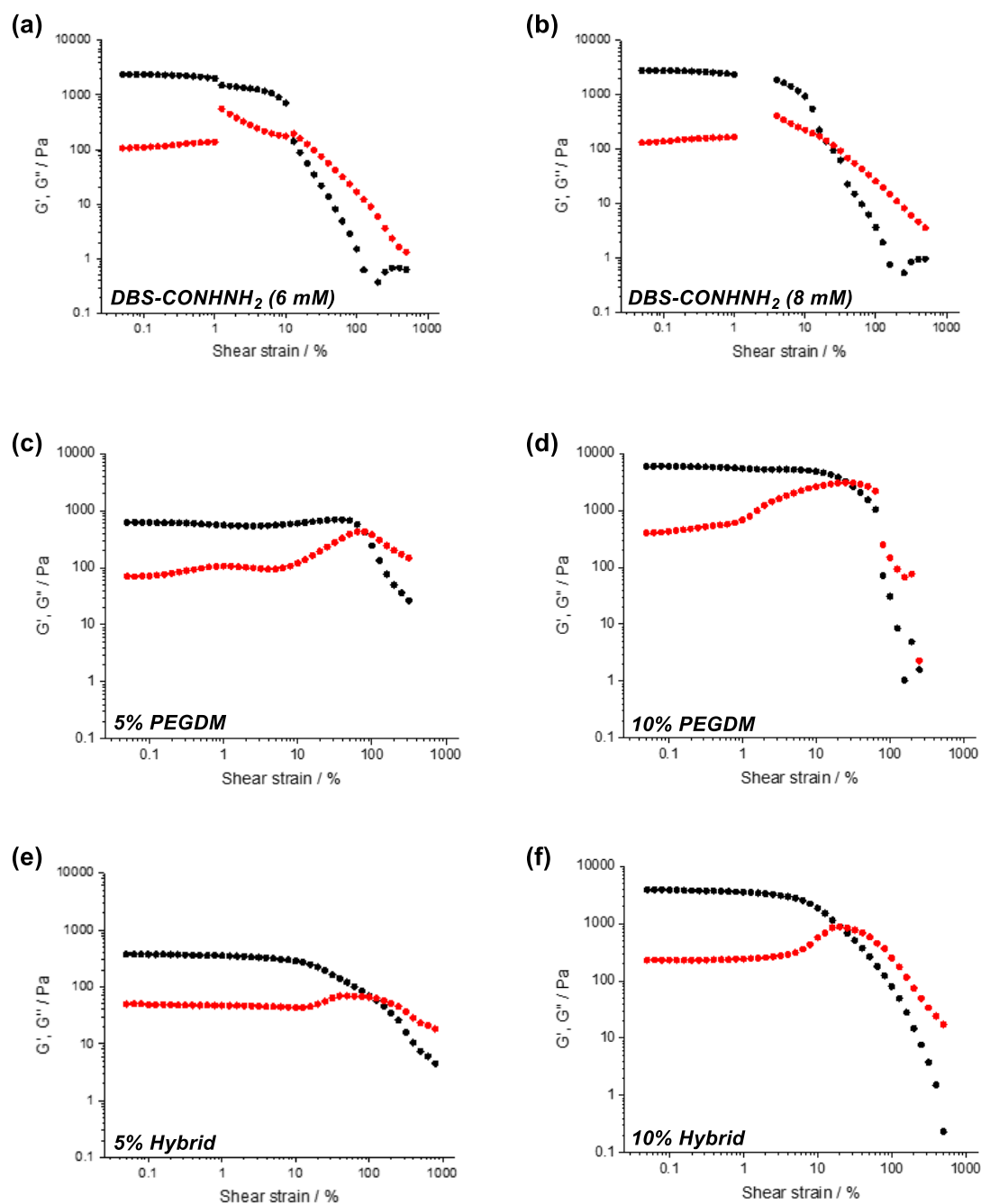


Figure 3.11: Storage (G' , black) and loss (G'' , red) moduli of NPX (6 mM) loaded hydrogels in response to varying shear strain at a constant frequency (1 Hz). Rheological traces for: 6 mM DBS-CONH₂ (a), 8 mM DBS-CONH₂ (b), 5% PEGDM (c), 10% PEGDM (d), 5% hybrid (e) and 10% hybrid (f). Errors are ca. $\pm 10\%$ for all samples. Breaks in the data in (a) and (b) are due to sample slipping.

is significantly more pronounced in the 10% hybrid gel, likely due to the greater polymer content. The incorporation of NPX also increases the breadth of the LVR in the hybrid gels compared to that seen in its absence, in contrast to the LMWGs and PGs alone. This suggests that the presence of NPX improves the stability of the gel networks with respect to shear strain, perhaps as a consequence of network stiffening.

Similarly, the response of the NPX loaded gels in response to changes in frequency (at a fixed shear strain) were then measured (Figure 3.12). An increased stiffness was again observed for 6 mM LMW hydrogels when NPX was incorporated compared to the drug-free samples from Chapter 2 (pages 76 and 77). G' values for NPX-loaded (6 mM) DBS-CONH₂ hydrogels were recorded as 3840 and 1994 Pa for 6 mM and 8 mM LMWG loadings respectively. In contrast, in the absence of NPX, the stiffness of 6 mM and 8 mM DBS-CONH₂ gels were 2500 and 2000 Pa respectively (pages 76 and 77). The fact that a significant difference in stiffness in the presence of NPX (compared to in its absence) is seen for the 6 mM LMW hydrogel and not for 8 mM gels, may suggest that equimolar interactions are responsible for these changes. In contrast, little change was observed for the PEGDM gels. 10% PEGDM gels have G' value 5500 Pa in the absence of NPX (pages 76 and 77) and 6700 Pa in the presence of NPX. The relatively small percentage changes here indicate that even in the presence of NPX, the properties of the PEGDM network determines the material stiffness. The stiffness of 5% hybrid gels approximately doubles from 770 Pa (pages 76 and 77) to 1600 Pa in the presence of NPX, whilst 10% hybrid gels show little difference between samples with (2900 Pa) and without (3400 Pa) NPX. This could suggest that at lower PEGDM loadings, the mechanical properties of the hybrid gels is more significantly influenced by the DBS-CONH₂ network, whilst at higher loadings the PEGDM network dominates these characteristics.

Interestingly, in the presence of NPX, the frequency at which gel stiffening occurs is almost identical for all samples (*ca.* 20 Hz). The stiffening frequency has been significantly reduced for both the DBS-CONH₂ and hybrid gel samples compared to those prepared without NPX (from *ca.* 40 and 25 Hz respectively). It is possible that the binding of NPX to DBS-CONH₂ lengthens the time over which the gel LMWG network relaxes due to a slight stiffening/rigidification effect. This would be in agreement with the idea that the high $\log P$ value encourages assembly into solid-like fibres. An increase in the hydrophobicity of nanofibres with bound NPX may also increase the energy required for rearrangement back to an energetic 'ground state' on removal of strain, resulting, again lengthening the relaxation timescale. Slipping of the PEGDM gel at 5% wt/vol prevented the collection of quality data for this sample. This illustrates that, despite the small contribution of NPX to the total expected error associated with these measurements (*ca.* 0.35%) its effect on the adhesive properties of this particular hydrogel may have resulted in the propagation of error

through unexpected mechanisms, and highlights the complexity of working with this class of materials.

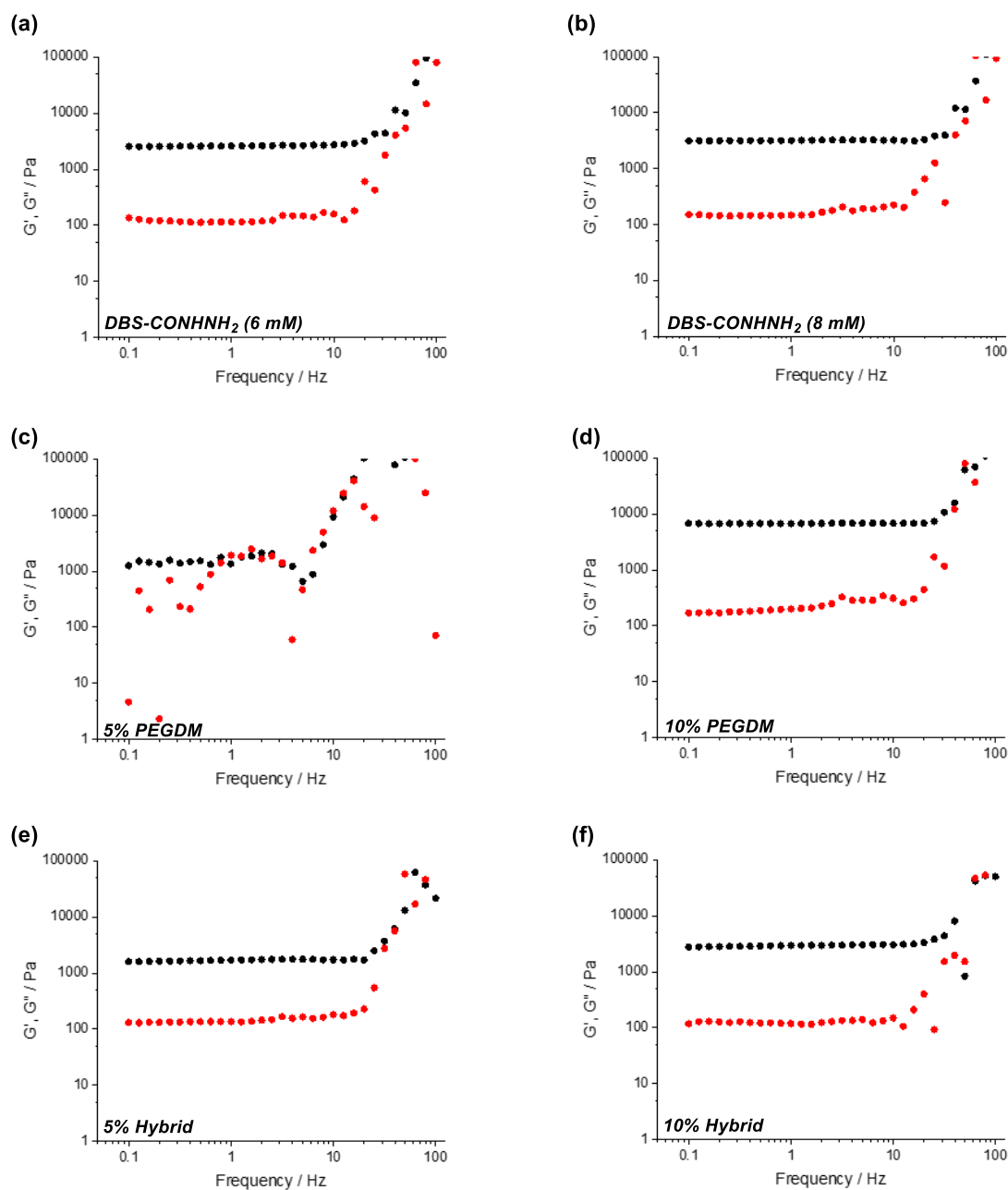


Figure 3.12: Storage (G' , black) and loss (G'' , red) moduli of NPX (6 mM) loaded hydrogels in response to varying frequency at a constant shear strain. Rheological traces for: 6 mM DBS-CONH₂ (a), 8 mM DBS-CONH₂ (b), 5% PEGDM – poor quality data due to gel slipping (c), 10% PEGDM (d), 5% hybrid (e) and 10% hybrid (f). Errors are ca. \pm 10% for all samples.

3.4.3 SEM imaging

Scanning electron microscopy was used to visualise the nanoscale networks of freeze-dried samples of hydrogels containing 6 mM NPX (Figure 3.13). In the electron micrograph of DBS-CONH₂ evidence of a nanofibrillar morphology is seen. The presence of NPX therefore does not appear to inhibit the self-assembly of DBS-CONH₂ or perturb the nanoscale structure. The nanofibres had an average diameter of 23 ± 10 nm, almost identical to that reported for LMW hydrogels in the absence of NPX (page 80). It does appear that slightly greater aggregation of the nanofibres can be seen in this SEM image compared to DBS-CONH₂ alone, with a slightly denser network and smaller pore structures visible for gels formed in the presence of NPX. Given that these are small differences however, the influence of drying artefacts cannot be ruled out. Importantly though, no evidence of NPX crystallisation is observed for these samples, indicating that NPX interacts with the DBS-CONH₂ nanofibres, and is not prevented from diffusing out of the gel (for example during hybrid gel preparation) due to physical constraint by the porous network.

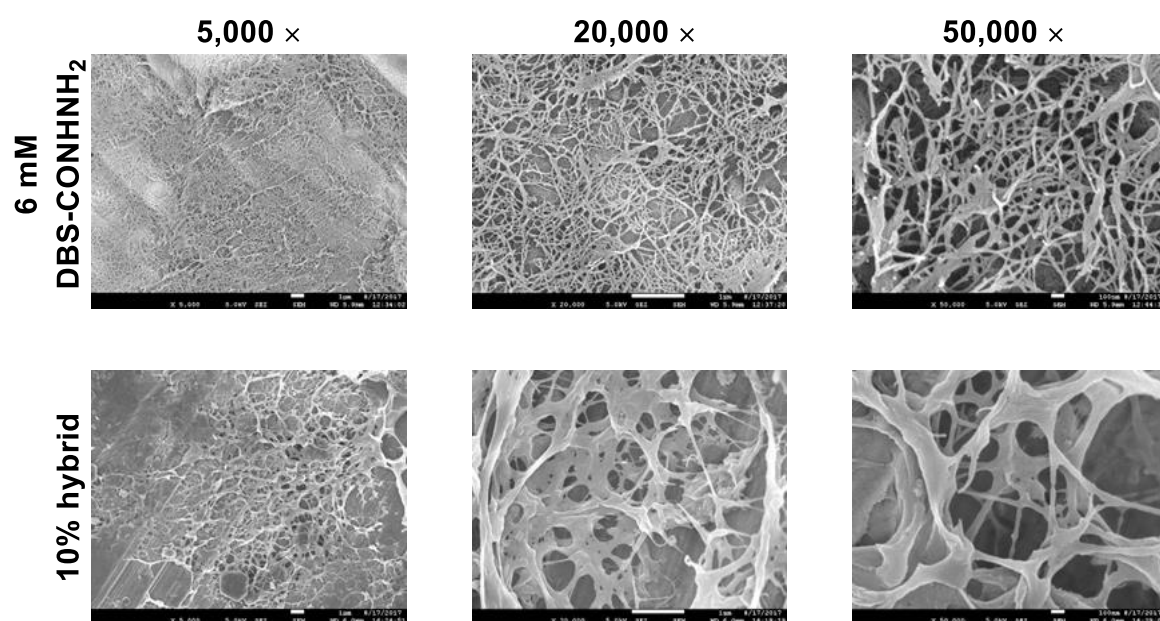


Figure 3.13: SEM images of 6 mM DBS-CONH₂ (top) and 10% hybrid (bottom) gels loaded with 6 mM NPX. Image magnification is given above each column. Scale bars are as follows: 5,000 x = 1 μ m, 20,000 x = 1 μ m, 50,000 x = 100 nm.

For NPX-loaded 10% hybrid gel samples, as for the samples without NPX, evidence of both DBS-CONH₂ nanofibres and the more sheet-like structures associated with PEGDM can be seen. However, in this material there appears to be less aggregation of the DBS-CONH₂ nanofibres along the PEGDM sheets. This may indicate that NPX preferentially interacts with the LMWG fibres, competing for any interactions it may have with PEGDM. Again, importantly, no evidence of NPX

crystallisation was observed within the gel matrix. Further SEM images are presented in Appendix 4.

3.4.4 IR spectroscopy

IR spectroscopy of dried NPX-containing xerogels was performed as described in Chapter 2 (page 82). Again, we focused on the O-H (3296 cm^{-1}) and N-H (3184 cm^{-1}) stretches of DBS-CONH₂. Additionally, the carbonyl stretch of NPX was used to infer interactivity between the API and the gel networks (full spectra given in Appendix 5).

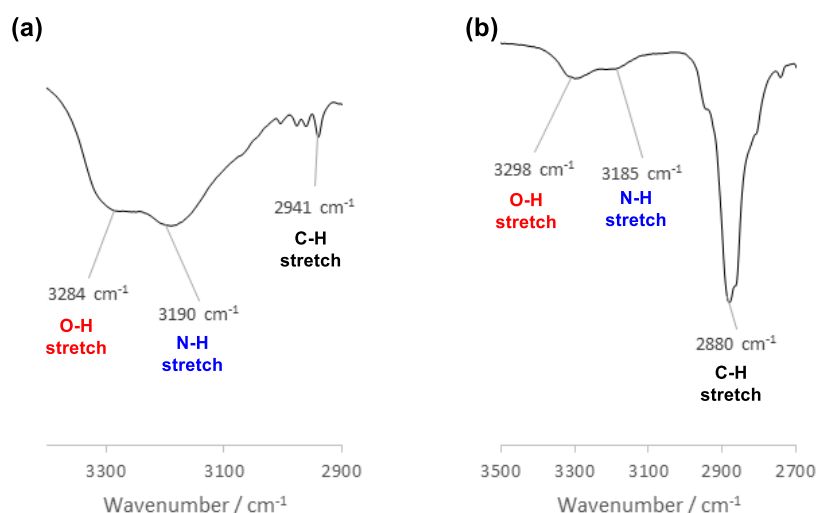


Figure 3.14: Excerpts from IR spectra of 6 mM DBS-CONH₂ (a) and 10% hybrid (b) gels. Changes in the O-H and N-H peaks of DBS-CONH₂ are observed.

The C=O stretching frequency of DBS-CONH₂ is 1640 cm^{-1} in both the NPX-loaded LMW and hybrid hydrogels. This is significantly shifted from the LMW hydrogel alone (1635 cm^{-1}), and indicates that in both samples, non-covalent interactions between the acyl hydrazide moiety and other the other components of the gel exist. The NPX C=O stretch shifts slightly from 1725 cm^{-1} to 1727 cm^{-1} when formulated in the DBS-CONH₂ hydrogel. This is accompanied by a significant shift in the O-H (-12 cm^{-1}) and N-H ($+6\text{ cm}^{-1}$) stretching frequencies of DBS-CONH₂. These data are indicative of interactions between the carboxylic acid of NPX and the acyl hydrazide and alcohol moieties on the gel nanofibres. As in Chapter 2, the importance of the changes in the O-H and N-H peaks should not be overstated. Whilst these shifts appear large, again the FWHM of the O-H and N-H peaks in this gel are *ca.* 140 and 300 cm^{-1} . However, the accompanying change in the carbonyl stretching frequency of NPX lends more weight to this argument. In contrast, when formulated in

PEGDM hydrogels, no change in the NPX C=O stretching frequency was observed, suggesting that no specific interactions are formed between the API and the sheet-like structures of PEGDM. Importantly, in the 10% hybrid gel, this stretch was shifted significantly to a value of 1732 cm⁻¹. This suggests that NPX interacts specifically with the DBS-CONH₂ nanofibres in the hybrid gel dual-network, as inferred from the SEM images. Additionally, in the 10% hybrid gel smaller shifts in the O-H (2 cm⁻¹) and N-H (1 cm⁻¹) peaks compared to in the absence of NPX (these shifts were 7 cm⁻¹ and the N-H peak was not visible). This data is possibly supportive of the idea that NPX competes with PEGDM for interaction with DBS-CONH₂, subtly altering the nanoscale structure of the gel network, although the small changes in peak maxima observed here are likely not significant given the breadth of the peaks of interest.

3.4.5 NMR study

To determine the proportion of NPX bound to the DBS-CONH₂ nanofibres, and hence immobilised, we prepared NPX-loaded DBS-CONH₂ hydrogels in an NMR tube. DBS-CONH₂ (1.99 mg, 6 mM) and NPX (0.97 mg, 6 mM) were suspended in D₂O containing DMSO as an internal standard (0.028 M). The sample was sonicated (15 min), then heated to dissolution. The hot sol was transferred to an NMR tube, with a gel forming on cooling. The ¹H NMR spectrum of this gel was recorded (Figure 3.15) and the concentration of unbound NPX calculated by comparison of relevant NMR signals to the DMSO internal standard ($\delta = 2.50$ ppm). An example calculation is given below:

$$\begin{aligned}
 I(\text{DMSO}, 6\text{H}) &= 60 \\
 I(\text{DMSO}, 1\text{H}) &= 10 \equiv 0.028 \text{ M} \\
 I(\text{NPX}, \text{CH}_3) &= 0.50 \\
 I(\text{NPX}, 1\text{H}) &= 0.17 \\
 [\text{Free NPX}] &= \left(\frac{0.17}{10}\right) \times 0.028 \text{ M} = 4.8 \times 10^{-4} \text{ M} \\
 \frac{4.8 \times 10^{-4} \text{ M}}{6 \times 10^{-3} \text{ M}} \times 100 \% &= 7.9 \%
 \end{aligned}$$

In DBS-CONH₂ hydrogels, *ca.* 92% of the NPX is NMR invisible and therefore considered bound to the gel fibres. This supports the conclusions drawn from the IR spectra, that interactions exist between NPX and the DBS-CONH₂ gelators. This high percentage of immobile NPX is not considered to be the result of crystallisation of NPX in the gel matrix, as no evidence of this was observed in the SEM images above.

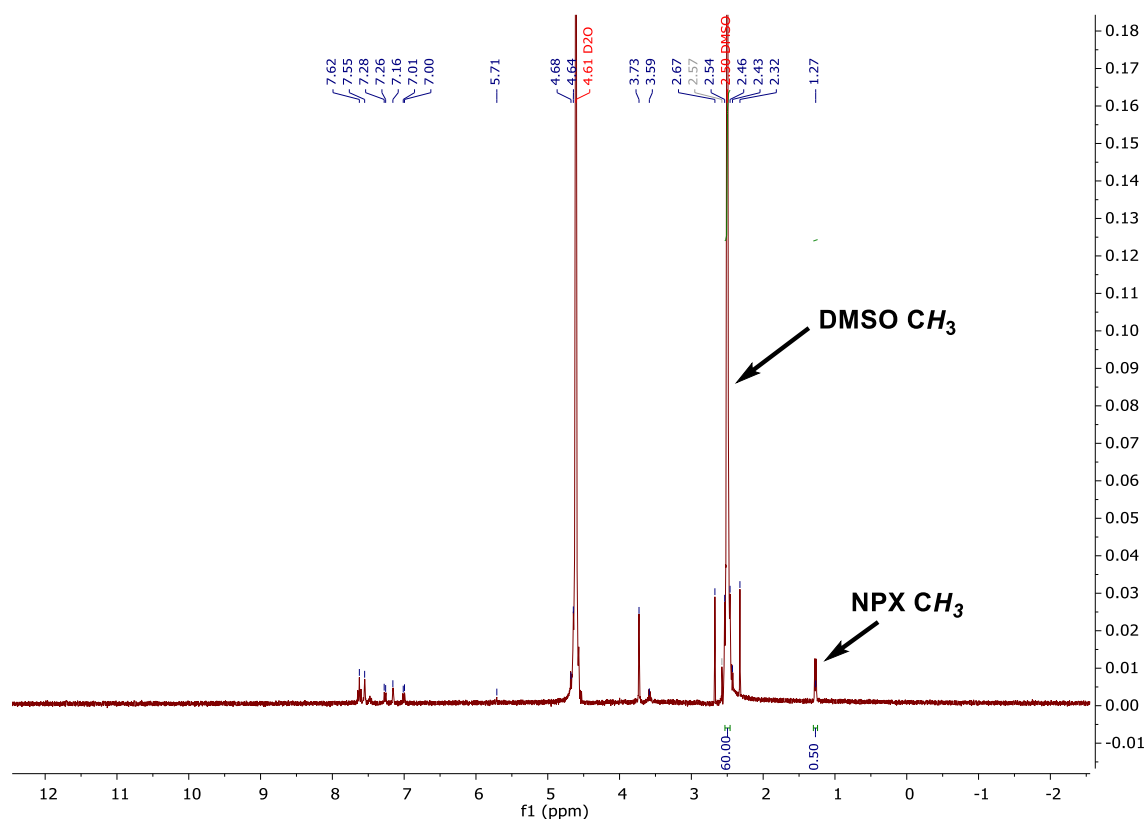


Figure 3.15: ^1H NMR spectrum of NPX (6 mM) loaded DBS-CONHNH₂ (6 mM) hydrogel made in D₂O solvent. Solution was spiked with DMSO (0.028 M) to quantify unbound NPX.

Using the same approach, the influence of the photo-polymerisation process on the interactions between NPX and DBS-CONHNH₂ was assessed. A solution of PEGDM (70 mg, 10% wt/vol) and PI (0.35 mg, 0.05% wt/vol) dissolved in a solution of DMSO (0.028 M) in D₂O (0.7 mL) and pipetted on top of the gel. The solution was left for 1 week to maximise PEGDM diffusion into the LMW hydrogel. The sample was then irradiated with UV light (0.5 h) and the ^1H NMR spectrum recorded. It was found in this gel that the proportion of mobile NPX in the sample was almost identical (7.2%) to that seen in the LMW hydrogels. It could be expected that competition with PEGDM for interactions with the DBS-CONHNH₂ nanofibres might increase the amount of mobile NPX, however this is not observed here. It could be that the competitive interactions weaken the binding between NPX and DBS-CONHNH₂, but not sufficiently to make it mobile within the gel sample.

3.5 pH controlled NPX release from hydrogels

As outlined in the Chapter aims, selective release of NSAIDs under intestinal conditions (pH 7-8), as opposed to the more acidic conditions found in the stomach (pH 2-4) has many potential benefits, including reduced dose frequency and incidence of side effects.²⁴⁸ Therefore, we studied the effect

of pH on the release of NPX from the prepared hydrogels. NPX-containing gels (1 mL) were prepared at a drug concentration of 6 mM (1.38 mg). These gels were covered with buffer solution (6 mL) and incubated at 37 °C. The concentration of NPX in the supernatant was monitored by UV-vis spectroscopy. NPX shows three distinct absorbances, at 285, 315 and 329 nm. We monitored the absorbance of NPX at 329 nm to minimise contributions from any DBS-CONH₂, PEGDM or PI released into the supernatant (Figure 3.16) and compared these values to those from control samples containing no NPX. When calculating percentage release, the volume of the gel (1 mL) was considered as the corresponding amount of solution, i.e. the concentration of NPX was considered in the 7 mL total volume, not only the 6 mL of supernatant.

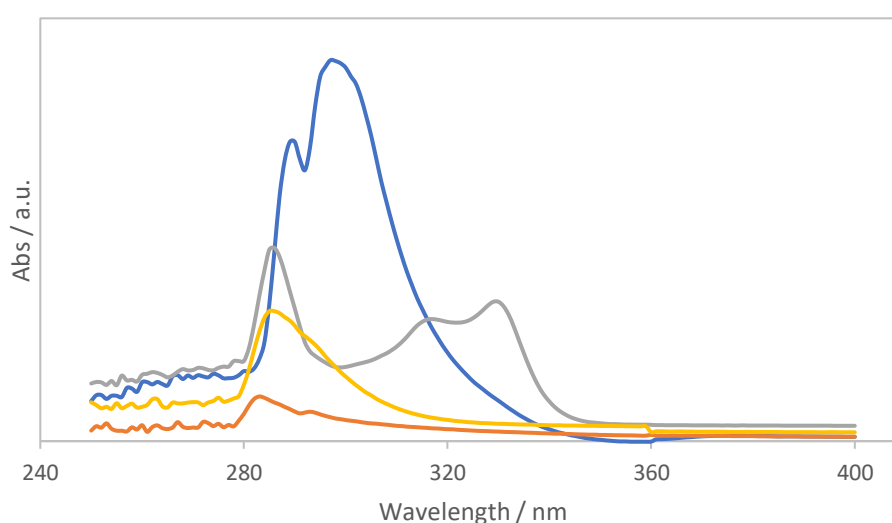


Figure 3.16: Representative absorption spectra of all gel components used in this study. PI = blue, DBS-CONH₂ = red, NPX = grey, PEGDM = orange.

When considering the results of the studies below, errors in addition to those associated with gel formation (estimated in Chapter 2 to be on the order of 0.4%) must be considered. Random error in the UV-vis absorption measurements has been considered and estimated as *ca.* $\pm 1\%$ of the value recorded, based on repeat measurements of standard samples. Such error may be the result of stray light and electronic noise. The temperature of the incubator is accurate to the nearest 0.05 °C and is verified using a thermometer encased within the equipment. More significantly, disruption of the gels on sampling may potentially have influenced the release profiles. Efforts were taken to minimise this any disruption through careful sampling, but the somewhat smaller standard deviations associated with release from the more robust PEGDM gels (see below) indicate that this may have contributed to errors. This is challenging to quantify, but we estimate that this could

account for up to *ca.* 5% error in the release percentage, relative to the recorded value, for LMW hydrogel samples.

DBS-CONHNH₂ hydrogels showed similar pH-dependent properties to those previously reported by Howe *et. al.* (Figure 3.17a), with greater NPX release observed at higher pH values.¹¹⁴ Differences were observed however due to the difference in receiving solution between the two studies. Here we used buffer solutions, which maintained a constant pH. In contrast, Howe monitored release into pH -adjusted solutions, which resulted in acidification of the supernatant over the course of the release study as NPX was released. In our experiment, over 24 h, a relatively small amount (*ca.* 25-30%) of NPX was released into pH 4 buffer from a DBS-CONHNH₂ (6 mM) hydrogel. No significant differences in the release of NPX into either acetate or citrate pH 4 buffered solution was seen. Only release into acetate is reported here. Comparatively large quantities of NPX were released into buffered solutions of pH 7 or pH 8 (80-90% release) over the same timescale. Similar release profiles were observed when NPX (6 mM) was encapsulated within an 8 mM DBS-CONHNH₂ hydrogel (Figure 3.17b). This difference in release can be rationalised by consideration of the Henderson-Hasselbalch relationship (Equation 3.1).

$$pH = pK_a + \log_{10} \left(\frac{[A^-]}{[HA]} \right) \quad \text{Equation 3.1}$$

By inputting the pH of each buffer and the pK_a of NPX (4.15)²⁴⁷ into this equation, the relative proportion of protonated and deprotonated forms of the API were calculated (Table 3.2). Good agreement is seen between the percentage of deprotonated NPX and the proportion of drug released into solution after 24 h over a wide range of pH values (2.8 – 8). Importantly, very little release into buffer solutions of pH 2.8 was seen. This result suggests that little release would be observed from DBS-CONHNH₂-containing hydrogels in the stomach, maximising uptake in the intestine where the conditions (pH 7-8) would encourage rapid release of the remaining NPX. Equally, the rapid release of NPX release at pH 5.5 – representative of the pH of the skin - potentially makes DBS-CONHNH₂ hydrogels appropriate materials for topical release of NSAIDs for pain relief of, for example, minor burns injuries, or potentially for transdermal delivery of pain relief medication to muscular injuries. The soft materials properties of these LMW hydrogels also lend themselves to this application, which is an interesting future avenue of research.^{249–251}

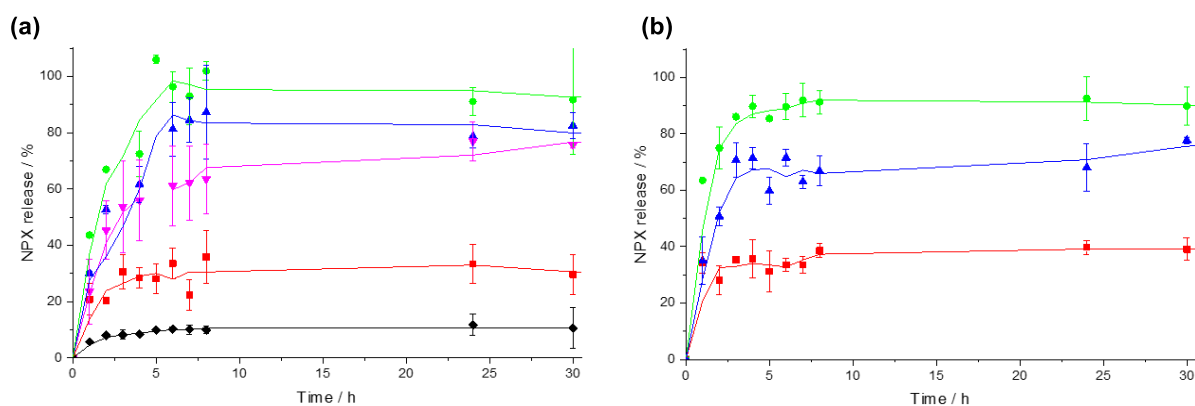


Figure 3.17: Release of NPX from DBS-CONH₂ hydrogels at LMWG concentration of 6 mM (a) and 8 mM (b) into buffers of different pH. Black diamond = pH 2.8, red square = pH 4, purple inverted triangle = pH 5.5, green circle = pH 7, blue triangle = pH 8.

Given that the proportion of deprotonated NPX correlates to the release, we suggest that the protonated form of NPX is unable to diffuse freely from the gels into the supernatant. Whilst this effect was thought to be the result of interactions with the DBS-CONH₂ nanofibres, some other interpretations were also considered. Crystallisation of NPX in the hydrogel matrix induced by pH change was a possibility. However, it was not observed by SEM after submersion of the gel in pH 4 buffer for 72 h (Figure 3.18). Nor was any significant change in the nanofibre morphology observed, consistent with previous findings that the macroscopic properties of DBS-CONH₂ do not change significantly with pH.¹⁴³ Therefore, the formation of large, entrapped crystals or changes in the gel properties were not considered to be the cause of lower release under acidic conditions.

Table 3.2: Percentage deprotonation of NPX in each buffer solution as calculated by the Henderson-Hasselbalch equation, and the observed release of NPX into buffer solution from 6 mM DBS-CONH₂ gels after 24 h.

pH	2.8	4	5.5	7	8
% deprotonated	4	42	96	100	100
% release (24 h)	12 ± 3	25 ± 4	77 ± 1	91 ± 4	79 ± 4

Similarly, the lower solubility of NPX in pH 4 buffer was also considered as an explanation for the lower release. However, given that complete dissolution of NPX was observed for calibration samples at a concentration of 0.86 mM – the maximum concentration in solution for this experiment – it was thought that this was an unlikely explanation of the experimental observations.

Therefore, specific interactions between NPX and DBS-CONHNH₂ are responsible for controlling the release of the API from the LMWG matrix. The similarity of the release profiles for 6 mM and 8 mM DBS-CONHNH₂ is supportive of the idea that these two species interact in a stoichiometric fashion.

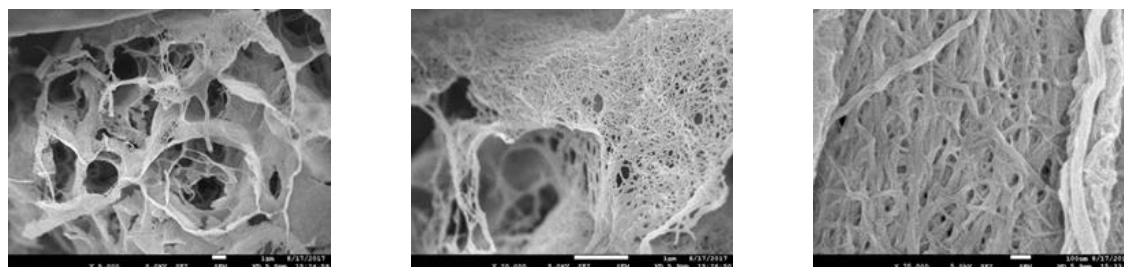


Figure 3.18: SEM images of NPX-loaded DBS-CONHNH₂ hydrogels after submersion in pH 4 buffer for 72 h. Magnifications are 5,000 × (left), 20,000 × (middle) and 75,000 × (right). Scale bars are as follows: 5,000 × = 1 μm, 20,000 × = 1 μm, 75,000 × = 100 nm.

In contrast to the LMW hydrogels, no differences in NPX release were demonstrated by PEGDM hydrogels into buffers of different pH. This supports the conclusion that no specific interactions exist between the PEGDM gel network and NPX (as suggested by IR spectroscopy). For a 5% PEGDM hydrogel, *ca.* 100% release of NPX was observed over the first 8 h into all buffers (Figure 3.19a). As well as demonstrating that no pH-dependent release properties from the PEGDM network, this result also confirms that the solubility of NPX is not the cause of limited NPX release from DBS-CONHNH₂ hydrogels at pH 4. PEGDM loading was also seen to have a significant influence on the kinetics of release of NPX from the hydrogel matrix, as well as the total amount released. A slower release rate was observed from a 10% PEGDM gel compared to the 5% wt/vol material. Furthermore, over 24 h, only 80% of the NPX was released (Figure 3.19b), suggesting that some of the API becomes trapped in the 10% PG network on photo-polymerisation, and is unable to diffuse out of the gel on the experimental timescale. Such effects have been previously described for polymer hydrogels.^{238–241} Again, though, the lack of specific interactions between PEGDM and NPX ensures that NPX release is consistent across all pH values studied.

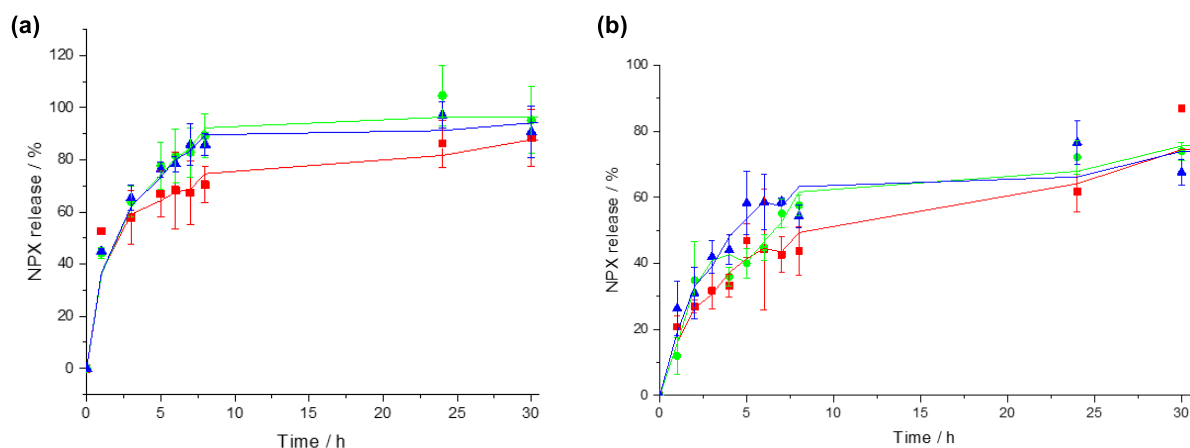


Figure 3.19: Release of NPX from 5% (a) and 10% (b) PEGDM hydrogels into buffers of different pH. Red square = pH 4, green circle = pH 7, blue triangle = pH 8.

Given the weak mechanical properties of DBS-CONH₂ hydrogels, these materials are not suitable for oral delivery of NSAIDs or other drugs, despite their excellent pH-dependent release properties and potential for transdermal applications. Breakdown of the gel is expected under significant strain, resulting in disruption of the self-assembled nanofibres and rapid release of the API. Conversely the PEGDM hydrogels, whilst robust enough to withstand this strain, demonstrate no pH-controlled release properties, meaning they will release the payload rapidly into the stomach, limiting useful uptake in the intestine. We therefore reasoned that the use of the hybrid gel developed here, containing largely orthogonal LMWG and PG network, would improve on the properties of both gels for oral drug delivery. The PG network should provide additional robustness (as seen in the rheological data), whilst the presence of the LMWG network may maintain its pH-dependent release properties.

On testing, the hybrid hydrogels did demonstrate a good degree of pH-dependence in the release of NPX (Figure 3.20). This effect was, however, slightly less pronounced than for the gels made from DBS-CONH₂ alone. Over 24 h the release of NPX into pH 4 buffer was *ca.* 50%, compared to the 30% release in the LMW hydrogel, whilst release at pH 7 and 8 decrease from 100 to *ca.* 70-80%. After 24 h, the release of NPX into pH 4 is significantly lower from both hybrid gel than into buffers of pH 5.5 and greater. Little change is seen for release into pH 5.5 buffer, the rate of which was slightly slower in DBS-CONH₂ gels than at pH 7 and 8. Importantly, given that the PEGDM hydrogels showed no pH-dependent release properties, we can infer that all the differences in release into different buffers are due to retention of the DBS-CONH₂ properties within the hybrid gel, and are not influenced by any changes in the swelling ratio of the polymer at different pH values.

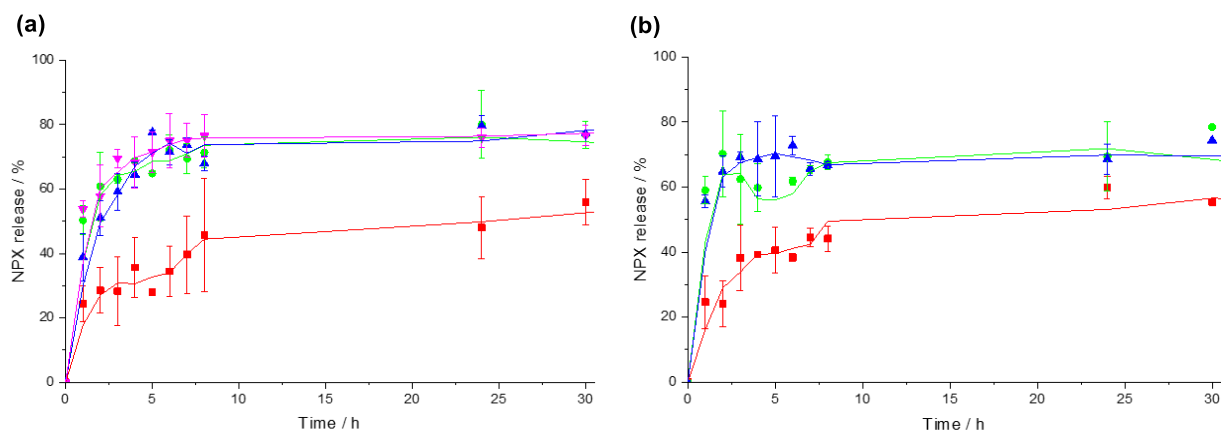


Figure 3.20: Release of NPX from 5% (a) and 10% (b) hybrid hydrogels into buffers of different pH. Red square = pH 4, pink inverted triangle = pH 5.5, green circle = pH 7, blue triangle = pH 8.

As outlined above, the controlled release properties of DBS-CONH₂ are slightly mediated by the presence of the PEGDM network. Similar total release percentages at pH 7 and pH 8 were seen over 24 h for the hybrid gels as for the 10% PEGDM gel, with *ca.* 20-30% of the formulated NPX not being released into solution. This suggests that in the hybrid gel, as proposed for PG samples, crosslinking of the PEGDM network results in entrapment of a proportion of the NPX in the more densely packed gel network. Hindrance of NPX diffusion, in particular for drug molecules situated far from the gel-sol interface, would account for the lesser total release over 24 h. Alternatively, some degree of NPX loss from the gel during the PEGDM diffusion loading step may account for some proportion of this decrease. However, this is considered a minor effect as little NPX was observed in the supernatant removed from the gel after 3 days (see Section 3.3).

A greater proportion of NPX was released from the hybrid gels into pH 4 buffer than in the DBS-CONH₂ gels. This observation is consistent with the observations from SEM and IR spectroscopy, which indicated that some interactions may exist between the PEGDM and DBS-CONH₂ networks in the hybrid gel. PEGDM is thus somewhat in competition with NPX for interactive sites on the DBS-CONH₂ network. Therefore, at pH 4, even though only *ca.* 30% of the NPX is deprotonated, the amount of 'free' NPX – that which is unbound to DBS-CONH₂ fibres – is closer to 50%. This effect is slightly greater for 10% hybrid gels than 5% hybrid gels, as is the decrease in release at pH 7 and pH 8. This suggests that PEGDM is responsible for mediation of the controlled release properties, rather than some general effect of formulation into the hybrid gels. As for the DBS-CONH₂ gels, no evidence of NPX crystallisation or morphological changes were observed (Figure 3.21).

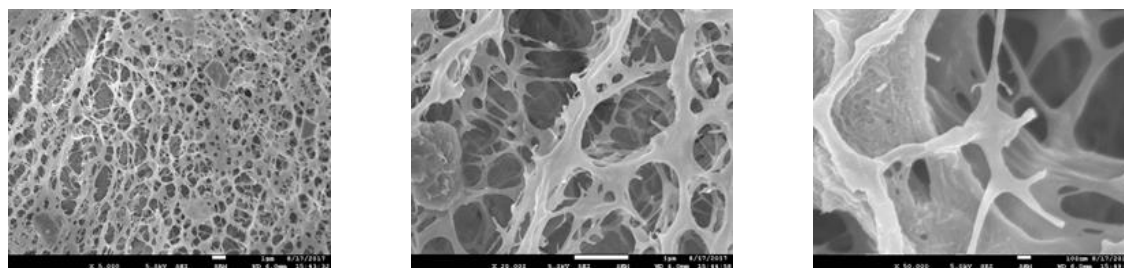


Figure 3.21: SEM images of NPX-loaded 10% hybrid hydrogels after submersion in pH 4 buffer for 72 h. Magnifications are 5,000 × (left), 20,000 × (middle) and 50,000 × (right). Scale bars are as follows: 5,000 × = 1 μm, 20,000 × = 1 μm, 50,000 × = 100 nm.

Table 3.3: Initial NPX release rates into buffers of varying pH. All rates assume zero-order release kinetics.

Buffer pH	Initial release rate × 10 ⁻⁹ / mol min ⁻¹					
	DBS-CONH ₂ 6 mM	DBS-CONH ₂ 8 mM	5% PEGDM	10% PEGDM	5% hybrid	10% hybrid
2.8	5.7	-	-	-	-	-
4	6.9	5.3	57.9	13.1	11.8	13.2
5.5	22.6	-	-	-	33.9	-
7	33.5	33.7	44.2	17.8	34.4	39.9
8	26.4	24.9	44.8	15.3	28.2	37.0

The initial rates of release from each of the gel matrices described above were also measured and are given in Table 3.3. For DBS-CONH₂ hydrogels, the initial rate of NPX release was significantly lower into pH 4 (and pH 2.8) buffer, than for less acidic buffers, the pH of which are greater than NPX's pK_a (4.15) – *ca.* 6 × 10⁻⁹ mol min⁻¹ compared to *ca.* 2.5 × 10⁻⁸ mol min⁻¹. These differences were consistent between DBS-CONH₂ gels with different LMWG loadings. Conversely, relatively similar release rates were observed from PEGDM hydrogels regardless of buffer pH – again demonstrating that DBS-CONH₂ is the active component determining pH-control of drug release. Release from the 5% and 10% PEGDM gels is significantly different however; diffusion from the former is approximately three times faster than from the latter (*ca.* 5.0 × 10⁻⁸ mol min⁻¹ vs 1.5 × 10⁻⁸ mol min⁻¹). This is reflective of the greater network density in the gel with a higher % wt/vol PEGDM. For both the 5% and 10% hybrid gels, the rate of NPX diffusion increased compared to the DBS-CONH₂ gels. They do, however, both release NPX at a significantly slower rate than 5% PEGDM alone. It is thought that the proposed competition between PEGDM and NPX, and the increase in 'free' API observed as a result, increases the release rate compared to the LMWG alone.

The combination of the two gel networks also, however, limits the rate of diffusion of NPX compared to the PG alone. Faster release kinetics were seen from the hybrid gels into buffers of elevated pH, again demonstrating the retained pH-dependent release properties of the LMWG network. The results of the above experiments should in the future be verified using a different analytical technique (such as NMR spectroscopy) to ensure the findings here are not influenced by systematic errors in, for example, the UV-vis spectrophotometer readings.

3.6 Photo-patterned NPX-loaded hybrid hydrogels

Importantly, the use of PEGDM as the PG component of these hybrid hydrogels afforded us the opportunity to induce spatial-control over the formation of NPX-loaded materials. We wished to demonstrate that the approach to spatial-resolution of the DBS-CONHNH₂/PEGDM hybrid gels outlined in Chapter 2 was compatible with the formulation of NPX. Therefore, we adapted the previously described methodology accordingly. DBS-CONHNH₂ (28.4 mg) and NPX (13.8 mg) were dissolved in DMSO (0.4 mL) by sonication and added to boiling water (9.6 mL). The hot solution was transferred to a square glass tray (5 cm × 5 cm × 1 cm) and allowed to cool to room temperature under ambient conditions, during which time a gel formed. The concentration of DBS-CONHNH₂ and NPX were both 6 mM in the 10 mL gel. On top of this gel, a 10 mL solution of PEGDM (10% wt/vol) and PI (0.05% wt/vol) was added and left for 3 days to allow diffusion into the LMWG hydrogel. After this time, the supernatant was removed.

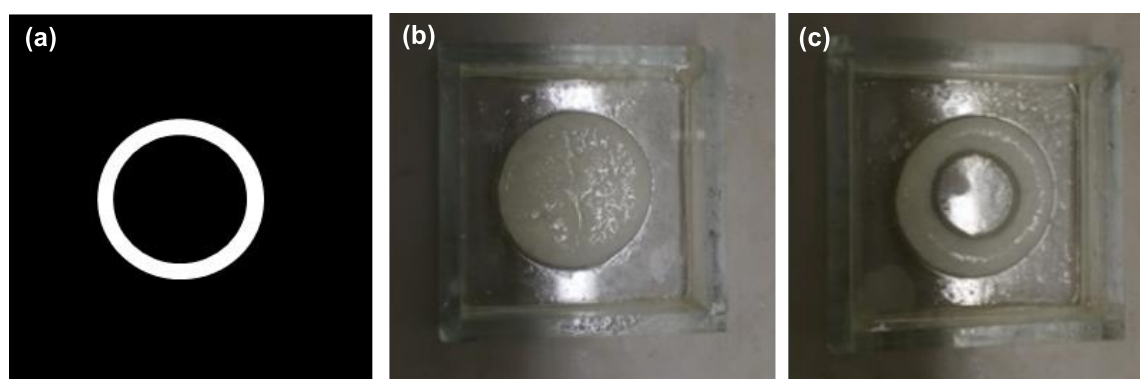


Figure 3.22: A ring-shaped photomask (a) was applied over the NPX-loaded LMWG gel and the pattern transferred to the gel by UV-photopatterning (b). The weak LMWG interior and exterior were easily removed to leave the more robust hybrid hydrogel ring (c).

As in Chapter 2, a ring-shaped photomask was chosen to exemplify the photo-patterning. An acetate photomask (four printed layers, Figure 3.22a) was applied over the top of the gel and the tray placed in ice. The masked gel was irradiated under a high power, long wavelength UV lamp (0.5

h) to induce photo-polymerisation in the exposed regions. In this way, an NPX-loaded multi-domain material was created. A robust, crosslinked hybrid gel ring with soft, LMWG regions both inside and outside this ring were created. The soft regions could be washed away (Figure 3.22b and c) to reveal a robust, drug-loaded, shaped gel.

3.7 Differential NPX release from photo-patterned hybrid gels

We proposed that shaped, pH-responsive hydrogels could afford unique controlled release properties and therefore chose to demonstrate the utility of our photo-patternable material by imposing spatial-control over NPX release. A 10 mL NPX-loaded hybrid hydrogel was prepared as above. In this case though, a simple band of hybrid gel (width = 2 cm, height = 0.5 cm) was 'patterned in' by spatially-controlling the exposure to UV irradiation (15 min) using an acetate photomask (4 layers thick). The LMWG each side of the band was removed using water to expose the hybrid gel pattern.

Given that differential release was observed into solutions above and below the pK_a of NPX, we reasoned that by exposing the two sides of the hybrid gel band to buffers of different pH, that selective release into the compartment of elevated pH may be observed. We chose to use the pH values for which the greatest difference in rate and overall percentage release were observed – pH 2.8 and pH 7 (Figure 3.23a). These buffers were pipetted onto opposite sides of the hybrid gel band (1.5 mL each) and both compartments stirred using magnetic fleas. NPX release into the two compartments at room temperature was monitored by UV-vis absorption spectroscopy over 3 hours. At each time point, a 100 μ L aliquot of each buffer solution was taken for analysis and diluted to 2 mL in a UV cuvette for analysis. This aliquot was replaced to maintain a constant solution volume and the removal of NPX at each time point accounted for in the release calculations.

NPX release into the pH 7 compartment was significantly faster than that into the pH 2.8 compartment over the experimental timescale (Figure 3.23b). Release into the neutral compartment occurred at a rate of $11.5 \times 10^{-9} \text{ mol min}^{-1}$, whilst the release rate into the acidic compartment was only $1.18 \times 10^{-9} \text{ mol min}^{-1}$ – approximately ten times slower. This clearly demonstrates the ability of the shaped gels to achieve differential release from the two separate gel-sol interfaces, dependent on the conditions to which it is exposed. Interestingly, this difference in release was not only observable by UV-vis spectroscopy. As NPX is released from the hybrid gel, it becomes more transparent. Therefore, on the side of the gel exposed to pH 7 buffer, a significantly greater proportion of the gel became transparent over time compared to the side of the gel which interfaces with pH 2.8 buffer (Figure 3.23c). The pH of the two compartments was

retained for the duration of the experiment, which demonstrates the ability of this hybrid gel to act as an effective barrier to separate the compartments on this timescale.

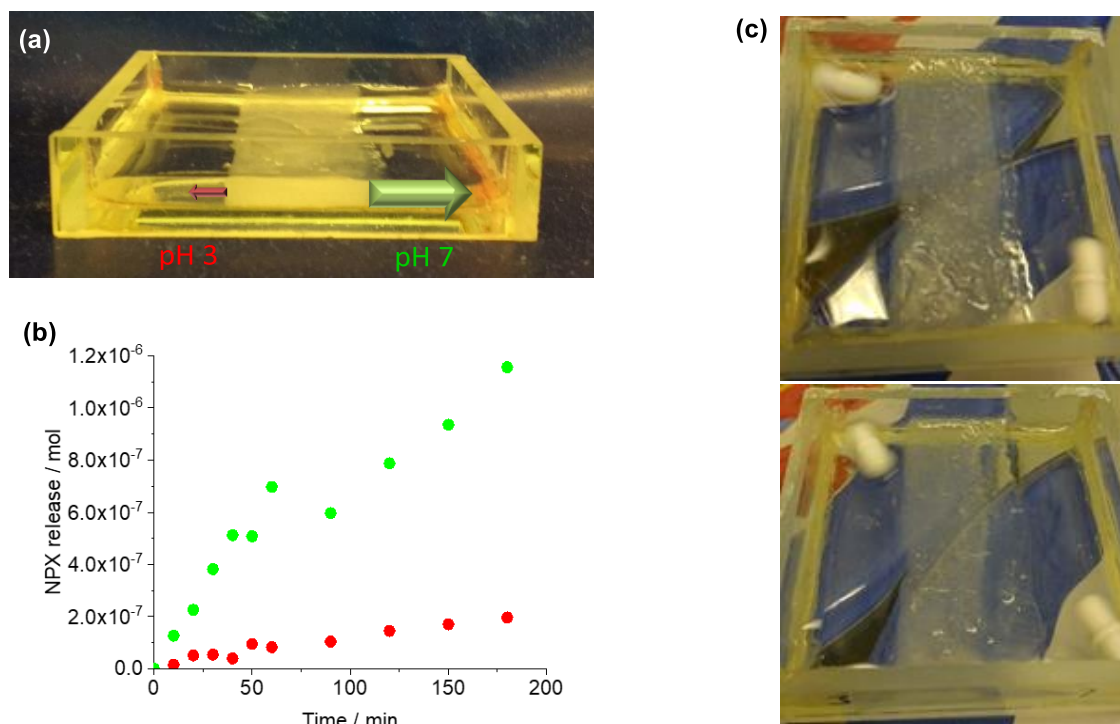


Figure 3.23: Summary of the differential release experiment (a). Release into two compartments of different pH values, separated by a gel band (diameter = 2 cm). NPX release profiles (b). Red circles = pH 2.8, green circles = pH 7. Increased transparency of the gel is observed from 0.5 h (top) to 3 h (bottom) as NPX is released (c).

The NPX release rates observed in this experiment are lower than those seen in the release studies above. For example, release from a 10% hybrid gel into pH 7 buffer in this experiment (11.5×10^{-9} mol min⁻¹) was *ca.* four times slower than in the experiment above (39.9×10^{-9} mol min⁻¹). This is likely due the differences in both temperature (37 °C vs room temperature) and the surface area of the gel:sol interface. In the ‘gel-in-vial’ experiments above, the calculated interface area based on a 1.8 cm gel diameter was *ca.* 10 cm², whereas for the photo-patterned gel this interface was much smaller (*ca.* 2 cm²). It is expected that ultimately an equilibrium (of both pH and NPX concentration) would eventually be reached for this system, but using the experimental setup outlined here, we are observing differences in initial release kinetics between the two compartments. If the drug was then ‘used up’ in one of the compartments, it would prevent equilibration through the system over longer timescales.

To date only one other example exists of a PG photo-patterned within a LMWG has been reported,⁵⁵ and never before has such a shaped gel been loaded with a bioactive component. Additionally, whilst prior literature has described control over the direction of drug release, this was never achieved without protection^{252–254} or deprotection^{255,256} of one face of a drug reservoir, or the application of an external magnetic field.²⁵⁷ Here, the difference in release was driven simply by a difference in pH at the gel:sol interfaces.

Given the wide range of pH interfaces in the body, it is easy to envisage the application of these types of differential release materials for controlled release *in vivo*. Simple devices such as that described here could be used for the release of pain relief medication specifically in the presence of inflamed tissue, or of acidity modifiers should the pH in the stomach cross a critical threshold. A similar hybrid gel could apply to transdermal delivery of drugs only towards the skin. Exciting future work may lie in the controlled release of chemotherapeutics, which utilise pH differences in the conditions surrounding cancers to selectively release drugs towards unhealthy tissue (e.g. latent tumour cells post-surgery), minimising the side effects of these APIs. Clearly, this specific simple pH-driven system is not necessarily appropriate for such an application, but this proof-of-principle study outlines the potential of controlled release matrices to maximise therapeutic benefits.

3.8 The influence of network order – reverse hybrid gels

For the hybrid gels described so far in this thesis, the LMWG network is self-assembled first, followed by triggering PG crosslinking. We have also carried out a preliminary investigation into the influence of the order of network formation on the properties of hybrid hydrogels, in particular controlled release. It was thought that through formation of the PEGDM network first, followed by self-assembly of DBS-CONHNH₂, different behaviours may be accessible to those described above, despite using the same gel components. It is becoming increasingly well known that the ‘pathway’ to materials assembly can influence their properties and performance.^{46,47,258,259} These PG/LMWG materials are termed ‘*x*% reverse hybrid’ gels here, where *x* refers to the % wt/vol of PEGDM loaded in the material.

The formation of these reverse hybrid gels is less simple than those in which the LMWG is formed first. We first attempted to prepare dual-network hydrogels through a diffusion approach. A 5% PEGDM hydrogel (0.5 mL) was prepared and a solution of DBS-CONHNH₂ (1.42 mg) dissolved in DMSO (0.04 mL) was added on top. The solution was left for 3 days and then removed. The resulting gel was dried to the xerogel and DMSO-*d*₆ added. The crosslinked PEGDM did not dissolve, however very small peaks corresponding to DBS-CONHNH₂ were observed in the spectrum. Given this

promising result, we repeated the experiment, but with both DBS-CONH₂ (1.42 mg) and NPX (0.69 mg) dissolved in the DMSO supernatant. In this case, after three days crystallisation was observed at the very top of the gel (Figure 3.24a). Given that this did not occur in the absence of NPX, it was assumed that this species was that crystallising. This was confirmed by sectioning the gel into two halves – top and bottom – using a razor blade, drying to the xerogel and dissolving the non-polymerised components in DMSO-*d*₆ as described above. Again, evidence of a very small amount of DBS-CONH₂ was observed throughout the gel. NPX, in contrast, was only observed in the top half, where crystallisation occurred, confirming the identity of the crystalline species.

Given the difficulties associated with formulation of NPX into the reverse hybrid gel *via* this method, we adopted a different approach to reverse hybrid gel formation (Figure 3.24b). Given the rapid gelation kinetics of DBS-CONH₂, we considered it necessary to retard this gelation process. To achieve this, a water bath was placed under the UV lamp so that a solution of mixed gelators could be held at the T_{gel} of DBS-CONH₂ (80 °C), significantly slowing the kinetics of self-assembly. A solution (0.5 mL) of PEGDM (10% wt/vol) and PI (0.1% wt/vol) was pre-warmed in the water bath at 80 °C. DBS-CONH₂ (2.84 mg) was dissolved in DMSO (0.04 mL) and added to boiling H₂O (0.46 mL). This hot sol was added to the PEGDM/PI solution and the mixture was immediately exposed to UV light (0.5 h) to crosslink the PG network.

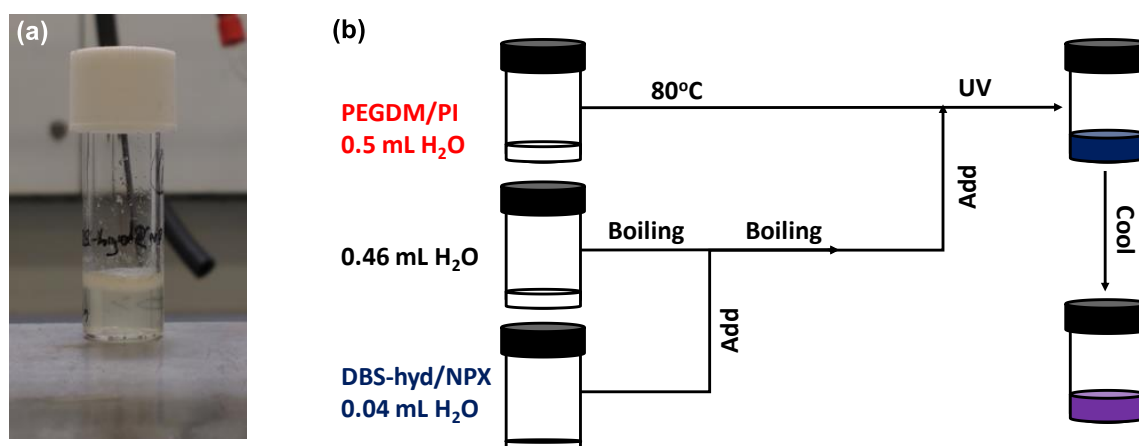


Figure 3.24: Crystallisation of NPX at the top of the PEGDM hydrogel during attempted diffusion-loading (a). Schematic of the optimised reverse hybrid gel fabrication methodology (b).

After crosslinking was complete, the gel was removed from the water bath and allowed to cool to ambient temperature, in theory inducing self-assembly of the LMWGs within the PG matrix. This process resulted in the formation of robust hydrogels which were slightly yellow in colour. The final concentrations of PEGDM and DBS-CONH₂ in this gel were 5% wt/vol and 6 mM respectively. If

the PEGDM/PI solution was not heated prior to addition of DBS-CONH₂, large, inhomogeneous aggregates of LMW hydrogel were seen in the resulting gels. NPX was formulated in these gels at a concentration of 6 mM simply by dissolving the solid (1.38 mg) in DMSO with DBS-CONH₂. NPX began to crystallise within these samples over *ca.* 24 h (Figure 3.25a).

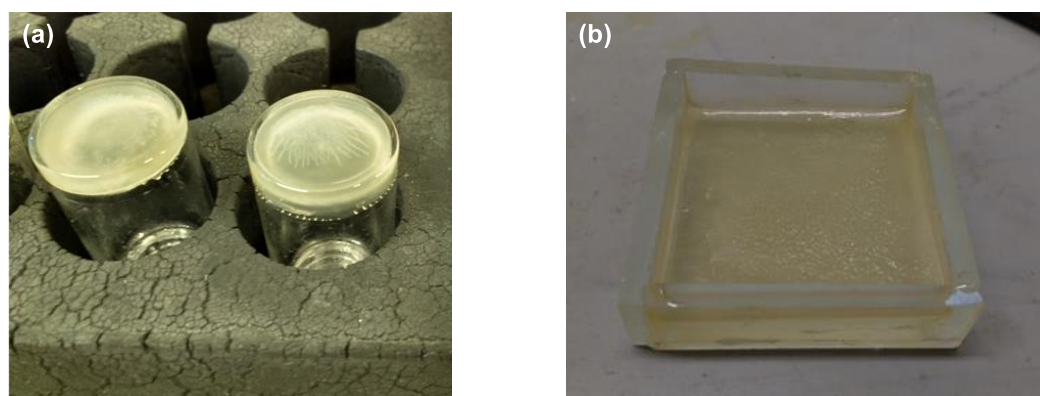


Figure 3.25: Images of 1 mL (a) and 10 mL (right) 5% reverse hybrid gels loaded with NPX (6 mM). Note that crystallisation of NPX is observed after 24 h, as seen in (a).

Reverse hybrid gels with volumes of 10 mL were prepared by scaling up the above procedure. PEGDM/PI was pre-heated in a glass tray (5 cm × 5 cm × 1 cm) to 80 °C before addition of the hot DBS-CONH₂/NPX solution. The sample was mixed thoroughly and placed under a UV lamp. Robust, homogeneous gels could be prepared using this approach (Figure 3.25b). However, attempts to induce spatial control of the PEGDM crosslinking by placing a ring-patterned acetate photo-mask over the solution during UV exposure led to no gel formation. Instead small aggregates were observed on cooling, attributable to self-assembling DBS-CONH₂. As for the attempts to form hybrid gels by simply mixing the components together, a sample-spanning DBS-CONH₂ network could not form from this solution. We propose that in this case, the failure of PEGDM to crosslink is caused by the absence of the pre-formed LMWG network and the high temperatures employed to prepare this gel. Both these factors would result in rapid diffusion of PI away from the site of irradiation. Control over diffusion rates and convection effects is an essential stepping-stone to achieving spatial resolution. A sufficient concentration of propagating radical species to induce methacrylate crosslinking is therefore not achieved in any one location.

Using homogeneously crosslinked reverse hybrid gels, we assessed the influence of network formation order on the rheological properties of the hydrogels in the absence of NPX. Following the same procedure as outlined previously, we exposed the hydrogels to changes in applied strain, frequency and temperature (Figure 3.26). Interestingly, in contrast to the 5% hybrid gels in which

the LMWG was formed first, the 5% reverse hybrid gel has a slightly greater storage modulus than DBS-CONHNH₂ (6 mM) hydrogels. More striking though, is the resistance of this material to strain. Even up to 1000%, the critical strain had not yet been reached. Neither the LMWG-first hybrid gels, nor PEGDM-only hydrogels, retain their gel-like properties at these high shears. Reversing the order of network formation clearly makes the material more elastic and gives significantly enhanced shear recovery properties. This suggests that forming the PG network first may encourage it to form a more effective sample-spanning chemical gel, whereas when it forms in the presence of a pre-formed LMWG network, its assembly is slightly limited. In contrast, little difference is seen in the response to shear or change in temperature compared to hybrid gels of a similar PG loading.

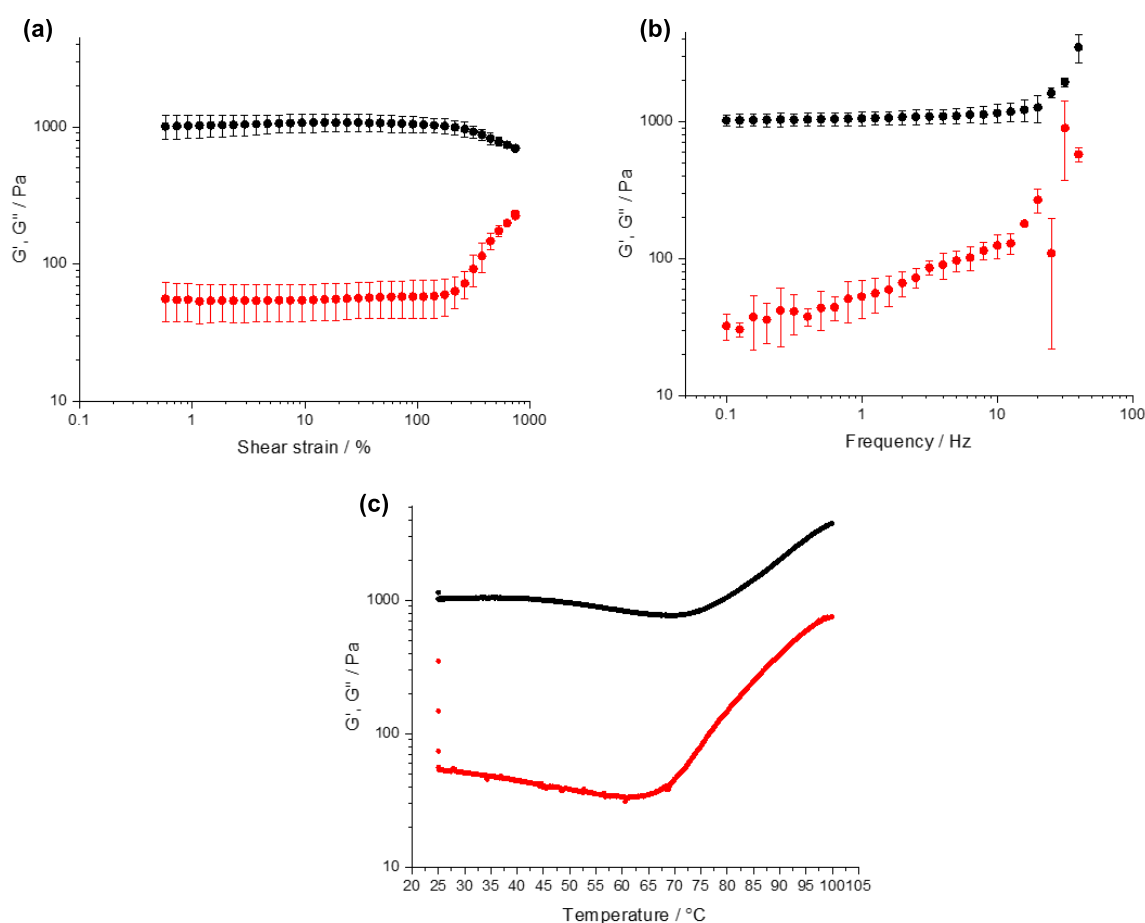


Figure 3.26: Storage (G' , black) and loss (G'' , red) moduli of a 5% reverse hybrid gel prepared using a pre-heated solution of PEGDM/PI. Changes in G' and G'' are given in response to increasing shear strain (a), frequency (b) and temperature (c). Errors are ca. $\pm 10\%$ for all samples.

Interestingly, the samples for which the PEGDM/PI solution was not pre-heated and for which significant heterogeneity was seen in the gel structure, possessed a much greater elastic modulus than the homogeneous gels (Figure 3.27). This is unusual, as such heterogeneity was expected to

weaken the gels. They also appear to be slightly less resistant to strain than the homogeneous samples, but as one might expect, the errors for these materials are quite large. Little difference other than the values of G' and G'' is observed in response to frequency. However, the profile of the temperature sweep was significantly different to that of the homogeneous gel (Figure 3.27c). No significant increase in G' and G'' was observed with increasing temperature. However, a break in the data is observed at *ca.* 75 °C. G'' increases significantly before decreasing again to a value similar to that before the jump. It is possible that this is an experimental artefact, however this occurs at almost the exact same temperature as the T_{gel} observed for DBS-CONH NH_2 gels. It is possible that breakdown of the DBS-CONH NH_2 component of these gels occurs at this temperature temporarily increases the sol-like properties of the material. On further increasing the temperature, rearrangement of the PEGDM network could then result in recovery of a stable gel state.

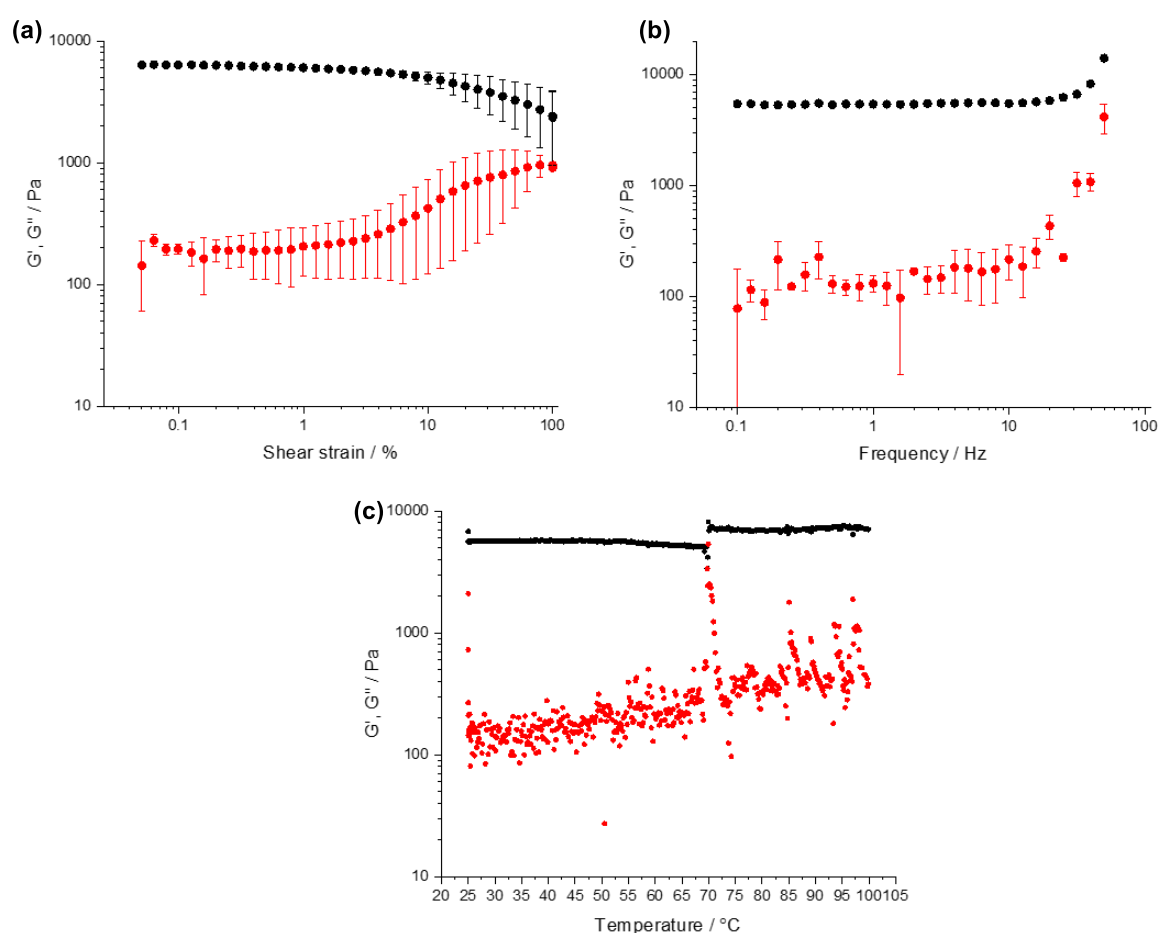


Figure 3.27: Storage (G' , black) and loss (G'' , red) moduli of a 5% reverse hybrid gel prepared using a room temperature solution of PEGDM/PI. Changes in G' and G'' are given in response to increasing shear strain (a), frequency (b) and temperature (c). Errors are *ca.* $\pm 10\%$ for all samples.

Clearly further study, such as that described for the hybrid gels earlier in this thesis, is required to gain a complete understanding of the molecular and nanoscale properties of these gels which govern the macroscopic behaviour (e.g. detailed IR, NMR, SEM studies). Nonetheless, for our initial study here we elected to determine the influence of network formation order on NPX release (Figure 3.28). As above, we prepared 1 mL gels in an 8.5 mL vial and added on top a buffer solution of pH 4, 7 or 8. As for the PEGDM and hybrid gels above, not all of the NPX was released from the gel even at elevated pH values where 100% should be free to diffuse. This is again rationalised by diffusional effects of entrapped NPX within the crosslinked PEGDM network. Significantly lower release percentages were observed at pH 8 than for any of the other gel types, whilst release into pH 7 buffer was comparable to that from the hybrid gels seen above. The reasons for the difference in release at pH 8 are not clear at this time, although we propose that changes in the swelling of the PEGDM network at different pH values within the reverse hybrid gel may be a contributing factor. A decrease in the pore size at pH 8 may prevent effective diffusion of NPX out of the gel matrix. Such effects were not evident from the release profiles of NPX from PEGDM gels alone. Additionally, previous studies indicate that PEG hydrogels containing no pH-sensitive groups (as for the PEGDM used here) do not show pH-dependent swelling properties.²⁶⁰ Therefore, if swelling does play a role in this case, the presence of the DBS-CONHNH₂ network must have a significant influence on this characteristic. Any differences in the porous network could be probed by comparing the diffusion of probe molecules through the gel network (see Section 4.4) or by SEM.

Interestingly, the release of NPX into pH 4 buffer was lower for these samples compared to the LMWG-first hybrid gels. Only *ca.* 40% release from the reverse hybrid was observed compared to 50% for the equivalent hybrid gels. The PEGDM network may compete less effectively for DBS-CONHNH₂ interactions under the gel formation conditions. Differences in the gel network density or pore size may also contribute to this difference. NPX release from this material was slower than from the hybrid gels, with release rates at pH 4, 7 and 8 of 5.1×10^{-9} , 27.9×10^{-9} and 24.3×10^{-9} mol min⁻¹ respectively. This may be indicative of a greater PEGDM network density than in the hybrid gel, due to the inverse order of network formation as described above. Alternatively, as suggested above, if PEGDM is less competitive with NPX for DBS-CONHNH₂ interactions, the rate of release may be slower due to enhanced interactions with the LMWG network. Interestingly, despite the difference in equilibrium NPX release from reverse hybrid gels at pH 7 and pH 8, the initial release rates are relatively similar. If swelling effects are responsible for these differences, they would likely be less pronounced at the beginning of the experiment – pH changes in the gel and nanoscale changes in morphology may take some time to manifest. Therefore, the fact that the initial release

rate into pH 8 buffer is relatively high may support the idea that differences in swelling have a significant influence on the release profiles.

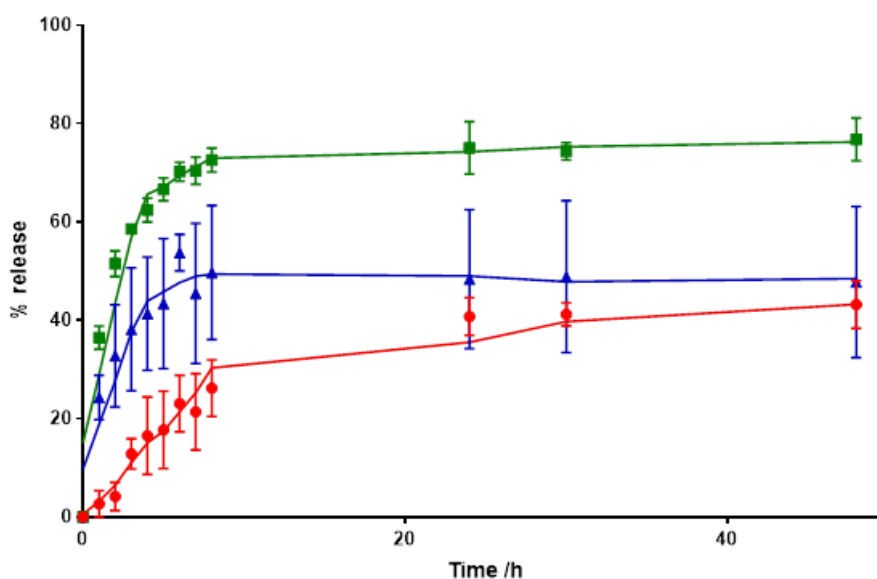


Figure 3.28: Release of NPX into buffers of different pH from a 5% reverse hybrid gel. Red circles = pH 4, green squares = pH 7, blue triangles = pH 8.

The release of NPX from these reverse hybrid gels is clearly quite complex, with both NPX deprotonation and pH-mediated swelling potentially playing a role in the kinetics. As well as studying the diffusion of probes through gels swollen in different buffers (as outlined above), release of model drug compounds which do not have specific interactions with the acyl hydrazide groups of DBS-CONHNH₂ may help to elucidate the relative importance of these two factors. Additionally, differences in the nature of the interactions between the LMWG, PG and NPX in the hybrid and reverse hybrid gels cannot be ruled out. Saturation Transfer Difference (STD) NMR spectroscopy, in which the saturation of signals corresponding to the nanoscale network is transferred selectively onto bound species, could show differences in the affinity and mode of binding of NPX to the individual networks in these materials.²⁶¹ Taken together, these additional experiments would greatly enhance our understanding of the processes determining NPX release under different conditions.

Clearly the order of network formation has a profound impact on the macroscopic (and presumably molecular and nanoscale) properties of DBS-CONHNH₂/PEGDM hybrid gels. This research may be of significant interest, as a material composed of identical components in the same quantities can express very different macroscopic properties. Such differences can be studied by utilising the techniques outlined for the characterisation of hybrid gels in this chapter (¹H NMR, IR, SEM) in

addition to further, complementary methods. Differences in the molecular scale properties of the gels could be probed by examining the differences in interactions with a range of probes using STD and NOESY NMR experiments.²⁶² Solid state NMR may also yield information regarding difference in packing of the two gel networks dependent on assembly order.²⁶³ On the nanoscale, as well as differences observed in xerogels observed by electron microscopy, small-angle neutron scattering could be used to determine the nature of the DBS-CONHNH₂ nanofibres in the solvated gels, elucidating any differences in assembly mode between the two materials.²⁶⁴

Developing an understanding of the influence of network order formation on gel properties is of key interest moving forwards and may assist with the design and fabrication of gel-phase devices in the future. As an example, the significantly greater elasticity of the reverse hybrid gel in this chapter compared to the hybrid gel (as well as the PG alone) may make it more useful as a material for wearable devices, which must be able to withstand significant movement-induced strain.¹⁰⁹ Elucidating the reasons for this enhanced elasticity, as well as the differences in interactions with a range of small molecules, may allow rational design of materials which can be processed into wearable sensors.

3.9 Conclusions

In this chapter, we have prepared and characterised DBS-CONHNH₂/PEGDM hybrid hydrogels containing the clinically relevant NSAID naproxen. It has been demonstrated that the fabrication methods developed in Chapter 2 can be readily modified for the facile incorporation of NPX in stoichiometric amounts. The presence of NPX is shown to alter the properties of the hydrogels in subtle ways. The hydrophobicity of API results in significant changes in the stiffness and temperature stability of DBS-CONHNH₂ hydrogels, whilst it also influences the response of LMW and hybrid hydrogels to high frequency oscillatory shear.

NPX has been demonstrated to bind to DBS-CONHNH₂ nanofibres in a pH-dependent manner. IR and NMR spectroscopy indicate that in unbuffered water, interactions between the carboxylic acid of NPX and the acyl hydrazide/alcohol functional moieties of DBS-CONHNH₂ result in >92% immobilisation of the API. Deprotonation of NPX at elevated pH values disrupts these interactions and allows free diffusion of the drug into solution. The proportion of the NPX which is bound to the nanofibres at a given time is determined by both the pK_a of the drug and the relative pH of the solution to which the gel is exposed. Despite the excellent release properties, this LMW hydrogel is not robust enough to be of significant utility for many drug delivery applications, although it has potential for transdermal drug delivery applications (skin pH ≈ 5.5).

The NPX-loaded hybrid hydrogels reported in this chapter possess a unique combination of properties which make them useful for controlled delivery. Key aspects include:

- The DBS-CONHNH₂ network largely retains its pH-dependent release properties within the hybrid gel. NPX is released in smaller amounts under acidic conditions, whilst at elevated pH almost total release is seen.
- The PG network, whilst unable to perform pH-mediated drug release, reinforces the material, making it robust enough for potential oral drug delivery applications.
- Both components are necessary for the formation of shaped, NPX-loaded gel-phase materials. PEGDM endows the material with UV-responsiveness and the potential to be photo-patterned, whilst spatial resolution (as reported in Chapter 2) is not achievable in the absence of the LMWG.

Photo-patterning of a drug-releasing gel allowed us to impose spatial control over the diffusion of NPX. By exposing the two sides of the hydrogel to different conditions of pH, the preferential release of a drug into different compartments has been demonstrated from a LMWG-containing material for the first time. No prior reports of such differential release without the use of physical barriers or strong magnetic fields has been reported. We propose that this concept of differential release may have important implications for targeted release of drugs towards sites of inflammation, infection or tumour growth *in vivo*. Future work in this area could focus on the development of different gel/drug combinations, exploiting different release triggers to target differences in tissues more complex than simple pH differences.

Additionally, we report preliminary findings regarding the influence of network formation order on the rheological and NPX release properties of hybrid hydrogels. A method for the fabrication of hybrid gels in which the PEGDM network is crosslinked prior to DBS-CONHNH₂ self-assembly has been developed. Despite containing the same component parts, gels formed in this fashion demonstrate greater resistance to shear and different NPX release properties compared to hybrid gels in which the PEGDM network is 'patterned into' a LMW hydrogel. To elucidate the reasons for the macroscopic differences observed, IR, NMR and SEM studies should be used to probe the properties of these hydrogels on the molecular and nanoscale. Few examples of LMWG-containing multicomponent gels exist, and to our knowledge, no systematic studies describing the influence of network formation order on the properties and applications of these materials have yet been reported.

4 Spatially-Resolved Enzyme Bioreactors

Acknowledgements are made to MChem student Jamie Kelly for his work towards some of the results in Sections 4.5 and 4.7.

4.1 Enzyme Bioreactions

Compartmentalisation of reactive components is a common and effective strategy employed in biology to maintain the integrity of biomolecules important for cellular function. Indeed, even on a larger scale the body can be thought of as being divided into a number of different ‘compartments’ or systems, each of which performs a given function.²⁶⁵ Rarely are the compartments (on any scale) completely isolated however. In fact, the ability of molecules to cross membrane barriers between compartments is often critical to their function. Oxygen crosses the barrier from the alveoli of the lungs into circulatory system, whilst nutrients are absorbed through the membrane of the intestine into the bloodstream to aid delivery to cells.

In a chemical setting - in particular for chemical engineering – the separation of catalyst and product is a key factor to consider when designing an industrial process. An effective separation of the desired compound from the reactive substrate can drastically reduce the processing time and cost to a company working on large scale fine chemical synthesis. For heterogenous catalysts a large range of techniques to achieve this are possible, including but not limited to the use of fluidised beds and immobilised catalysts in flow reactors, and simple filtration/centrifugation technologies to separate the catalyst in a batch reactor. For a reaction requiring a homogeneous catalyst however, the problem facing an industrial chemist is not so simple. The soluble catalyst can in principle be separated from the reaction mixture, but this often requires comparatively costly and solvent-intensive processes such as chromatography and/or precipitation.^{266,267}

Of increasing industrial importance is the use of enzymatic processes in the production of pharmaceuticals and fine chemicals,^{268–270} processing of food^{271,272} and the development of so-called ‘value-added’ products from industrial by-products.²⁷³ Enzymes overcome many of the difficulties associated with these industrial processes - including poor efficiency, selectivity and enantioselectivity – whilst operating under mild conditions.²⁷⁴ The application of enzymes in an industrial setting is limited however, by the fact that their separation and subsequent recycling can be challenging. Some strategies to enforce spatial separation of the enzyme ‘catalyst’ from reaction products are outlined below.

4.1.1 Membrane Bioreactors

Membrane bioreactors (MBRs) have been demonstrated to represent an effective method for the separation of large catalysts from the reaction products (Figure 4.1). In this approach, a porous membrane is used to separate a 'reactant' compartment from a 'product' compartment. The size of the pores in these membranes is such that macromolecules, including enzymes, are too large to cross between compartments, whilst smaller reaction substrates or products are able to diffuse freely between the two. These reactions are usually conducted under flow to prevent equilibration of the product concentration across the reactor. MBRs have become relatively common in the rapidly expanding field of biocatalysis.^{275–277} With a push towards synthesising fine chemicals from renewable resources such as plant matter rather than fast-depleting reserves of crude oil, enzymatic catalysts will continue to become of increasing importance in the future.^{278,279}

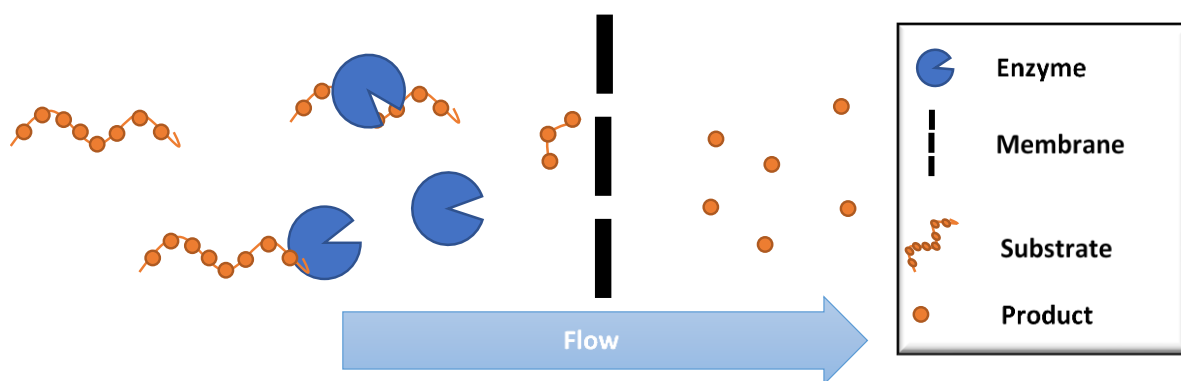


Figure 4.1: Schematic representation of a traditional MBR. Macromolecules and biocatalysts can't pass the membrane, whereas small molecule products can diffuse through, eliminating the need for post-reaction separation.

Whilst not using a pure enzyme, a representative example of an industrially relevant MBR process was recently reported by Najafpour.²⁸⁰ Using *Lactobacillus bulgaricus* (a lactase source), the conversion of lactose into lactic acid was achieved with high yields ($17.21 \text{ g L}^{-1} \text{ h}^{-1}$ compared to $7.2 \text{ g L}^{-1} \text{ h}^{-1}$ for a conventional bioreactor) and good separation of product and starting material (Figure 4.2a). Similarly, Liu *et. al.* developed a 'small scale' MBR to screen a wide range of reaction parameters in the hydrolysis of cellulose (Figure 4.2b) - cellulase concentration, pH, temperature etc.²⁸¹ Crucially, the mesh size of the polyethersulfone membrane allowed for exclusion of not only enzyme, but also oligosaccharides from the product stream, essentially ensuring complete conversion to glucose. Cellulose hydrolysis provides a renewable route to monosaccharides which are valuable feedstocks for chemical synthesis and biofuel production.²⁸² Separation of such monosaccharides is an important industrial challenge. Pinelo and co-workers developed a dual-enzyme MBR to address this issue.²⁸³ GOx-mediated oxidation of glucose (Figure 4.2c) was fuelled

by the hydrolysis of H_2O_2 by catalase, and the gluconic acid formed was separated *via* membrane from other monosaccharides in the reaction mixture.

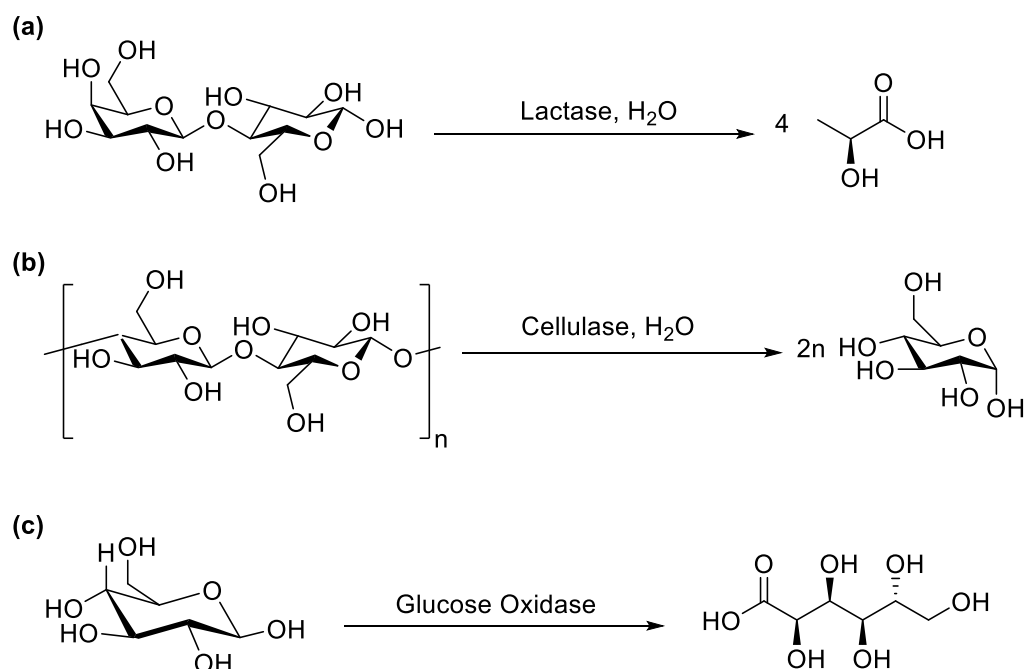


Figure 4.2: Industrially relevant MBR reactions. Effective separation of lactase starting material and lactic acid was demonstrated by Najafpour (a), whilst Liu demonstrated that only glucose and no oligosaccharide species could pass through a PES membrane (b). Pinelo used the selective oxidation of glucose (c) to achieve efficient separation from xylose in solution.

In the above examples the biocatalysts are free in solution in the ‘reactant’ compartment. An increasingly common approach is the immobilisation of an enzyme within the membrane. This approach ensures contact between reactant and enzyme, and allows for easy replacement of the biocatalyst by replacement of the membrane.^{284,285} In general, two approaches to enzyme immobilisation are used (Figure 4.3):

- i. Covalent attachment of the enzyme to the MBR;
- ii. Physical encapsulation in the MBR porous structure. This approach relies on the enzymes being too large to diffuse out of the membrane.

Sulaiman *et. al.* used the first of these approaches to fabricate cellulosic membranes which were catalytically proficient in the conversion of starch into cyclodextrin,²⁸⁶ whilst Kamaruddin and co-workers crosslinked polyethyleneimine in the presence of β -galactosidase to entrap the enzyme in a porous membrane.²⁸⁷ The dual-enzyme monosaccharide separation described above was also carried out using enzymes encapsulated in a polydopamine membrane.²⁸³ A novel approach to

catalyst immobilisation was recently reported by Zhu *et al.*, who used simple physical adsorption to allow laccase enzymes to enter the radial pores of a membrane before entrapping them by covalent crosslinking (Figure 4.3c).²⁸⁸ This improved the stability of the membrane reactor compared to reactors relying on physical adsorption alone.

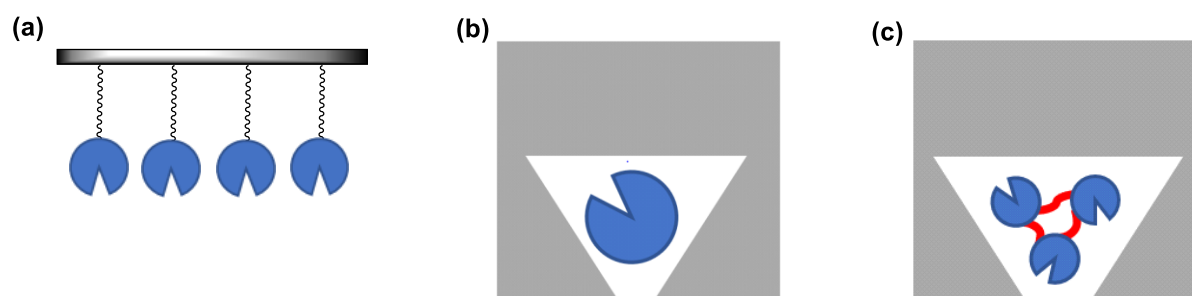


Figure 4.3: Cartoon representation of strategies for enzyme immobilisation in MBRs. Covalent immobilisation (a), physical entrapment (b) and crosslinking-mediated physical entrapment (c).

Innovations in gas-exchange MBR reactors are being developed to widen the accessible chemistries of these systems. A recent example of a ‘tube-in-tube’ microreactor demonstrated the enzymatic hydroxylation of 2-hydroxybiphenol to 3-phenylcatechol (Figure 4.4a).²⁸⁹ In a conventional bioreactor, CO₂ produced in the reaction process deactivates the hydroxybiphenyl 3-monooxygenase (HbpA) enzyme, resulting in poor yield and recyclability. In this reactor configuration however, the reaction compartment is contained by a gas-permeable Teflon membrane which allows escape of the CO₂ as well as the reintroduction of oxygen to aid HbpA activity (Figure 4.4b). Optimisation of the reactor conditions enabled facile synthesis of the desired catechol with significantly greater yields (14.5 g L⁻¹ h⁻¹) than other MBRs described to this date.

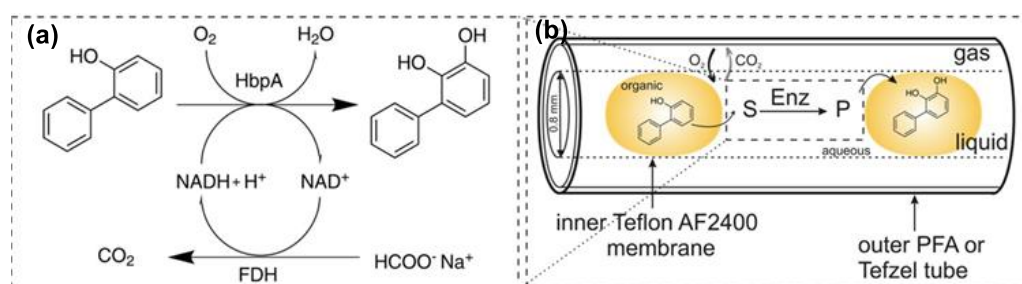


Figure 4.4: (a) Scheme of 2-hydroxybiphenyl hydroxylation catalysed by HbpA with concomitant NADH regeneration by formate dehydrogenase (FDH). (b) Schematic representation of the tube-in-tube reactor including separation of gas and liquid phases by inner membrane. Figure adapted from [289].

4.1.2 Enzymatic Reactions in LMW Hydrogels

An alternative approach to enzyme/product separation is to formulate enzymes within a gel matrix. The encapsulation of the enzyme within the porous material is conceptually similar to the physical entrapment of enzymes in an MBR membrane as described above. The large peptide catalysts are too large to diffuse through the gel nanopores, whilst small reactant and product molecules can diffuse freely. Separation of the enzyme from the reaction mixture can then be achieved by simply removing the gel. Many examples of enzymatic reactions in polymer gels have been reported throughout the years.²⁹⁰ However, despite the fact that enzymes are widely used to trigger LMWG assembly (Chapter 1) and to control gel degradation and drug release (Chapter 3), surprisingly few examples exist where an enzyme-loaded LMWG has been used as a 'heterogeneous' catalyst.

Pioneering work in this area was published in 2007 by Xu and co-workers (Figure 4.5a).²⁹¹ They formulated haemoglobin (Hb) into a LMW amino acid hydrogel and demonstrated that the process (a gentle heat/cool cycle) did not alter the conformation of the enzyme. This enzyme-gel showed superactivity in the oxidation of pyrogallol (Figure 4.5b) carried out in toluene compared to free enzymes in both toluene (no reaction, enzyme inactivation) and water (*ca.* 9 times slower), as well as compared to Hb in a polyacrylamide PG (Figure 4.5c). The authors postulate that the amphiphilic nature and large pore size in the LMWG facilitate mass transport of the reaction products into the organic phase, reducing enzyme inhibition and increasing the enzyme activity. Additionally, the aqueous environment in the hydrogel prevented deactivation by organic solvent - little loss of activity was shown over three reaction cycles in toluene. This increased activity extended to other tested enzymes (including horseradish peroxidase, laccase and chymotrypsin).

The following year, the same group demonstrated that the enzyme acid phosphatase (AP) could be used to trigger formation of amino acid hydrogels, and that the resulting encapsulated enzyme retained its activity.¹⁰⁴ Again, enhanced activity and stability were demonstrated in organic solvents. Wang *et. al.* recently used a similar dual-purpose enzyme approach.⁴⁹ In their case alkaline phosphatase (ALP) was used to trigger formation of a robust tetrapeptide hydrogel and subsequent dephosphorylation of *para*-nitrophenylphosphate (*p*NPP). Good recyclability of the enzyme was reported in these gels compared to calcium alginate hydrogels. However, the authors do not report the washing of product from the gels between reactions, so the reported turnover of each cycle may be influenced by the residual products of earlier reactions. In innovative work, Mao *et. al.* used a dual-enzyme approach to form a dual-network hybrid gel.⁵⁰ Dephosphorylation of Fmoc-tyrosine phosphate with AP resulted in formation of a LMW hydrogel, which was then reinforced by GOx-initiated crosslinking of a PG network (mechanism described in Chapter 1.3). Both enzymes remained active within the hybrid gel and retained their activity over five reaction cycles.

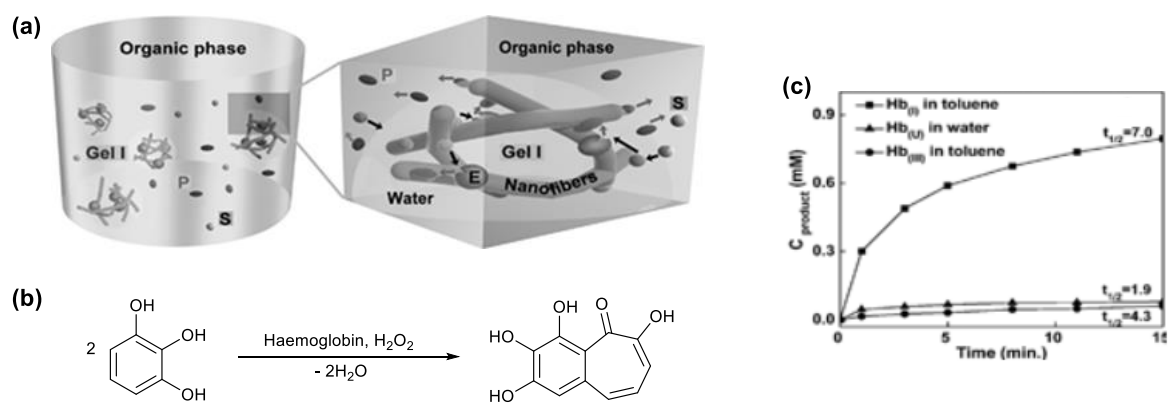


Figure 4.5: Schematic representation of Xu's super-active LMWG-immobilised enzyme (a). The amphiphilic nature of the LMWG accompanied by large pore size facilitates mass transfer of substrate (S) and products (P) to and from the enzyme (E) sites in the hydrogel. The Hb catalysed oxidation of pyrogallol was tested (b). Turnover rates (c) of Hb immobilised in the LMW hydrogel (squares) were much greater than free Hb in water (triangles) and Hb immobilised in a PG matrix (circles). Figure adapted from [291].

Other novel examples of enzymatically active LMWGs have been reported. Early work by Li and co-workers reported enhanced activity of horseradish peroxidase (HRP) in tetraethylorthosilicate gels prepared in an ionic liquid (IL)/water mixture compared to water alone,²⁹² and later developed this into a stable and sensitive biosensor electrode.²⁹³ Sun and Huang prepared gels from 1-dodecylpyridinium bromide, a cationic surfactant, and loaded them with laccase to carry out oxidation reactions in ionic liquid media.²⁹⁴ An interesting recent report from Aline Miller and co-workers describes the covalent conjugation of enzymes to a β -sheet forming octapeptide sequence. Self-assembly of the short peptide sequence results in presentation of a selective reductase enzyme on the surface of the nanofibres. No loss of enzyme mass from these hydrogels was observed over one year. By comparison, 98% of a non-covalently encapsulated enzyme diffused out of the gels over 7 hours. The immobilised reductase catalysed the reduction of ketoisophorone with excellent conversion (>99%) and enantioselectivity (95%). To our knowledge this is the only reported example of an enzyme covalently bound to a self-assembled LMWG.

Researchers have begun to utilise the high activity and selectivity of enzyme-containing LMWGs for advanced sensing applications. A notable early example came from the Hamachi group, who encapsulated amino acid-specific proteases in a saccharide-amino acid hydrogel.²⁹⁵ A fluorescent dansyl species was liberated from a protected oligopeptide by cleavage at the adjacent amino acid, and migrated into the hydrophobic environment within the gel nanofibres. This change in environment enhanced dansyl fluorescence, providing a visible readout for the reaction and allowing the detection of specific amino acid residues in a sample (Figure 4.6a). No fluorescence

enhancement was observed in the absence of the LMWG. More recently, this group developed a high throughput peptide-gel-based assay for a range of biologically relevant species based on the action of oxidative enzymes such as GOx and urate oxidase (UOx).²⁹⁶ Addition of an appropriate biomolecule (glucose for GOx, uric acid for UOx) resulted in the production of H₂O₂, which reduced and cleaved the gelator protecting group (nitrophenyl methyloxycarbonyl, NPMoc). Loss of the head group caused the gels to break down rapidly and specifically in the presence of each enzyme's substrate (Figure 4.6b).

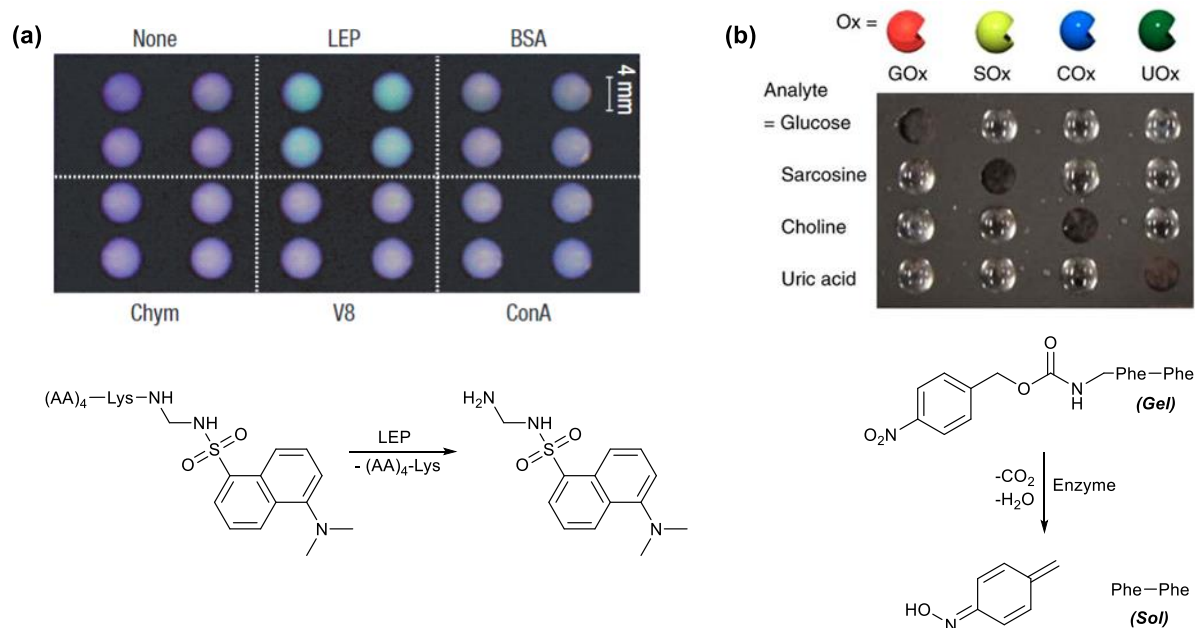


Figure 4.6: Immobilised enzyme assays reported by Hamachi et. al. Fluorescence assay for N-terminal lysine residues (a). 5-Dimethylaminonaphthalene-1-(N-2-aminoethyl)sulfonamide is liberated selectively in LMWG hydrogels containing lysyl endoprotease (LEP), resulting in a change in colour from pink to green for these samples only. Adapted from [34]. Oxidase-mediated LMWG breakdown assay (b). Oxidation of the relevant biomolecule results in formation of H₂O₂, which reductively cleaves the NPMoc protecting group and induces LMWG disassembly. Adapted from [296].

In other recent work, Park and co-workers have incorporated both an enzyme (GOx) and quantum dots (QDs) in a Fmoc-Phe-Phe hydrogel to enhance the detection of glucose.²⁹⁷ H₂O₂ produced during the oxidation of glucose quenches QD photoluminescence at clinically relevant concentrations for diabetes diagnosis. In a unique report, Lev and co-workers used an HRP-containing electro-osmotic gel as a bioreactor with built in separation functionality.²⁹⁸ Intermolecular interactions between gelators lowered the pK_a of the primary amides in the nanofibres, allowing them to accumulate charge on application of a current. This charge drives progress of neutral compounds down the gel 'column'. Conversion of pyrogallol by the HRP gel could be seen and quantified using the resulting electropherogram, although due to the continuous

production of purpurogallin down the length of the ‘column’, complete separation of starting material and product was not achieved in this case. Longer reactor lengths or higher enzyme concentration may overcome this limitation in the future.

4.2 Chapter Aims

Despite the progress made in recent years on the application of enzyme/LMWG systems for functional reactivity, the inherent mechanical weakness associated with most LMW hydrogels limits their applicability in real-world applications. Additionally, for sophisticated sensing devices, spatial control of reactivity is of vital importance to their applications.

In this chapter, we aimed to utilise the photo-patternable DBS-CONHNH₂/PEGDM hybrid hydrogel described in Chapter 2 to create shaped enzyme bioreactors. Substrates and reactants were expected to pass relatively freely through the gel matrix, whilst enzymes would be unable to diffuse through the small pores of the gel membrane. In principle this would allow easy separation of enzyme, starting material and product. By developing a shaped gel ‘membrane’ we aimed to impose a degree of spatiotemporal control over an enzymatic reaction, with a longer term view to future development of multi-step reactor systems (Figure 4.7). To our knowledge no such bioreactor, where reactants diffuse through two separate gels to perform sequential reaction steps, has been developed to date,^{299,300} and it constitutes a highly challenging target for shaped gel technology. Here we will attempt to take steps towards such reactors with a simpler system, using a single gel barrier and a single enzyme to demonstrate the potential for these shaped materials to act as reactor ‘devices’.

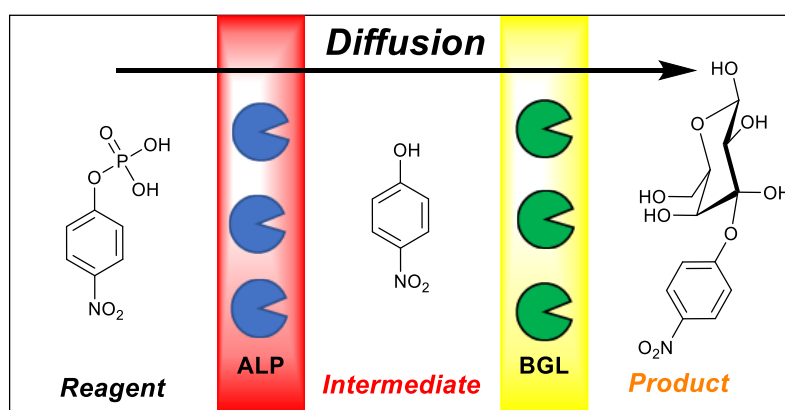


Figure 4.7: Cartoon representation of a challenging two-step photo-patterned enzyme reactor configuration. To proceed to the next compartment, each reagent must pass through an enzyme-loaded gel barrier. In theory this results in a ‘product’ compartment with no reactant impurities. Example reaction shown here is the dephosphorylation of para-nitrophenyl phosphate by alkaline phosphatase (ALP),⁴⁹ followed by O-glucosylation using β-glucosidase (BGL).³⁰¹

4.3 Alkaline Phosphatase

Alkaline phosphatase (ALP) is a widely studied metalloenzyme, found in a wide range of organisms on the surfaces of most cell membranes.^{302,303} It is a homodimeric enzyme containing zinc and magnesium at the active sites (Figure 4.8a). The enzyme is considered somewhat promiscuous, catalysing the hydrolysis of a wide range of phosphate-containing organic compounds under basic conditions.^{304,305} The two zinc metals are thought to be intimately involved in the binding of such substrates by this enzyme. X-ray crystallography and NMR studies suggest that one zinc site coordinates to the phosphoester oxygen, whilst the second zinc (as well as an arginine residue within the active site) interact with the phosphate hydroxyl groups.³⁰² Attack at the phosphorous centre by a serine residue results in cleavage of the P-O bond yielding the dephosphorylated product. Under basic conditions decomplexation of inorganic phosphate from the enzyme active site is the rate-limiting step of this reaction. As well as performing a regulatory role in the intestine,³⁰⁶ ALP is widely regarded as having an important role in promoting mineralisation during osteogenic differentiation. Indeed, the upregulation of ALP is considered a reliable indicator of bone-forming processes in tissue engineered cell cultures.^{307,308}

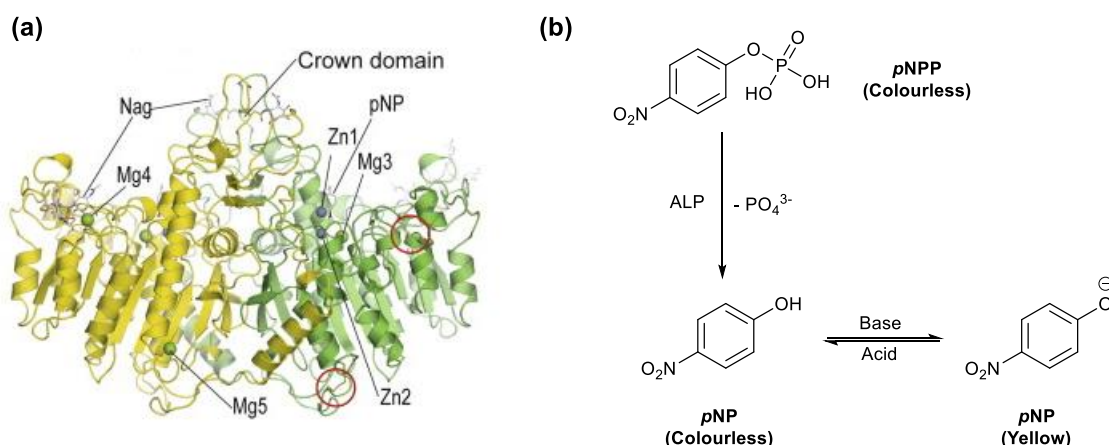


Figure 4.8: Structure of rat intestinal alkaline phosphatase with pNP located at the active site (a). Enzyme was recombinantly expressed in *Sf9* lepidoptera cells and the two monomers are coloured in green and yellow respectively.³⁰⁹ Image from [309]. ALP-catalysed dephosphorylation of pNPP yields pNP, which undergoes a pH-induced colour change based on deprotonation of the phenol (b).

Given that ALP displays relatively high thermal stability and has been shown to retain activity on immobilisation,^{49,310} it was selected as an appropriate enzyme for encapsulation and reaction in the gel-phase. For this proof-of-principle study, the enzymatic dephosphorylation of *para*-nitrophenyl phosphate (pNPP) to form *para*-nitrophenol (pNP) and inorganic phosphate was identified as a suitable test reaction (Figure 4.8b) due to the rapid turnover rates reported in the prior literature.³¹¹

In addition, a striking change in the colour of the solution on dephosphorylation (from colourless to yellow) afforded simple qualitative (visual) and quantitative (UV-visible spectroscopy) assessment of reaction turnover.³¹² A reactor design in which *p*NPP diffuses through a photo-patterned hybrid gel ring, containing ALP, and reacts to yield pure *p*NP in a product compartment was envisaged (Figure 4.9). In this reactor design, the hybrid gel acts as a semi-permeable membrane which allows diffusion of the small substrate/product molecules, whilst confining the much larger enzymes to the gel phase.

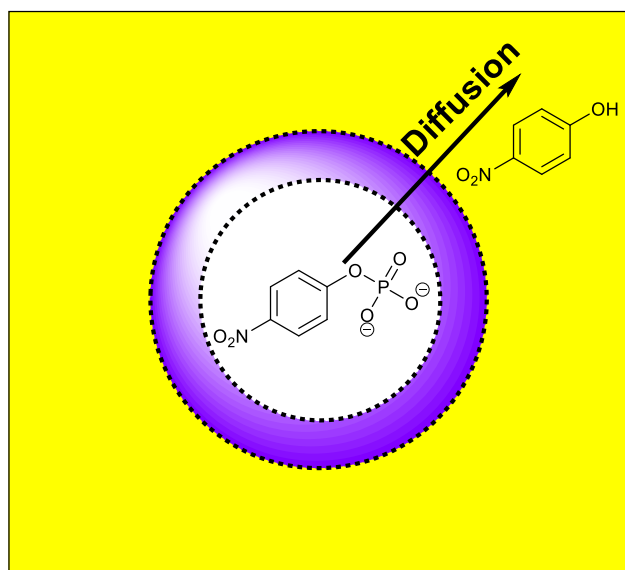


Figure 4.9: Schematic representation of the proposed enzyme bioreactor. *p*NPP (colourless) diffuses from a central ‘reactant’ compartment through an ALP-loaded gel membrane (purple ring) which catalyses its dephosphorylation into *p*NP (yellow). Therefore, the outer ‘product’ compartment should consist solely of *p*NP.

4.4 Gel Permeability

For effective immobilisation of ALP, it is important that it is unable to diffuse through the porous matrix of the gel within which it has been encapsulated. For reactor efficiency it is equally important that small reactants and products can move freely through the gel matrix. To assess the feasibility of our gels for use in enzyme bioreactors, we designed an experiment to probe the diffusion of fluorescent biomolecules through a gel-phase material.

Gel samples of a known volume were prepared in a fluorescence cuvette. For DBS-CONHNH₂ samples, the LMW hydrogels were prepared by heating a known quantity of the gelator to dissolution in a glass vial. This hot sol was transferred to the cuvette and a gel was formed on standing at room temperature. 10% hybrid gels were prepared using the same procedure, followed by the addition of a solution of PEGDM (10% wt/vol) and PI (0.05% wt/vol) on top of the gel and

leaving covered for 3 days. The supernatant was then removed and the cuvette gel placed under a long wavelength UV lamp for 0.5 h to crosslink the PG network. PEGDM hydrogels were prepared by simply charging the cuvette with a solution of PEGDM (10% wt/vol) and PI (0.05% wt/vol) and crosslinking by UV for 0.5 h.

Onto these gels was pipetted a 50 μ M solution of either fluorescein (332 Da) or a fluorescein isothiocyanate-dextran (FITC-dextran) of a known molecular weight between 4 and 70 kDa. FITC-dextran adopt a somewhat condensed and coiled conformation in solution and are therefore considered good substitutes for the study of macromolecule diffusion kinetics.^{313,314} They are commonly used to assess the permeability and diffusivity of biological membranes.^{315–317} The fluorescence intensity of the probes was recorded at the base of the gel samples (away from the interface with the supernatant) every 5 min over a 3 hour time period to collect information on the initial rate of diffusion. An additional reading was taken at 24 and 48 h to ascertain equilibrium uptake. Fluorescence was recorded at the emission maximum (λ_{\max} , Table 4.1). An excitation wavelength (λ_{exc}) for all fluorophores of 470 nm was selected. When recording the fluorescence in gel samples a large peak was observed at λ_{exc} , presumably due to elastic scattering of the incident light. This peak obscured any changes in intensity resulting from fluorophore diffusion. Using λ_{exc} of 470 nm ensured that no overlap of peaks corresponding to scattering and fluorescence occurred.

Table 4.1: Physical characteristics of the fluorophores used in this study. Absorption maxima (recorded at 50 μ M), calculated Stokes radius and literature gyration radius values for each compound.

Fluorophore	λ_{\max} nm	Calculated Radius nm	Gyration Radius ³¹⁴ nm
Fluorescein	512	-	-
FITC-dextran (3-5 kDa)	521	1.50	2.0
FITC-dextran (10 kDa)	522	2.28	-
FITC-dextran (20 kDa)	526	3.14	3.4
FITC-dextran (40 kDa)	528	4.32	5.0
FITC-dextran (70 kDa)	521	5.59	6.3

Initially we prepared gels of 2 mL volume (cross-sectional area = 1 cm \times 1 cm, height = 2 cm) and pipetted 2 mL of the fluorophore solution on top. However, over the first three hours, essentially no change in fluorescence was observed (data not shown). Increases in the fluorophore concentration at the base of the gel were observed after 24 h, but it was unclear whether the system had reached equilibrium. Additionally, as no information on the rate of diffusion could be abstracted, we chose to modify the experiment and prepared gels of a smaller volume (0.5 mL, 0.5 cm gel height) and fluorophore solution (50 μ M, 0.5 mL). This yielded much improved data, with

changes in fluorophore concentration observed over the experiment timescale (Figure 4.10). No significant changes in concentration were observed for any samples between 24 and 48 h, so these data have been omitted from the graphs.

The errors associated with the data presented here are similar to those outlined for the UV-vis absorption studies described in Chapter 3. Repeat measurements of calibration samples have allowed estimation of the random error associated with instrument readings as *ca.* 0.5%. The errors associated with gel formation are also similar to those described earlier in this thesis (*ca.* 0.4%). The preparation and measurement of the fluorescent stock solutions is of a similar magnitude (*ca.* 0.5%). The errors seen below are slightly greater than those outlined here. The contribution of temperature fluctuations is one which is likely significant in this case, as the fluorimeter was not temperature controlled during this experiment.

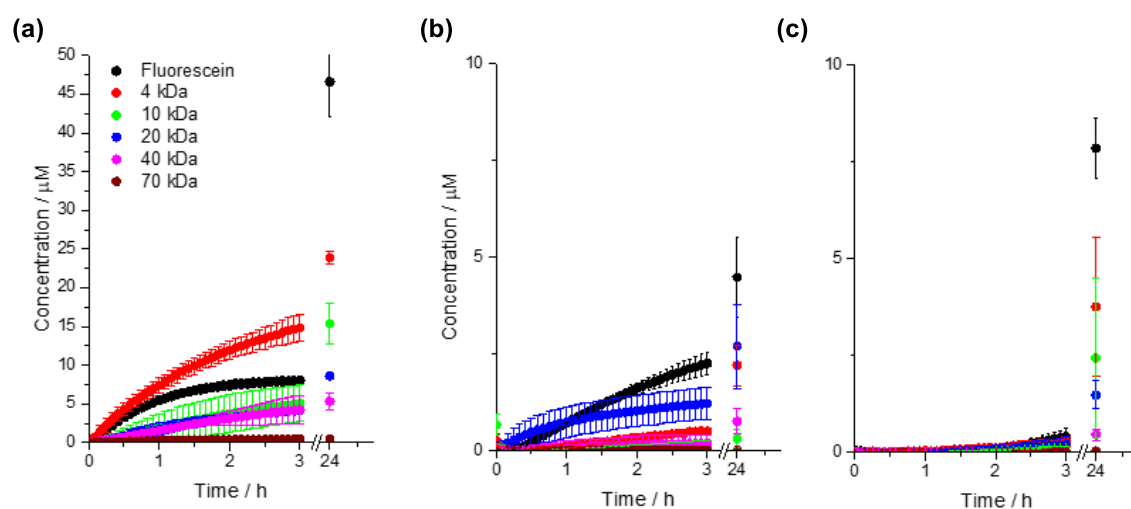


Figure 4.10: Concentration of fluorophores at the base of gels of dimension 1 cm × 1 cm × 0.5 cm (height). Diffusion through 6 mM DBS-CONHNH₂ (a), 10% hybrid (b) and 10% PEGDM (c) hydrogels. Errors given as standard deviation (*n* = 3).

Diffusion of the fluorescent probes is clearly influenced by the internal structure of the hydrogels. A significantly greater proportion of all species (with the exception of 70 kDa FITC-dextran) diffused through the LMW hydrogel (Figure 4.10a) than either the 10% hybrid gel (Figure 4.10b) or the 10% PEGDM (Figure 4.10c). LMW hydrogels typically have a larger mesh size than PGs, so this result was expected. A lower rate of diffusion is also observed for the 10% PEGDM gels than the 10% hybrid gels. This indicates that the self-assembly of the LMWG network prior to PEGDM curing reduces the

density of the second network compared to in the PG alone. The Stokes radius of FITC-dextrans can be calculated using Equation 4.1.^{318,319}

$$r = 0.33(M_w^{0.46}) \quad \text{Equation 4.1}$$

The radii for the FITC-dextrans used in this study are given in Table 4.1. Similar sizes can be inferred based on literature values for the radius of gyration (R_g) of FITC-dextrans recorded by light scattering. Given that 70 kDa FITC-dextran does not diffuse into any of the gels over 24 h, it can be inferred that the pore sizes of the DBS-CONHNH₂, 10% PEGDM and 10% hybrid gels are all less than *ca.* 11 nm.

Table 4.2: Initial diffusion rates through each gel and concentration at the base of the gel after 24 h. Diffusion rates calculated assuming zero order kinetics.

FITC-dextran M_w kDa	Initial diffusion rate $\mu\text{M cm}^{-1} \text{s}^{-1} (\times 10^{-3})$			Concentration After 24 h μM		
	LMWG	Hybrid	PG	LMWG	Hybrid	PG
Fluorescein	168	28	10	47	4.5	7.8
4	202	6.8	4.3	24	2.2	3.8
10	64	1.4	2.8	15	0.3	2.4
20	56	25	3.3	8.6	2.7	1.5
40	56	2.5	0.7	5.3	0.8	0.5
70	5.4	0.3	0.1	0.5	0.02	0.04

For DBS-CONHNH₂, the rate of diffusion of the fluorophores broadly decreases with increasing molecular mass of the molecule (Table 4.2). Complete exclusion of the 70 kDa FITC-dextran was observed, with increasing diffusion rates and equilibrium quantities observed decreasing FITC-dextran mass as expected. Interestingly, the initial rate of fluorescein diffusion was slower than that of the 4 kDa FITC-dextran. This, combined with the fact that essentially all of the fluorescein is incorporated in the LMWG after 24 h, is indicative of interactions between fluorescein and the DBS-CONHNH₂ nanofibres, perhaps between the gel acyl hydrazide groups and an equilibrium free acid form of fluorescein (Figure 4.11).^{320–322} High interactivity between fluorescein and the gel fibres would slow diffusion to the base of the gel, as the fluorophore would remain near the surface of the gel rather than diffusing freely through the material. Eventually, as the nanofibres become ‘saturated’ and attractive interactions cannot be formed with additional fluorescein molecules, then the diffusion front will move. This effect is not seen for either the hybrid or PEGDM hydrogels.

This finding is in agreement with those reported in Chapter 3, where the incorporation of PEGDM in the DBS-CONHNH₂ network has a slight disruptive effect on the interaction of NPX and DBS-CONHNH₂. Unlike for NPX release though, where this effect has a negative impact on the pH-dependent release of the drug, in this case prevention of interactions with the LMWG network should enhance the ability of the gel to act as a passive matrix for enzyme encapsulation.

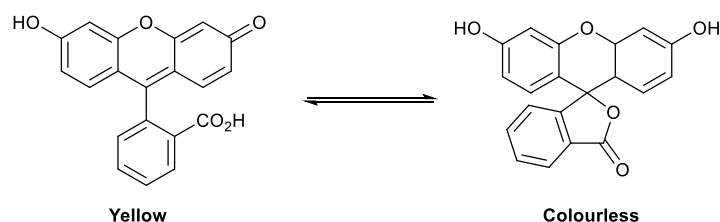


Figure 4.11: Two possible tautomeric forms of fluorescein – free acid (left) and lactone (right).

Diffusion to the base of the 10% PEGDM was low over the first 3 hours for all samples (Table 4.2). After 24 h though, the same trends in uptake into the gel were observed as in the LMWG. Fluorescein showed the greatest uptake, whilst total exclusion of 70 kDa FITC-dextran was observed. In the 10% hybrid gel however, fluorescein still diffuses comparatively rapidly through the gel matrix, but of the FITC-dextrans, the 20 kDa displays the fastest rate of incorporation. The reasons for the change in order of diffusion rate (20 > 4 > 40 > 10 > 70 kDa) compared to the two individual components has not been fully elucidated, although it is possible that an interplay between the mesh size and the affinity of the fluorophores for the gel network account for this behaviour.

Importantly, no diffusion of the 70 kDa FITC-dextran was observed through any of the gels. This suggests that it should be possible to encapsulate ALP ($M_w = 140$ kDa) in any of these hydrogels without significant loss from the matrix over time. Of equal importance is the fact that fluorescein - a small molecule, similar in size to the proposed bioreactor substrates/products - is able to diffuse through the 10% hybrid gel. This promising result suggested that the fabrication of enzymatically active, photo-patterned gel reactors was feasible.

4.5 Solution-phase studies

Having demonstrated the potential for immobilising molecules similar in size to ALP, we then studied the behaviour of this enzyme in solution. As described above, the hydrolysis of *p*NPP by ALP yields *para*-nitrophenol (*p*NP), a compound which displays a significant bathochromic shift on deprotonation. Below its pK_a (7.15) *p*NP is colourless in aqueous solution, whereas above this value (as the phenolate anion) it displays a prominent yellow colour. Given that optimum ALP activity is reported as pH 9, we expected that all *p*NP formed would be in this deprotonated form and would therefore show no overlap with peaks corresponding to the starting material (Figure 4.12a). Therefore, this reaction was simple to monitor by UV-vis spectroscopy. By studying the reaction in solution phase, we aimed to identify suitable conditions for the gel-phase dephosphorylation of *p*NPP.

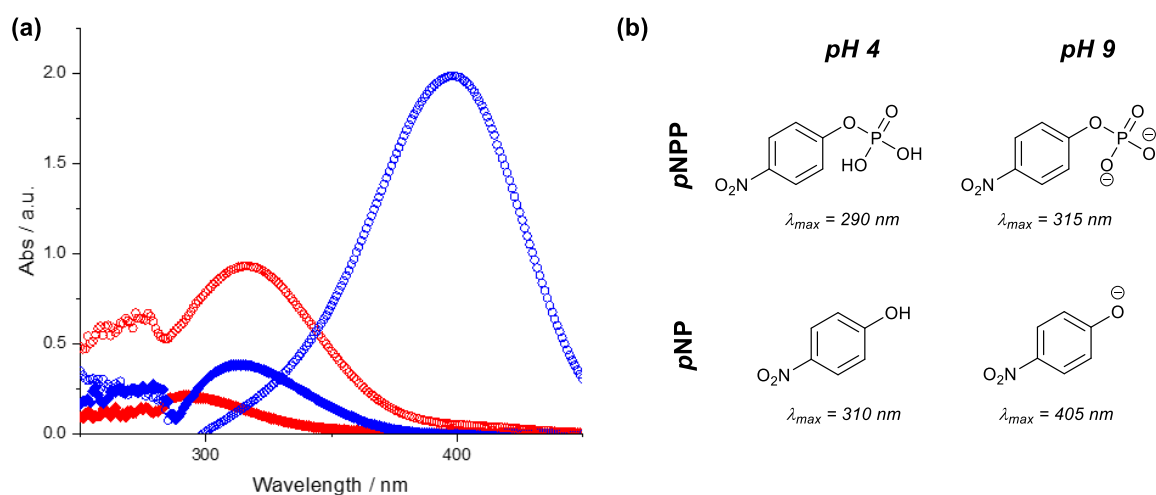


Figure 4.12: UV spectra of *p*NPP (solid) and *p*NP (hollow) at pH 4 (red) and pH 9 (blue). All spectra recorded at a concentration of 0.016 mM (a). Structures and absorption maxima of *p*NPP and *p*NP at pH 4 and pH 9 (b).

Initially, we studied the influence of *p*NPP concentration on dephosphorylation kinetics. Given that the active pH range of ALP is *ca.* 8-11, and for ease of comparison with previously reported results, these initial studies were carried out in buffer solution at pH 9 (glycine buffer, 0.2 M). According to the Henderson-Hasselbalch equation, at this pH >99% of the *p*NP produced in the reaction should be deprotonated and therefore contribute to the UV peak at 405 nm. This also ensured that there was no contribution from *p*NPP to this peak. Comparison of the intensity at this wavelength to a calibration curve allowed the evolution of *p*NP to be monitored over time.

A concentrated solution of ALP was placed in a UV cuvette at room temperature. The cuvette was placed in the spectrometer and monitoring of the absorbance at 405 nm was started. The ALP was

diluted by addition of a solution containing a known concentration of *p*NPP to a total volume of 2 mL. We elected to add *p*NPP to ALP rather than the other way around as the volume of the former solution was much greater. We reasoned that this would ensure rapid and thorough mixing of enzyme and substrate and eliminate any diffusional effects on the observed rate.

We initially performed this experiment at an ALP concentration of 26 units per mL (U mL^{-1}), a figure reported in the literature.⁴⁹ However, the rate of reaction at this concentration was too fast (complete conversion in < 100 s) to obtain an accurate measure of the kinetics using this experimental setup. Using a lower ALP concentration of 0.1 U mL^{-1} sufficiently slowed the rate of reaction such that linear changes in product concentration ($R^2 > 0.99$ in all cases) were observed for the first minute of the reaction (Figure 4.13). For ease of viewing, the first 15 seconds of each plot has been removed. Significant deviation from linearity is seen at these short times because the addition of *p*NPP solution to the cuvette necessitated exposure of the detector to ambient light. As expected, the rate of change in *p*NP concentration is greater for samples containing a greater concentration of starting material. The increase in the substrate availability would logically increase the turnover rate.

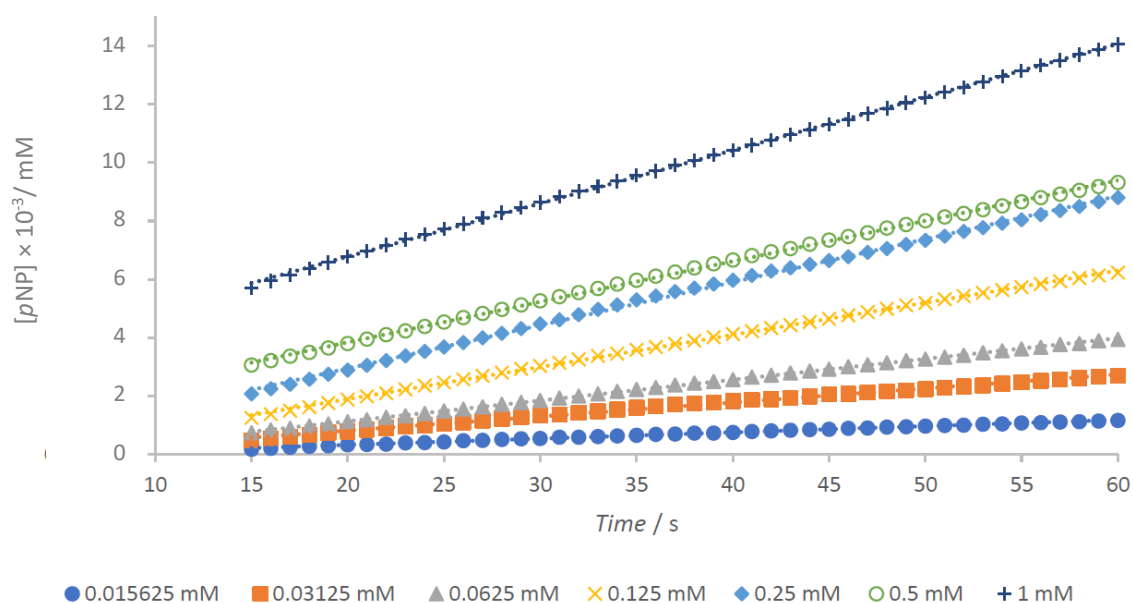


Figure 4.13: Representative changes in ALP-catalysed *p*NP formation over time at different substrate concentrations. ALP concentration was 0.1 U mL^{-1} for all samples.

From the rates of *p*NPP hydrolysis, it was possible to derive the Michaelis constant (K_m) and the maximum velocity (V_{\max}) under these reaction conditions. Under basic conditions, the rate of

hydrolysis is determined by the enzyme-phosphate decomplexation kinetics, such that a general equation for the reaction can be considered as:



Where E = enzyme (ALP), S = substrate (pNPP) and P = product (pNP). The enzyme-substrate complex, ES, is assumed to be in a quasi-steady state, as the rate of its formation greatly exceeds that of decomplexation. Given this assumption, the rate of formation of product can be given as:

$$\frac{dP}{dt} = \frac{k_{cat}[E]_0[S]}{K_M + [S]} \quad \text{Equation 4.3}$$

Here, K_M is considered to be the concentration of substrate at which the reaction velocity is half of V_{max} . The maximum velocity is equivalent to the product of the concentration of enzyme and the rate constant of catalysis (k_{cat}). Equation 4.3 can therefore be rewritten as:

$$V_0 = V_{max} \left(\frac{[S]}{K_M + [S]} \right) \quad \text{Equation 4.4}$$

V_0 is defined as the initial rate of product formation (i.e. dP/dt). Taking the gradient of each line in Figure 4.13 and plotting it against the initial concentration of pNPP, a so-called Michaelis-Menten plot can be generated (Figure 4.14).

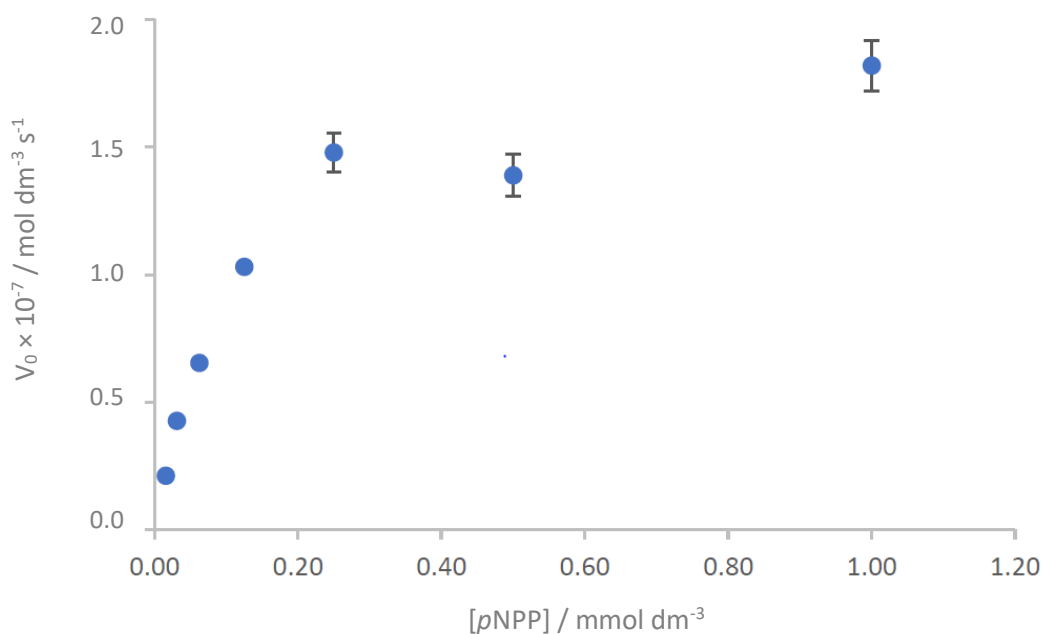


Figure 4.14: Michaelis-Menten kinetic plot for the hydrolysis of pNPP using ALP at a concentration of 0.1 U mL⁻¹. Error bars represent one standard deviation and where not seen are smaller than the data points (n = 3).

An initial increase in the rate of *p*NPP hydrolysis is seen with increasing substrate concentration. The rate of *p*NP formation does begin to plateau at concentrations greater than 0.25 mM, likely due to saturation of the active sites of ALP. Above this concentration the reaction rate is limited by the decomplexation of enzyme and substrate. To generate values for K_M and V_{max} , the double reciprocal of Equation 4.4 (Equation 4.5) was plotted in what is known as a Lineweaver-Burk plot (Figure 4.15).

$$\frac{1}{V_0} = \frac{K_M}{V_{max}} \cdot \frac{1}{[S]} + \frac{1}{V_{max}} \quad \text{Equation 4.5}$$

From this plot K_M and V_{max} can be calculated from the inverse of the x and y intercepts respectively. The values of these parameters are 0.14 mM and 2.1×10^{-4} mM s^{-1} respectively, in relatively good agreement with literature values.⁴⁹ The maximum velocity is slightly slower than that reported by Wang *et. al.*, however, likely due to differences in the operating temperatures of the reactions. They were able to incubate all enzymatic reaction at a fixed temperature of 22°C. The limitations of our UV-vis spectroscopy setup did not allow us to control the temperature in this way, and it is possible that the temperature at which we carried out these experiments was lower than in Wang's report. This likely also contributes to the errors associated with the measurements above.

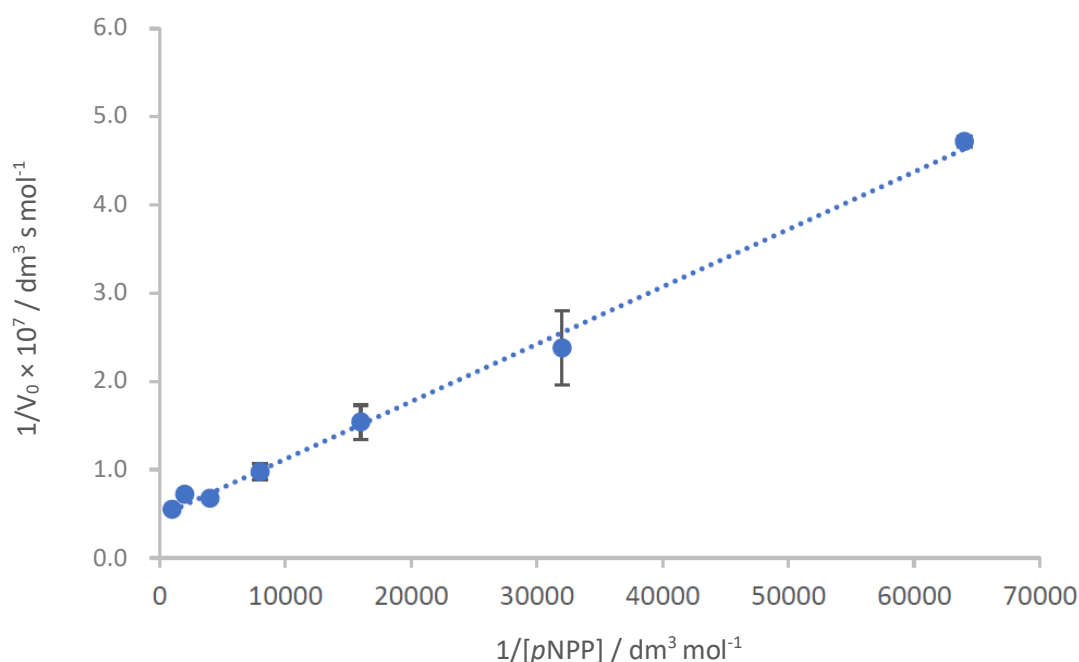


Figure 4.15: Lineweaver-Burk plot for the hydrolysis of *p*NPP using ALP at a concentration of 0.1 U mL⁻¹. Error bars represent one standard deviation and where not seen are smaller than the data points ($n = 3$).

As well as the effect of changing *p*NPP concentration, we also probed the influence of ALP concentration on the rate of hydrolysis. A similar experiment as that outlined above was designed.

A solution containing a known amount of ALP was placed in a UV cuvette and was diluted with *p*NPP solution to a total volume of 2 mL. A fixed *p*NPP concentration of 0.1 mM was studied in these experiments. In the previous experiment the kinetics of the reaction at this concentration were relatively rapid but were also not limited by the number of available active sites. The activity of the enzyme was assessed at various pH values: pH 4, pH 7, pH 9 and pH 11 (buffer solutions) as well as in unbuffered water. All concentrations were calculated based on calibration curves at the appropriate pH.

From Figure 4.16 it can be seen that the initial rate of reaction is low across a wide pH range below 0.05 U mL⁻¹ ALP. As expected, no ALP activity was observed at pH 4 at any loading. It should be noted that significant overlap of the *p*NPP ($\lambda_{\text{max}} = 316 \text{ nm}$) and *p*NP ($\lambda_{\text{max}} = 310 \text{ nm}$) peaks was observed at pH 4, making analysis challenging. However, given that no changes in the spectral features were seen over 48 h we assumed that no reaction had taken place in these samples. Denaturation of the enzyme under these acidic conditions likely leads to this effect.^{323,324} Similarly, very little turnover is seen at pH 7. In alkaline buffer however, V_0 increases significantly with ALP concentration. The greatest rates of reaction are observed when the greatest quantity of ALP is used, and no plateau in the activity is seen in the range tested. A significantly greater activity was observed in pH 9 buffer at 0.4 U mL⁻¹ ALP than under any of the other tested conditions, in line with previous literature.^{323,324} Interestingly, at the higher concentration of ALP, the rate of reaction in unbuffered water was comparable with that in pH 11 buffer solution. We propose that dissolution of *p*NPP and *p*NP raises the pH in the reaction mixture, resulting in an enhanced reaction rate.

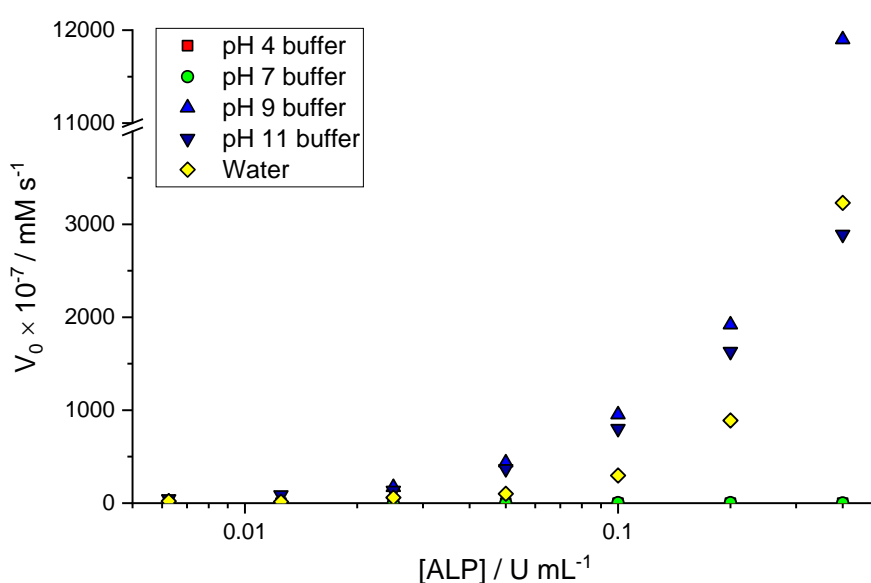


Figure 4.16: Change in the initial rate of hydrolysis of *p*NPP (0.1 mM) with ALP concentration.

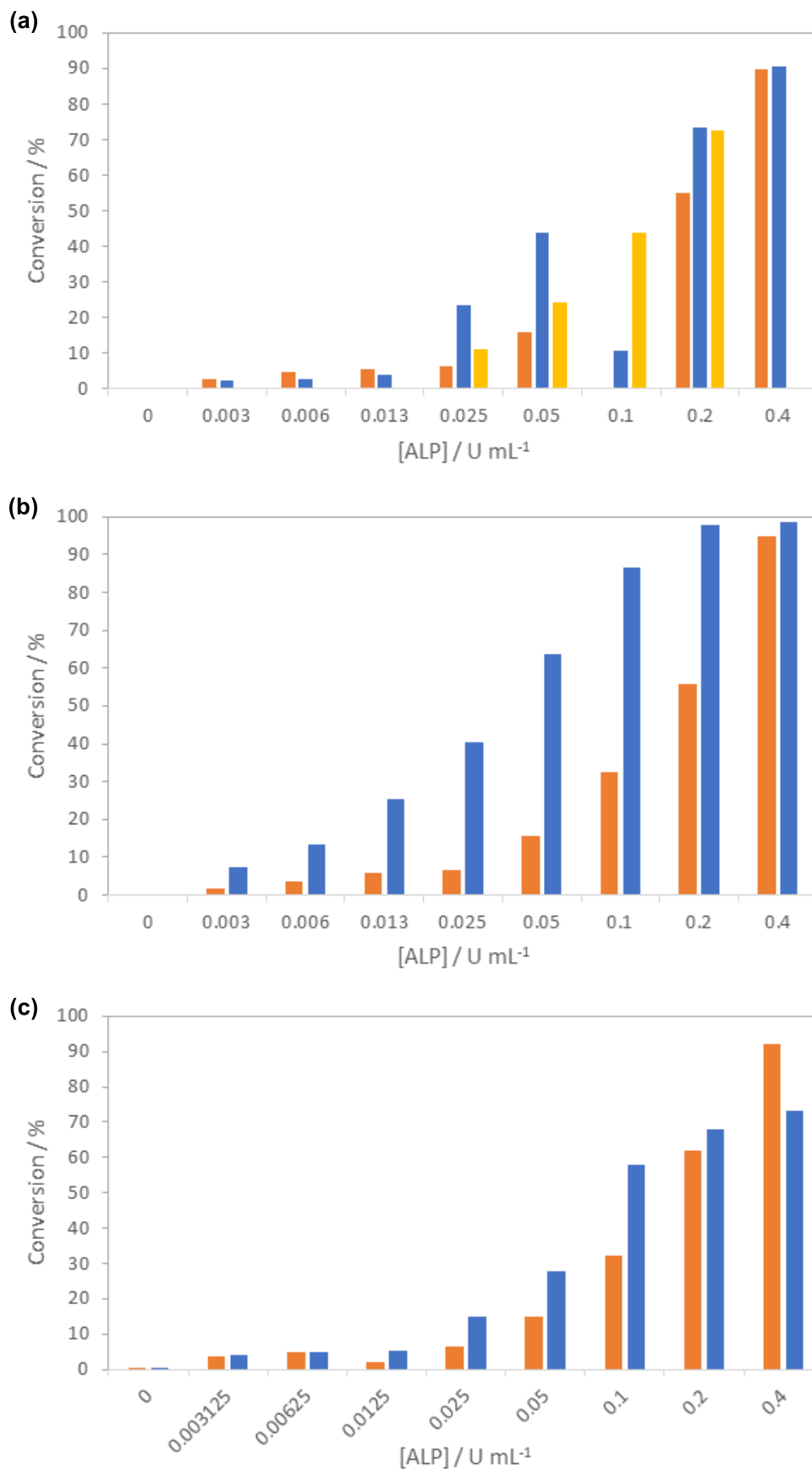


Figure 4.17: Total conversion of pNPP over time at different concentrations of ALP in pH 9 buffer (a), pH 11 buffer (b) and in unbuffered water (c). Orange bars = 2 h, blue bars = 24 h, yellow bars = 48 h.

We also considered the total percentage conversion of *p*NPP over longer time periods (example UV spectra are given in Appendix 9. Reactions in pH 4 buffer, as stated above, showed no evidence of *p*NP in the samples. Similarly, the maximum turnover after 24 h at pH 7 was only *ca.* 4% at ALP concentration 0.4 U mL⁻¹. Little to no conversion was seen at lower concentrations. In pH 9 buffer (Figure 4.17a) almost 100% conversion of *p*NPP occurs over the first 2 hours of reaction with 0.4 U mL⁻¹ ALP. At lower concentrations the reaction does not reach completion, even after 48 h. In contrast, at pH 11, lower concentrations (0.2 U mL⁻¹) of ALP were able to convert *ca.* 100% of the *p*NPP over the first 24 hours of reaction (Figure 4.17b). Despite the slower initial kinetics of the reaction at this pH, the reaction appears more likely to go to completion over long time periods. In unbuffered water the percentage conversions seen after 24 h are lower than those in buffered solutions (Figure 4.17c). A decrease in the observed conversion was seen after 24 h for a reaction catalysed by ALP at a concentration of 0.4 U mL⁻¹. It is possible that a drop in the pH of the solution resulted in a degree of protonation of the sample, reducing the peak intensity at 405 nm. Importantly though, given that the gels which will be used for ALP encapsulation are made in water, rather than buffered solutions (for consistency, see Section 4.6) the fact that a reasonable rate of reaction is observed in unbuffered water is promising for the proposed bioreactor.

The aim of this solution-phase study was to determine appropriate conditions for the conversion of *p*NPP into *p*NP by immobilised ALP. In the patterned reactors, we envisaged the *p*NPP diffusing through a relatively thin, reactive membrane (Figure 4.9). Therefore, rapid turnover would help to ensure maximum conversion over this short distance. Therefore, despite the greater equilibrium conversion of *p*NPP in pH 11 buffer, we elected to use the conditions above, which showed the fastest initial kinetics i.e. pH 9 buffer, 0.4 U mL⁻¹ ALP for our patterned reactor system.

4.6 ALP-encapsulation and activity

Having studied ALP activity in solution, we next assessed the behaviour of this system when ALP is encapsulated within our hydrogel. By comparison to literature examples of enzyme-containing LMWGs, relatively harsh conditions are required to initiate gel network formation for the gels described in this report.^{49,291} We therefore aimed to determine the impact of gelation conditions on the activity of ALP, initially through a qualitative study. All gels prepared in this section were washed by pipetting 1 mL H₂O on top and leaving for 24 h prior to removal and reaction. It was thought this should remove any ALP which is not immobilised, but sits on the surface of the gels, which would create false positive signals for gel-encapsulated ALP activity.

4.6.1 Solution-phase

DBS-CONHNH₂ LMW hydrogels are usually prepared by first sonicating a suspension of the gelator in water, followed by heating to dissolution (*ca.* 100 °C) and cooling. ALP was dissolved in pH 9 buffer at a concentration of 0.2 U mL⁻¹. One 0.5 mL aliquot was taken and sonicated for 15 min. Another was heating to boiling and allowed to cool to room temperature. To these samples a solution of *p*NPP (10 mM, 0.5 mL) in pH 9 buffer was added such that the concentration of ALP and *p*NPP in the sample were 0.1 U mL⁻¹ and 5 mM respectively. Over the course of 1 h, the sonicated sample developed a bright yellow colour (Figure 4.18a) - attributed to the formation of *p*NP - at a similar rate to an untreated control (0.1 U mL⁻¹ ALP, 5 mM *p*NPP), whereas the heated sample showed no colour change in the same period (Figure 4.18b). This is suggestive of the fact that ALP is relatively unperturbed by sonication, but that heating to 100 °C results in denaturation even of this relatively thermostable enzyme.

In the standard DBS-CONHNH₂ gelation procedure, the hot sol is left to stand under ambient conditions to allow cooling and network formation. We considered that the resulting period at relatively high temperature may have contributed to the seemingly total denaturation of the enzyme. Therefore, we repeated the above experiment. However, after heating to boiling, the ALP solution was placed immediately into an ice bath, rapidly cooling the solution (Figure 4.18b). No activity was evident in this sample, either indicating that the heat/cool cycle employed for DBS-CONHNH₂ LMW hydrogel formation is incompatible with ALP formulation.

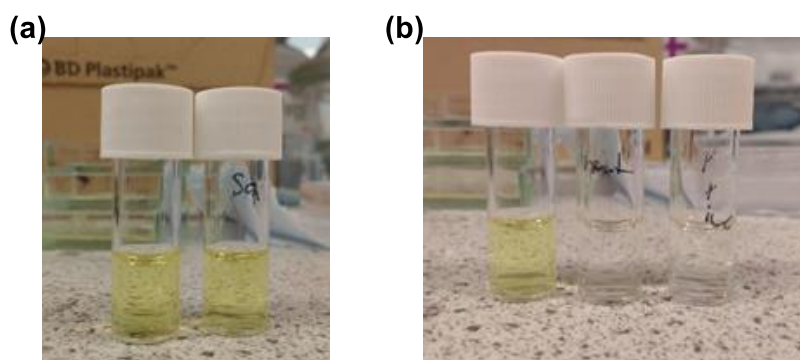


Figure 4.18: Solution-phase studies of gelation stimuli on the bioactivity of ALP (0.2 U mL⁻¹). Activity in the hydrolysis of *p*NPP (5 mM) was tested in response to sonication (a: left = control, right = sample) and heat (b: left = control, middle = heated, right = heated and cooled in ice).

4.6.2 DBS-CONH₂ gels

To determine whether the presence of gelator or formation of a gel network enhanced the thermal stability of ALP we carried out a similar experiment to that described above. DBS-CONH₂ (6 mM) was suspended in a 0.2 U mL⁻¹ solution of ALP in water (0.5 mL). The sample was sonicated for 15 min, then heated to dissolution. The hot sol was cooled either by standing in ambient conditions, or by placing in an ice bath. The pH of these gels was *ca.* 12 after network formation. Gels formed in both cases, and an aqueous solution of *p*NPP (10 mM, 0.5 mL) was added on top. No colour change was seen for either sample (Figure 4.19a). It should be noted that similar studies were attempted using gels formed in pH 9 buffer, however these were too weak to support a solution on top and rapid breakdown of the gels occurred. No reactivity was evident on gel breakdown.

In practise, these results indicate that for ALP encapsulation in our LMWG, the enzyme must be formulated into the gel after the heating step. However given the barrier to diffusion, the enzyme cannot be pipetted on top of the gel after formation and left to penetrate into the gel matrix. Therefore the enzyme must be either injected into the gel after formation or encapsulated during the cooling step of LMWG formation. To test the feasibility of ALP injection, a DBS-CONH₂ gel was formed, and 1 μ L ALP solution (0.2 U μ L⁻¹) injected in via micropipette (ALP concentration = 0.4 U mL⁻¹). 0.5 mL *p*NPP solution was pipetted on top and conversion followed qualitatively (Figure 4.19b). A yellow colour quickly developed in these gels (< 2 h), however, given that these gels are not self-healing, it was unclear whether the ALP is encapsulated in the matrix or if damage of the gel induced by the injection process allows it to diffuse freely into the *p*NPP solution. It is also clear that the enzyme will not be homogeneously distributed within the gel.

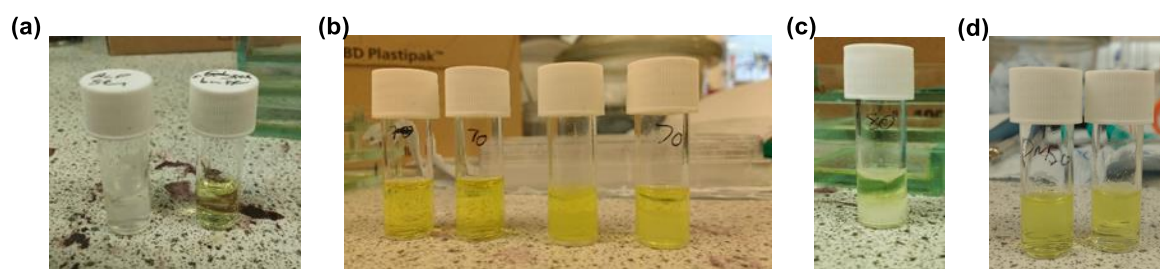


Figure 4.19: Gel-phase studies of gelation stimuli on the bioactivity of ALP (0.4 U mL⁻¹ in each gel). All gels are 6 mM DBS-CONH₂. Gel prepared by standard DBS-CONH₂ procedure (a: left = sample, right = control). Gels prepared by holding the hot sol at 70°C (b: left = untreated solution control, middle-left = treated solution control, middle-right = gel injected with ALP, right = gel sample). ALP gel prepared by holding the hot sol at 80°C (c). ALP-gel containing DMSO has similar activity to a gel with no DMSO (d: left = DMSO gel, right = gel control).

Injection of two dyes, fluorescein and methylene blue, into DBS-CONH₂, 10% PEGDM and 10% hybrid gels via syringe suggested that gel damage occurs (Figure 4.20). The location of the dyes in these samples was largely limited to the 'cavity' left by the syringe and the surface of the gel. For these small molecules, diffusion throughout the sample was then observed over time, however this is unlikely to be the case for much larger molecules such as enzymes. Therefore, this method of enzyme encapsulation was not appropriate for the materials used here, leading to inhomogeneous loading and material damage. The use of self-healing gels as an injectable carrier for enzymes is, however, an interesting avenue for future research and to our knowledge no such study has been undertaken using LMW hydrogels.

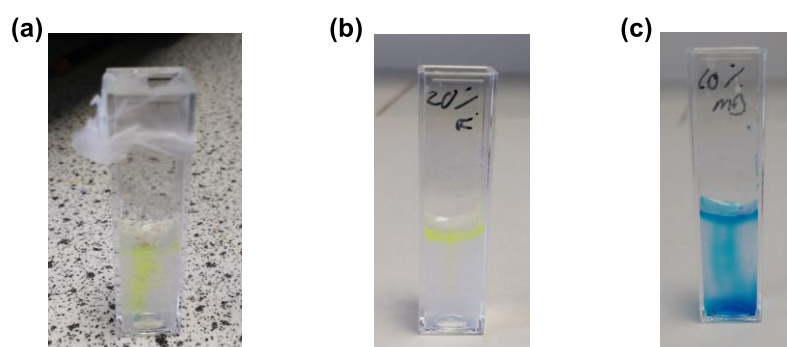


Figure 4.20: Images of dyes injected into hydrogels. Fluorescein injected into DBS-CONH₂ (a) and hybrid (b) gels. Methylene blue injected into a hybrid gel (c).

Encapsulation of the enzyme during the gel cooling step was then tested. The procedure for the preparation of DBS-CONH₂ gels was therefore modified. After heating to dissolution, the hot sol was placed in a thermoregulated oil bath. The possibility of using a slow cooling rate to form DBS-CONH₂ gels was explored, with the hypothesis that addition of ALP to the gel at a lower temperature would help retain its bioactivity. However, cooling from 90 °C at rates of 1, 5 and 10 °C min⁻¹ all resulted in incomplete gelation.

We reasoned that cooling the LMWG sol to a temperature around its T_{gel} , followed by ALP addition and rapid cooling, may result in the formation of more robust, bioactive gels. First we tried this approach at a temperature of 70°C. The beginnings of a gel network formed quickly when held at this temperature, but the sample was left in the oil bath to equilibrate to 70°C for 5 min. At this point 1 μ L of a 0.2 U μ L⁻¹ ALP solution was added and the sample immediately placed in an ice bath to complete gel formation. 0.5 mL pNPP (10 mM in pH 9 buffer) was added on top of the weak gel, which appeared to be catalytically active (Figure 4.19b). However, given the degree of gelation prior to enzyme addition and the weakness of the gel it is again unclear whether the ALP was truly

encapsulated in the gel matrix. Importantly, the enzyme remained active during this treatment, but the gel formation required optimisation.

In an attempt to slow gelation sufficiently to allow complete ALP encapsulation, we repeated the previous experiment, but held the gel at 80°C after heating (rather than 70°C). When allowed to equilibrate at 80°C after dissolution (5 min), the very beginnings of a gel network can be seen forming. ALP solution (1 μL , 0.2 U μL^{-1}) was added at this point, the sample was mixed and then placed immediately into an ice bath (final ALP concentration = 0.4 U mL^{-1}). A robust, homogeneous gel formed on cooling. Enzymatic activity was evidenced in this gel by the evolution of a yellow colour over 1 h (Figure 4.19c). ALP is likely preserved in the gel as a result of the relatively high pH of the gel matrix, measured as *ca.* 11. This method was reproducible and was therefore used for the preparation of all DBS-CONH₂ gels described later in this chapter. For DBS-CONH₂ gels of large volume (i.e. for photo-patterning) DMSO is also added to the gelator solution at a concentration of 4% vol/vol. DBS-CONH₂ gels prepared with DMSO at this concentration showed no loss of activity compared to a gel containing no DMSO (Figure 4.19d). Aqueous DMSO (4% vol/vol) solution also showed no significant change in turnover rate ($7.3 \times 10^{-5} \text{ mM s}^{-1}$) or conversion after 2 h (*ca.* 100%) of a pNPP solution (0.1 mM) compared to the same concentration of enzyme in water ($6.0 \times 10^{-5} \text{ mM s}^{-1}$, *ca.* 100% conversion).

4.6.3 PEGDM and hybrid gels

For the formation of enzyme-loaded PG and hybrid gels, UV light exposure is necessary. Therefore, we tested the activity of ALP after exposure to conditions mimicking the photo-polymerisation process. An ALP-loaded DBS-CONH₂ gel was prepared as described above and exposed to UV light for 0.5 h (the maximum exposure time used for photo-patterned gels). UV-irradiation had no qualitative impact on ALP activity compared to a 'untreated' solution. No loss of activity was observed for irradiated ALP in the solution phase either (Figure 4.21).

For photo-polymerisation, however, the presence of a photo-initiator is also required to induce crosslinking. ALP dissolved in a 0.05% wt/vol solution of PI showed no activity after 0.5 h UV exposure (Figure 4.21). Normal activity was observed compared to a control sample when ALP was dissolved in the PI solution without UV exposure. Proteins are well known to undergo inactivation *via* free-radical initiated processes. Modification of amino acid residues in the protein can lead to peptide cleavage, oxidation processes and protein-protein crosslinking, all of which may render an enzyme non-functional. It is likely therefore, that enzyme inactivation occurs here through one of these mechanisms.

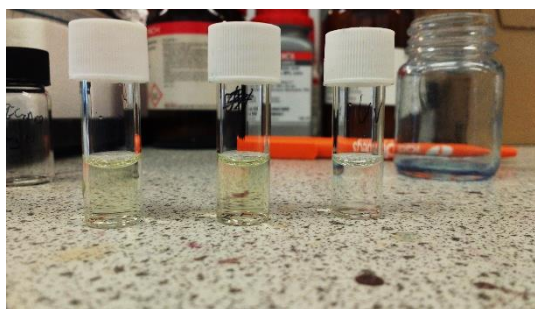


Figure 4.21: Effect of UV light on the bioactivity of ALP in solution (0.2 U mL^{-1}). Control (left), 0.5 h UV exposure (middle) and 0.5 h UV exposure in 0.05% wt/vol PI solution (right). pNPP concentration was 5 mM in all cases.

Despite the inactivation of ALP under these conditions, we proposed that the presence of the PEGDM may enhance the stability of the enzymes to free-radical mediated modification. Mettler and co-workers have previously shown that the presence of acrylated PEG macromolecules during hydrogel curing at 0.2% wt/vol PI loading (using 2-hydroxy-4'-(2-hydroxyethoxy)-2-methylpropiophenone, as in our studies) helped preserve the structure and activity of lysozyme, a thermally stable enzyme.³²⁵ They proposed that the acrylates convert primary radicals – produced by photo-initiation – into a less damaging propagating radical species. They also found (by SDS-PAGE) evidence of covalent conjugation of the enzyme to the PEG monomers. Similar results were previously reported in organogels.³²⁶ We were therefore confident that the bioactivity of ALP may be retained in our hybrid gels.

PEGDM gels containing immobilised ALP were prepared by simply dissolving PEGDM (10% wt/vol) and PI (0.05% wt/vol) in a solution of ALP (0.1 U mL^{-1} , 0.5 mL). These solutions were exposed to UV light for 0.5 h to induce crosslinking, resulting in the formation of a transparent gel. Relatively slow conversion of pNPP (10 mM, 0.5 mL) was observed for these samples, although yellowing of the solution did occur over time. The gel did not take on a significant yellow colour throughout however – only the top of the gel changed colour. This suggests, in agreement with the diffusion studies in Section 4.4, that diffusion of the substrate through the PEGDM network is relatively slow, and likely limits the rate of reaction achievable with these materials. However, it does indicate that bioactivity is preserved in the presence of PEGDM.

To fabricate an ALP-loaded 10% hybrid gel we first prepared a DBS-CONHNH₂ gel containing the enzyme as described above (0.5 mL). On top of this an aqueous solution containing PEGDM (10% wt/vol) and PI (0.05% wt/vol) was added on top and left for 3 days to allow diffusion into the gel. The supernatant was removed after this time and the gel placed under the high-power UV lamp for 0.5 h. Onto this gel a solution of pNPP (10 mM, 0.5 mL) was added. In contrast to the PEGDM gels, rapid hydrolysis of pNPP was seen. In the first hour, only the gel became yellow in colour, indicating

that the enzyme is encapsulated within the gel and retains bioactivity. Over the subsequent hour this yellow colour intensified in both the gel and the solution phase. This result was extremely promising and served to highlight the importance of both the LMWG and PG in our hybrid gels.

It is unclear at present whether ALP is physically encapsulated within the hybrid gel matrix or covalently bound to the PEGDM network. The photo-polymerised sample is not soluble and therefore we could not analyse the enzyme using electrophoretic methods. It may be possible to use lower concentrations of polymer or shorter UV exposure times to partially crosslink the network, but not sufficiently to form a sample-spanning network. These samples could be tested by SDS-PAGE to determine whether any covalent linkages between enzyme and PEGDM have formed.

4.6.4 Enzyme leaching

During the PEGDM diffusion step in hybrid gel preparation, some ALP was lost from the gel network structure. When *p*NPP was added to the removed supernatant, a yellow colour developed, indicative of the presence of enzyme in this sample. For effective separation of enzyme and product, it is important that loss of enzyme from the hydrogels is minimal. We therefore attempted to study the quantity of enzyme lost from each type of gel matrix – LMWG, PG and hybrid gel – over time. To do this we prepared gels of each type as outlined above. Onto each of these gels was pipetted an equal volume of pH 9 buffer. After 24 h this buffer was removed and diluted to 2 mL with *p*NPP such that the final concentration of the substrate was 0.1 mM. The initial rate of *p*NP formation was calculated and therefore a concentration of ALP could be extrapolated from the data. This concentration was converted to a percentage loss of ALP from the gel matrix (Table 4.3). Fresh *p*NPP solution was placed on top of the gel and this process repeated twice more. Errors associated with gel formation (and ALP measurement) were estimated to be *ca.* 0.5% as described previously, whilst the lack of temperature control may have also resulted in an unspecified magnitude of error in the experiments (enzyme reactivity can be significantly influenced by small changes in temperature).

Table 4.3: Calculated percentage ALP release from each gel type into pH 9 buffer. Errors given as standard deviation (*n* = 3).

Gel	Wash 1 release %	Wash 2 release %	Wash 3 release %	Total release %
DBS-CONHNH ₂	0.59 ± 0.04	0.01 ± 0.01	0.00 ± 0.01	0.60 ± 0.06
PEGDM	0.04 ± 0.02	0.00 ± 0.00	0.00 ± 0.01	0.04 ± 0.03
Hybrid	0.06 ± 0.01	0.00 ± 0.01	0.01 ± 0.01	0.07 ± 0.03

Only a small proportion of ALP was lost from each of the gels, and after the first 'wash', essentially no loss was observed for any of the gels. This suggests that the ALP released in these studies was ALP on the surface of the material which had not been immobilised within the gel matrix. According to this interpretation, PEGDM hydrogels display a slightly greater encapsulation efficiency than the DBS-CONHNH₂ LMW hydrogels, perhaps due to a smaller pore size, or perhaps due to covalent conjugation of the enzyme to the PG network.

Similar levels of ALP loss are observed in this study for the 10% hybrid gels as for PEGDM gels. However, as seen in the qualitative experiments, a large enough proportion of the ALP is lost into the supernatant during the 72 h diffusion step to elicit a significant colour change on pNPP addition. It was not possible to directly compare this sample to those used in this experiment, as the PEGDM content of the supernatant can influence ALP reactivity, however it is likely that a similar ALP percentage is lost to solution in this step as for the LMW hydrogel. Overall, however, it appears that little ALP is lost from the gel matrices to surrounding solution, and therefore these appear to be suitable materials for enzyme encapsulation. This also validates the qualitative experiments above, as one wash should have been sufficient to remove all residual ALP on the surface of the gel.

An underlying issue with this experiment for validation of ALP loss is that it is a measure of the bioactive ALP released into the solution. Therefore, should a significant proportion of the enzyme be denatured during gel formation, these results may be misleading for the determination of active ALP concentration in the gels. We attempted to assess the influence of the heat/cool cycle and UV exposure on samples of ALP in the gel-phase by circular dichroism (CD) spectroscopy. CD can be used to assess the secondary structure of proteins by differential absorption of right- and left-handed circularly polarised light. On denaturation, a decrease in the peak intensity corresponding to α -helices and β -sheet forming regions in ALP would therefore be expected as these structures disassemble.^{327,328} Unfortunately, the samples did not contain a great enough concentration of ALP to be able to perform such studies. Typical protein concentrations for CD spectroscopy are *ca.* 1 mg mL⁻¹. The ALP purchased contained 1 mg ALP at a concentration of *ca.* 10 mg mL⁻¹. The large quantities of material required for this study therefore made it prohibitively expensive. The question of how much damage formulating the enzyme in the gel has on the bioactivity is a question which therefore still needs to be addressed. Alternative characterisation techniques such as tryptophan fluorescence may provide a means to determine this at lower enzyme concentrations.^{329,330} However, changes in tryptophan fluorescence due to confinement and solvophobic effects are likely for ALP immobilised in the gel matrices, which would make the abstraction of meaningful data a significant challenge.

4.6.5 Gel-phase studies

Thus far, we had demonstrated ALP bioactivity in LMWG, PG and hybrid hydrogels in a qualitative manner. We then sought to quantify the reactivity using UV-visible spectroscopy. We prepared ALP-loaded gels (0.4 U mL^{-1} , 0.5 mL) in UV cuvettes and added pH 9 buffer (0.5 mL) on top for 24 hours to remove any non-immobilised enzyme. This supernatant was removed and replaced with a solution of *p*NPP (2 mL , 0.1 mM) in pH 9 buffer solution. The absorption at 405 nm was recorded over time in the solution. Little increase in *p*NP concentration was observed for reactions with any of the gels over 24 h, despite yellowing of the hydrogels suggesting that the hydrolysis was occurring. These observations were suggestive of the fact that *p*NP was being formed within the hydrogel by the immobilised ALP but was then being retained in the hydrogel under the experimental conditions. Wang *et. al.* provided pictures of an ALP-loaded gel after reaction with *p*NPP.⁴⁹ Their samples were also bright yellow in colour, but they did not comment on the reasons for this, or attempt to quantify the amount of *p*NP remaining in their hydrogel after each reactive cycle.

To explore this phenomenon further, we pipetted solutions of either *p*NPP or *p*NP (1 mM , 6 mL) onto 2 mL hydrogel samples in 8 mL sample vials. Solutions were buffered at one of three values: pH 4, pH 7 and pH 11. These values were chosen as they represent conditions under which 100% of the *p*NP should be protonated (pH 4), 100% deprotonated (pH 11) and an equal proportion of the two species respectively (pH 7). A sample of the supernatant was taken after 24 and 48 h, and the UV spectrum recorded. From the intensities of the spectral features ($\lambda = 316 \text{ nm}$ for *p*NPP, $\lambda = 310 \text{ nm}$ and 405 nm for *p*NP), the concentration of each species in the solution could be calculated, which in turn allowed inference of the percentage taken up by the gel. The results are summarised in (Figure 4.22). The dotted lines on the graphs represent 25% uptake by the gel. This is the value which would be expected based purely on free diffusion of the small molecules within the solvent i.e. there is no preference for either the gel or solution phase. The errors associated with the instrumentation and measurements are similar to those described earlier in this thesis.

*p*NPP uptake into DBS-CONHNH₂ hydrogels was broadly similar across all pH values tested, and was slightly lower than that predicted based on diffusion alone. For 10% PEGDM gels, relatively slow uptake is observed at pH 4 compared to the neutral and basic samples. After 48 h, however, there was no significant difference in uptake across the pH range. In contrast, for solutions pipetted onto the 10% hybrid gel, a lower proportion of the *p*NPP was present in the gel phase at both time points compared to the LMWG and PG-based materials. Of particular interest was the uptake at pH 11. At this pH, essentially none of the *p*NPP diffused into the hybrid gel over 48 h. This was a curious

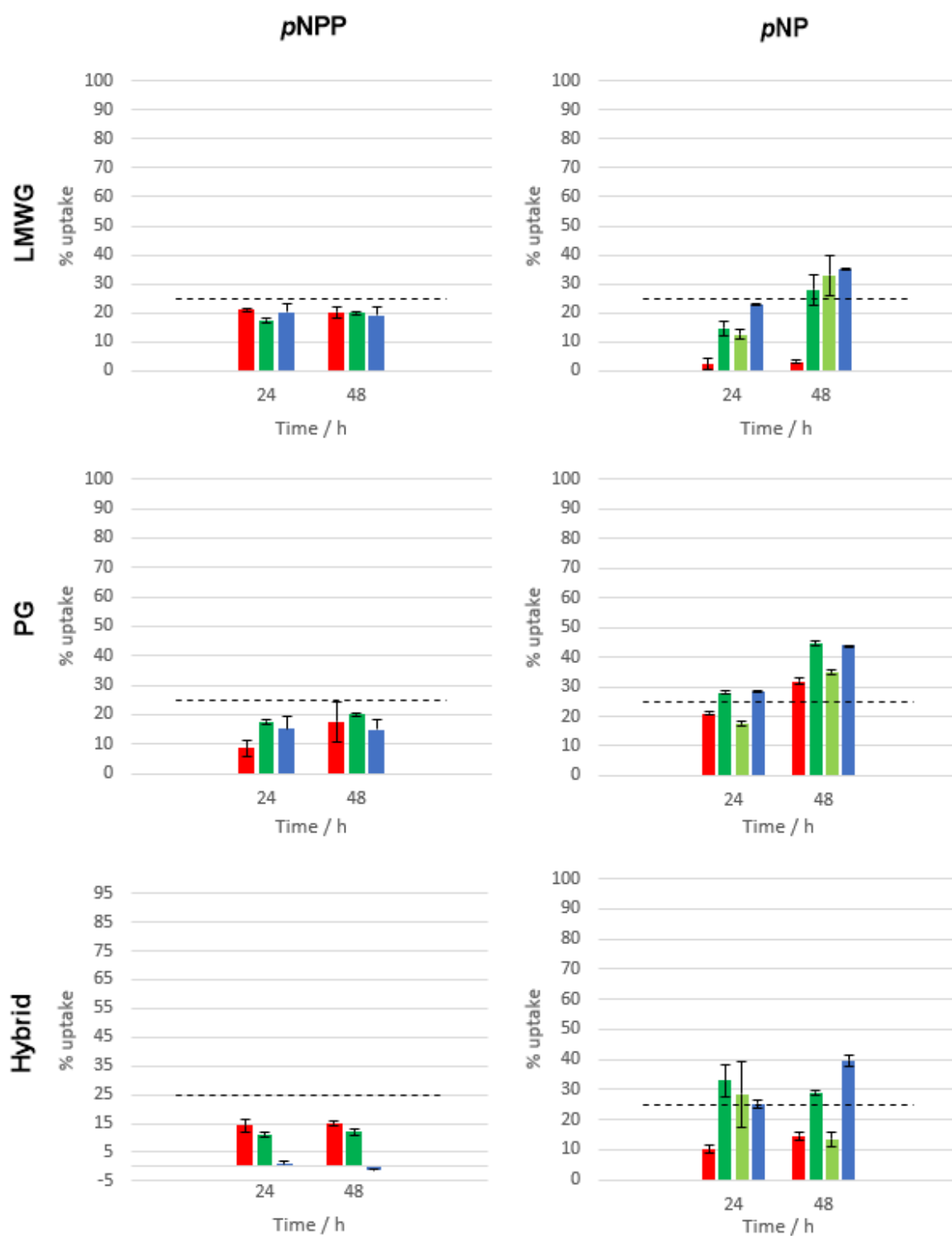


Figure 4.22: Uptake of pNPP (left) and pNP (right) into DBS-CONHNH₂ (top), 10% PEGDM (middle) and 10% hybrid (bottom) hydrogels. Red bars = pH 4, blue bars = pH 11. Green bars are uptakes at pH 7. For pNP two distinct species are observed by UV at pH 7. The protonated and deprotonated forms are denoted by the dark and light green bars respectively. The dashed black line represents 25% uptake, the expected dilution based solely on equilibration of concentration. Errors given as standard deviation ($n = 3$).

finding. It was anticipated that *p*NPP, with its highly charged phosphate group, would show a preference for the hydrophilic solution phase, rather than the somewhat more hydrophobic gel.

However, the effects were expected to be uniform, as no change in the overall charge of this species should be seen in the studied pH range. It is possible that at pH 11 some change in the properties of the hybrid gel is manifested which serves to repel *p*NPP from the gel matrix. Any such change does not result in significant changes in either of the single component gels.

The uptake of *p*NP into the gel phase was studied in the same manner. Interestingly, the protonation state of *p*NP appears to have a significant effect on the proportion of the compound in the solution and gel phases respectively. For DBS-CONH₂ and 10% hybrid gels, significantly less *p*NP was found in the gel at pH 4 than at either pH 7 or pH 11. Given that *ca.* 25% uptake of *p*NP was found for 10% PEGDM gels, this result suggests that a specific repulsive interaction between the protonated form of *p*NP and the DBS-CONH₂ network in both gels. Elevated uptake of *p*NP was observed at pH 11 across all samples compared to what is expected based on diffusion alone. This suggests that a more general preference for the gel-phase is preferred for deprotonated *p*NP. This was a surprising result. A previous report by Okesola *et. al.* described the preferential uptake of methylene blue dye at pH values which minimised the overall charge on the molecule.¹⁴³ In this study, the inverse effect was seen. The more highly charged species partitions preferentially into the gels, whilst the uncharged form of *p*NP is not taken up by the LMWG or hybrid gels effectively.

To elucidate the reasons for elevated *p*NP uptake in the LMW gels, we used NMR spectroscopy to assess the mobility of this species in a DBS-CONH₂ hydrogel. The theory behind this approach was described in Chapter 2. Briefly, mobile species will be visible in the NMR spectrum, whilst immobile species are “NMR invisible”. DBS-CONH₂ (6 mM) was suspended in a solution of *p*NPP (10 mM) in D₂O. DMSO was added at a concentration of 0.56 M. The sample was heated to dissolution and transferred to an NMR tube. On cooling, gel formation was observed. The ¹H NMR of this sample was recorded (Figure 4.23).

From the ratios of the peak integrals relating to DMSO and the aromatic *p*NP protons, the concentration of mobile *p*NP was calculated as follows:

$$I(\text{DMSO}, 6\text{H}) = 23.02$$

$$I(\text{DMSO}, 1\text{H}) = 3.84 \equiv 0.56 \text{ M}$$

$$I(\text{pNP}, 2\text{H}) = 0.15$$

$$I(\text{pNP}, 1\text{H}) = 0.075 \equiv 0.01 \text{ M} \equiv 10 \text{ mM}$$

All of the *p*NP was mobile in the gel phase suggesting, as inferred from the uptake assay, that no specific interaction between the gel fibres and *p*NP are responsible for the elevated uptake. It should be noted that the errors associated with NMR are estimated at *ca.* 5%. However, this does not significantly influence the findings in this case. Unfortunately, we were unable to perform a more rigorous NMR study on the influence of pH on *p*NP mobility. Gels did not form properly in the NMR tube when prepared in buffer solution. It was not possible to study *p*NPP mobility in this way either – heating the gelator suspension in the presence of *p*NPP resulted in hydrolysis of the phosphate group. These results go some way to explaining the observations in the gel-phase reactivity studies described above.

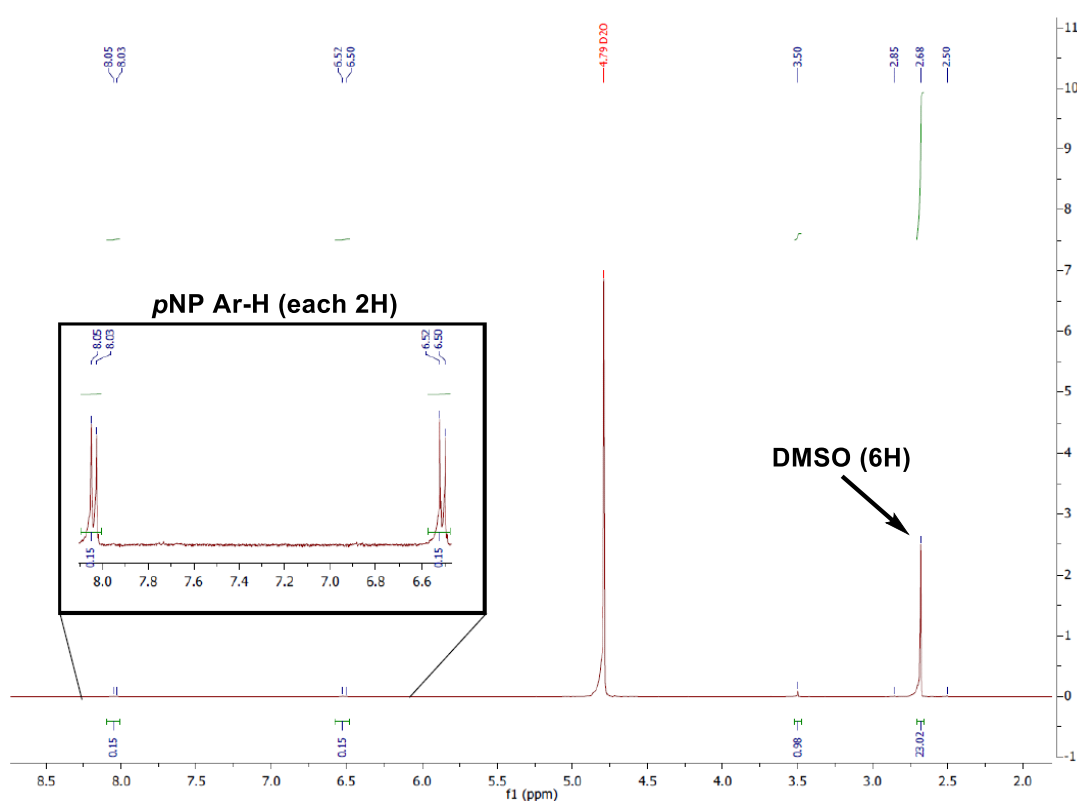


Figure 4.23: NMR spectrum of a DBS-CONHNH₂ (6 mM) hydrogel formed in an aqueous solution of *p*NP (10 mM). Peaks of interest for determining the proportion of mobile and immobile *p*NP are highlighted.

4.7 Photo-patterned bioreactors

Having studied the reactivity of ALP within a hydrogel, we designed and fabricated a photo-patternable bioreactor for the dephosphorylation of *p*NPP. We envisaged that in the absence of flow, an increase in the volume of the ‘product’ compartment compared to the ‘reactant’ compartment would create a concentration gradient that would somewhat drive the diffusion of material through the reactive gel (Figure 4.9). We therefore chose to pattern a ring of bioactive gel

within a glass mould, such that the inner 'reactant' compartment could hold a volume of 0.3 mL, whilst the larger outer 'product' held 2 mL solution. We elected to carry out all reactions in the photo-patterned reactor at pH 9. As outlined above, reaction kinetics were fastest at this pH. Additionally, whilst the reaction was also shown to turn over at a reasonable rate in both pH 11 buffer and in unbuffered water, uptake of *p*NP into the hybrid gel was similarly high under both conditions, therefore no benefit was perceived from using these conditions.

The procedure for preparing photo-patterned hybrid gels is similar to that described in Chapter 2. 28.4 mg DBS-CONHNH₂ was dissolved in DMSO, and then added to boiling water (9.6 mL). The resulting solution was placed in a thermostatted oil bath at a temperature of 80 °C. The sample was left to equilibrate for 5 min until the very beginning of a gel network could be seen forming. At this point ALP solution (20 μL, 0.2 U μL⁻¹, in pH 9 buffer) was added. The mixture was stirred briefly before adding to a glass tray (5 cm × 5 cm × 1 cm) which had been pre-cooled in an ice bath. A sample-spanning gel was formed rapidly on cooling. On top of this gel, a 10 mL aqueous solution of PEGDM (10% wt/vol) and PI (0.05% wt/vol) was pipetted and left for 3 days. After this time, the solution was removed. An acetate photomask (4 layers) with printed ring pattern was placed over the gel and the sample irradiated with UV light for 30 min to photo-polymerise the exposed regions. The soft, shielded regions were washed away with a low power water jet to yield ALP-loaded, photo-patterned hybrid gels. All gels were washed with water prior to carrying out reactions to remove any ALP on the surface of the hybrid gels. Propagation of error in the following experiments is the result of a number of factors, including gel formation inconsistency, UV-vis spectrometer error and temperature fluctuations. All of these have been discussed earlier in this work.

Initially, the rate of diffusion of *p*NPP through the gel and into the outer compartment was studied. A solution of *p*NPP (0.3 mL, 10 mM) in pH 9 buffer solution was pipetted into the inner compartment of a photo-patterned, ring-shaped hybrid gel in which no ALP was encapsulated. The solution in the outer compartment (pH 9 buffer, 2 mL) was stirred to ensure material diffused away from the surface of the gel. The concentration of *p*NPP in the outer compartment was measured over time. The solution was sampled and analysed before returning the solution to the outer compartment (λ_{max} *p*NPP = 310 nm). The concentration of *p*NPP increased linearly in the product compartment over the course of 3 h, demonstrating that in this configuration, small molecules are able to diffuse across the gel barrier. The rate of diffusion of *p*NPP was calculated to be $49 \pm 10 \times 10^{-3} \mu\text{M cm}^{-1} \text{s}^{-1}$ based on a ring diameter of 0.8 cm. This diffusion rate is consistent with those described in Section 4.4, and we can therefore infer that the slight alteration in fabrication procedure has not had a significant impact on the internal pore structure of the hybrid gel.

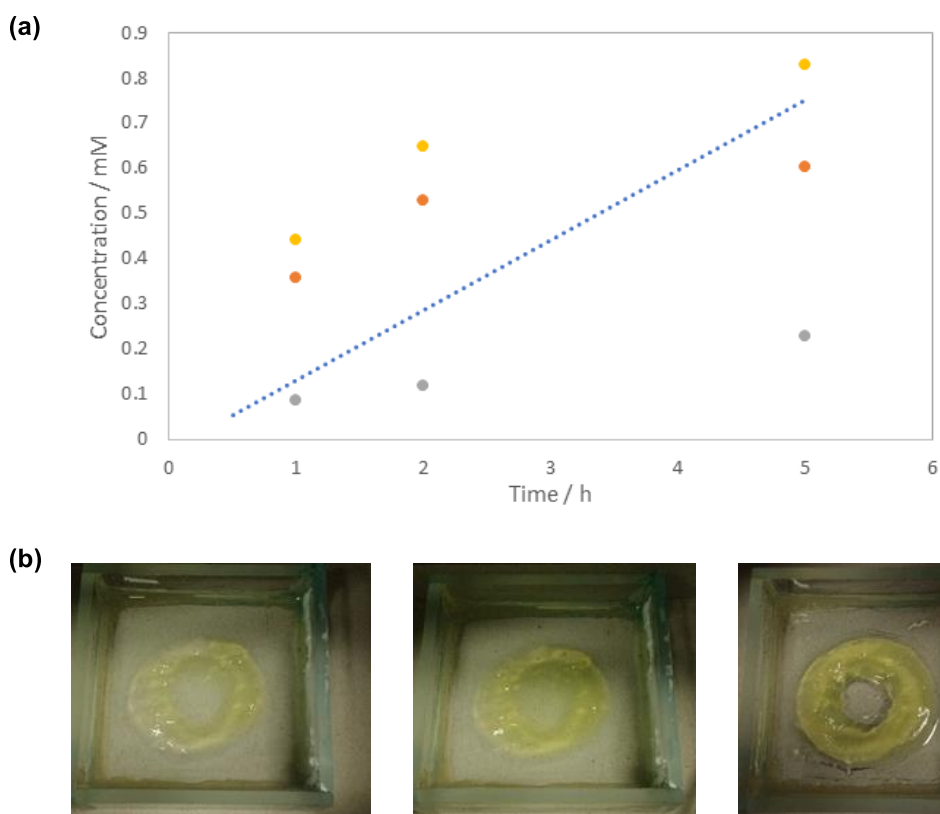


Figure 4.24: Change in concentration of *pNPP* (red), *pNP* (grey) and the total molar concentration (yellow) in the 'product' compartment over time for an ALP-loaded hybrid gel reactor (a). The dotted blue line represents the rate of diffusion of *pNPP* into the 'product' compartment with no ALP present. Images of the bioreactor taken after 1 h (left), 2 h (middle) and 5 h (right) reaction time.

Having established the rate of diffusion of *pNPP* through the hybrid gel ring, we then repeated this experiment with a photo-patterned ring containing 0.4 U mL^{-1} ALP. Again, the UV-vis spectrum of the whole product compartment was recorded over time and returned to the compartment immediately after measurement. In the presence of ALP, a much greater proportion of the soluble components diffuse across the membrane and into the product compartment over the course of the experiment (Figure 4.24a). We suggest that the conversion of *pNPP* into *pNP* may increase the concentration gradient of the substrate compared to when no reaction occurs, encouraging a greater rate of diffusion towards the exterior of the reactor. However, the concentration of *pNP* observed in the outer compartment was very low, with no greater than 2% of converted product measured in this solution. A comparatively high proportion (*ca.* 6%) of *pNPP* diffused into the outer compartment over this time. Clearly, in this reactor design, a greater concentration of ALP is required for the reaction to proceed to completion as some of the *pNPP* diffused through the ring without reacting. Significantly, however, a marked yellow colour developed in the hybrid gel over

the course of the reaction (Figure 4.24b), again suggesting that conversion was taking place, but that a large proportion of the *p*NP remained within the gel after conversion. The volume of the gel used in this experiment is approximately 1.44 cm³ (based on a 2.0 cm inner diameter, 2.8 cm outer diameter and 0.5 cm height). This is less than the volume of solution (total = 2.3 cm³), therefore the retention seen is not simply due to free diffusion of the substrate/product. We suggest that reaction is occurring but that *p*NP is being retained within the gel ring. Additionally, it should be noted that ALP encapsulated in the hybrid gels at room temperature retain a reasonable degree of reactivity over at least 3 months at room temperature (Appendix 10).

To try to decouple some of the effects which may contribute to the above findings, we performed a similar experiment to that described for analysis of *p*NPP diffusion. A photo-patterned ring-shaped hydrogel containing no enzyme was fabricated, and a solution of *p*NPP (0.3 mL, 10 mM, pH 9 buffer) was added to the central compartment. In this case however, the outer compartment was loaded with a solution of ALP in pH 9 buffer, at a concentration of 26 U mL⁻¹. This should ensure a much greater extent of reaction than for the ALP in the gel, which was at a concentration of 0.4 U mL⁻¹. The concentration of *p*NP in the product compartment increased over the first 3 h of the reaction, and then began to decrease at longer reaction times (Figure 4.25a). Much greater *p*NP concentrations are observed at this higher ALP loading as expected.

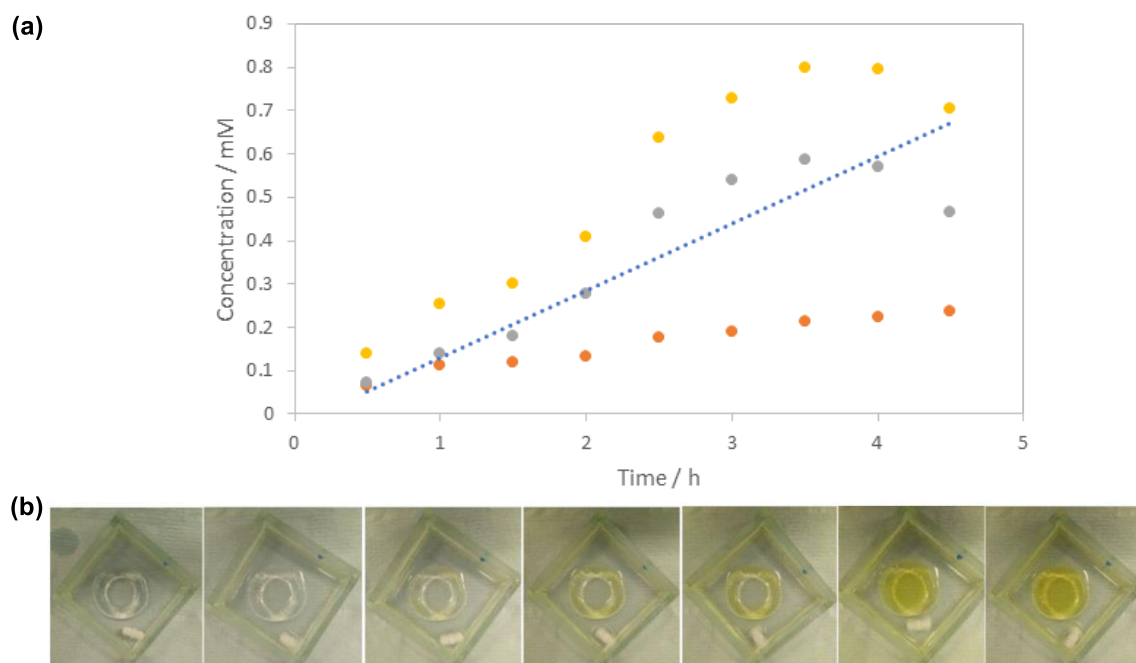


Figure 4.25: Change in concentration of *p*NPP (red), *p*NP (grey) and the total molar concentration (yellow) in the 'product' compartment over time for a reactor with ALP present in the 'product' compartment (a). The dotted blue line represents the rate of diffusion of *p*NPP into the 'product' compartment with no ALP present. Images of the bioreactor taken every 30 min (b). Pictures span the time from 0 h (left) to 3 h (right).

The constant increase in *p*NPP concentration in this compartment suggests that no significant changes in substrate diffusion are seen over this time. The decrease in *p*NP concentration must therefore be the result of partitioning of the product from the outer solution-phase compartment back into the gel. At these high enzyme loadings, *p*NPP is likely used up relatively quickly, resulting in slower production of *p*NP over time. After 4 hours the rate of *p*NP uptake outstrips its production, and the concentration in the product compartment decreases. This indicates that irrespective of whether *p*NP is produced in the gel ring or in the outer compartment, it ultimately ends up in the gel.

In this experiment, the gel developed a significant yellow colour as reported for the reactor with ALP loaded into the hybrid gel (Figure 4.25b). Interestingly, the reactant compartment also turned a bright yellow over the course of the reaction. This prompted us to determine the contents of the interior compartment and to calculate the proportion of substrate and product in the gel and solution phase respectively for each of the bioreactors described above. The contents of the central compartment were removed after 6 h reaction time and diluted to 2 mL in pH 9 buffer before recording the UV spectrum.

The number of moles of *p*NPP and *p*NP in each compartment are given in Table 4.4 for the reactions with ALP encapsulated within the gel, or contained in the product compartment. As expected from the UV study, a significantly smaller amount of *p*NPP is present in the reaction mixture when the ALP is present in solution. The higher turnover rate ensures that almost all of the substrate is hydrolysed over the first 6 h. For this experiment, a greater proportion of *p*NP is also present in the reactant compartment compared to the product compartment. This is in agreement with the qualitative observations from this experiment, but is still surprising. Based simply on the volumes of the two compartments, a 6-fold excess of *p*NP was expected in the product compartment. Additionally, given that the *p*NP is formed in the product compartment, it must be preferentially released into the smaller reactant compartment after partitioning into the gel ring. It is possible that the smaller interfacial area between the gel and solution at the interior of the ring slows uptake of *p*NP from this solution. Alternatively, stirring of the outer compartment may increase the uptake rate from the outer compartment by increasing the rate at which the product is brought into contact with a gel surface. Whilst less pronounced, a greater than expected *p*NP content is also observed for the reactant compartment for bioreactors with immobilised enzyme, suggesting that these observations are a result of the specific shape and reaction employed for this bioreactor. No differences in pH were seen in the different compartments after 6 h.

Given that *p*NPP shows little to no uptake into hybrid gels at pH 9, we can infer that the gel contains a relatively small amount of the substrate at the time when these measurements were made. Given this assumption, the approximate percentage conversion achieved by the bioreactors could be calculated. An example calculation is given for the immobilised enzyme:

$$\text{Mol } (pNPP) = (38 + 60) \times 10^{-8} \text{ mol} = 98 \times 10^{-8} \text{ mol}$$

$$\% \text{ unreacted} = \frac{98 \times 10^{-8} \text{ mol}}{300 \times 10^{-8} \text{ mol}} \times 100\% = 33\%$$

$$\% \text{ conversion} = 100\% - 33\% = 67\%$$

Relatively high conversions of *p*NPP into *p*NP are achieved with both configurations of the bioreactor, with 67 and 98% conversion for the immobilised and free enzyme respectively. This suggests that the encapsulation, or confinement within an enzyme ‘reactive’ compartment (Figure 4.26) are both feasible approaches for this type of photo-patterned bioreactor. Unfortunately, despite the high conversion, the affinity of the product for the gel meant that obtainable ‘yields’ – the percentage of product free in solution after 6 h - was relatively low. Only 11 and 23% yields were obtainable using these reactor configurations. This specific combination of enzymatic reaction and supporting hydrogel matrix may not be optimal, however the proof-of-principle study here lays groundwork for the development of more functional patterned reactors in the future.

Table 4.4: Quantities of *p*NPP and *p*NP in the different compartments of the photo-patterned bioreactor after 6 h reaction time. The initial amount of *p*NPP added to the reactant compartment was $300 \times 10^{-8} \text{ mol}$ (10 mM, 0.3 mL).

ALP in	Compartment	<i>p</i> NPP ($\times 10^{-8}$) mol	<i>p</i> NP ($\times 10^{-8}$) mol	Sum ($\times 10^{-8}$) mol	% in sol	Conversion %						
Gel	Reactant	38	10	131	44	67						
	Product	60	23				Sol	Reactant	2.3	39	76	25
Sol	Reactant	2.3	39	76	25	98						
	Product	4.4	30									

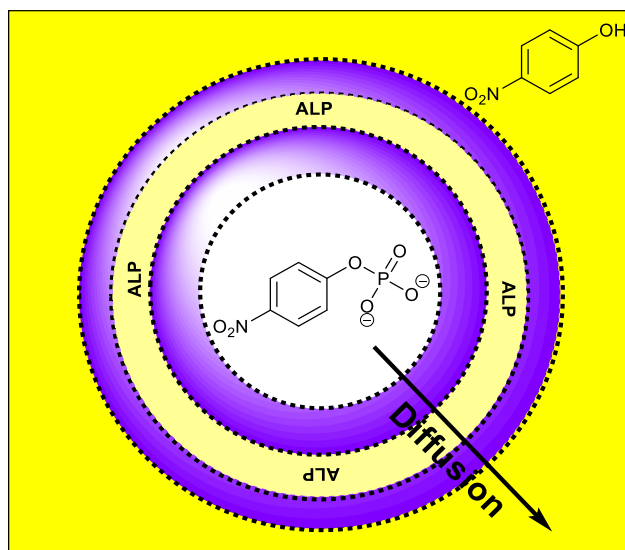


Figure 4.26: Schematic of how a bioreactor with ‘reactive’ enzyme compartment would function. ALP is encapsulated between two photo-patterned hybrid gel rings. pNPP must diffuse from the ‘reactant’ compartment (centre, white), through the ‘reactive’ compartment (middle), conceptually yielding pure pNP in the ‘product’ compartment (outside, yellow).

In particular we are interested in enhancing the obtainable yield of this reaction by utilising the fact that low pNP uptake is observed at pH 4. It can be envisaged that flushing the reactor with pH 4 buffer after conversion is complete may drive the product out of the gel. However, subjecting the immobilised enzyme to these conditions is likely to result in denaturation, limiting the recyclability of these materials. Another potential solution is to use the related enzyme acid phosphatase (AP) in place of alkaline phosphatase. This enzyme catalyses the same hydrolysis reaction as ALP, but under significantly more acidic conditions (optimum pH *ca.* 4.8 - 5.8).³²³ At these depressed pH values, partitioning of the reaction product into the gel membrane should not be seen, increasing the proportion available in solution and therefore the effective yield. This may also prevent back-flow of the product into the reagent compartment. More generally, a range of different enzymatic reactions and/or patternable gels could be screened for both catalytic activity and product retention. For example, the acid-triggered DBS-COOH/PEGDM hybrid gel reported by Smith and co-workers⁵⁵ is formed under acidic conditions (*ca.* pH 4) which would appear highly amenable to AP incorporation.

We briefly investigated the suitability of AP as the reactive component of these DBS-CONHNH₂/PEGDM bioreactors. In a simple experiment, we fabricated a 10% hybrid gel ring as described above. The ‘reactant’ compartment was loaded with a solution of pNPP (10 mM, 0.3 mL) in pH 5.8 buffer solution – the pH optimum of the enzyme. The pNPP product is predicted, using

the Henderson-Hasselbalch relationship, to be 96% protonated under these conditions. The 'product' compartment contained a solution containing AP (26 U mL^{-1}) in pH 5.8 buffer solution. The outer compartment was stirred and an aliquot (0.5 mL) of the solution in this compartment was taken every hour. This aliquot was diluted to 2 mL in pH 9 buffer to quench the reaction and to convert any *p*NP into the deprotonated, yellow form. This was a necessary step due overlap between the UV peaks of protonated *p*NP and the starting material *p*NPP, but made recording the spectrum and returning the solution to the reactor (as for the ALP reaction) infeasible. The aliquot taken was replaced with fresh AP (26 U mL^{-1}) solution (in pH 5.8 buffer). Absorbances were compared to a sample of the enzyme solution to account for contributions from the brown AP solution and a calibration curve used to quantify the concentration of *p*NPP and *p*NP in the compartment.

In this preliminary experiment, it can be seen that the rate of *p*NP accumulation in the product compartment in the AP bioreactor (Figure 4.27a) is similar to that of the ALP bioreactor (as seen in Figure 4.25), despite there being no clear visual indication of this due to the comparatively low pH used (Figure 4.27b). However, in contrast to the ALP reactor, the concentration of *p*NPP in the product compartment in the AP reactor is greater than that of *p*NP. The rate of turnover of the enzyme appears to be similar (due to the similar *p*NP concentration profile), so the differences must be due to a greater rate of *p*NPP diffusion through the hybrid gel ring. As seen in Section 4.6.5, the uptake of *p*NPP into the hybrid gel is significantly greater at pH values of 4 and 7 than at pH 11. As the amount of *p*NPP entering the gel is presumably higher under these mildly acidic conditions than in the pH 9 ALP reactor, and therefore a greater amount of *p*NPP is present at the outer gel-sol interface, increasing the rate of *p*NPP accumulation in the product compartment.

The contents of the reactant compartment were also analysed by UV-vis spectroscopy. The molar quantity of *p*NPP and *p*NP in this compartment were *ca.* 0.40 and 0.82 mM respectively. The accumulation of product within the reactant compartment is still an inherent issue with this reactor design. However, it was calculated that, in this case, that *ca.* 68% of the total substrate and product is present in the solution phase. This is a marked improvement over the equivalent experiment at pH 9, in which only *ca.* 25% of the small molecules were in solution. This preliminary study suggests that AP, employed under acidic conditions, is a more suitable reaction to use in these hybrid gel bioreactors. Incorporation of AP into the photo-patterned hybrid gel ring is a key next step to study this combination further.

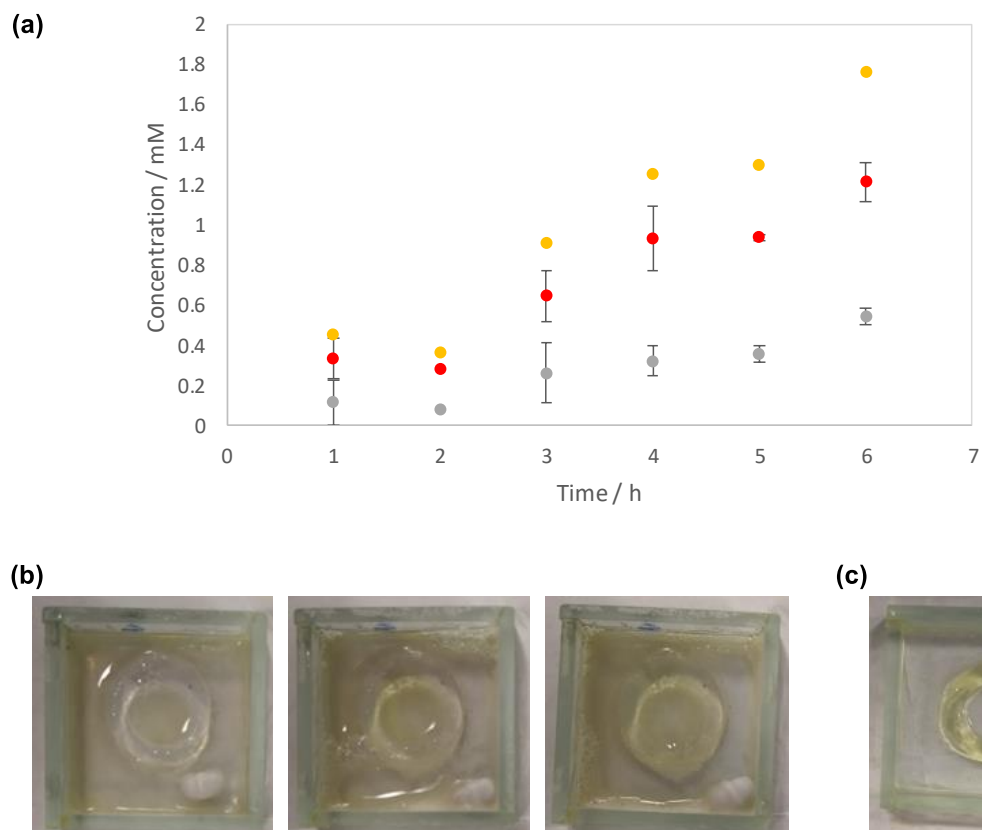


Figure 4.27: (a) Change in concentration of pNPP (red), pNP (grey) and the total molar concentration (yellow) in the 'product' compartment over time for a reactor with AP present in the 'product' compartment. (b) Images of the bioreactor taken after 2 h (left), 4 h (middle) and 6 h (right). (c) Image of the bioreactor after being submerged in pH 9 buffer for 24 h. Errors given as standard deviation ($n = 3$).

4.8 An alternative reactor design – small molecule exclusion

As well as the studies outlined above, we also aimed to overcome the limitations of the hybrid gel bioreactors using a different approach to spatial control of reactivity. Given that at 10% PEGDM loading in a hybrid gel, significant depression of diffusion kinetics was observed even for small molecules, it was expected that by raising the concentration of the PG, the exclusion of small molecules could also be achieved. Therefore, by photo-patterning a high-loading hybrid gel, we reasoned that reactants could in effect be channelled down the soft, lower density, non-irradiated regions (Figure 4.28). In contrast with the bioreactors above, where the hybrid gel acts as a semi-permeable membrane, in this case the hybrid gel will be used to direct diffusion through a lower density gel phase. The whole bioreactor in this section is in the gel-phase.

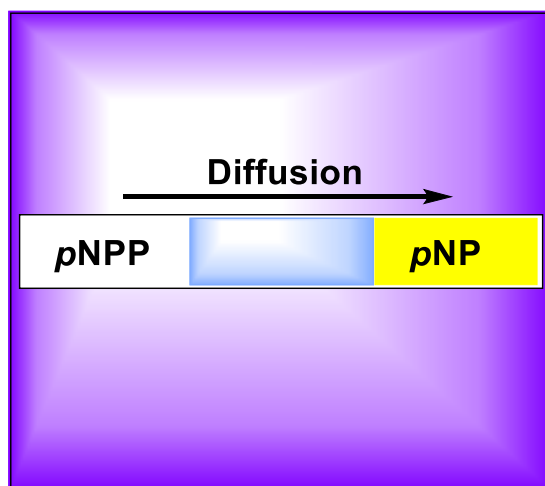


Figure 4.28: Schematic representation of an exclusion bioreactor. Dense, photo-patterned hybrid gel (purple) does not allow passage of reactant or product, whilst an enzyme-loaded, soft LMWG (blue) allows reagent diffusion and reaction.

As seen in Section 4.4, the 10% hybrid gels allow diffusion of small molecules such as fluorescein through the gel matrix. We therefore prepared hybrid gels using the same methodology as described in Chapter 2. PEGDM uptake over 3 days was assessed by ^1H NMR spectroscopy on gels as described in Chapters 2 and 3. The actual PEGDM content of the 20%, 40% and 60% hybrid gels were found to be *ca.* 10, 21, and 27% respectively. The mechanical properties of these hybrid gels were assessed by rheological studies (Figure 4.29). These were carried out as described in Chapter 2. Good quality data was obtained for the 20% hybrid gel. However, at higher PEGDM loadings, gel slipping led to inconsistency in the data obtained, particularly in the frequency sweep experiments (Figure 4.29b). From the amplitude sweeps, the G' values for the 20%, 40% and 60% hybrid gels were approximated as *ca.* 8000, 30000 and 37000 Pa respectively. We consider this stiffening of the material to be the result of a greater density of a crosslinked PEGDM network, which should, in principle, correlate to a decrease in pore size as required for small molecule exclusion. The critical shear strain of these materials also increased with higher PEGDM loading, from *ca.* 40% for the 20% hybrid to *ca.* 60% hybrid. The increasing PEGDM content provides a greater resistance to shear, as described in Chapter 2. The behaviour of these materials in response to increasing shear is similar to the hybrid gels described in Chapters 2 and 3. Due to the high PG loadings in these examples, nanoscale rearrangements of the PEGDM networks results in an increase in the G'' values before an accompanying decrease in G' is observed. At these higher PG loadings, the critical strain values here are much closer to those of the PEGDM hydrogels described in Chapter 2 (page 75, *ca.* 100%). Overall, the rheological behaviour of these materials is dominated by the PG content.

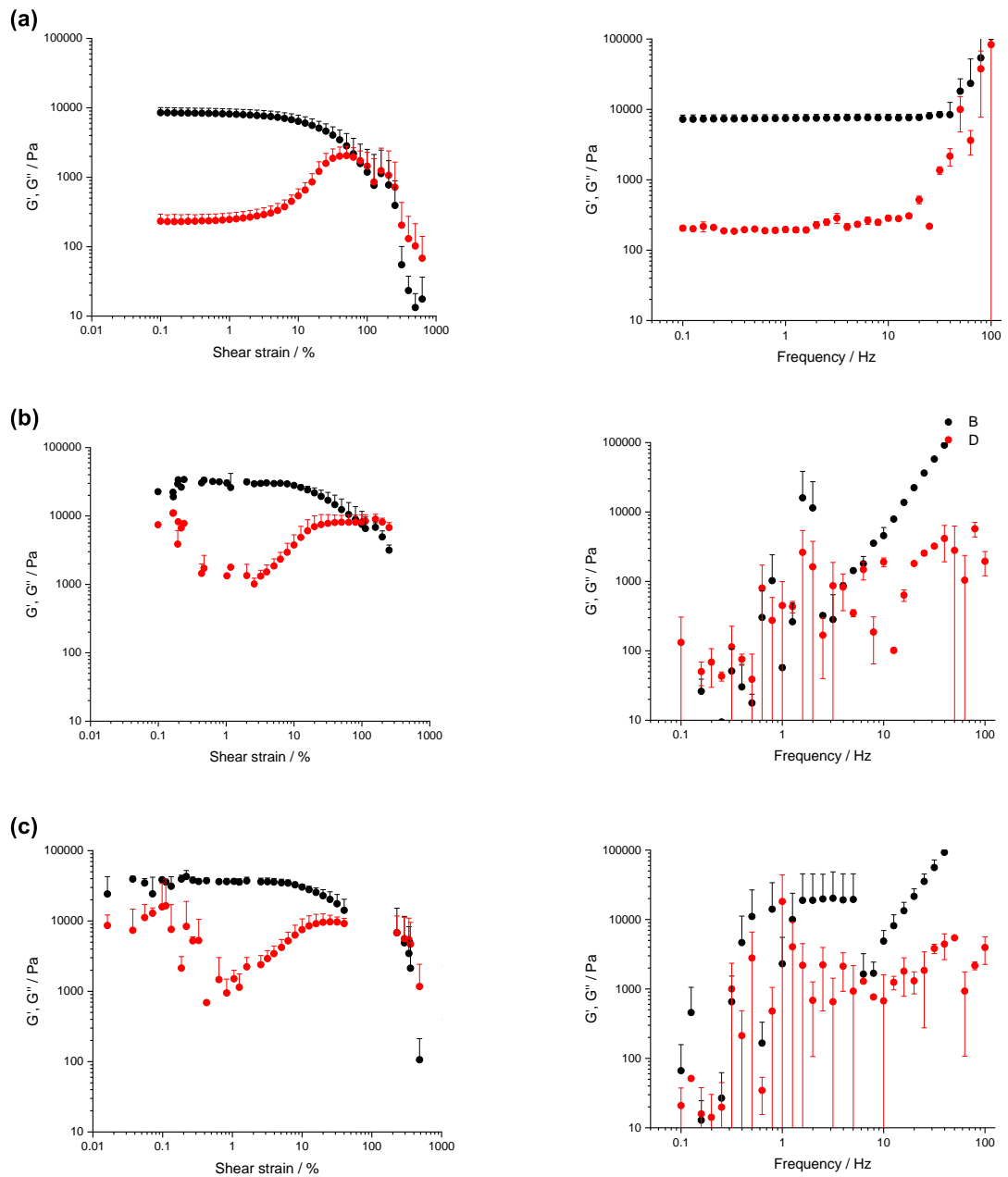


Figure 4.29: Storage (G' , black) and loss (G'' , red) moduli of the different prepared hydrogels in response to varying shear strain at a constant frequency (1 Hz, left) and to varying frequency at a constant shear strain (right). Rheological traces for: 20% hybrid (a), 40% hybrid (b), and 60% hybrid (c) hydrogels. At 40 and 60% PEGDM loading slipping of the gels lead to poor quality data, in particular in the frequency sweep experiments. Errors given as standard deviation ($n = 3$).

To assess the feasibility of small molecule exclusion using these higher PEGDM-loading hybrid gels, we performed diffusion studies on gels using the same methodology described for the diffusion

studies above. Hybrid gels (0.5 mL) were prepared in UV cuvettes as previously described, but using supernatant solutions containing 20, 40 and 60% wt/vol PEGDM (all 0.05% wt/vol PI). As above, these materials have significantly greater stiffness than 10% hybrid gels, which we assumed to be the result of their greater network densities. On top of these hybrid gels a solution of fluorescein (0.5 mL, 50 μ M) was then pipetted and the fluorescence intensity recorded at the base of the gel over time (Figure 4.30). Some diffusion of fluorescein through the 20% hybrid gel was recorded over the first 3 hours of the experiment, however 40 and 60% hybrid gels almost totally prevented fluorescein diffusion through the 0.5 cm gel height on this timescale. No significant difference in fluorescein concentration was observed after 24 h. This suggests that the diffusion of even small molecules can be prevented by hybrid gels with higher PEGDM loading.

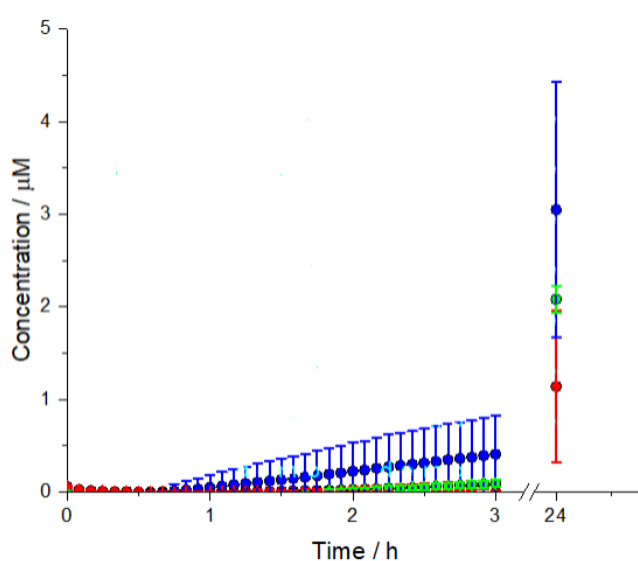


Figure 4.30: Concentration of fluorophores at the base of gels of dimension 1 cm \times 1 cm \times 0.5 cm (b). Diffusion through 20% (blue), 40% (red) and 60% (green) hybrid gels. Errors give as standard deviation ($n = 3$).

Encouraged by this result, we then aimed to demonstrate that the flow of small molecules could be directed down channels of soft LMWG, which had not been exposed to UV light within a highly crosslinked hybrid gel matrix. We prepared 10 mL hybrid gels as described previously. DBS-CONHNH₂ was dissolved in DMSO before addition to boiling water. The resulting solution was transferred to a glass tray (dimensions = 5 cm \times 5 cm \times 1 cm) and allowed to cool to room temperature, resulting in formation of a gel. On top of this gel a solution containing PI (0.05% wt/vol) and a known quantity of PEGDM (40 or 60% wt/vol) was pipetted and left for 3 days. After this time the supernatant was removed, and the gels exposed to UV light (with or without a photomask) to induce photo-polymerisation. Short curing times were required to induce PG

network formation (6 min for the 20% hybrid), (4 min for 40 and 60% hybrids). Significantly longer times resulted in poor patterning resolution.

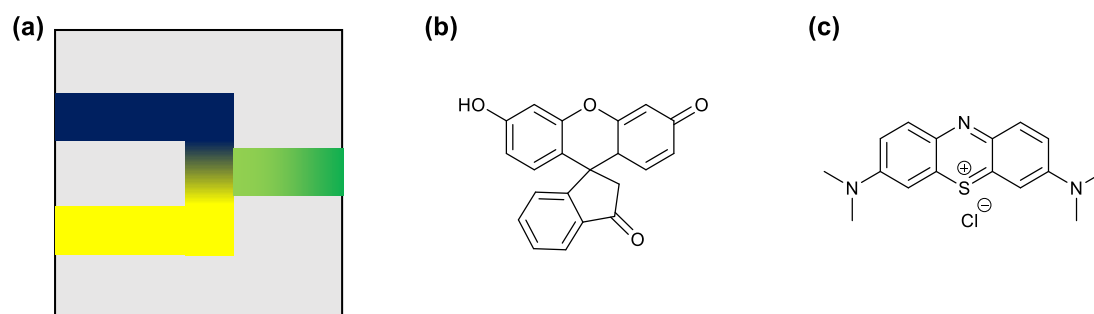


Figure 4.31: Cartoon representation of the reactor design (a). Fluorescein (b, yellow) and MB (c, blue) diffuse through the less dense reactor channels and mix prior to collection in the 'product' well.

We chose to study these patterned hydrogels using fluorescein and methylene blue (MB) as model 'reactants', which were guided to the same point in the LMWG channels to mix (simulating reaction) and further diffuse into a 'product' collection well (Figure 4.31a). The area of each well is 1 cm × 1 cm. We selected these dyes as the diffusion into DBS-CONHNH₂ gels is relatively well understood within the research group. In this work we have shown that fluorescein (Figure 4.31b) diffused relatively freely through the LMWG matrix, whilst a previous publication in the group describes the relative affinity for MB (Figure 4.31c) of this hydrogel.¹⁴³ All gels and dye solutions used in this study were prepared in deionised water.

Initially we studied the diffusion of the dyes through gels which had not had structural inhomogeneity introduced. Wells were cut using upturned UV cuvettes. 0.2 mL of dye was placed in each of the 'reactant' wells and 0.2 mL H₂O in the 'product' well. Relatively rapid and uncontrolled diffusion of the two dyes was observed through a DBS-CONHNH₂ hydrogel. Some leakage was seen down the sides of the glass tray when the two 'reactant' wells were cut at the edge of the gel. This resulted in leaching of the dyes between the two wells. Therefore this experiment was repeated with these two wells cut *ca.* 1 cm in from the edge of the tray (Figure 4.32a) In comparison, in a 60% hybrid gel, diffusion of the coloured front was much slower (Figure 4.32b), with neither dye diffusing the 1 cm distance across into the other 'reactant' well over the first 5 h. These results suggested that by photo-patterning channels into the hybrid gels, a degree of spatiotemporal control over dye diffusion could be achieved.

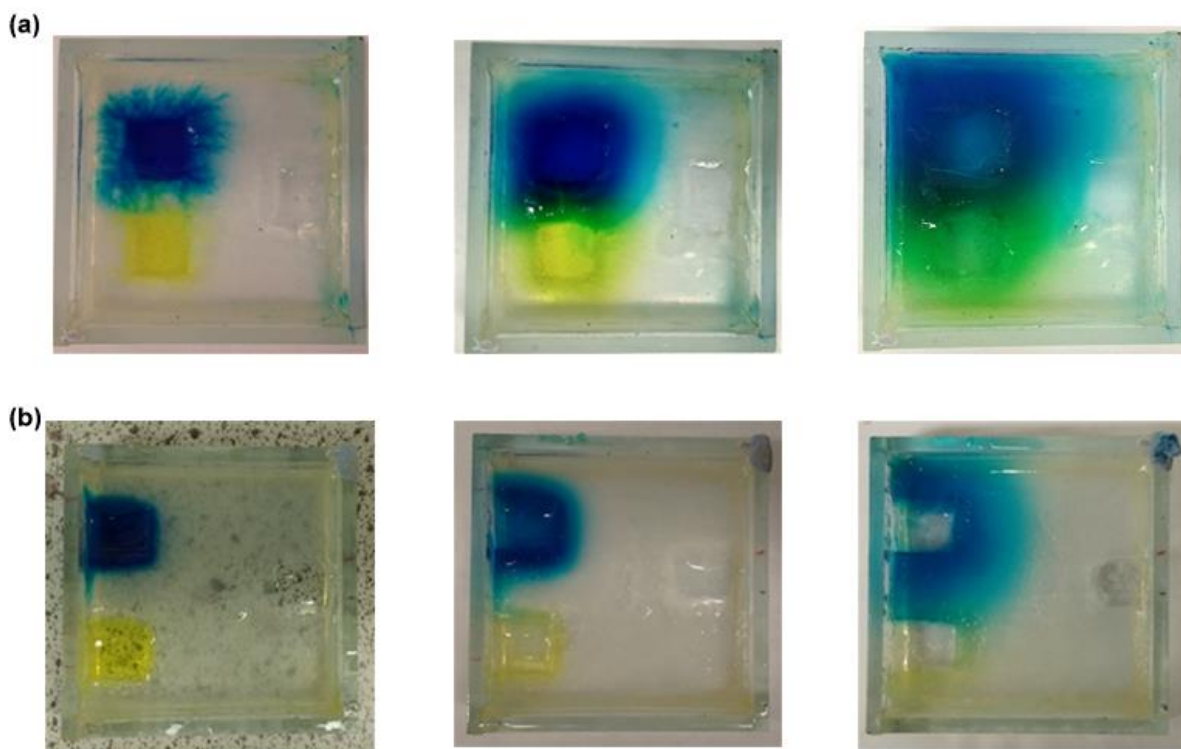


Figure 4.32: Diffusion of MB and fluorescein through 6 mM DBS-CONHNH₂ (a) and 60% hybrid (b) hydrogels. Pictures were taken after 0 h (left), 5 h (middle) and 24 h (right). Both dyes are at concentrations of 0.5 M.

A degree of dye leaching was also seen for the 60% hybrid gel if the reactant compartments were cut at the tray edge. Similar observations were made for initial photo-patterned reactors with reactant wells in the same location. We therefore developed a mask where the shielded regions of the gel end *ca.* 0.5 cm from the edge of the glass tray (Figure 4.33a). This was designed such that no unrestricted diffusion of dye was observed as a result of imperfect contact between gel and glass (Figure 4.33b). Using this optimised reactor design, we explored the influence of dye concentration on diffusion rate. As expected, higher concentrations of dye resulted in faster diffusion, most significantly through the LMWG channels (Figure 4.33c and d). Additionally, replacing the dye solution at regular intervals also increased the rate at which the dyes accumulated in the product compartment. For all subsequent experiments, we therefore replaced the dye solution every 0.5 h for the first 7 h of diffusion in an attempt to use the concentration gradient to induce a greater difference in diffusion rate between the LMWG and hybrid gel regions of the gel.

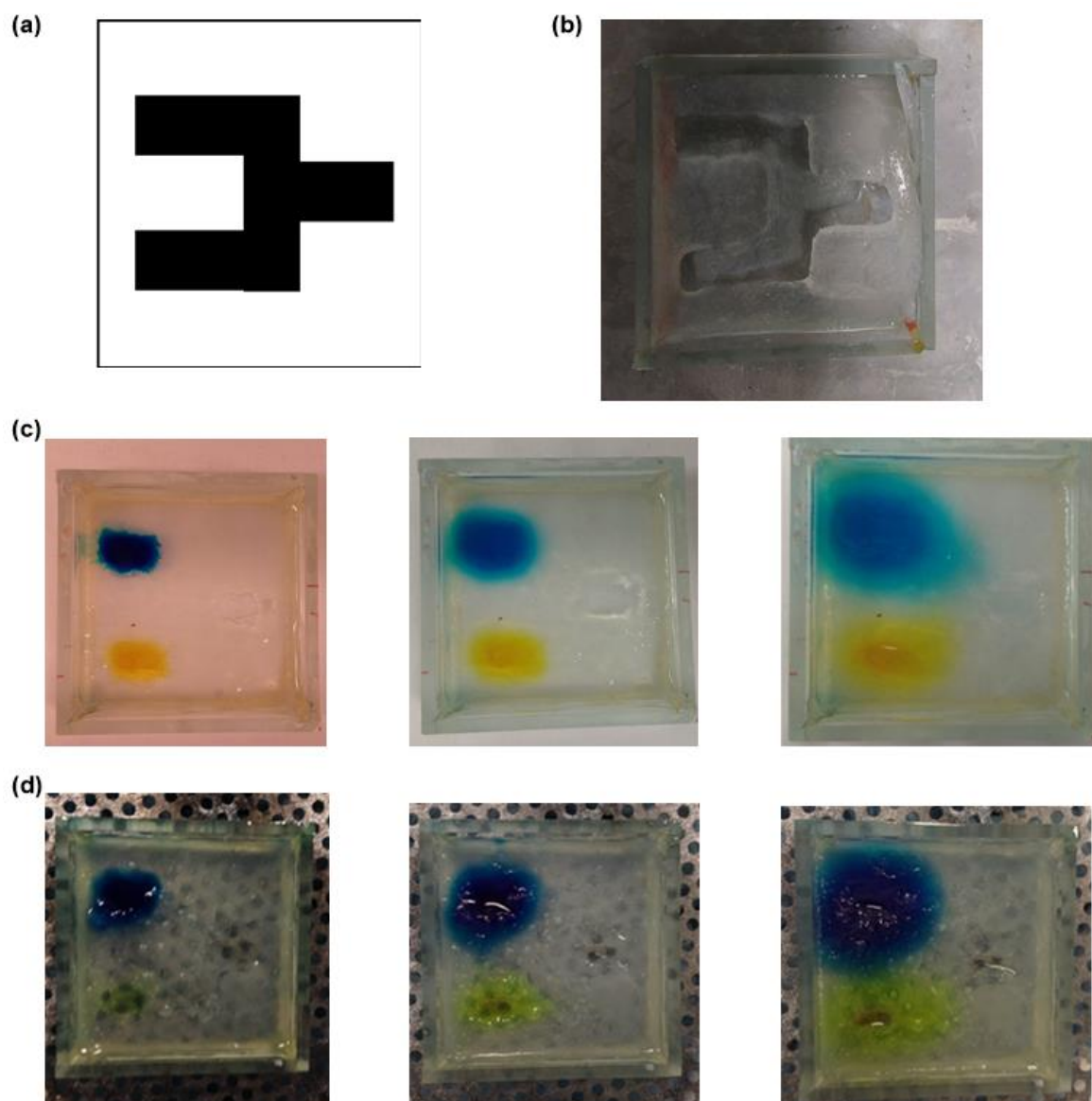


Figure 4.33: Photomask (a) and resulting pattern (b) used to study the diffusion of MB and fluorescein in photo-patterned 60% hybrid gels. MB and fluorescein at 0.5 M (a) and as saturated solutions (b) after 0 h (left), 5 h (middle) and 24 h (right).

Having established a basic methodology to study diffusion in these patterned reactors, we then compared the efficiency of 20%, 40% and 60% hybrid gels in directing the diffusion of dye molecules in this configuration. Patterned gels were prepared as described above. Wells were removed from the LMWG channels which were loaded with MB, fluorescein and water respectively (all 0.2 mL, both dyes were saturated solutions). All solutions were replaced every 0.5 h. The product compartment was taken, diluted to 2 mL and the UV spectrum recorded at each time point.

At room temperature, very little of either dye was able to diffuse into the product compartment over the experimental timescale for any of the patterned gels. Over 24 h some dye content was measured in the product compartment. However, over these lengths of time (typically 24 h) diffusion and mixing of the dyes within the photo-polymerised regions also occurred. Using the 20% hybrid gel this mixing was observed in just a few hours (Figure 4.34a), making it unsuitable for these spatially-controlled diffusion reactors. Better separation of the two dyes was seen in the 40% hybrid reactor (Figure 4.34b).

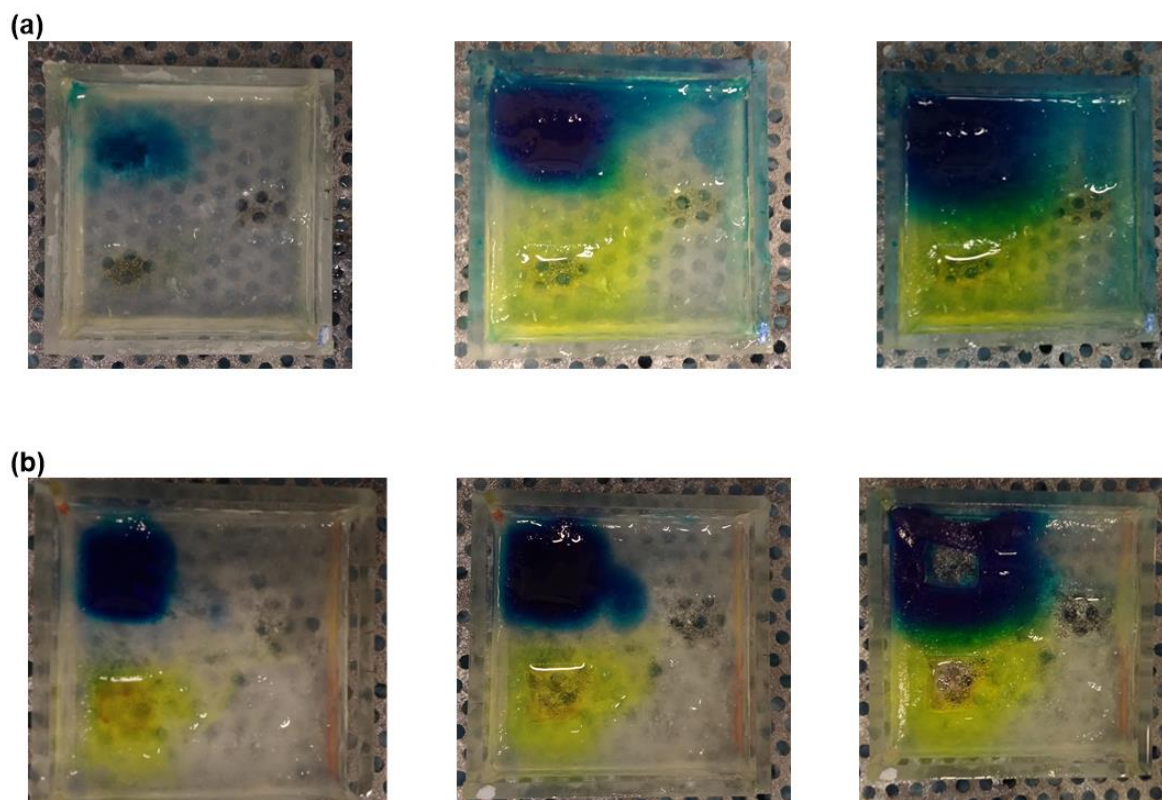


Figure 4.34: Diffusion of saturated solution of MB and fluorescein in photo-patterned 20% hybrid (a) and 40% hybrid (b) reactors.

To increase the flow of dyes specifically down the LMWG channels, we experimented with the effect of temperature on dye diffusion. It was thought that at higher temperature, a greater increase in diffusion rate might be observed in the LMWG channels compared to the hybrid regions. The experiments above were repeated with the gels incubated at 50 °C. A much greater rate of dye diffusion was observed through the channels than for the equivalent experiment at room temperature (Figure 4.35a), and good separation of the dyes between the two reactant wells is seen for the 60% hybrid gel over the first 7 h of diffusion.

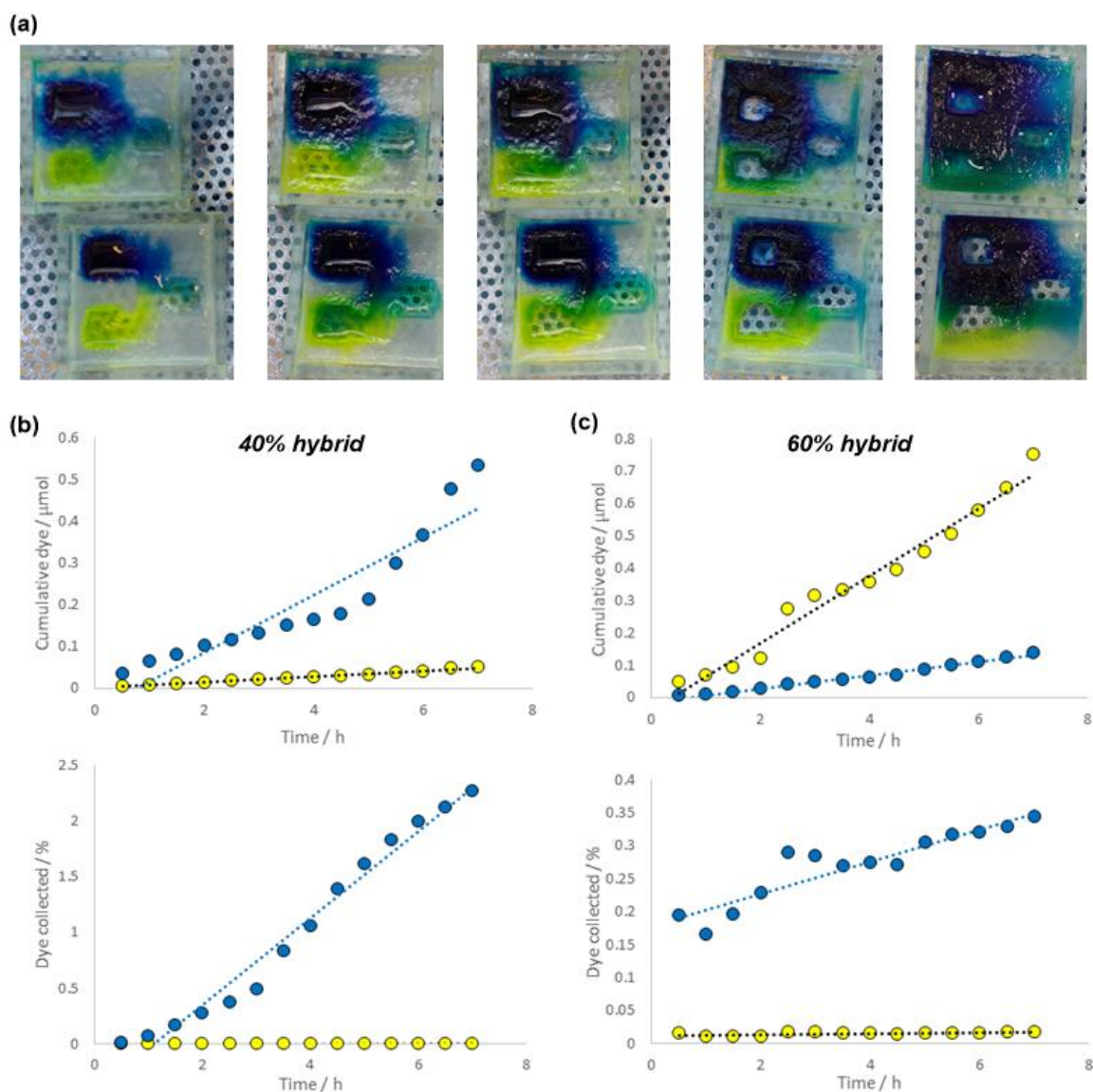


Figure 4.35: Diffusion of saturated MB and fluorescein solutions through photo-patterned 40% hybrid (top) and 60% hybrid (bottom) gels (a). Pictures represent the reactor (from left to right) after 1, 3, 5, 7 and 24 h. Cumulative molar quantities of dyes (top graph) and percentage of total added moles (bottom graph) measured in the 'product' compartment for 40% hybrid (b) and 60% hybrid (c) reactors. Yellow circles = fluorescein, blue circles = MB.

The rate of diffusion of MB is, by eye, much faster than that of fluorescein. This is reflected in the relative molar quantities of dye measured in the product compartment of the 40% hybrid gel reactor (Figure 4.35b, top graph). However, in the 60% hybrid gel this is not the case (Figure 4.35c, top graph). The total collected fluorescein in molar terms is significantly higher than that of MB. This is likely due to the much greater saturation concentration of fluorescein (1.5 M) compared to MB (0.15 M). Therefore, if the dye collected in the product well is considered as a percentage of the total loaded into the reactant wells, the relative efficiency of diffusion through the LMWG

channels can be assessed. In these terms, a significantly greater quantity of MB diffuses into the product well compared to fluorescein. The effect of the molar mass of the two dyes on their respective diffusion rates could also be assessed by using an inert polymer matrix as a diffusional barrier, however given the similarity of the two species in this respect (fluorescein = 332.31 g mol⁻¹, methylene blue = 319.85 g mol⁻¹), it was not expected to have significantly influenced the results of this experiment.

These differences can be rationalised by considering the relative affinities of the two dyes for the LMW hydrogel phase. Okesola *et. al.* reported that little uptake of MB into DBS-CONH₂ hydrogels is observed at pH 7 compared to solutions at pH 12, due to lessening of the overall charge on the molecule *via* amine deprotonation. In contrast, the diffusion studies reported in this chapter suggest that fluorescein interacts with DBS-CONH₂ gels (Section 4.4). It is considered that this high affinity for the LMWG effectively prevents fluorescein from diffusing out of the gel and into the product well effectively, whilst the comparatively low affinity of MB for the gel phase encourages diffusion into the aqueous environment of the product well. High concentrations of this dye were necessary to induce this diffusion, as the 'reactant' wells must be effectively 'overloaded' to encourage diffusion into the LMWG to begin with.

The above results demonstrate that preferential diffusion of small molecules through the LMWG channels of the photo-patterned reactor is feasible. Diffusion of fluorescein and MB through the non-patterned LMWG and hybrid gels (Figure 4.32), where no dye was seen in the product wells after 7 h, it is clear that the use of photo-patterned gel channels has the potential to guide the diffusion of small molecules down pre-defined paths. These preliminary experiments demonstrate the potential of these patterned materials to act as bioreactors. Improvements must be made however, for this system to become a viable tool for spatiotemporal reaction engineering. In particular, in its current iteration, precise control of the 'flow' is not possible. Replacement of the dye solution is a relatively crude method of achieving this, and as such proper diffusion kinetics are difficult to obtain with this system.

Notwithstanding this drawback, we aimed to illustrate the potential of this material as an ALP bioreactor. For this experiment, we simply patterned a straight LMWG channel (4 cm) within a surrounding 60% hybrid gel matrix. The LMWG strip was washed away, and 1 cm at each end of the empty channel was blocked with cotton wool. An ALP-containing DBS-CONH₂ hydrogel was prepared in a similar method as described to above. A 6 mM suspension of DBS-CONH₂ (1 mL) was sonicated and heated to dissolution. This sol was held at 80 °C for 5 min, after which time ALP was added to a concentration of 0.4 U mL⁻¹ and the solution transferred into the middle section of

the empty gel channel. This reactor configuration was illustrated in Figure 4.28a. The blocking objects were removed from the ends of the channel. One end (the 'reactant well' was charged with a solution of *p*NPP (0.2 mL, 10 mM) in pH 9 buffer, whilst the other (the 'product' well) contained pH 9 buffer (0.2 mL) only. The solution in the 'product' well was removed periodically, diluted to 2 mL and the UV spectrum recorded. The product well was refilled with pH 9 buffer and the reactant well with *p*NPP solution (10 mM in pH 9 buffer) at each time point. The experiment was carried out at room temperature and at 50 °C.

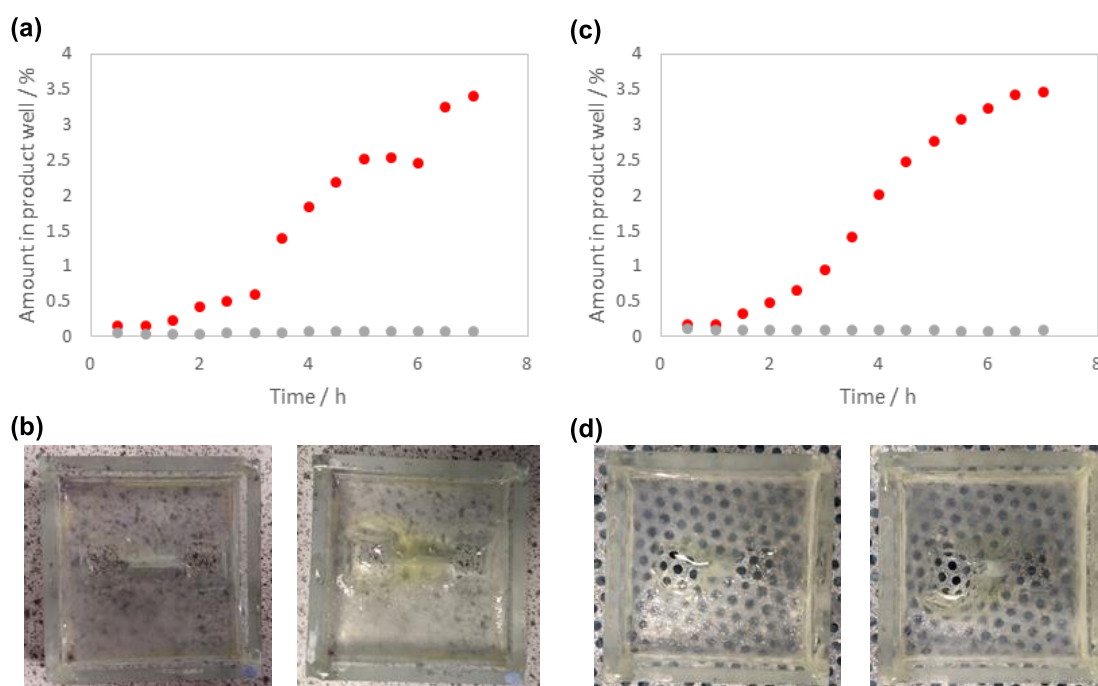


Figure 4.36: Change in concentration of *p*NPP (red) and *p*NP (grey) in the product well of the diffusion bioreactor at room temperature (a) and images of the bioreactor (b) after 1 h (left) and 6 h. Change in concentration of *p*NPP (red) and *p*NP (grey) in the product well of the diffusion bioreactor at 50 °C (c) and images of the bioreactor (d) after 1 h (left) and 6 h.

Only *p*NPP was able to diffuse through the LMW hydrogel channel and into the product well at either temperature (Figure 4.36). No significant amount of *p*NP was observed even after 7 h. No *p*NP was present in the reactant compartment either. No significant difference between the reactors at room temperature and 50 °C were measured. However, from the images given in Figure 4.36b and c, it can be seen that the reaction was occurring. We refer to the previous discussion of *p*NP uptake at pH 9 to explain these observations. Some *p*NP can clearly be seen diffusing into the hybrid gel regions of the reactor (across the length of the gel channel, not only at the reactant well end) over longer periods of time, so this is not a case of the product being unable to diffuse the distance to the product well. It appears, as above, unfavourable for the *p*NP to partition out of the

gel phase to achieve reasonable yields of reaction product. The yields in the product well are likely particularly low because of the high volume of the gel phase (*ca.* 11.5 cm³) compared to the solution phase (0.3 cm³ per well) in this experiment. As for the preliminary study with the ring bioreactor above, we propose that the use of a different enzyme, such as AP, under more acidic conditions may drive diffusion of the product into the product well.

4.9 Conclusions

In this chapter we have described work towards creating photo-patterned, functional, gel-based enzyme bioreactors. Using the dephosphorylation of *para*-nitrophenyl phosphate by alkaline phosphatase as a model reaction, our key achievements so far have been:

1. Demonstrating that the DBS-CONH₂/PEGDM hybrid gel is suitable for ALP encapsulation
2. That ALP retains bioactivity within the hybrid gel matrix
3. The development of shaped bioreactors which impose a degree of spatiotemporal control over the diffusion and reaction of small molecules

Both the LMWG and PG in the hybrid gel are essential components determining the properties of the reactors developed here. As outlined in previous chapters, both DBS-CONH₂ and PEGDM are important for spatial resolution of photo-patterning to be achieved. In this chapter though, we have shown that altering the composition of the gel also has an impact on the permeability and interactivity of the gel phase. The PEGDM content of the hybrid gel can be tailored to control the diffusion rate of both low-molecular weight molecules and larger polymeric species. We also propose that the DBS-CONH₂ network retains its ability to interact non-covalently with species such as fluorescein, *p*NPP and MB, introducing a further level of diffusional control in these materials, although in many cases this has actually been frustrating. Despite the issues faced with the initial reactor design, relatively high product conversions were achieved over a short timescale for certain configurations. We anticipate that optimisation of this reactor will result in greater efficiency and reusability. To our knowledge, the spatially-resolved activity of an enzymatic species immobilised within an LMWG-containing material has never been demonstrated prior to this work. Most reports simply describe the addition of an enzyme-loaded gel 'block' to a reaction mixture.

Differential interactions between the different gel compositions and reactant molecules has important implications for the design of reactors in the future. Tuning the rate of diffusion through selection of appropriate diffusing species and gel media could become a powerful approach for the complex spatiotemporal control of reactivity, in what can be considered in analogy to microfluidics

approaches. Spatially controlled diffusion⁹⁴ and enzymatic activity⁹⁷ have been shown to have applications for 2-dimensional materials. Retention of bioactivity within gels is also a key consideration when developing materials for tissue engineering which express biological cues in addition to the mechanical and chemical cues inherent to the hydrogel.^{163,331} With further development this preliminary work could be utilised for such high-tech applications.

Key future work to realise the potential of these hybrid gels as bioreactors includes the screening of a range of enzymes and substrates to identify more suitable reactions and elucidate the factors governing the partitioning effect at the sol-gel interface. Acid phosphatase is of particular interest for immediate study. The acidic conditions under which this enzyme operates may help to increase the yield of *p*NP obtainable in this reactor. Preliminary studies with this enzyme highlight the promise for this combination of enzyme and hybrid gel, and future work should focus on the incorporation of this enzyme within both reactors described in this chapter to enhance product diffusion and yield. Previous reports by Xu and Wang have also shown that performing hydrogel-phase enzymatic reaction in non-aqueous solvents can significantly enhance the product yield due to preference of the products for the organic phase. Investigations into the influence of reaction solvent on the partitioning of *p*NP may also assist in the development of more efficient bioreactors in the future.

5 Towards Spatially-Programmed Stem Cell Behaviour

Acknowledgments are made to Andrew Stone, who engineered the Y201 XGreen cells used in Sections 5.4, 5.5 and 5.9 of this chapter.

5.1 Introduction

Tissue engineering is a highly interdisciplinary field combining chemistry, biology, materials science and engineering, with the ultimate goal of repairing or replacing damaged organs or tissue.³³² Unlike an allograft, a tissue engineered material is derived from a patient's own stem cells, reducing the immunogenic response on implantation and preventing eventual rejection. The reduction in reliance on organ donation is an added benefit of this approach.³³³

Stem cells are a type of unspecialised biological cell which have the potential to undergo a process known as differentiation.³³⁴ Differentiation describes the increasing specialisation of a stem cell as it develops features defining it as a given cell type. For example, in the early stages of mammalian development, the inner mass of a developing blastocyst consists largely of embryonic stem cells (ESCs).³³⁵ Later in development, these ESCs proliferate and specialise to become each of the cell types required for the development of the various systems of the developed individual.

A major focus in tissue engineering is on the stimulation of stem cells to generate desired tissues or organs. Current strategies to induce programmed differentiation include the delivery of small molecules, growth factors and morphogenetic factors, as well as surface topography^{336,337} and the application of mechanical signals, and external forces.^{338–340} As a deeper understanding of the mechanisms behind stem cell differentiation is established, it is becoming increasingly clear that the interception of key signalling pathways is crucial in determining phenotypic fate.^{341,342} Therefore, the development of scaffolds which can deliver chemical, biological and physical cues with spatial and temporal control are of particular importance for the development of complex tissue for clinical use.

5.1.1 Polymer gels for the spatiotemporal control

Hydrogels have emerged as leading materials for regenerative medicine due to their inherent similarity to the extracellular matrix.³⁴³ For example, both are porous, elastic and have a high water content. In addition, the tunability of these materials makes them highly valuable as potential tissue engineering scaffolds.^{31,344–347} In particular, polymer gels have been widely used to support and direct cell behaviour through presentation of biomechanical cues.^{154,348} Several reports have

described the spatiotemporal modification of polymer hydrogels to impose some degree of spatiotemporal control over stem cell differentiation,³⁴² a few of which will be described here.

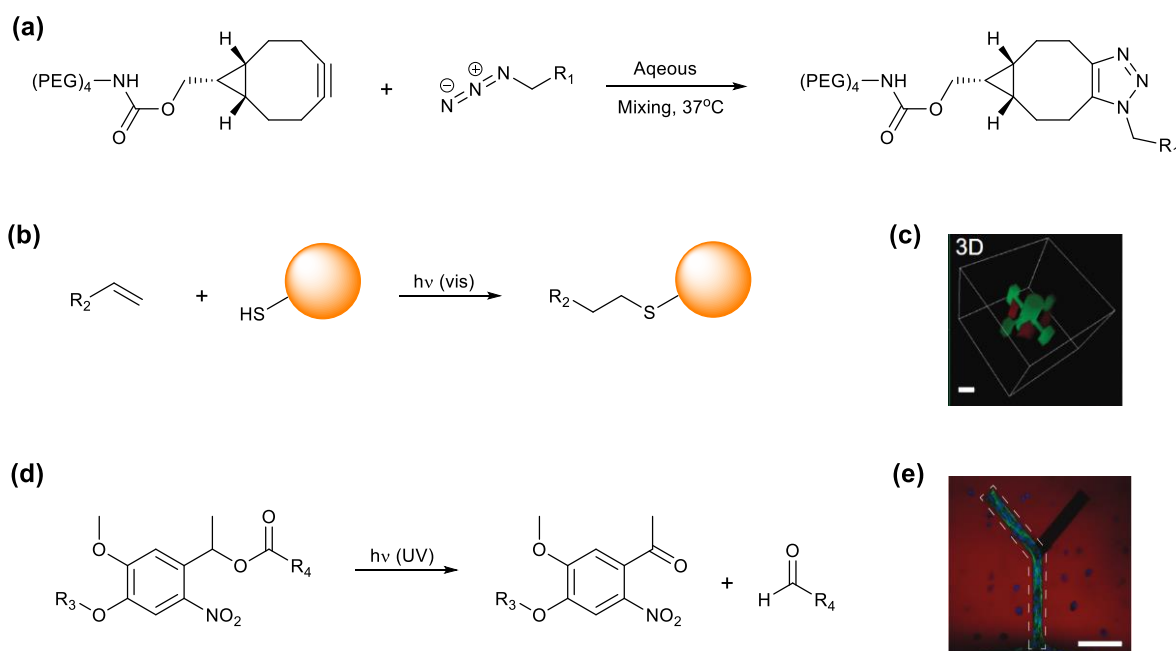


Figure 5.1: Orthogonal triggers can be used to achieve complex control of gel properties and stem cell behaviour. Anseth and co-workers used SPAAC reactivity between a tetra-arm PEG and a functionalised aldehyde to form a PG network (a). Conjugation of biomolecules to the gel network was achieved with spatial control via a visible light-initiated thiol-ene reaction (b). Orange circle = biomolecule. Two-photon laser methods were used to spatially control the expression of fluorescent peptides in 3-dimensions (c). Gel breakdown was initiated by UV-mediated cleavage of a nitrobenzyl ether (d). UV light was used to pattern channels in the PEG hydrogel. Cell migration was only seen in the channel which had been functionalised with an RGD peptide (e). Adapted from [349].

Anseth and co-workers have developed a number of PEG-based hydrogels for tissue engineering applications. Functionalisation of the PEG network with appropriate moieties has endowed these materials with spatiotemporally addressable properties. For example, azide-appended PEG monomers were crosslinked by cyclooctyne-functionalised peptide sequences through a strain-promoted azide-alkyne cycloaddition (SPAAC, Figure 5.1a).³⁴⁹ These peptide sequences were cleavable by matrix metalloproteinases, allowing the mechanical properties of the hydrogels to change in response to cell growth. Interestingly, when these linkers were further functionalised with a pendant alkene, photochemically activated thiol-ene reactivity (Figure 5.1b) allowed the conjugation of peptides only in regions exposed to UV light (Figure 5.1c). In subsequent work similar PGs were prepared, except with a photo-cleavable nitrobenzyl ether moiety within the linking group (Figure 5.1d).¹⁵⁵ Because the wavelengths of the photo-degradation and thiol-ene photocoupling reactions were orthogonal, spatiotemporal (but irreversible) control over the delivery of

biological and mechanical stimuli could be achieved (Figure 5.1e). By exposing the gel matrices to different proteins at different times, followed by photo-coupling, multiple proteins could be presented by the gel network over time. Controlled photo-degradation was used to liberate stem cells from the gel at defined locations for further study.

In 2015 DeForest *et. al.* developed a polymer hydrogel which could reversibly bind proteins for more precise spatiotemporal control of protein expression.³⁵⁰ Using a photo-induced oxime ligation strategy, aldehyde-functionalised proteins were attached to the gel network in defined locations (Figure 5.2a). The incorporation of a photo-cleavable nitrobenzyl linker in the aldehyde spacer enabled removal of the conjugated protein by mild UV exposure (Figure 5.2b). This regenerated the alkoxyamine groups required for further oxime ligation with a second protein. The spatiotemporal display of these proteins within the hydrogel was used to demonstrate spatial control of stem cell differentiation through the photo-reversible patterning of vitronectin, a glycoprotein which promotes osteogenesis – the formation of bone cells. Only in the regions where vitronectin ligation was maintained over ten days was there evidence of differentiation into bone cells (Figure 5.2c). Cells cultured in regions of the gel which were exposed to UV light after 3 days (triggering vitronectin release) showed much lower levels of osteocalcin, suggesting bone cells were not formed in these areas.

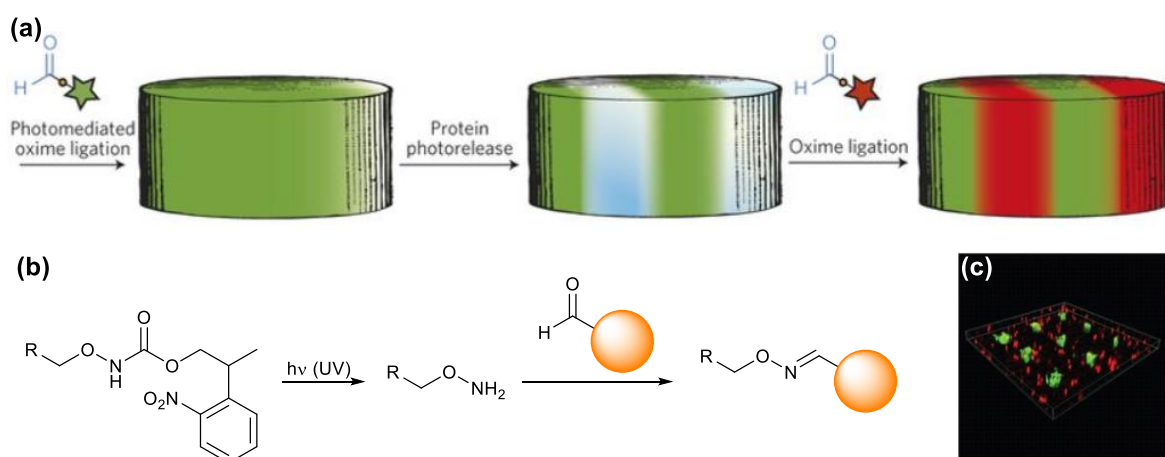


Figure 5.2: Reversible oxime ligation can be used to conjugate proteins to the PEG hydrogel with spatiotemporal control (a). UV-initiated cleavage of the nitrobenzyl ether moiety reveals an alkoxyamine, which in turn reacts with an aldehyde-functionalised protein to form an oxime linkage between hydrogel and protein (b). Reversible oxime ligation was used to spatiotemporally control mesenchymal stem cell (MSC) adherence to the gel network (c, MSCs shown in green). Images adapted from [350].

As well as biomolecule expression, the spatiotemporal control of polymer gel rheology has been shown to have a profound impact on stem cell behaviour. Hydrogels based on mixed octa-arm PEG hydrogels with boronic acid and 1,2-*cis*-diol end-groups were shown to have much greater rates of stress relaxation than the corresponding SPAAC-crosslinked networks. Stem cells cultured on the fast-relaxing gels crosslinked by reversible boronate bonds showed much lower sphericity and greater concentrations of YAP/TAZ (a marker for osteogenesis) compared to the SPAAC-crosslinked gels.³⁵¹ Hydrogel networks which undergo a dual-stiffening process have also been shown to influence the development of bone cells.³⁵² Initial crosslinking of an octa-arm PEG by SPAAC is followed by photo-crosslinking of pendant alkenes in the network, allowing further stiffening of the network to be spatiotemporally controlled. Greater YAP/TAZ expression was observed in stem cells when the secondary crosslinking reaction was delayed until day 7 of cell culture, compared to materials which were stiffened prior to cell seeding. These studies highlight the importance of matrix properties and timing of mechanical cues on gel-mediated control of stem cell behaviour.

5.1.2 LMW hydrogels for cell growth

Unlike PGs, there is a relative paucity of literature describing the use of LMW hydrogels to control tissue growth, either *in vitro* or *in vivo*.¹³ The majority of the examples that do exist describe the use of relatively long (> 7 amino acids) peptide amphiphiles (PAs).³⁵³ In these amphiphilic species, amino acid sequences responsible for self-assembly and biological function are separate, enabling facile presentation of bioactive sequences by the self-assembled nanofibres.

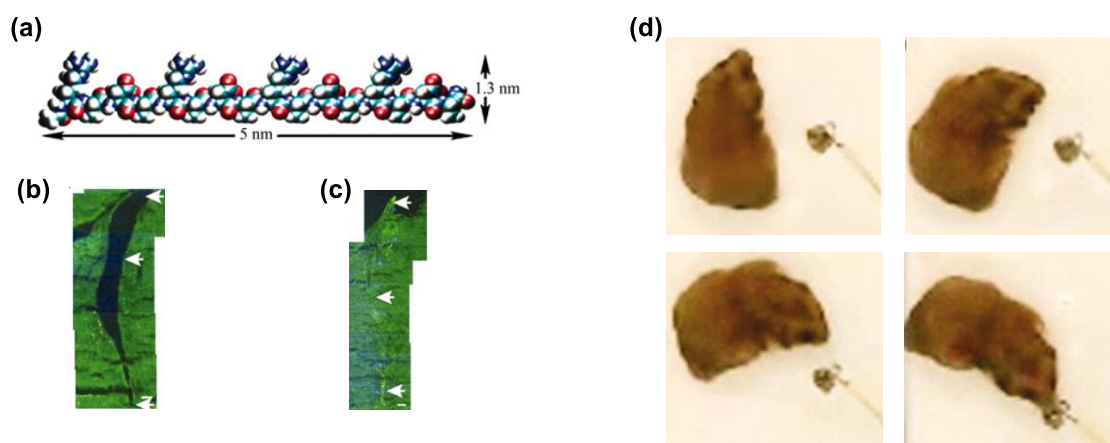


Figure 5.3: Peptide amphiphile developed by Schneider and co-workers (a). Peptide amphiphile gels implanted into a brain lesion (b) allows migration and growth of cells into the gap (c). Hamsters treated with the peptide amphiphile recovered vision in most cases, as evidenced by the response of the subjects to a visual stimulus (d). Images adapted from [358].

An early example of the applications of these materials came from Stupp and co-workers, who designed a PA to present a neurite-promoting pentapeptide.³⁵⁴ When encapsulated in this material, neural progenitor cells underwent rapid differentiation into neuronal cells compared to the peptide in solution, highlighting the advantages of the multivalent presentation of biomolecules or binding moieties by self-assembled species.³⁵⁵ Functional *in vivo* treatments have also been achieved with such systems.^{356,357} A particularly eye-catching example was the peptide hydrogel-supported healing of brain lesions in hamster models (Figure 5.3).³⁵⁸ The hydrogels connected tissue each side of the lesion and promoted cell migration into the gap between the two (Figure 5.3 b and c). Behavioural tests indicated that hamsters treated with the peptide gel showed increased vision regeneration compared to untreated subjects (Figure 5.3d). Another peptide hydrogel developed by Stupp and co-workers promoted growth of neurites at the site of spinal cord injury.³⁵⁶ In a mouse model, treated subjects showed some regeneration of motor function after treatment.

Reports of smaller, less complex LMWGs in tissue engineering are comparatively very rare. Ulijn and co-workers first demonstrated that short Fmoc-dipeptide hydrogels supported chondrocyte (cartilage cell) growth as early as 2006.³⁵⁹ Co-assembly of Fmoc-Phe-Phe with Fmoc-Arg-Gly-Asp resulted in the formation of LMW hydrogels with superior cell adhesion properties than the former, whilst improving the mechanical stability compared to the latter.³⁶⁰ The stiffness and bioactive sequence density could be tuned in the bulk materials by modifying the ratio of the two gelators.

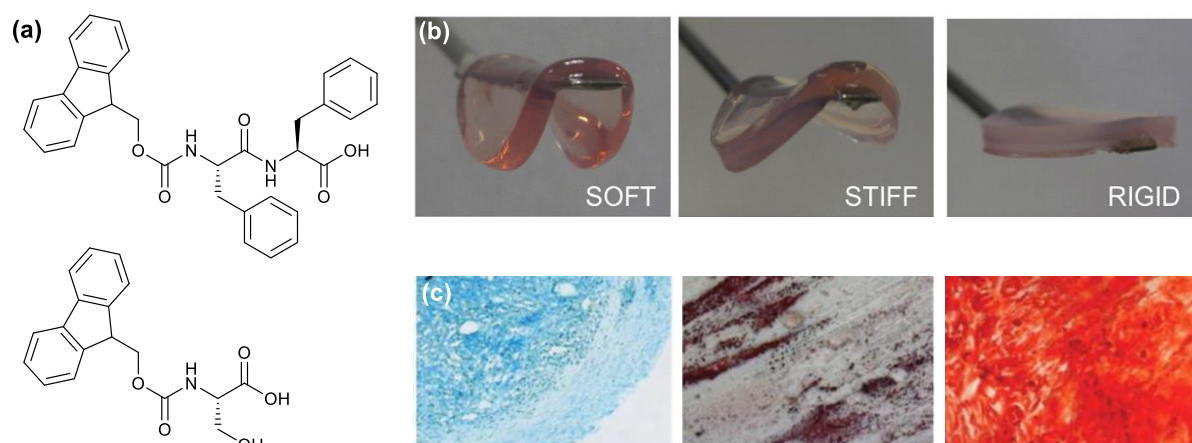


Figure 5.4: (a) Co-assembly of Fmoc-Phe-Phe (top) and Fmoc-Ser (bottom) allowed the fabrication of robust, cytocompatible amino acid hydrogels. (b) The ratio of the two gelators could be altered to control hydrogel stiffness. Greater proportions of Fmoc-Phe-Phe increased hydrogel stiffness. (c) Soft, stiff and rigid gels could be used to stimulate the formation of adipocytes (left), chondrocytes (middle) and osteocytes (right) respectively. Images taken from [64].

Hu *et.al.* have demonstrated the ability of amino acid hydrogels to direct stem cell differentiation based on gelator loading.³⁶¹ Greater LMWG concentrations resulted in the formation of stiffer gel

networks, which stimulated the differentiation of stem cells into the osteoblastic lineage. In contrast, stem cells cultured on softer gels favoured the specialisation to form chondrocytes. Dalby and co-workers demonstrated a similar dependence of stem cell behaviour on matrix stiffness.⁶⁴ Co-assembly of Fmoc-Phe-Phe and Fmoc-Ser (Figure 5.4a) LMWGs resulted in the formation of robust, bioactive nanofibrous scaffolds (Figure 5.4b). Again, greater loadings increased the stiffness of the nanofibres and promoted osteogenesis (Figure 5.4c).

A number of further examples of amino acid-based LMW hydrogels have been used in preliminary tissue engineering studies.^{362–364} Whilst few in number, reports of LMWGs containing other functional groups have begun to emerge. In 2014 Feng and co-workers showed that the chirality of amide nanofibres had a significant impact on the adhesion and proliferation of a range of cell lines.³⁶⁵ This gelator was later combined with a photo-responsive azobenzene gelator to fabricate materials which could be disassembled by exposure to UV light.³⁶⁶ Controlled encapsulation and release of fibroblasts was demonstrated using this system. Importantly, the gel assembly and disassembly conditions did not result in significant cell death. Hamachi and co-workers have also used a photo-responsive hydrogelator to control stem cell behaviour. Spatially-resolved gel disassembly allowed the fabrication of sol channels within the gel matrix. Cells proliferated faster in these channels than in the gel matrix. In this way, a degree of spatially controlled cell growth was achieved.³⁶⁷

Barthélémy and co-workers have developed a range of nucleobase-derived LMW hydrogelators with potential application in regenerative medicine. The glycosylated thymidine derivatives underwent a relatively mild thermally-induced gelation, enabling encapsulation of cells throughout the hydrogel matrix in a 3D culture.³⁶⁸ Further elaboration at the thymidine core allowed the properties of the bulk materials to be tailored. Bola-amphiphilic structures showed consistent self-assembly and cytocompatibility with human adipose-derived stem cells (ASCs).³⁶⁹ These gels also exhibited thixotropic properties, recovering their elasticity after shear-induced breakdown. Thixotropic gels are of great interest as injectable materials for drug delivery and tissue engineering applications.^{370–373} Thymidine-based LMWGs were also combined with collagen in hybrid gels to increase the durability of the materials for *in vivo* applications (Figure 5.5). The hybrid gels showed greater osteogenic potential than either of the individual gel networks and persisted in a mouse model after injection for at least 60 days (Figure 5.5b and c).³⁷⁴

Guanosine derivatives are also relatively well known as LMWGs. Often, as in research reported by Barboui *et. al.*, these gelators self-assemble into G-quartets which subsequently stack to form nanofibres. Crosslinking with Mg²⁺ resulted in formation of a soft hydrogel, which showed good

fibroblast viability.³⁷⁵ Rowan and co-workers reported a novel bromoguanosine gelator which self-assembled in a helical assembly rather than the more common G-quartet.³⁷⁶ These gels were mechanically robust and showed good cell adhesion. A hybrid gel comprising the guanosine LMWG and a gelatin PG network showed improved cell adhesion and lower cytotoxicity compared to the LMWG alone.

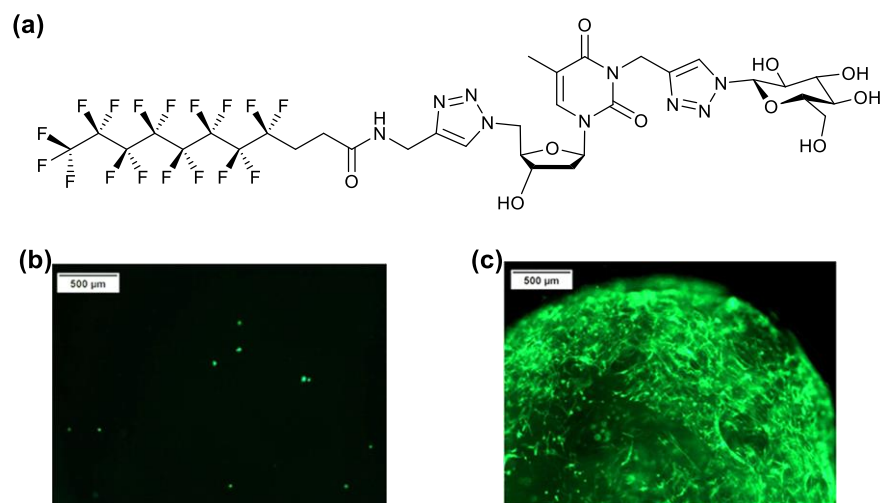


Figure 5.5: Barthelemy's glycosylated thymidine gelator (a). Little ASC adherence is seen after 14 days on the LMWG hydrogel alone (b). When co-assembled with collagen however, much greater ASC adherence and proliferation is observed. Figure adapted from [374].

A small number of sugar-containing LMWGs have also been shown to support cell growth. Disaccharide amphiphiles containing photo-responsive azobenzene groups formed LMW hydrogels at relatively low concentrations.³⁷⁷ These amphiphiles self-assembled to form micelle-like structures through aromatic interactions between the azobenzene groups. The sugar head groups were shown by lectin adhesion to be presented on the surface of the micellar fibres. These sugars promoted cell adhesion, whilst the 'burial' of the azobenzene moieties on the interior of the nanofibres prevented them from showing cytotoxicity. These gels exhibited azobenzene isomerisation-induced, reversible gel-sol transitions. The authors suggest this reversibility could have future uses in cell culture applications. Li and co-workers have prepared similar micellar assemblies using glycopeptide LMWGs. Self-assembly of the peptide sections of these gelators results in presentation of sugars on the nanofibre surfaces. These gels were highly biocompatible, supporting the growth of a range of cell types *in vitro*.³⁷⁸ In later *in vivo* studies, these gels were shown to persist after injection in a mouse model for 10 days.³⁷⁹ Formulation of deferoxamine in the gel encouraged the generation of blood capillaries in treated subjects.

5.2 Chapter aims

Despite the increasing interest in the use of small molecule gelators for tissue engineering, no LMWG-containing materials have been developed which come close to controlling stem cell behaviour in the way that polymer gels are currently able to. For this gap to be bridged, spatial control of stem cell behaviour is a key barrier which must be overcome.

In this chapter we aimed to carry out preliminary investigations into the applications of our LMWG/PG hybrid and multidomain gels for tissue engineering applications. In particular, we hoped to demonstrate control of stem cell fate by exploiting a process known as mechanotransduction. Put simply, this is the response of cells to the mechanical forces to which they are exposed (Figure 5.6a). In terms of tissue engineering, these forces can be utilised to direct stem cell differentiation. External factors which have been shown to play a role in the determination of stem cell fate include flow, compression and tension.^{380,381}

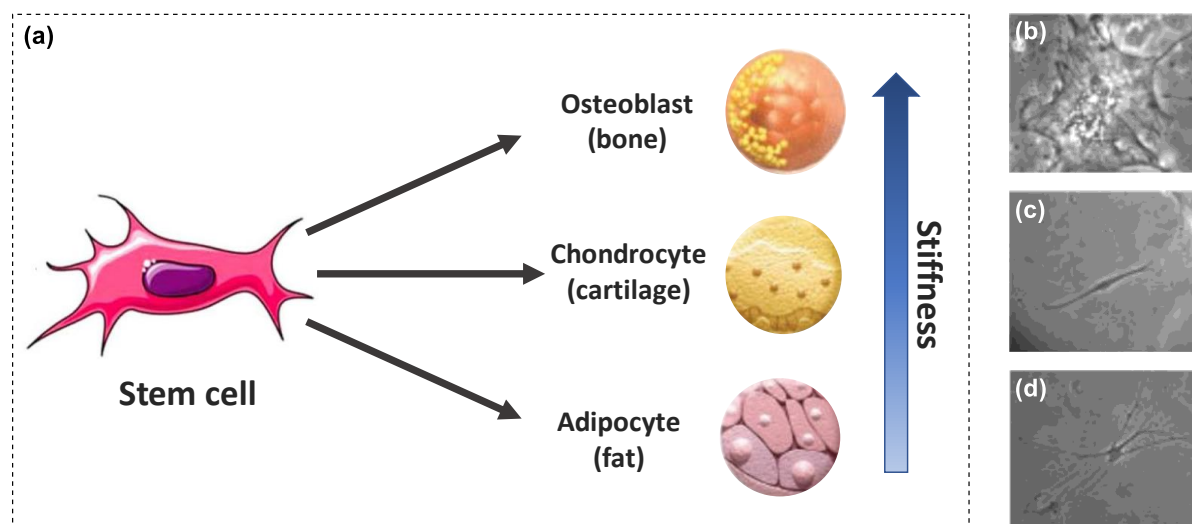


Figure 5.6: Cartoon representation of the influence of matrix stiffness on mesenchymal stem cell fate (a). The example fates given here are those of human bone marrow mesenchymal stem cells. The specific stem cell type alters the available lineages, and other possible stem cell fates are possible. For example, with a different subset of stem cells, Engler *et. al.* showed that MSCs undertook different morphologies when cultured on gels of high (b), medium (c) and low (d) stiffness. These different morphologies were the result of the formation of bone, muscle and fat tissue respectively. Images taken from [63].

Of particular interest in this chapter, is the role that substrate stiffness plays in differentiation. In seminal work, Engler *et. al.* observed that stem cells cultured on collagen gels of different stiffnesses committed to different specialisation lineages (Figure 5.6b-d).⁶³ In particular, the cells grown on soft matrices differentiated to form neuronal cells, whilst those on gels mimicking the stiffness of

muscle tissue displayed markers of myogenesis. Significantly stiffer gels induced the formation of osteoblasts. Interestingly, they observed that over time, matrix stiffness was found to override the directing effects of soluble growth factors. This work was the first to illustrate the immense importance of the supporting matrix on determining stem cell fate.

Previous work in the Smith group demonstrated the compatibility of DBS-CONHNH₂ hydrogels with 3T3 mouse fibroblasts.⁵⁸ Interestingly, cells grown on a hybrid DBS-CONHNH₂/agarose hybrid gel also showed good adhesion and proliferation, where the agarose gel alone does not. Given this information, we hypothesised that similar cytocompatibility may be expressed by the DBS-CONHNH₂/PEGDM hybrid gels developed in Chapter 2. Given that the stiffness of these materials can be controlled by PG loading, we aimed to study how the changes in mechanical properties influence the behaviour of mesenchymal stem cells (MSCs) *via in vitro* 2D culture studies. More significantly, we aimed to use photo-patterned multidomain gels to demonstrate spatial control over stem cell differentiation, a level of control not previously demonstrated for LMWG-based materials.

5.3 Mesenchymal stem cells

We elected to study the cytocompatibility and directing effects of a range of LMWG, PG and hybrid gels using mesenchymal stem cells (MSCs). These are multipotent stromal cells which are able to undergo differentiation to become connective tissue such as fat, muscle, cartilage and bone.³⁸² Commonly, MSCs are derived from either adipose tissue (AMSC) or bone marrow (BMSC), and depending on their source, may be able to differentiate into a subtly different range of cell types.³⁸³ The differentiation capacity and relative ease of accessibility has made MSCs attractive candidates for regenerative medicine.^{384–386}

In vitro MSC differentiation is classically controlled by the administration of specific mixtures of growth factors and/or chemical stimuli. More recently, culturing this class of cells on materials with different mechanical^{387–389} and topographical properties^{389–391} has become of interest. Differences in the material properties are thought to induce changes in the signalling pathways controlled by the transmembrane cell adhesion proteins known as integrins, resulting in changes in gene expression and ultimately the MSC physical properties.^{392,393}

We were particularly interested in using matrix stiffness to direct stem cell lineage selection. Previous studies reporting stiffness-controlled differentiation are inconsistent in the specific ranges required to promote the formation of specific cell types. For example, in collagen gels, Engler *et. al.*

found that neuronal, myogenic and osteogenic cells grew on matrices of < 1 kPa, 8-17 kPa and 25-40 kPa respectively.⁶³ Similar values were reported by Dalby and co-workers when using amino acid-based LMW hydrogels (intermediate stiffnesses in this case induced chondrogenesis rather than myogenesis).⁶⁴ However, a recent report from Gao and co-workers suggested that on a phenylboronic acid LMW hydrogel, the formation of cartilage cells was observed at much lower stiffnesses (1-10 kPa).³⁹⁴ Clearly, whilst stiffer matrices are more likely to induce the formation of stiffer tissue, the chemical properties and nanoscale morphology of the materials may also influence stem cell fate (as can the specific cell line used).

In this study we have used an immortalised line of MSCs developed by Genever and co-workers. From human BMSCs they isolated four individual subsets of cell which each possessed distinct colony forming, migratory and differentiation potentials.³⁹⁵ The Y201 cell line was used here to study the influence of gel mechanical properties on MSC behaviour. This subset showed a fibroblastoid morphology, were highly migratory and formed well dispersed colonies *in vitro*. Importantly, these cells are tripotent – able to undergo adipogenic, chondrogenic and osteogenic differentiation. It was hoped that by using this single immortalised cell line rather than a heterogeneous population of primary cells, that errors typically associated with biological studies would be minimised.

5.4 MSC compatibility and seeding density

We initially set out to determine the cytocompatibility of DBS-CONHNH₂, PEGDM and hybrid hydrogels with Y201 MSCs. Given the difficulties which can be associated with imaging cells through a gel matrix, for these experiments, we used a line of Y201 cells which had been engineered to express the fluorophore ZsGreen (Y201 XGreen cells). These fluorescent cells should be visible even if the gels obstruct the passage of light through the material, because the incident light and the fluorescence detector are both located above the sample.

Following a significant optimisation process, gels of volume 50 µL were formed in the interior of stainless steel washers, which had been adhered to the surface of a 24-well plate using a small amount of silicone grease (Figure 5.7a). The formation of each gel type (DBS-CONHNH₂, PEGDM and hybrid) followed the same process as outlined in Chapter 2. The metal washer prevented the formation of a meniscus within the wells, ensuring a uniform thickness across the sample.³⁹⁶ Changes in matrix thickness have been shown to influence cell behaviour, so it was important to minimise the influence of this factor on the Y201 cells.

5.4.1 DBS-CONH₂ hydrogels

Initially, we aimed to determine the biocompatibility of DBS-CONH₂ (6 mM) gels. Gels were prepared in the washer interiors under non-sterile conditions. Two different post-gelation sterilisation methods were then applied. Half the gels were exposed to short wavelength UV light (100 - 290 nm). The other half were exposed to UV light, washed with 70% aqueous ethanol solution (0.5 mL) and then washed three times with phosphate buffered saline (PBS, 0.5 mL). Y201 XGreen cells were seeded on these gels at cell densities between 0 and 50,000 cells mL⁻¹ (Figure 5.7b). The samples were incubated at 37 °C for 24 h, after which time cell adherence was assessed by optical microscopy.

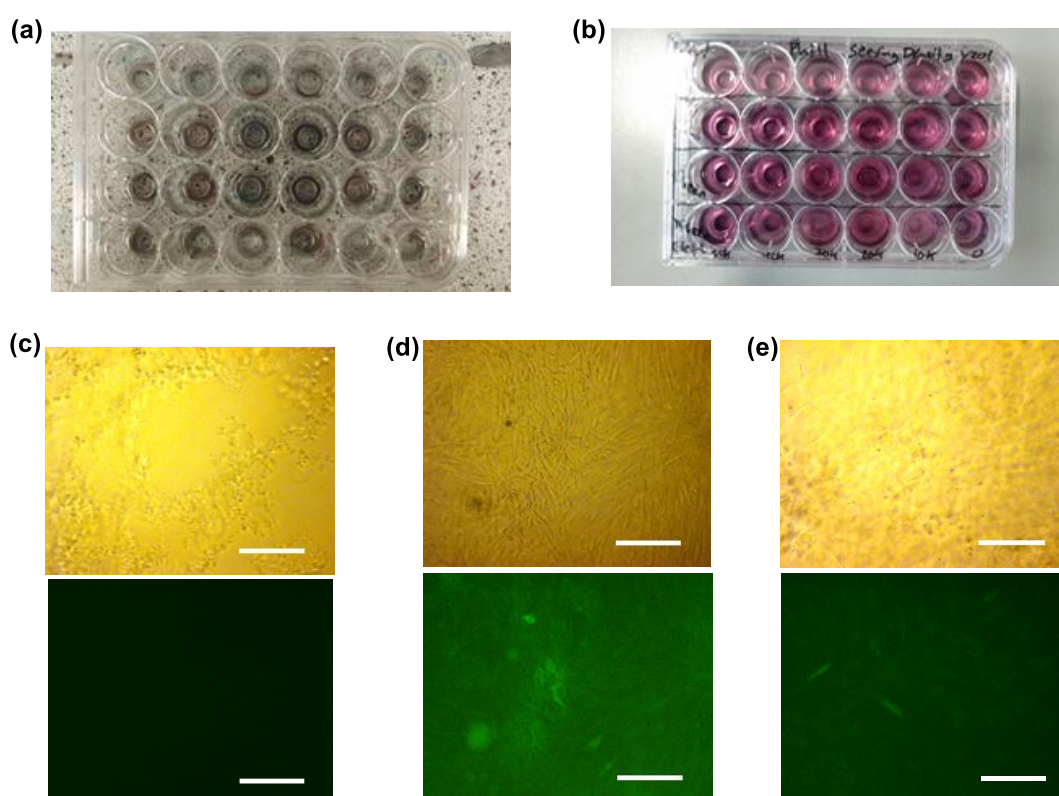


Figure 5.7: Gels were prepared in the centre of washers adhered to the bottom of the wells in a 24 well plate (a). A typical experiment is shown in (b). Brightfield (top) and fluorescence (bottom) images of a DBS-CONH₂ (6 mM) hydrogel incubated in media for 24 h (c). The LMW hydrogel features seen in the Brightfield images are not observed in the fluorescence image. Cells seeded on LMW hydrogels at densities of 10,000 (d) and 50,000 (e) cells mL⁻¹ showed good adherence after 24 h and adopted extended, fibroblast-like morphologies. Scale bars = 500 μm.

Importantly, cells could be imaged through the gel samples using normal optical microscopy. Some structures associated with the gels are seen, however these do not have significant adverse effects on the imaging process. Additionally, the DBS-CONH₂ gels in media (cell seeding density = 0 cells mL⁻¹) do not fluoresce (at 506 nm) under irradiation at 496 nm. The lack of autofluorescence for

these gel samples allows the cells to be imaged using fluorescence microscopy (Figure 5.7c), which yields slightly clearer images than those from light microscopy. Taking the brightfield and fluorescence images of the different sample treatments, it is clear that cell adhesion was observed only for two samples – on ethanol washed gels with cell seeding densities of 10,000 (Figure 5.7d) and 50,000 cells mL⁻¹ (Figure 5.7e). This result suggested that DBS-CONHNH₂ is not inherently cytotoxic or non-adherent, however the more general lack of cell growth demonstrated that further optimisation of the gel formation and cell seeding process was necessary. Two reasons for the general lack of cell growth were proposed:

- i) Non-sterility of the gels and/or washers introduced some factor which inhibited MSC adherence and proliferation
- ii) Cytotoxicity of the stainless steel washers

Given previous reports of the growth of ASCs using a similar ‘gel-in-washer’ approach, the latter explanation seemed unlikely.³⁹⁶ Nonetheless, we assessed the effect of cell growth of these washers in comparison to cells seeded in wells with no washers. After 24 h no significant differences in MSC growth were observed by microscopy. Given these results we considered that the lack of cell adhesion was more likely the result of gel formation under non-sterile conditions.

We therefore performed a similar experiment to that described above, in which the gels were prepared under more rigorously sterile conditions. The metal washers were sterilised in 100% ethanol for 24 h and washed thoroughly with PBS prior to adherence in well plates. Autoclaved, sterile water was used to prepare all gels, which were fabricated in a sterile cell culture hood using sterilised equipment. The gels were subsequently washed using one of the following procedures:

- i) 70% aqueous ethanol solution (1 mL, 10 min), followed by PBS (3 × 1 mL, 24 h each)
- ii) PBS (3 × 1 mL, 24 h each)

Y201 XGreen cells were seeded onto gels at concentrations between 10,000 and 50,000 cells mL⁻¹.

Additionally, cells were seeded at a concentration of 30,000 cells mL⁻¹ in a plate with only washers (no LMW hydrogel) for comparison. Significantly improved adhesion was observed for the samples washed with ethanol (Figure 5.8) compared to the PBS-washed gels (Figure 5.9) and to those prepared under non-sterile conditions, highlighting the importance of sterile handling for this class of cell. The improved adhesion was evidenced by the adoption of the typical fibroblastoid morphology associated with BMSCs. Greater numbers of cells were also seen compared to the non-sterile samples shown above. The ethanol/PBS washing procedure was therefore used for all subsequent studies in this chapter.

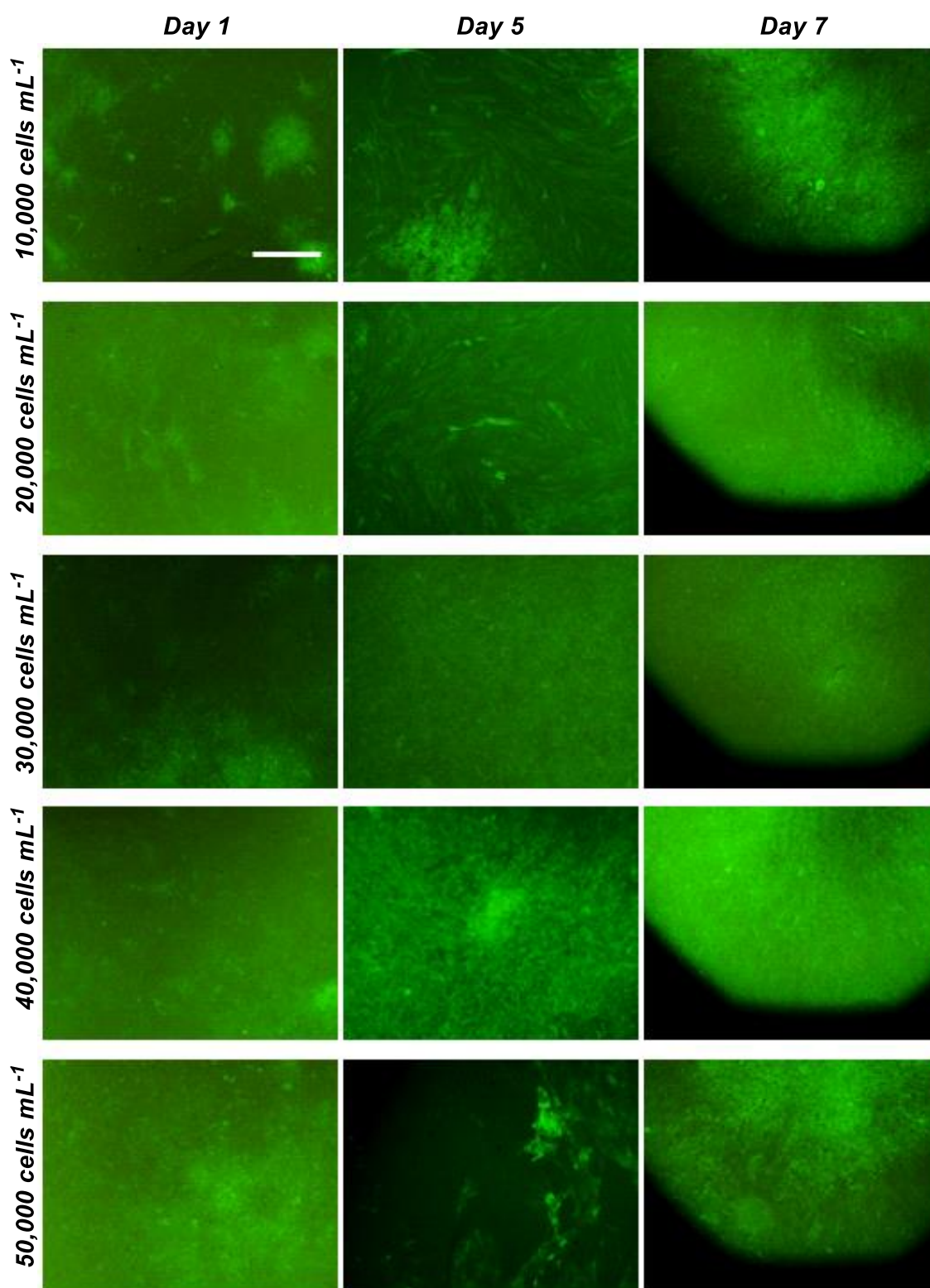


Figure 5.8: Representative fluorescence microscopy images of Y201 XGreen cells cultured on DBS-CONHNH₂ hydrogels washed with 70% ethanol followed by three washes with PBS. Cells were cultured for 1, 5 and 7 days. Seeding densities are given on the left-hand side of the figure. Good adherence and proliferation were seen for cells up to 40,000 cells mL⁻¹. At a seeding density of 50,000 cells mL⁻¹ aggregated structures were observed. This is indicative of cell apoptosis and agglomeration occurring at high cell confluency. Scale bar = 500 μm.

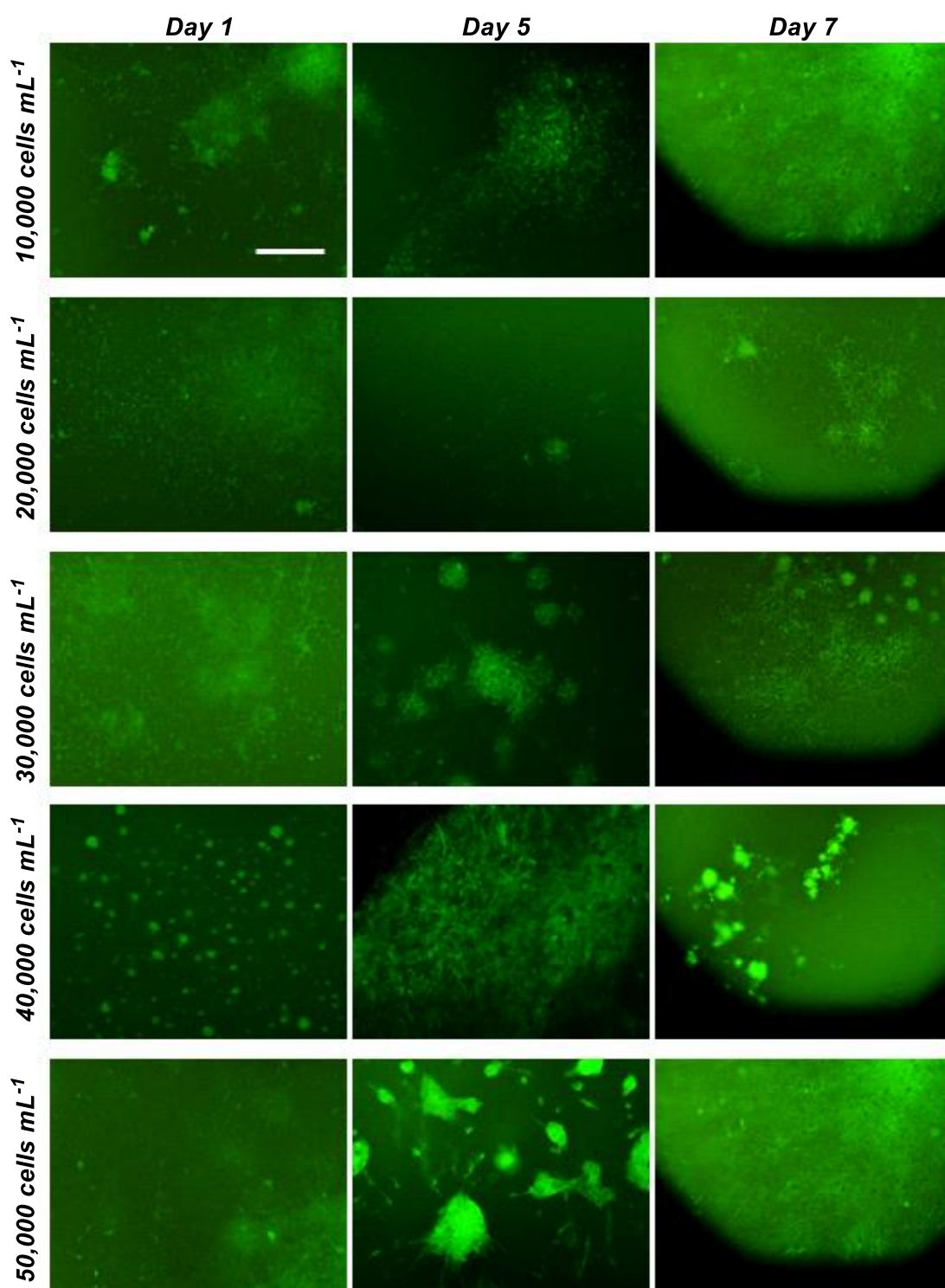


Figure 5.9: Representative fluorescence microscopy images of Y201 XGreen cells cultured on DBS-CONHNH₂ hydrogels washed with PBS only for 1, 5 and 7 days. Seeding densities are given on the left-hand side of the figure. Good adherence and proliferation were seen for cells seeded at 10 and 20,000 cells mL⁻¹. At higher seeding densities large, round, aggregated structures were observed. This is indicative of cell apoptosis and agglomeration occurring at high cell confluency. Scale bar = 500 μm.

Importantly, the initial results outlined here indicated that, as previously demonstrated for 3T3 mouse fibroblasts, DBS-CONHNH₂ gels are cytocompatible and, in this case, able to support MSC adherence and proliferation.⁵⁸ Over longer periods of time (5-7 days), cells seeded at higher initial densities began to undergo apoptosis and agglomeration, as evidenced by the formation of round, aggregated structures. This cell death is likely due to the competition between cells for nutrients in the media as well as adhesion sites on the gel surface. However, given that the differentiation process of MSCs is typically upwards of 7 days, these high seeding densities were therefore considered inappropriate for later studies aimed at assessing stem cell fate.^{382,395,397} It is important for cell signalling during differentiation that a relatively high confluency is achieved (confluency here is defined here as the percentage of a surface covered by cells), but not so high that further cell proliferation is inhibited. MSC seeding densities of *ca.* 10,000 cells mL⁻¹ therefore appeared to be appropriate for further studies on the LMW hydrogels. To rule out the influence of impurities on MSC adhesion and proliferation, a more rigorous interrogation of the purity of DBS-CONHNH₂ must be carried out. As outlined in Chapter 2, elemental analysis and HPLC could be used to ascertain the purity of the compounds used in these studies. In the case of DBS-CONHNH₂, any such impurities do not appear to inhibit the growth of the Y201 MSCs.

Acyl hydrazide linkages are frequently utilised in tissue engineering for the conjugation of bioactive moieties to gel matrices and are not shown to have an inhibitory effect on the cell growth.^{398,399} Much fewer examples of gels displaying free hydrazide moieties have been reported. In addition to the previous work from the Smith group described above,⁵⁸ Kilian and co-workers have shown that hydrazine-treated polyacrylamide gels support MSC growth *in vitro* over 13 days.^{400,401} In contrast, the introduction of hydrazide moieties into a number of small molecules has been shown to enhance their cytotoxic effects in fibroblastic and cancer cell lines in certain cases.^{402,403} In other examples, hydrazide derivatisation either has not had such negative effects on cell survival.^{404,405} Clearly, the influence of the hydrazide functional group is complex and context-dependent, but in our case (and for other reported gel matrices) it does not have an inhibitory effect on cell growth.

5.4.2 PEGDM hydrogels

We next assessed the growth of MSCs on PEGDM hydrogels. Polymer hydrogels were prepared by dissolving PEGDM (10% wt/vol) and PI (0.05% wt/vol). 50 μ L aliquots were pipetted into the centre of the 6 mm washers and crosslinked with long wavelength UV light for 0.5 h. This resulted in the formation of clear hydrogels. Crosslinking was clearly observed throughout the depth of the gel. Given the finding in Chapter 2 that no differences in mechanical properties through the depth of a 1 cm gel were observed following photopatterning, we are confident that uniform crosslinking is present throughout these much thinner gels. The presence of the polystyrene between the UV lamp

and the gel is not expected to interfere with the crosslinking process (or that of the hybrid gel, see below). This plastic absorbs strongly at 260 nm, but in the region of UV light accessible with the lamp used for this study (*ca.* 315 – 400 nm), no interference is expected.⁴⁰⁶

Gels were washed with ethanol and PBS ($\times 3$) prior to Y201 XGreen seeding. Cells were seeded at densities ranging from 0 to 50,000 cells mL^{-1} . As for the LMW hydrogels, no autofluorescence was evident in the control samples (Figure 5.10a). Interestingly, in contrast to the MSCs cultured on DBS-CONHNH₂ hydrogels, when cultured on 10% PEGDM gels very few cells were observed on the surface of the materials after 24 h (at any cell seeding density). Those that were adopted a much more rounded morphology (Figure 5.10b). This suggested that the Y201 XGreens are unable to adhere and proliferate on the polymer gels. It is widely reported in the literature that, whilst biocompatible, PEG hydrogels do not themselves support cell adhesion.⁴⁰⁷ Only when modified or co-polymerised with cell adhesive moieties do they show such behaviour. The lack of MSC growth on the polymer gels was considered to be the result of this effect, rather than the product of non-sterile handling, because good cell growth and proliferation was observed on the polystyrene well plates around the outside of the washer over 24 h (Figure 5.10c). These findings suggest that PEGDM alone is not compatible with the growth of MSCs.

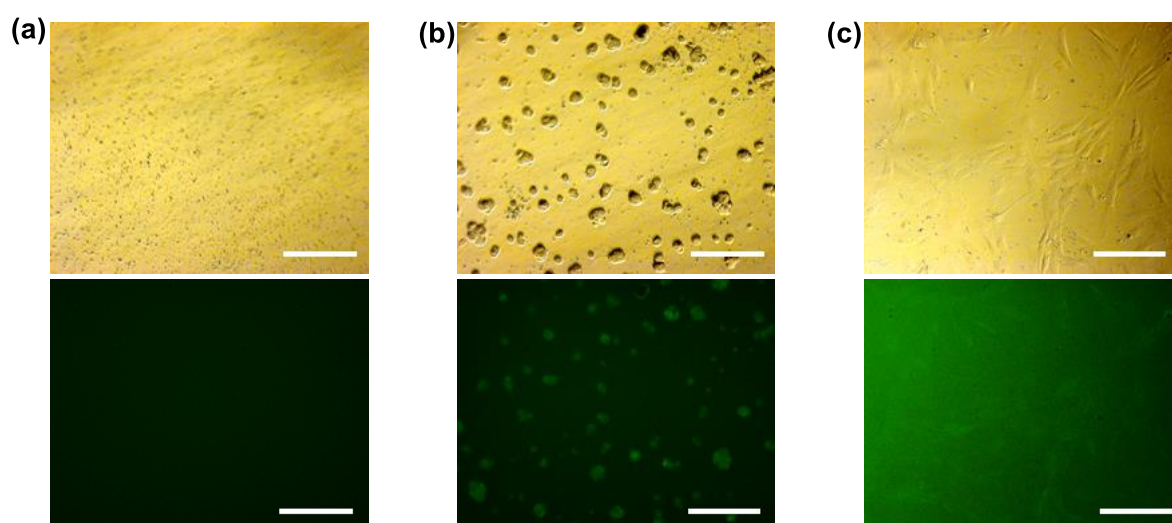


Figure 5.10: Brightfield (top) and fluorescence (bottom) images of PEGDM samples. Gels were washed with 70% ethanol followed by three washes with PBS. Images of the gel seeded with no cells indicate that the gel does not fluoresce under ZsGreen excitation conditions (a). Poor Y201 XGreen adherence was seen on PEGDM gels, shown at a seeding of 30,000 cells mL^{-1} (b). This is indicated by the rounded morphology of the cells after 24 h. Similar cell morphologies were observed at higher and lower Y201 XGreen seeding densities (see Appendix 13). Good adherence of cells to the polystyrene well plate surrounding the gel and washer was observed over 24 h (c), indicating that lack of adhesion is a property of the gel and not of experiment error.

It is possible that residual DCM from the synthesis of the gelator may have influenced the cell behaviour observed here. Given that MSC proliferation is observed in the well plates surrounding the gels, this seems unlikely to be playing a significant role. Solvent exchange between the gel and surrounding media should be relatively rapid, therefore residual DCM would be expected to affect all the cells in each well. A number of experiments would confirm whether DCM is responsible for the lack of cell growth on PEGDM hydrogels. Elemental analysis of the gelator would reveal whether the drying steps taken were sufficient to remove all the residual solvent. Having established the proportion of residual DCM in the PG, control experiments in which MSCs are grown in media (and on PEGDM gels) dosed with a representative concentration of DCM would determine its influence on their growth.

5.4.3 Hybrid hydrogels

10% hybrid gels were then prepared for study. DBS-CONH₂ gels were made in the washer as described above. A solution (50 μ L) of PEGDM (10% wt/vol) and PI (0.05% wt/vol) was added on top of the gel and left for 3 days. After this time the supernatant was removed and the gels irradiated with long wavelength UV light for 0.5 h, crosslinking the PEGDM network. Gels were washed with ethanol and PBS as described above. Y201 XGreen cells were then seeded on the gels at initial densities between 0 and 50,000 cells mL⁻¹. As for the two individual networks, the hybrid gels do not exhibit any fluorescence when irradiated under 496 nm light (Appendix 13). This was largely expected due to the relative orthogonality of the two gel networks within the hybrid gel. Cells showed good adherence on these materials after 24 h (Figure 5.11). As for the DBS-CONH₂ gels, the cells largely adopted an extended, fibroblast-like morphology, although a small number of round, non-adherent cells were also seen. Qualitatively, there did appear to be fewer cells adhered to the hybrid gel than the LMW hydrogels after this time. However, over the course of 7 days, evidence of proliferation was seen as the cells expanded to cover the surface (Figure 5.11). As for the LMW hydrogels, seeding at higher densities resulted in cell agglomeration over the course of a week, making them unsuitable for longer-term differentiation studies. Importantly, this result shows that the incorporation of the DBS-CONH₂ network provides the hybrid gel with cell adherent properties not possessed by the PEGDM gel alone. It is likely that DBS-CONH₂ provides the hybrid gel with the necessary cell adhesion potential that is absent in the PEGDM-only gels. Again, any influence of residual DCM from the synthesis of PEGDM has not been elucidated. If solvent effects are responsible for the differences in MSC behaviour, the concentration of DCM is presumably lower in the hybrid gels compared to the PEGDM hydrogels, as MSC adherence and proliferation was not significantly inhibited in this case.

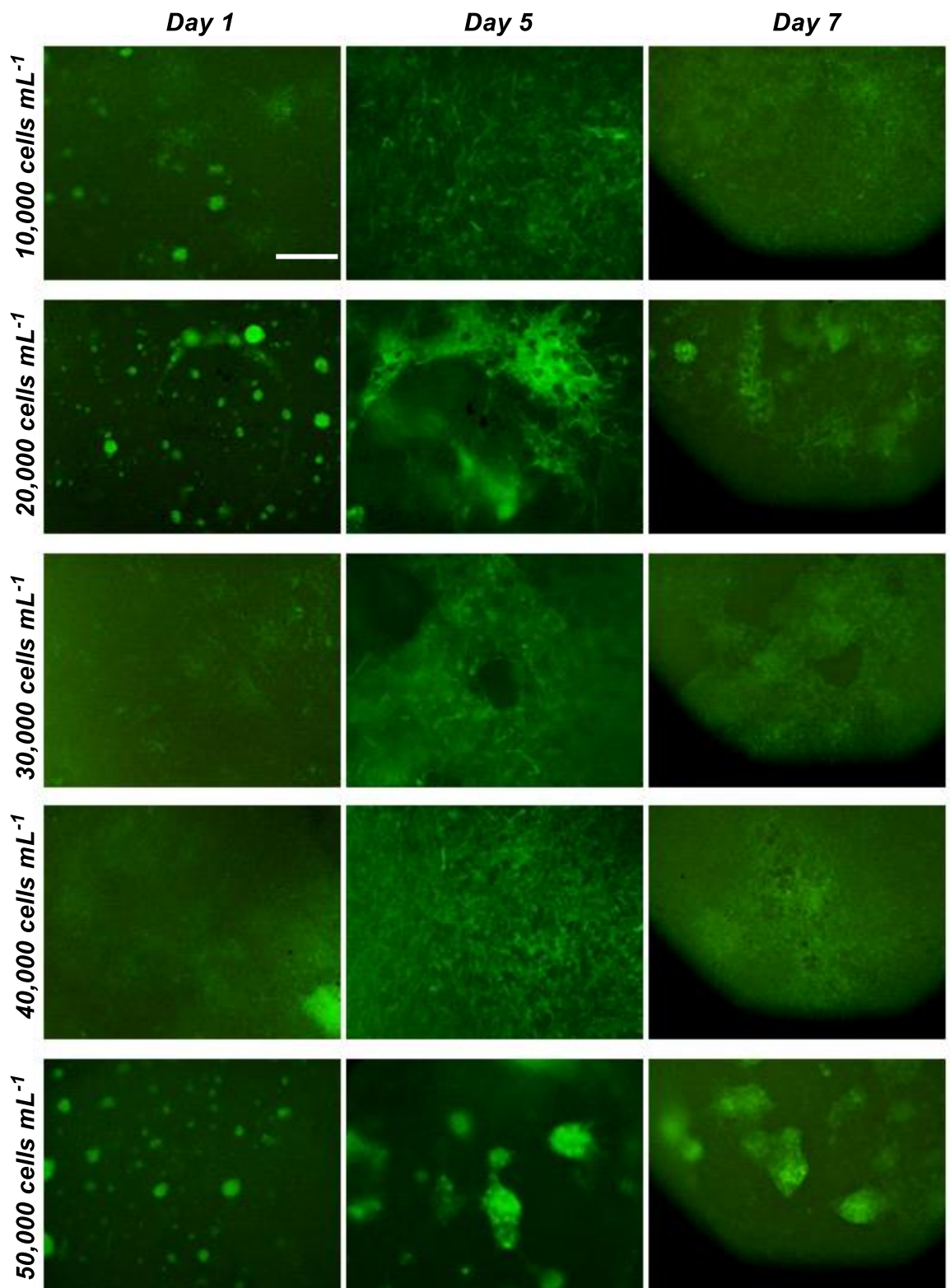


Figure 5.11: Representative fluorescence microscopy images of Y201 XGreen cells cultured on 10% hybrid hydrogels washed washed with 70% ethanol followed by three washes with PBS. Cells were imaged after 1, 5 and 7 days culture. Seeding densities are given on the left-hand side of the figure. Good adherence and proliferation is seen for cells seeded between 10,000 and 40,000 cells mL⁻¹ over 7 days. Poor adherence is seen in some samples after 24 h At an initial seeding density of 50,000 cell mL⁻¹, evidence of large, round, aggregated structures were observed. This is indicative of cell apoptosis and agglomeration occurring at high cell confluency. Scale bar = 500 μm.

Whilst the 10% hybrid gels are significantly stiffer (4.4 kPa) than the DBS-CONH₂ LMW hydrogels (1.4 kPa), they fall significantly short of the stiffnesses previously reported to induce osteogenesis (see Section 5.3). We therefore chose to screen a number of the stiffer hydrogels developed in Chapter 4 for compatibility with the Y201 XGreen MSCs. Specifically, we tested hybrid gels containing 20, 40 and 60% wt/vol PEGDM. These gels show significantly greater stiffness than the gels tested above. The 20% hybrid gel displayed a G' value of *ca.* 8 kPa, the 40% hybrid *ca.* 30 kPa and the 60% hybrid *ca.* 37 kPa (Figure 5.12). The enhanced stiffness of these materials with greater PG loadings should make them more conducive to the formation of stiffer tissue such as cartilage or bone.

The 20, 40 and 60% hybrid gels were prepared using the same procedure outlined for the 10% hybrid gels. The cytocompatibility of these materials was assessed by seeding Y201 XGreen cells on the gels at a density of 10,000 cells mL⁻¹ – based on the optimal seeding density of the 10% hybrid gels - and monitoring cell growth over the course of a week. The 20% hybrid gels showed reasonable cell adherence in the short term (Figure 5.13a). In contrast, cells did not adhere well to the 40% (Figure 5.13b) and 60% (Figure 5.13c) hybrid gels, adopting a rounded morphology similar to that

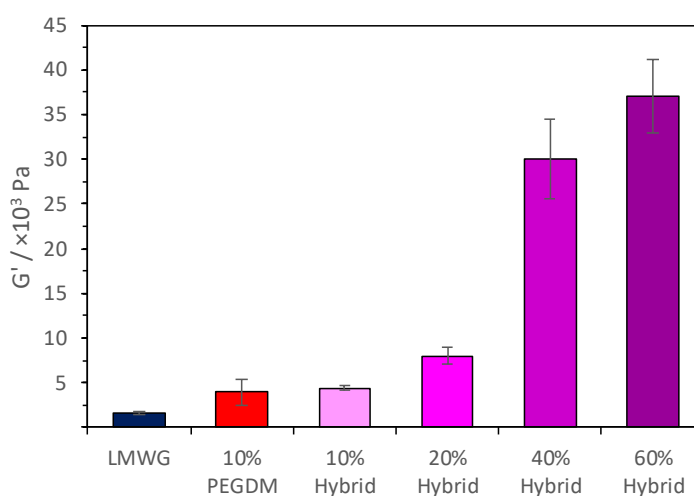


Figure 5.12: Elastic moduli (stiffnesses) of the gels tested in this cytocompatibility study. Errors given as standard deviation (n=3).

seen for PEGDM. The number of cells observed on the surface of the gel was also lower for these samples than the 20% hybrid gel. No improvement in adhesion or proliferation was seen over the course of a week for these materials, whilst the Y201 XGreen cells appeared to multiply on the 20% hybrid gels, reaching medium-to-high confluency after 7 days. These findings illustrate the importance of the two orthogonal gel networks in determining material properties. At lower

PEGDM loadings (10 and 20%) even a relatively small quantity of DBS-CONH₂ is able to impart cell adhesion properties to the hybrid gels. However, at high PEGDM loadings the positive effects of cell growth imparted by this network are no longer observed. Due to interactions between the networks (as described in Chapter 2) it may simply be that the PEGDM network competes with cell for adhesive moieties on the DBS-CONH₂ nanofibres, or it may be simply that the increased density of the non-adherent network prevents cell access to the LMWGs and dominates the overall gel surface properties. These findings align with those of Smith and co-workers, who demonstrated that incorporation of agarose in a hybrid gel slightly inhibits fibroblast adhesion and growth compared to DBS-CONH₂ gels alone.⁵⁸ As outlined above, solvent effects can not be ruled out at this stage. An increase in DCM concentration with higher PEGDM loading could also explain the lack of cell adhesion on 40 and 60% hybrid hydrogels.

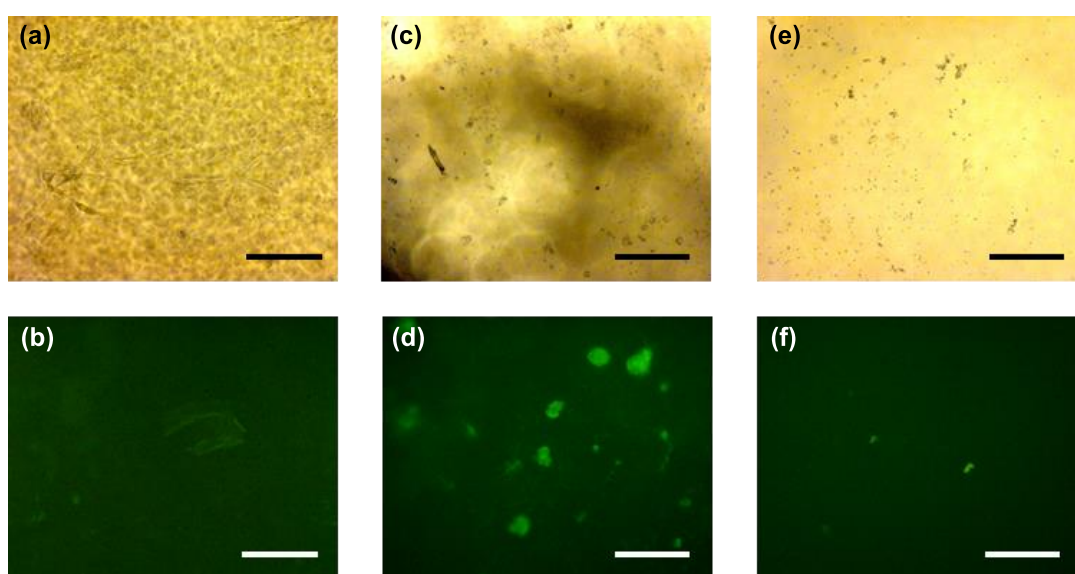


Figure 5.13: Y201 XGreen cells cultured on 20% (a, b), 40% (c, d) and 60% (e, f) hybrid gels for 7 days. Reasonable cell adhesion is seen on the 20% hybrid gels, with cells adopting an extended morphology. MSCs cultured on 40% hybrid gels show no adherence and display spherical morphology reminiscent of that seen for PEGDM hydrogels. Almost no cells were observed on the surface of the 60% hybrid gels, indicating that they are not compatible with Y201 cells. Scale bar = 500 μ m.

5.4.4 Gel swelling

In addition to the lack of cell adhesion, work with the 40% and 60% hybrid gels was challenging due to the significant swelling observed when these materials were submerged in aqueous solution. This prompted us to consider more generally the swelling of the different materials used in this study. We prepared representative LMW, hybrid and PG hydrogels to determine the swelling of each type of material. Gels were prepared at a volume of 0.5 mL in a vial of diameter 10 mm.

Deionised water (1 mL) was pipetted on top of each gel and the sample left to equilibrate over 3 days before the supernatant was removed. Swelling was assessed by the change in gel height over this time (Table 5.1). DBS-CONHNH₂ (6 mM) hydrogels showed no change in gel height. We therefore consider swelling effects to be insignificant for these LMWG materials. In contrast, 10% PEGDM hydrogels swelled significantly in water, increasing in height by *ca.* 20%. Hybrid gels showed some degree of swelling, with the total height change determined by the PEGDM content of the material. 20% hybrid gels showed similar swelling properties to the 10 % PG, probably due to the similar PEGDM content of the two materials (see Chapter 4). It is noted that the errors seen in this data may be the result of slight differences in the mass of prepared gelators or volume of water pipetted. Differences in the volume of LMW hydrogel retained after cooling is the major source of error in this case. The effect of temperature is not expected to have been significant as all samples were studied in parallel.

Table 5.1: Swelling of DBS-CONHNH₂, PEGDM and hybrid hydrogels in water; measured by changes in gel height. LMWG and PG tests were carried out in triplicate, hybrid gel samples in duplicate. Errors given as standard deviation.

Sample	Height before / mm	Height after / mm	Difference (% change)
LMWG	4.7 ± 1.2	4.7 ± 1.2	0 ± 0 (0)
10% PG	6.7 ± 0.3	8.0 ± 0.0	1.3 ± 0.3 (20)
10% hybrid	5.0 ± 0.0	5.5 ± 0.0	0.5 ± 0 (10)
20% hybrid	4.0 ± 1.4	5.3 ± 1.8	1.3 ± 0.4 (31)

5.4.5 Cell seeding on larger gels

The above studies were repeated with 0.5 mL gels. However, with these samples, poorer adherence of the gels to the well plate (presumably due to swelling), as well as poorer adherence of the Y201 XGreens to the surface of the gels was seen. Given these results, alongside the greater fabrication time and gelator quantity required, we elected to abandon this approach and continue study with the smaller scale ‘gel-in-washer’ approach.

5.4.6 Photoinitiator concentration in cell culture media

As well as matrix effects, the presence (and release) of photoinitiator in the PEGDM and hybrid gels was considered to be a potential factor inhibiting potential MSC growth. To assess this, we prepared

a range of gels in washers (50 μ L) as described for the cell seeding tests above, namely DBS-CONH₂ and 10 and 20% hybrid gels. The DBS-CONH₂ hydrogel was prepared in a 0.05% solution of PI to assess PI release from uncured regions of any photo-patterned hybrid gels. These gels were submerged in 1 mL PBS for 24 h. After this time, the solution was removed, diluted to 2 mL in PBS and the absorbance recorded at 286 nm. Absorbance values were compared to that of PBS controls (with washers) and, for LMWG and hybrid samples, to a DBS-CONH₂ gel control.

Significant amounts of PI were indeed released from the hydrogel structures into solution during the first wash (Figure 5.14). By comparison to a calibration curve, it was calculated that the concentrations of PI in PBS solution used to wash DBS-CONH₂, 10% hybrid and 20% hybrid gels were *ca.* $5 - 6 \times 10^{-4}$ % wt/vol. A greater concentration was released into the solutions used to wash the PEGDM hydrogels. Concentrations of *ca.* 12×10^{-4} % wt/vol were recorded in these samples. These concentrations are far below those reported to have adverse effects on cell viability (*ca.* 100×10^{-4} % wt/vol)^{177,178,408} and therefore the effect of PI is considered to be negligible.

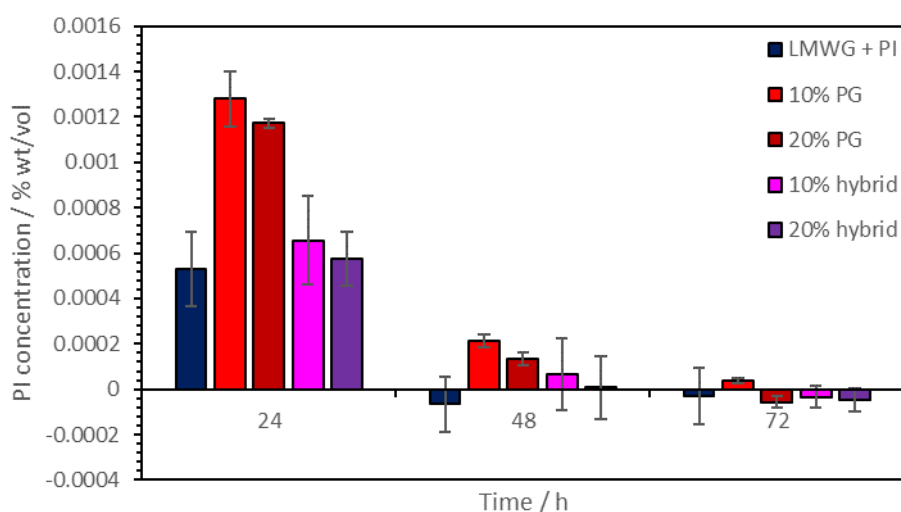


Figure 5.14: Concentration of PI in PBS solution used to wash gels in prepared in well plates. Errors given as standard deviation ($n = 4$).

The above process was repeated to determine the number of washes required to remove all mobile PI from the gel matrices. A small contribution of PI to the UV-vis absorption spectrum of the supernatant was seen after a second wash of the PEGDM hydrogels. No PI was seen in any of the other samples. After three washes all washings showed no evidence of PI by UV-vis spectroscopy, validating the washing procedure outlined above. As all samples were exposed to the same conditions of temperature, this is unlikely to have played a role in the results seen here. Errors in

the readings are more likely the results of instrument error (*ca.* 1%), and the result of measuring out relatively small amounts of PI for stock solution (0.5 mg in 1 mL H₂O, error *ca.* 1%).

5.5 Matrix-dependent Y201 growth

Having screened the LMWG, PG and hybrid gels for cytocompatibility, we then aimed to assess whether any qualitative differences in MSC behaviour were evident in cells cultured on these materials for longer periods of time. To determine the influence of the gels themselves on MSC differentiation, we cultured the Y201 XGreen cells using non-conditioned (basal) media in the absence of any differentiation directing factors. As described above, the MSC differentiation process typically takes upwards of 7 days, in particular in the absence of stimulating conditions. We therefore hoped to see changes in cell growth and/or morphology on the different materials. It should be noted that the formation of cartilage from Y201 cells requires a cell pelleting procedure which – to perform in these hydrogels – would require significant optimisation. Therefore, at this stage we have considered only the formation of adipose and bone cells.

Given the lack of cell adherence observed on PEGDM hydrogels, we elected to use these materials as a negative control for MSC growth during the subsequent studies. In addition, we studied longer term MSC growth on the cell-adhesive gels seen above, namely DBS-CONHNH₂ (6 mM), 10% hybrid and 20% hybrid gels (Figure 5.15 and Figure 5.16). Cells were also cultured directly on polystyrene well plates, and wells filled with media in the absence of cells were used as a negative control for fluorescence.

After 1 week, as in the experiments in Section 5.4, little difference in MSC morphology was seen for cells cultured on the different gel types. High confluency was seen in the polystyrene cultured samples. Similarly high surface coverage was seen in the LMW hydrogel samples. Lower confluency was observed on the 10% hybrid gels, and lower again on the 20% hybrid gels, consistent with the findings above. As expected, MSCs did not adhere at all to PEGDM hydrogels, adopting spherical morphologies on the gel surface.

After 2 weeks, very high confluency of the polystyrene plated samples was seen. In contrast, Y201 XGreen cells appeared to have decreased in number on the LMW hydrogel surface. Interestingly, the cells appeared to be dispersed throughout the gel matrix. This indicates that, despite being cultured in a 2D monolayer, the MSCs were able to migrate through the relatively permeable LMW hydrogel structure. Such migration has previously been seen for LMW hydrogels and xerogels previously.^{409,410} Smith and co-workers did not observe migration of 3T3 fibroblasts through a DBS-

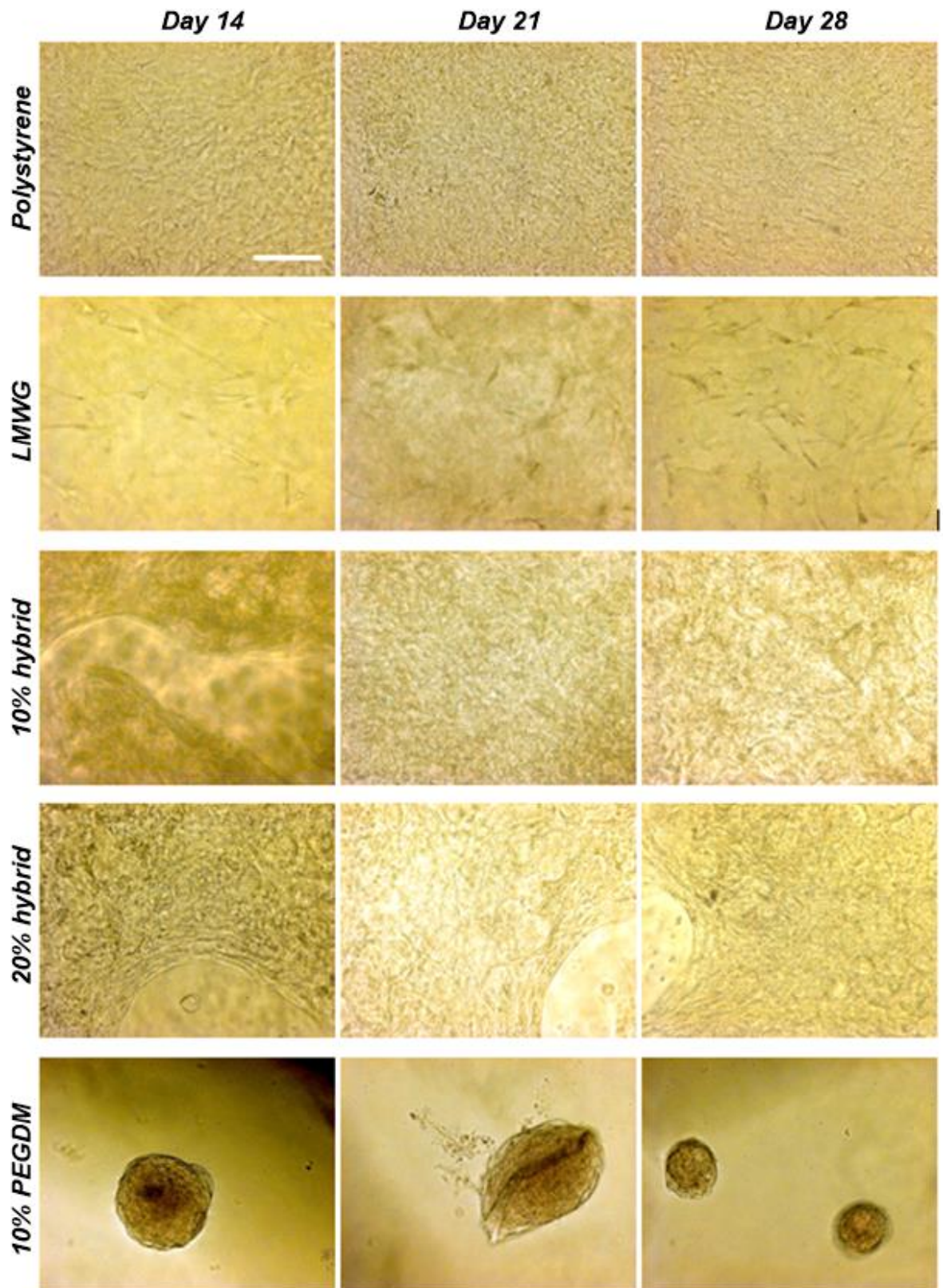


Figure 5.15: Representative optical microscopy images of Y201 XGreen cells cultured on plastic and gel matrices. Images were taken after 7, 14 and 21 days. Initial cell seeding densities of $10,000 \text{ cells mL}^{-1}$ were used for all samples. Cells cultured on LMW hydrogel matrices appear more disperse than those cultured on the stiffer hybrid gels. All individual cells showed elongated morphologies on these materials. Cells grown on 10% PEGDM hydrogels showed no adherence over 21 days, indicated by the rounded aggregates. Scale bar = $500 \mu\text{m}$.

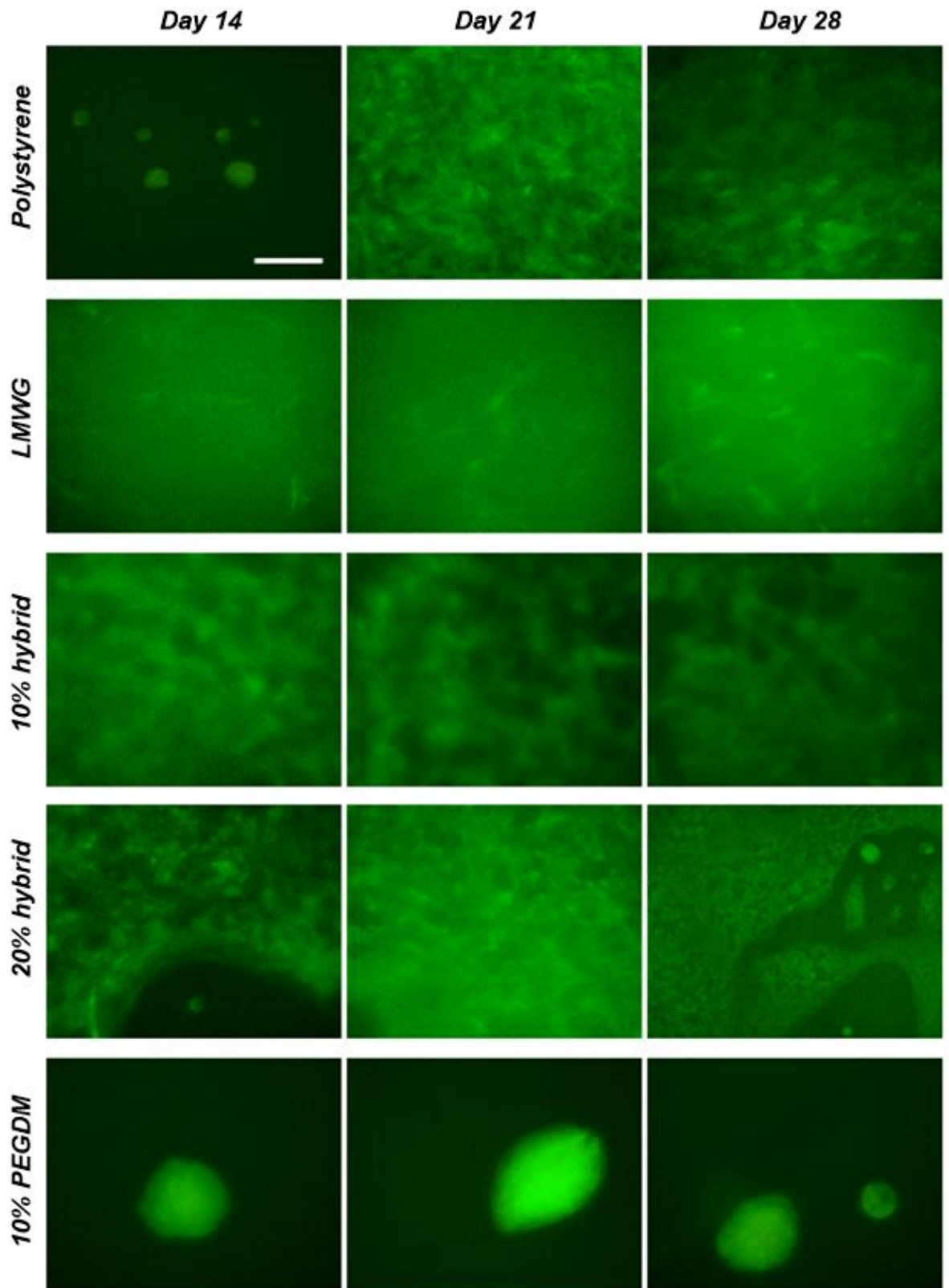


Figure 5.16: Representative fluorescence microscopy images of Y201 XGreen cells cultured on plastic and gel matrices. Images were taken after 7, 14 and 21 days. Initial cell seeding densities of $10,000 \text{ cells mL}^{-1}$ were used for all samples. Cells cultured on LMW hydrogel matrices appear more disperse than those cultured on the stiffer hybrid gels. All individual cells showed elongated morphologies on these materials. Cells grown on 10% PEGDM hydrogels showed no adherence over 21 days, indicated by the rounded aggregates. Scale bar = $500 \mu\text{m}$.

CONHNH₂ matrix, however, in this study, cells were only cultured for 7 days.⁵⁸ In contrast to the LMW hydrogels, Y201 XGreen cells were only observed on the surface of the 10% and 20% hybrid gels. Significant cell growth was observed between weeks 1 and 2. The MSCs now showed high confluency on the hybrid materials and now appeared to have formed more densely packed colonies compared to those grown on the LMW hydrogel. Cells cultured on PEGDM gels again showed no adherence.

No significant changes in the MSC properties were observed by microscopy after 2 weeks cell culture. Some evidence of cell aggregation was seen in the 20% hybrid samples after 4 weeks, but the number of these aggregates was very small compared to that seen on the PEGDM hydrogels. The differences in morphology and cell density between the LMW and hybrid hydrogels was interesting. It was considered that the formation of more dense structures on the stiffer hybrid gel may be an indication of the formation of a more dense and rigid tissue type – in this case osteogenesis. In contrast, the more disperse nature of the cells in the softer LMW hydrogels may provide evidence of the formation of a softer, less dense tissue such as adipose.

In addition to the fluorescence images shown above, we also attempted to characterise the morphology and dispersion of Y201 cells on the LMW and hybrid hydrogels by SEM. Unfortunately, the DBS-CONHNH₂ hydrogels which had been incubated in the presence of cells were too weak to be removed from the well plates for analysis. Given that DBS-CONHNH₂ gels incubated in cell culture media for upwards of a month showed excellent stability (Figure 5.17), the weakness of these materials is not considered to be the result of weakened intermolecular interactions in the presence of this complex solution. Instead we propose that mechanical action of cell migration irreversibly weakens the (non-thixotropic) LMWG nanofibres. This observation therefore provides supporting evidence that these cells can migrate into the DBS-CONHNH₂ hydrogel network.

The 10% and 20% hybrid gels were easy to remove for SEM analysis due to the robustness of these materials provided by the PEGDM. Samples prepared for SEM imaging by a solvent gradient method were unsuitable for analysis. The addition of bis(trimethylsilyl)amine in the last step of this process resulted in destruction of the dried gels. Samples were instead freeze-dried for SEM. Better samples were obtained, but on imaging it became clear that significant cell breakdown had occurred. It is therefore difficult to draw any meaningful conclusions from this data.

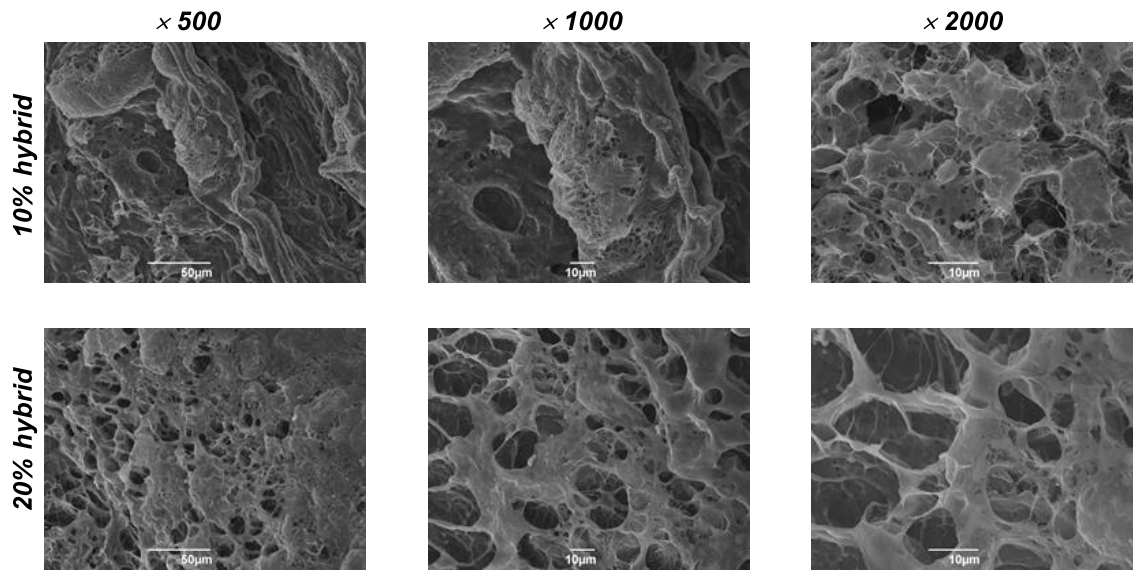


Figure 5.17: SEM images of 10% hybrid (top) and 20% hybrid (bottom) hydrogels with Y201 MSCs cultured on top for 3 weeks. Further images are provided in Appendix 14.

We used similar samples to assess the migratory potential of cells using confocal microscopy. Using this technique, the cells could be imaged live, without the need for pre-processing. This should, in principle, allow the visualisation of MSC location in the hydrogel matrices. We cultured Y201 XGreen cells which did not require staining to visualise due to their intrinsic fluorescent properties. Additionally, these samples were prepared in washers, but removed to maximise available surface area through which MSCs could migrate over 2 weeks.

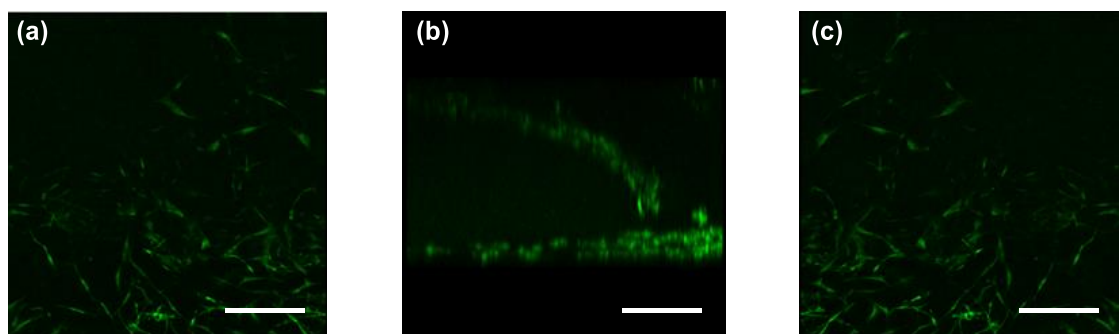


Figure 5.18: Confocal microscopy images of Y201 XGreen cells cultured on a 20% hybrid gel. Views are from beneath (a), side-on (b) and above (c). Scale bar = 500 μm .

Interestingly, on 20% hybrid gels, no MSC migration through the hydrogels was observed. Evidence of cell growth was seen in two layers – at the top and at the bottom of the gel (Figure 5.18, Supplementary Video 2). This provides evidence that the hybrid gel network structure is too dense

for the cells to migrate through (pore size in Chapter 4 was estimated at < 11 nm). As for the SEM samples, the LMWG hydrogel broke down during the course of the experiment. Key future work involves the optimisation of sample preparation to allow visualisation of MSC migration in these less dense samples.

5.6 Quantifying cell growth

In addition to the qualitative differences in cell growth seen above, quantified cell growth on each material using a bicinchnic acid (BCA) assay. This assay gives a value for the concentration of protein in a sample which can be used as a proxy for the number of cells. A reading is generated through the sequential reduction of CuSO_4 by peptide bonds, followed by bicinchnic acid chelation of the resulting Cu^+ ion (Figure 5.19a). This complexation results in the formation of a strong purple coloration, the intensity of which is proportional to the concentration of protein in the sample.⁴¹¹

The protein content of the MSCs cultured on polystyrene, DBS- CONH_2 gels, 10% hybrid and 20% hybrid gels for 3 weeks was determined using this BCA assay. Cells were lysed using Triton-X solution (0.1% vol/vol) in combination with a freeze/thaw cycle. An aliquot of lysed cells was taken and added to the BCA assay working reagent (containing copper sulfate and bicinchnic acid). The samples were incubated at 37°C for 0.5 h, after which time the absorbance of each solution at 562 nm was recorded. Readings were compared to those of control samples, in which gels were incubated in media (without cells) for the same length of time. This should account for protein originating from the media rather than cellular activity. The total protein was quantified by comparison to prepared standards (Figure 5.19b).

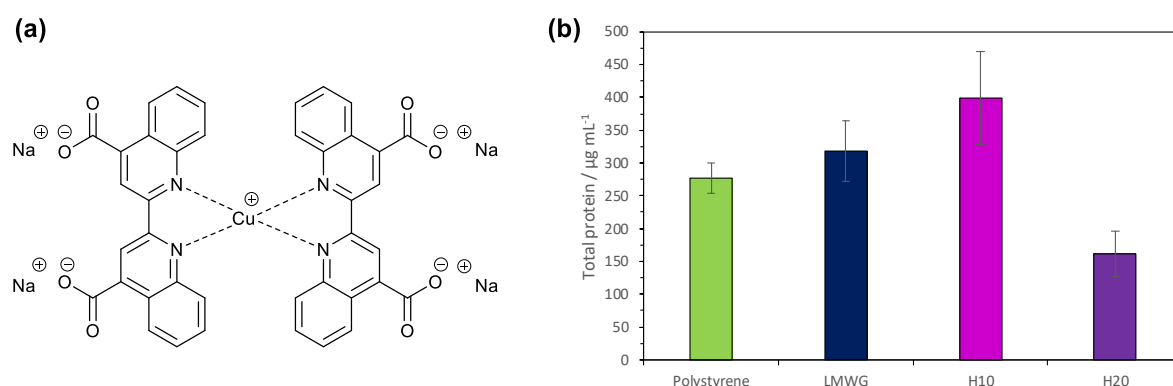


Figure 5.19: Complexation of Cu^+ by bicinchnic acid (a). This complex is responsible for purple coloration in the presence of protein. Total protein recorded for each of the cell treatments (b). Errors given as standard deviation ($n = 6$).

Interestingly, despite the qualitative observation that Y201 XGreen cells appeared to grow fastest on the polystyrene plates, the protein content of the solutions removed from the 10% hybrid gels was actually higher ($399 \pm 71 \mu\text{g mL}^{-1}$). However, no significant difference was seen between this sample and the DBS-CONHNH₂ hydrogels ($318 \pm 46 \mu\text{g mL}^{-1}$). In line with the visual observations discussed earlier in this chapter, the 20% hybrid gels did indeed appear to induce the lowest degree of MSC proliferation, as the total protein seen for these samples was significantly lower ($161 \pm 35 \mu\text{g mL}^{-1}$). This is probably a result of the higher PG loading in these materials slightly reducing the ability of the gels to support cell adhesion and spreading. Errors resulting from the assay kit itself were quantified using standard solutions as *ca.* 2% of the recorded protein value.

5.7 Oil Red O Adipogenesis Assay

Given the differences in MSC morphology and migration evident from fluorescence microscopy after some weeks, we can infer that the mechanical properties of the gel influence the behaviour of cultured stem cells. We next aimed to determine whether the observed morphological differences are the result of MSCs undergoing differential differentiation pathways, dependent on the material they are seeded onto.

The adipogenic potential of cells cultured on polystyrene well plates as well as DBS-CONHNH₂ (6 mM), 10% hybrid and 20% hybrid gels was first assessed using an Oil Red O assay. Oil Red O is a lipophilic stain which has found use in a range of applications, including fingerprint staining and pathology.⁴¹²⁻⁴¹⁴ In the context of tissue engineering, this species partitions into the lipid droplets formed by adipocytes, providing a marker for the formation of fat cells.^{415,416} Such studies have previously been reported for cells cultured on hydrogels.^{417,418}

For this study we used unmodified Y201 cells, as isolated by Genever and co-workers. Gels were prepared as previously described within washers adhered to the base of the wells in a 24-well plate. Following washing, Y201 cells were seeded in each well at a density of 10,000 cells mL⁻¹. Cells were cultured for 3 weeks (to allow differences in MSC behaviour to emerge) with regular media changes to ensure sufficient nutrients were provided to prevent apoptosis. Cell adherence and proliferation were confirmed visually. After 3 weeks, the cells were fixed and each well incubated with Oil Red O staining solution (7.3 mM in 60% aqueous propan-2-ol) for 30 min. Wells were washed once with 60% aqueous propan-2-ol followed by washes with water until the washing solution was colourless.

It should be noted that, consistent with the observations in Section 5.5, the LMW hydrogels became significantly weaker over the course of cell growth, and were unable to withstand the fixing and washing procedures required for cell staining. This may be explained in the context of the

observations made in Section 5.5. Migration of cells into the bulk could weaken the LMWG hydrogel structure through mechanical action on the nanofibres.

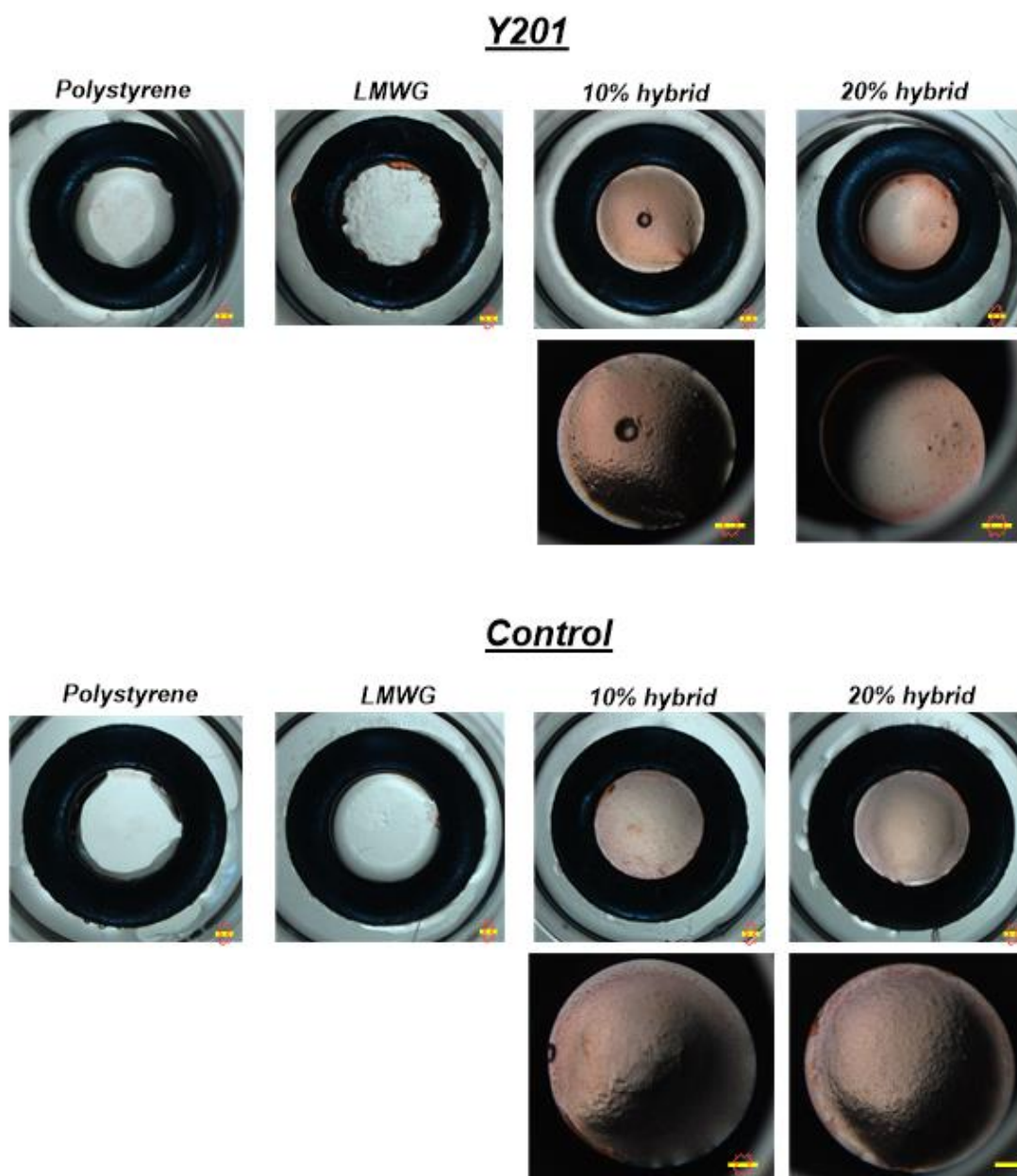


Figure 5.20: Oil Red O staining of Y201 cells cultured on different materials after 3 weeks (top). Images of Oil Red O stained control samples with no cells seeded (bottom). Scale bar = 1 mm.

Qualitatively, little of the stain appeared to be taken up by any of the samples (Figure 5.20). A slight pink coloration was observed in the hybrid gels, suggestive of some Oil Red O in the porous matrices. No stain uptake was seen for the cells around the outside of the gel, or for samples where no gel was present. Optical microscopy of the gels cultured with Y201 cells revealed what appeared

to be small droplets of stain on the surface of the gel. Whilst it is possible that this droplet-like staining pattern is the result of the formation of lipid droplets associated with adipogenesis, given that control samples incubated in media appeared visually similar, this would seem an unlikely explanation. It may be that the formation of these droplets may occur within small hydrophobic pockets in the gel, possibly in regions of particularly high gel fibre density. However, at this stage this is purely speculative.

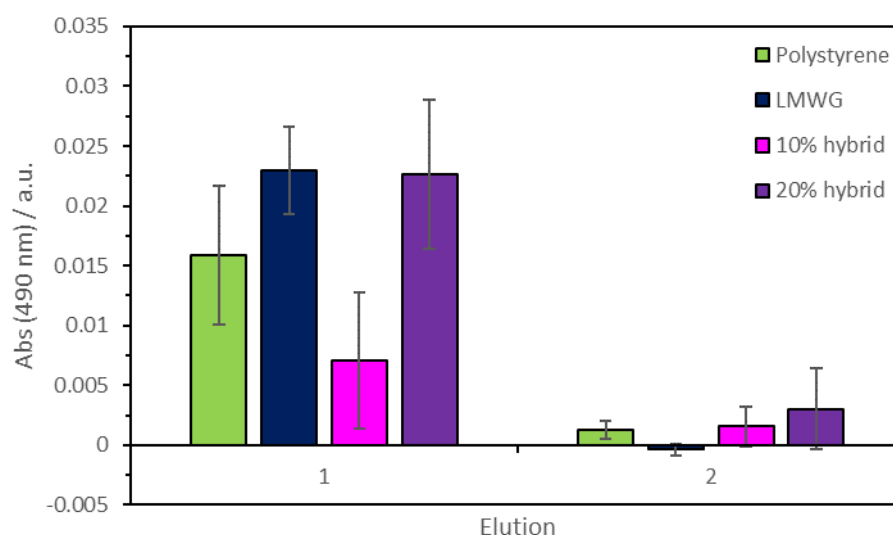


Figure 5.21: Absorption of solutions of Oil Red O eluted from Y201 cells cultured for 3 weeks. Absorbance of eluent from control samples with no seeded cells were subtracted from the original absorbance to yield these values. Errors given as standard deviation ($n = 6$).

Despite there being no obvious differences between the wells in which cells were cultured and the control wells, we determined the uptake of Oil Red O by each sample to assess any differences in the lipid production of cells cultured on different surfaces (Figure 5.21). The stain was eluted into 100% propan-2-ol and the absorbance of each solution recorded at 490 nm. Very little Oil Red O was present in any of the samples and no significant differences between samples grown on either polystyrene or any of the gels was seen. The gels became largely clear after the elution step. However, to ensure that all stain was removed from the gels, we repeated the process. Little to no absorbance was recorded in this eluent, suggesting that the low Oil Red O release is not the result of the stain remaining within the hybrid gels. Overall, we can conclude that it is unlikely that significant adipogenesis is observed using any of the conditions tested here.

5.8 Osteogenesis Assays

Having seen no evidence of adipogenesis by Oil Red O assay, we aimed to determine the osteogenic potential of Y201 cells cultured on gels of different stiffnesses. Being unsure of the influence of the gels on the standard assays for osteogenesis, we utilised a range of investigations to determine whether any differences could be observed between the cell 'treatments'.

5.8.1 Alizarin Red S

Y201 cells were again seeded on polystyrene well plates, and a range of gels - DBS-CONHNH₂ (6 mM), 10% hybrid and 20% hybrid – at a density of 10,000 cells mL⁻¹. Cells were cultured for 3 weeks as described for the adipogenesis studies (Section 5.6). After 3 weeks, the cells were fixed and washed, prior to incubation with Alizarin Red S staining solution (40 mM). Alizarin Red S is a deep red dye which has historically been used to dye textiles.⁴¹⁹ More recently it has found use in histology due to its ability to bind multivalent cations, with calcium being of specific interest in this work (Figure 5.22a). On osteogenesis, MSCs begin to deposit calcium in the extracellular environment. Alizarin red stains these calcium deposits through the formation of a salt which possesses a deep red colour. Therefore, cells which show osteogenic potential can be identified using this method.^{420,421}

After Alizarin Red S staining, the samples were washed with PBS, followed by washes in water. As for adipogenic staining, DBS-CONHNH₂ gels which had been seeded with Y201 cells were unable to survive this process. Deep red staining remained in both the test samples (with cultured cells, Figure 5.22b) and in the control samples (Figure 5.22c). This suggests that Alizarin Red S has an affinity for the gel phase in preference to the aqueous phase. Similar observations have been previously reported by Okesola *et. al.*, who showed that dyes with low net charges showed significant uptake into gels from aqueous solution than highly charged dyes. Alizarin Red S has only one anionic charge – on the sulfonate group. Combined with the structural similarities to the water insoluble anthraquinone, it is perhaps unsurprising that this dye demonstrates a preference for the comparatively hydrophobic gel interior.

Practically, the intense staining of the gels made it impossible to determine any differences in osteogenic potential based on optical microscopy (Appendix 15). In general, the 20% hybrid gels appeared to take on a slightly deeper red hue than the 10% hybrid gels. The surviving LMW hydrogel controls were also a deep red, however this is due to the fact that these materials could not be washed as vigorously due to their weak mechanical properties. In contrast to the adipogenic staining, some amount of Alizarin Red stain was retained by cells cultured outside the washer diameter in all cases. This is likely due to small quantities of calcium produced in general in the cells,

rather than being any indication of osteogenesis. Y201 cells treated with osteogenic media over 21 days retain a much greater quantity of Alizarin Red S than the cells seen here.³⁹⁵

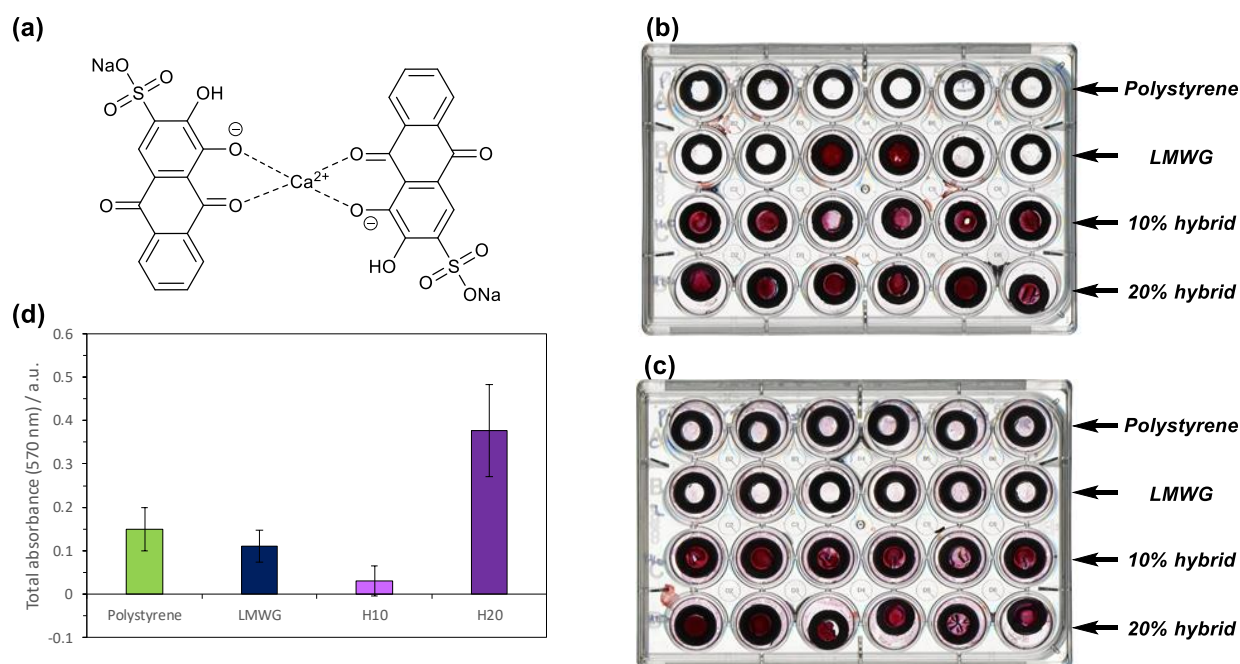


Figure 5.22: Mode of calcium binding by Alizarin Red S (a). Cumulative elution of Alizarin Red S from each cell growth matrix (d) Scanned images of the 24 well plates containing Alizarin Red S stained samples. Controls without cells are shown in (b). Stained test samples with cells cultured for 3 weeks are shown in (c). Values are corrected for staining on control samples where no cells were seeded and against. Errors given as standard deviation ($n = 6$).

For elution of the osteogenesis stain, cetyl pyridinium chloride (CPC, 100 mM) in deionised water (0.5 mL) was applied to each sample and the well plates stirred vigorously over 3 hours. The optical density of the solutions was then recorded at 570 nm to quantify the amount of Alizarin Red in each sample. The remaining LMW hydrogel control samples were broken down during this process and therefore released the total encapsulated stain. In contrast, the hybrid gels still showed distinct coloration, indicative of entrapped Alizarin Red S within the gel networks. The elution process was repeated until no further stain was removed from the gels. The total encapsulated Alizarin Red is given for each of the cell treatments in Figure 5.22d. All values are given as the average of six samples, having been corrected for both the absorbance of CPC solution and the Alizarin Red elution from control samples. As no LMW hydrogels remained in the wells after washing, the polystyrene controls were considered more appropriate for these samples than the stained LMW hydrogels.

No significant differences in the amount of Alizarin Red released from the polystyrene and LMWG-cultured Y201s. Given that the cells adhered to the DBS-CONHNH₂ gels were likely lost along with

the hydrogel during washing, this is not surprising. All cells recorded in the 'LMWG' sample were essentially polystyrene-cultured Y201s. Interestingly, the 10% hybrid gels showed essentially no uptake of Alizarin Red which was not due to partitioning of the dye into the gel phase. These gels are less stiff than those previously reported to induce chondro- or osteogenesis, so this result was, to a degree, expected.^{63,64} In contrast, 20% hybrid gels eluted a much greater amount of Alizarin Red S in samples seeded with cells compared to the control samples. The Alizarin Red S considered to be associated with calcium deposits from cells is therefore significantly greater for the 20% hybrid gel samples compared to cells cultured on polystyrene plates or 10% hybrid gels. This data may therefore indicate some osteogenic potential induced by the gel matrix stiffness – cells were treated with media containing no osteogenic factors. However, given the uptake of Alizarin Red S into all the gel samples, these results must be treated with caution. The errors associated with these readings are quite large, possibly as a result of differences in MSC growth on the materials. An additional consideration though, is that differences in the nature of the gel samples results in different amounts of Alizarin Red elution during the washing step. The quantification of such differences is challenging to quantify and represents a significant study in its own right. Lee and co-workers recently reported the use of an Alizarin Red S staining within a chitosan hydrogel.⁴²² They reported no issues such as the ones faced with the removal of the dye from the gel matrix (and no non-specific staining as seen in the images presented), possibly due to the more hydrophilic nature of the PG used in their material, which would discourage partitioning of the dye into the gel phase.

5.8.2 Wnt reporter cells

To address the limitations of the Alizarin Red staining protocol (in particular the partitioning of the stain into the gel phase) we then chose to utilise histological methods which did not involve staining of cells *in situ*. First, we looked for evidence of endogenous Wnt signalling. Canonical Wnt signalling is initiated by the binding of Wnt ligand to membrane receptors.⁴²³ Through a series of intracellular signals, this activates the genes which promote osteogenesis. Therefore, intercepting a step in the Wnt signalling cascade can provide indirect evidence for the formation of osteoblasts.^{424–426}

For this study, we used a line of Y201 cells that express enhanced green fluorescent protein (EGFP) in response to activation of transcription factors implicated in the Wnt signalling pathway.⁴²⁷ These cells (referred to as Y201 Wnt reporters in this chapter) show dose-dependent fluorescence in the presence of Wnt. Y201 Wnt reporters were seeded onto polystyrene well plates, and DBS-CONHNH₂ (6 mM), 10% hybrid and 20% hybrid gels at a seeding density of 10,000 cells mL⁻¹. Control samples incubated with media in the absence of cells were also prepared. The samples were left for 2 weeks, after which time, half were treated with Wnt3a protein at a concentration of 300 ng mL⁻¹. This treatment provides a positive control for Wnt response to compare against the untreated cells.

Cells were incubated for a further 24 h after treatment, after which time they were lysed by addition of surfactant and freeze/thaw cycling. This lysing step breaks down the cell membrane, releasing the contents of the cell into solution. Aliquots of the lysis solution transferred to a 96-well plate with black surfaces for fluorescence readings. The LMW hydrogels again broke down during the lysis process, however, given that the contents of the cell interior were being analysed in this case, this was not considered to have a significant effect on the assay results. Further aliquots were taken for analysis of total protein content by BCA assay (see Section 5.5) and fluorescence was normalised against this value.

Cells treated with Wnt3a showed high fluorescence intensity in all cases, indicating that EGFP was expressed in the presence of Wnt. Much lower fluorescence intensities were observed for untreated cells (Figure 5.23) and little to no fluorescence was observed in the control samples as expected. Interestingly, when expressed as the fluorescence per unit of protein (used here as a proxy for the number of cells in the sample), cells cultured on the polystyrene plate were seen to produce the greatest quantity of EGFP. This trend held for both the treated and untreated cells, but was much more significant for the Wnt-treated samples. Little difference was observed between the EGFP expression of cells cultured on the different types of hydrogel. It is unclear at this time why the Y201 Wnt reporters are more fluorescent when cultured on the polystyrene well rather than on the gels. Recent literature has highlighted the role of surface topography on the regulation of Wnt signalling pathways.^{391,428} This may be playing a role here.

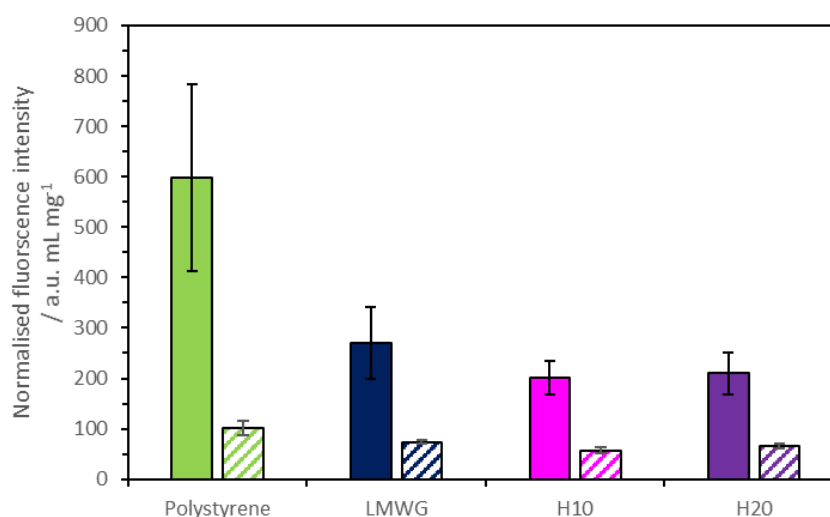


Figure 5.23: Fluorescence intensity normalised against total sample protein content for cells cultured on four different matrices. Solid bars represent fluorescence from Wnt-3a treated positive controls for fluorescence, whilst striped bars represent fluorescence from the untreated test samples. Errors given as standard deviation (n = 6).

Given the data above it can be considered that none of the gels show any significant osteogenic activation through the canonical Wnt signalling pathway. However, if correcting the data to compare the amount of EGFP expressed by the untreated materials relative to that induced by Wnt, the data appear very different. The untreated cells seeded onto polystyrene plates only express 17% of the amount of EGFP seen for those treated with Wnt. In contrast, DBS-CONHNH₂, 10% hybrid and 20% hybrid gels expressed 27, 28 and 31% of their 'potential' EGFP respectively. The total protein recorded by BCA for the treated and untreated samples were very similar in all cases. This observation is therefore not an effect of enhanced MSC proliferation after Wnt treatment. The errors associated with these values are relatively small in most cases, likely highlighting the influence of the washing procedures on the results of the Alizarin Red and Oil Red O elution studies.

The data are clearly quite complex, and a number of contributing factors may influence the expression of EGFP in the samples. Additionally, there is currently a lack of consensus among the MSC community as to the role of Wnt signalling in 2D MSC differentiation. Genever and co-workers found that MSC monolayers which were stimulated to undergo osteogenesis did not show any increase in EGFP expression during the process.⁴²⁷ In contrast, Benoit and Oh have both in recent years showed that stimulation of the canonical Wnt pathway led to enhanced osteogenic capability in 2D cultures.^{429,430}

5.8.3 Alkaline phosphatase

Given the complexity of the Wnt reporter system, we returned to the assessment of osteoblast formation using a simpler assay. Alkaline phosphatase (ALP, see Chapter 4) is a homodimeric enzyme that is expressed in greater quantities in osteoblasts than either adipocytes or chondrocytes.⁴³¹ For MSCs, ALP is therefore a useful marker by which differentiation can be assessed.^{307,432}

Y201 cells were seeded as described in Section 5.7.1, at a density of 10,000 cells mL⁻¹. Samples were incubated for 3 weeks, after which time the cells were lysed as described in Section 5.7.2. Aliquots of the lysed cells were taken for a BCA assay to determine the total protein in each experiment. A sample of the lysis buffer was removed and diluted with *para*-nitrophenylphosphate (*p*NPP) solution (1 mM) and incubated for 1 h at 37 °C. A yellow colour developed in the samples due to the hydrolysis of *p*NPP by ALP, which forms *para*-nitrophenol (*p*NP), a strong chromophore in basic solution. The absorbance of these samples was measured at 405 nm and compared to a calibration curve to calculate *p*NP concentration in each sample. A greater absorbance at 405 nm indicates the more rapid hydrolysis of *p*NPP, in turn indicating elevated levels of ALP, which can be considered a sign of osteogenesis. Control samples with no cells were prepared for comparison. As described for

the Wnt reporter cells, given that total lysis of the cells has occurred, LMW hydrogel breakdown during the freeze-thaw cycle is not considered to have a significant impact on the results.

All the samples showed relatively similar concentration of *p*NP after 1 h incubation. However, when normalised for total protein (Figure 5.24), it was seen that Y201 cells cultured on the 20% hybrid gels express significantly greater amounts of ALP ($12 \pm 1.2 \times 10^{-4} \mu\text{mol mg}^{-1}$) than cells grown on the polystyrene well plates, or the LMW or hybrid hydrogels (*ca.* $7 \times 10^{-4} \mu\text{mol mg}^{-1}$). This data is in agreement with the observations from the Alizarin Red S assay above (Section 5.7.1) and indicates that the osteogenic potential of MSCs grown on the stiffest of the gel matrices studied here is comparatively high.

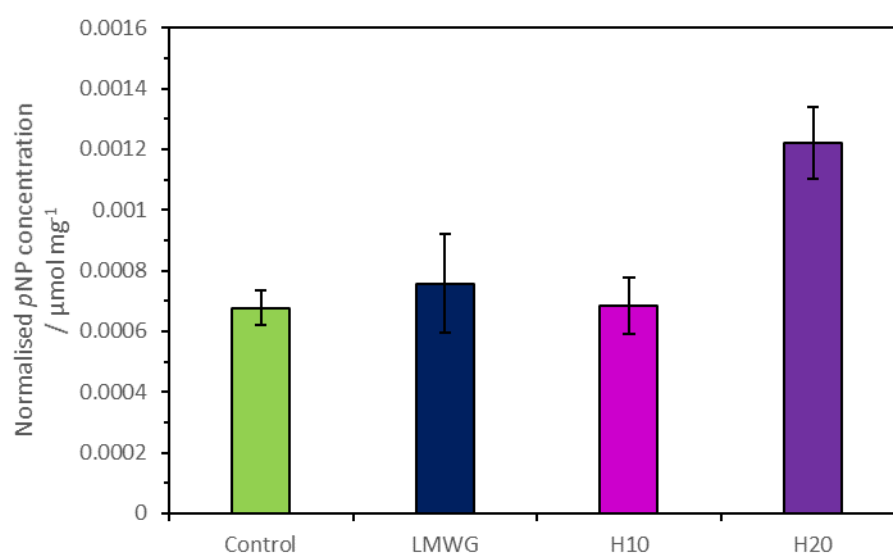


Figure 5.24: ALP content normalised against total protein for samples cultured on different matrices. Errors given as standard deviation ($n = 6$).

Unfortunately, the exact values reported here cannot be compared directly to literature values, where the concentration of *p*NP is usually normalised against DNA concentration. However, for the same cell type, Genever and co-workers showed that cells which underwent osteogenesis displayed a much greater increase in *p*NP concentration per unit DNA than the increase observed here.³⁹⁵ However it must be considered that in this work, no osteogenic factors are being used to help induce differentiation – the differences observed are solely caused by the properties of the gel matrix on which the cells are grown. Additionally, as in the Alizarin Red assay, the contents of the entire well plate were lysed and a sample of these contents were taken for assaying, including those not directly attached to the gel surface. If only the cells adhered to the gels were sampled, the difference in *p*NP concentration (and therefore in cell ALP content) would likely be amplified. As for

the Wnt reporter assay, the errors in this study are relatively small, and can likely be largely accounted for by biological variability. In the case of studies of cell growth on gels, lysing the whole population of a well appears to lead to more reproducible results than protocols requiring staining and washing steps. We propose that these kinds of assays may prove more useful for the study of gels as biomaterials by minimising the influence of the supporting matrix.

The preliminary studies outlined here indicate that 20% hybrid gels may induce osteogenesis in Y201 MSCs in the absence of any chemical or biological stimuli. Importantly, these effects are solely due to the interactions between MSCs and the gel matrix. Whilst these results are promising, they also highlight the importance of assay selection in gathering meaningful data from these experiments. Unlike simple monolayer cultures seeded on polystyrene well plates, the gel matrices may not be passive bystanders in the assay protocol. For this reason, we propose that further histological examinations of the cultured cells are necessary future work, both to optimise the materials for the direction of differentiation, and to understand the chemical and biological processes governing these changes. For example, quantitative polymerase chain reaction (qPCR) and flow cytometry would yield information on gene expression and physicochemical characteristics of the cultured cells.

It is also important that the results outlined here are verified by comparison to a range of other gel-phase materials with known stiffnesses to help determine whether or not the differences in differentiation potential are solely the result of differences in matrix stiffness, or whether surface topology/chemistry are also playing a role. These factors have been shown to play a significant role in the determination of stem cell fate, although findings are inconsistent between studies and materials used.^{337,433,434}

We could assess the impact of such effects on the differentiation observed in this work using, for example, gels prepared by combining PEGDM with a range of other LMW hydrogelators (such as the amino acid-based materials outlined in Section 5.1.2). Materials of comparable stiffness to those used in this research could be prepared, but with significantly altered chemical adhesion properties, could be used to elucidate the specific effects of the two individual gel networks on MSC behaviour. Additionally, comparison of the assay results with those of MSCs which have been cultured in osteogenic media is important to quantify the extent to which the hydrogels here are influencing MSC differentiation.

5.9 Photo-patterned gels for spatially-resolved stem cell properties

Having assessed the adherence, proliferation and differentiation of MSCs on a range of gels, we then returned to the chapter aim set out in Section 5.2. Given that the 20% hybrid gels appear to induce osteogenesis, whilst the DBS-CONH₂ gels do not, we aimed to create photo-patterned gels in which the growth of cells in different domains of soft (non-crosslinked PG network) and stiff (crosslinked PG network) may be significantly different.

An optimised method for photo-patterning of hybrid gels formed in washers at the bottom of a 24-well plate was developed. Briefly, hybrid gels were prepared as outlined previously in this chapter. However, rather than exposing the whole well plate to UV irradiation, half the gel was shielded using a photomask. To ensure sterility of the gels, masks were applied on the outside of the well plates, which remained sealed throughout the patterning process. Samples in which the mask was placed on the lid of the well plate showed poor patterning resolution due to the distance between the mask and the surface of the gel (*ca.* 15 mm). Therefore, the plates were inverted, and a photomask applied to the bottom of the well plate (Figure 5.25). In this way, excellent patterning resolution, even using the 50 μ L gels (diameter = 6 mm) was achieved. A UV exposure time of 20 minutes was found to be optimal, allowing time for PG crosslinking, but preventing loss of pattern fidelity.

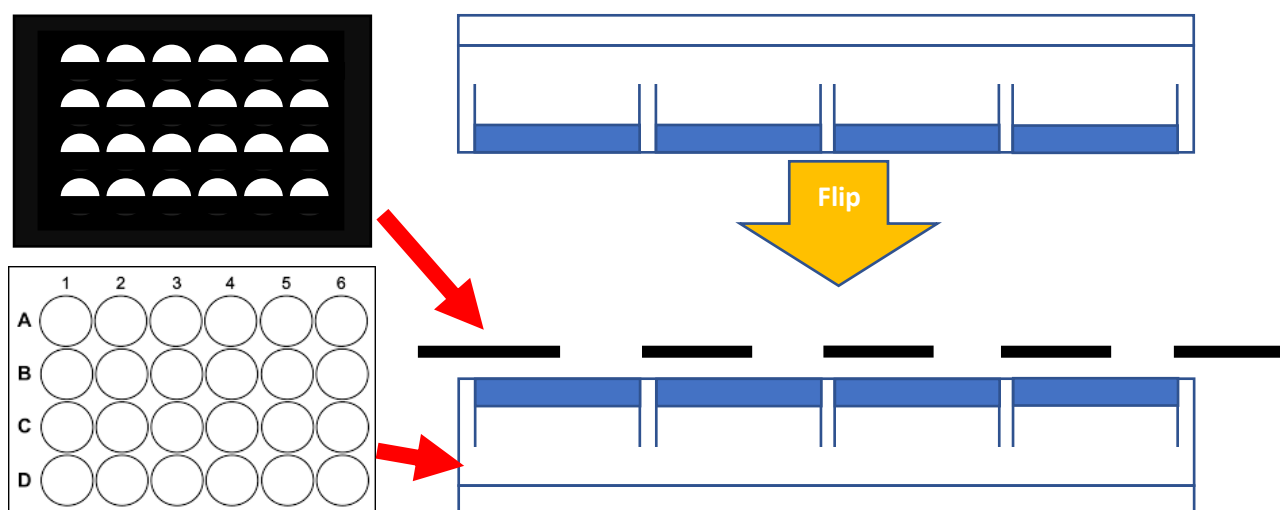


Figure 5.25: Cartoon representation of photopatterning of gels in well plates. Gels are formed in the well plates. The plate is turned upside down and a photomask placed over the top such that half of each well is shielded from UV irradiation. Gels are then irradiated with long wavelength UV light for 20 min.

In this way, 20% hybrid gel regions were patterned into a pre-existing LMWG matrix. A simple ‘half-half’ pattern was used at this stage for simplicity. The patterned gels were washed and Y201 XGreen

cells were seeded at a density of $10,000 \text{ cells mL}^{-1}$. However, after *ca.* 24 h, breakdown of the soft, non-crosslinked region of the gel was observed. This was considered to be the results of swelling of the hybrid gel portion of the matrix (Section 5.5), which would weaken the soft LMW hydrogel region sufficiently to break down under very slight strain.

Therefore, we adapted the procedure for the preparation of multidomain gels. Patterned 20% hybrid gels were prepared as described above. However, after the patterning and washing procedure, the gels were incubated in media overnight to complete swelling. Any remaining 'soft', non-hybridised regions of the gels were removed, and the resulting gaps in the washers replaced with new DBS-CONH₂ hydrogel. Y201 XGreen cells were seeded on the patterned gels at a density of $10,000 \text{ cells mL}^{-1}$ and the samples incubated for 2 weeks. Fluorescence microscopy showed that the morphology of the MSCs after this time was significantly different on the two halves of the gel (Figure 5.26). A difference in the density of the cells was seen between the two halves at the interface after this time, indicating that differences in MSC growth can be influenced with spatial control. The observed differences may be because after two weeks, the MSCs have not fully committed to a specific lineage, and are able to change their morphology in response to the

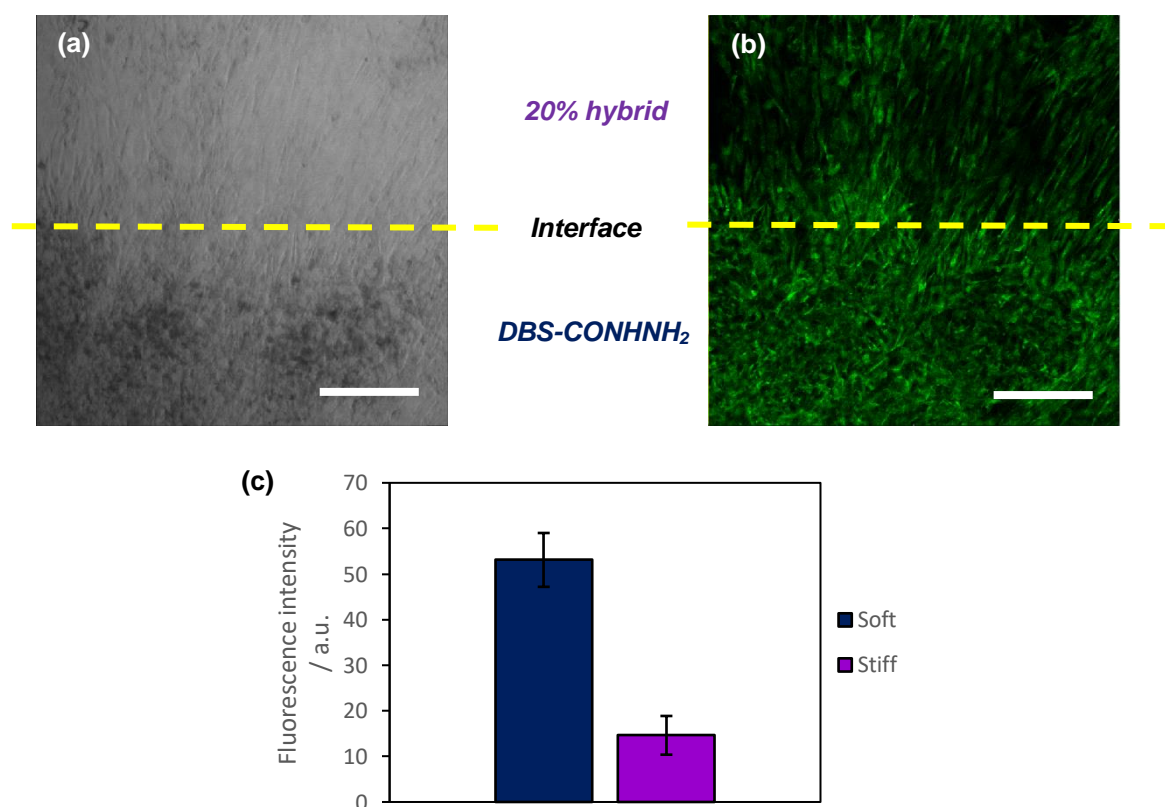


Figure 5.26: Brightfield (a) and fluorescent (b) images of cells growing at the interface of 'stiff' hybrid gel (top half) and 'soft' LMW hydrogel (bottom half) after 2 weeks. The yellow dashed lines guide the eye as to the location of the interface. Scale bars = $500 \mu\text{m}$. Average fluorescence intensity from the 'stiff' and 'soft' regions of the multi-domain gels (c). Errors given as standard deviation ($n = 3$).

changes in the matrix stiffness they experience.⁶³ Additionally, given that the whole gel sample was submerged in PEGDM solution prior to photo-patterning, this suggests that the influence of any residual DCM from the gelator synthesis may play a minimal role in limiting MSC growth – unless it is entrapped specifically within the crosslinked regions of the hybrid gel.

Assuming no differences in the fluorescence intensity of the cells on each side of the interface, the average brightness of the image in the soft and stiff regions was measured as a proxy for Y201 XGreen cell density (Fig. 5.26c). On average, the recorded fluorescence intensity was significantly (*ca.* 3.5 times) greater from the soft regions of the multi-domain gels than from the stiff regions – an effect which was reproducible across a number of samples. These trends in Y201 proliferation are consistent with those seen on the LMW and 20% hybrid hydrogels reported earlier in the chapter (Section 5.6). Given that the MSC behaviour observed here is similar to that on the individual gels (with no differences in stiffness across the gel), this suggests that over a longer timescale, matrix-dependent – and spatially-resolved - MSC differentiation may also be observed on these photo-patterned gels.

5.10 Conclusions

In this chapter we have reported preliminary studies aimed at the development of hybrid and multidomain gels for the spatial control of MSC behaviour. We have demonstrated the biocompatibility of DBS-CONH₂, 10% and 20% hybrid gels with an immortalised human stem cell line. The presence of both components of the hybrid gel – DBS-CONH₂ and PEGDM – are essential for the development of appropriate cell culture matrices. DBS-CONH₂ gels show excellent biocompatibility and cell adhesion properties, but broke down over time in the presence of growing cells. On the other hand, MSCs showed no adherence to the robust PEGDM matrix over 7 days. Therefore, both of the networks in the hybrid gel play a crucial role in mitigating the drawbacks of the other network.

Observation of MSC growth over the course of a month indicated that the gel matrix on which the cells were cultured could have a profound impact on their behaviour. On DBS-CONH₂ gels, the MSCs were more spread out and appeared to migrate through the gel matrix over time. In contrast, cells cultured on hybrid gels formed more dense superstructures on the surface of the gels. Preliminary studies suggest that this difference in behaviour may be indicative of differences in the osteogenic potential of MSCs cultured on the gels of different stiffnesses. In particular, the 20% hybrid gel showed greater ALP expression and calcium deposition, suggesting some formation of osteoblasts over 3 weeks. The stiffness of this gel (8 kPa) is lower than others previously reported

to induce osteogenesis. Preliminary experiments to demonstrate the use of spatially-resolved gels to induce spatially-resolved stem cell behaviour show different cell morphologies on a gel patterned with soft and stiff domains.

Overall, the hydrogels developed in this thesis appear to be promising candidates for tissue engineering applications, in particular with regards to the spatial control of MSC differentiation. Future work with these materials will likely focus on the development of materials to induce spatially-resolved differentiation and analytical methods to prove that this is indeed the case, in addition to comparison of differentiation potential with materials which have known stem cell directing properties. To overcome the limitations of the LMW hydrogel weakness, gradient patterning of hybrid gels could also be explored. Rather than total exclusion of UV light from a region of the gel, controlled exposure in different regions could be used to modify the crosslinking density, and therefore the stiffness, of different regions of the gel. Gradient biomaterials are of significant interest in tissue engineering for the creation of complex materials mimicking the stiffness gradients in the body.⁴³⁵ However, this area remains almost completely unexplored for LMWG-based materials. We have carried out limited preliminary studies in this area using large-scale (10 mL) gels. Using a mask with a gradient pattern, small differences in stiffness were observed between the 'most' and 'least' exposed regions of the gel after UV-irradiation for 10 minutes (Figure 5.27). Clearly, significant optimisation is required for these gradient patterns to demonstrate sufficient differences in stiffness (and sufficient patterning resolution) to be useful for control of MSC differentiation. Developing these patterned materials and demonstrating their applications as tissue engineering matrices are key aims of future work in this area.

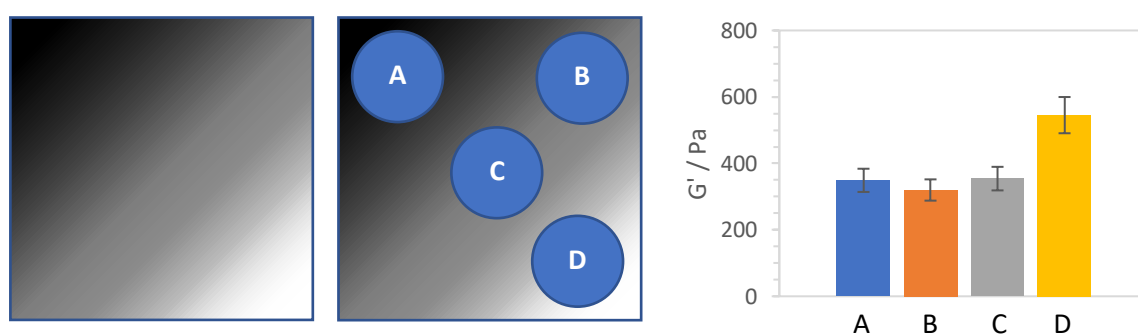


Figure 5.27: Gradient patterning mask (left). Increasingly light regions of the mask (moving from top-left to bottom-right) should allow greater UV penetration and PG crosslinking, resulting in greater gel stiffness. Sampling pattern for rheology is given in (middle). Storage modulus (G') of the gels sampled from each region of the gel (right). Errors given as standard deviation ($n = 3$).

6 Conclusions and Future Work

In this project, we aimed to develop a photo-patternable hybrid hydrogel comprising two orthogonal gel networks; a responsive LMWG network and a robust PG network. By incorporating a PG which underwent crosslinking in response to UV irradiation, it was thought that shaped materials which demonstrated the properties of both networks could be fabricated. In addition to studying the assembly of such hybrid gels, the potential for these materials to intervene in high-tech applications was to be explored. Specifically, in this thesis we aimed to demonstrate in 'proof-of-principle' studies that these gels may represent a suitable underpinning technology with potential for further development as materials with applications in: (i) drug delivery, (ii) enzyme reactors and (iii) tissue engineering.

6.1 Fabrication and characterisation of hybrid hydrogels

In Chapter 2 we investigated the possibility of forming hybrid hydrogels by combining the commercially relevant LMWG DBS-CONH₂ with the biocompatible PG PEGDM. By employing a sequential assembly approach - in which a heat/cool cycle first induces formation of the DBS-CONH₂ network prior to addition and UV-initiated crosslinking of PEGDM monomers - orthogonal assembly of the two gel networks was achieved. SEM images of the nanoscale structure of the hybrid gels showed evidence of networks associated with both DBS-CONH₂ and PEGDM. The two networks appeared to somewhat aggregate along each other. IR spectroscopy indicated that the two networks do interact with each other to some extent.

The mechanical properties of the hybrid hydrogels could be tuned by varying the loading of PG in the materials. The stiffness of these materials increased with PEGDM content. However, the DBS-CONH₂ network is not passive in rheological terms. The hybrid gel shows an increased resistance to high frequency oscillations compared to PEGDM gels alone. As seen in Chapter 4, altering the PEGDM content of the hybrid gels also has a significant influence on the porosity of the hybrid gels. Increasing concentrations of PEGDM slowed the diffusion of fluorescent molecules between 300 and 70,000 Da in mass. The DBS-CONH₂ network also modifies the diffusion rate of certain species through interactions between the nanoscale network. This indicated that DBS-CONH₂ retains its properties within the hybrid gel structure.

Spatial control of PEGDM crosslinking, and therefore gel stiffening, was achieved by shielding regions of the gel from UV light during irradiation. Using laser printed acetate photomasks, two-dimensional hybrid gel patterns could be written into a soft DBS-CONH₂ gel. Importantly, in the absence of the DBS-CONH₂ supporting network, no spatial control of the crosslinking process

could be imposed, highlighting the importance of both gel networks in determining the properties of this material.

6.2 Drug delivery

In Chapter 3, the potential of these hybrid gels for controlled drug release was investigated. NPX, a model drug used in this study, was encapsulated in the hybrid gels in an equimolar ratio with DBS-CONHNH₂. IR and NMR spectroscopy showed that, when protonated, NPX interacts strongly with DBS-CONHNH₂ fibres *via* the carboxylic acid group. However, in the presence of the PEGDM network, these interactions are slightly weakened. This suggests that there is a degree of competition for the acyl hydrazide groups of the LMWG nanofibres, and is consistent with the finding in Chapter 2 that non-covalent interactions exist between the LMWG and PG networks. NPX was not found to have any interactions with the PEGDM network.

DBS-CONHNH₂ hydrogels released NPX in a pH-dependent manner. At pH values below the pK_a of NPX (4.15), little drug release was observed. In contrast, almost all of the encapsulated NPX was released quickly into neutral or alkaline buffer solution. We suggest that at elevated pH values, deprotonation of NPX disrupts the drug:LMWG interactions and allows rapid release into solution. Hybrid gels containing NPX also demonstrated pH-dependent drug release properties. Again, slower release into acidic buffer was observed, although the difference in release was smaller than that of the LMW hydrogel. Therefore, DBS-CONHNH₂ largely retains its interactivity when formulated in a dual-network hybrid gel. In contrast, PEGDM hydrogels released NPX at an equal rate independent of the pH of the receiving solution, a result consistent with the lack of specific interactions with the drug molecules.

Photo-patterned hybrid gels were then used to demonstrate spatial control over drug release. An NPX-loaded hybrid gel band was exposed to solutions of different pH on each side. The gel released the drug into a compartment pH 7 buffer at a significantly greater rate than into a pH 2.8 compartment. This is significant as it represents the first example of differential release from a gel which does not require modification of one surface or the application of a strong magnetic field. In this example, the differential release is an equilibrium-controlled process. Coupling this differential release to a second process, such as an enzymatic reaction, could move them away from equilibrium – this is of key interest in future work.

The importance of the two individual networks is clear for this application. DBS-CONHNH₂ nanofibres enable controlled release in the presence of a stimulus, whilst the PEGDM network provides robustness to withstand oral ingestion, and the ability to make shaped materials for

implantation. For significant impact, future work on differential release could focus on the delivery of drugs which have significant side effects, for example chemotherapeutic agents. The development of new hybrid gels which can respond to biologically relevant stimuli are essential for these materials to progress towards *in vivo* applications. It can be envisaged that a shaped, hybrid gel implant which directs release towards tissue exhibiting a certain stimulus may have significant potential in a medicinal setting.

6.3 Enzyme bioreactors

Studies aimed at determining the relative permeability of the gels revealed that both the LMW and hybrid hydrogels effectively excluded large compounds of high molecular weight, whilst allowing diffusion of relatively small molecules through the porous matrix. Varying the PEGDM concentration allowed tuning of the diffusion process, with higher PG density preventing the diffusion of increasingly small molecular species. These findings prompted us to explore the possibility of encapsulating enzymes within the gels developed in this research. Alkaline phosphatase (ALP) was incorporated into LMWG, PG and hybrid hydrogels and its retained activity in the hydrolysis of *p*NPP (to form *p*NP) was demonstrated.

Photo-patterned hybrid gel reactors, comprising a central reactant compartment, a ring of ALP-loaded gel and an outer product compartment were fabricated. These were designed such that to reach the product compartment, *p*NPP must diffuse through the bioactive gel layer, forcing reaction. In an unoptimised system, 67% conversion of *p*NPP was achieved over 5 h. However, the majority of the *p*NP partitioned into the gel phase, preventing easy product retrieval.

A second reactor mode was designed in which a densely crosslinked hybrid gel framework directs the diffusion of small molecules through a LMW hydrogel channels. A range of conditions were screened to maximise diffusion of fluorescein and methylene blue dyes through the soft gel channels. A simple reactor was then designed to direct the diffusion of *p*NPP through an ALP-loaded LMW hydrogel channel. Spatial control of *p*NP formation was demonstrated, however partitioning of reaction products into the gel phase remained an issue.

Future work in this area will focus on the identification of more suitable enzymes or reactions for use in photo-patterned hybrid gel bioreactors. Acid phosphatase, which also catalysed *p*NPP hydrolysis, operates under acidic conditions which may minimise product uptake by the hybrid gel.³²³ Longer term future work will focus on the development of multi-step bioreactor through encapsulation of different enzymes in multiple gel barriers. The recently reported activity of palladium nanoparticle-loaded DBS-CONHNH₂ gels could also be utilised in such reactors.

6.4 Tissue engineering

Stem cell growth and differentiation can be directed by the properties of the matrix on which they are grown. To achieve complex tissue growth, such materials must be able to direct stem cell growth with spatiotemporal control. Such resolution has been achieved for limited numbers of PG systems,^{155,350,436} but no such example has yet been reported for LMW hydrogels.

In Chapter 5 we described our preliminary work towards this goal. Using an immortalised line of tripotent mesenchymal stem cells (MSCs), we demonstrated that DBS-CONH₂ is a biocompatible matrix for cell growth, in agreement with a previous report from Smith and co-workers. In contrast, MSCs showed no adherence on PEGDM hydrogels, whilst the compatibility of hybrid hydrogels was determined by the quantity of PEGDM. Cells cultured on LMW hydrogels appeared different to those grown on hybrid gels. MSCs grown on the soft material appeared more disperse, and migration through the gel was evident. In contrast, on hybrid gels denser cell growth was seen. In addition, MSCs cultured on a photo-patterned hybrid gel adopted different morphologies in the soft regions compared to the stiffer, crosslinked domains.

Preliminary histological analysis suggests that cells cultured on stiff hybrid gels ($G' \approx 8$ kPa) differentiate down an osteogenic lineage in basal media (with no osteogenic factors). Cells cultured on these gels appeared to deposit more calcium and contained greater levels of ALP, both markers of osteoblast formation.^{420,421,431} Cells grown on softer gels ($G' ca. 1 - 4$ kPa) showed no signs of adipogenesis by Oil Red O staining.

The promising preliminary results reported in this thesis suggest that photo-patterned hybrid hydrogels may be able to direct MSC differentiation with spatial control. Continued efforts towards this goal require, initially, a more thorough histological analysis of MSC differentiation on the different hydrogels in the absence of directing factors. Techniques such as qPCR and flow cytometry may be used to determine the gene expression and cell markers of these cells for example. The relative influence of matrix stiffness on stem cell fate could also be studied by culturing MSCs on gels in either osteogenic or adipogenic media. Co-polymerisation of PEGDM with cell adhesion moieties such as Arg-Gly-Asp, has been shown to improve the cytocompatibility of PEG hydrogels.^{36,437,438} Adopting a similar approach in this work may endow hybrid gels of greater PEGDM loading (and hence stiffness) with greater biocompatibility than those reported in this study.

6.5 Summary

In summary, the work reported in this thesis described the development of a robust yet responsive hybrid gel which has shown promise in a range of biological applications. In all the studies reported

herein, functionality not accessible with either of the individual components was demonstrated in the dual-network gels. The tuneability and versatility demonstrated by these gels highlights the utility of a LMWG/PG hybrid approach for the development of shaped, functional gel-phase materials.

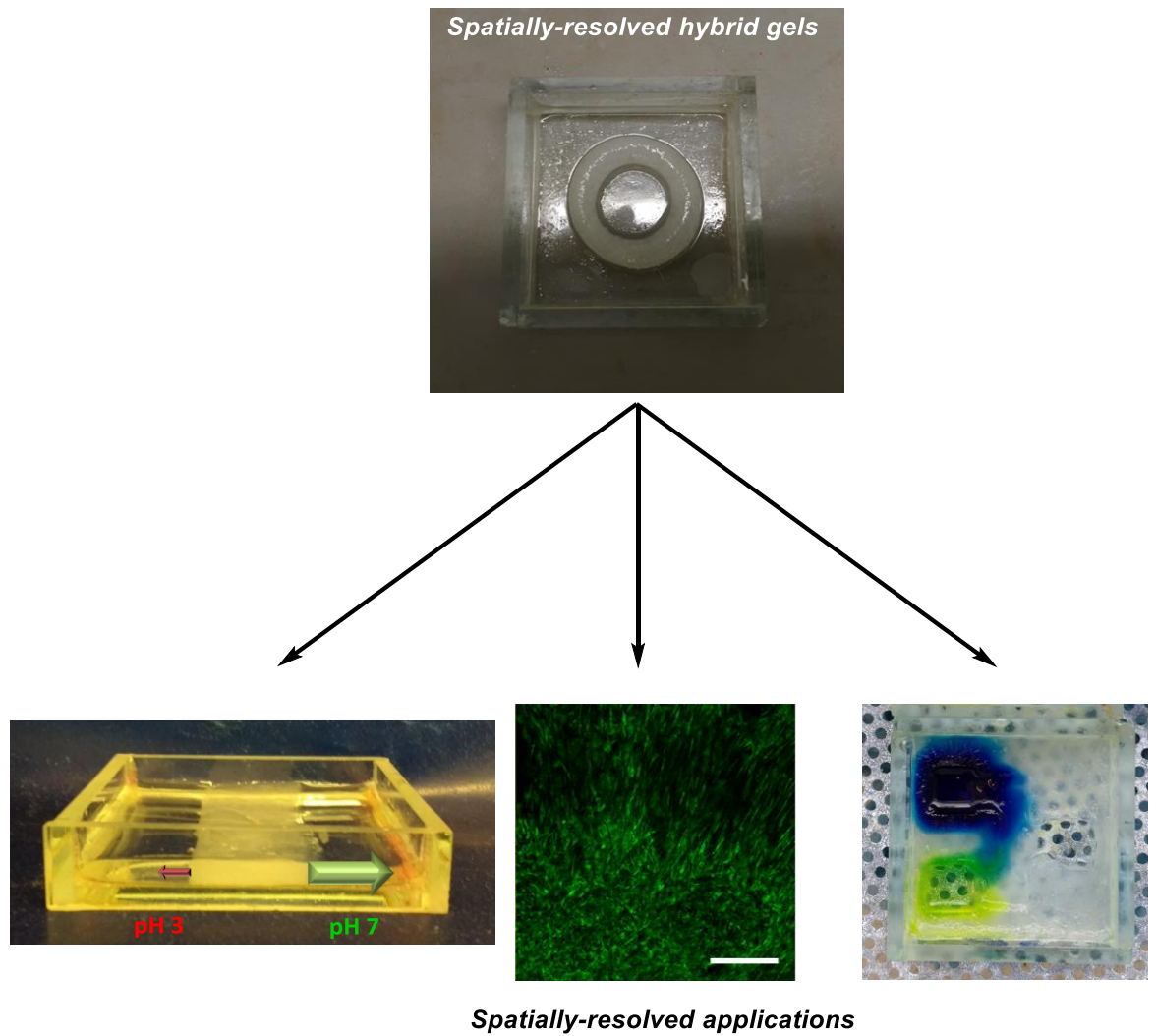


Figure 6.1: *Spatially-resolved hybrid hydrogels have been shown to have potential applications for differential release (left), spatially-controlled tissue engineering (middle) and spatially-resolved bioreactors (right).*

7 Experimental

7.1 General Experimental Methods

All compounds required for synthesis and analysis were purchased from standard chemical suppliers and were used without further purification. Proton and carbon NMR spectra were recorded on a Jeol ECX 400 spectrometer (^1H 400 MHz, ^{13}C 100 MHz). Samples were recorded as solutions in deuterated NMR solvents as stated. Chemical shifts (δ) are quoted in parts per million and coupling constants (J) are given in Hz. NMR assignment was achieved using model compounds, literature data and standard knowledge of NMR assignment and was assisted using 2D NMR experiments. DEPT experiments were undertaken to assist in assignment of the ^{13}C NMR spectra. Positive ion ESI and MALDI mass spectra were recorded on a Bruker solariX FTMS 9.4T mass spectrometer. ATR-FTIR spectra were recorded on a PerkinElmer Spectrum Two FT-IR spectrometer. Melting points were measured on a Stuart SMP3 melting point apparatus and are uncorrected. Transparent glass screw-capped vials (2.5 or 8.5 mL) were used in the preparation of gels. T_{gel} values were recorded using a high precision thermoregulated oil bath. Rheological measurements were recorded using a Malvern Instruments Kinexus Pro+ rheometer fitted with a parallel plate geometry and data were processed using rSpace software. Circular dichroism spectra were recorded on a Jasco J810 CD spectrophotometer fitted with a Peltier temperature controller, using a quartz cell with a path length of 1 mm and using the following settings: Data pitch 0.5 nm, Scanning mode = continuous, Scanning speed = 1 nm min⁻¹, Response = 1 s, Accumulation = 5, Bandwidth = 2 nm, Temperature = 20 °C. SEM was carried out on freeze-dried samples sputtered with gold/palladium on a JEOL JSM-7600F FEG-SEM. Microscope parameters are provided alongside the corresponding image. Images were collected by Meg Stark at the Biology Technology Facility at the University of York. UV-vis absorbance spectroscopy was recorded on Shimadzu UV-2401 PC and Shimadzu UV-1800 spectrophotometers. Fluorescence spectroscopy was recorded on a Hitachi F-4500 fluorimeter, with emission and excitation slit widths both set to 2.5 nm. pH readings were carried out using a Hanna Instruments Checker[®] pH Tester HI98103, calibrated using buffer solutions to pH 7 and either pH 4 or 10, depending on the target pH of the test solution. Analysis of gel pattern dimensions was performed in ImageJ. Gel nanofibre diameters were calculated in ImageJ using the DiameterJ plugin.

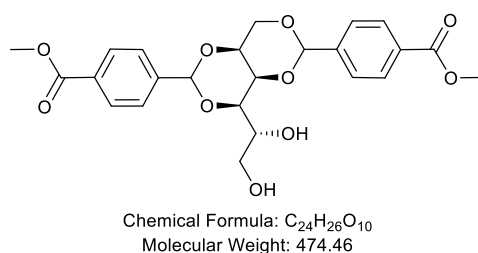
For biological studies, all reagents were purchased from standard suppliers. Cryo-preserved cells were revived from a solution of 10% DMSO in foetal bovine serum into cell growth medium. Y201 XRed and XGreen cells were expanded in T75 flasks, whilst Y201 and Y201 Wnt Reporter cells were expanded in T175 flasks. All cells were cultured in Dulbecco's Modified Eagle's Medium (supplemented with pyruvate and 4.5 g L⁻¹ D-glucose and L-glutamine), 10% foetal bovine serum

and 1% penicillin/streptomycin. Cell growth medium was changed every 3-4 days. Cells were passaged upon reaching 80-90% confluency. All cells were incubated at 37 °C in an atmosphere of 5% CO₂ and 95% relative humidity. Cells were routinely checked for mycoplasma infections using a standard protocol: Cells were washed with PBS, fixed with methanol, then washed again. Fixed cells were then incubated at room temperature in the dark with 4',6-diamidino-2-phenylindole (DAPI). DAPI was removed and the cells washed again with PBS before observation under a fluorescent microscope (Zeiss Invert 880).

7.2 Chapter 2

7.2.1 Synthetic procedures

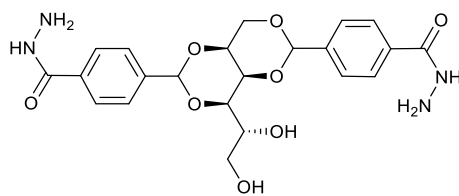
7.2.1.1 Synthesis of DBS-CO₂Me



The synthesis of DBS-CO₂Me was carried out as described in the literature.¹⁴³ D-Sorbitol (4.90 g, 26.90 mmol, 95% purity, VWR) was weighed into a 3-neck round bottom flask fitted with Dean-Stark apparatus. Cyclohexane (35 mL) and methanol (10 mL) were added and the mixture was stirred under N₂ at 50 °C for 20 min. 4-Methylformylbenzoate (7.50 g, 45.69 mmol, 98.5% purity, Alfa Aesar) and *p*-toluenesulfonic acid hydrate (1.00 g, 5.80 mmol, 99% purity, Acros Organics) were dissolved in methanol (20 mL) and stirred for 20 min at room temperature and added dropwise to the reaction mixture. The reaction temperature was raised to 70 °C and the mixture stirred for a further 2 h, topping up with 1:1 cyclohexane:methanol as required. The white paste formed was washed with methanol (3 × 100 mL) before drying under high vacuum for 2 h. The crude product was washed further with boiling water (5 × 100 mL) and boiling DCM (3 × 100 mL) to remove mono- and tri- substituted derivatives respectively. The clean product was dried *in vacuo*. Yield 8.00 g (74%). M.p: 209-215 °C; lit. 210-213 °C.¹⁴³ ¹H NMR (400 MHz, DMSO-*d*₆): δ 8.00 (2H, d, *J*=8 Hz, Ar-*H*), 7.97 (2H, d, *J*=8 Hz, Ar-*H*), 7.62 (2H, d, *J*=8 Hz, Ar-*H*), 7.59 (2H, d, *J*=8 Hz, Ar-*H*), 5.76 (s, Ar-CH, 2H), 4.93 (d, CH-OH, *J*=6 Hz, 1H), 4.47 (br, CH₂OH, 1H), 4.24 (1H, dd, *J*=2,13 Hz, COCHH'), 4.22 (1H, dd, *J*=2,9 Hz, CHCHCH), 4.18 (1H, dd, *J*=2,13 Hz, COCHH'), 4.01 (1H, br., CH₂CH(O)CH), 3.89 (1H, dd,

$J=2,9$ Hz, CHCHCHOH), 3.85 (6H, s, CH_3), 3.79 (1H, br, CHOH), 3.62 (1H, br. d, $J=12$ Hz, CHH' OH), 3.47 (1H, br. d, CHH' OH). ^{13}C NMR (100 MHz, DMSO- d_6): 166.01 (COO), 143.34 (aromatic p -C), 143.07 (aromatic p -C), 129.77 (aromatic o -C), 129.72 (aromatic o -C), 129.04 (aromatic, m -H), 128.95 (aromatic, m -H), 126.51 (aromatic, m -H), 98.53 (Ph-C), 98.45 (Ph-C), 77.58 (CH), 70.18 (CH), 69.31 (CH_2), 68.53 (CH), 67.58 (CH), 62.56 (CH_2), 52.21 (CH_3). ν_{max} (cm^{-1}): 3251w, 2956w, 1983w, 1724s, 1276s, 1093s, 1018s, 854m, 750s. ESI-MS (m/z) calc. for $C_{24}H_{26}O_{10}Na$ 497.1424; found 497.1424 (100% $[M+Na]^+$). Spectra given in Appendix 1.

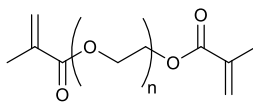
7.2.1.2 Synthesis of DBS-CONHNH₂



Chemical Formula: $C_{22}H_{26}N_4O_8$
Exact Mass: 474.18

The synthesis of DBS-CONHNH₂ was carried out as described in the literature. DBS-CO₂Me (1.10 g, 2.32 mmol) was weighed into a round-bottomed flask and dissolved in THF (40 mL). Hydrazine monohydrate (6.19 g, 12 mmol, 98% purity, TCI) was added to the reaction mixture, which was stirred under reflux at 70 °C for 16 h. Upon reaction completion (monitored by TLC) the white precipitate formed was filtered and washed with deionised water (3 × 100 mL). The product was dried first under high vacuum, then in a vacuum oven at 80 °C to constant mass. The final product was ground to yield a white powder. Yield 1.01 g (92%). 1H NMR (400 MHz, DMSO- d_6): δ 9.81 (s, CONHNH₂, 2H), 7.82 (2H, d, $J=8$ Hz, Ar-H), 7.81 (2H, d, $J=8$ Hz, Ar-H), 7.53 (2H, d, $J=8$ Hz, Ar-H), 7.50 (2H, d, $J=8$ Hz, Ar-H), 5.71 (s, Ar-CH, 2H), 4.95 (d, CH-OH, $J=6$ Hz, 1H), 4.51 (s, CONHNH₂, 4H), 4.47 (1H, dd, $J=6,6$ Hz, CH_2OH), 4.22 (1H, dd, $J=2,13$ Hz, COCHH'), 4.19 (1H, dd, $J=2,9$ Hz, CHCHCH), 4.17 (1H, dd, $J=2,13$ Hz, COCHH'), 3.98 (1H, ddd, $J=1,1,2$ Hz, $CH_2CH(O)CH$), 3.87 (1H, dd, $J=2,9$ Hz, CHCHCHOH), 3.77 (1H, dddd, $J=2,6,6,6$ Hz, CHOH), 3.62 (1H, ddd, $J=2,6,12$, CHH' OH), 3.47 (1H, ddd, $J=2,6,12$ Hz, CHH' OH). ^{13}C NMR (100 MHz, DMSO- d_6): 165.67 (C=O), 141.30 (aromatic p -C), 141.03 (aromatic p -C), 133.56 (aromatic o -C), 133.47 (aromatic o -C), 126.81 (aromatic, m -H), 126.73 (aromatic, m -H), 126.13 (aromatic, m -H), 126.10 (aromatic, m -H), 98.80 (Ph-C), 98.73 (Ph-C), 77.60 (CH), 70.16 (CH), 69.37 (CH_2), 68.51 (CH), 67.69 (CH), 62.62 (CH_2). ν_{max} (cm^{-1}): 3295s, 2881w, 1569m, 1091s. ESI-MS (m/z) calc. for $C_{22}H_{27}O_8N_4$ 475.1829; found 475.1823 (100% $[M+H]^+$). Spectra given in Appendix 2.

7.2.1.3 Synthesis of poly(ethylene glycol) dimethacrylate



Chemical Formula: $C_{2n+8}H_{4n+10}O_{n+3}$

The synthesis of PEGDM was carried out as described in the literature.¹⁶⁰ PEG 8000 (8.00 g, 1.00 mmol, 95% purity, Fisher Scientific), was dissolved in dry DCM (15 mL) and stirred at room temperature with methacrylic anhydride (0.34 g, 2.2 mmol, 94% purity, Alfa Aesar) and triethylamine (0.2 mL, 0.15 mmol) over activated molecular sieves (3.00 g, 3Å sieve) for 4 days. The solution was filtered over alumina, which was washed with further DCM (*ca.* 100 mL). The product was then precipitated by addition of diethyl ether. The product was filtered and dried under high vacuum to yield a white solid. Yield 6.10 g (75%). M.p: 58-60 °C; lit. 59-61 °C.⁵⁵ ¹H NMR (400 MHz, CDCl₃): δ 6.13 (s, =CH, 4H), 5.57 (t, =CH, *J*=2, 2H), 4.29 (t, OCH₂, *J*=5, 4H), 3.83-3.44 (m, polymer chain OCH₂, 620H), 1.94 (s, CH₃, 6H). ¹³C NMR (100 MHz, CDCl₃): δ 175.03 (COO), 135.91 (C=CH₂), 125.63 (C=CH₂), 70.36 (OCH₂), 68.91 (OCH₂), 63.69 (OCH₂), 18.15 (CH₃). ν_{max} (cm⁻¹): 2881s, 1716w, 1466m, 1341m, 1279w, 1241w. MALDI-MS (*m/z*): M_n = 6138.00 ≡ (C₄H₅O_{1.5})₂(C₂H₄O)₁₃₆, M_w = 6981.81 ≡ (C₄H₅O_{1.5})₂(C₂H₄O)₁₅₅, PDI = 1.14. Spectra given in Appendix 3.

7.2.2 Preparation of hydrogels

7.2.2.1 Preparation of DBS-CONH₂ hydrogels

A known quantity of DBS-CONH₂ was weighed into a 2.5 mL sample vial and 0.5 mL deionised water was added. The vial was then sonicated to disperse the solid and gels formed by a simple heat-cool cycle. Gels formed in a few minutes at room temperature following the removal of the heat source.

7.2.2.2 Preparation of PEGDM hydrogels

A known concentration (% wt/vol) of PEGDM was dissolved in 0.5 mL of 2-hydroxy-4'-(2-hydroxyethoxy)-2-methylpropiophenone (photoinitiator, PI) solution (0.05% wt/vol) in 2.5 mL sample vials. The solutions were cured in uncapped vials under a long wavelength UV lamp (30 min) to form transparent hydrogels.

7.2.2.3 Preparation of DBS-CONH₂/PEGDM hybrid hydrogels

DBS-CONH₂ gels (1.42 mg in 0.15 mL, 6 mM) were prepared as above. A solution (0.5 mL) of PEGDM (known concentration) dissolved in PI solution (0.05% wt/vol) was pipetted into the vial on

top of the gel and allowed to stand in the sealed vial for 72 hours. The supernatant was then removed, and the discs cured in the uncapped vials under a long wavelength UV lamp for between 10 and 30 min to yield translucent hybrid gel samples.

7.2.3 Estimation of DBS-CONHNH₂ gelation percentage

DBS-CONHNH₂ (1.99 mg) was suspended in 0.7 mL D₂O and DMSO (1.4 μL) was added. The mixture was sonicated for 15 min to disperse the solid. The sample was heated to dissolution before transferring to a hot NMR tube and leaving to cool at room temperature. Upon cooling, a transparent gel formed which was analysed by ¹H NMR spectroscopy. Signals in the NMR spectrum were considered to represent free DBS-CONHNH₂ in solution, and were compared to the DMSO internal standard to estimate the concentration of 'free' DBS-CONHNH₂ in the gel.

7.2.4 Estimation of PEGDM concentration in hybrid gels

An NMR experiment allowed the PEGDM uptake in the LMWG to be quantified. PEGDM solutions of a known concentration (0.5 mL) were pipetted onto pre-formed DBS-CONHNH₂ (6 mM, 0.5 mL) gels. The samples were allowed to stand for a given length of time before removal of the supernatant. The gels were dried *in vacuo* and dissolved in DMSO-*d*₆. The resulting solution was analysed by ¹H NMR spectroscopy. The ratio of the integrals of the PEGDM methyl peak ($\delta = 1.93$) and a DBS-CONHNH₂ hydrazide peak (CONHNH₂, $\delta = 9.77$) was measured against a calibration curve to allow the mass of PEGDM in the gel to be calculated. This mass was converted to a % wt/vol to give the concentration in the gel.

7.2.5 Preparation of samples for FT-IR analysis

ATR-FTIR spectra were recorded on a PerkinElmer Spectrum Two FT-IR spectrometer.

Gels (0.5 mL) were prepared as described above. These samples were then dried *in vacuo*, first at room temperature, and then at 80 °C. The dried xerogels were removed from the vials and then analysed directly by FT-IR.

7.2.6 Preparation of samples for SEM analysis

SEM was carried out on freeze-dried samples sputtered with gold/palladium on a JEOL JSM-7600F FEG-SEM.

Gels (0.5 mL) were prepared as described in Sections 7.2.2.1 to 7.2.2.3. A sample of gel was spread onto a supporting copper shim. Excess water was removed using a filter paper. The gel was frozen on the copper shim by submersion in liquid nitrogen. The water was then removed through

lyophilisation on a Peltier stage, with a maximum temperature of -50 °C. Once dry, the shim was mounted on an SEM stub using a carbon sticky tab. The sample was then sputtered with a thin layer of gold/palladium coating to prevent sample charging before SEM imaging.

7.2.7 T_{gel} analysis

Gels (0.5 mL) were prepared as described in Sections 7.2.2.1 to 7.2.2.3 in 2.5 mL sample vials. These vials were then placed in a thermoregulated oil bath, which was heated from 20 °C at a rate of 0.5 °C min⁻¹. Vials were carefully removed at each whole degree and inverted. Samples in which greater than half the gel no longer adhered to the vial walls were considered to have undergone the gel-sol transition. Samples which had not yet undergone the transition were carefully replaced in the oil bath.

7.2.8 Rheology sample preparation

7.2.8.1 DBS-CONH₂ hydrogels

A known amount of DBS-CONH₂ (2.84 – 3.79 mg) was suspended in H₂O (1 mL) and sonicated for 15 min to disperse the solid. The mixture was heated to dissolution and then transferred to a bottomless 8.5 mL vial which had been adhered directly to the lower plate of the rheometer. Upon cooling at room temperature, the vial was removed to yield a gel disc (diameter = 1.8 cm, height = ca. 0.2-0.3 cm). A slight syneresis occurs on gel formation and again on compression between the two rheometer plates. Excess water was carefully removed with a filter paper prior to taking rheological measurements.

7.2.8.2 PEGDM hydrogels

A known amount of PEGDM (50 – 100 mg) was dissolved in an aqueous solution of PI (0.05% wt/vol, 1 mL in an 8.5 mL vial) and cured under a long-wavelength UV lamp for 0.5 h. The polymerised hydrogels were removed from the sample vials and the discs (width = 1.8 cm, height = ca. 0.3 cm) were placed on the lower plate of the rheometer.

7.2.8.3 Hybrid hydrogels

A known amount of DBS-CONH₂ (2.84 – 3.79 mg) was suspended in H₂O (1 mL in an 8.5 mL vial) and sonicated for 15 min to disperse the solid. The mixture was heated to dissolution and allowed to cool to room temperature. On cooling a gel formed. A solution of PEGDM (5 – 10% wt/vol) dissolved in PI solution (0.05% wt/vol) was pipetted into the vial on top of the gel and allowed to stand in the sealed vial for 72 hours. The supernatant was then removed and the discs cured in the uncapped vials under a long wavelength UV lamp for 30 min to yield a translucent hybrid gel. This

gel disc (diameter = 1.8 cm, height = *ca.* 0.3 cm) was carefully removed from the vial and placed on the lower plate of the rheometer.

7.2.8.4 *Crosslinking density test*

A hybrid gel was prepared as described as in Section 7.2.8.3, but in this case on a 2 mL scale and with a PEGDM concentration of 10% wt/vol. This yielded a gel disc of height 0.6 cm. This disc was carefully sectioned using a razor blade to yield two identical gel discs of height 0.3 cm. These were placed on the lower plate of the rheometer and analysed as normal.

7.2.9 Rheology methods

Rheological measurements were recorded using a Malvern Instruments Kinexus Pro+ rheometer fitted with a parallel plate geometry and data were processed using rSpace software.

7.2.9.1 *Amplitude sweep*

Gels, as described in Section 7.2.8, were loaded onto the rheometer and compressed carefully with the upper plate such that the whole plate (diameter = 2 cm) was in contact with the surface of the gel. Oscillation frequency was fixed at a value of 1 Hz and the shear strain increased from 0.05 to 100%. Ten readings per decade were recorded at 25 °C.

If the critical shear strain was not reached in the first amplitude sweep, the experiment was repeated after performing a frequency sweep (Section 7.2.9.2). The process was identical to that outlined above, but in this case the shear strain was increased to 1000%. This almost invariably resulted in permanent gel breakdown, hence this experiment was always performed last.

Shear strain was plotted against the storage and loss moduli to identify the LVR.

7.2.9.2 *Frequency sweep*

The gel was retained in place on the rheometer plate after the amplitude sweep (Section 7.2.9.1) was complete. The shear strain was then fixed to a value identified as being in LVR. The storage and loss moduli were recorded at 25 °C (ten samples per decade) on reducing the oscillation frequency from 100 to 0.1 Hz.

7.2.9.3 *Temperature sweep*

A gel was loaded and compressed as described above. The shear strain was fixed at a value in the LVR, and the oscillation frequency at a value in the plateau region of the frequency sweep. The temperature was increased from 25 to 100 °C at a rate of 1 °C min⁻¹. G' and G'' were recorded at 5 second intervals.

7.2.10 Photo-patterned hybrid gels

7.2.10.1 *Glass slide method (hybrid gels)*

A known amount of DBS-CONHNH₂ was suspended in H₂O (total concentration 6 mM) and sonicated for 15 min to disperse the solid. The mixture was heated to dissolution and then transferred to a bottomless 8.5 mL vial which had been adhered to the surface of a glass plate using silicone. On cooling a LMWG formed. A solution of PEGDM (10% wt/vol) dissolved in PI solution (0.05% wt/vol) was pipetted into the vial on top of the gel and allowed to stand in the sealed vial for 72 hours. The supernatant and the vial were removed to leave a self-standing gel. A glass slide with a cardboard photomask attached was placed on top of the gel, which was then cured under a long-wavelength UV lamp for a period of time (10-30 min). The glass slide was carefully removed to yield multidomain hybrid gels.

7.2.10.2 *Large-scale square mould solvent mixture testing (hybrid gels)*

DBS-CONHNH₂ (28.4 mg) was suspended in a known solvent mixture (10 mL) and sonicated to disperse the solid. The suspension was heated to dissolution or thorough boiling, whichever occurred first, and was then transferred to a large, square, glass mould (5 cm × 5 cm × 1 cm). The sample was allowed to cool to room temperature, at which point the phase of the material was assessed qualitatively.

7.2.10.3 *Optimised large-scale square mould method (hybrid gels)*

DBS-CONHNH₂ (28.4 mg) was weighed into a sample vial and dissolved in 0.4 mL DMSO. This solution was added to boiling deionised H₂O (9.6 mL) and mixed before transferring to a square glass mould (5 cm × 5 cm × 1 cm). On cooling a gel was formed. A 10 mL solution of PI (0.05% wt/v) and PEGDM (known quantity, 5-10% wt/vol) was then added on top of the gel and left for three days, during which the cloudy solution became transparent. The solution was removed and a laser-printed acetate photomask (4 layers) placed on the top of the tray so only part of the gel was exposed. The mask sits *ca.* 0.5 cm from the top of the DBS-CONHNH₂ gel in this configuration. The mould was then sat in a tray of ice (to minimise heating) and placed under a long-wave UV light. The solution was cured for a period of time (10-30 min), after which time the exposed region had formed a hybrid gel. This region was very robust whereas the uncured (non-hybrid) region was mechanically weak. The pattern was exposed using a low-power water stream from a 'squeazy bottle'.

7.3 Chapter 3

7.3.1 Preparation of NPX-loaded hydrogels

7.3.1.1 Preparation of NPX-loaded DBS-CONH₂ hydrogels

Known quantities of DBS-CONH₂ (1.42 – 1.89 mg, 6 – 8 mM) and NPX (0.69 mg, 6 mM) were weighed into a 2.5 mL sample vial and 0.5 mL deionised water was added. The vial was then sonicated to disperse the solid and gels formed by a simple heat-cool cycle. Gels formed in a few minutes at room temperature following the removal of the heat source.

7.3.1.2 Preparation of NPX-loaded PEGDM hydrogels

NPX (0.69 mg, 6 mM) was suspended in a 0.5 mL solution of PEGDM (known concentration) and PI (0.05% wt/vol) in 2.5 mL sample vials. The suspension was sonicated to ensure even dispersion and then cured in uncapped vials under a long wavelength UV lamp (30 min) to form transparent hydrogels.

7.3.1.3 Preparation of NPX-loaded DBS-CONH₂/PEGDM hybrid hydrogels

NPX-loaded DBS-CONH₂ gels were prepared as above. A solution of PEGDM (known concentration) dissolved in PI solution (0.05% wt/vol) was pipetted into the vial on top of the gel and allowed to stand in the sealed vial for 72 hours. The supernatant was then removed and the discs cured in the uncapped vials under a long wavelength UV lamp for between 10 and 30 min to yield translucent hybrid gel samples.

7.3.2 NPX-loaded rheology sample preparation

7.3.2.1 NPX-loaded DBS-CONH₂ hydrogels

Known amounts of DBS-CONH₂ (2.84 – 3.78 mg, 6 – 8 mM) and NPX (1.38 mg, 6 mM) were suspended in H₂O (1 mL) and sonicated for 15 min to disperse the solid. The mixture was heated to dissolve and then transferred to a bottomless 8.5 mL vial which had been adhered directly to the lower plate of the rheometer. Upon cooling at room temperature, the vial was removed to yield an opaque gel disc (diameter = 1.8 cm, height = ca. 0.2-0.3 cm). A slight syneresis occurs on gel formation and again on compression between the two rheometer plates. Excess water was carefully removed with a filter paper prior to taking rheological measurements.

7.3.2.2 PEGDM hydrogels

NPX (1.38 mg, 6 mM) was suspended in a 1 mL solution of PEGDM (known concentration) and PI (0.05% wt/vol) in an 8.5 mL sample vial. The suspension was sonicated to ensure even dispersion and then cured in uncapped vials under a long wavelength UV lamp (30 min). The polymerised

hydrogels were removed from the sample vials and the discs (width = 1.8 cm, height = ca. 0.3 cm) were placed on the lower plate of the rheometer.

7.3.2.3 Hybrid hydrogels

DBS-CONHNH₂ (2.84 mg, 6 mM) and NPX (1.38 mg, 6 mM) were suspended in H₂O (1 mL in an 8.5 mL vial) and sonicated for 15 min to disperse the solid. The mixture was heated to dissolve and allowed to cool to room temperature. On cooling, a gel formed. A solution of PEGDM (known concentration) dissolved in PI solution (0.05% wt/vol) was pipetted into the vial on top of the gel and allowed to stand in the sealed vial for 72 hours. The supernatant was then removed and the discs cured in the uncapped vials under a long wavelength UV lamp for 30 min to yield a translucent hybrid gel. This gel disc (diameter = 1.8 cm, height = ca. 0.3 cm) was carefully removed from the vial and placed on the lower plate of the rheometer.

7.3.3 Characterisation of NPX-loaded hydrogels

Procedures for the characterisation of NPX-loaded hydrogels were carried out as described in Sections 7.2.5 to 7.2.9.

7.3.4 NPX encapsulation study

DBS-CONHNH₂ (1.99 mg, 6 mM) and NPX (0.97 mg, 6 mM) were suspended in D₂O (0.7 mL). DMSO (1.4 µL) was added and the mixture was sonicated for 15 min to disperse the solids. The mixture was then heated to dissolved and allowed to cool to room temperature. On cooling, a gel formed which was analysed by solution phase ¹H NMR spectroscopy. The ratio of the integrals of peaks corresponding to an NPX methyl group ($\delta = 1.27$) and the DMSO internal standard ($\delta = 2.50$) were used to calculate the concentration of unbound NPX in the sample.

7.3.5 NPX release studies

Gel samples (1 mL) were prepared by the methods outlined above. 6 mL of one of (i) pH 2.8 citrate buffer, (ii) pH 4.0 acetate buffer, (iii) pH 5.5 phosphate-citrate buffer, (iv) pH 7.0 phosphate buffer and (v) pH 8.0 phosphate buffer was pipetted onto the gel and the release of NPX monitored at 329 nm by UV-vis spectroscopy. The samples were incubated at 37 °C for the duration of the study. NPX concentration in the supernatant was quantified using calibration curves. All experiments were carried out in duplicate and control experiments using gels containing no NPX were also carried

out. Citrate buffer (pH 4.0) was also used for some experiments. No significant differences in release were observed compared to when using acetate buffer.

7.3.6 Preparation of NPX-loaded photo-patterned hybrid gels

The procedure outlined in Section 7.2.10.3 was followed using an equimolar mixture of DBS-CONHNH₂ (28.4 mg, 6 mM in the 10 mL gel) and NPX (13.8 mg, 6 mM).

7.3.7 Differential release

7.3.7.1 *Preparing the photo-patterned gel*

DBS-CONHNH₂ (28.4 mg) and NPX (13.8 mg) were weighed into a sample vial and dissolved in DMSO (0.4 mL). This solution was added to boiling deionised H₂O (9.6

mL) and mixed before transferring to a square glass mould (25 mL capacity). On cooling, a gel was formed. A solution (10 mL) of PI (0.05% wt/vol) and PEGDM (10% wt/vol) was then added on top of the gel and left for three days. The solution was removed and acetate photomasks placed over the top so that only part of the gel was exposed. The mould was then sat in a tray of ice (to minimise heating) and placed under a long-wavelength UV lamp. The solution was cured for 15 min, after which the exposed region had formed a hybrid gel.

7.3.7.2 *Release study*

The weak LMWG was removed by washing with water, leaving a band of robust hybrid gel. Buffer solutions (1.5 mL) of pH 2.8 and pH 7.0 were pipetted into either side of the band and stirred using magnetic fleas. The mould was covered using a glass slide for the duration of the experiment. NPX release was monitored by UV-vis spectroscopy (at 329 nm) over 3 h. At each time point 100 µL of each of the stirred solutions was taken and diluted to 2 mL. The solution removed was replaced with fresh buffer. This experiment was repeated using hybrid gels containing no NPX.

7.3.8 Preparation of reverse hybrid gels

7.3.8.1 *Diffusion method*

A 5% PEGDM hydrogel was prepared as outlined in Section 7.2.2. DBS-CONHNH₂ (1.42 mg) was dissolved in DMSO (0.04 mL) and pipetted on top of the PEGDM hydrogel. The samples were left for 3 days to allow diffusion of DBS-CONHNH₂ into the PEGDM gel.

This procedure was also carried out using an equimolar quantity of NPX (0.69 mg) and DBS-CONHNH₂ (1.42 mg).

7.3.8.2 Optimised reverse hybrid gel method

An aqueous solution (0.5 mL) of PEGDM (10% wt/vol) and PI (0.1% wt/vol) was added to a glass vial (8.5 mL, diameter = 1.8 cm) and heated to 80 °C in a water bath which was held under a high-powered UV lamp. DBS-CONHNH₂ (2.84 mg) was suspended in H₂O (0.5 mL) and dispersed by sonication. The sample was heated to dissolution and added quickly to the vial containing the PEGDM/PI solution. The mixture was stirred briefly to ensure complete mixing and the sample exposed to UV-light for a known period of time (10-30 min). The temperature was maintained at 80 °C throughout this process. After UV-exposure, the sample was taken from the water bath and allowed to cool to room temperature under ambient conditions. The final concentrations of DBS-CONHNH₂, PEGDM and PI were 6 mM, 5% wt/vol and 0.05% wt/vol respectively.

This procedure was also carried out using an equimolar quantity of NPX (1.38 mg) and DBS-CONHNH₂ (2.84 mg).

7.3.8.3 Optimised large-scale square mould reverse hybrid gel method

An aqueous solution (5 mL) of PEGDM (10% wt/vol) and PI (0.1% wt/vol) was added to a square glass mould (dimensions = 5 cm × 5 cm × 1 cm) and heated to 80 °C in a water bath which was held under a high-powered UV lamp. DBS-CONHNH₂ (28.4 mg) was dissolved in DMSO (0.3 mL) and heated. This hot solution was added to boiling H₂O (4.7 mL) and then quickly transferred into the glass mould. The solution was stirred briefly to ensure complete mixing, a photo-mask placed over the gel (if required), then the sample exposed to UV-light for a known period of time (10-30 min). The temperature was maintained at 80 °C throughout this process. After UV-exposure, the sample was taken from the water bath and allowed to cool to room temperature under ambient conditions. The final concentrations of DBS-CONHNH₂, PEGDM and PI were 6 mM, 5% wt/vol and 0.05% wt/vol respectively.

This procedure was also carried out using an equimolar quantity of NPX and DBS-CONHNH₂.

7.3.9 Preparation of reverse hybrid rheology samples

Reverse hybrid gels were prepared as described in 7.3.8.2. The gel disc (diameter = 1.8 cm, height = *ca.* 0.3 cm) was carefully removed from the vial by separating the gel from the sides of the vial using a small spatula. The sample were then placed on the lower plate of the rheometer.

7.3.10 NPX release study

NPX-loaded reverse hybrid gels (1 mL) were prepared according to the procedure outlined in Section 7.3.8.2. Release of NPX was monitored as described in Section 7.3.7.2.

7.4 Chapter 4

7.4.1 Preparation of hydrogels in cuvettes

7.4.1.1 DBS-CONH₂ hydrogels

DBS-CONH₂ was weighed into a 2.5 mL sample vial and deionised water was added such that the LMWG was at a concentration of 6 mM. The vial was then sonicated to disperse the solid and the suspension heated to dissolution before transferral to a polystyrene cuvette (1 cm × 1 cm × 4.5 cm). The sol was allowed to cool under ambient conditions. Gel formation was observed after a few minutes.

7.4.1.2 PEGDM hydrogels

A solution of PEGDM (10% wt/vol) and PI (0.05% wt/vol) was added to a UV cuvette (cross-sectional dimensions = 1 cm × 1 cm). The solution was placed under a long wavelength UV lamp (0.5 h), after which time a transparent gel had formed.

7.4.1.3 DBS-CONH₂ / PEGDM hybrid hydrogels

LMW hydrogels were first made in a UV cuvette as described above. An aqueous solution of PEGDM (known concentration, 10 – 60% wt/vol) and PI (0.05% wt/vol) was pipetted on top of the gel and left for three days to allow diffusion. After this time the supernatant was removed and the PG network cured by exposure to long wavelength UV light (0.5 h).

7.4.2 Diffusion studies

An aqueous solution of either 50 μM fluorescein or fluorescein-isothiocyanate-dextran (M_w from 4-70 kDa) was pipetted on top of the gel sample and the fluorescence after excitation ($\lambda_{exc} = 470$ nm) monitored at the λ_{max} of the fluorophore solution as recorded at 50 μM. Control experiments in the absence of fluorophore were carried out for comparison. The emission and excitation slit widths were set to 2.5 nm in all cases.

Table 7.1: Suppliers, stated mass and wavelengths of fluorescence intensity maxima for each fluorophore at 50 μM .

Solution	Supplier	Purity / %	Supplied M_w / Da	λ_{max} (50 μM)
Fluorescein	Aldrich	98	332.31	512
FITC-dextran (4 kDa)	Sigma	-	3430	521
FITC-dextran (10 kDa)	Sigma	-	Ca. 10000	522
FITC-dextran (20 kDa)	Sigma	-	Ca. 20000	526
FITC-dextran (40 kDa)	Sigma	-	36198	528
FITC-dextran (70 kDa)	Sigma	-	75090	521

Quantification was achieved by comparison to calibration curves. Decreasing fluorescence intensity at greater fluorophore concentrations – caused by increasing optical density of the solution - was compensated for using a calculation reported by Lakowicz:⁴³⁹

$$F_{\text{corr}} \cong F_{\text{obs}} \cdot 10^{\frac{OD_{\text{exc}} + OD_{\text{em}}}{2}}$$

Where F_{corr} is the corrected fluorescence intensity, F_{obs} is the observed fluorescence intensity, and the optical density of the sample at the emission and excitation wavelengths are OD_{em} and OD_{exc} respectively.

7.4.3 Preparation of enzyme stock solution

Bovine intestinal ALP (2 μL , 21.6 U μL^{-1} , from Sigma) was dissolved in buffer solution or water (1.998 mL) to give a stock solution of concentration 21.6 U mL^{-1} . This was further diluted as required.

7.4.4 Solution phase studies

A UV cuvette was charged with a known volume of ALP stock solution. This solution was diluted to 2 mL with *p*NPP disodium salt hexahydrate (*p*NPP, $M_w = 371.14 \text{ g mol}^{-1}$) such that the final concentrations of ALP and *p*NPP were known. The formation of *p*NP was monitored by UV-vis spectroscopy at the maximum absorbance of the product in the given solvent. The solvents used the maximum absorbance values in each are:

- pH 4 citrate buffer (0.1 M): $\lambda_{\text{max}} = 310 \text{ nm}$
- pH 7 phosphate buffer (0.2 M): $\lambda_{\text{max}} = 310 \text{ nm} + 405 \text{ nm}$
- pH 9 glycine-NaOH buffer (0.2 M): $\lambda_{\text{max}} = 405 \text{ nm}$
- pH 11 carbonate buffer (0.1 M): $\lambda_{\text{max}} = 405 \text{ nm}$
- Unbuffered water: $\lambda_{\text{max}} = 310 \text{ nm} + 405 \text{ nm}$

UV-vis spectra were also recorded at various time points in the range 250 – 450 nm. Concentrations of *p*NPP and *p*NP were calculated by comparison of the experimental absorbances to those of calibration curves in each solvent.

7.4.5 DBS-CONHNH₂ pH determination

A 6 mM DBS-CONHNH₂ hydrogel (1 mL) was prepared as previously described. On dissolution a pH probe was introduced to the solution and the pH monitored during cooling and gel formation.

7.4.6 Qualitative ALP activity tests

All ALP activity tests were carried out using 10 mM *p*NPP solution (0.5 mL) made up in pH 9 glycine/NaOH buffer (0.2 M). Gels were washed once with water prior to addition of substrate.

ALP solutions were treated as required followed by mixing with *p*NPP solution.

DBS-CONHNH₂ gels were prepared by suspending DBS-CONHNH₂ (1.42 mg) in either H₂O or pH 9 buffer (0.5 mL). The suspension was sonicated (15 min) followed by heating to dissolution. On cooling a gel formed. *p*NPP solution was then pipetted on top.

For ALP-containing LMWGs, DBS-CONHNH₂ gels were prepared as described above, but on dissolution the vial was placed in a thermoregulated oil bath at a known temperature. After 5 min the vial was removed and ALP (1 μ L, 0.2 U μ L⁻¹) was added (ALP concentration in gel = 0.4 U mL⁻¹). For slow cooling, the vial was replaced in the oil bath and the cooling rate set to a known speed. For rapid cooling, the vial was placed immediately into an ice bath. On rapid cooling, gelation occurs. These gels were allowed to warm to room temperature before evaluating enzyme activity by pipetting *p*NPP solution on top.

For ALP-containing hybrid gels, the above procedure was followed until gelation. Following gel formation, a solution (0.5 mL) of PEGDM (10% wt/vol) and PI (0.5% wt/vol) was added on top and left for 3 days. After this time the supernatant was removed and the gel cured under a long-wavelength UV lamp (30 min) to initiate formation of the PG. *p*NPP solution was then pipetted on top.

7.4.7 Enzyme leaching experiments

Gels were prepared as described above, but at a total volume of 2 mL. A solution of pH 9 buffer (2 mL) was pipetted on top of the gel. After 24 h the supernatant was removed and diluted to 4 mL with a 0.2 mM solution of *p*NPP (final *p*NPP concentration = 0.1 mM). The evolution of *p*NP was monitored over time using UV-vis spectroscopy by recording the absorbance at 405 nm. The rate of change in *p*NP concentration was compared to those from the solution phase studies (see above) at 0.1 mM *p*NPP concentration. The rate of evolution was correlated to an ALP concentration, which

was considered to be the approximate concentration of enzyme in the solution (i.e. leached enzyme).

7.4.8 CD spectroscopy

Solutions of ALP (0.2 U mL^{-1}) in pH 9 buffer were analysed before and after UV irradiation (0.5 h). 100 μL of each solution was pipetted into a glass CD cuvette (path length 1 mm) and the CD spectrum recorded. A background glycine buffer sample was also run and subtracted from these spectra. CD spectroscopy parameters were: Range = 180 – 260 nm, Band Width = 2 nm, Accumulations = 5, Scan Speed = 1 nm min^{-1} , Pitch = 0 - 5 nm, Response = 1 s. All spectra were recorded at a temperature of 20 °C.

7.4.9 Gel-phase ALP activity

ALP-loaded gels (0.5 mL) were prepared in UV cuvettes. All gels were washed with 0.5 mL H_2O prior to reaction testing.

DBS-CONHNH₂ (1.42 mg) was suspended in H_2O (0.5 mL) and sonicated (15 min). The solution was heated to dissolution and then the vial was placed in a thermoregulated oil bath at 80 °C. The solution was allowed to equilibrate to this temperature (5 min). The vial was then removed from the oil bath and 2 μL ALP stock solution (21.6 U mL^{-1}) was added (ALP concentration in gel = 0.4 U mL^{-1}). The solution was mixed and then placed immediately in an ice bath to induce gelation.

10% hybrid gels were prepared by taking a DBS-CONHNH₂ gel in a UV cuvette. A 0.5 mL solution of PEGDM (10% wt/vol) and PI (0.05% wt/vol) was added on top and left for 3 days. The supernatant was then removed and the PG network crosslinked by exposure to UV light (0.5 h).

10% PEGDM gels were prepared by dilution of ALP stock solution (1 μL , 21.6 U mL^{-1}) in a 0.5 mL solution of PEGDM (10% wt/vol) and PI (0.05% wt/vol) in a UV cuvette. The solution was placed under a long wavelength UV lamp (0.5 h) to induce crosslinking. After this time a transparent gel had formed.

For reactivity tests of all gel samples, *p*NPP solution (2 mL, 0.1 mM) in pH 9 buffer was pipetted on top of the gels. The absorbance at 405 nm was recorded over time *in situ* to monitor *p*NP evolution. At given time points UV spectra of the solution were recorded in the range 250 – 450 nm. Experiments were repeated in triplicate.

7.4.10 Substrate/product uptake studies

Hydrogels of 2 mL volume were prepared in 8 mL vials as described previously. Solutions of *p*NP and *p*NPP were prepared in pH 4, 7 and 11 buffer solutions, at a concentration of 1 mM, and each was pipetted on top of a hydrogel. The samples were left for 24 h, after which time 2 mL of the solution was removed and analysed by UV-vis spectroscopy, before returning to the sample vial. This process was repeated at 48 h. Each combination of pH, gel and solution-phase component was tested in triplicate.

7.4.11 NMR study

DBS-CONHNH₂ (1.99 mg) was suspended in a solution of *p*NP (0.01 M) dissolved in D₂O (0.7 mL) containing 28 μL DMSO as internal standard (0.56 M). The suspension was sonicated (15 min) and heated to dissolution. The hot sol was transferred to an NMR tube and allowed to cool under ambient conditions. A gel formed quickly in the NMR tube. ¹H NMR of the gel was performed.

7.4.12 *p*NPP diffusion through a hybrid gel ring

A hybrid gel ring was prepared as previously described (see Chapter 2). The compartment contained within the ring was charged with a solution of *p*NPP in pH 9 buffer (0.3 mL, 10 mM), whilst the outer compartment contained pH 9 buffer only (2 mL). The whole reactor was placed in a dark container to prevent light-induced *p*NPP degradation. The outer compartment was stirred for the duration of the experiment. At each time point, the contents of the outer compartment were removed, placed in a UV cuvette, and the UV spectrum of the solution recorded. This solution was returned to the outer compartment after each measurement.

7.4.13 ALP bioreactor with enzyme immobilised in the hybrid gel ring

DBS-CONHNH₂ (28.4 mg) was dissolved in DMSO (0.4 mL) with sonication. This solution was mixed with boiling H₂O (9.6 mL) and the flask placed in a thermoregulated oil bath at 80 °C. The sample was left to equilibrate at this temperature for 5 min, at which point ALP solution (20 μL, 0.2 U μL⁻¹) was added (final ALP concentration = 0.4 U mL⁻¹). The hot solution was transferred immediately to a glass tray (5 cm × 5 cm × 1 cm) cooled in ice. Rapid gel formation was observed on cooling. Onto this gel was added a 10 mL solution of PEGDM (10%wt/vol) and PI (0.05% wt/vol). The sample was left for three days, then the supernatant was removed, and acetate photomasks placed over the top of the gel, such that only a ring-shaped section was exposed. The tray was placed in ice to

minimise heating effects and irradiated with long-wavelength UV light (0.5 h). In this time, the exposed region had formed a robust hybrid gel. The remaining, soft LMW hydrogel was washed away using a low-pressure water jet to reveal the ring pattern.

The central compartment of the reactor was loaded with a solution of *p*NPP (0.3 mL, 10 mM) in pH 9 buffer. The outer compartment was charged with pH 9 buffer (2 mL). The whole reactor was placed in a dark container to prevent light-induced *p*NPP degradation. The outer compartment was stirred for the duration of the experiment. At each time point, the contents of the outer compartment were removed, placed in a UV cuvette, and the UV spectrum of the solution recorded. This solution was returned to the outer compartment after each measurement.

After 6 h, in addition to the removal of the buffer solution, the contents of the central compartment were pipetted into a UV-vis cuvette and diluted to 2 mL with pH 9 buffer. This solution was also analysed by UV-vis spectroscopy. Calibration curves plotted from absorbances of known concentrations of *p*NP and *p*NPP in pH 9 buffer were used to calculate the concentration of these compounds in each compartment.

7.4.14 ALP bioreactor with enzyme free in the outer compartment

A hybrid gel ring was prepared as previously described (see Chapter 2). The compartment contained within the ring was charged with a solution of *p*NPP in pH 9 buffer (0.3 mL, 10 mM), whilst the outer compartment contained ALP dissolved in pH 9 buffer (26 U mL⁻¹, 2 mL). The whole reactor was placed in a dark container to prevent light-induced *p*NPP degradation. The outer compartment was stirred for the duration of the experiment. At each time point, the contents of the outer compartment were removed, placed in a UV cuvette, and the UV spectrum of the solution recorded. This solution was returned to the outer compartment after each measurement.

After 6 h, in addition to the removal of the buffer solution, the contents of the central compartment were pipetted into a UV-vis cuvette and diluted to 2 mL with pH 9 buffer. This solution was also analysed by UV-vis spectroscopy. Calibration curves plotted from absorbances of known concentrations of *p*NP and *p*NPP in pH 9 buffer were used to calculate the concentration of these compounds in each compartment.

7.4.15 AP bioreactor with enzyme in the outer compartment

A hybrid gel ring was prepared as previously described (see Chapter 2). The compartment contained within the ring was charged with a solution of *p*NPP in pH 9 buffer (0.3 mL, 10 mM), whilst the outer

compartment contained AP (2 U mg^{-1} , from TCI) dissolved in pH 5.8 buffer (26 U mL^{-1} , 2 mL). The whole reactor was placed in a dark container to prevent light-induced *p*NPP degradation. The outer compartment was stirred for the duration of the experiment. At each time point, the contents of the outer compartment were removed and diluted to 2 mL using pH 9 buffer (final pH *ca.* 9) and the UV spectrum of the solution recorded. The product compartment was replenished with fresh pH 5.8 buffer at each time point.

After 6 h, in addition to the removal of the buffer solution, the contents of the central compartment were reduced to dryness and dissolved in 2 mL pH 9 buffer. This solution was also analysed by UV-vis spectroscopy. Calibration curves plotted from absorbances of known concentrations of *p*NP and *p*NPP in pH 9 buffer were used to calculate the concentration of these compounds in each compartment.

7.4.16 Dye diffusion through DBS-CONH₂ LMW hydrogels

DBS-CONH₂ (28.4 mg) was weighed into a sample vial and dissolved in 0.4 mL DMSO. This solution was added to boiling deionised H₂O (9.6 mL) and mixed before transferring to a square glass tray (5 cm × 5 cm × 1 cm). On cooling a gel was formed. Two 'reactant' wells and one 'product' well (all 1 cm × 1 cm) were cut in the gel using an upturned UV cuvette. The two reactant wells were located at the opposite edge of the tray to the product well, which was filled with H₂O (0.2 mL). The reactor was transferred to a chamber in which the atmosphere was saturated with water vapour, to maintain hydration of the gel and dye solutions over time. The two reactant wells were filled with aqueous methylene blue (MB) and fluorescein solutions of a known concentration. The contents of the product well were taken periodically and diluted to 2 mL. This solution was analysed by UV-vis spectroscopy. The product well was replenished with fresh H₂O at each time point.

7.4.17 Dye diffusion through hybrid hydrogels

DBS-CONH₂ (28.4 mg) was weighed into a sample vial and dissolved in 0.4 mL DMSO. This solution was added to boiling deionised H₂O (9.6 mL) and mixed before transferring to a square glass tray (5 cm × 5 cm × 1 cm). On cooling a gel was formed. A 10 mL solution of PI (0.05% wt/vol) and PEGDM (60% wt/vol) was then added on top of the gel and left for three days, during which the cloudy solution became transparent. The supernatant was removed, the tray placed in ice and the whole sample exposed to UV irradiation for 4 min. Significant stiffening of the gel occurred.

Two 'reactant' wells and one 'product' well (all 1 cm × 1 cm) were cut in the gel using an upturned UV cuvette. The two reactant wells were located at the opposite edge of the tray to the product well, which was filled with H₂O (0.2 mL). The reactor was transferred to a chamber in which the atmosphere was saturated with water vapour, to maintain hydration of the gel and dye solutions over time. The two reactant wells were filled with aqueous methylene blue (MB) and fluorescein solutions of a known concentration. The contents of the product well were taken periodically and diluted to 2 mL. This solution was analysed by UV-vis spectroscopy. The product well was replenished with fresh H₂O at each time point.

7.4.18 Dye diffusion through photo-patterned hybrid hydrogels

DBS-CONHNH₂ (28.4 mg) was weighed into a sample vial and dissolved in 0.4 mL DMSO. This solution was added to boiling deionised H₂O (9.6 mL) and mixed before transferring to a square glass mould (5 cm × 5 cm × 1 cm). On cooling a gel was formed. A 10 mL solution of PI (0.05% wt/vol) and PEGDM (known quantity, 20-60% wt/vol) was then added on top of the gel and left for three days, during which the cloudy solution became transparent. The solution was removed and a laser-printed acetate photomask (4 layers) placed on the top of the tray so only part of the gel was exposed. The mould was then sat in a tray of ice (to minimise heating) and placed under a long-wave UV light. The solution was cured for a known amount of time (4-6 min), after which the exposed region had formed a hybrid gel. This region was very robust whereas the uncured (non-hybrid) region was mechanically weak.

Two 'reactant' wells and one 'product' well (all 1 cm × 1 cm) were cut into the ends of the soft LMWG channels using an upturned UV cuvette. The two reactant wells were located at the opposite edge of the tray to the product well, which was filled with H₂O (0.2 mL). The reactor was transferred to a chamber in which the atmosphere was saturated with water vapour, to maintain hydration of the gel and dye solutions over time. The two reactant wells were filled with aqueous methylene blue (MB) and fluorescein solutions of a known concentration. The contents of the product well were taken periodically and diluted to 2 mL. This solution was analysed by UV-vis spectroscopy. The product well was replenished with fresh H₂O at each time point, whilst the reactant wells were replenished at known intervals.

7.4.19 ALP controlled diffusion reactor

A photo-patterned 60% hybrid gel reactor following the method outlined above. In this case, an acetate photomask (4 layers) printed with a straight-line shielded region (length = 4 cm, width = 1 cm) was used. The channel pattern was revealed by washing with a low pressure water jet. 1 cm at each of the two ends of the channel were plugged with cotton wool and the tray transferred into an ice bath.

DBS-CONHNH₂ (1.42 mg) was suspended in H₂O (0.5 mL) and sonicated (15 min). The solution was heated to dissolution and then the vial was placed in a thermoregulated oil bath at 80 °C. The solution was allowed to equilibrate to this temperature (5 min). The vial was then removed from the oil bath and 2 µL ALP stock solution (21.6 U mL⁻¹) was added (ALP concentration in gel = 0.4 U mL⁻¹). The solution was mixed and then transferred to unblocked portion of the gel channel. On cooling rapid gel formation was observed. The cotton wool plugs were then removed.

The 'reactant' well was charged with *p*NPP (0.2 mL, 10 mM) in pH 9 buffer, and the 'product' well with pH 9 buffer only. The contents of the reactant and product wells were removed at given time points and diluted to 2 mL with pH 9 buffer in a UV cuvette. The solution was analysed by UV-vis spectroscopy. At each time point the product well was replenished with fresh buffer solution (0.2 mL) and the reactant well with fresh *p*NPP solution (0.2 mL, 10 mM) in pH 9 buffer. The concentration of *p*NPP and *p*NP in each well was calculated at each time point by comparison to a calibration curve.

7.5 Chapter 5

7.5.1 Preparation of gels in 24-well plates

Stainless steel washers (interior diameter = 6 mm, exterior diameter = 12 mm) were adhered to the base of each well of a 24 well plate (well diameter = 15.6 mm) using silicone grease. For sterile gel preparation all gels were prepared in autoclaved water, and solutions and well plates were only opened to the atmosphere when inside the sterile tissue culture hood.

7.5.1.1 DBS-CONHNH₂ hydrogels

DBS-CONHNH₂ (1.42 mg) was suspended in H₂O (0.5 mL, LMWG concentration = 6 mM) and sonicated (15 min) to disperse the solid. The resulting suspension was heated to dissolution and 50 µL of the hot sol was transferred by pipette into the inside of the washers. The solution was allowed to cool to room temperature under ambient conditions. Translucent gels formed in *ca.* 1 minute (gel height *ca.* 1.5 mm).

For the preparation of gels filling each well, no washers were adhered to the base of the wells. DBS-CONHNH₂ (1.42 mg) was dissolved in H₂O as described above. The entire hot sol (0.5 mL) was transferred to the well plate on dissolution. Cooling under ambient conditions resulted in gel formation over *ca.* 5 minutes (gel height *ca.* 2.5 mm).

7.5.1.2 PEGDM hydrogels

Solutions of PEGDM (10 to 60 % wt/vol) and PI (0.05 % wt/vol) were prepared. A 50 µL aliquot of this solution was pipetted into the inside of a washer. The solutions were placed under a long wavelength UV lamp (0.5 h) over which time PEGDM crosslinking resulted in the formation of a transparent gel (height *ca.* 1.5 mm).

For the preparation of gels filling each well, no washers were adhered to the base of the wells. PEGDM (50 to 300 mg) and PI (0.25 mg) were dissolved in 0.5 mL H₂O (PEGDM concentrations 10 to 60% wt/vol). The entire solution was transferred to a well and irradiated with long wavelength UV light (0.5 h), after which a transparent gel (height *ca.* 2.5 mm) was formed.

7.5.1.3 Hybrid hydrogels

DBS-CONHNH₂ LMW hydrogels were prepared as described in Section 7.5.1.1. A solution of PEGDM (10 to 60 % wt/vol) and PI (0.05% wt/vol) was prepared and 50 µL pipetted on top of the LMW hydrogel. The sample was left for 3 days, after which time the supernatant was removed. The gel was placed under a long wavelength UV lamp and irradiated for 0.5 h. Stiff, translucent gels were formed on irradiation (height *ca.* 1.5 mm).

For the preparation of gels filling each well, no washers were adhered to the base of the wells. DBS-CONHNH₂ hydrogels were prepared as described in Section 7.5.1.1. PEGDM (50 to 300 mg) and PI (0.25 mg) were dissolved in 0.5 mL H₂O (PEGDM concentrations 10 to 60% wt/vol). This solution was pipetted on top of the LMW hydrogel. The sample was left for 3 days, after which time the supernatant was removed. The gel was placed under a long wavelength UV lamp and irradiated for 0.5 h. Stiff, translucent gels were formed on irradiation (height *ca.* 2.5 mm).

7.5.2 Gel sterilisation

Gels were prepared as described above and sterilised using one of two methods:

7.5.2.1 Ethanol / PBS wash

70% aqueous ethanol solution (1 mL) was pipetted on top of the gels and left for 10 minutes to sterilise the gel. The ethanol was removed and a solution of phosphate buffered saline solution (PBS, 1 mL, 1.76 mM, pH 7.4) pipetted on top. The gels were left in the incubator at 37 °C overnight,

then the PBS removed. The PBS wash was repeated twice more to remove any residual ethanol. Polystyrene surfaces with no gel were treated in the same manner.

7.5.2.2 Ethanol / PBS wash

PBS solution (1 mL, 1.76 mM, pH 7.4) was pipetted on top of the gels, which were then left in the incubator at 37 °C overnight. The PBS was removed and this process repeated twice more. Polystyrene surfaces with no gel were treated in the same manner.

7.5.3 2D cell culture

Cell culture medium was removed from the desired cells, which were washed with PBS (10 mL) and trypsinised (2 mL trypsin/EDTA solution). Cells were resuspended in media, and a 10 µL aliquot mixed with trypan blue solution (10 µL, 0.4% wt/vol) to stain dead/permeable cells. 10 µL of the cell/trypan blue mixture was loaded into a haemocytometer with glass coverslip. Live cells were counted and dilutions accounted for to calculate the concentration of cells in the suspension. The suspension was diluted to the desired concentration (between 50,000 and 10,000 cells mL⁻¹) with cell culture medium. 1 mL cell suspension was added into each well. Media was replaced completely every 3-4 days.

7.5.4 Optical and fluorescence microscopy

The morphology of the cells was assessed by placing the 24 well plates on the imaging stage of a Leica DM IRB microscope. Brightfield images were taken by exposure to visible light from beneath the gels. Fluorescence images were taken by exposure of the sample to light of wavelength 465 nm (ZsGreen λ_{ex} maximum = 496 nm). Fluorescence emission was detected at a wavelength of 510 nm (ZsGreen λ_{em} maximum = 506 nm). Images were taken using a Leica DMC2900 camera.

7.5.5 Gel swelling test

Glass vials (diameter = 1 cm) were weighed prior to the formation of hydrogels. DBS-CONHNH₂, 10% PEGDM, 10% hybrid and 20% hybrid gels (0.5 mL) were prepared in the vials as described in Section 7.2.2. The mass of the vials containing gels were recorded, as well as the height of the gels. H₂O (1 mL) was pipetted onto each of the gels and the samples sealed and left for 3 days. The supernatant was removed and the gels were dabbed dry with blue roll. Care was taken not to

disrupt the gels during this process. The gel was weighed in the glass vial. The gel height was also measured.

7.5.6 PI leaching

Gels (50 μ L) were prepared in washers in a 24 well plate as described above. A DBS-CONHNH₂ gel containing PI was prepared by suspension of the LMWG (1.42 mg) in 0.5 mL aqueous PI solution (0.05% wt/vol). The suspension was sonicated to disperse the solid and heated to dissolution. 50 μ L aliquots were pipetted into the inside of a stainless steel washer. The solution was allowed to cool to room temperature. A translucent gel formed in *ca.* 1 min.

PBS (1 mL, 1.76 mM, pH 7.4) was pipetted on top of each of the gels to simulate the washing process. Samples were left for 24 h, after which time the solution from each well was removed and diluted to 2 mL total volume. The absorbance of the solution was recorded at 286 nm. LMW hydrogel and PBS controls were also measured. The washing process was repeated twice more, and UV absorbance recorded each time. The concentration of PI in each solution was calculated by comparison to a calibration curve. Each experiment was performed in quadruplicate.

7.5.7 SEM sample preparation

Gels were removed from the well plate and placed on a square of copper shim. Double strength fixative (8 % formaldehyde, 5 % glutaraldehyde in 100 mM phosphate buffer was diluted 1:1 in cell culture medium. Gels were submerged in the fixative for 2 h, after which time the fixative was removed. Any excess liquid was removed with filter paper. Gels were frozen in liquid nitrogen before loading the samples onto a Peltier stage. Samples were freeze-dried over a few hours and the samples sputter-coated with a thin layer (< 20 nm) of gold/palladium.

7.5.8 Confocal microscopy

Samples were imaged using a Zeiss LSM 880 confocal microscope. Images were taken by exposure of the sample to light of wavelength 465 nm (ZsGreen λ_{ex} maximum = 496 nm). Fluorescence emission was detected at a wavelength of 510 nm (ZsGreen λ_{em} maximum = 506 nm). Images were taken over a depth of 780 μ m, with an image taken each 10 μ m.

7.5.9 Cell lysis

Samples were washed with carbonate buffer (500 μL per well, pH 10.2, 0.2 M) and the cells lysed in the 24 well plates by addition of 0.1% Triton-X in carbonate buffer (0.5 mL). Samples were rapidly cooled to $-80\text{ }^{\circ}\text{C}$. Upon freezing of the Triton-X solution, the samples were removed from the freezer and incubated at $37\text{ }^{\circ}\text{C}$ until melted. This freeze/thaw cycle was repeated twice more and the sample allowed to cool to room temperature. The solution was pipetted up and down to ensure complete cell lysis.

7.5.10 BCA total protein assay

BCA Protein Assay kit was purchased from ThermoFisher Scientific. Bovine Serum Albumin (BSA) standards were prepared in 0.1% Triton-X solution (in 0.2 M carbonate buffer) by dilution from a $2000\text{ }\mu\text{g mL}^{-1}$ stock solution. The BCA working reagent was prepared as per the assay instructions.

Cells were lysed as described in Section 7.5.9. $25\text{ }\mu\text{L}$ of lysed cell sample (in buffered 0.1 % Triton-X solution) was pipetted into a well in a 96 well plate. BCA working reagent ($200\text{ }\mu\text{L}$) was added to the sample and mixed well on a plate shaker for 30 s. The plate was covered and incubated at $37\text{ }^{\circ}\text{C}$ for 0.5 h. The plate was allowed to cool to room temperature and the absorbance of the solution recorded at 562 nm using a plate reader. Absorbance of 0.1% Triton-X solution blank was subtracted from these values. Protein concentration was calculated by comparison to a calibration curve created by treating the BSA standards ($25\text{ }\mu\text{L}$) with BCA working reagent ($200\text{ }\mu\text{L}$). Samples were compared to control samples with no seeded cells.

7.5.11 Oil Red O assay

7.5.11.1 Staining procedure

Samples were washed with PBS (1 mL, 1.76 mM, pH 7.4). PBS was removed and the cells were fixed in aqueous paraformaldehyde solution (1 mL, 4% wt/vol) for 10 minutes. The fixative was removed and the samples washed with H_2O (1 mL). After the H_2O was removed, the samples were submerged in 60% propan-2-ol solution (aqueous) and left for 5 min before removal. Oil Red O staining solution (1 mL, 7.3 mM in 60% propan-2-ol) was added to the wells and the samples incubated for 10 minutes. The staining solution was removed and the samples washed once with 60% propan-2-ol solution, and then with H_2O (1 mL) to remove non-specific staining. H_2O washes were carried out until no further stain eluted from the samples.

7.5.11.2 Imaging

Oil Red O staining was imaged on a stereo microscope (Zeiss) using Brightfield settings. Microscope was fitted with an AxioCam MRc5 camera.

7.5.11.3 Elution

The remaining stain was eluted by adding propan-2-ol (0.5 mL) to each well plate. Samples were mixed for 3 h using a plate shaker to ensure maximum elution from gel samples. 100 μ L of this eluent was added to a 96 well plate and the absorbance recorded at 490 nm using a plate reader and the absorbance of propan-2-ol (100 μ L) subtracted. The elution process was repeated until no absorbance was observed.

7.5.12 Alizarin Red S assay

7.5.12.1 Staining procedure

Samples were washed once with PBS (1 mL, 1.76 mM, pH 7.4). PBS was removed and the cells were fixed in aqueous paraformaldehyde solution (1 mL, 4% wt/vol) for 20 minutes. The fixative was removed and the samples washed three times with PBS (1 mL, 1.76 mM, pH 7.4). The cells were stained with Alizarin Red S solution (1 mL, 40 mM, pH 4.2) for 20 minutes at room temperature, after which time the staining solution was removed. The cells were washed three times in PBS (1 mL, 1.76 mM, pH 7.4) before washing with tap water (1 mL) until no further stain was eluted from the samples.

7.5.12.2 Imaging

Alizarin Red S staining was imaged on a stereo microscope (Zeiss) using Brightfield settings. Microscope was fitted with an AxioCam MRc5 camera.

7.5.12.3 Elution

Alizarin Red S stain was eluted using cetylpyridinium chloride solution (CPC, 0.5 mL, 100 mM in H₂O). The plates were covered and mixed on a plate shaker for 3 h. A sample of eluent (100 μ L) was pipetted into a 96 well plate. The absorbance of the eluent solution was recorded at 570 nm and the absorbance of 100 mM CPC solution subtracted. The elution process was repeated until no absorbance was observed.

7.5.13 Wnt Reporter Assay

7.5.13.1 *Wnt treatment*

Cells were treated after 2 weeks of growth with recombinant human Wnt3a protein (300 ng mL⁻¹). Half (0.5 mL) the cell culture medium was removed from the samples to be treated, and replacement with 0.5 mL Wnt3a solution (600 ng mL⁻¹ in cell culture medium). Cells were left a further 24 h before lysing as described in Section 7.5.9.

7.5.13.2 *EGFP expression*

50 µL cell lysis solution was pipetted into a black 96 well plate. Using a fluorescence plate reader, EGFP fluorescence was stimulated with light of wavelength 488 nm. Emission intensity was recorded at 507 nm and compared to 0.1% Triton-X (50 µL) in 0.2 M carbonate buffer as a control sample.

7.5.14 ALP assay

A solution of *p*NPP (3 mM) was prepared by dissolving 10 mg *p*NPP in 9 mL carbonate buffer (0.2 M, pH 10.2) and adding MgCl₂ solution (1 mL, 100 mM). From this stock, a working *p*NPP solution was prepared by mixing 1 mL stock with 2 mL H₂O.

Cells were lysed as described in Section 7.5.9. Aliquots (50 µL) of lysed cell solution were transferred to a 96 well plate. 50 µL *p*NPP solution was added to the sample. The well plate was covered and the sample incubated for 1 h. The absorbance of the sample at 405 nm was recorded. The absorbance of 0.1% Triton-X in carbonate buffer (0.2 M) was recorded as a control. The concentration of *p*NP in each sample was quantified by comparison to a calibration curve prepared by dilution of a 10 mM *p*NP solution with carbonate buffer (0.2 M).

7.5.15 Photo-patterned gels in well plates

DBS-CONHNH₂ (6 mM) hydrogels were prepared as described above. 50 µL of a solution of PEGDM (10 or 20% wt/vol) and PI (0.05% wt/vol) was pipetted on top of the gels and left for 3 days, after which time the supernatant was removed. Well plates were placed upside down and an acetate laser printed photomask (4 layers) applied to the outside. The mask was designed such that half the gel was exposed to UV light and half was shielded. The gel was exposed to long wavelength UV irradiation for 20 min, yielding gels which were half soft and half stiff.

7.5.16 Spatially-resolved stem cell growth

The gels prepared in Section 7.5.15 were submerged in 1 × PBS for 24 h to induce swelling of the hybrid gel network. After this time the PBS was removed and the soft LMWG region of the photo-patterned gels was removed. DBS-CONHNH₂ (1.42 mg) was suspended in autoclaved H₂O (0.5 mL) with sonication. The suspension was heated to dissolution and 25 μL aliquots of the hot sol added to the empty region of the inside of the washer. On cooling to room temperature, a gel formed in these regions (*ca.* 1 min) The gels were washed once with ethanol (1 mL, 10 min) and three times with 1 × PBS (1 mL, 24 h).

Cells were seeded on the multidomain gels in a 2D culture at a density of 10,000 cells mL⁻¹ (1 mL) following the procedure outlined in Section 7.5.3. Cell growth and morphology were monitored by optical and fluorescent microscopy using a Zeiss LSM 880. Image analysis was performed in ImageJ.

7.5.17 Gradient patterning

7.5.17.1 Gel preparation

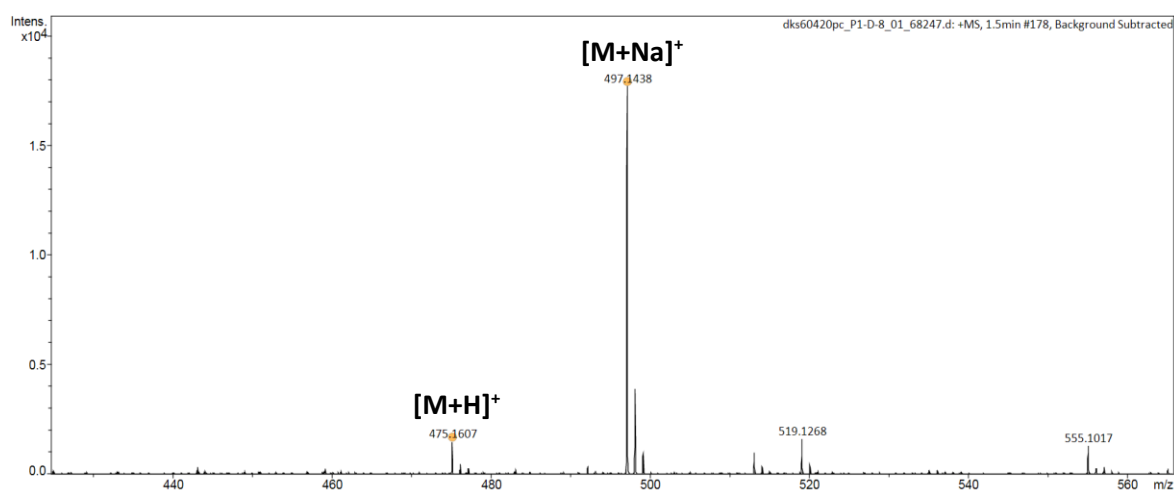
Hybrid gels (10 mL) were prepared in 5 cm × 5 cm × 1 cm glass trays as described in Section 7.2.10.3. A gradient photomask (4 layers, Figure 5.27) was placed over the gel and the sample irradiated with long-wavelength UV light (10 min).

7.5.17.2 Rheology sample preparation

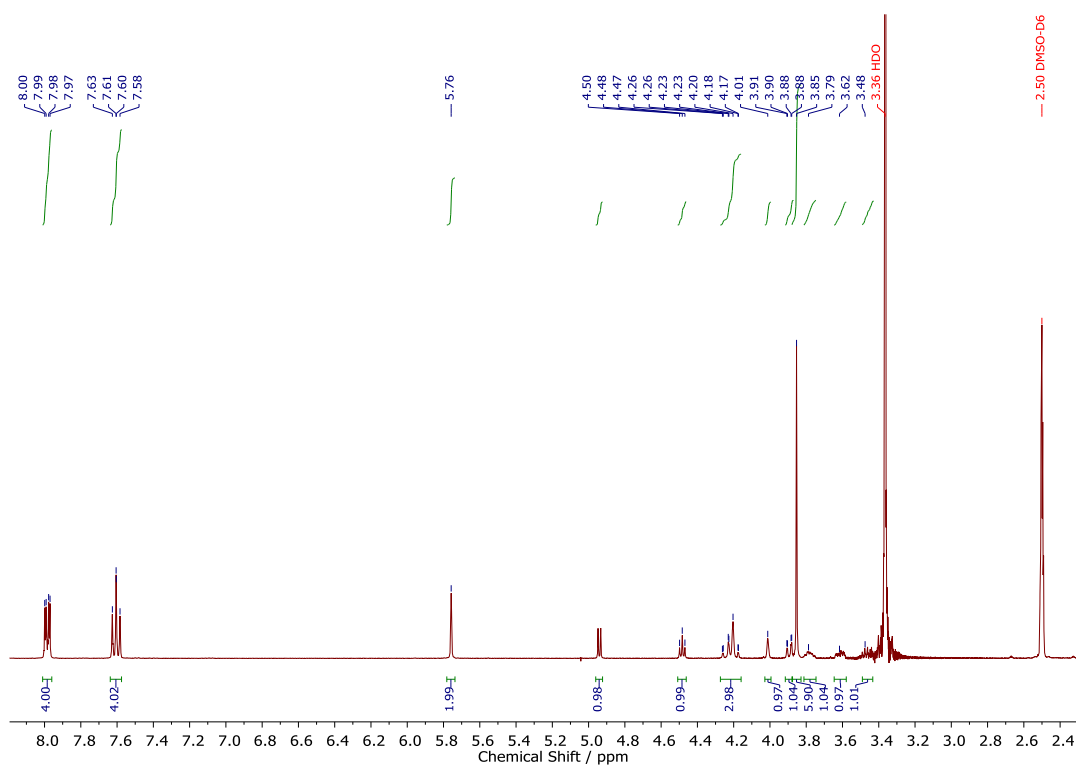
Regions of the hybrid gel were sampled by cutting of a circular gel disc (diameter = 1.8 cm, height = 0.5 cm) using a bottomless 8.5 mL vial. The gel discs were transferred to the lower plate of the rheometer. Rheology methods were employed as described in Section 7.2.9.

Appendices

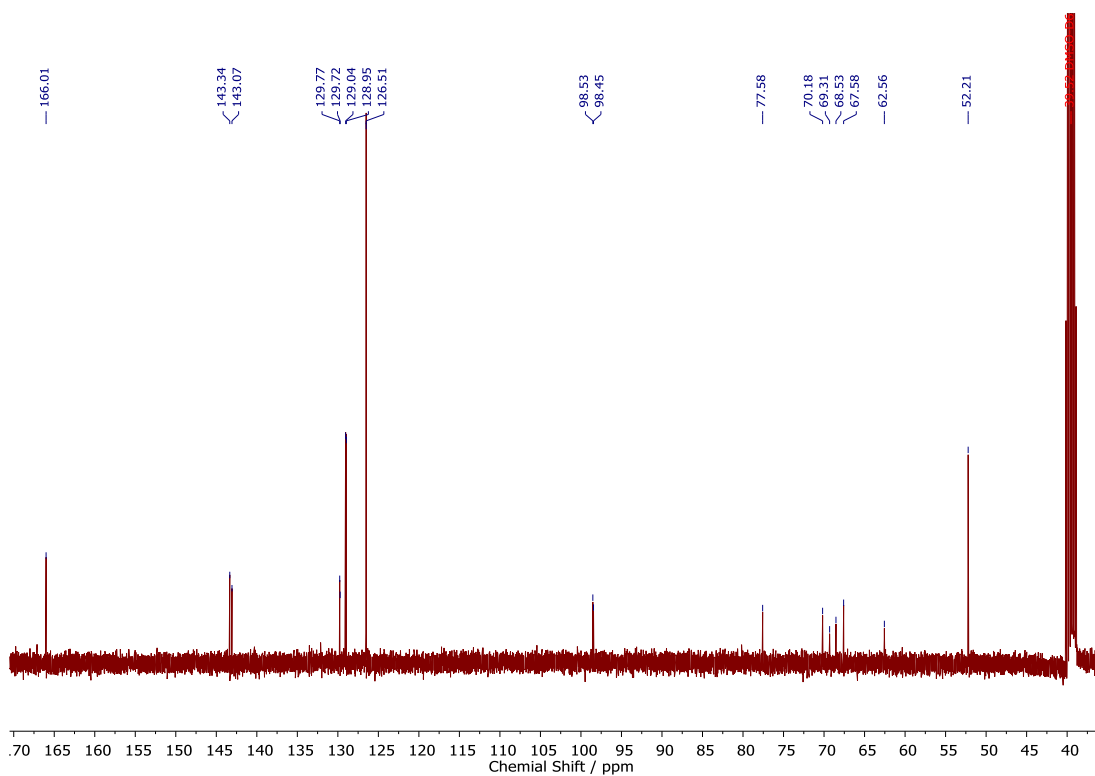
Appendix 1: Characterisation of DBS-CO₂Me



ESI MS of DBS-CO₂Me. Peaks at 475.1607 and 497.1438 are [M+H]⁺ and [M+Na]⁺. Peaks representing MBS-CO₂Me (C₁₅H₂₀O₈, [M+H]⁺ = 329.12, [M+Na]⁺ = 351.11) and TBS-CO₂Me (C₃₃H₃₂O₁₂, [M+H]⁺ = 621.20, [M+Na]⁺ = 643.18) are not seen.

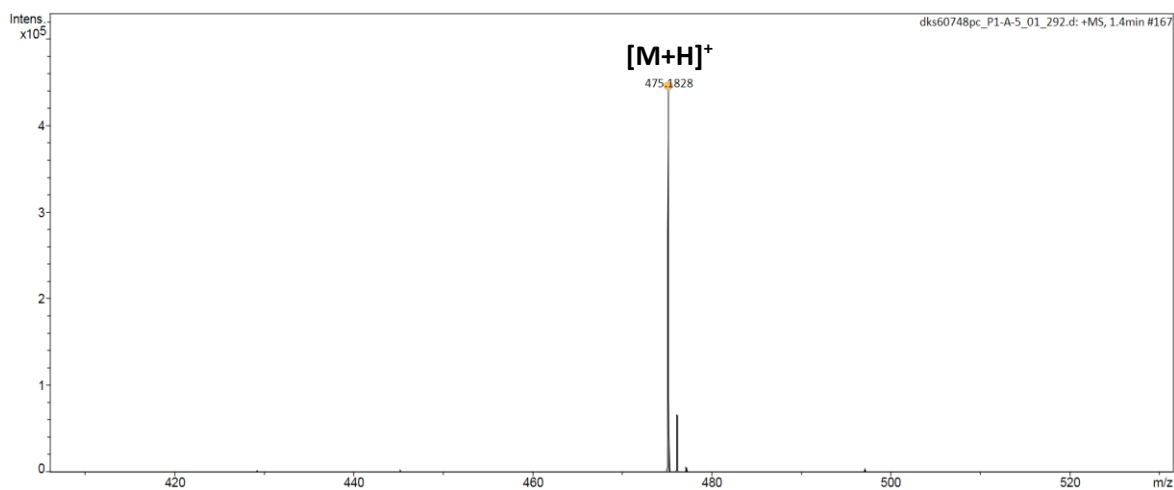


¹H NMR spectrum of DBS-CO₂Me

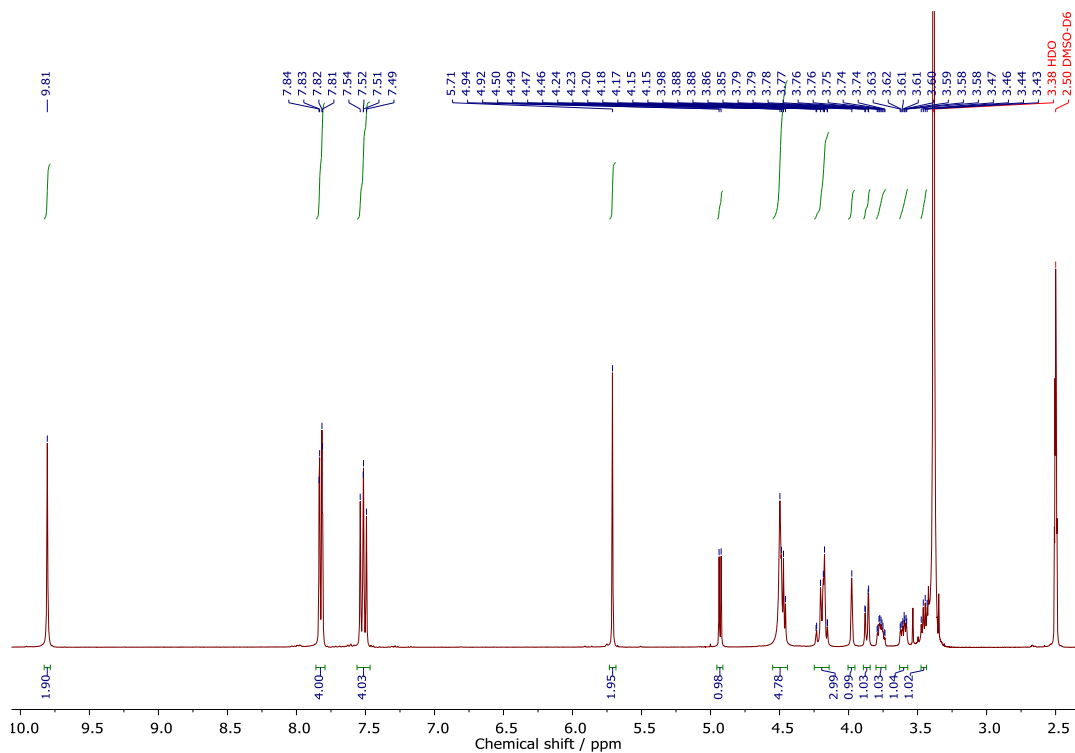


^{13}C NMR spectrum of DBS- CO_2Me

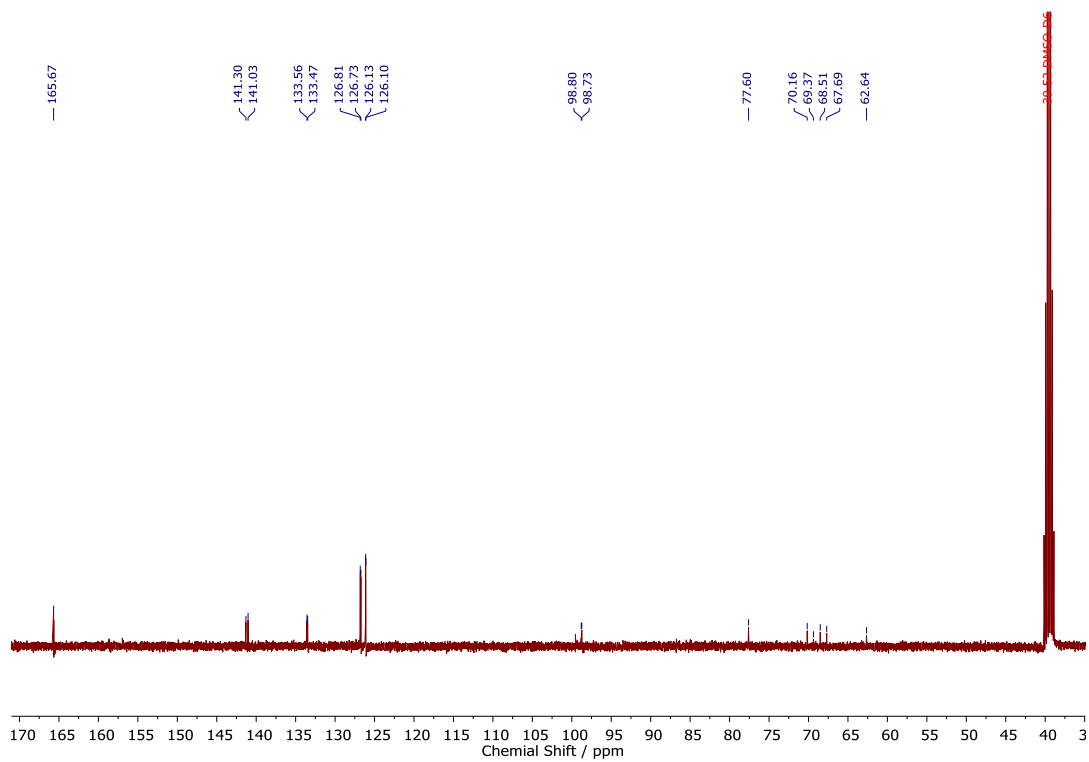
Appendix 2: Characterisation of DBS-CONHNH₂



ESI MS of DBS-CONHNH₂. Peak at 475.1828 is $[\text{M}+\text{H}]^+$. Peaks representing MBS-CONHNH₂ ($\text{C}_{15}\text{H}_{20}\text{O}_8$, $[\text{M}+\text{H}]^+ = 329.13$) and TBS-CONHNH₂ ($\text{C}_{33}\text{H}_{32}\text{O}_{12}$, $[\text{M}+\text{H}]^+ = 621.23$) are not seen.

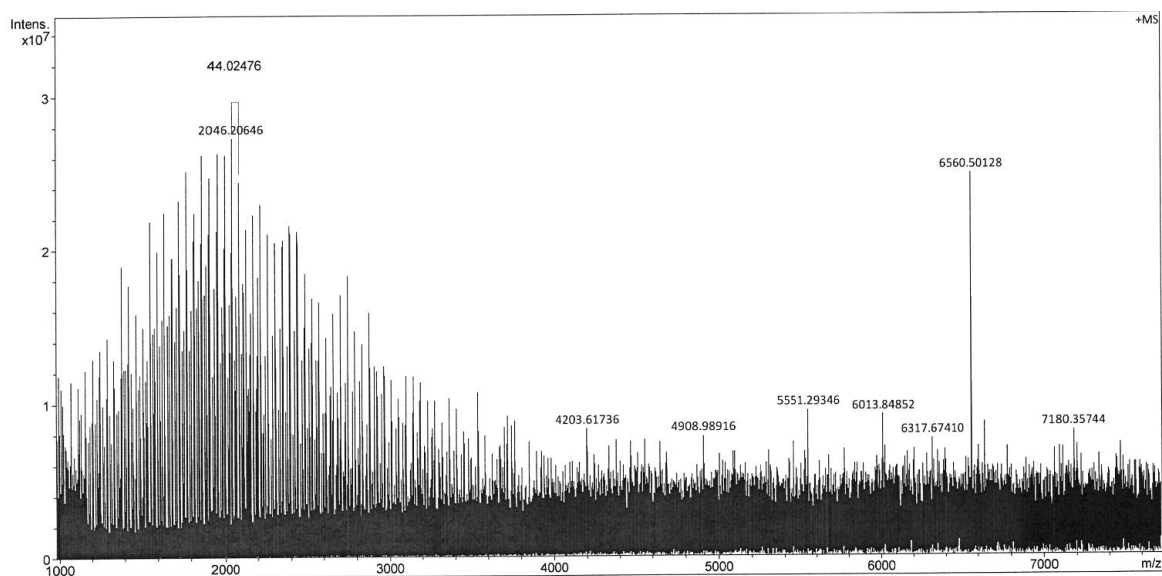


^1H NMR spectrum of DBS-CONHNH₂

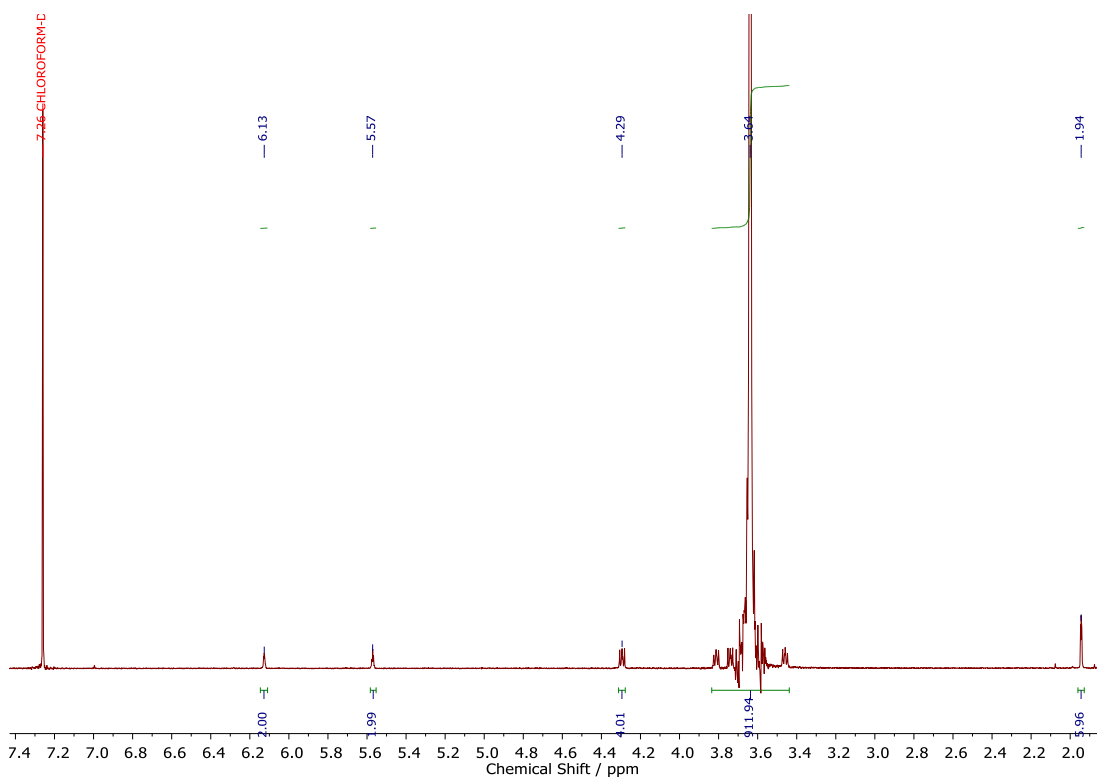


^{13}C NMR spectrum of DBS-CONHNH₂

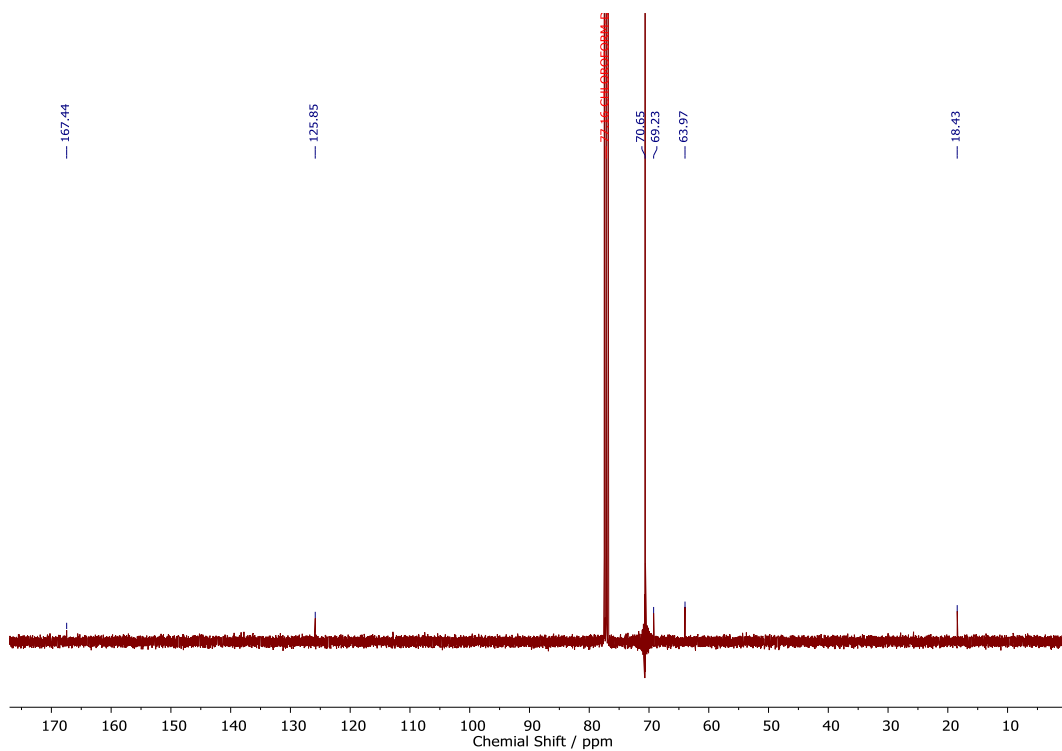
Appendix 3: Characterisation of PEGDM



ESI MS of PEGDM

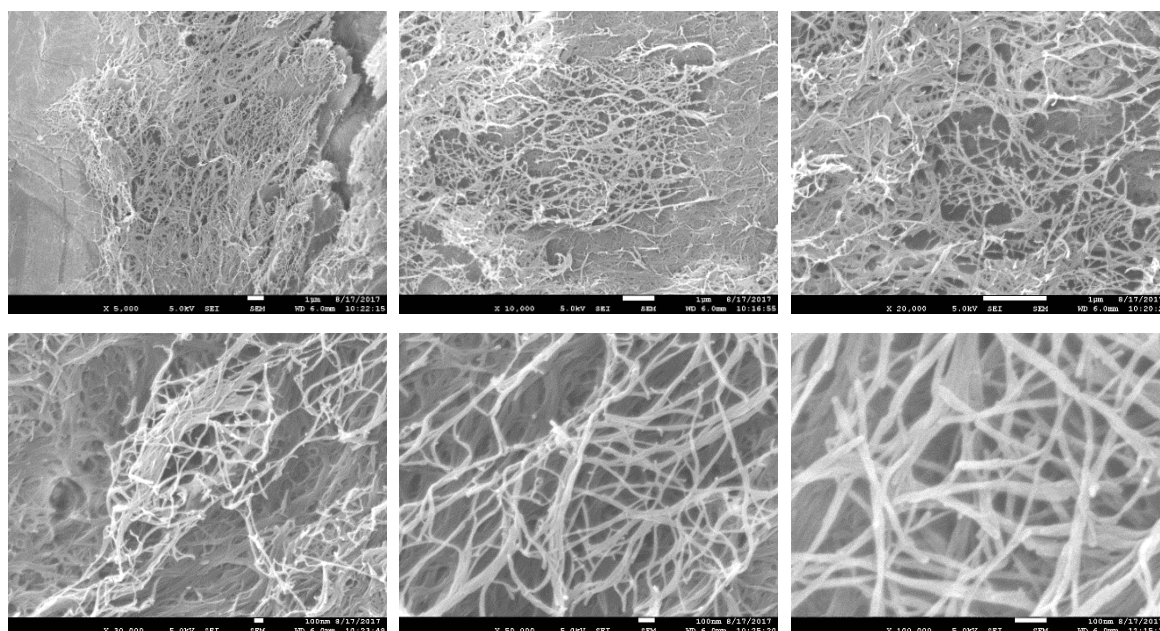


¹H NMR spectrum of PEGDM

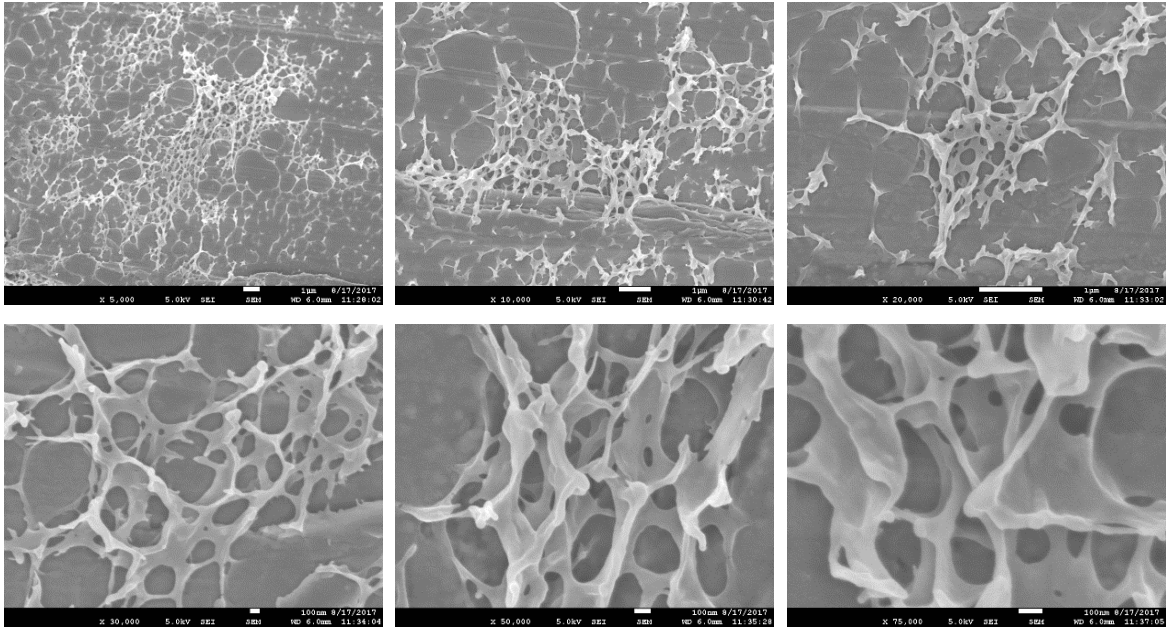


^{13}C NMR spectrum of PEGDM

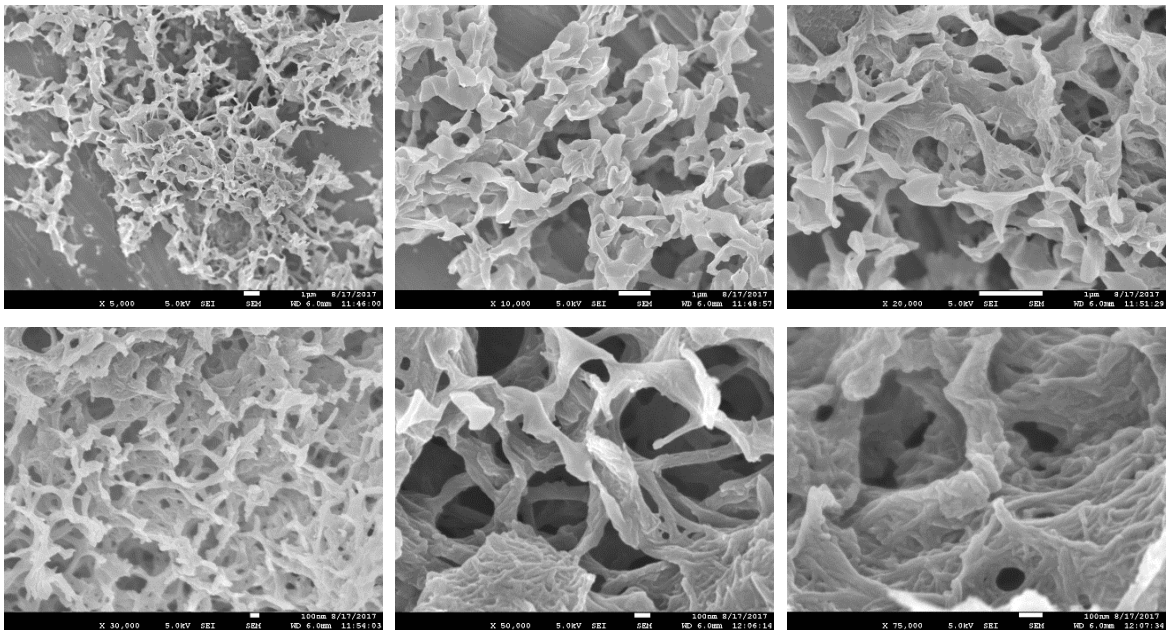
Appendix 4: Scanning Electron Micrographs of Hydrogels



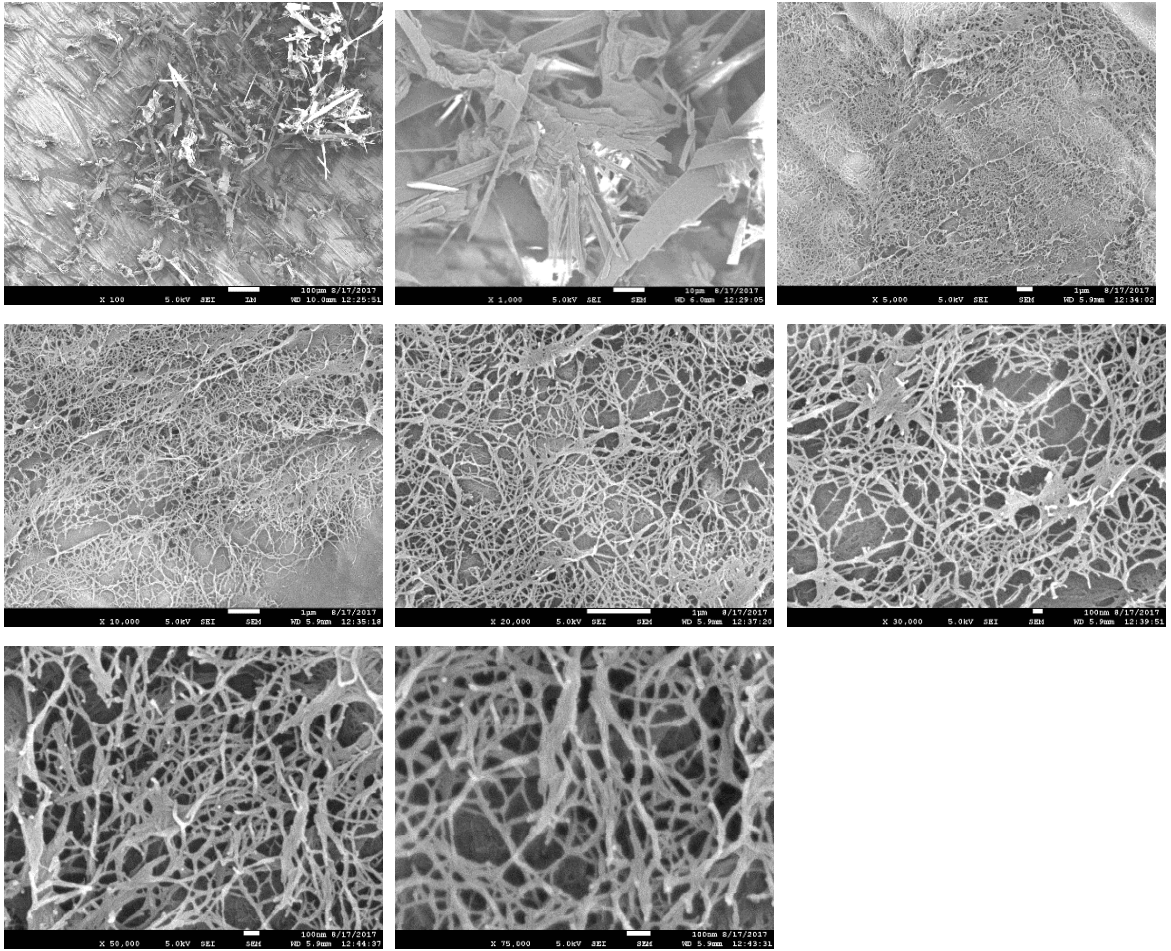
DBS-CONHNH₂ (6 mM)



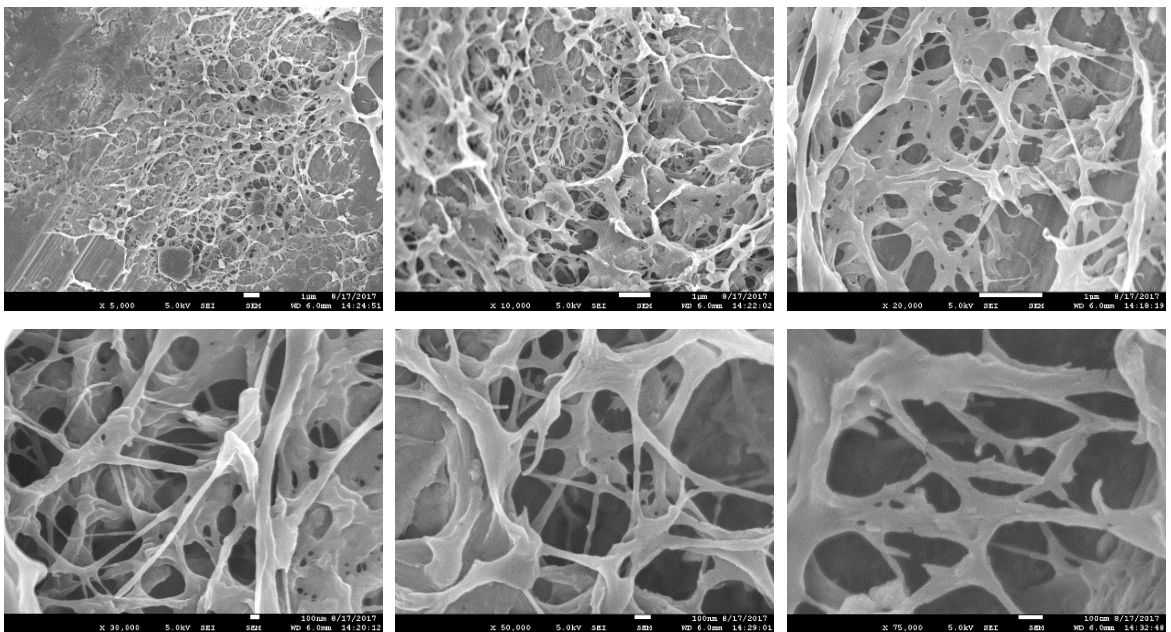
PEGDM (10% wt/vol)



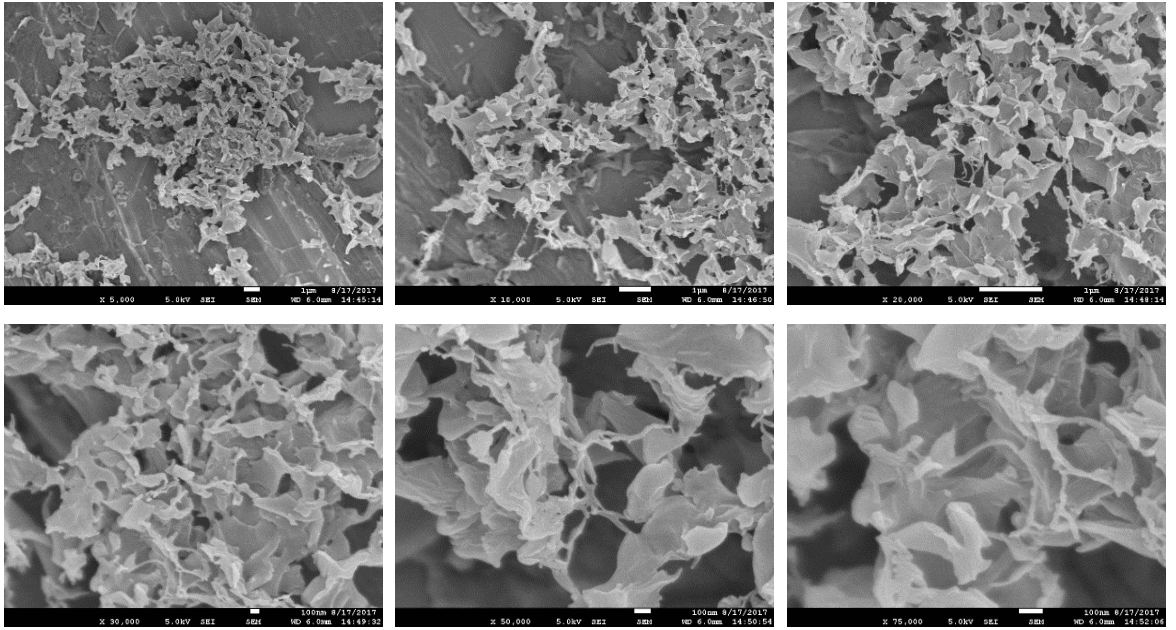
10% Hybrid



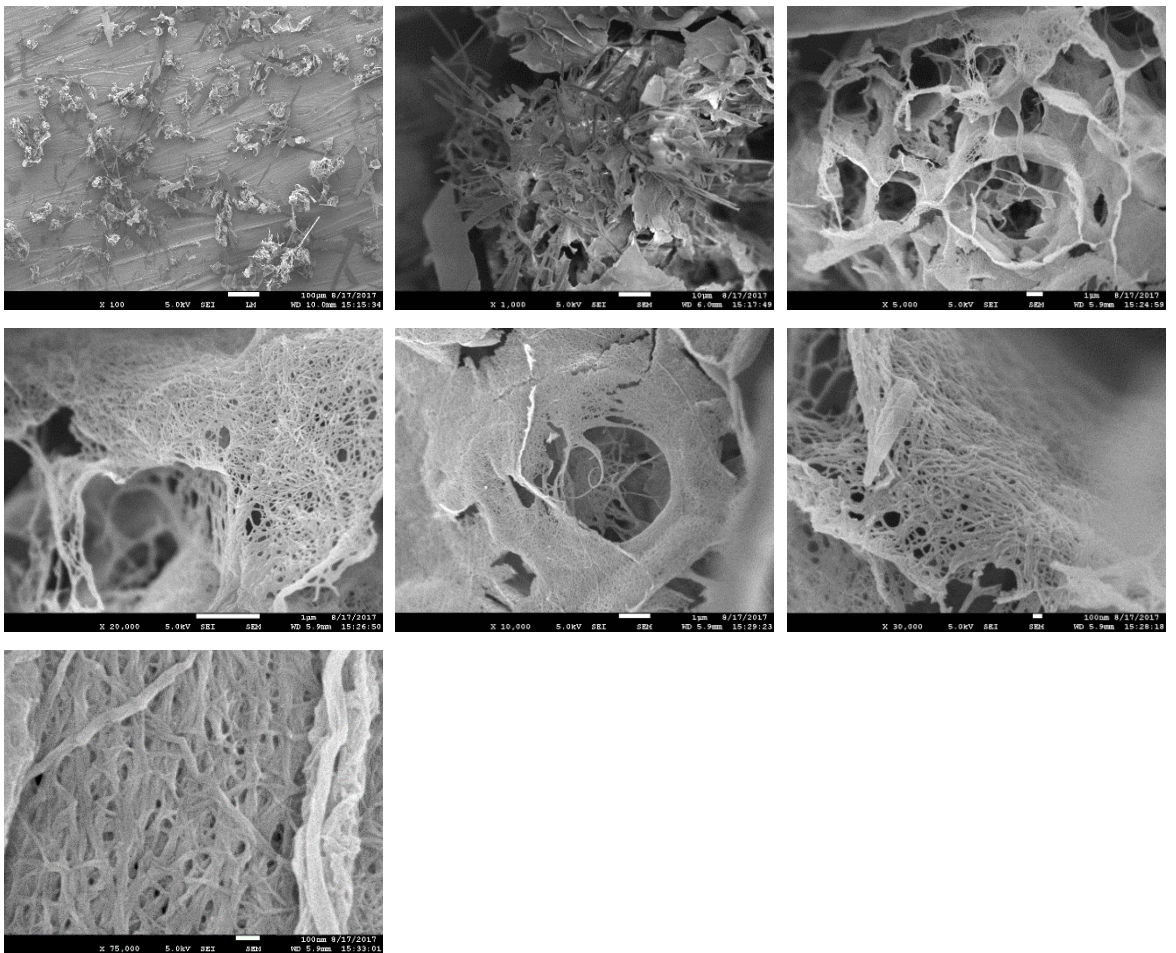
DBS-CONHNH₂ (6 mM) + NPX (6 mM)



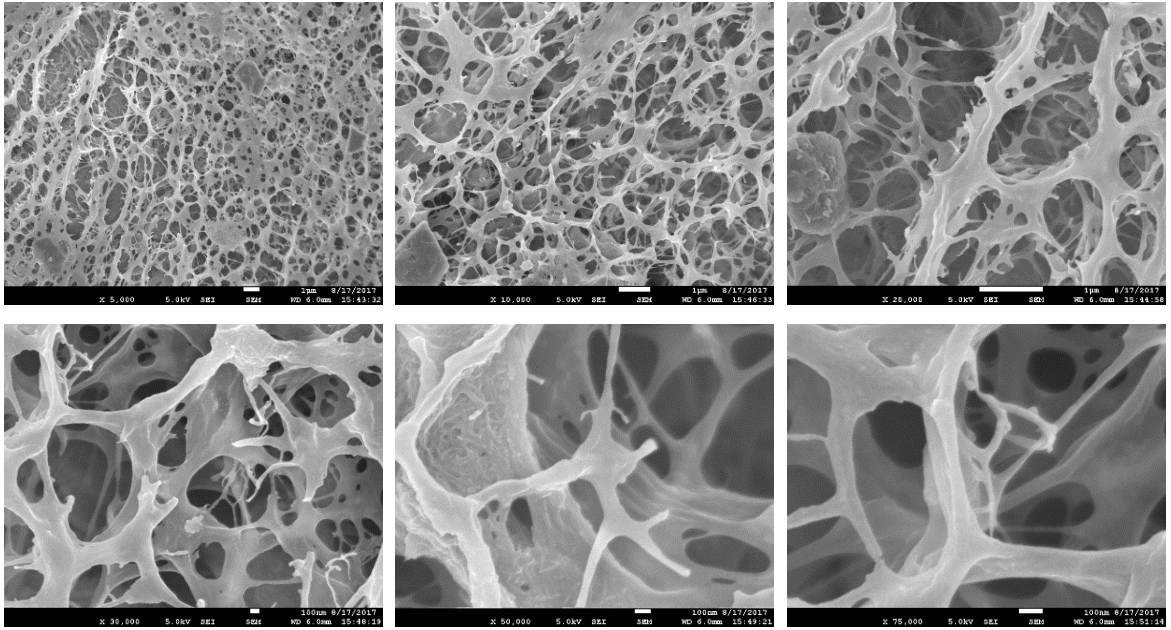
10% Hybrid + NPX (6 mM)



10% hybrid before UV-exposure

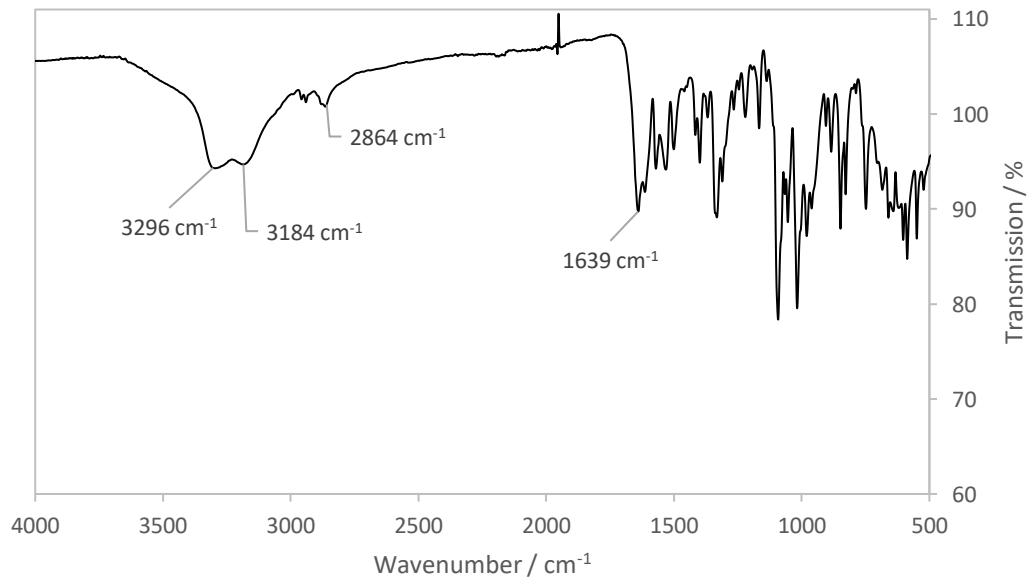


DBS-CONHNH₂ (6 mM) + NPX (6 mM) submerged in pH 4 buffer (72 h)

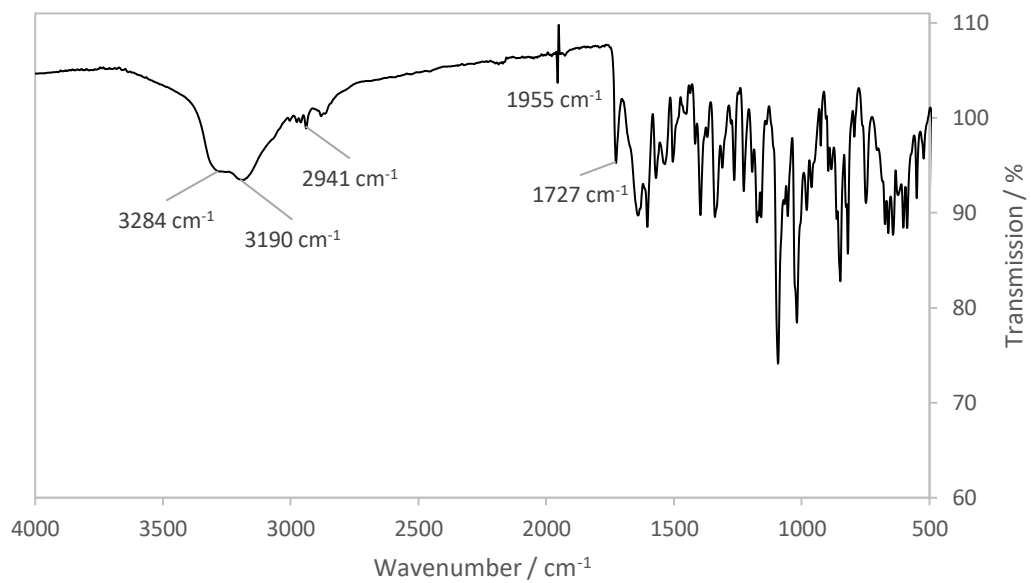


10% Hybrid + NPX (6 mM) submerged in pH 4 buffer (72 h)

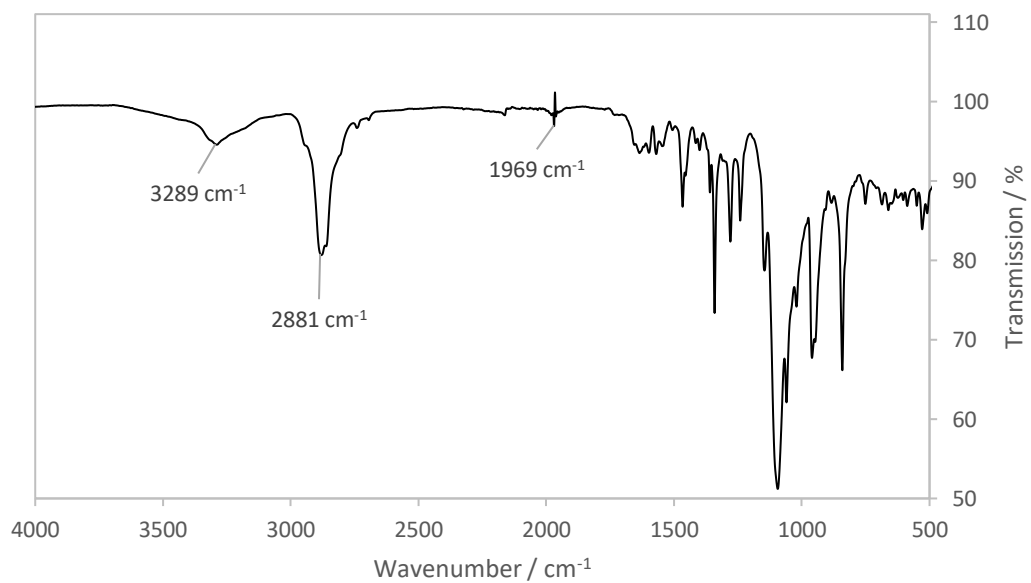
Appendix 5: IR spectra (all gels are xerogels)



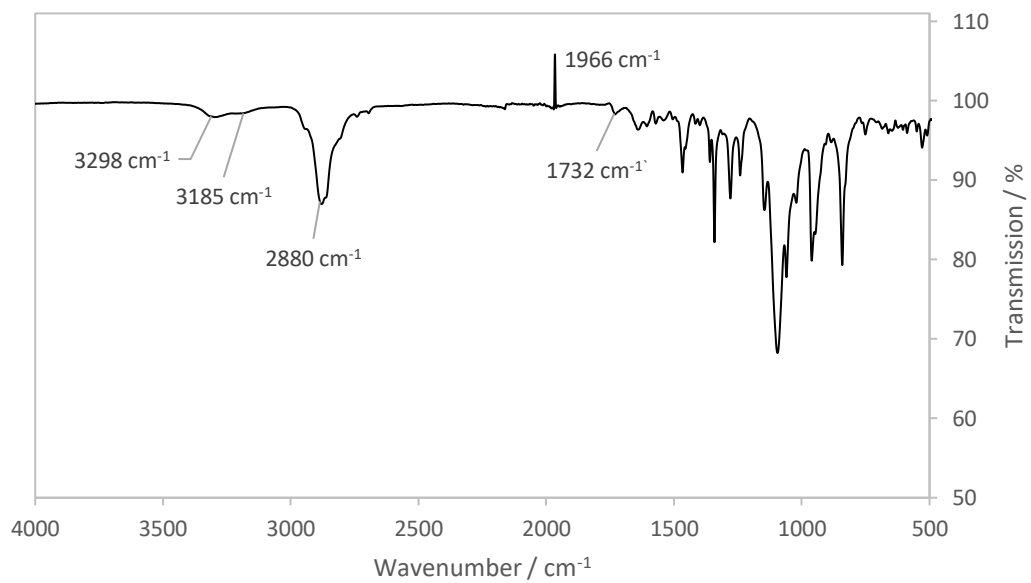
DBS-CONHNH₂ gel (6 mM)



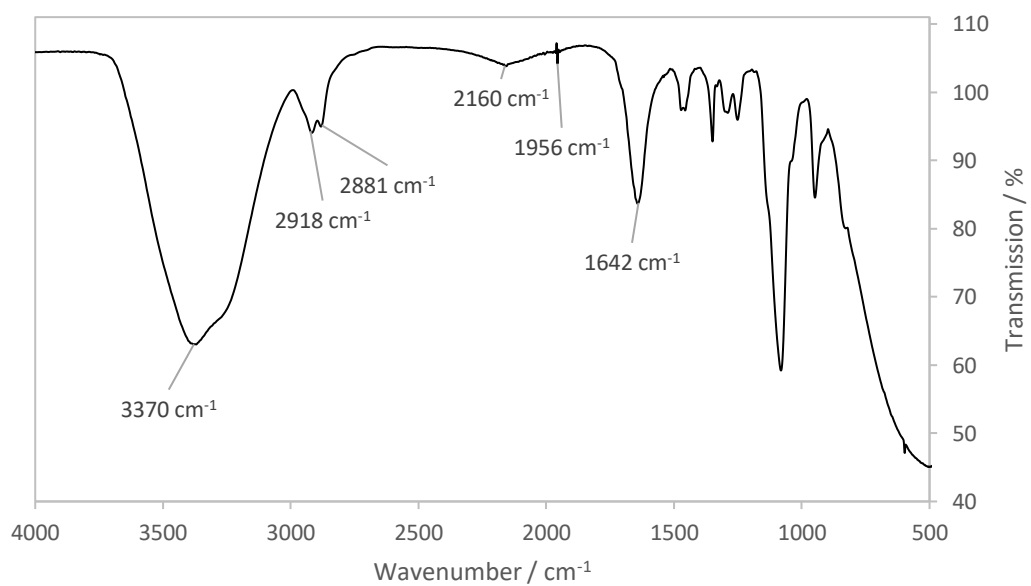
DBS-CONH₂ gel (6 mM) + NPX (6 mM)



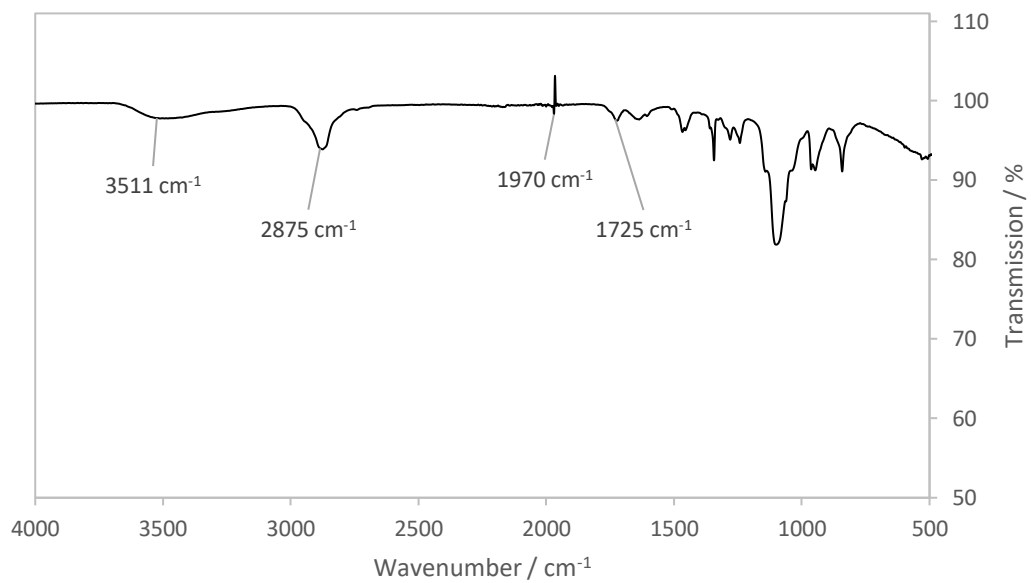
10% hybrid gel (6 mM)



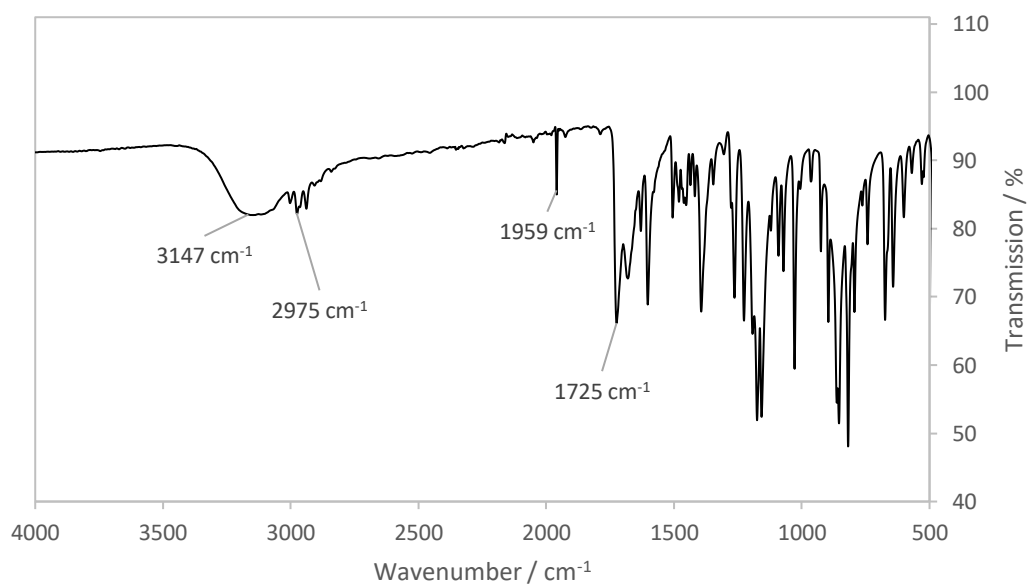
10% hybrid gel + NPX (6 mM)



PEGDM gel (10% wt/vol)



PEGDM gel (10% wt/vol) + NPX (6 mM)

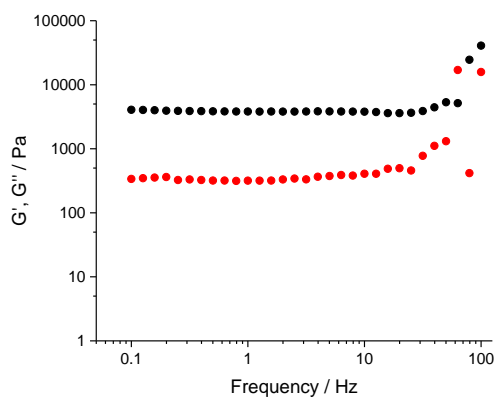


NPX powder

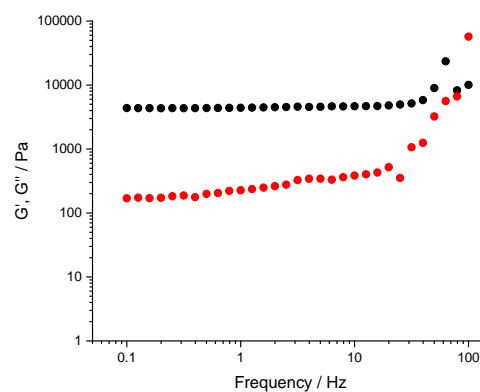
Appendix 6: Representative rheology traces of hydrogels

In all cases black circles represent the elastic modulus (G') and red circles represent the loss modulus (G'') of the material.

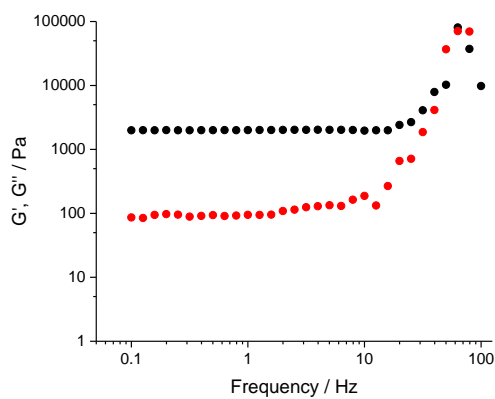
Gels without NPX: Frequency sweeps



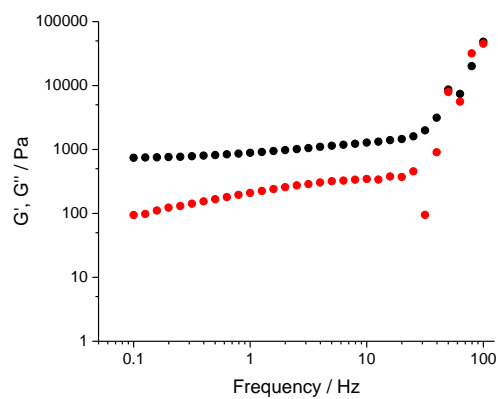
DBS-CONH₂ (6 mM)



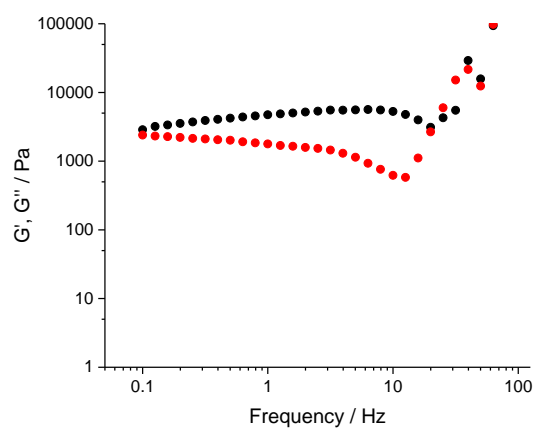
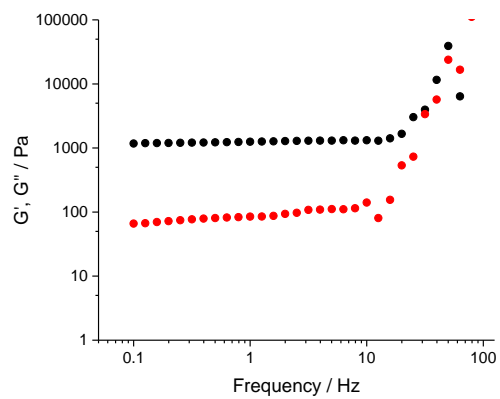
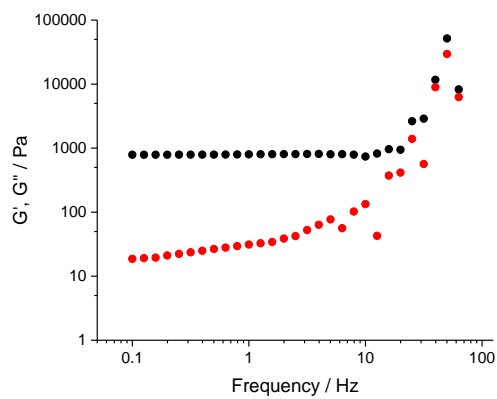
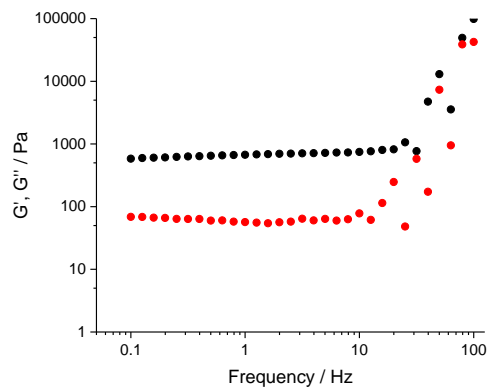
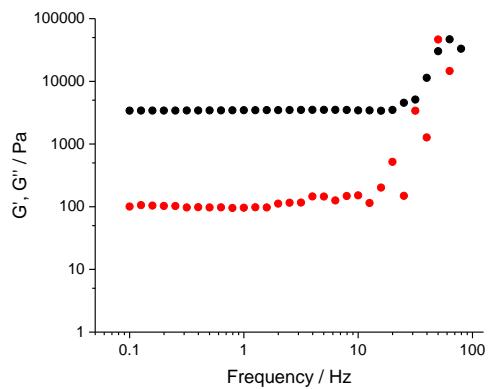
DBS-CONH₂ (6 mM) – UV exposure for 0.5 h



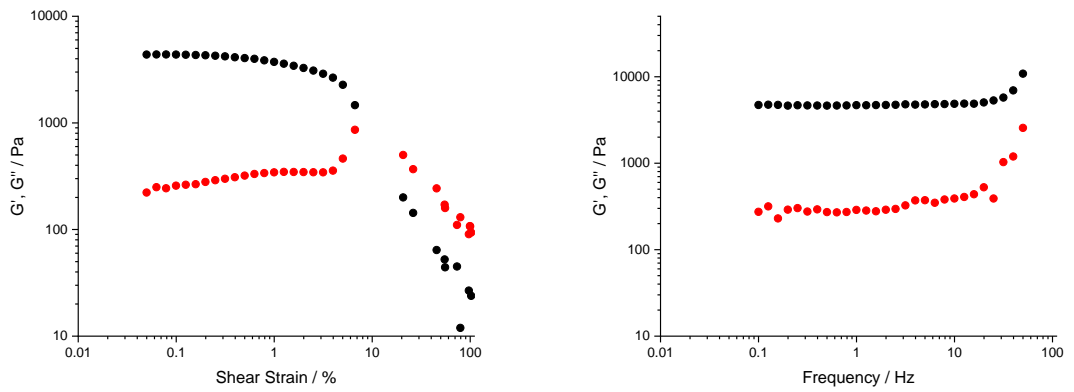
DBS-CONH₂ (8 mM)



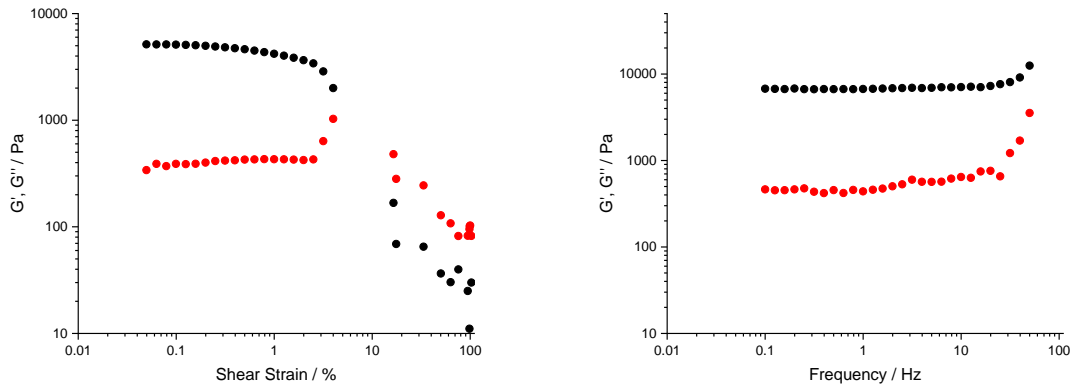
5% Hybrid



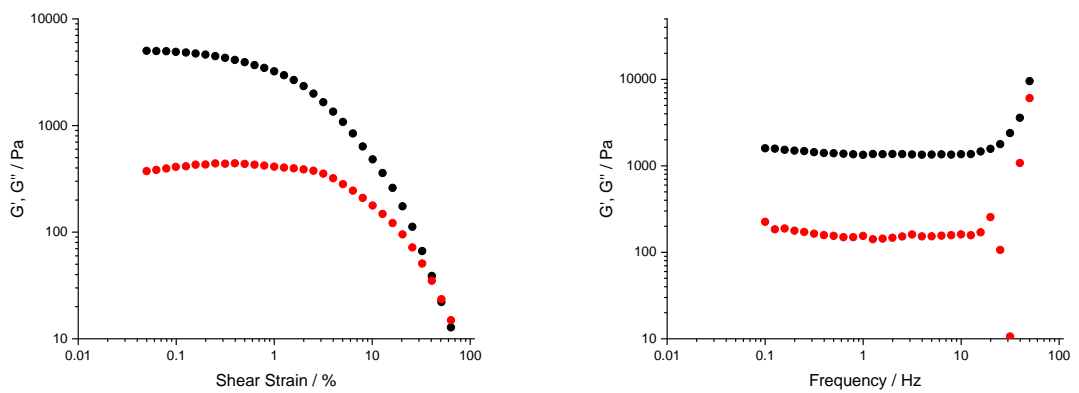
DBS-CONHNH₂ gels (6 mM) – solvent system test



0% EtOH in H₂O: Amplitude sweep (left), frequency sweep (right)

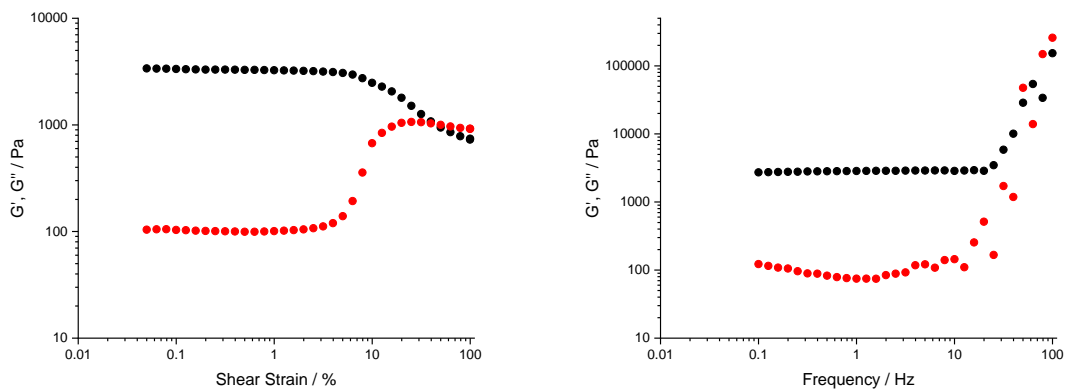


10% EtOH in H₂O: Amplitude sweep (left), frequency sweep (right)

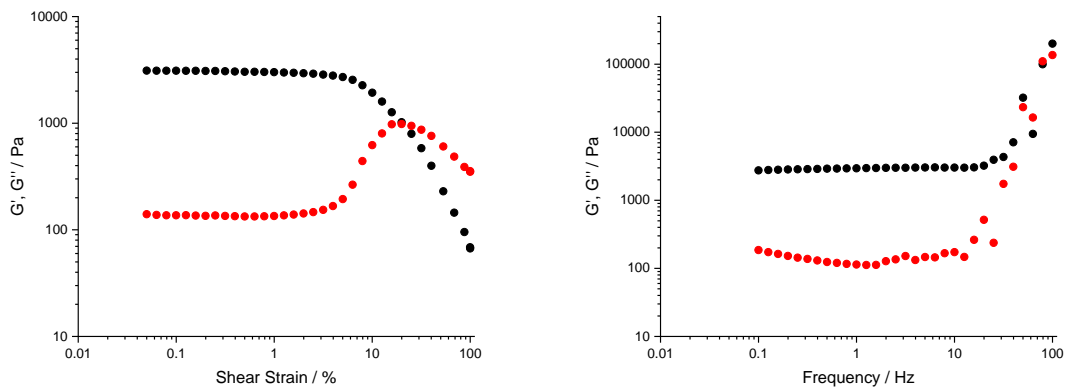


20% EtOH in H₂O: Amplitude sweep (left), frequency sweep (right)

Crosslinking Density Test (10% hybrid gel)

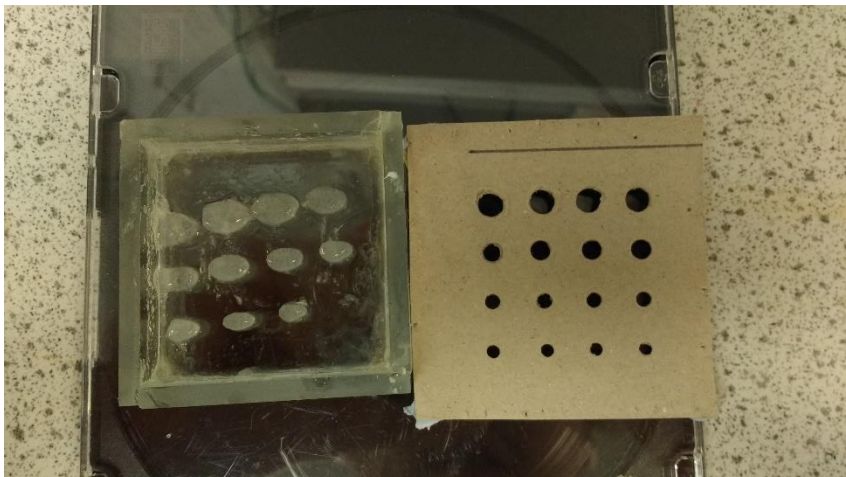


Top half: Amplitude sweep (left), frequency sweep (right)



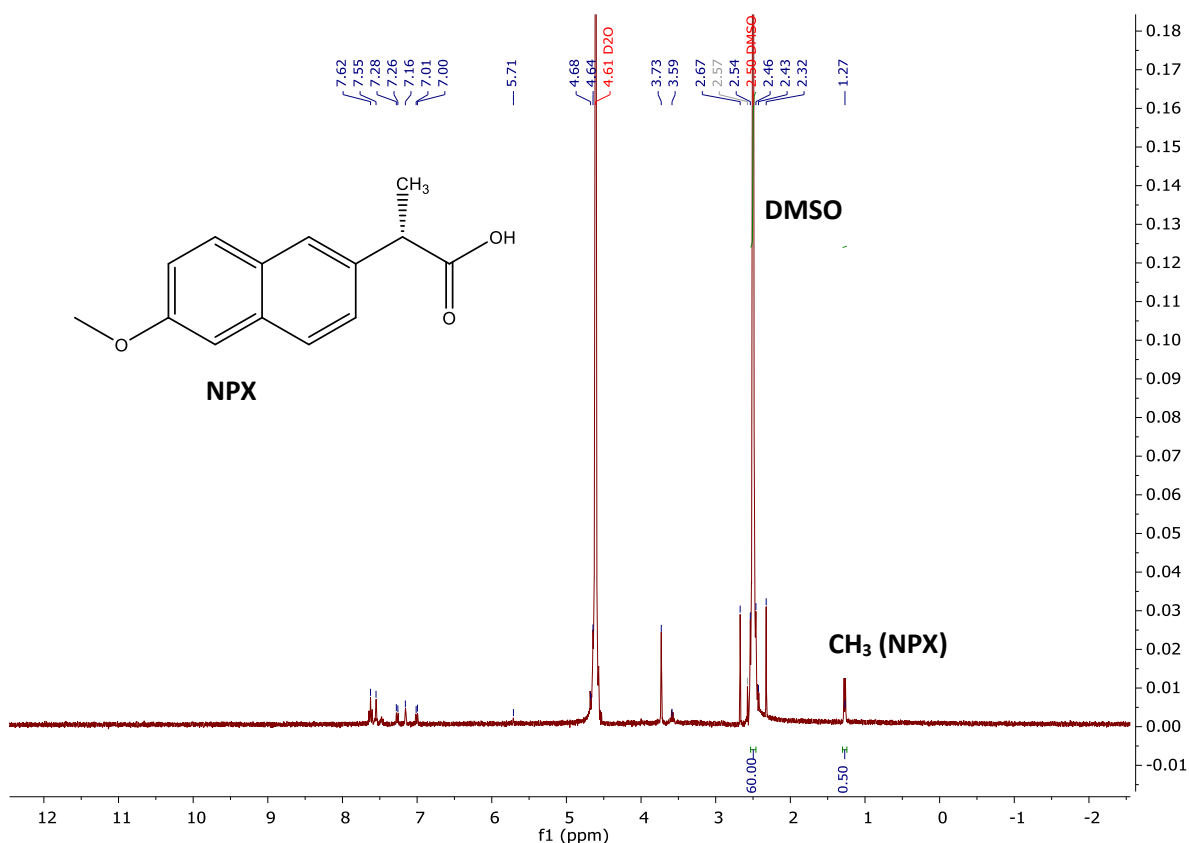
Bottom half: Amplitude sweep (left), frequency sweep (right)

Appendix 7: Photo-patterning resolution test, 20% EtOH gel



Appendix 8: Example NMR quantification experiment

Calculation of the unbound NPX in a DBS-CONH₂ is given as an exemplar here. The same methodology was applied to calculate e.g. percentage gelation of DBS-CONH₂, comparing known peaks for the compound of interest to the DMSO standard in each case.



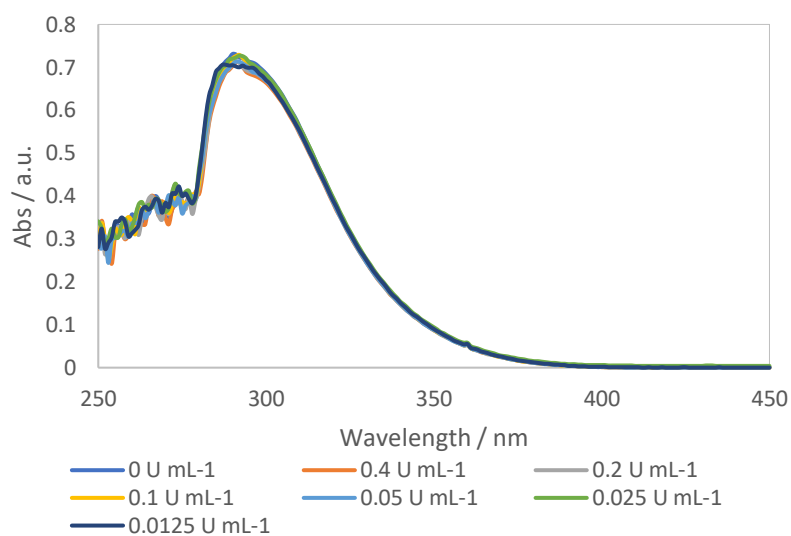
¹H NMR spectrum of NPX (6 mM) loaded DBS-CONH₂ (6 mM) hydrogel made in D₂O solvent. Solution was spiked with DMSO (0.028 M) to quantify unbound NPX.

$$0.50/3 = 0.17$$

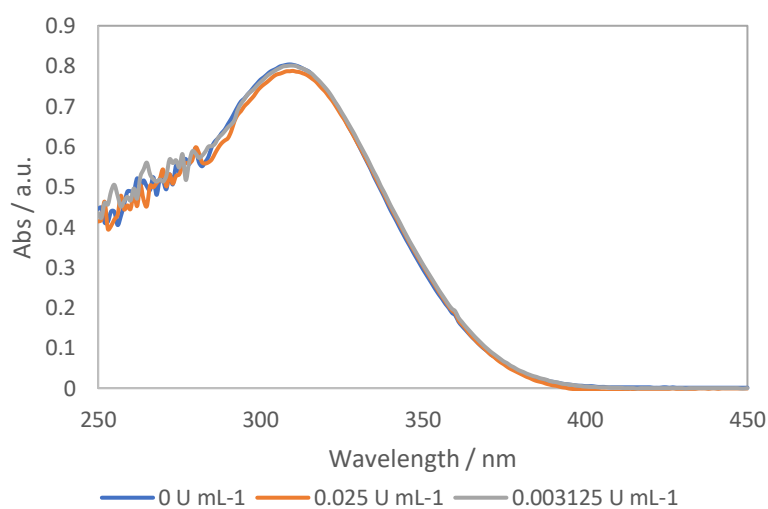
$$\left(\frac{0.17}{10}\right) \times 0.028 M = 4.8 \times 10^{-4} M$$

$$\frac{4.8 \times 10^{-4} M}{6 \times 10^{-3} M} \times 100\% = 7.93\%$$

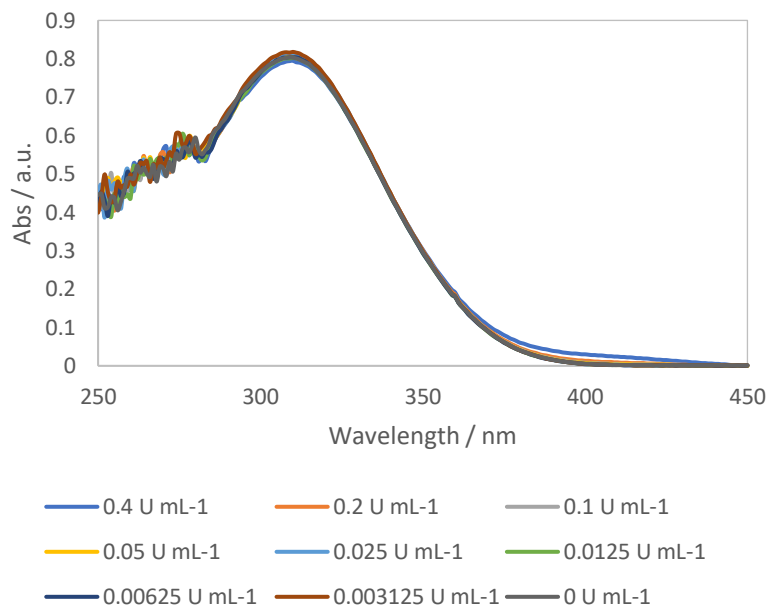
Appendix 9: UV-vis spectra of ALP solution-phase reactions



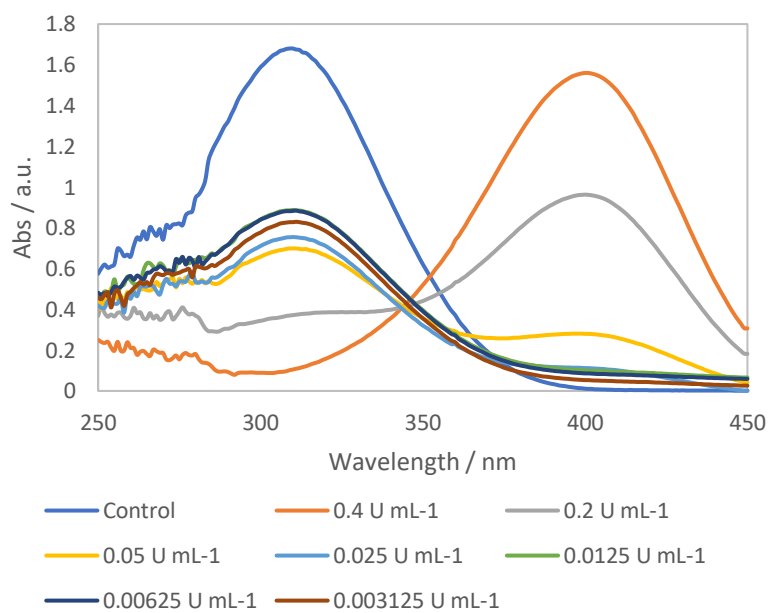
UV-vis spectra of ALP solution-phase reaction with pNPP after 2 h in pH 4 acetate buffer



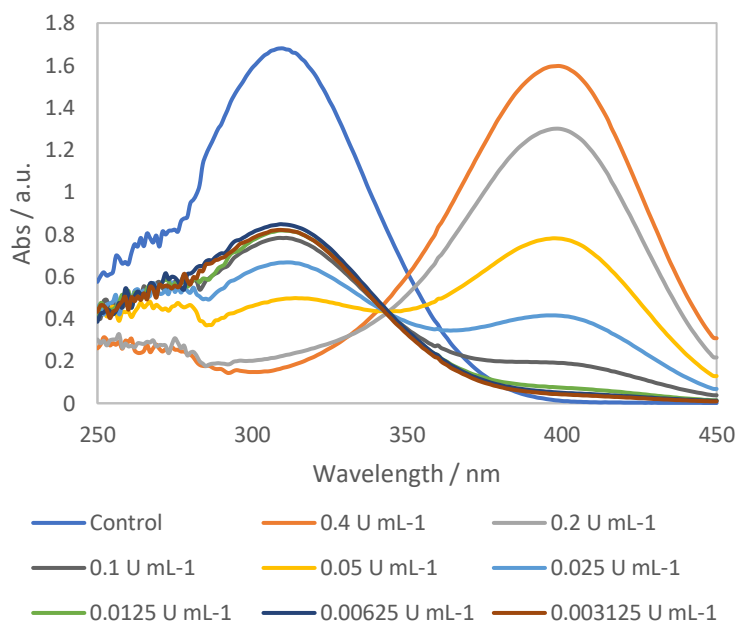
UV-vis spectra of ALP solution-phase reaction with pNPP after 2 h in pH 7 phosphate buffer



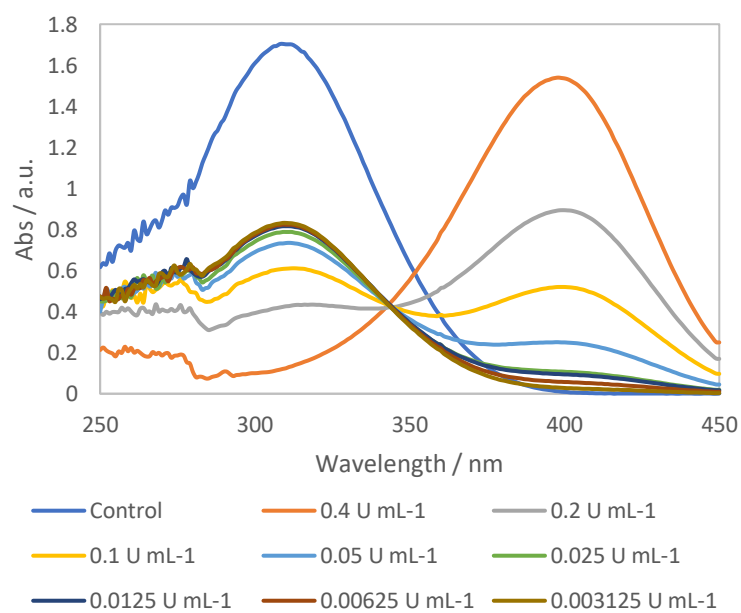
UV-vis spectra of ALP solution-phase reaction with pNPP after 24 h in pH 7 phosphate buffer



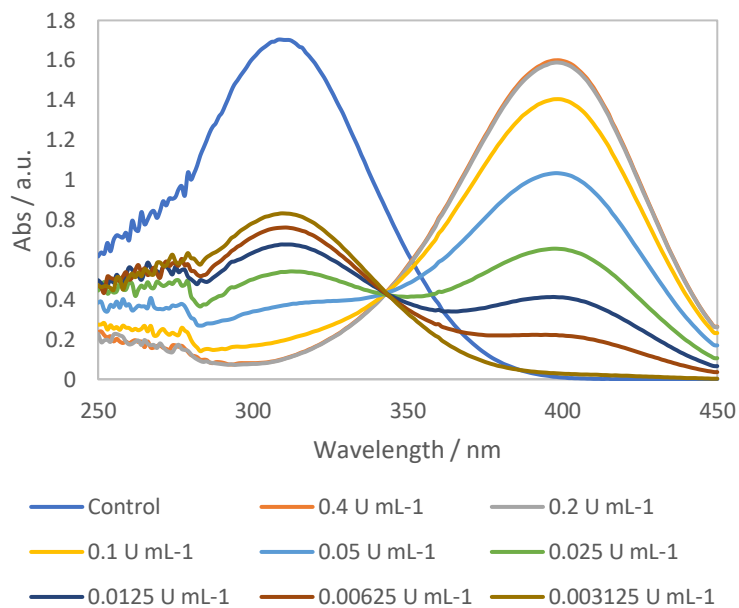
UV-vis spectra of ALP solution-phase reaction with pNPP after 2 h in pH 9 glycine/NaOH buffer



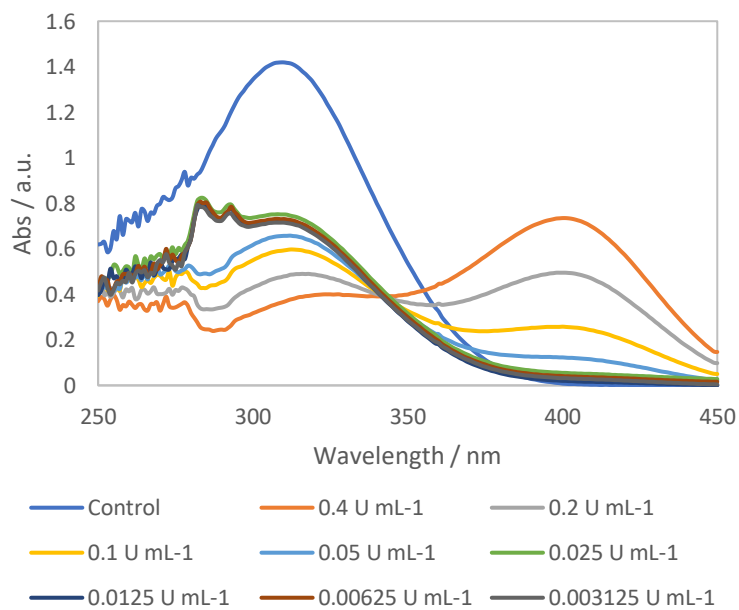
UV-vis spectra of ALP solution-phase reaction with pNPP after 24 h in pH 9 glycine/NaOH buffer



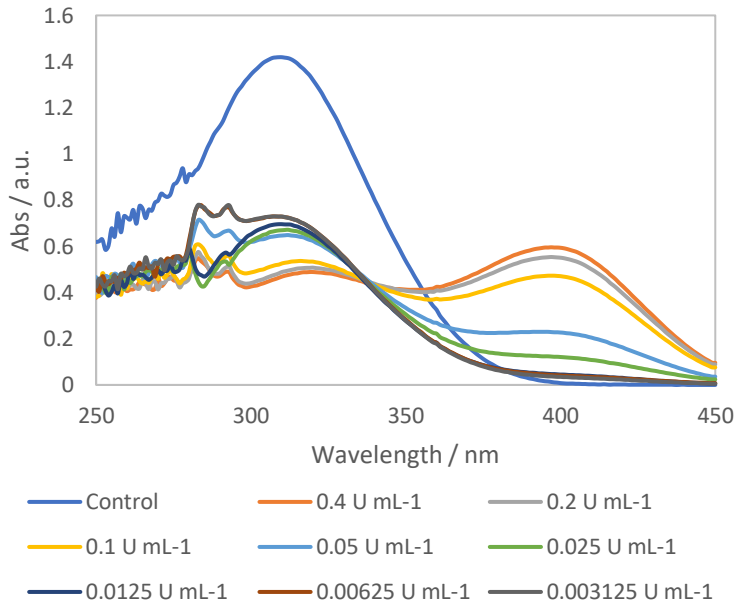
UV-vis spectra of ALP solution-phase reaction with pNPP after 2 h in pH 11 carbonate buffer



UV-vis spectra of ALP solution-phase reaction with pNPP after 24 h in pH 11 carbonate buffer

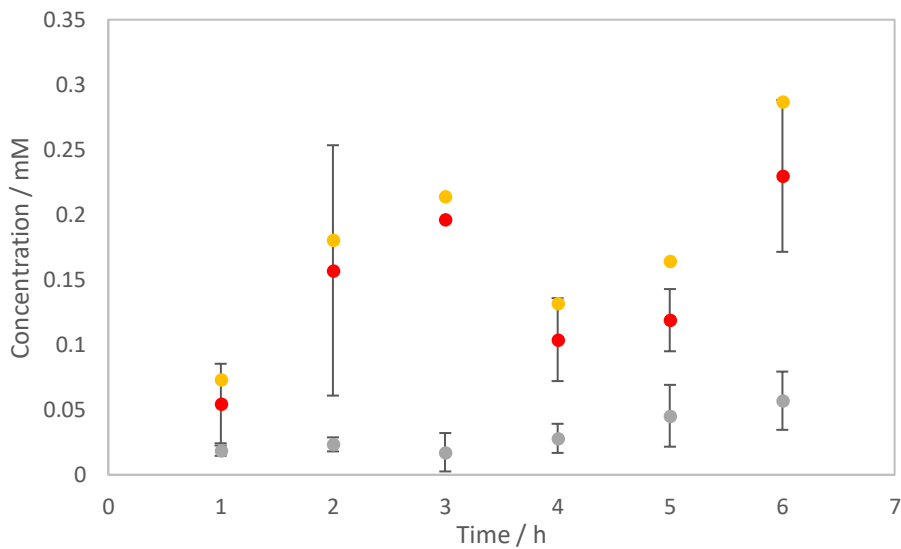


UV-vis spectra of ALP solution-phase reaction with pNPP after 2 h in unbuffered water

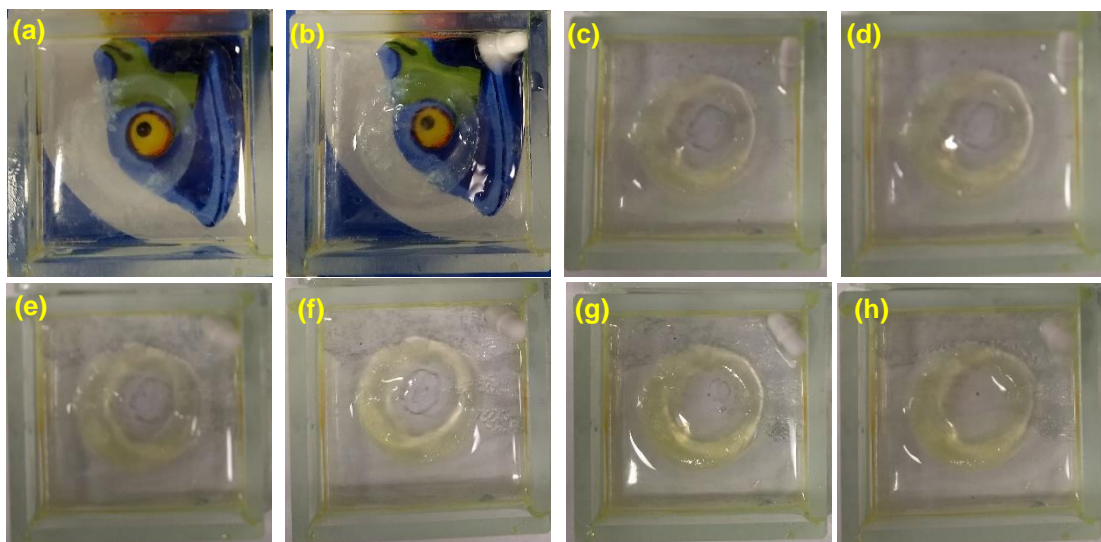


UV-vis spectra of ALP solution-phase reaction with pNPP after 24 h in unbuffered water

Appendix 10: 3-month old bioreactors

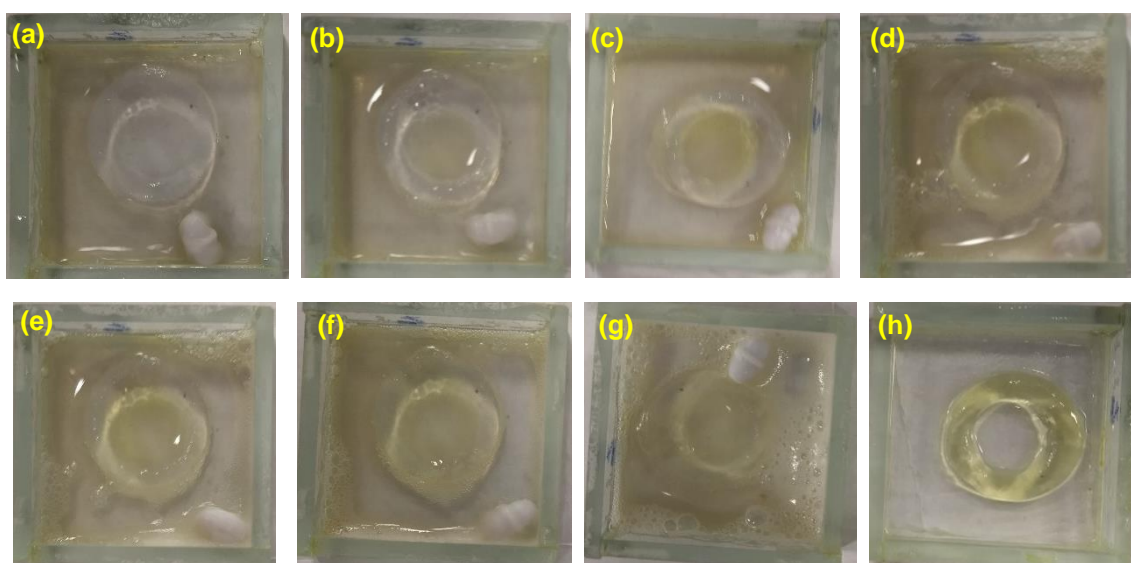


Concentration of pNPP (red), pNP (grey) and summed total of both (yellow) in the ring bioreactor product compartment



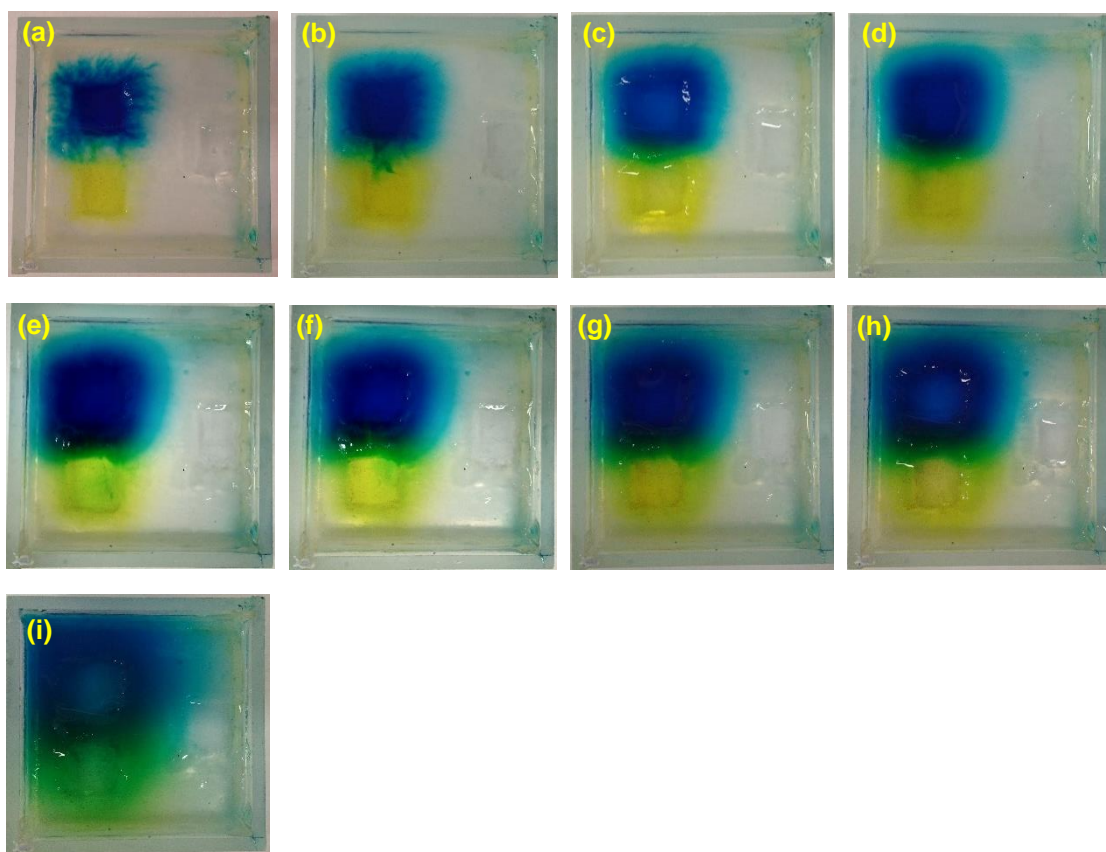
Representative images of bioreactor activity after 3 months at room temperature. Images were taken at one hour intervals from 0 h (a) to 7 h (h).

Appendix 11: Acid phosphatase reactor

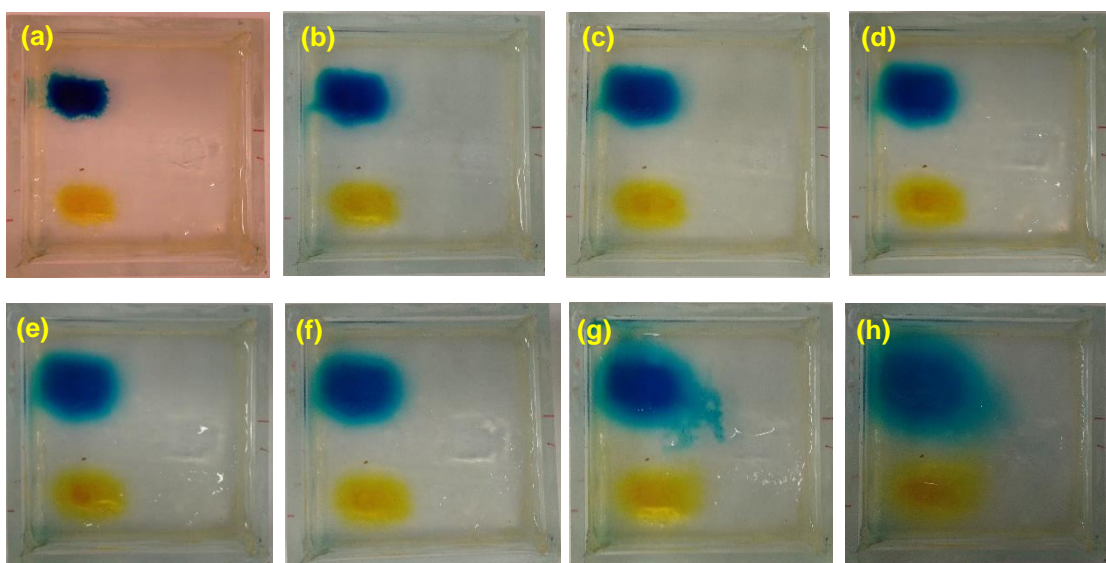


Images of acid phosphatase ring bioreactor. Images taken at one hour intervals from 0 h (a) to 6 h (g). Image of the bioreactor after 6 h reaction and 24 h submersion in pH 9 buffer (h).

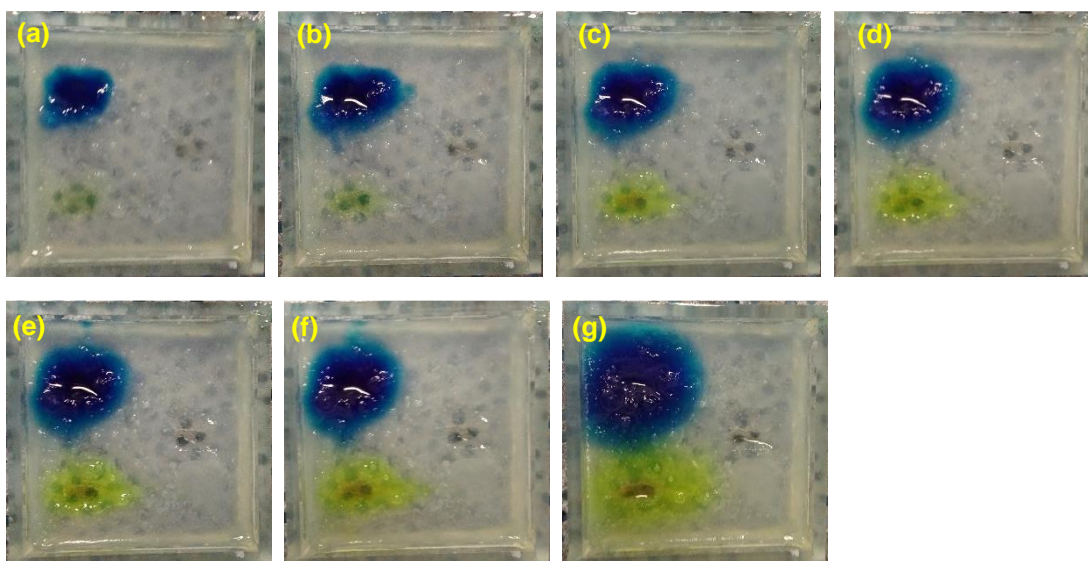
Appendix 12: Diffusion reactor images



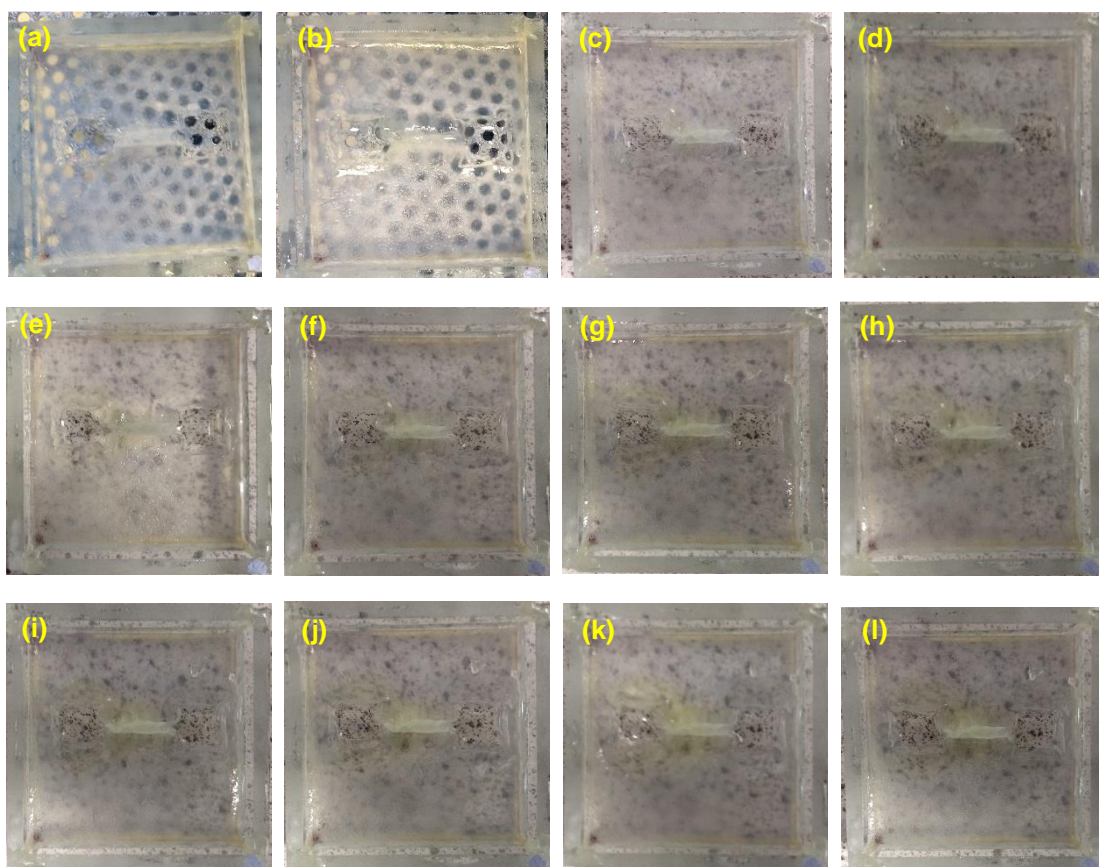
Images of fluorescein and MB (0.5 M) diffusion through DBS-CONHNH₂ gel (10 mL) at room temperature. Tray dimensions = 5 cm × 5 cm Images taken at one hour intervals from 0 h (a) to 7 h (h) and after 24 h (i)

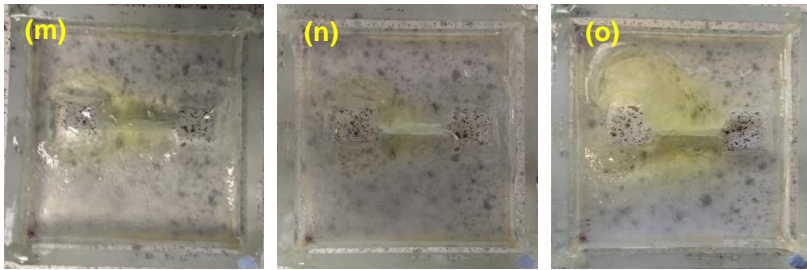


Images of fluorescein and MB (0.5 M) diffusion through a photo-patterned 60% hybrid gel (10 mL) at room temperature. Tray dimensions = 5 cm × 5 cm Images taken at one hour intervals from 0 h (a) to 6 h (g) and after 24 h (h)

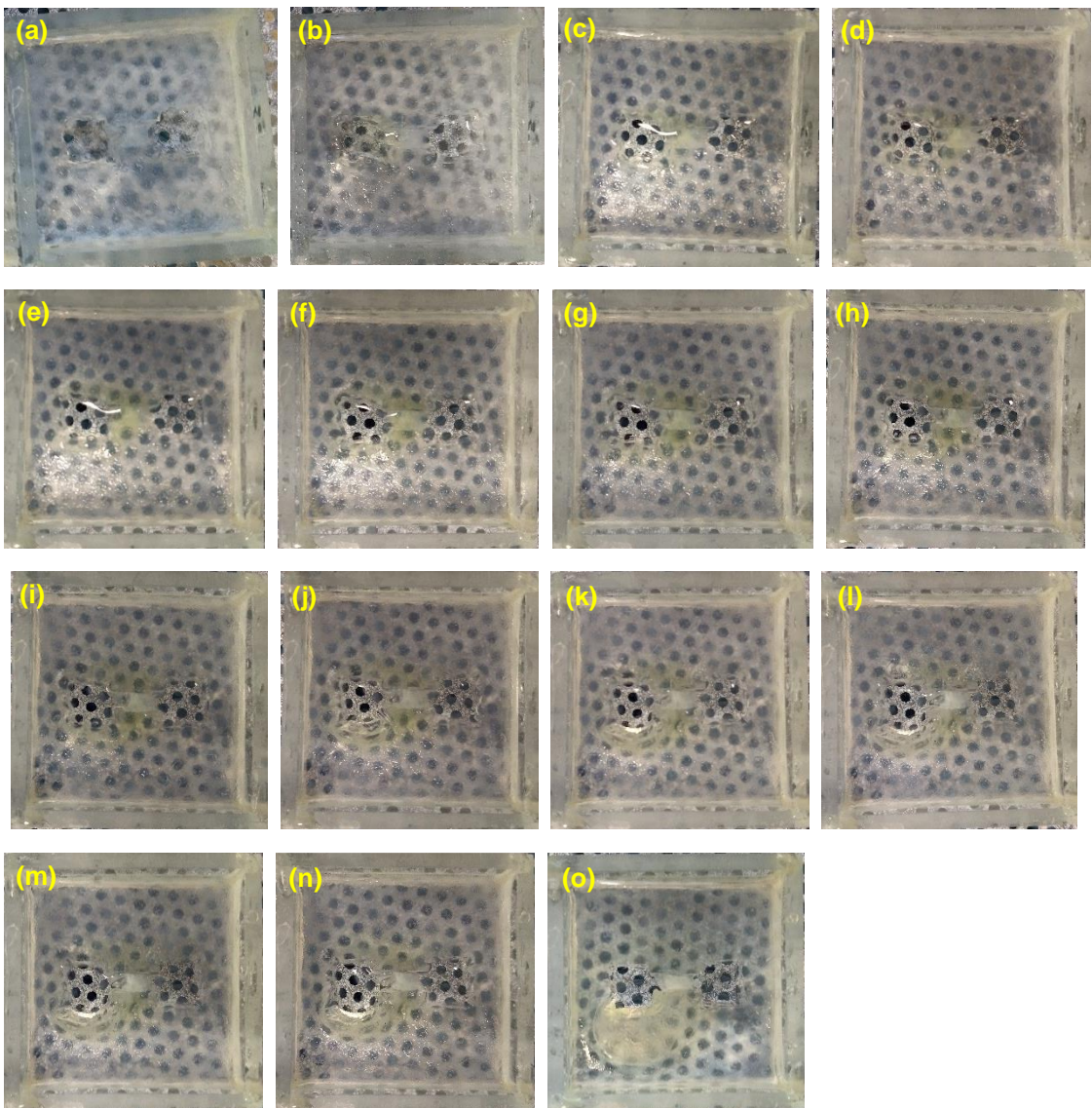


Images of fluorescein and MB (saturated solutions) diffusion through a photo-patterned 60% hybrid gel (10 mL) at room temperature. Tray dimensions = 5 cm × 5 cm Images taken at one hour intervals from 0 h (a) to 6 h (f) and after 24 h (g)



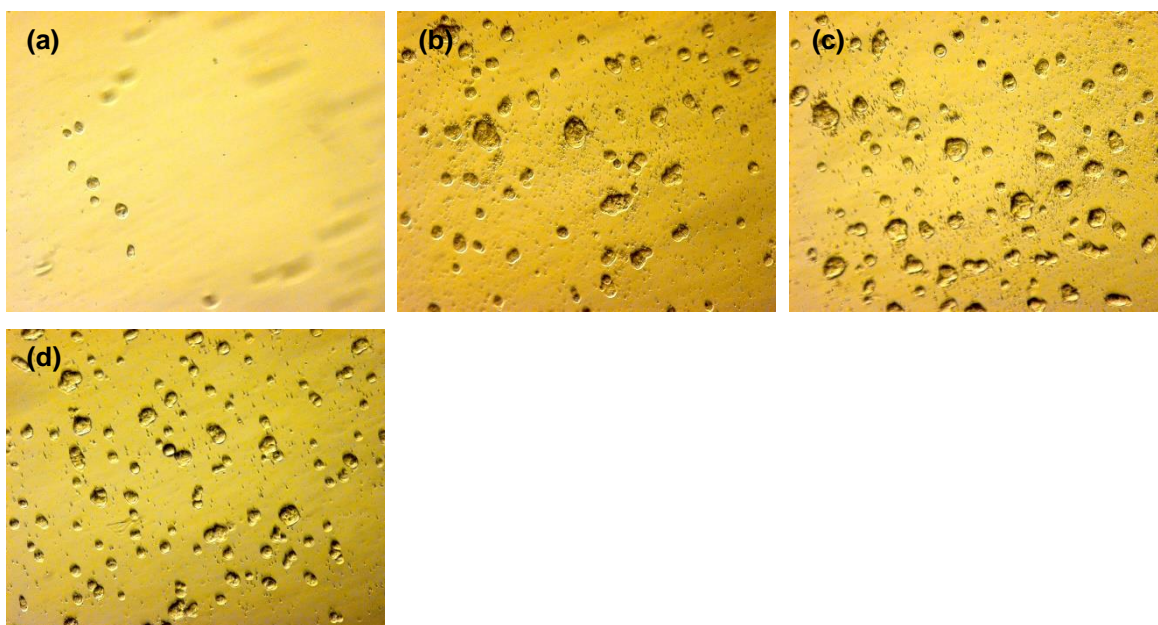


Images of fluorescein alkaline phosphatase reaction in a photo-patterned 60% hybrid gel (10 mL) at room temperature. Tray dimensions = 5 cm × 5 cm Images taken at 0.5 h intervals from 0 h (a) to 6.5 h (n) and after 24 h (o)

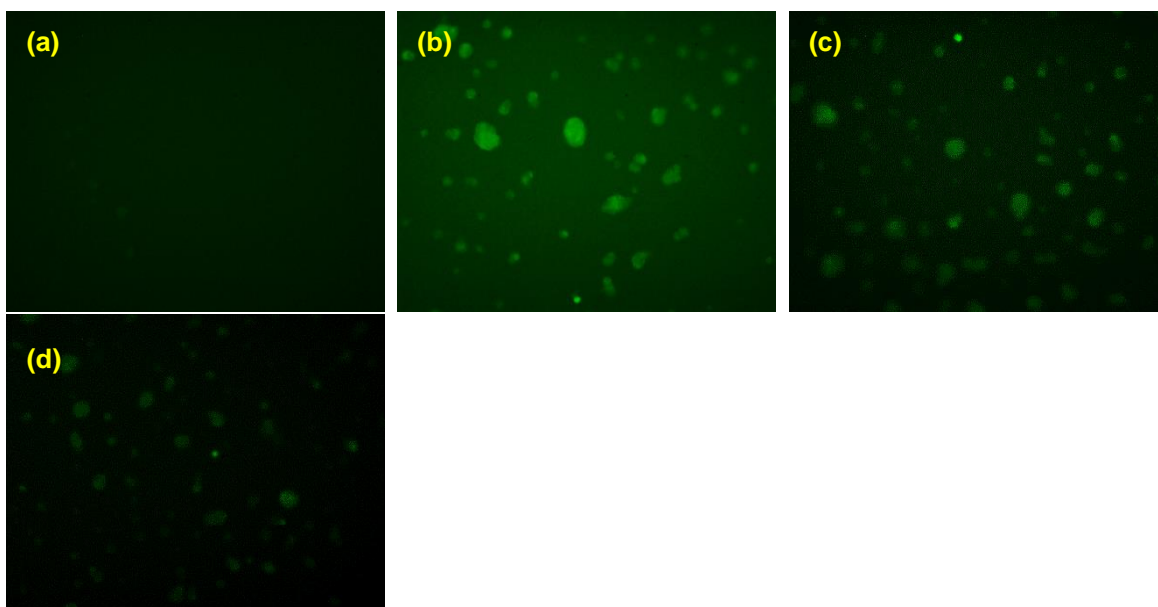


Images of fluorescein alkaline phosphatase reaction in a photo-patterned 60% hybrid gel (10 mL) at 50 °C. Tray dimensions = 5 cm × 5 cm Images taken at 0.5 h intervals from 0 h (a) to 6.5 h (n) and after 24 h (o)

Appendix 13: Fluorescence microscopy images

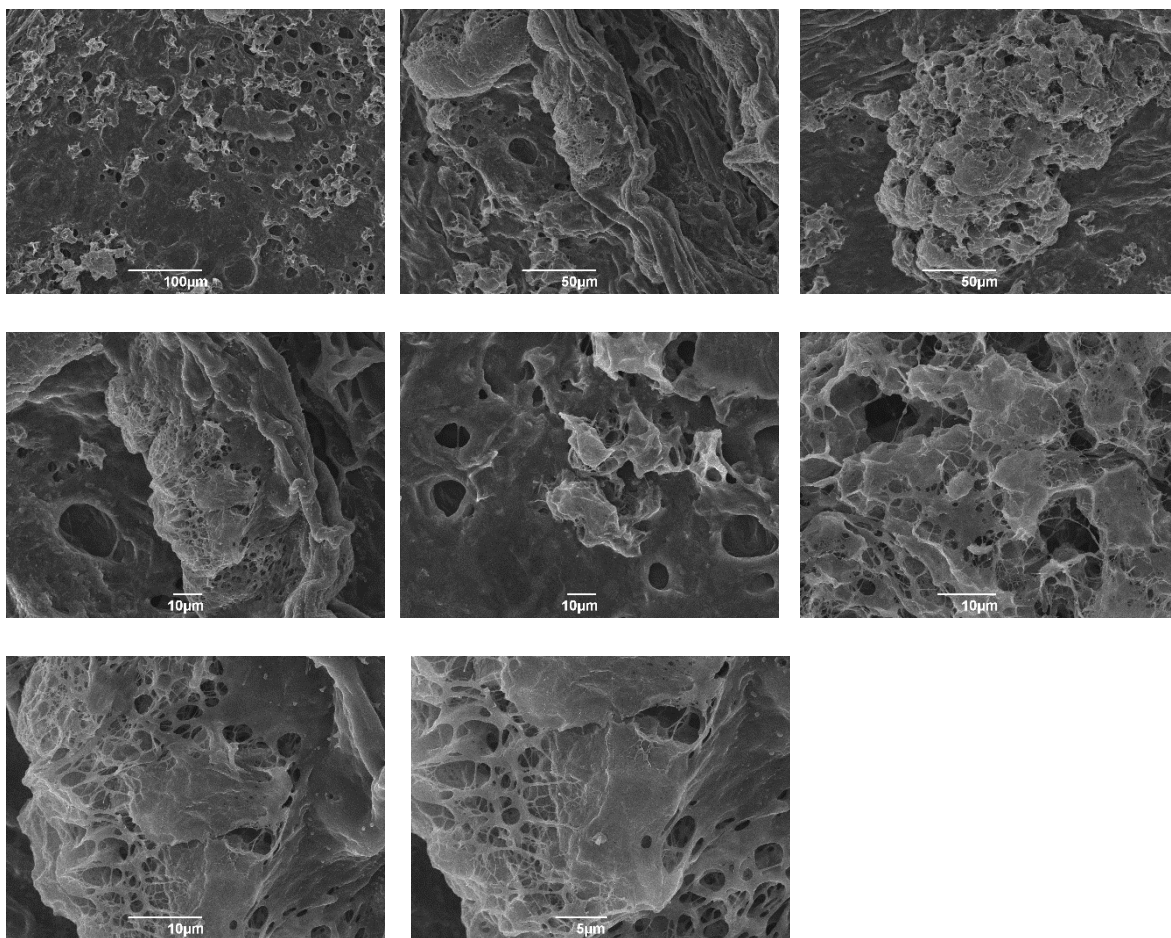


Brightfield images of Y201 XGreen cells cultured on 10% PEGDM hydrogels for after 1 day, at densities of 10,000 (a), 20,000 (b), 40,000 (c) and 50,000 (d) cells mL⁻¹

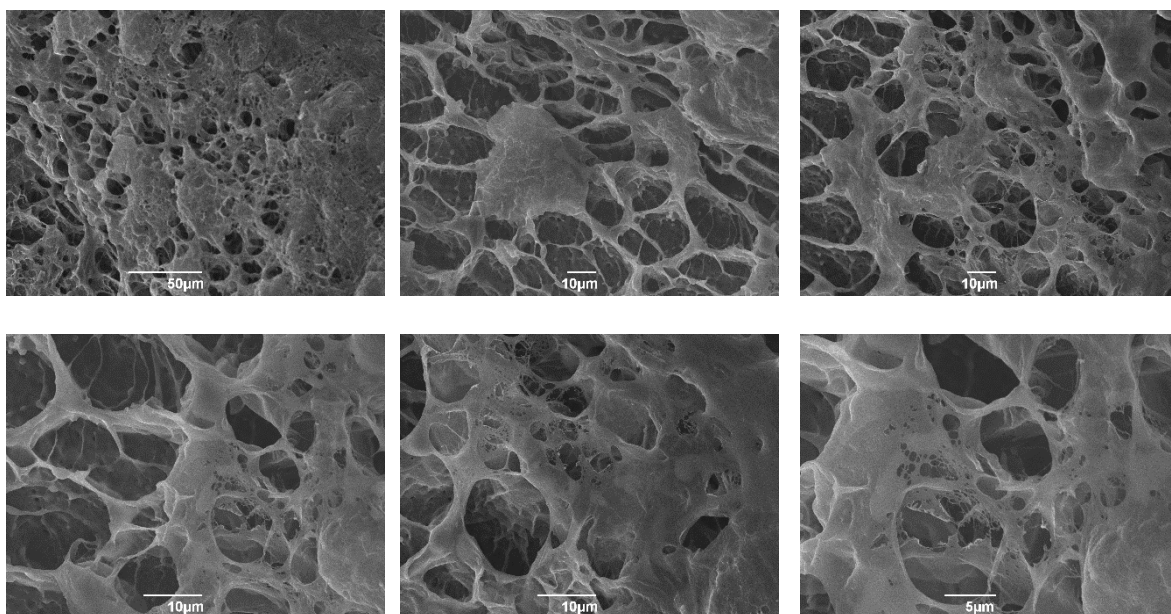


Fluorescence images of Y201 XGreen cells cultured on 10% PEGDM hydrogels for after 1 day, at densities of 10,000 (a), 20,000 (b), 40,000 (c) and 50,000 (d) cells mL⁻¹

Appendix 14: Scanning electron micrographs of MSCs cultured on hybrid hydrogels



SEM images of Y201 cells cultured on 10% hybrid gels for 3 weeks

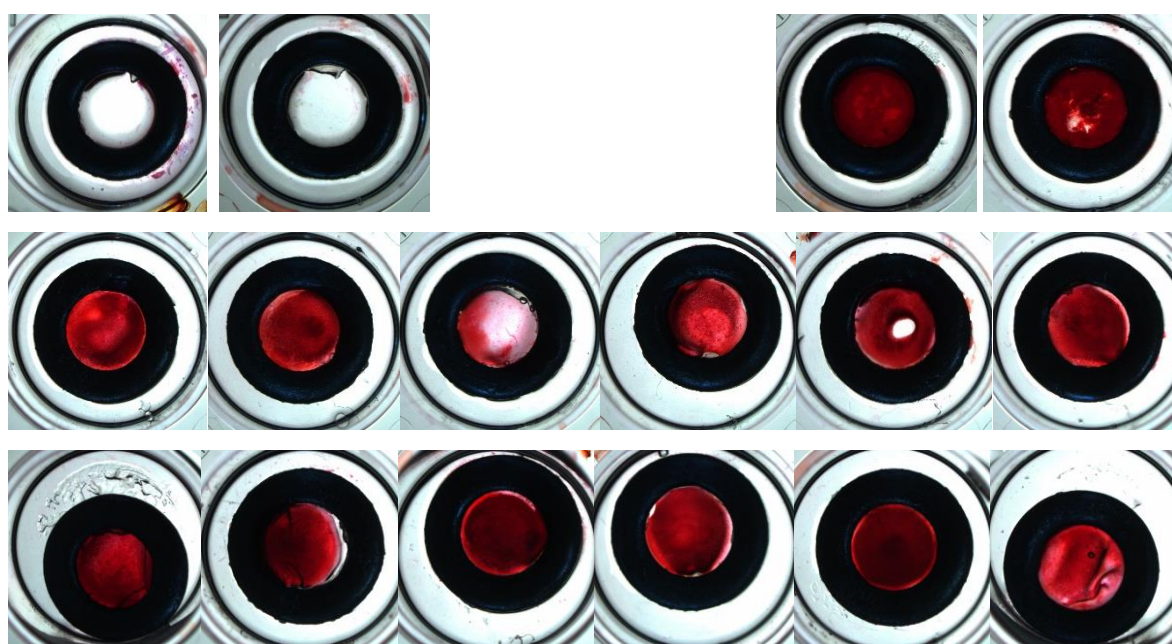


SEM images of Y201 cells cultured on 20% hybrid gels for 3 weeks

Appendix 15: Optical microscopy images of Alizarin Red S stained samples



Images of Alizarin Red S stained samples of Y201 cells cultured on polystyrene (row 1), DBS-CONHNH₂ hydrogel (row 2), 10% hybrid gel (row 3) and 20% hybrid gel (row 4).



Images of Alizarin Red S stained control samples polystyrene (row 1, left), DBS-CONHNH₂ hydrogel (row 1, right), 10% hybrid gel (row 2) and 20% hybrid gel (row 3).

List of Abbreviations

1D	One-dimensional
2D	Two-dimensional
3D	Three-dimensional
AcAc	Acetylacetone
AFM	Atomic force microscopy
ALP	Alkaline phosphatase
AP	Acid phosphatase
API	Active pharmaceutical ingredient
Ar	Aromatic
Arg	Arginine
ASC	Adipose-derived stem cells
Asp	Aspartic acid
ATR-FTIR	Attenuated Total Reflectance-Fourier Transform Infrared
BCA	Bicinchonic acid
br.	Broad (NMR)
CD	Circular Dichroism
CDCl ₃	Deuterated chloroform
Col _h	Columnar hexagonal
COX	Cyclooxygenase
CPC	Cetyl pyridinium chloride
d	Doublet (NMR)
D ₂ O	Deuterated water
Da	Daltons
DAPI	4',6-diamino-2-phenylindole
DBS	1,3:2,4-Dibenzylidene-d-sorbitol
DBS-CO ₂ H	1,3:2,4-dibenzylidene-d-sorbitol- <i>p,p'</i> -dicarboxylic acid
DBS-CO ₂ Me	1,3:2,4-Dibenzylidene-d-sorbitol- <i>p,p'</i> -dimethyl ester
DBS-CONHNH ₂	1,3:2,4-Dibenzylidene-d-sorbitol- <i>p,p'</i> -diacylhydrazide
DBS-glycine	1,3:2,4-Dibenzylidene-d-sorbitol- <i>p,p'</i> -dicarbonyl glycine
DCM	Dichloromethane
dd	Double doublet (NMR)
ddd	Double double doublet (NMR)

dddd	Double double double doublet (NMR)
DFT	Density functional theory
DMEM	Dulbecco's Modified Eagle's Medium
DMSO	Dimethyl sulfoxide
DMSO- d_6	Deuterated DMSO
DNA	Deoxyribonucleic acid
DPIN	Diphenyliodonium nitrate
DSC	Differential scanning calorimetry
EC	Ethyl cellulose
EDTA	Ethylenediaminetetraacetic acid
EGFP	Enhanced green fluorescent protein
EM	Electron microscopy
ESC	Embryonic stem cell
ESI	Electrospray Ionisation
FITC-dextran	Fluorescein isothiocyanate dextran
Fmoc	Fluorenylmethyloxycarbonyl
FT-IR	Fourier transform infrared
FTO	Fluorine-doped tin oxide
FWHM	Full width half maximum
G'	Storage modulus
G''	Loss modulus
GdL	Glucono- δ -lactone
Gly	Glycine
GOx	Glucose oxidase
h	Hours
H ₂ O ₂	Hydrogen peroxide
Hb	Haemoglobin
HbpA	Hydroxybiphenyl 3-monooxygenase
HCl	Hydrochloric acid
HRP	Horseradish peroxidase
Hz	Hertz
IPN	Interpenetrating polymer network
IR	Infrared
J	Coupling constant (in ppm)

KOH	Potassium hydroxide
LC	Liquid crystal
LMW	Low-molecular-weight
LMWG	Low-molecular-weight gelator
log <i>P</i>	Partition coefficient
LVR	Linear viscoelastic region
<i>m</i>	Medium (IR)
m	Multiplet
M.p.	Melting point
m/z	Mass to charge ratio
MALDI	Matrix Assisted Laser Desorption Ionisation Mass Spectrometry
MB	Methylene blue
MB	Methylene blue
MBR	Membrane bioreactor
MGC	Minimum gelation concentration
MHz	Megahertz
min	Minutes
mL	Millilitres
mm	Millimetre
mM	Millimolar per dm ³
MS	Mass spectrometry
MSC	Mesenchymal Stem Cell
M _w	Molecular weight
nm	Nanometre
NMR	Nuclear magnetic resonance
Npmoc	Nitrophenyl methyloxycarbonyl
NPX	Naproxen
NSAID	Non-steroidal anti-inflammatory drug
OPV	Oligo(<i>p</i> -phenylenevinylene)
PA	Peptide amphiphile
PAG	Photoacid generator
PASP	Polyaspartic acid
PBI	Perylene-bisimide
PBS	Phosphate-buffered saline

PEG	Poly(ethylene glycol)
PEGDM	Poly(ethylene glycol) dimethacrylate
PEGMA	Poly(ethylene glycol) methacrylate
PG	Polymer gel
pH	Negative logarithm of the concentration of hydrogen ions
Phe	Phenylalanine
PI	Photoinitiator, here used to refer to 2-hydroxy-4'-(2-hydroxyethoxy)-2-methylpropiophenone
pK _a	Negative logarithm of the acid dissociation constant
PNIPAAm	Poly(<i>N</i> -isopropyl)acrylamide
<i>p</i> NP	<i>para</i> -Nitrophenol
<i>p</i> NPP	<i>para</i> -Nitrophenyl phosphate
PPV	Poly(<i>para</i> -phenylene vinylene)
<i>p</i> -TsOH	<i>para</i> -Toluene sulfonic acid (monohydrate)
QD	Quantum dot
rad s ⁻¹	Radians per second
R _g	Gyration radius
s	Singlet (NMR)
<i>s</i>	Strong (IR)
SANS	Small-angle neutron scattering
SEM	Scanning electron microscopy
Ser	Serine
Sol	Solution
SPAAC	Strain-promoted azide-alkyne cycloaddition
t	Triplet
TEM	Transmission electron microscopy
T _{gel}	Gel-sol transition temperature
Tyr	Tyrosine
U	Units
Uox	Urate oxidase
UV	Ultraviolet
UV-vis	Ultraviolet-visible
Vis	Visible
<i>w</i>	Weak (IR)

wt/vol	Weight to volume ratio
δ	NMR chemical shift (in ppm)
δ	Phase angle (rheology)
λ_{em}	Emission wavelength
λ_{exc}	Excitation wavelength
λ_{max}	Wavelength at maximum intensity
μg	Microgram
μL	Microlitre
μm	Micrometre
ν_{max}	Wavenumber at maximum peak intensity (IR)

References

- 1 P. Terech and R. G. Weiss, *Chem. Rev.*, 1997, **97**, 3133–3160.
- 2 J. F. Douglas, *Gels*, 2018, **4**, 19.
- 3 R. G. Weiss, in *Molecular Gels: Structure and Dynamics*, ed. R. G. Weiss, Royal Society of Chemistry, Cambridge, 2018, pp. 1–27.
- 4 D. J. Lloyd and J. Alexander, *Colloid Chem. Chem. Cat. Co New York*, 1926, **1**, 767.
- 5 J.-M. Guenet, in *Organogels: Thermodynamics, Structure, Solvent Role, and Properties*, ed. J.-M. Guenet, Springer, New York, 2016, pp. 7–15.
- 6 A. R. Hirst, I. A. Coates, T. R. Boucheteau, J. F. Miravet, B. Escuder, V. Castelletto, I. W. Hamley and D. K. Smith, *J. Am. Chem. Soc.*, 2008, **130**, 9113–9121.
- 7 V. J. Nebot and D. K. Smith, in *Functional Molecular Gels*, eds. B. Escuder and J. F. Miravet, Royal Society of Chemistry, Cambridge, 2013, pp. 30–66.
- 8 X. Yang, G. Zhang and D. Zhang, *J. Mater. Chem.*, 2012, **22**, 38–50.
- 9 E. R. Draper and D. J. Adams, in *Chemoresponsive Materials: Stimulation by Chemical and Biological Signals*, ed. H.-J. Schneider, Royal Society of Chemistry, Cambridge, 2015, pp. 332–363.
- 10 C. D. Jones and J. W. Steed, *Chem. Soc. Rev.*, 2016, **45**, 6546–6596.
- 11 J. Raeburn and D. J. Adams, *Chem. Commun.*, 2015, **51**, 5170–5180.
- 12 A. R. Hirst, B. Escuder, J. F. Miravet and D. K. Smith, *Angew. Chem. Int. Ed.*, 2008, **47**, 8002–8018.
- 13 K. J. Skilling, F. Citossi, T. D. Bradshaw, M. Ashford, B. Kellam and M. Marlow, *Soft Matter*, 2014, **10**, 237–256.
- 14 J. Boekhoven and S. I. Stupp, *Adv. Mater.*, 2014, **26**, 1642–1659.
- 15 M. J. Webber, E. A. Appel, E. W. Meijer and R. Langer, *Nat. Mater.*, 2016, **15**, 13–26.
- 16 B. O. Okesola and D. K. Smith, *Chem. Soc. Rev.*, 2016, **45**, 4226–4251.
- 17 S. R. Jadhav, P. K. Vemula, R. Kumar, S. R. Raghavan and G. John, *Angew. Chem. Int. Ed.*, 2010, **49**, 7695–7698.

- 18 C. S. Kesava Raju, B. Pramanik, R. Ravishankar, P. V. Chalapathi Rao and G. Sriganesh, *RSC Adv.*, 2017, **7**, 37175–37180.
- 19 S. S. Babu, V. K. Praveen and A. Ajayaghosh, *Chem. Rev.*, 2014, **114**, 1973–2129.
- 20 S. Ghosh, V. K. Praveen and A. Ajayaghosh, *Annu. Rev. Mater. Res.*, 2016, **46**, 235–262.
- 21 J. Buendía, E. Matesanz, D. K. Smith and L. Sánchez, *CrystEngComm*, 2015, **17**, 8146–8152.
- 22 J. A. Foster, K. K. Damodaran, A. Maurin, G. M. Day, H. P. G. Thompson, G. J. Cameron, J. C. Bernal and J. W. Steed, *Chem. Sci.*, 2017, **8**, 78–84.
- 23 C. R. King, D. W. Bristol and M. L. English, US Pat., 20140178480, 2014.
- 24 D. K. Smith, in *Molecular Gels: Structure and Dynamics*, ed. R. G. Weiss, Royal Society of Chemistry, Cambridge, 2018, pp. 300–371.
- 25 D. DeRossi, K. Kajiwara, Y. Osada and A. Yamauchi, *Polymer Gels: Fundamentals and Biomedical Applications*, Springer US, New York, 1991.
- 26 Y. Osada, J. Ping Gong and Y. Tanaka, *J. Macromol. Sci. Part C Polym. Rev.*, 2004, **44**, 87–112.
- 27 D. Saha and S. Bhattacharya, *J. Food Sci. Technol.*, 2010, **47**, 587–597.
- 28 D. C. Turner, R. B. Steffen, C. Wildsmith and T. A. Matiocio US Pat., 6861123, 2000.
- 29 Y. Liu, Y. Ji, D. Morsley, C. Francis and A. Back, EU Pat., 2483737, 2010.
- 30 N. J. Manesis and A. Back, US Pat., 20140200286, 2013.
- 31 E. Caló and V. V. Khutoryanskiy, *Eur. Polym. J.*, 2015, **65**, 252–267.
- 32 S. Ahn, R. M. Kasi, S.-C. Kim, N. Sharma and Y. Zhou, *Soft Matter*, 2008, **4**, 1151–1157.
- 33 D. J. Cornwell and D. K. Smith, *Mater. Horizons*, 2015, **2**, 279–293.
- 34 E. S. Dragan, *Chem. Eng. J.*, 2014, **243**, 572–590.
- 35 B. G. Cooper, R. C. Stewart, D. Burstein, B. D. Snyder and M. W. Grinstaff, *Angew. Chem. Int. Ed.*, 2016, **55**, 4226–4230.
- 36 G. C. Ingavle, S. H. Gehrke and M. S. Detamore, *Biomaterials*, 2014, **35**, 3558–3570.
- 37 Y. Jiang, Y. Wu and Y. Huo, *J. Biomater. Sci. Polym. Ed.*, 2015, **26**, 917–930.
- 38 D. Dasgupta, S. Srinivasan, C. Rochas, A. Ajayaghosh and J. M. Guenet, *Langmuir*, 2009, **25**, 8593–8598.

- 39 J. Wang, Z. Wang, J. Gao, L. Wang, Z. Yang, D. Kong and Z. Yang, *J. Mater. Chem.*, 2009, **19**, 7892–7896.
- 40 J. Wang, H. Wang, Z. Song, D. Kong, X. Chen and Z. Yang, *Colloid. Surface. B*, 2010, **80**, 155–160.
- 41 C. Yang, M. Bian and Z. Yang, *Biomater. Sci.*, 2014, **2**, 651–654.
- 42 R. Huang, W. Qi, L. Feng, R. Su and Z. He, *Soft Matter*, 2011, **7**, 6222–6230.
- 43 Y. Xie, J. Zhao, R. Huang, W. Qi, Y. Wang, R. Su and Z. He, *Nanoscale Res. Lett.*, 2016, **11**, 184.
- 44 E. Çelik, C. Bayram, R. Akçapınar, M. Türk and E. B. Denkbaş, *Mater. Sci. Eng. C*, 2016, **66**, 221–229.
- 45 J. S. Foster, J. M. Žurek, N. M. S. Almeida, W. E. Hendriksen, V. A. A. le Sage, V. Lakshminarayanan, A. L. Thompson, R. Banerjee, R. Eelkema, H. Mulvana, M. J. Paterson, J. H. van Esch and G. O. Lloyd, *J. Am. Chem. Soc.*, 2015, **137**, 14236–14239.
- 46 P. A. Korevaar, T. F. A. de Greef and E. W. Meijer, *Chem. Mater.*, 2014, **26**, 576–586.
- 47 P. A. Korevaar, S. J. George, A. J. Markvoort, M. M. J. Smulders, P. A. J. Hilbers, A. P. H. J. Schenning, T. F. A. De Greef and E. W. Meijer, *Nature*, 2012, **481**, 492–496.
- 48 J. Chen, N. Tao, S. Fang, Z. Chen, L. Liang, X. Sun, J. Li and Y.-N. Liu, *New J. Chem.*, 2018, **42**, 9651–9657.
- 49 J. Wang, X. Miao, Q. Fengzhao, C. Ren, Z. Yang and L. Wang, *RSC Adv.*, 2013, **3**, 16739–16746.
- 50 Y. Mao, T. Su, Q. Wu, C. Liao and Q. Wang, *Chem. Commun.*, 2014, **50**, 14429–14432.
- 51 J. Rubio-Magnieto, M. Tena-Solsona, B. Escuder and M. Surin, *RSC Adv.*, 2017, **7**, 9562–9566.
- 52 Y. Yu, Y. Wang and C. Feng, *Chem. Res. Chinese Univ.*, 2016, **32**, 872–876.
- 53 D. J. Cornwell, B. O. Okesola and D. K. Smith, *Soft Matter*, 2013, **9**, 8730–8736.
- 54 V. M. P. Vieira, L. L. Hay and D. K. Smith, *Chem. Sci.*, 2017, **8**, 6981–6990.
- 55 D. J. Cornwell, B. O. Okesola and D. K. Smith, *Angew. Chem. Int. Ed.*, 2014, **53**, 12461–12465.
- 56 B. O. Okesola, S. K. Suravaram, A. Parkin and D. K. Smith, *Angew. Chem. Int. Ed.*, 2016, **55**, 183–187.
- 57 P. Slavík, D. W. Kurka and D. K. Smith, *Chem. Sci.*, 2018, **9**, 8673–8681.

- 58 V. M. P. Vieira, A. C. Lima, M. de Jong and D. K. Smith, *Chem. Eur. J.*, 2018, **24**, 15112–15118.
- 59 P. Li, X.-Q. Dou, C.-L. Feng and D. Zhang, *Soft Matter*, 2013, **9**, 3750–3757.
- 60 J. Zhang, W. Ji, T. Liu and C. Feng, *Macromol. Chem. Phys.*, 2016, **217**, 1197–1204.
- 61 Y. Ohseido, M. Taniguchi, K. Saruhashi and H. Watanabe, *RSC Adv.*, 2015, **5**, 90010–90013.
- 62 F. Chen, Q. Chen, L. Zhu, Z. Tang, Q. Li, G. Qin, J. Yang, Y. Zhang, B. Ren and J. Zheng, *Chem. Mater.*, 2018, **30**, 1743–1754.
- 63 A. J. Engler, S. Sen, H. L. Sweeney and D. E. Discher, *Cell*, 2006, **126**, 677–689.
- 64 E. V. Alakpa, V. Jayawarna, A. Lampel, K. V. Burgess, C. C. West, S. C. J. Bakker, S. Roy, N. Javid, S. Fleming, D. A. Lamprou, J. Yang, A. Miller, A. J. Urquhart, P. W. J. M. Frederix, N. T. Hunt, B. Péault, R. V. Ulijn and M. J. Dalby, *Chem*, 2016, **1**, 298–319.
- 65 W. S. Leong, C. Y. Tay, H. Yu, A. Li, S. C. Wu, D.-H. Duc, C. T. Lim and L. P. Tan, *Biochem. Biophys. Res. Commun.*, 2010, **401**, 287–292.
- 66 T. Liebmann, S. Rydholm, V. Akpe and H. Brismar, *BMC Biotechnol.*, 2007, **7**, 88.
- 67 E. R. Draper and D. J. Adams, *Chem. Commun.*, 2016, **52**, 8196–8206.
- 68 C. K. Karan and M. Bhattacharjee, *ACS Appl. Mater. Interfaces*, 2016, **8**, 5526–5535.
- 69 L. Yan, L. Shen, M. Lv, W. Yu, J. Chen, S. Wang, X. Fu and Z. Ye, *Chem. Commun.*, 2015, **51**, 17627–17629.
- 70 J. Eastoe, M. Sánchez-Dominguez, P. Wyatt and R. K. Heenan, *Chem. Commun.*, 2004, **0**, 2608–2609.
- 71 M. Moriyama, N. Mizoshita, T. Yokota, K. Kishimoto and T. Kato, *Adv. Mater.*, 2003, **15**, 1335–1338.
- 72 M. Moriyama, N. Mizoshita and T. Kato, *Polym. J.*, 2004, **36**, 661–664.
- 73 J. J. D. de Jong, P. R. Hania, A. Pugžlys, L. N. Lucas, M. de Loos, R. M. Kellogg, B. L. Feringa, K. Duppen and J. H. van Esch, *Angew. Chem. Int. Ed.*, 2005, **44**, 2373–2376.
- 74 C. Maity, W. E. Hendriksen, J. H. van Esch and R. Eelkema, *Angew. Chem. Int. Ed.*, 2015, **54**, 998–1001.
- 75 J. Raeburn, T. O. McDonald and D. J. Adams, *Chem. Commun.*, 2012, **48**, 9355–9357.

- 76 S. Matsumoto, S. Yamaguchi, S. Ueno, H. Komatsu, M. Ikeda, K. Ishizuka, Y. Iko, K. V. Tabata, H. Aoki, S. Ito, H. Noji and I. Hamachi, *Chem. Eur. J.*, 2008, **14**, 3977–3986.
- 77 S. Lee, S. Oh, J. Lee, Y. Malpani, Y.-S. Jung, B. Kang, J. Y. Lee, K. Ozasa, T. Isoshima, S. Y. Lee, M. Hara, D. Hashizume and J.-M. Kim, *Langmuir*, 2013, **29**, 5869–5877.
- 78 S.-T. Tung, H.-T. Cheng, A. Inthasot, F.-C. Hsueh, T.-J. Gu, P.-C. Yan, C.-C. Lai and S.-H. Chiu, *Chem. Eur. J.*, 2018, **24**, 1522–1527.
- 79 J. T. van Herpt, M. C. A. Stuart, W. R. Browne and B. L. Feringa, *Chem. Eur. J.*, 2014, **20**, 3077–3083.
- 80 E. R. Draper, R. Schweins, R. Akhtar, P. Groves, V. Chechik, M. A. Zwijnenburg and D. J. Adams, *Chem. Mater.*, 2016, **28**, 6336–6341.
- 81 J. H. Lee, S. H. Jung, S. S. Lee, K.-Y. Kwon, K. Sakurai, J. Jaworski and J. H. Jung, *ACS Nano*, 2017, **11**, 4155–4164.
- 82 E. R. Draper, E. G. B. Eden, T. O. McDonald and D. J. Adams, *Nat. Chem.*, 2015, **7**, 848–852.
- 83 X. Che, B. Bai, T. Zhang, C. Zhang, C. Zhang, P. Zhang, H. Wang and M. Li, *New J. Chem.*, 2017, **41**, 8614–8619.
- 84 D. J. Cornwell, O. J. Daubney and D. K. Smith, *J. Am. Chem. Soc.*, 2015, **137**, 15486–15492.
- 85 K. Hajash, B. Sparrman, C. Guberan, J. Laucks and S. Tibbits, *3D Print. Addit. Manuf.*, 2017, **4**, 123–132.
- 86 B. Duan, L. A. Hockaday, K. H. Kang and J. T. Butcher, *J. Biomed. Mater. Res. A*, 2013, **101**, 1255–1264.
- 87 T. Christoff-Tempesta, A. Lew and J. Ortony, *Gels*, 2018, **4**, 40.
- 88 M. Nadgorny, Z. Xiao and L. A. Connal, *Mol. Syst. Des. Eng.*, 2017, **2**, 283–292.
- 89 I. Roppolo, A. Chiappone, A. Angelini, S. Stassi, F. Frascella, C. F. Pirri, C. Ricciardi, E. Descrovi, Y. Lassailly and J. Peretti, *Mater. Horiz.*, 2017, **4**, 396–401.
- 90 Q. Wei, M. Xu, C. Liao, Q. Wu, M. Liu, Y. Zhang, C. Wu, L. Cheng and Q. Wang, *Chem. Sci.*, 2016, **7**, 2748–2752.
- 91 H. Yang, S. Zhang, K. Liu and Y. Fang, *RSC Adv.*, 2016, **6**, 109969–109977.
- 92 M. C. Nolan, A. M. Fuentes Caparrós, B. Dietrich, M. Barrow, E. R. Cross, M. Bleuel, S. M. King

- and D. J. Adams, *Soft Matter*, 2017, **13**, 8426–8432.
- 93 S. S. Rohner, J. Ruiz-Olles and D. K. Smith, *RSC Adv.*, 2015, **5**, 27190–27196.
- 94 M. Lovrak, W. E. J. Hendriksen, C. Maity, S. Mytnyk, V. van Steijn, R. Eelkema and J. H. van Esch, *Nat. Commun.*, 2017, **8**, 15317.
- 95 R. W. Jagers and S. A. F. Bon, *J. Mater. Chem. B*, 2017, **5**, 7491–7495.
- 96 J. Ruíz-Olles and D. K. Smith, *Chem. Sci.*, 2018, **9**, 5541–5550.
- 97 R. J. Williams, A. M. Smith, R. Collins, N. Hodson, A. K. Das and R. V. Ulijn, *Nat. Nanotechnol.*, 2009, **4**, 19–24.
- 98 M. P. Conte, K. H. A. Lau and R. V. Ulijn, *ACS Appl. Mater. Interfaces*, 2017, **9**, 3266–3271.
- 99 J. Zhou, X. Du, C. Berciu, H. He, J. Shi, D. Nicastro and B. Xu, *Chem*, 2016, **1**, 246–263.
- 100 J. Li, Y. Gao, Y. Kuang, J. Shi, X. Du, J. Zhou, H. Wang, Z. Yang and B. Xu, *J. Am. Chem. Soc.*, 2013, **135**, 9907–9914.
- 101 P. K. Vemula, G. A. Cruikshank, J. M. Karp and G. John, *Biomaterials*, 2009, **30**, 383–393.
- 102 J. M. Karp, P. K. Vemula, N. R. Campbell, A. M. Syed, S. Zhang, O. C. Farokhzad and R. S. Langer, US Pat., 20170000888, 2017.
- 103 J. Li, Y. Kuang, J. Shi, Y. Gao, J. Zhou and B. Xu, *Beilstein J. Org. Chem.*, 2013, **9**, 908–917.
- 104 Q. Wang, Z. Yang, Y. Gao, W. Ge, L. Wang and B. Xu, *Soft Matter*, 2008, **4**, 550–553.
- 105 A. G. L. Olive, N. H. Abdullah, I. Ziemecka, E. Mendes, R. Eelkema and J. H. van Esch, *Angew. Chem.*, 2014, **126**, 4216–4220.
- 106 J. Raeburn, B. Alston, J. Kroeger, T. O. McDonald, J. R. Howse, P. J. Cameron and D. J. Adams, *Mater. Horiz.*, 2014, **1**, 241–246.
- 107 A. C. Balazs, *Mater. Today*, 2007, **10**, 18–23.
- 108 Z. Wei, J. H. Yang, J. Zhou, F. Xu, M. Zrínyi, P. H. Dussault, Y. Osada and Y. M. Chen, *Chem. Soc. Rev.*, 2014, **43**, 8114–8131.
- 109 J. Li, L. Geng, G. Wang, H. Chu and H. Wei, *Chem. Mater.*, 2017, **29**, 8932–8952.
- 110 S. Bera and D. Haldar, *J. Mater. Chem. A*, 2016, **4**, 6933–6939.
- 111 K. E. Inostroza-Brito, E. Collin, O. Siton-Mendelson, K. H. Smith, A. Monge-Marcet, D. S.

- Ferreira, R. P. Rodríguez, M. Alonso, J. C. Rodríguez-Cabello, R. L. Reis, F. Sagués, L. Botto, R. Bitton, H. S. Azevedo and A. Mata, *Nat. Chem.*, 2015, **7**, 897–904.
- 112 A. Mendoza-Meinhardt, L. Botto and A. Mata, *Sci. Rep.*, 2018, **8**, 2900.
- 113 C. L. Hedegaard, E. C. Collin, C. Redondo-Gómez, L. T. H. Nguyen, K. W. Ng, A. A. Castrejón-Pita, J. R. Castrejón-Pita and A. Mata, *Adv. Funct. Mater.*, 2018, **28**, 1703716.
- 114 E. J. Howe, B. O. Okesola and D. K. Smith, *Chem. Commun.*, 2015, **51**, 7451–7454.
- 115 M. J. Meunier, *Ann. Chim. Phys.*, 1891, **22**, 412.
- 116 J. K. Wolfe, R. M. Hann and C. S. Hudson, *J. Am. Chem. Soc.*, 1942, **64**, 1493–1497.
- 117 S. J. Angyal and J. V. Lawler, *J. Am. Chem. Soc.*, 1944, **66**, 837–838.
- 118 B. O. Okesola, V. M. P. Vieira, D. J. Cornwell, N. K. Whitelaw and D. K. Smith, *Soft Matter*, 2015, **11**, 4768–4787.
- 119 E.-L. Roehl and B.-H. Tan, US Pat., 4154816, 1976.
- 120 E.-L. Roehl, US Pat., 4346079, 1980.
- 121 T. J. Schamper, M. M. Perl and J. D. Warren, US Pat., 4720381, 1986.
- 122 N. G. Telyan, D. R. McCarthy, L. Wilson and R. B. Kasat, US Pat., 5490979, 1996.
- 123 J. P. Luebbe, P. R. Tanner and J. D. Melanson, US Pat., 4816261, 1987.
- 124 M. H. Randhawa and T. J. Schamper, US Pat., 4719102, 1985.
- 125 J. Mattai, C. Ortiz, E. Guenin and J. Afflitto, US Pat., 6338841, 2001.
- 126 A. Esposito, T. Schamper and E. C. Henry, US Pat., 7799318, 2007.
- 127 H. Kamada and H. Uchiyama, US Pat., 4016118, 1977.
- 128 Y. Kawai, K. Sasagawa, M. Maki, H. Ueda and M. Miyamoto, US Pat., 4314039, 1980.
- 129 H. Uchiyama, US Pat., 4483956, 1984.
- 130 J. W. Rekers, US Pat., 5049605, 1989.
- 131 J. Xu, J. Li, B. W. Bolt, K. D. Lake Jr., J. D. Sprinkle, B. M. Burkhart and K. A. Keller, US Pat., 8022133, 2005.
- 132 T. Sutthatang and S. Wangsoub, *J. Met. Mater. Miner.*, 2013, **23**, 1–8.

- 133 J. M. Gardlik and R. V. Burkes, *US Pat.*, 5106999, 1990.
- 134 R. Stan, S. Rosca, C. Ott, E. Perez, I. Rico-Lattes and A. Lattes, *Rev. Roum. Chim.*, 2006, **51**, 609–613.
- 135 K. Fan, Z. Yin, X. Yang, X. Wang and H. Kong, *Ch. Pat.*, 106117233, 2016.
- 136 R. Feng, C. Ligong, Z. Hou and J. Song, *Trans. Tianjin Univ.*, 2007, **13**, 35–41.
- 137 G. Malle and T. Luukas, *US Pat.*, 20130039862, 2011.
- 138 S. Yamasaki and H. Tsutsumi, *Bull. Chem. Soc. Jpn.*, 1995, **68**, 123–127.
- 139 S. Yamasaki, Y. Ohashi, H. Tsutsumi and K. Tsujii, *Bull. Chem. Soc. Jpn.*, 1995, **68**, 146–151.
- 140 M. Watase, Y. Nakatani and H. Itagaki, *J. Phys. Chem. B*, 1999, **103**, 2366–2373.
- 141 J. Li, K. Fan, X. Guan, Y. Yu and J. Song, *Langmuir*, 2014, **30**, 13422–13429.
- 142 D. Alperstein and D. Knani, *Polym. Adv. Technol.*, 2013, **24**, 391–397.
- 143 B. O. Okesola and D. K. Smith, *Chem. Commun.*, 2013, **49**, 11164–11166.
- 144 K. Kyburz and K. Anseth, *Ann. Biomed. Eng.*, 2015, **43**, 489–500.
- 145 A. M. Diez-Pascual and A. L. Diez-Vicente, *RSC Adv.*, 2016, **6**, 79507–79519.
- 146 C.-C. Lin and K. S. Anseth, *Pharm. Res.*, 2009, **26**, 631–643.
- 147 J. Jagur-Grodzinski, *Polym. Adv. Technol.*, 2010, **21**, 27–47.
- 148 M. B. Mellott, K. Searcy and M. V. Pishko, *Biomaterials*, 2001, **22**, 929–941.
- 149 N. A. Peppas, K. B. Keys, M. Torres-Lugo and A. M. Lowman, *J. Control. Release*, 1999, **62**, 81–87.
- 150 A. K. S. Chandel, C. U. Kumar and S. K. Jewrajka, *ACS Appl. Mater. Interfaces*, 2016, **8**, 3182–3192.
- 151 A. Arya and A. L. Sharma, *J. Phys. D. Appl. Phys.*, 2017, **50**, 443002.
- 152 M. R. Arkenberg and C.-C. Lin, *Biomater. Sci.*, 2017, **5**, 2231–2240.
- 153 M. Ehrbar, S. C. Rizzi, R. G. Schoenmakers, B. S. Miguel, J. A. Hubbell, F. E. Weber and M. P. Lutolf, *Biomacromolecules*, 2007, **8**, 3000–3007.
- 154 B. D. Polizzotti, B. D. Fairbanks and K. S. Anseth, *Biomacromolecules*, 2008, **9**, 1084–1087.

- 155 C. A. DeForest and K. S. Anseth, *Nat. Chem.*, 2011, **3**, 925–931.
- 156 M. Malkoch, R. Vestberg, N. Gupta, L. Mespouille, P. Dubois, A. F. Mason, J. L. Hedrick, Q. Liao, C. W. Frank, K. Kingsbury and C. J. Hawker, *Chem. Commun.*, 2006, **0**, 2774–2776.
- 157 M. Doytcheva, D. Dotcheva, R. Stamenova and C. Tsvetanov, *Macromol. Mater. Eng.*, 2001, **286**, 30–33.
- 158 C. Zhou, Q. Wang and Q. Wu, *Carbohydr. Polym.*, 2012, **87**, 1779–1786.
- 159 L. A. Sawicki and A. M. Kloxin, *J. Vis. Exp.*, 2016, **29**, e54462.
- 160 S. Lin-Gibson, S. Bencherif, J. A. Cooper, S. J. Wetzel, J. M. Antonucci, B. M. Vogel, F. Horkay and N. R. Washburn, *Biomacromolecules*, 2004, **5**, 1280–1287.
- 161 B. D. Fairbanks, M. P. Schwartz, C. N. Bowman and K. S. Anseth, *Biomaterials*, 2009, **30**, 6702–6707.
- 162 A. Berdichevski, Y. Shachaf, R. Wechsler and D. Seliktar, *Biomaterials*, 2015, **42**, 1–10.
- 163 J. Zhu and R. E. Marchant, *Expert Rev. Med. Devices*, 2011, **8**, 607–626.
- 164 D. L. Hern and J. A. Hubbell, *J. Biomed. Mater. Res.*, 1998, **39**, 266–276.
- 165 J. Zhu, *Biomaterials*, 2010, **31**, 4639–4656.
- 166 S. P. Zustiak and J. B. Leach, *Biomacromolecules*, 2010, **11**, 1348–1357.
- 167 B. K. Mann, A. S. Gobin, A. T. Tsai, R. H. Schmedlen and J. L. West, *Biomaterials*, 2001, **22**, 3045–3051.
- 168 B. V Sridhar, J. L. Brock, J. S. Silver, J. L. Leight, M. A. Randolph and K. S. Anseth, *Adv. Healthc. Mater.*, 2015, **4**, 702–713.
- 169 J. Yu, F. Chen, X. Wang, N. Dong, C. Lu, G. Yang and Z. Chen, *Polym. Degrad. Stab.*, 2016, **133**, 312–320.
- 170 S. Lin-Gibson, R. L. Jones, N. R. Washburn and F. Horkay, *Macromolecules*, 2005, **38**, 2897–2902.
- 171 D. Perera, M. Medini, D. Seethamraju, R. Falkowski, K. White and R. M. Olabisi, *J. Microencapsul.*, 2018, **30**, 1–7.
- 172 J. P. Mazzoccoli, D. L. Feke, H. Baskaran and P. N. Pintauro, *J. Biomed. Mater. Res. A*, 2010, **93**, 558–566.

- 173 J. A. Killion, L. M. Geever, D. M. Devine, J. E. Kennedy and C. L. Higginbotham, *J. Mech. Behav. Biomed. Mater.*, 2011, **4**, 1219–1227.
- 174 S. R. Raghavan and B. H. Cipriano, in *Molecular Gels: Materials with Self-Assembled Fibrillar Networks*, eds. R. G. Weiss and P. Terech, Springer Netherlands, Dordrecht, 1st edn., 2006, pp. 235–236.
- 175 S. Raddatz, J. Mueller-Ibeler, J. Kluge, L. Wäss, G. Burdinski, J. R. Havens, T. J. Onofrey, D. Wang and M. Schweitzer, *Nucleic Acids Res.*, 2002, **30**, 4793–4802.
- 176 Y. Liu, Y. Fu, J. Wang, B. Xue and E. Liu, *Russ. J. Phys. Chem. B*, 2017, **11**, 722–728.
- 177 C. G. Williams, A. N. Malik, T. K. Kim, P. N. Manson and J. H. Elisseeff, *Biomaterials*, 2005, **26**, 1211–1218.
- 178 C. Bahney, T. Lujan, C. Hsu, M. Bottlang, J. West and B. Johnstone, *Eur. Cells Mater.*, 2011, **15**, 43–55.
- 179 D. L. Blair, in *Molecular Gels: Structure and Dynamics*, ed. R. G. Weiss, Royal Society of Chemistry, Cambridge, 2018, pp. 28–56.
- 180 A. M. Grillet, N. B. Wyatt and L. M. Gloe, in *Rheology*, ed. J. De Vicente, InTech, Rijeka, 2012, pp. 59–80.
- 181 E. R. Draper, L. L. E. Mears, A. M. Castilla, S. M. King, T. O. McDonald, R. Akhtar and D. J. Adams, *RSC Adv.*, 2015, **5**, 95369–95378.
- 182 Y. Abidine, V. M. Laurent, R. Michel, A. Duperray, L. I. Palade and C. Verdier, *Europhys. Lett.*, 2015, **109**, 38003.
- 183 M. Brass, F. Morin, T. Meldrum, M. Brass, F. Morin and T. Meldrum, *Magnetochemistry*, 2018, **4**, 8.
- 184 L. Zedler, M. D. Hager, U. S. Schubert, M. J. Harrington, M. Schmitt, J. Popp and B. Dietzek, *Mater. Today*, 2014, **17**, 57–69.
- 185 D. J. Adams, *Gels*, 2018, **4**, 32.
- 186 L. L. E. Mears, E. R. Draper, A. M. Castilla, H. Su, Z. Zhuola, B. Dietrich, M. Nolan, G. N. Smith, J. Douth, S. E. Rogers, R. Akhtar, H. Cui and D. J. Adams, *Biomacromolecules*, 2017, **18**, 3531–3540.
- 187 T. Gulik-Krzywicki, *Curr. Opin. Colloid Interface Sci.*, 1997, **2**, 137–144.

- 188 S. G. Sunol, O. Keskin, O. Guney and A. K. Sunol, in *Innovations in Supercritical Fluids*, eds. K. W. Hutchenson and N. R. Foster, American Chemical Society, Washington D.C., 1995, pp. 258–268.
- 189 K. Cieřła, B. Sartowska and E. Królak, *Radiat. Phys. Chem.*, 2015, **106**, 289–302.
- 190 J.-M. Guenet, P. Mesini and M. Schmutz, in *Molecular Gels*, ed. R. G. Weiss, Royal Society of Chemistry, London, 2018, pp. 227–299.
- 191 J. Rubio, V. Martí-Centelles, M. I. Burguete and S. V. Luis, *Tetrahedron*, 2013, **69**, 2302–2308.
- 192 C. Zhuan, Y. Li, X. Yuan, J. Zhao and X. Hou, *J. Appl. Polym. Sci.*, 2018, **135**, 47052.
- 193 B. Bai, Z. Li, H. Wang, M. Li, Y. Ozaki and J. Wei, *R. Soc. Open Sci.*, 2018, **5**, 170492.
- 194 Y. Lan, M. G. Corradini, R. G. Weiss, S. R. Raghavan and M. A. Rogers, *Chem. Soc. Rev.*, 2015, **44**, 6035–6058.
- 195 J. Raeburn, C. Mendoza-Cuenca, B. N. Cattoz, M. A. Little, A. E. Terry, A. Zamith Cardoso, P. C. Griffiths and D. J. Adams, *Soft Matter*, 2015, **11**, 927–935.
- 196 J. Galvao, B. Davis, M. Tilley, E. Normando, M. R. Duchen and M. F. Cordeiro, *FASEB J.*, 2014, **28**, 1317–1330.
- 197 L. de Abreu Costa, M. Henrique Fernandes Ottoni, M. dos Santos, A. Meireles, V. Gomes de Almeida, W. de Fátima Pereira, B. Alves de Avelar-Freitas and G. Eustáquio Alvim Brito-Melo, *Molecules*, 2017, **22**, 1789.
- 198 J. Mayr, C. Saldías and D. Díaz Díaz, *Chem. Soc. Rev.*, 2018, **47**, 1484–1515.
- 199 C. L. Esposito, P. Kirilov and V. G. Roullin, *J. Control. Release*, 2018, **271**, 1–20.
- 200 S. Soukasene, D. J. Toft, T. J. Moyer, H. Lu, H.-K. Lee, S. M. Standley, V. L. Cryns and S. I. Stupp, *ACS Nano*, 2011, **5**, 9113–9121.
- 201 N. B. Graham and M. E. McNeill, *Biomaterials*, 1984, **5**, 27–36.
- 202 R. J. Mitra, D. Das, S. Roy and P. K. Das, *J. Phys. Chem. B*, 2007, **111**, 14107–14113.
- 203 S. Cao, X. Fu, N. Wang, H. Wang and Y. Yang, *Int. J. Pharm.*, 2008, **357**, 95–99.
- 204 A. Nishimura, T. Hayakawa, Y. Yamamoto, M. Hamori, K. Tabata, K. Seto and N. Shibata, *Eur. J. Pharm. Sci.*, 2012, **45**, 1–7.
- 205 J. Liu, L. Zhang, Z. Yang and X. Zhao, *Int. J. Nanomedicine*, 2011, **6**, 2143–2153.

- 206 S. Zarzhitsky and H. Rapaport, *J. Colloid Interface Sci.*, 2011, **360**, 525–531.
- 207 C. K. Thota, N. Yadav and V. S. Chauhan, *Sci. Rep.*, 2016, **6**, 31167.
- 208 L. McDougall, E. R. Draper, J. D. Beadle, M. Shipman, P. Raubo, A. G. Jamieson and D. J. Adams, *Chem. Commun.*, 2018, **54**, 1793–1796.
- 209 M. Kurbasic, C. Romano, A. Garcia, S. Kralj and S. Marchesan, *Gels*, 2017, **3**, 29.
- 210 H. Wang, Z. Feng and B. Xu, *Adv. Drug Deliv. Rev.*, 2017, **110–111**, 102–111.
- 211 Y. Nagai, L. D. Unsworth, S. Koutsopoulos and S. Zhang, *J. Control. Release*, 2006, **115**, 18–25.
- 212 L. Chronopoulou, S. Margheritelli, Y. Toumia, G. Paradossi, F. Bordi, S. Sennato and C. Palocci, *Gels*, 2015, **1**, 179–193.
- 213 D. Limón, E. Amirthalingam, M. Rodrigues, L. Halbaut, B. Andrade, M. L. Garduño-Ramírez, D. B. Amabilino, L. Pérez-García and A. C. Calpena, *Eur. J. Pharm. Biopharm.*, 2015, **96**, 421–436.
- 214 D. Limón, C. Jimenez-Newman, A. C. Calpena, A. Gonzalez-Campo, D. B. Amabilino and L. Perez-Garcia, *Chem. Commun.*, 2017.
- 215 Y. Huang, Z. Qiu, Y. Xu, J. Shi, H. Lin and Y. Zhang, *Org. Biomol. Chem.*, 2011, **9**, 2149–2155.
- 216 Z. L. Pianowski, J. Karcher and K. Schneider, *Chem. Commun.*, 2016, **52**, 3143–3146.
- 217 L. Qin, P. Duan, F. Xie, L. Zhang and M. Liu, *Chem. Commun.*, 2013, **49**, 10823–10825.
- 218 S.-L. Zhou, S. Matsumoto, H.-D. Tian, H. Yamane, A. Ojida, S. Kiyonaka and I. Hamachi, *Chem. Eur. J.*, 2005, **11**, 1130–1136.
- 219 H. Komatsu, S. Matsumoto, S. Tamaru, K. Kaneko, M. Ikeda and I. Hamachi, *J. Am. Chem. Soc.*, 2009, **131**, 5580–5585.
- 220 B. Xing, C.-W. Yu, K.-H. Chow, P.-L. Ho, D. Fu and B. Xu, *J. Am. Chem. Soc.*, 2002, **124**, 14846–14847.
- 221 Y. Gao, Y. Kuang, Z.-F. Guo, Z. Guo, I. J. Krauss and B. Xu, *J. Am. Chem. Soc.*, 2009, **131**, 13576–13577.
- 222 J. Majumder, M. R. Das, J. Deb, S. S. Jana and P. Dastidar, *Langmuir*, 2013, **29**, 10254–10263.
- 223 S. Bhuniya, Y. J. Seo and B. H. Kim, *Tetrahedron Lett.*, 2006, **47**, 7153–7156.

- 224 X. Li, J. Li, Y. Gao, Y. Kuang, J. Shi and B. Xu, *J. Am. Chem. Soc.*, 2010, **132**, 17707–17709.
- 225 J. B. Matson and S. I. Stupp, *Chem. Commun.*, 2011, **47**, 7962–7964.
- 226 H. Liu, Z. Song and X. Chen, *J. Nanosci. Nanotechnol.*, 2014, **14**, 4837–4842.
- 227 C. Valéry, M. Paternostre, B. Robert, T. Gulik-Krzywicki, T. Narayanan, J.-C. Dedieu, G. Keller, M.-L. Torres, R. Cherif-Cheikh, P. Calvo and F. Artzner, *Proc. Natl. Acad. Sci. U. S. A.*, 2003, **100**, 10258–10262.
- 228 Z. Yang, H. Gu, Y. Zhang, L. Wang and B. Xu, *Chem. Commun.*, 2004, **0**, 208–209.
- 229 P. Casuso, P. Carrasco, I. Loinaz, H. J. Grande and I. Odriozola, *Org. Biomol. Chem.*, 2010, **8**, 5455–5458.
- 230 R. Roy, J. Deb, S. S. Jana and P. Dastidar, *Chem. Eur. J.*, 2014, **20**, 15320–15324.
- 231 R. Parveen, B. Sravanthi and P. Dastidar, *Chem. Asian J.*, 2017, **12**, 792–803.
- 232 R. Roy and P. Dastidar, *Chem. Eur. J.*, 2016, **22**, 14929–14939.
- 233 A. Saha, B. Roy, A. Esterrani and A. K. Nandi, *Org. Biomol. Chem.*, 2011, **9**, 770–776.
- 234 G. J. Gross and J. Moore, *Pharmacology*, 2004, **71**, 135–142.
- 235 N. Bhala and J. Emberson, *Lancet*, 2016, **382**, 769–779.
- 236 V. A. de Mello and E. Ricci-Júnior, *Quim. Nova*, 2011, **34**, 933–939.
- 237 C. Bombardier, L. Laine, A. Reicin, D. Shapiro, R. Burgos-Vargas, B. Davis, R. Day, M. B. Ferraz, C. J. Hawkey, M. C. Hochberg, T. K. Kvien and T. J. Schnitzer, *N. Engl. J. Med.*, 2000, **343**, 1520–1528.
- 238 C. H. Hsiao and J. S. Kent, US Pat., US 4803079, 1989.
- 239 E. K. Solak, *J. Biomater. Nanobiotechnol.*, 2011, **2**, 445–453.
- 240 S. Joshi, P. Patel, S. Lin and P. L. Madan, *Asian J. Pharm. Sci.*, 2012, **7**, 134–142.
- 241 Ö. B. Ünlüer, L. Genç, Ş. G. Kahyaoğlu and A. Ersöz, *J. Pharm. Pharmacol.*, 2014, **2**, 527–533.
- 242 V. Georgiadou, G. Makris, D. Papagiannopoulou, G. Vourlias and C. Dendrinou-Samara, *ACS Appl. Mater. Interfaces*, 2016, **8**, 9345–9360.
- 243 M. Gasztych, J. V. Valh, V. Kokol, A. J. Szumny, A. Gola and W. Musiał, *J. Sol-Gel Sci. Technol.*, 2016, **79**, 466–474.

- 244 S. Das and U. Subuddhi, *Ind. Eng. Chem. Res.*, 2013, **52**, 14192–14200.
- 245 H. Cao, J. Zhu, H. Su, L. Fang and T. Tan, *J. Appl. Polym. Sci.*, 2009, **113**, 327–336.
- 246 N. Goyal, H. P. R. Mangunuru, B. Parikh, S. Shrestha and G. Wang, *Beilstein J. Org. Chem.*, 2014, **10**, 3111–3121.
- 247 F. Barbato, M. I. La Rotonda and F. Quaglia, *J. Pharm. Sci.*, 1997, **86**, 225–229.
- 248 J. Fallingborg, *Dan. Med. Bull.*, 1999, **46**, 183–196.
- 249 J. Majumder, J. Deb, A. Husain, S. S. Jana and P. Dastidar, *J. Mater. Chem. B*, 2015, **3**, 6634–6644.
- 250 J. Majumder, P. Yedoti and P. Dastidar, *Org. Biomol. Chem.*, 2015, **13**, 2300–2309.
- 251 R. Parveen and P. Dastidar, *Chem. Eur. J.*, 2016, **22**, 9257–9266.
- 252 K. M. Ainslie, C. M. Kraning and T. A. Desai, *Lab Chip*, 2008, **8**, 1042–1047.
- 253 M. McGinity, J. R. Floyd, J. McGinity and F. Zhang, *Drug Dev. Ind. Pharm.*, 2017, **43**, 1421–1429.
- 254 P. Govindasamy, B. R. Kesavan and J. K. Narasimha, *Asian Pac. J. Trop. Biomed.*, 2013, **3**, 995–1002.
- 255 P. Marizza, S. S. Keller, A. Müllertz and A. Boisen, *J. Control. Release*, 2014, **173**, 1–9.
- 256 M. F. Bédard, B. G. De Geest, H. Möhwald, G. B. Sukhorukov and A. G. Skirtach, *Soft Matter*, 2009, **5**, 3927–3931.
- 257 X.-H. Ge, J.-P. Huang, J.-H. Xu and G.-S. Luo, *Lab Chip*, 2014, **14**, 4451–4454.
- 258 D. van der Zwaag, P. A. Pieters, P. A. Korevaar, A. J. Markvoort, A. J. H. Spiering, T. F. A. de Greef and E. W. Meijer, *J. Am. Chem. Soc.*, 2015, **137**, 12677–12688.
- 259 X. Huang, S. R. Raghavan, P. Terech and R. G. Weiss, *J. Am. Chem. Soc.*, 2006, **128**, 15341–15352.
- 260 H. Huang, L. Hou, F. Zhu, J. Li and M. Xu, *RSC Adv.*, 2018, **8**, 9334–9343.
- 261 S. M. Ramalhete, K. P. Nartowski, N. Sarathchandra, J. S. Foster, A. N. Round, J. Angulo, G. O. Lloyd and Y. Z. Khimyak, *Chem. Eur. J.*, 2017, **23**, 8014–8024.
- 262 B. Escuder, M. LLusar and J. F. Miravet, *J. Org. Chem.*, 2006, **71**, 7747–7752.

- 263 Nonappa and E. Kolehmainen, *Soft Matter*, 2016, **12**, 6015–6026.
- 264 E. C. Barker, A. D. Martin, C. J. Garvey, C. Y. Goh, F. Jones, M. Mocerino, B. W. Skelton, M. I. Ogden and T. Becker, *Soft Matter*, 2017, **13**, 1006–1011.
- 265 P. L. Urban, *New J. Chem.*, 2014, **38**, 5135–5141.
- 266 D. J. Cole-Hamilton, *Science*, 2003, **299**, 1702–1706.
- 267 D. Nair, S. S. Luthra, J. T. Scarpello, L. S. White, L. M. Freitas dos Santos and A. G. Livingston, *Desalination*, 2002, **147**, 301–306.
- 268 J. M. Woodley, *Trends Biotechnol.*, 2008, **26**, 321–327.
- 269 R. Wohlgemuth, in *Biocatalysis for Green Chemistry and Chemical Process Development*, John Wiley & Sons, Inc., Hoboken, NJ, USA, 2011, pp. 277–298.
- 270 R. J. Bayer, S. Defrees and M. Ratcliffe, EU Pat., 0820520, 1996.
- 271 P. Fernandes, *Enzyme Res.*, 2010, **2010**, 862537.
- 272 F. A. Castillo Martinez, E. M. Balciunas, J. M. Salgado, J. M. Domínguez González, A. Converti and R. P. de S. Oliveira, *Trends Food Sci. Technol.*, 2013, **30**, 70–83.
- 273 J. Pradima, M. R. Kulkarni and Archana, *Resour. Technol.*, 2017, **3**, 394–405.
- 274 J. Adrio, A. Demain, J. L. Adrio and A. L. Demain, *Biomolecules*, 2014, **4**, 117–139.
- 275 W. Yang, N. Cicek and J. Ilg, *J. Memb. Sci.*, 2006, **270**, 201–211.
- 276 R. de Regil and G. Sandoval, *Biomolecules*, 2013, **3**, 812–847.
- 277 M. G. Adsul, M. S. Singhvi, S. A. Gaikawai and D. V. Gokhale, *Bioresour. Technol.*, 2011, **102**, 4304–4312.
- 278 R. A. Sheldon and P. C. Pereira, *Chem. Soc. Rev.*, 2017, **46**, 2678–2691.
- 279 J.-M. Choi, S.-S. Han and H.-S. Kim, *Biotechnol. Adv.*, 2015, **33**, 1443–1454.
- 280 H. G. Taleghani, A. A. Ghoreyshi and G. Najafpour, *Appl. Food Biotechnol.*, 2017, **4**, 27–34.
- 281 J. Liu, J. Lu and Z. Cui, *Bioprocess Biosyst. Eng.*, 2011, **34**, 525–532.
- 282 J. B. Binder and R. T. Raines, *Proc. Natl. Acad. Sci. U. S. A.*, 2010, **107**, 4516–4521.
- 283 S. T. Morthensen, A. S. Meyer, H. Jørgensen and M. Pinelo, *Biochem. Eng. J.*, 2017, **117**, 41–47.

- 284 G. M. Rios, M. P. Belleville, D. Paolucci and J. Sanchez, *J. Memb. Sci.*, 2004, **242**, 189–196.
- 285 E. P. Cicolatti, A. Valério, R. O. Henriques, D. E. Moritz, J. L. Ninow, D. M. G. Freire, E. A. Manoel, R. Fernandez-Lafuente, D. de Oliveira and E. Csöregi, *RSC Adv.*, 2016, **6**, 104675–104692.
- 286 S. Sulaiman, N. L. Cieh, M. N. Mokhtar, M. N. Naim and S. M. M. Kamal, *Process Biochem.*, 2017, **55**, 85–95.
- 287 F. N. Gonawan, M. Z. Abu Bakar, K. Abd Karim and A. H. Kamaruddin, *RSC Adv.*, 2016, **6**, 59865–59874.
- 288 X.-Y. Zhu, C. Chen, P.-C. Chen, Q.-L. Gao, F. Fang, J. Li and X.-J. Huang, *RSC Adv.*, 2016, **6**, 30804–30812.
- 289 B. Tomaszewski, A. Schmid and K. Buehler, *Org. Process Res. Dev.*, 2014, **18**, 1516–1526.
- 290 D. Díaz Díaz, D. Kühbeck and R. J. Koopmans, *Chem. Soc. Rev.*, 2011, **40**, 427–448.
- 291 Q. Wang, Z. Yang, L. Wang, M. Ma and B. Xu, *Chem. Commun.*, 2007, **0**, 1032–1034.
- 292 Y. Liu, M. Wang, J. Li, Z. Li, P. He, H. Liu and J. Li, *Chem. Commun.*, 2005, **0**, 1778–1780.
- 293 Y. Liu, L. Shi, M. Wang, Z. Li, H. Liu and J. Li, *Green Chem.*, 2005, **7**, 655–658.
- 294 Y. Sun and X. Huang, *Supramol. Chem.*, 2015, **27**, 21–27.
- 295 S. Kiyonaka, K. Sad, I. Yoshimura, S. Shinkai, N. Kato and I. Hamachi, *Nat. Mater.*, 2004, **3**, 58–64.
- 296 H. Shigemitsu, T. Fujisaku, S. Onogi, T. Yoshii, M. Ikeda and I. Hamachi, *Nat. Protoc.*, 2016, **11**, 1744–1756.
- 297 J. H. Kim, S. Y. Lim, D. H. Nam, J. Ryu, S. H. Ku and C. B. Park, *Biosens. Bioelectron.*, 2011, **26**, 1860–1865.
- 298 S. Mizrahi, D. Rizkov, N. Hayat and O. Lev, *Chem. Commun.*, 2008, **0**, 2914–2916.
- 299 C. Schmidt-Dannert and F. Lopez-Gallego, *Microb. Biotechnol.*, 2016, **9**, 601–609.
- 300 M. B. Quin, K. K. Wallin, G. Zhang and C. Schmidt-Dannert, *Org. Biomol. Chem.*, 2017, **15**, 4260–4271.
- 301 T. Balogh, L. Boross and J. Kosáry, *Tetrahedron*, 2004, **60**, 679–682.

- 302 J. E. Coleman, *Annu. Rev. Biophys. Biomol. Struct.*, 1992, **21**, 441–483.
- 303 U. Sharma, D. Pal and R. Prasad, *Indian J. Clin. Biochem.*, 2014, **29**, 269–278.
- 304 M. H. Ross, J. O. Ely and J. G. Archer, *J. Biol. Chem.*, 1951, **192**, 561–568.
- 305 P. J. O'Brien and D. Herschlag, *Biochemistry*, 2001, **40**, 5691–5699.
- 306 J. Fawley and D. M. Gourlay, *J. Surg. Res.*, 2016, **202**, 225–234.
- 307 R. S. Siffert, *J. Exp. Med.*, 1951, **93**, 415–426.
- 308 E. E. Golub and K. Boesze-Battaglia, *Curr. Opin. Orthop.*, 2007, **18**, 444–448.
- 309 K. Ghosh, D. Mazumder Tagore, R. Anumula, B. Lakshmaiah, P. P. B. S. Kumar, S. Singaram, T. Matan, S. Kallipatti, S. Selvam, P. Krishnamurthy and M. Ramarao, *J. Struct. Biol.*, 2013, **184**, 182–192.
- 310 Z. M. Saiyed, S. Sharma, R. Godawat, S. D. Telang and C. N. Ramchand, *J. Biotechnol.*, 2007, **131**, 240–244.
- 311 D. R. Trentham and H. Gutfreund, *Biochem. J.*, 1968, **106**, 455–460.
- 312 V. Sancenon, W. H. Goh, A. Sundaram, K. S. Er, N. Johal, S. Mukhina, G. Carr and S. Dhakshinamoorthy, *Biomol. Detect. Quantif.*, 2015, **4**, 1–9.
- 313 F. Xiao, C. Nicholson, J. Hrabe and S. Hrabětová, *Biophys. J.*, 2008, **95**, 1382–1392.
- 314 Karine Andrieux, P. Lesieur, Sylviane Lesieur, Michel Ollivon and C. Grabielle-Madelmont, *Anal. Chem.*, 2002, **74**, 5217–5226.
- 315 F. Pincet, V. Adrien, R. Yang, J. Delacotte, J. E. Rothman, W. Urbach and D. Tareste, *PLoS One*, 2016, **11**, 0158457.
- 316 M. B. Bellhorn, R. W. Bellhorn and D. S. Poll, *Exp. Eye Res.*, 1977, **24**, 595–605.
- 317 P. Gribbon and T. E. Hardingham, *Biophys. J.*, 1998, **75**, 1032–1039.
- 318 K. A. Granath and B. E. Kvist, *J. Chromatogr. A*, 1967, **28**, 69–81.
- 319 P. Aimar, M. Meireles and V. Sanchez, *J. Memb. Sci.*, 1990, **54**, 321–338.
- 320 L. D. Lavis, T. J. Rutkoski and R. T. Raines, *Anal. Chem.*, 2007, **79**, 6775–6782.
- 321 N. O. Mchedlov-Petrosyan, V. I. Kukhtik and V. I. Alekseeva, *Dye. Pigment.*, 1994, **24**, 11–35.

- 322 N. A. Vodolazkaya, P. V. Shakhova and N. O. Mchedlov-Petrosyan, *Russ. J. Gen. Chem.*, 2009, **79**, 1437–1445.
- 323 D. M. Mobley, M. M. Chengappa, W. L. Kadel and J. G. Stuart, *Can. J. Comp. Med. Rev. Can. Med. Comp.*, 1984, **48**, 175–178.
- 324 S. Zappa, J. L. Rolland, D. Flament, Y. Gueguen, J. Boudrant and J. Dietrich, *Appl. Environ. Microbiol.*, 2001, **67**, 4504–4511.
- 325 C.-C. Lin, S. M. Sawicki and A. T. Metters, *Biomacromolecules*, 2008, **9**, 75–83.
- 326 F. Gu, R. Neufeld and B. Amsden, *Eur. J. Pharm. Biopharm.*, 2007, **66**, 21–27.
- 327 C. F. Rigos, H. de L. Santos, G. Thedei, R. J. Ward and P. Ciancaglini, *Biochem. Mol. Biol. Educ.*, 2003, **31**, 329–332.
- 328 N. J. Greenfield, *Nat. Protoc.*, 2006, **1**, 2876–2890.
- 329 S. Ghosh, A. Misra, A. Ozarowski, C. Stuart and A. H. Maki, *Biochemistry*, 2001, **40**, 15024–15030.
- 330 C. L. Ladner, J. Yang, R. J. Turner and R. A. Edwards, *Anal. Biochem.*, 2004, **326**, 13–20.
- 331 S. Stratton, N. B. Shelke, K. Hoshino, S. Rudraiah and S. G. Kumbar, *Bioact. Mater.*, 2016, **1**, 93–108.
- 332 R. Langer and J. P. Vacanti, *Science*, 1993, **260**, 920–926.
- 333 A. Heidary Rouchi and M. Mahdavi-Mazdeh, *Int. J. Organ Transplant. Med.*, 2015, **6**, 93–98.
- 334 P. Arpornmaeklong, S. E. Brown, Z. Wang and P. H. Krebsbach, *Stem Cells Dev.*, 2009, **18**, 955–968.
- 335 G. Keller, *Genes Dev.*, 2005, **19**, 1129–1155.
- 336 M. J. Dalby, N. Gadegaard, R. Tare, A. Andar, M. O. Riehle, P. Herzyk, C. D. W. Wilkinson and R. O. C. Oreffo, *Nat. Mater.*, 2007, **6**, 997–1003.
- 337 M. J. Dalby, N. Gadegaard and R. O. C. Oreffo, *Nat. Mater.*, 2014, **13**, 558–569.
- 338 N. S. Hwang, S. Varghese and J. Elisseeff, *Adv. Drug Deliv. Rev.*, 2008, **60**, 199–214.
- 339 R. R. Nadig, *J. Conserv. Dent.*, 2009, **12**, 131–138.
- 340 F. J. O'Brien, *Mater. Today*, 2011, **14**, 88–95.

- 341 M. A. Kinney and T. C. McDevitt, *Trends Biotechnol.*, 2013, **31**, 78–84.
- 342 T. E. Brown and K. S. Anseth, *Chem. Soc. Rev.*, 2017, **46**, 6532–6552.
- 343 I. M. El-Sherbiny and M. H. Yacoub, *Glob. Cardiol. Sci. Pract.*, 2013, **2013**, 316–342.
- 344 I. Tomatsu, K. Peng and A. Kros, *Adv. Drug Deliv. Rev.*, 2011, **63**, 1257–1266.
- 345 S. A. Fisher, A. E. G. Baker and M. S. Shoichet, *J. Am. Chem. Soc.*, 2017, **139**, 7416–7427.
- 346 S. J. Bryant, J. L. Cuy, K. D. Hauch and B. D. Ratner, *Biomaterials*, 2007, **28**, 2978–2986.
- 347 K. T. Nguyen and J. L. West, *Biomaterials*, 2002, **23**, 4307–4314.
- 348 H. Wang and S. C. Heilshorn, *Adv. Mater.*, 2015, **27**, 3717–3736.
- 349 C. A. Deforest, E. A. Sims and K. S. Anseth, *Chem. Mater.*, 2010, **22**, 4783–4790.
- 350 C. A. DeForest and D. A. Tirrell, *Nat. Mater.*, 2015, **14**, 523–531.
- 351 S. Tang, H. Ma, H.-C. Tu, H.-R. Wang, P.-C. Lin and K. S. Anseth, *Adv. Sci.*, 2018, **5**, 1800638.
- 352 T. E. Brown, J. S. Silver, B. T. Worrell, I. A. Marozas, F. M. Yavitt, K. A. Günay, C. N. Bowman and K. S. Anseth, *J. Am. Chem. Soc.*, 2018, **140**, 11585–11588.
- 353 W. Y. Seow and C. A. E. Hauser, *Mater. Today*, 2014, **17**, 381–388.
- 354 G. A. Silva, C. Czeisler, K. L. Niece, E. Beniash, D. A. Harrington, J. A. Kessler and S. I. Stupp, *Science*, 2004, **303**, 1352–1355.
- 355 V. M. P. Vieira, V. Liljeström, P. Posocco, E. Laurini, S. Pricl, M. A. Kostianen and D. K. Smith, *J. Mater. Chem. B*, 2017, **5**, 341–347.
- 356 V. M. Tysseling-Mattiace, V. Sahni, K. L. Niece, D. Birch, C. Czeisler, M. G. Fehlings, S. I. Stupp and J. A. Kessler, *J. Neurosci.*, 2008, **28**, 3814–3823.
- 357 V. A. Kumar, Q. Liu, N. C. Wickremasinghe, S. Shi, T. T. Cornwright, Y. Deng, A. Azares, A. N. Moore, A. M. Acevedo-Jake, N. R. Agudo, S. Pan, D. G. Woodside, P. Vanderslice, J. T. Willerson, R. A. Dixon and J. D. Hartgerink, *Biomaterials*, 2016, **98**, 113–119.
- 358 R. G. Ellis-Behnke, Y.-X. Liang, S.-W. You, D. K. C. Tay, S. Zhang, K.-F. So and G. E. Schneider, *Proc. Natl. Acad. Sci. U. S. A.*, 2006, **103**, 5054–5059.
- 359 V. Jayawarna, M. Ali, T. A. Jowitt, A. F. Miller, A. Saiani, J. E. Gough and R. V. Ulijn, *Adv. Mater.*, 2006, **18**, 611–614.

- 360 M. Zhou, A. M. Smith, A. K. Das, N. W. Hodson, R. F. Collins, R. V. Ulijn and J. E. Gough, *Biomaterials*, 2009, **30**, 2523–2530.
- 361 Y. Hu, W. Gao, F. Wu, H. Wu, B. He and J. He, *J. Mater. Chem. B*, 2016, **4**, 3504–3508.
- 362 T. Suga, S. Osada, T. Narita, Y. Oishi and H. Kodama, *Mater. Sci. Eng. C*, 2015, **47**, 345–350.
- 363 W. Sun, B. Xue, Y. Li, M. Qin, J. Wu, K. Lu, J. Wu, Y. Cao, Q. Jiang and W. Wang, *Adv. Funct. Mater.*, 2016, **26**, 9044–9052.
- 364 B. Cheng, Y. Yan, J. Qi, L. Deng, Z.-W. Shao, K.-Q. Zhang, B. Li, Z. Sun and X. Li, *ACS Appl. Mater. Interfaces*, 2018, **10**, 12474–12484.
- 365 G.-F. Liu, D. Zhang and C.-L. Feng, *Angew. Chem. Int. Ed.*, 2014, **53**, 7789–7793.
- 366 G.-F. Liu, W. Ji, W.-L. Wang and C.-L. Feng, *ACS Appl. Mater. Interfaces*, 2015, **7**, 301–307.
- 367 H. Komatsu, S. Tsukiji, M. Ikeda and I. Hamachi, *Chem. Asian J.*, 2011, **6**, 2368–2375.
- 368 S. Ziane, S. Schlaubitz, S. Miraux, A. Patwa, C. Lalande, I. Bilem, S. Lepreux, B. Rousseau, J.-F. Le Meins, L. Latxague, Barthélémy and O. Chassande, *Eur. Cells Mater.*, 2012, **23**, 147–160.
- 369 L. Latxague, M. A. Ramin, A. Appavoo, P. Berto, M. Maisani, C. Ehret, O. Chassande and P. Barthélémy, *Angew. Chem. Int. Ed.*, 2015, **54**, 4517–4521.
- 370 M. Guvendiren, H. D. Lu and J. A. Burdick, *Soft Matter*, 2012, **8**, 260–272.
- 371 X. Ding, Y. Wang, E. Ruiz-Hernandez, K. Schenke-Layland, C. J. Walsh, G. P. Duffy, M. Sayegh, M. M. Hossain, A. Paul, E. W. Meijer, S. A. Chamuleau, P. Y. Dankers, G. Fytas and E. W. Meijer, *J. Mater. Chem. B*, 2017, **5**, 887–906.
- 372 N. Zanna, S. Focaroli, A. Merlettini, L. Gentilucci, G. Teti, M. Falconi and C. Tomasini, *ACS Omega*, 2017, **2**, 2374–2381.
- 373 B. Serban, K. Stipe, J. Alverson, E. Johnston, N. Priestley, M. Serban, B. A. Serban, K. T. Stipe, J. B. Alverson, E. R. Johnston, N. D. Priestley and M. A. Serban, *Gels*, 2017, **3**, 19.
- 374 M. Maisani, S. Ziane, C. Ehret, L. Levesque, R. Siadous, J.-F. Le Meins, P. Chevallier, P. Barthélémy, H. De Oliveira, J. Amédée, D. Mantovani and O. Chassande, *J. Tissue Eng. Regen. Med.*, 2018, **12**, e1489–e1500.
- 375 A. Rotaru, G. Pricope, T. N. Plank, L. Clima, E. L. Ursu, M. Pinteala, J. T. Davis and M. Barboiu, *Chem. Commun.*, 2017, **53**, 12668–12671.

- 376 L. E. Buerkle, H. A. von Recum and S. J. Rowan, *Chem. Sci.*, 2012, **3**, 564–572.
- 377 Y. Ogawa, C. Yoshiyama and T. Kitaoka, *Langmuir*, 2012, **28**, 4404–4412.
- 378 J. Liu, Z. Sun, Y. Yuan, X. Tian, X. Liu, G. Duan, Y. Yang, L. Yuan, H.-C. Lin and X. Li, *ACS Appl. Mater. Interfaces*, 2016, **8**, 6917–6924.
- 379 J. Qi, Y. Yan, B. Cheng, L. Deng, Z. Shao, Z. Sun and X. Li, *ACS Appl. Mater. Interfaces*, 2018, **10**, 6180–6189.
- 380 A. J. Steward and D. J. Kelly, *J. Anat.*, 2015, **227**, 717–731.
- 381 Y. Han, T. Bai and W. Liu, *Sci. Rep.*, 2014, **4**, 126–131.
- 382 I. Ullah, R. B. Subbarao and G. J. Rho, *Biosci. Rep.*, 2015, **35**, e00191.
- 383 I. V Kholodenko, A. A. Konieva, R. V Kholodenko and K. N. Yarygin, *J. Regen. Med. Tissue Eng.*, 2013, **2**, 4.
- 384 R. Schäfer, G. Spohn and P. C. Baer, *Transfus. Med. Hemother.*, 2016, **43**, 256–267.
- 385 H. Shyam, S. K. Singh, R. Kant and S. K. Saxena, *Regen. Med.*, 2017, **12**, 111–114.
- 386 R. E. B. Fitzsimmons, M. S. Mazurek, A. Soos and C. A. Simmons, *Stem Cells Int.*, 2018, **2018**, 1–16.
- 387 H. Lv, L. Li, M. Sun, Y. Zhang, L. Chen, Y. Rong and Y. Li, *Stem Cell Res. Ther.*, 2015, **6**, 103.
- 388 R. J. McMurray, M. J. Dalby and P. M. Tsimbouri, *J. Tissue Eng. Regen. Med.*, 2015, **9**, 528–539.
- 389 Y. Wu, Z. Yang, J. B. K. Law, A. Y. He, A. A. Abbas, V. Denslin, T. Kamarul, J. H. P. Hui and E. H. Lee, *Tissue Eng. Part A*, 2017, **23**, 43–54.
- 390 K. Metavarayuth, P. Sitasuwan, X. Zhao, Y. Lin and Q. Wang, *ACS Biomater. Sci. Eng.*, 2016, **2**, 142–151.
- 391 A. M. Loye, E. R. Kinser, S. Bensouda, M. Shayan, R. Davis, R. Wang, Z. Chen, U. D. Schwarz, J. Schroers and T. R. Kyriakides, *Sci. Rep.*, 2018, **8**, 8758.
- 392 F. D’Angelo, R. Tiribuzi, I. Armentano, J. M. Kenny, S. Martino and A. Orlacchio, *J. Funct. Biomater.*, 2011, **2**, 67–87.
- 393 E. K. F. Yim and M. P. Sheetz, *Stem Cell Res. Ther.*, 2012, **3**, 41.

- 394 J. He, Y. Hu, F. Wu, B. He and W. Gao, *J. Bionic Eng.*, 2018, **15**, 682–692.
- 395 S. James, J. Fox, F. Afsari, J. Lee, S. Clough, C. Knight, J. Ashmore, P. Ashton, O. Preham, M. Hoogduijn, R. D. A. R. Ponzoni, Y. Hancock, M. Coles and P. Genever, *Stem Cell Rep.*, 2015, **4**, 1004–1015.
- 396 A. L. Barnes, P. G. Genever, S. Rimmer and M. C. Coles, *Biomacromolecules*, 2016, **17**, 723–734.
- 397 I. Han, B.-S. Kwin, H.-K. Park and K. S. Kim, *Int. Neurorol. J.*, 2017, **21**, S24–S31.
- 398 N. Boehnke, C. Cam, E. Bat, T. Segura and H. D. Maynard, *Biomacromolecules*, 2015, **16**, 2101–2108.
- 399 G. D. Prestwich, D. M. Marecak, J. F. Marecek, K. P. Vercruysse and M. R. Ziebell, *J. Control. Release*, 1998, **53**, 93–103.
- 400 J. Lee, A. A. Abdeen, D. Zhang and K. A. Kilian, *Biomaterials*, 2013, **34**, 8140–8148.
- 401 J. Lee, A. A. Abdeen and K. A. Kilian, *Sci. Rep.*, 2015, **4**, 5188.
- 402 T. Dzimbova, I. Iliev, K. Georgiev, R. Detcheva, A. Balacheva and T. Pajpanova, *Biotechnol. Biotechnol. Equip.*, 2012, **26**, 180–184.
- 403 P. Sur, S. P. Chatterjee, P. Roy and B. Sur, *Cancer Lett.*, 1995, **94**, 27–32.
- 404 K. Noguchi, T. F. S. Ali, J. Miyoshi, K. Orito, T. Negoto, T. Biswas, N. Taira, R. Koga, Y. Okamoto, M. Fujita, M. Otsuka and M. Morioka, *Eur. J. Med. Chem.*, 2019, **163**, 207–214.
- 405 Y. Fu, Y. Zhag, S. Zhou, Y. Liu, J. Wang, Y. Wang, C. Lu and C. Li, *Int. J. Pharmacol.*, 2013, **9**, 416–429.
- 406 T. Li, C. Zhou and M. Jiang, *Polym. Bull.*, 1991, **25**, 211–216.
- 407 Y.-H. Tsou, J. Khoneisser, P.-C. Huang and X. Xu, *Bioact. Mater.*, 2016, **1**, 39–55.
- 408 N. E. Fedorovich, M. H. Oudshoorn, D. van Geemen, W. E. Hennink, J. Alblas and W. J. A. Dhert, *Biomaterials*, 2009, **30**, 344–353.
- 409 P. Li, Z. Yin, X.-Q. Dou, G. Zhou and C.-L. Feng, *ACS Appl. Mater. Interfaces*, 2014, **6**, 7948–7952.
- 410 Y. Wang, Y. Shao, X. Ma, B. Zhou, A. Faulkner-Jones, W. Shu and D. Liu, *ACS Appl. Mater. Interfaces*, 2017, **9**, 12311–12315.

- 411 P. K. Smith, R. I. Krohn, G. T. Hermanson, A. K. Mallia, F. H. Gartner, M. D. Provenzano, E. K. Fujimoto, N. M. Goeke, B. J. Olson and D. C. Klenk, *Anal. Biochem.*, 1985, **150**, 76–85.
- 412 E. J. Kasdon, S. Rosen, R. B. Cohen and W. Silen, *Am. J. Surg. Pathol.*, 1981, **5**, 381–384.
- 413 K. Guigui and A. Beaudoin, *J. Forensic Identif.*, 2007, **57**, 550–581.
- 414 Y. Wang, R. A. Goulart and L. Pantanowitz, *Diagn. Cytopathol.*, 2011, **39**, 272–273.
- 415 R. D. Lillie and L. L. Ashburn, *Arch. Pathol.*, 1943, **36**, 432–440.
- 416 N. A. Kraus, F. Ehebauer, B. Zapp, B. Rudolphi, B. J. Kraus and D. Kraus, *Adipocyte*, 2016, **5**, 351–358.
- 417 T. Debnath, S. Ghosh, U. S. Potlapuvu, L. Kona, S. R. Kamaraju, S. Sarkar, S. Gaddam and L. K. Chelluri, *PLoS One*, 2015, **10**, e0120803.
- 418 T. Bai, A. Sinclair, F. Sun, P. Jain, H.-C. Hung, P. Zhang, J.-R. Ella-Menye, W. Liu and S. Jiang, *Chem. Sci.*, 2016, **7**, 333–338.
- 419 H. Puchtler, S. N. Meloan and M. S. Terry, *J. Histochem. Cytochem.*, 1969, **17**, 110–124.
- 420 P. Virtanen and K. Isotupa, *Acta Anat.*, 1980, **108**, 202–207.
- 421 E. Castrén, T. Sillat, S. Oja, A. Noro, A. Laitinen, Y. T. Konttinen, P. Lehenkari, M. Hukkanen and M. Korhonen, *Stem Cell Res. Ther.*, 2015, **6**, 167.
- 422 Z.-K. Cui, J. Fan, S. Kim, O. Bezouglaia, A. Fartash, B. Wu, T. Aghaloo and M. K. Lee, *J. Control. Release*, 2015, **217**, 42–52.
- 423 G. Liu, S. Vijayakumar, L. Grumolato, R. Arroyave, H. Qiao, G. Akiri and S. A. Aaronson, *J. Cell Biol.*, 2009, **185**, 67–75.
- 424 T. Gaur, C. J. Lengner, H. Hovhannisyan, R. A. Bhat, P. V. N. Bodine, B. S. Komm, A. Javed, A. J. van Wijnen, J. L. Stein, G. S. Stein and J. B. Lian, *J. Biol. Chem.*, 2005, **280**, 33132–33140.
- 425 J. H. Kim, X. Liu, J. Wang, X. Chen, H. Zhang, S. H. Kim, J. Cui, R. Li, W. Zhang, Y. Kong, J. Zhang, W. Shui, J. Lamplot, M. R. Rogers, C. Zhao, N. Wang, P. Rajan, J. Tomal, J. Statz, N. Wu, H. H. Luu, R. C. Haydon and T.-C. He, *Ther. Adv. Musculoskelet. Dis.*, 2013, **5**, 13–31.
- 426 Y. Wang, X. Zhang, J. Shao, H. Liu, X. Liu and E. Luo, *Sci. Rep.*, 2017, **7**, 3652.
- 427 F. Saleh, A. Carstairs, S. L. Etheridge and P. Genever, *Stem Cells Int.*, 2016, **2016**, 7132529.
- 428 E. Maffioli, C. Schulte, S. Nonnis, F. Grassi Scalvini, C. Piazzoni, C. Lenardi, A. Negri, P. Milani

- and G. Tedeschi, *Front. Cell. Neurosci.*, 2018, **11**, 417.
- 429 M. D. Hoffman and S. W. Benoit, Danielle, *J. Tissue. Eng. Regen. Med.*, 2015, **9**, E13–E26.
- 430 J.-A. Kim, H.-K. Choi, T.-M. Kim, S.-H. Leem and I.-H. Oh, *Stem Cell Res.*, 2015, **14**, 356–368.
- 431 J. R. Farley, S. L. Hall, M. A. Tanner and J. E. Wergedal, *J. Bone Miner. Res.*, 2009, **9**, 497–508.
- 432 Y.-L. Cheng, Y.-W. Chen, K. Wang and M.-Y. Shie, *J. Mater. Chem. B*, 2016, **4**, 6307–6315.
- 433 A. Higuchi, Q.-D. Ling, Y. Chang, S.-T. Hsu and A. Umezawa, *Chem. Rev.*, 2013, **113**, 3297–3328.
- 434 B. D. Boyan, E. M. Lotz and Z. Schwartz, *Tissue Eng. Part A*, 2017, **23**, 1479–1489.
- 435 A. Seidi, M. Ramalingam, I. Elloumi-Hannachi, S. Ostrovidov and A. Khademhosseini, *Acta Biomater.*, 2011, **7**, 1441–1451.
- 436 P. E. Farahani, S. M. Adelmund, J. A. Shadish, C. A. DeForest, S. L. Bane, R. Y. Tsien, Y. Wang and L. Zhu, *J. Mater. Chem. B*, 2017, **5**, 4435–4442.
- 437 A. H. Zisch, M. P. Lutolf, M. Ehrbar, G. P. Raeber, S. C. Rizzi, N. Davies, H. Schmökel, D. Bezuidenhout, V. Djonov, P. Zilla and J. A. Hubbell, *FASEB J.*, 2003, **17**, 2260–2262.
- 438 J. C. Grim, I. A. Marozas and K. S. Anseth, *J. Control. Release*, 2015, **219**, 95–106.
- 439 J. R. Lakowicz, in *Principles of Fluorescence Spectroscopy*, Plenum Press, New York, London, 1983, p. 44–46.